PROCEEDINGS OF THE NASA SYMPOSIUM ON
GLOBAL WIND MEASUREMENTS

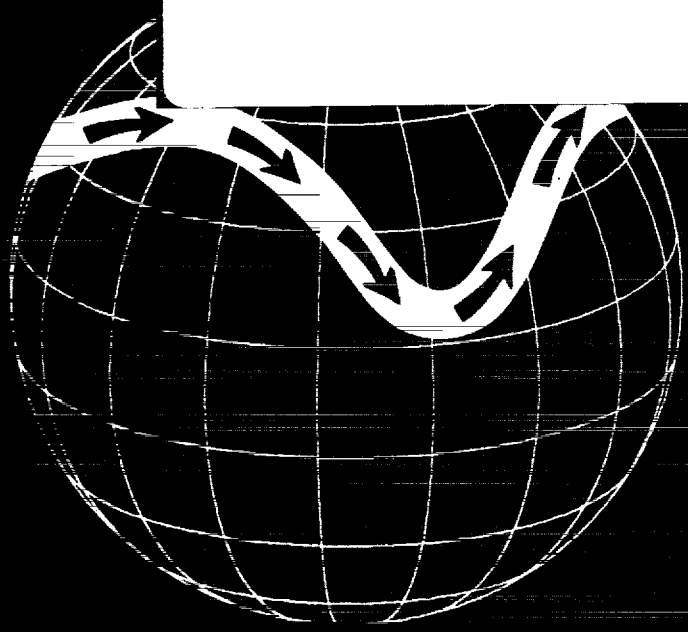

PROCEEDINGS OF A SYMPOSIUM
CONVENED IN COLUMBIA, MARYLAND
JULY 29-AUGUST 1, 1985

PROCEEDINGS OF THE NASA SYMPOSIUM ON
GLOBAL WIND MEASUREMENTS

Edited by

WAYMAN E. BAKER

NASA Goddard Space Flight Center
Greenbelt, MD

and

ROBERT J. CURRAN

NASA Headquarters
Washington, DC

A. DEEPAK PUBLISHING 1985
A Division of Science and Technology Corporation

Hampton, Virginia

PROCEEDINGS OF THE NASA SYMPOSIUM ON

GLOBAL WIND MEASUREMENTS

Proceedings of the Symposium on
GLOBAL WIND MEASUREMENTS
Convened in Columbia, MD
July 29–August 1, 1985

Sponsored by the

NASA Global Scale Atmospheric Processes Research Program
under NASA Langley Research Center Contract No. NAS1-18057

Organized by

Science and Technology Corporation
101 Research Drive, Hampton, VA 23666-1340

CONTENTS

OPERATIONAL WIND SENSING TECHNIQUES

POTENTIAL SPACE-BORNE TECHNIQUES

ATMOSPHERIC AEROSOLS AND RELATED TRACERS

ORGANIZING COMMITTEE

Lt. Col. Charles P. Arnold, Jr.
United States Air Force

Dr. Robert M. Atlas
NASA Goddard Space Flight Center

Dr. Wayman E. Baker
NASA Goddard Space Flight Center

Mr. James Bilbro
NASA Marshall Space Flight Center

Lt. Col. John S. Bohlson
United States Air Force

Dr. Robert J. Curran
NASA Headquarters

Dr. Clifford H. Dey
NOAA National Meteorological Center

Maj. Gary Duke
United States Air Force

Dr. G. David Emmitt
Simpson Weather Associates, Inc.

Dr. George Fichtl
NASA Marshall Space Flight Center

Dr. Dan Fitzjarrald
NASA Marshall Space Flight Center

Dr. Freeman F. Hall
NOAA Wave Propagation Laboratory

Mr. R. Milton Huffaker
Coherent Technologies, Inc.

Dr. Eugenia Kalnay
NASA Goddard Space Flight Center

Dr. James B. Laudenslager
NASA Jet Propulsion Laboratory

Dr. M. Patrick McCormick
NASA Langley Research Center

Dr. S. H. Melfi
NASA Goddard Space Flight Center

Dr. Robert T. Menzies
NASA Jet Propulsion Laboratory

Dr. Joanne Simpson
NASA Goddard Space Flight Center

PRIMARY

PREFACE

This Proceedings contains a collection of the papers which were presented at the Symposium and Workshop on Global Wind Measurements held 29 July–1 August 1985 at the Columbia Inn in Columbia, Maryland. The objectives and agenda for the Symposium and Workshop were decided during a planning meeting of the Organizing Committee (see page ix) held in Washington, DC, on 5 February 1985.

Invited papers were presented at the Symposium by meteorologists and leading experts in wind sensing technology from the United States and Europe on: (1) the meteorological uses and requirements for wind measurements, (2) the latest developments in wind sensing technology, and (3) the status of our understanding of the atmospheric aerosol distribution. A special session was also held on the latest developments in wind sensing technology by the United States Air Force. The Workshop participants were then divided into discussion groups in order to focus on key issues raised during the Symposium presentations (a Report containing the conclusions of the Workshop discussions with recommendations has been published separately). It is hoped that this document will serve as a useful reference for the current research and development activities involving the meteorological uses of wind data and wind sensing technology and will contribute to the enhancement of our current wind observing capability.

The editors would like to acknowledge the excellent support and cooperation of the session chairmen and speakers which were essential to the success of the Symposium and Workshop as well as the many contributors to this Proceedings (see Appendix B). Their efforts are gratefully appreciated. Mr. James Bilbro, NASA Marshall Space Flight Center, Dr. Freeman Hall, NOAA Wave Propagation Laboratory, and Dr. Joanne Simpson, NASA Goddard Space Flight Center, contributed substantially to the organization of the Symposium sessions. Thanks are also due to Dr. John Theon, NASA Headquarters, for his helpful comments during the Workshop discussions. It is a pleasure to acknowledge the outstanding support provided by the Meetings Division staff of Science and Technology Corporation (STC), particularly the assistance of Carolyn Keen and Marilou Phillips with the Symposium and Workshop. The STC Publication Division staff, especially Mary Goodwin and Diana McQuestion, did a superb job in the production of this document.

Wayman E. Baker
Robert J. Curran

THE RELATIVE IMPORTANCE OF MASS AND WIND DATA IN THE FGGE OBSERVING SYSTEM

E. Kalnay, J. C. Jusem* and J. Pfaendtner*

Laboratory for Atmospheres
NASA/Goddard Space Flight Center
Greenbelt, Maryland, USA

1. BACKGROUND

There are two theoretical arguments that have been used to discuss the relative importance of mass and wind data in numerical weather prediction (NWP). We will analyze these arguments in this section as clearly as possible in order to draw conclusions which may help to interpret experimental results on four-dimensional data assimilation, simulations of future observing systems, as well as give guidance on how to improve the efficiency with which we use the present observing system.

The evolution of an NWP model depends, to a very good approximation, only on the initial value of the slow (Rossby) modes of the model. The dynamics of the slow modes are characterized by the conservation of potential vorticity, and by the presence of a balance constraint. For a shallow water model on a β-plane, we can write the potential vorticity as

$$\eta \simeq f_o + \beta y + \nabla^2 \psi - f_o \frac{\phi}{gD} \qquad (1)$$

where f_o is the mean Coriolis parameter, β is the gradient df/dy, ψ is the streamfunction of the rotational wind, and $\phi = gz$, the departure of the geopotential from its mean value gD.

The quasigeostrophic balance constraint is, in its simplest form, the geostrophic relationship

$$\psi_g = \frac{\phi_g}{f_o} \qquad (2)$$

For strongly nonlinear flows, equation (2) has to be replaced by the gradient wind equation or by a form of the nonlinear balance equation, both of which will also provide a relationship between ψ and φ.

Since the evolution of the forecast is determined by equations (1) and (2), it is clear that we have to provide the model with an initial field of a single variable, η or ψ, as accurately as possible.

The first argument that has provided insight on the importance of winds for "small scales" has been the geostrophic adjustment argument (e.g. Rossby, 1938; Blumen, 1972). It provides a very powerful theoretical framework, but we believe its interpretations have not always been completely appropriate (e.g., Washington, 1964; Daley, 1980).

Consider a small mass perturbation field δφ of horizontal wavenumber n introduced in the initial conditions of the model:

$$\delta\phi = Ae^{i(kx + \ell y)}, \quad k^2 + \ell^2 = n^2 = (2\pi/L)^2 \qquad (3)$$

After a short period of geostrophic adjustment, during which fast inertia-gravity waves disperse, the system reaches a new state of balance with the same perturbation potential vorticity:

$$-f_o \frac{\delta\phi}{gD} = \nabla^2 \delta\psi_g - f_o \frac{\delta\phi_g}{gD} \qquad (4)$$

where the wind and the mass are in balance:

$$\delta\psi_g = \frac{\delta\phi_g}{f_o} \qquad (5)$$

Therefore, the balanced geopotential height perturbation is given by

$$\delta\phi_g = \frac{1}{n^2R^2+1}\,\delta\phi \qquad (6)$$

where $R^2 = gD/f_o^2$ is the square of the Rossby radius of deformation.

Equation (6) indicates that for long waves ($n^2R^2 \ll 1$), $\delta\phi_g \simeq \delta\phi$, ie, the model retains the mass data, and, from (5), the wind adapts to the mass field. For short waves ($n^2R^2 \gg 1$), however, $\delta\phi_g \simeq 0$, the model does not retain the mass information, which disperses away as gravity waves. In effect, the model does not believe short wave mass information which is not in a state of balance.

Conversely, for a small wind perturbation δψ in the initial conditions,

$$\delta\psi_g = \frac{n^2R^2}{n^2R^2+1}\,\delta\psi \qquad (7)$$

which indicates that for short waves the model believes in the wind data ($\delta\psi_g \simeq \delta\psi$), and the mass field adapts to the wind. For long waves, $\delta\psi_g \simeq 0$, the model does not retain wind information.

The traditional interpretation (Washington, 1964, Daley, 1980) has been similar to this: "Wind data must be used for short scales (e.g. tropics and small synoptic scales). For large scales mass data may be used". The reason why this interpretation is somewhat misleading, is that it does not exploit the fact that the atmosphere itself is in balance, and therefore the mass and wind data must also be in balance (Eq. (2)).

A more positive interpretation is the following: "In order to maximize the retention of useful information in the model, we should use the balance constraint on the data". Note that if

*M/A-COM Sigma Data Corp.

for example, we apply the geostrophic wind correction on the data ($\delta\psi = \delta\phi/f_o$), we can force the model to retain all of the mass information even at small scales.

There are two comments that should be made. The first one is that, as pointed out by Daley (1980), most of the atmospheric waves can be considered short ($n^2R^2 > 1$). For an equivalent depth D = 10 km, typical of the external mode, waves are "short" if L < 20,000 km, i.e., even for planetary scale waves the model will tend to believe wind data much more than it will believe mass data. For the first baroclinic mode, D ≈ 1 km, waves are short if L < 6000 km, i.e., for most synoptic scale waves. For higher vertical modes, the mass data becomes increasingly important, but, with few exceptions, these modes do not have much energy.

Another comment is that although we can force the model to retain mass information even at small scales by imposing a geostrophic wind relationship on the data, we may only want to do so if we believe the mass data to be accurate at such scales.

This brings us to the subject of relative accuracy of mass and wind data, and to the second argument that emphasizes the importance of wind data at small scales: the differential versus integral measurement argument. From the geostrophic relationship $v = -kx\,\nabla\phi/f_o$, winds are related to the gradient of the mass field, and therefore they should be more accurate at small scales. This is the argument that is implicit in the analysis by Phillips (1983), which we present here in a considerably simplified form.

We start, once again, from the premise that we want to estimate the initial value of the slow modes, or, equivalently, the geostrophic streamfunction. Consider a component of the streamfunction of horizontal wavenumber n: $\psi_n = B\,e^{i(kx + \ell y)}$, $k^2 + \ell^2 = n^2$. Suppose we have both mass (ϕ) and wind (v) measurements, with observational errors $\delta\phi_o, |\delta v_o|$ respectively. From these measurements we obtain two estimates of ψ, $\psi_g^{(mass)} = \phi/f_o$, and $\nabla\psi^{(wind)} = \underset{\sim}{k} \times \underset{\sim}{v}$, with corresponding errors

$$\delta\psi_n^{(mass)} = \delta\phi_o/f_o, \text{ and } \delta\psi_n^{(wind)} = \frac{|\delta v_o|}{n} \qquad (8)$$

Equation (8) provides a simple estimate of the relative accuracy of wind and mass measurements. Winds will be "more accurate" than mass data if

$$\frac{|\delta v_o|}{n} < \frac{g\delta z_o}{f_o} .$$

For example, if we assume $|\delta v_o| \sim 3$ m sec^{-1}, and $\delta z_o \sim 10$ m, winds are more accurate than heights for L < 2000 km. We can combine optimally both estimates of ψ (with weights inversely proportional to the square of the error), and then the accuracy of the weighted average estimate will be the sum of the accuracies of the two measurements (Gandin, 1963, Phillips, 1983):

$$\frac{1}{|\delta\psi|^2} = \frac{f_o^2}{g^2|\delta z_o|^2} + \frac{n^2}{|\delta v_o|^2} \qquad (9)$$

Equation (9) shows that the mass field will contribute very little accuracy at low latitudes, and that winds become increasingly accurate at short wavelengths.

From these theoretical arguments, it is clear that winds are extremely useful data at small scales (or in the tropics) because of two independent reasons: (a) they have higher accuracy, and (b) the model believes them better. However, if we have mass data that we consider reliable even at small scales (e.g. sea level pressure data or satellite temperature gradient data), we should force the model to retain it by imposing a balance constraint in the data itself.

2. FORECAST IMPACT EXPERIMENTS

Simulation experiments (Halem et al., 1985; Atlas et al., 1985) have indicated that 3-dimensional fields of horizontal wind data are more effective than mass data in reducing forecast errors. In this section we address the question: "Which data are more important in the present observing system, winds or heights?"

For this purpose we performed four real data assimilation experiments using the GLA Analysis/Forecast system (Baker, 1983, Kalnay et al., 1983).

In the first experiment, denoted "FGGE", we assimilated all available FGGE II-C data for the period 5 January - 2 February. These data include both rawinsonde and satellite (TIROS-N) temperature and moisture, and cloud-tracked winds data. In the other three experiments we omitted the assimilation of temperature and moisture ("NOTEMP"), of winds ("NOWIND"), and of cloud-track winds ("NOCTW"). We then performed seven 5-day forecasts from the different analyses every four days, and verified the forecasts against the ECMWF analysis.

Figures 1 and 2 present the extratropical (poleward of 20°) anomaly correlation averaged for the seven forecasts in the Southern and Northern Hemispheres respectively. It is clear from Fig. 1 that in the Southern Hemisphere, temperature data (mostly from satellite temperature soundings) are of essential importance. The forecasts which without temperatures are skillful for less than one day (correlation > 60%), become skillful for more than 3 days when the temperature data are utilized. Winds are useful in that they increase skill by about 9 hours, and cloud-track winds alone by less than six hours.

In the Northern Hemisphere (Fig. 2) there is much more redundancy in the data, but it is clear that the 3-dimensional wind fields provided by rawinsondes are the most important component of the observing system. Their absence results in a degradation of about 6 hours. The absence of temperature has a smaller effect, and cloud-track winds have actually a small negative impact. If we look at the North American region separately (Fig. 3), the impacts are larger, with a small positive impact of cloud-track winds, and larger impact of temperatures and especially winds.

In the tropics, Fig. 4, the winds are useful throughout the 5-day forecast, and the temperatures have a positive impact on the first two days, although the skill, measured by the S1 score of the geopotential height, is small throughout the period.

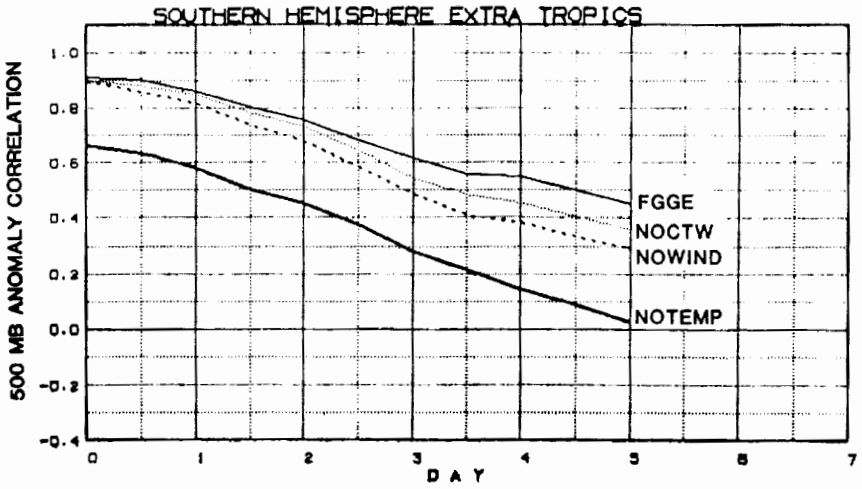

Figure 1. Average of anomaly correlation as a function of forecast day for seven forecasts each from the "FGGE", "NOTEMP", "NOWIND" and "NOCTW" assimilation experiments. Verifications are made against the ECMWF analysis and the region of verification is the extratropical Southern Hemisphere (polewards of 20°).

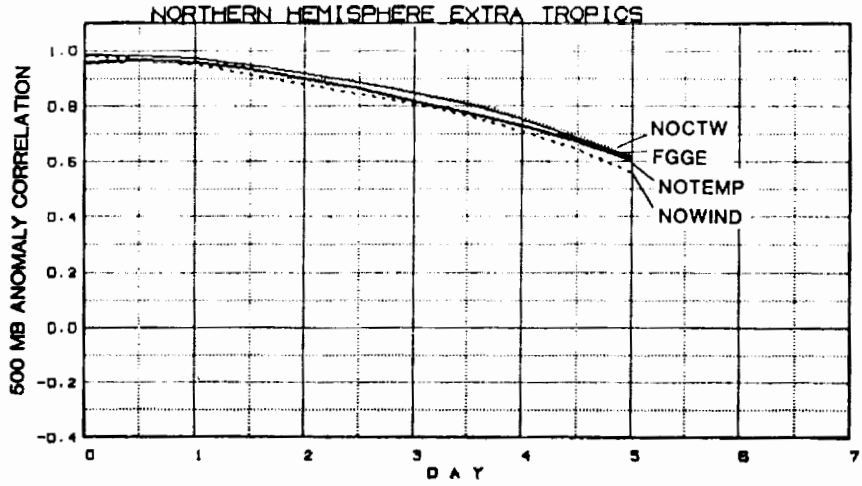

Figure 2. Same as Fig. 1 but for the Northern Hemisphere.

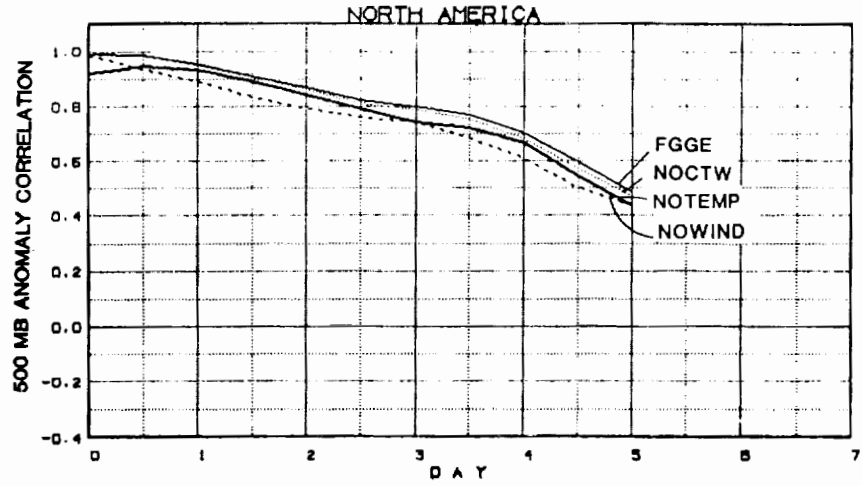

Figure 3. Same as Fig. 1 but for North America.

3. DISCUSSION

We have reviewed, in a very simple fashion, two independent arguments that emphasize the importance of wind observations for small scales and in the tropics: the geostrophic adjustment argument, and the differential measurement argument. They indicate that winds are very effective at small scales and in the tropics because (a) the model "believes" the wind data better than the mass data and (b) winds observations are more accurate than mass observations. As pointed out by Daley (1980), in the geostrophic adjustment argument, "small scale" includes most of the energy-containing modes of the atmosphere. This is especially true for the barotropic model, which explains why sea level pressure data were found to be quite ineffective in specifying the initial state (Smagorinsky et al., 1970). On the other hand, simulation studies of Halem et al. (1985) and Atlas et al. (1985) show that wind data are extremely effective.

Although these observations are explained by the traditional application of geostrophic adjustment theory to initialization (e.g. Washington, 1964, Daley, 1980), this theory also indicates that we can make much more effective use of mass data by imposing the geostrophic balance constraint on the data. If we have mass observations that are considered reliable we should force the model to retain them by forcing the wind to be in balance with the mass data. One effective way to do this is by the "geostrophic correction" of the wind, currently used at least in a partial form in many operational systems (Puri, 1981, Kistler and McPherson, 1975). However, if not performed carefully, this correction can easily result in an actual deterioration of the model's initial conditions. The use of mass data of heterogeneous origin (e.g. rawinsonde and satellite temperatures), which have different biases and are not even coincident in time, and the fact that the accuracy of geostrophic winds becomes poorer at small scales, can result in synthetic wind data which is not only inaccurate, but which is completely retained by the model. The use of multivariate optimal interpolation may be less desirable in data sparce regions, because the balance is introduced in a statistical fashion, assuming a "typical" correlation distance between mass and wind field rather than the observed wavelengths. The use of initialization methods, such as non-linear normal mode initialization, has no effect on the amount of information extracted, because their role is to filter out the information that the model would not retain anyway.

The second argument, that winds are more accurate at small scales because they are a measurement of the mass field gradient, (Phillips, 1983), provides a quantitative relationship with which both types of measurements can be optimally weighted.

It is possible that the application of these simple ideas, for example in the use of synthetic "satellite thermal wind" data together with appropriate filtering of the small scale noise in the temperature gradients (eq. 8) may be useful in increasing the amount of useful information extracted from the present observing system. A striking example of the potential improvement that the use of "satellite thermal winds" might produce, is presented in Fig. 5. We adapted a simulation system of an idealized data assimilation (Halem et al., 1985), where perfect data derived from a "nature" run are directly inserted into the GLA GCM. The figure presents the 12-hour 500 mb rms forecast error during the simulated assimilation cycle. The top two curves, adapted from Halem et al. (1985), show that perfect wind data is much more effective than mass data (surface pressure and complete temperature fields) in reducing the 12-hour forecast error. On the other hand, when we use mass data both directly and through the assimilation of geostrophic winds, the reduction of error is faster than with either mass or wind data alone.

Real data experiments with the current GLA Analysis/Forecast System show that in the present observing system, temperature data (mostly from polar orbiter satellites) is absolutely essential in the Southern Hemisphere. It is in this hemisphere that the use of satellite thermal winds has the largest potential for producing a significant improvement upon the current forecast skill. In the Northern Hemisphere, rawinsonde winds are already somewhat more important than temperatures. However, realistic simulation experiments (Atlas et al., 1985), indicate that lidar wind profile observations with a better geographical coverage will result in improved numerical weather prediction even in this hemisphere.

REFERENCES

Atlas, R., E. Kalnay, W. E. Baker, J. Susskind, D. Reuter, and M. Halem, 1985: Simulation studies of the impact of future observing systems on weather prediction. Proceedings of the 7th Conference on NWP, AMS, Montreal, June, 1985.

Baker, W. E., 1983: Objective analysis and assimilation of observational data from FGGE. Mon. Wea. Rev., 111, 328-342.

Blumen, W., 1972: Geostrophic adjustment. Rev. Geophys. Space Phys., 10, 485-528.

Daley, R., 1980: On the optimal specification of the initial state for deterministic forecasting. Mon. Wea. Rev., 108, 1719-1755.

Gandin, L., 1963: Objective analysis of meteorological fields. Translated from Russian by the Israeli Program for Scientific Translations, 1965. 242 pp.

Halem, M., J. Susskind and R. Atlas, 1985: Future observing systems simulation studies. Proceedings of the First National Workshop on FGGE results, T. O'Neill, editor, NAS, Woodshole, July 1984.

Kalnay, E., R. Balgovind, W. Chao, D. Edelmann, J. Pfaendtner, L. Takacs and K. Takano, 1983: Documentation of the GLAS Fourth Order GCM. NASA TM 86064.

Kistler, R. E. and R. McPherson, 1975: On the use of a local wind convection technique in four-dimensional assimilation. Mon. Wea. Rev., 103, 445-559.

Phillips, N. A., 1983: An accuracy goal for a comprehensive satellite wind measuring system. Mon. Wea. Rev., 111, 237-239.

Puri, K., 1981: Local geostrophic wind correction in the assimilation of height data and its relationship to the slow manifold. Mon. Wea. Rev., 109, 52-55.

Rossby, C. G., 1938: On the mutual adjustment of pressure and velocity distribution in certain simple current systems. J. of Marine Research, 1, 239-263.

Smagorinsky, J., K. Miyakoda and R. Strickler, 1970: The relative importance of variables in initial conditions for dynamical weather prediction. Tellus, 22, 141-154.

Washington, W. M., 1964: A note on the adjustment towards geostrophic equilibrium in a simple fluid system. Tellus, 16, 530-534.

ACKNOWLEDGEMENTS

Dr. M. Halem has kindly allowed us to reproduce some of his simulation experiments, performed by R. Dlouhy, L. Takacs and M. Almeida. We had useful discussions with F. Semazzi, W. Baker, A. Dalcher and S. Bloom. The text was typed by M. A. Wells and the figures prepared by L. Rumburg.

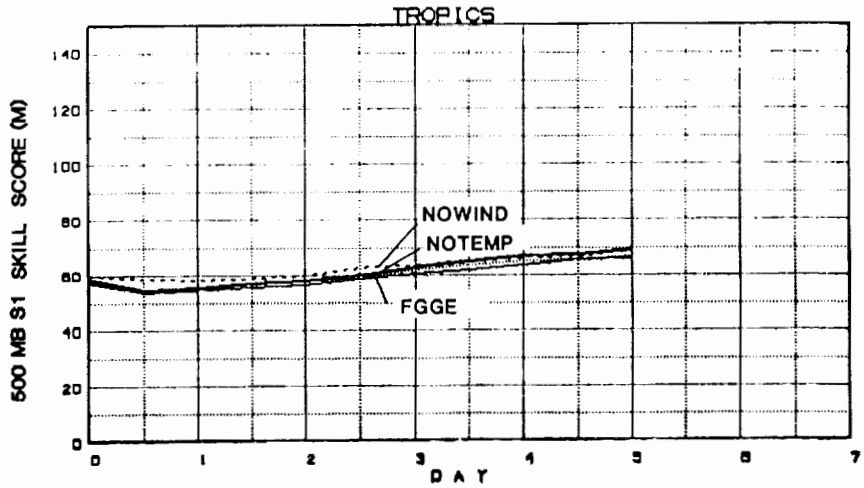

Figure 4. Same as Fig. 1 but for the tropics (30°S to 30°N). The skill score S1 measures the relative error in the pressure gradient forecast at 500 mb.

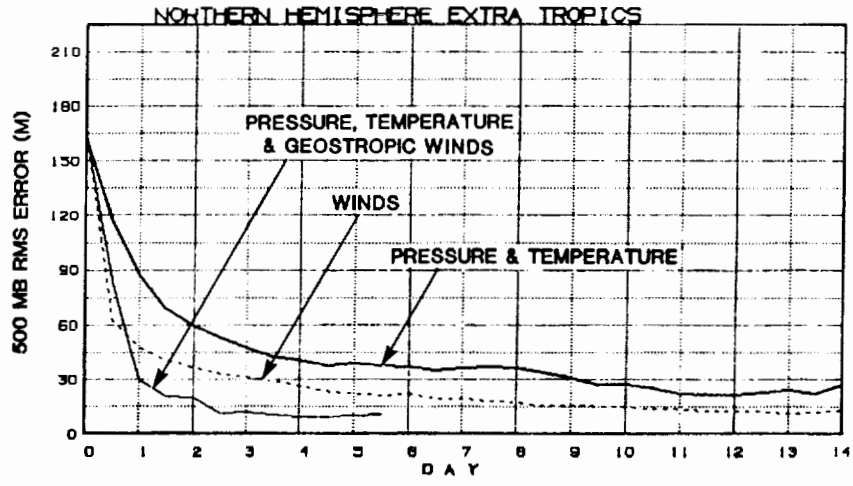

Figure 5. Idealized 12-hour cycle assimilation experiment using as data exact 3-D fields of a) surface pressure and temperature, b) u and v wind components, and c) surface pressure, temperature and geostrophic winds. Experiments a) and b) adapted from Halem et al. (1985).

THE IMPACT OF TROPICAL WIND DATA ON THE ANALYSIS AND FORECASTS OF THE GLA GCM FOR THE GLOBAL WEATHER EXPERIMENT

Jan Paegle

Department of Meteorology, University of Utah, Salt Lake City, UT, USA

W. E. Baker

GLA/NASA, Goddard Space Flight Center, Greenbelt, Maryland, USA

1. BACKGROUND

It is well-known that divergent wind estimates are much more dependent upon the analysis system than are estimates of the rotational wind. This conclusion is supported in recent analyses of FGGE SOP1 data produced by the Goddard Laboratory for Atmospheres (GLA), the Geophysical Fluid Dynamics Laboratory (GFDL) and the European Center for Medium Range Weather Forecasting (ECMWF, see Fig. 1.) These analyses differ in the forecast models that are used for the four-dimensional assimilation, in the data rejection criteria, and, to a certain extent, in the data density.

Because the final divergent wind is a product of both model constraints and observation, it is relevant to inquire how much of each goes into the final product. We presently investigate this question through a systematic analysis of tropical data that are sampled at different densities by the GLA GCM.

Four experiments using differing amounts of tropical wind data were run on each of three different analysis times. In the first experiment, all available tropical wind data were used. In the second experiment, all the tropical wind data were suppressed between 20°S and 20°N, whereas in the third experiment, the tropical wind data with a westerly wind component were retained and tropical easterly wind data were suppressed within these latitudes. Analogously, in the final experiment, tropical wind data were retained in regions of easterlies and suppressed in regions of westerlies. The first two experiments are identical to those described by Paegle et al. (1983).

One motivation for the design of Experiments 3 and 4 is that convectively active regions of the deep tropics tend to be co-located with upper tropospheric easterly winds, and the less active regions of the deep tropics tend to display westerly winds (Paegle et al., 1984.) Thus, Experiment 4 should resolve more of the convectively heated regions, whereas Experiment 3 should resolve more of the tropically inactive regions of the upper troposphere.

The model utilized in this study is the global fourth order GLAS general circulation model described in detail by Kalnay-Rivas et al., (1977), Kalnay-Rivas and Hoitsma (1979) and, more recently, by Kalnay et al., (1983.) The analysis cycle for all of the experiments began on 0000 GMT, 29 January 1979 and provided initial data for forecasts from 0000 GMT on 4, 5, 6 February 1979. Further details on the data assimilation procedure are given by Baker (1983) and Baker and Paegle (1983).

2. INFLUENCE OF THE TROPICAL WIND DATA

We have selected 200-mb for the analysis comparisons because this level is close to the level that tropical wind data are assigned from cirrus motion vectors, and also because this is near the level of maximum outflow from deep convection. Consequently, the signal/noise ratio for the analyses using tropical wind data should be especially favorable around 200 mb.

2.1 Rotational and Divergent Wind

All results for the rotational and divergent wind are taken from the analysis time 0000 GMT, 6 February 1979, since the results are rather similar at other times.

Figure 2a presents the 200-mb long-wave rotational wind field for Experiment 1 (with all tropical wind field data); Figure 2b presents the difference of this analysis from the analysis without tropical wind data (Experiment 2-1); Figure 2c presents the equivalent difference for the case with only tropical westerlies (Experiment 3-1); and Figure 2d presents the difference for the case with only tropical easterlies (Experiment 4-1). The scale in the difference fields is amplified by a factor of 3.3 with respect to the scale for Experiment 1.

Strong jets (with speeds on the order of 60 m/s) are apparent in Figure 2a near the east coasts of Asia and North America. The Southern Hemisphere flow is somewhat weaker and in the deep tropics the winds are generally less than 20 m/s. Figure 2b indicates that, in the absence of tropical winds, the assimilation model tends to generate westerly rotational flow in the tropics with peak error values on the order of 20 m/s (assuming that Experiment 1 reflects an accurate analysis.) These errors are on the order of the peak tropical wind in the analysis invoking all available tropical wind data. We conclude that Experiment 1 (retaining all data) produces results that are significantly different from an analysis depending entirely on extratropical data and the interpolating

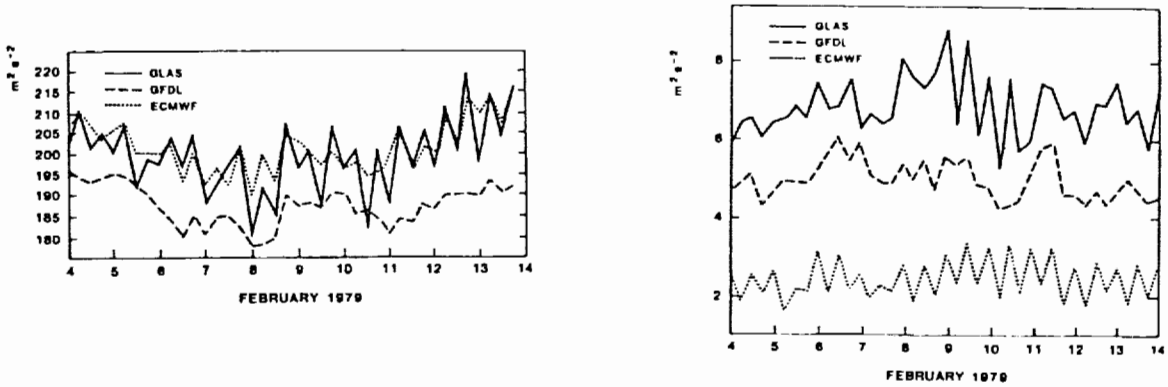

Figure 1: Global average of 200-mb kinetic energy of the rotational wind (left) and divergent wind (right) for the period 4-13 Feb. 1979.

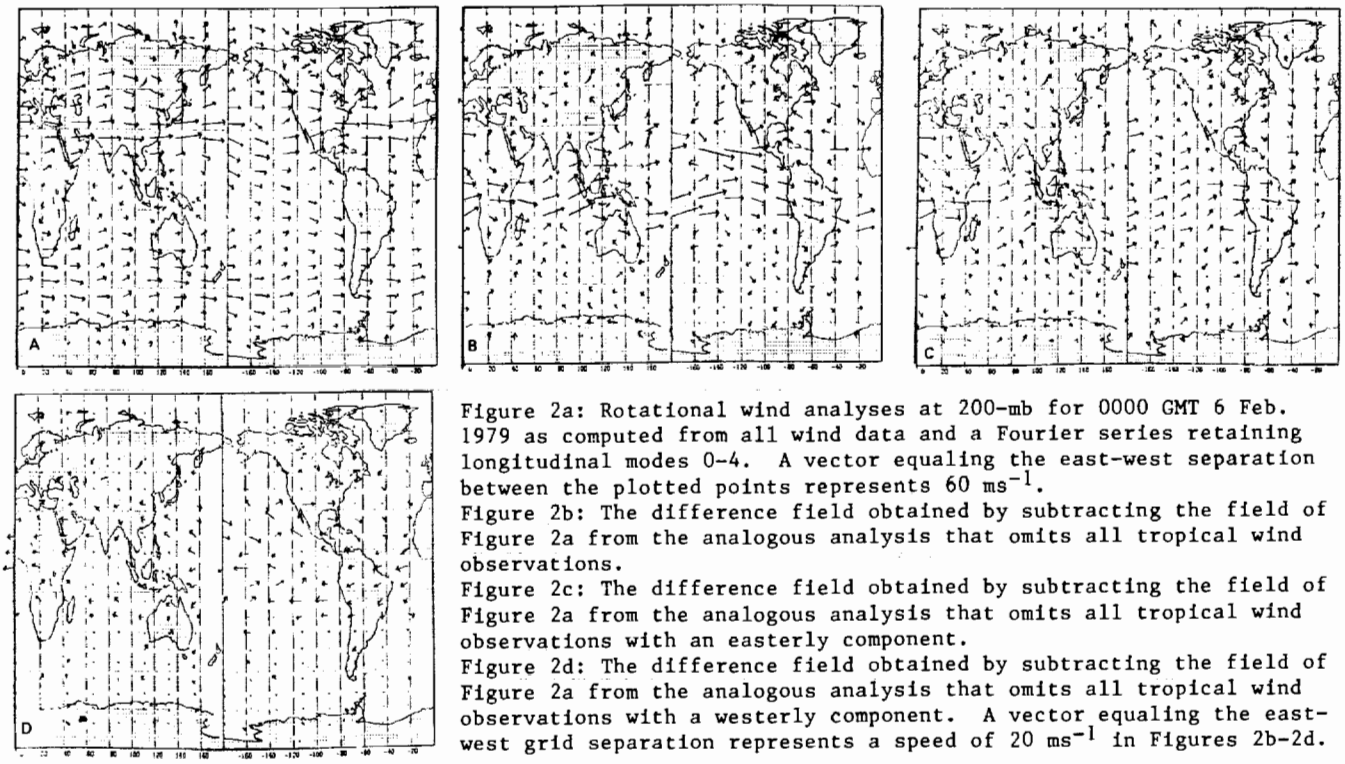

Figure 2a: Rotational wind analyses at 200-mb for 0000 GMT 6 Feb. 1979 as computed from all wind data and a Fourier series retaining longitudinal modes 0-4. A vector equaling the east-west separation between the plotted points represents 60 ms^{-1}.

Figure 2b: The difference field obtained by subtracting the field of Figure 2a from the analogous analysis that omits all tropical wind observations.

Figure 2c: The difference field obtained by subtracting the field of Figure 2a from the analogous analysis that omits all tropical wind observations with an easterly component.

Figure 2d: The difference field obtained by subtracting the field of Figure 2a from the analogous analysis that omits all tropical wind observations with a westerly component. A vector equaling the east-west grid separation represents a speed of 20 ms^{-1} in Figures 2b-2d.

model. Figures 2c and 2d suggest that neither easterly wind data nor westerly wind data alone are sufficient to produce a good tropical analysis, with the westerly case (Fig. 2c) having somewhat larger local errors.

Figures 3a, 3b, 3c, 3d present 200-mb divergent wind of the long waves for Experiments 1, 2,3,4, respectively, whereas Figures 3e, 3f, 3g show the differences between Experiments 2 and 1, 3 and 1, and 4 and 1, respectively. All analyses display peak divergent winds on the order of 10 m/s from the strong outflow regions above the western tropical Pacific Ocean and Indian Ocean. Somewhat weaker divergent winds emanate from the Amazon Basin of South America. The difference fields (Figs. 3e,3f, 3g) display maxima that are a significant fraction of the individual analyses, but it is interesting to note that all analyses seem to capture the same outflow centers of the deep tropics. This is true even for the case lacking all tropical wind data (Experiment 2, Fig. 3b) which appears to produce the strongest outflow. Thus, while tropical wind data modify the details of the tropical divergent wind rather strongly, they do not seem to be essential for the longitudinal placement of the major divergence centers in this case. However, at least in this case, tropical wind data are essential in maintaining the maximum tropical outflow centers in the Southern Hemisphere.

In all three cases presently studied, as well as the 15 January 1979 case of Baker and Paegle (1983), assimilating the tropical wind data slightly weakens the tropical divergence in the analysis. The Burger (1958) scaling appears to be valid within the tropics for all of the present analyses because the ratio of the divergent to the rotational wind magnitude is on the order of 1-2.

2.2 Rotational and Divergent Kinetic Energy

Plots of the 200-mb rotational and diver-

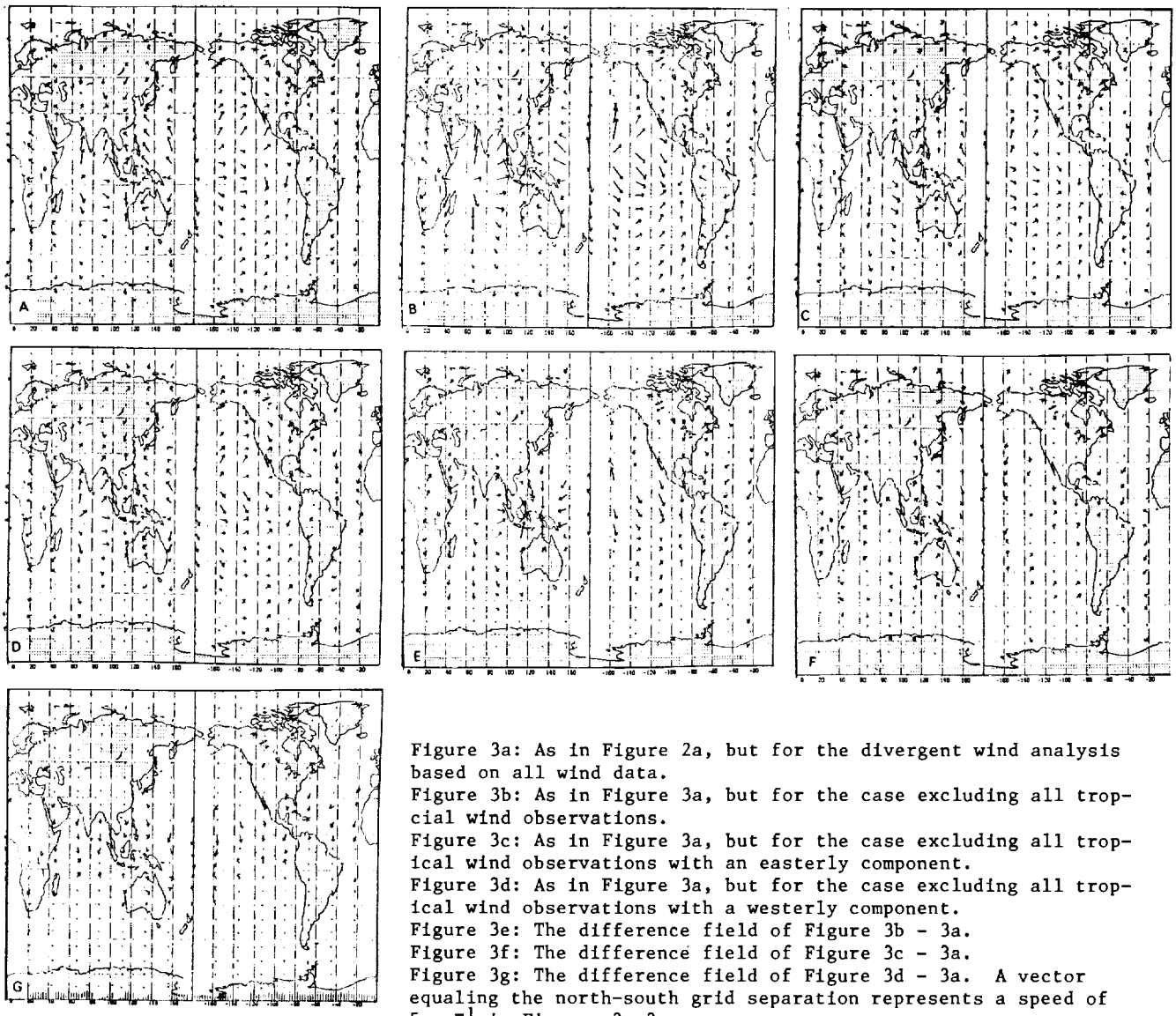

Figure 3a: As in Figure 2a, but for the divergent wind analysis based on all wind data.
Figure 3b: As in Figure 3a, but for the case excluding all tropcial wind observations.
Figure 3c: As in Figure 3a, but for the case excluding all tropical wind observations with an easterly component.
Figure 3d: As in Figure 3a, but for the case excluding all tropical wind observations with a westerly component.
Figure 3e: The difference field of Figure 3b - 3a.
Figure 3f: The difference field of Figure 3c - 3a.
Figure 3g: The difference field of Figure 3d - 3a. A vector equaling the north-south grid separation represents a speed of 5 ms^{-1} in Figures 3e-3g.

gent kinetic energies of the long waves are displayed in Figure 4. Experiment 2 (without tropical winds) possesses about 10% more rotational kinetic energy than does Experiment 1 (with all tropical winds), and the former has about twice as much divergent kinetic energy as the latter. The case with easterly data only exhibits a level of kinetic energy more similar to the case with all the data utilized than does the case of westerly data only. These differences are similar to those found between different analyses that use similar observations (Fig. 1).

3. FORECAST EXPERIMENTS

The present section describes the impact of the tropical wind data upon the 72 h forecast of the upper troposphere. We select 200-mb for the same reasons as in Section 2. All results of the present section are based upon stream-function and velocity potential representations in terms of Fourier modes 0-4 in longitude with full latitude resolution.

Unless otherwise specified, the results

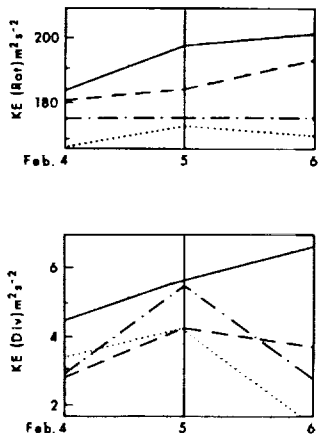

Figure 4: The global average of the 200-mb rotational (top) and divergent (bottom) flow kinetic energy obtained from a flow representation retaining longitudinal Fourier modes 0-4. Experiments 1, 2, 3, 4, are shown as the dashed-dotted, solid, dashed, and dotted curves, respectively.

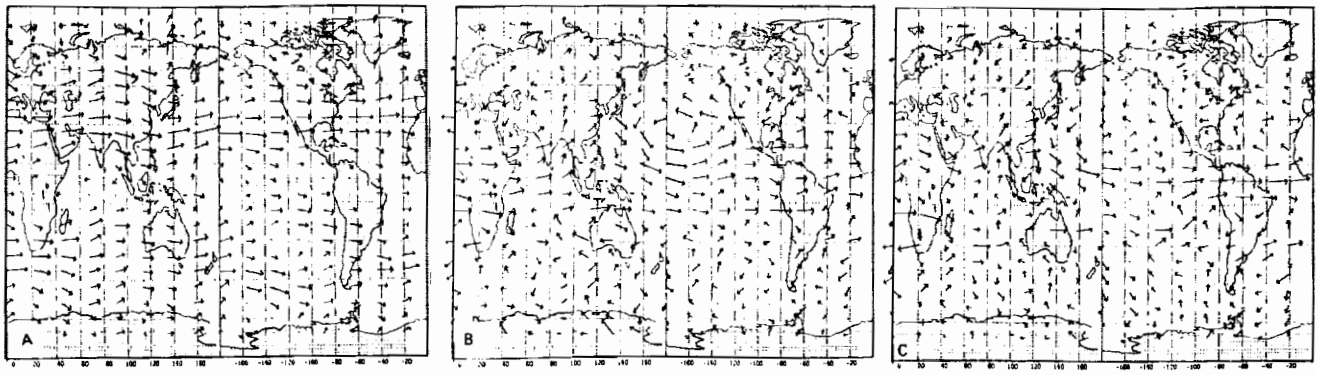

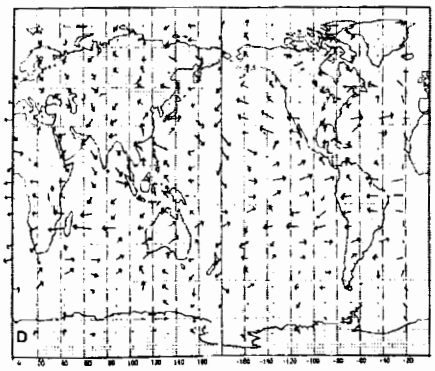

Figure 5a: 72 h rotational wind forecast at 200-mb made from initial time 0000 GMT, 6 Feb. 1979, using all available initial wind data. The figure displays a Fourier series representation retaining the zonal mean and longitudinal modes 1-4. A vector equaling the east-west grid separation represents 60 ms^{-1}.
Figure 5b: The difference field obtained by subtracting the field of Figure 5a from the analogous forecast based on an initial data set that omits all tropical wind observations.
Figure 5c: The difference field obtained by subtracting the field of Figure 5a from the analogous forecast based on an initial data set that omits all tropical wind data with an easterly component.
Figure 5d: The difference field obtained by subtracting the field of Figure 5a from the analogous forecast based on an initial data set that omits all tropical wind data with a westerly component. A vector equaling the east-west grid separation represents 20 ms^{-1} in Figures 5b, 5c, 5d.

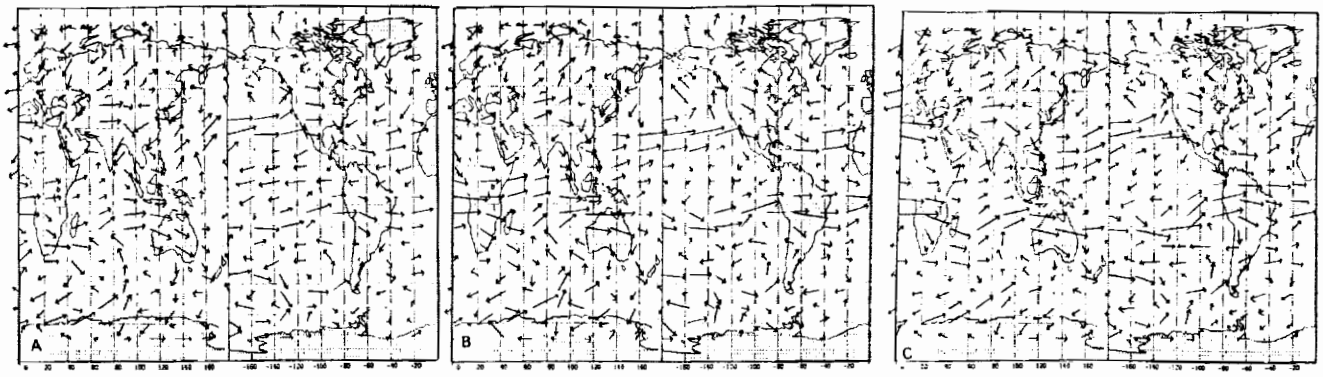

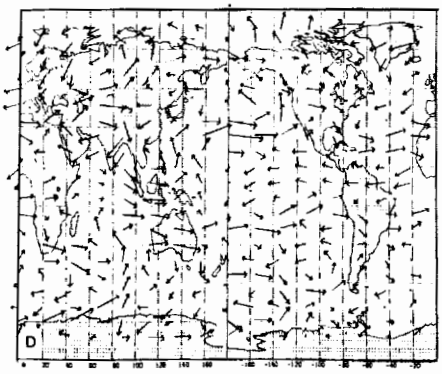

Figure 6a: 72 h rotational wind forecast error at 200-mb for a forecast made from initial time 0000 GMT, 6 Feb. 1979, using all available initial wind data. The figure displays a Fourier series representation retaining the zonal mean and longitudinal modes 1-4.
Figure 6b: As in Figure 6a, but for a forecast made from an initial analysis lacking all tropical wind observations.
Figure 6c: As in Figure 6a, but for a forecast made from an initial analysis lacking all tropical wind observations with an easterly component.
Figure 6d: As in Figure 6a, but for a forecast made from initial analyses lacking tropical wind observations with a westerly component. A vector equaling the east-west grid separation represents 20 ms^{-1} in these diagrams.

for the rotational and divergent wind decompositions are taken from verification time 0000 GMT on 9 February 1979, for the 72 h forecast initialized on 0000 GMT on 6 February 1979.

Figure 5a presents the 200-mb rotational wind field forecast for Experiment 1 (with all tropical wind data); Figure 5b presents the difference of this forecast from the forecast made without tropical wind data (Experiment 2-1); Figure 5c presents the difference of the 200-mb forecast retaining only tropical westerlies from Experiment 1 (Experiment 3-1); Figure 5d presents the difference of the 72 h 200-mb forecast retaining only tropical easterlies from Fxperiment 1 (Experiment 4-1). In comparing these figures with the initial analysis differences of Figures 1b, 1c, 1d it is clear that the 72 h differences have spread substantially into higher latitudes during the forecast. This condition is also true for the 72 h forecasts initialized on 4 and 5 February.

It is also clear that the 72 h extratropical spread of forecast difference that arises from the use of easterly winds alone (Fig. 5d) is similar to the 72 h spread of forecast differences that arises from the use of westerly winds alone (Fig. 5c.) In higher latitudes of the Northern Hemisphere, the former show somewhat greater differences than the latter, even though the corresponding initial difference fields in the tropics (Figs. 1c and 1d) are somewhat greater in the westerly case. Thus, critical latitude trapping of Rossby waves is not a dominant mechanism with respect to the evolution of the present forecast fields. The influence of tropical data within local easterlies does not appear to be more effectively restricted to the tropical sector than is the influence of tropical wind data within local westerlies.

Figures 6a, 6b, 6c, 6d display the forecast 200 mb long wave rotational wind errors of Experiments 1, 2, 3, 4, respectively. The similarity of these errors in high latitudes indicates that the forecasts in these regions are more similar to each other than to the atmosphere. The relatively large differences among the tropical forecast errors indicates that the tropical wind data has a greater impact in tropical prediction than in extra-tropical prediction. Regions where the forecast errors in Fig. 6a exceed the sensitivity to the tropical wind data in Fig. 5a denote areas where the tropical wind data

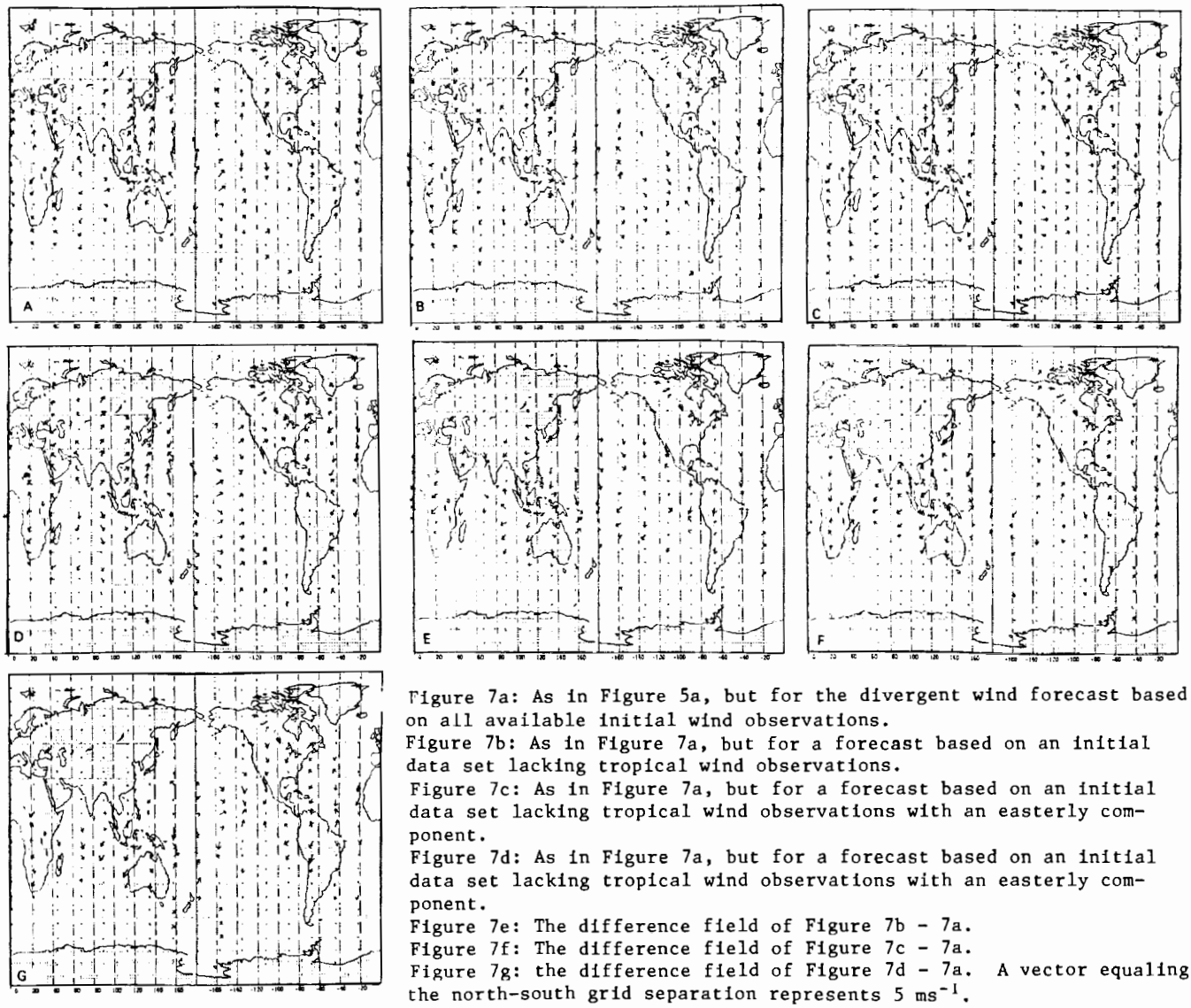

Figure 7a: As in Figure 5a, but for the divergent wind forecast based on all available initial wind observations.
Figure 7b: As in Figure 7a, but for a forecast based on an initial data set lacking tropical wind observations.
Figure 7c: As in Figure 7a, but for a forecast based on an initial data set lacking tropical wind observations with an easterly component.
Figure 7d: As in Figure 7a, but for a forecast based on an initial data set lacking tropical wind observations with an easterly component.
Figure 7e: The difference field of Figure 7b - 7a.
Figure 7f: The difference field of Figure 7c - 7a.
Figure 7g: the difference field of Figure 7d - 7a. A vector equaling the north-south grid separation represents 5 ms^{-1}.

is of less importance than other data or model errors. In the present case this appears to be true poleward of approximately 40°latitude.

Figures 7a, 7b, 7c, 7d present the 72 h forecast 200-mb divergent wind of the long waves for Experiments 1, 2, 3, 4, respectively, whereas Figures 7e, 7f, 7g present the differences between Experiments 2 and 1, 3 and 1, and 4 and 1, respectively. In comparison with Figure 2, it is clear that all forecasts lose divergent flow amplitude with respect to the initial state, and that this change is larger than the difference between individual divergent wind predictions. As in Baker and Paegle (1983), the effect of the divergent wind differences is confined to the tropics.

Figures 8a, 8b, 8c, 8d present the forecast 200 mb long wave divergent wind errors of Experiments 1, 2, 3, 4, respectively. As opposed to the divergent wind differences in Figs. 7e, 7f, 7g, the forecast divergent wind errors are not confined only to tropical latitudes, but are quite prominent in the extratropics as well. The long wave divergent wind errors possess peak magnitudes of approximately 10 m/s, and are nearly isotropic with respect to direction, unlike the rotational wind errors which are dominated by the zonal flow component.

The meridional component of the divergent wind error has magnitude similar to the meridional component of the rotational wind error (see Fig. 6), whereas the zonal component of the divergent flow error is about half as large as the zonal component of the rotational flow error. Thus, the contribution of the divergent flow to the long wave error is not much less than that of the rotational long wave error.

4. GEOPOTENTIAL FIELD CALCULATIONS USING WIND DATA

The geopotential height of pressure surfaces can be computed either from temperature data using the hydrostatic equation or from wind data using a differentiated version of the equations of motion (i.e., the divergence equation.) Within the tropics, where the temperature variations are commonly obscured by the radiosonce uncertainty which is on the order of 1/2°C, it may be more practical to use wind data and the divergence equation to compute the geopotential field. Paegle et al. (1983) explore this approach and find that it is systematically superior to using temperature data and the hydrostatic equation in application to GATE data. Stout and Young (1983) have also used this technique to obtain boundary layer pressure fields associated with the Somali jet.

We now describe the sensitivity of the geopotential calculation to the different wind analyses in Experiment 1-4. Figure 9a displays the 200 mb geopotential height analysis obtained from the wind data of Figs. 2a and 3a, using a version of the divergence equation that retains all terms except vertical advection and tilting terms (which are probably small around 200 mb), and the time tendency term (which is also generally small, Paegle et al, 1983.) The differences of this calculation from those based upon Experiments 2, 3, and 4 are shown in Figs. 9b, 9c and 9d, respectively. These differences are on the order of 10-30 m in the deep tropics and peak around 100 m in the cases neglecting all tropical wind data, or by using only westerly tropical data (Figs. 9b and 9c). The case retaining only tropical easterly wind data displays much less difference with the full fields (Fig. 9d.)

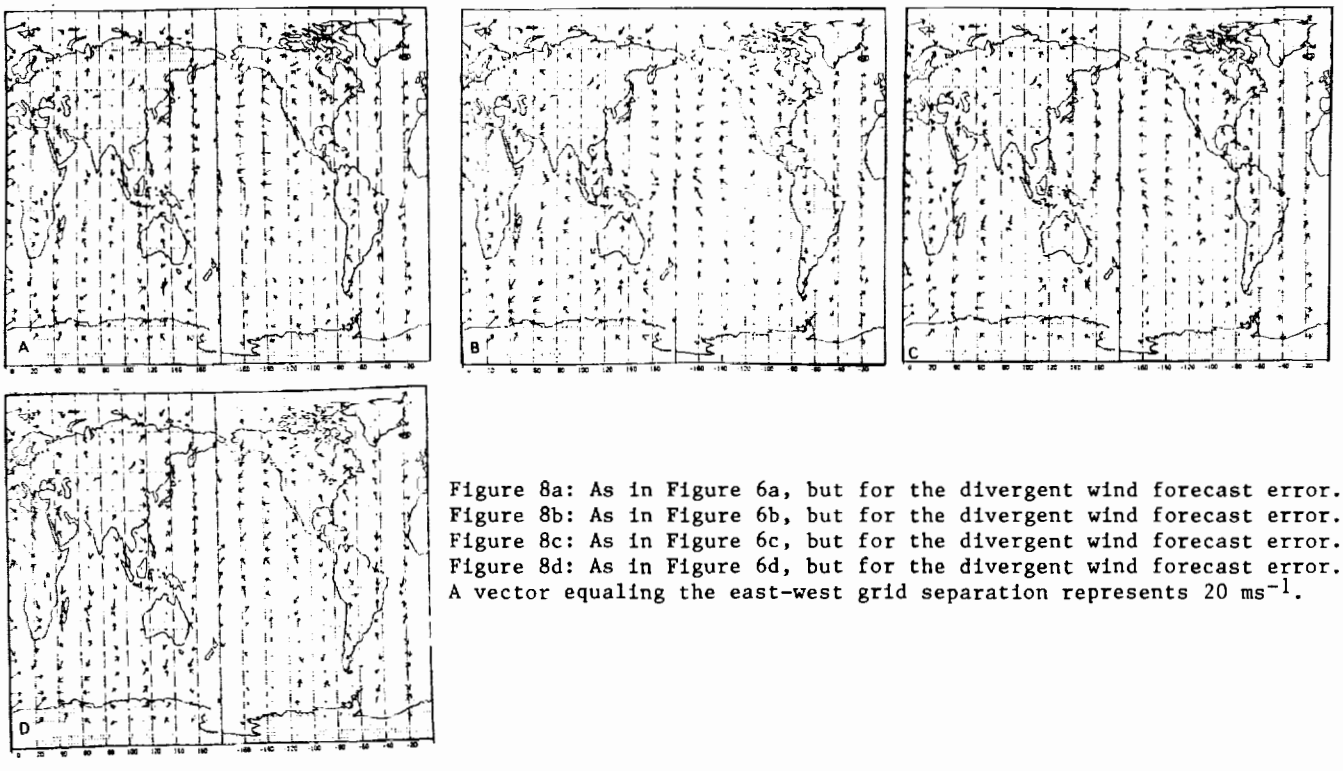

Figure 8a: As in Figure 6a, but for the divergent wind forecast error.
Figure 8b: As in Figure 6b, but for the divergent wind forecast error.
Figure 8c: As in Figure 6c, but for the divergent wind forecast error.
Figure 8d: As in Figure 6d, but for the divergent wind forecast error.
A vector equaling the east-west grid separation represents 20 ms^{-1}.

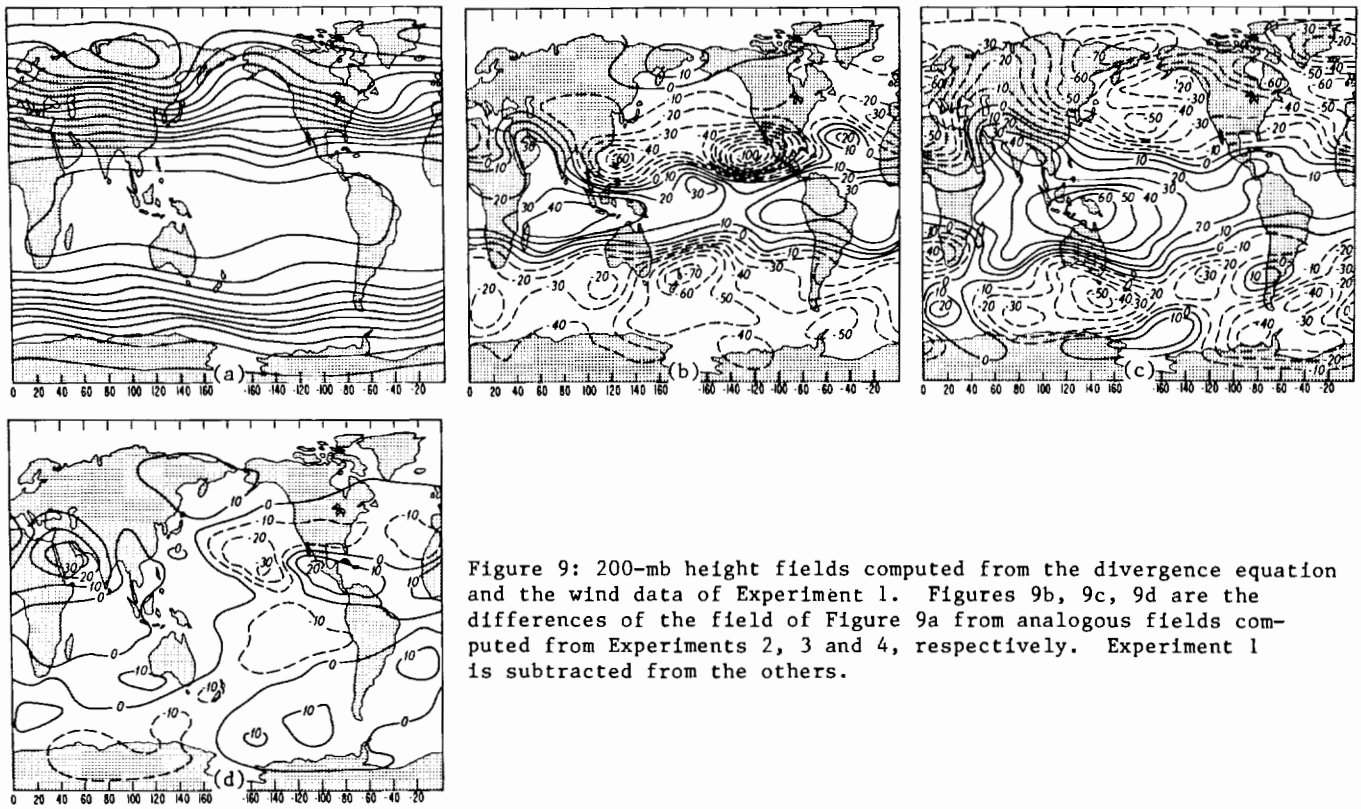

Figure 9: 200-mb height fields computed from the divergence equation and the wind data of Experiment 1. Figures 9b, 9c, 9d are the differences of the field of Figure 9a from analogous fields computed from Experiments 2, 3 and 4, respectively. Experiment 1 is subtracted from the others.

5. CONCLUDING REMARKS

Regarding the biases of the GLAS analysis cycle, it appears that the model, given only extratropical observations, generates excessively strong upper tropospheric westerlies. These biases are sufficiently pronounced to amplify the globally integrated rotational flow kinetic energy by about 10% and the global divergent flow kinetic energy by about a factor of 2.

Including only easterly wind data in the tropics is more effective in controlling the model error than including only westerly wind data. This conclusion is especially noteworthy because approximately twice as many upper tropospheric westerly winds were available in these cases as easterly winds. However, more easterly winds were available at low levels.

With respect to the influences of the tropical wind data on the forecast, it is necessary to differentiate between the extratropical spread (or impact) of tropical wind data as opposed to development of forecast error. For the present study, changes of the tropical wind data propagate out of the tropics as essentially rotational waves.

However, the long-wave error field of the forecast flow is almost as large in the divergent wind as in the rotational wind at almost all latitudes. One reason that the extratropical spread of the divergent wind impact is rather small may simply be that the model systematically loses divergent flow amplitude and this loss diminishes the final difference of any two forecast divergent fields.

This model tendency suggests that the rather large initial divergent wind of the analysis is not simply a model result, but also reflects the input data. Analogously, we conclude that the active initial tropical wave energetics and ageostrophic winds (Paegle et al., 1985) are not merely artifacts of the interpolating model.

A related conclusion is that the tropical wind impact upon the prediction is not uniformly positive. Other data errors and model errors dominate the final forecast error fields to the point that the commonality in all error fields is greater than the differences poleward of approximately 40° latitude.

ACKNOWLEDGMENT

Part of this research was supported by NASA Grant NAG 5-127 to the University of Utah.

REFERENCES

Baker, W., and J. Paegle, 1983: The influence of the tropics on the prediction of ultralong waves. Part I: Tropical wind field. Mon. Wea. Rev., 111, 1341-1355.

Burger, A., 1958: Scale considerations of planetary motions in the atmosphere. Tellus, 10, 195-205.

Kalnay, E., R. Balgovind, W. Chao, B. Edelmann, J. Pfaendtner, L. Takacs, and K. Takano, 1983: Documentation of the GLAS fourth order general circulation model. NASA Tech. memo. 86064, [NTIS W842028].

Kalnay-Rivas, E., A. Bayliss, and J. Storch, 1977: The fourth order GISS model of the global atmosphere. Beitr. Phys. Atmos., 50, 229-311.

Kalnay-Rivas, E., and D. Hoitsma, 1979: The effect of accuracy, conservation and filtering on numerical weather forecasting. Preprint volume, Fourth Conference on Numerical Weather Prediction. Silver Springs, American Meteorological Society, 302-312.

Paegle, J., W.E. Baker, and J.N. Paegle, 1985: The analysis sensitivity to tropical winds from the global weather experiment. Accepted by Mon. Wea. Rev.

Paegle, J., J.N. Paegle, and G. Dodd, 1983: On the occurrence of atmospheric states that are non-elliptic for the balance equation. Mon. Wea. Rev., 111, 1341-1355.

Paegle, J., J.N. Paegle, and F.P. Lewis, 1984: Large-scale motions of the tropics in observation and theory. PAGEOPH, 121, 948-982.

Stout, J.E., and J.A. Young, 1983: Low-level monsoon dynamics derived from low-level winds. Mon. Wea. Rev., 111, 774-798.

TROPICAL UPPER TROPOSPHERIC MOTION FIELD [1]

T.N. Krishnamurti

Department of Meteorology
Florida State University
Tallahassee, Florida 32306-3034 USA

1. INTRODUCTION

Upper tropospheric cloud motion vectors and commercial aircraft wind reports have enabled a detailed definition of the motion field. These two data sets have enhanced our observational capability since the launch of 4 to 5 geostationary satellites around the globe and the implementation of the ASDAR program. (A list of acronyms is presented in Table 1.) Figure 1 illustrates a sample of recent commercial aircraft wind reports at the 300, 250, and 200 mb surfaces over parts of the Pacific Ocean, North America, and Atlantic Ocean. This data coverage is impressive. The rms difference between these data and those obtained from rawinsonde ascents (colocated) is around $\pm$ 4 ms^{-1}. In a recent study of the cloud winds, from geostationary satellites, Johnson (1984) noted almost 15 ms^{-1} vector wind differences between estimates from GMS, GOES, and METEOSAT with respect to the rawinsonde obserations. Figure 2 based on the assessment of Johnson (1984) illustrates these results. Overall, the commercial aircraft winds are the more accurate of these two observing systems. However, it is apparent that because of the sparcity of airline routes across southern oceans, one has to rely rather heavily on the cloud winds as a primary data source over the tropical southern oceans. The operational rawinsonde coverage over the tropics is generally very poor. The overall data coverage based primarily on the collections at the ECWMF is shown in the next section.

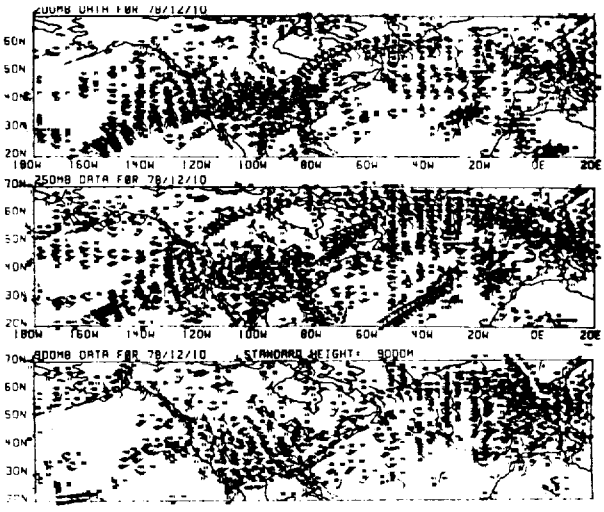

Figure 1. Location of commercial aircraft wind reports on a single synoptic time ($\pm$ 03 hrs). Top 200 mb; middle 250 mb; bottom 300 mb.

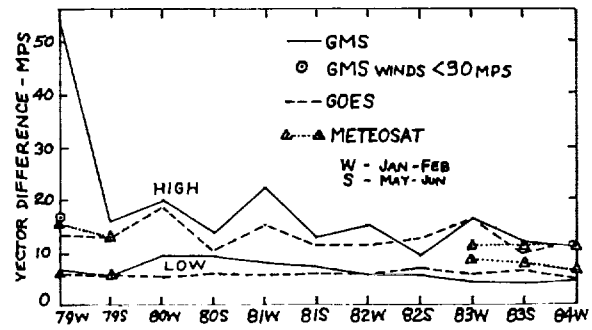

Figure 2. Comparison of high and low-cloud wind estimates from GMS, GOES, and METEOSAT with radio-wind observations (Johnson, 1984).

2. OPERATIONAL TROPICAL DATA SETS

The following are component data sets of the operational stream:

(a) Surface observations (SYNOPS)
(b) Radiosonde/rawinsonde (TEMPS)
(c) Rawinsonde (PILOT)
(d) Commercial aircraft (AIREP)
(e) Cloudwinds from geostationary satellite (SATOBS)
(f) Satellite soundings (SATEMS)

The operational coverage of data from data sets (b) and (c) is marginal to poor over the tropics. Besides the near total data gaps over the tropical oceans, the situation over the continental areas (especially over South America and Africa) is also quite inadequate. Figure 3 from a

1 The research reported here was jointly supported by NOAA grant No. NA82AA-D-00004 and NFS grant No. ATM-8304809.

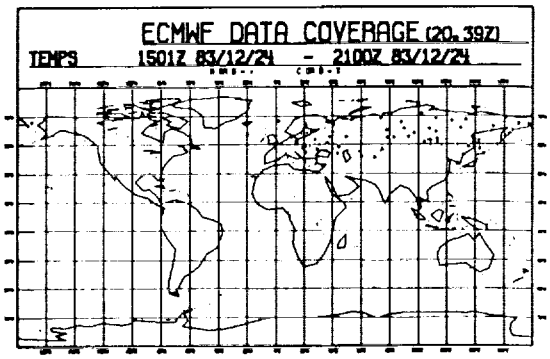

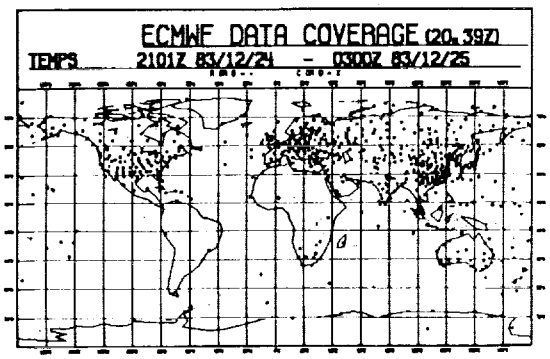

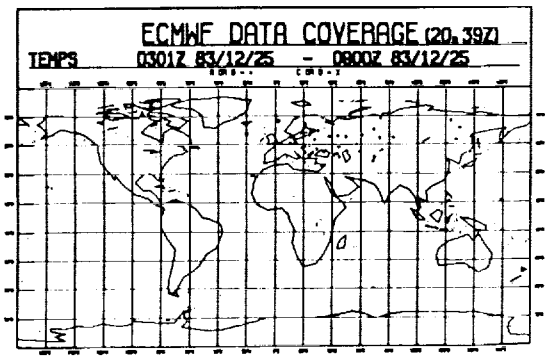

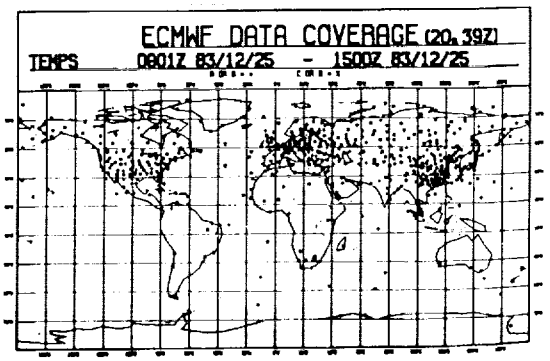

(a) Radiosonde observations (Note the big gaps over most of tropics and southern hemisphere).

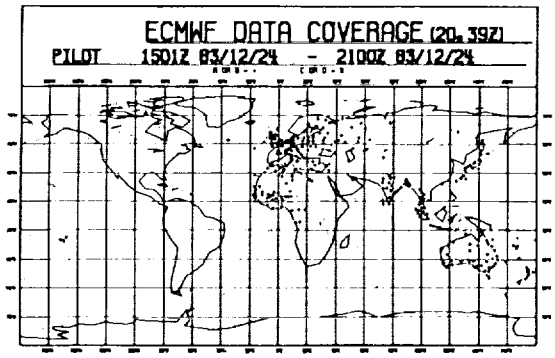

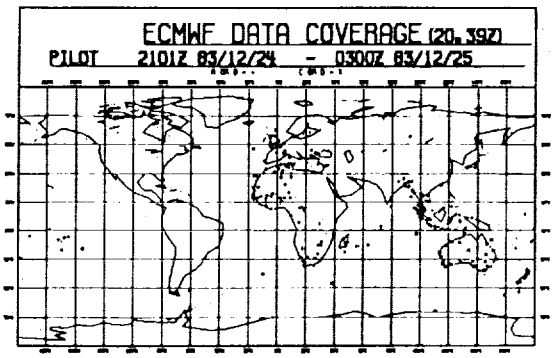

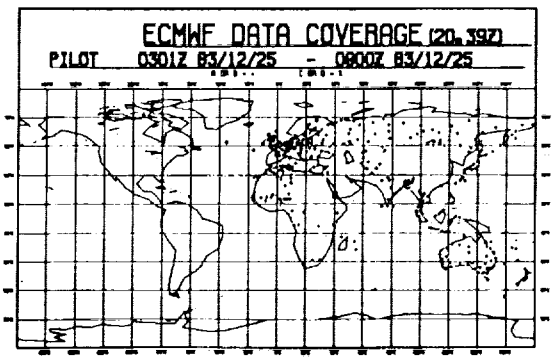

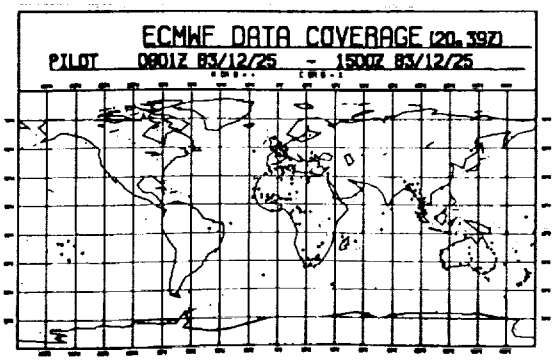

(b) Pilot balloon data (Note the general lack of coverage).

Figure 3. Radiosonde observations and pilot balloon data as received at ECMWF at 1800, 0000, and 1200 GMT.

recent summary shows the typical daily distribution of upper air data from TEMPS and PILOT over Africa and South America. It is apparent that this operational coverage by itself is not a useful data set for research or operational practice.

The operational coverage of surface data, shown in figure 4, appears to be quite adequate for the definition of the planetary and synoptic scale weather systems over most tropical areas of the northern hemisphere. However, major data gaps over the southern hemisphere are apparent.

The distribution of rawinsonde wind reports (PILOT) adds only a little more to the TEMPS data. The distribution of data over Africa is poor, over South America the distribution at 12 Z is marginally better for the description of tropical weather systems. It is poor at all other map times. (See Figure 3.)

The current operational commercial aircraft data are based on AIREP and ASDAR collections. The AIREP data are either directly sent by aircraft on radio messages or collected at airports (flight data debriefing forms) and transmitted via GTS. The ASDAR is an aircraft-satellite data acquisition relay system that was implemented during FGGE and is undergoing major improvement and extensions at the present time. The addition of these data between 300 and 200 mbs over the tropics enhances the capability of the overall observing system considerably. Over the southern hemisphere tropical oceans, this is not an adequate data source.

The cloud motion vectors from the geostationary satellites are a major operational data source. Low- and high-level cloud winds enhance the composite observing system immensely. The present coverage from the Indian Ocean satellite INSAT is poor; however, an improvement in the quantity of data is expected. Operationally, some 300 vectors at each of the two levels are generally transmitted at 00 and 12 GMT. These are usually assigned to the cloud-base level (around 900 or 850 mb level) and the 200 mb level. Figure 5 illustrates a typical coverage based on the operational NMC data base.

The temperature retrieval soundings from the polar orbiting satellites (SATEM) have not been very satisfactory over the tropics. The temperature gradients from these data sets over the tropics are very weak and do not describe the thermal structure of tropical disturbances. This present operational system can provide some useful broad scale data sets for totally data sparse tropics. It is not of the same quality as the current VAS system which is based on the U.S. geostationary satellite data sets. The careful man-machine mix in the extraction of VAS soundings all around the cloud-free regions of major storms off the North American coasts have provided some of the best applications. Such a procedure, if implemented, with all the five geostationary satellites can provide very useful satellite soundings. The quality of the radiance data is, however, not uniform at the present time. The horizontal resolution of the satllite radiance data sets are also nonuniform. Thus, a uniform quality of retrieval soundings from a VAS type system may not be easy to implement for the entire tropics. Some degree of intercalibration

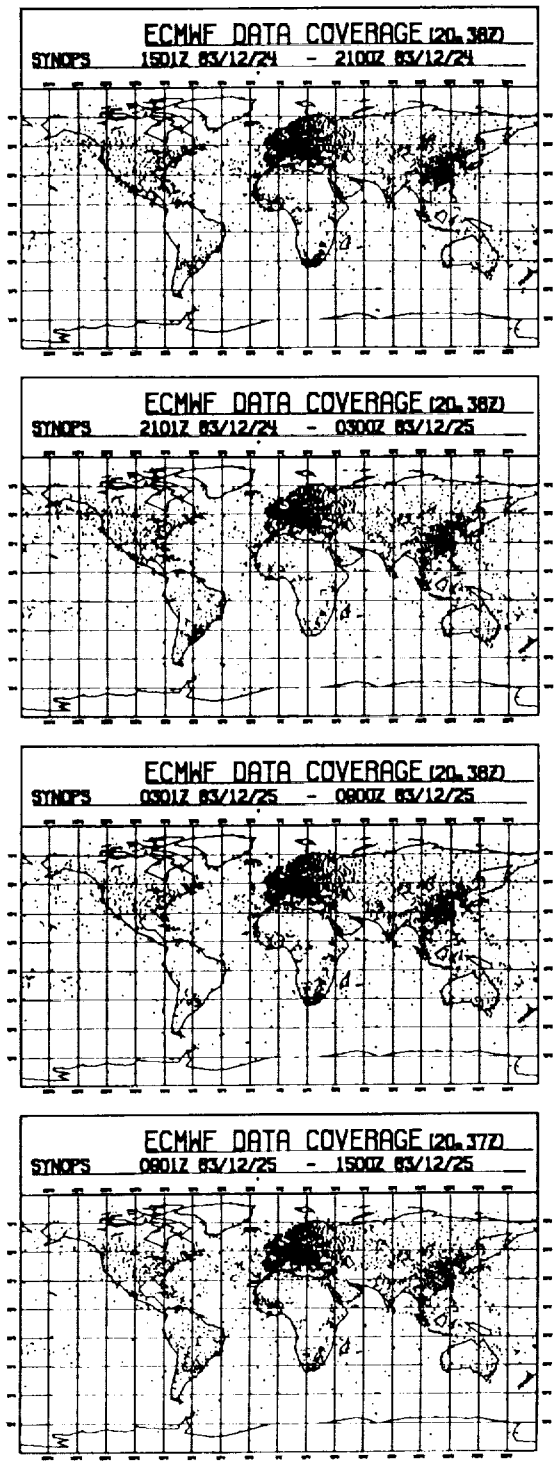

Figure 4. Surface synoptics data as received at the ECMWF at 1800, 0000, 0600, and 1200 GMT (Note the data gaps over southern oceans).

of the radiance information may be necessary to obtain a useful data set. At the present time, the SATEM data set is not very useful over the tropics.

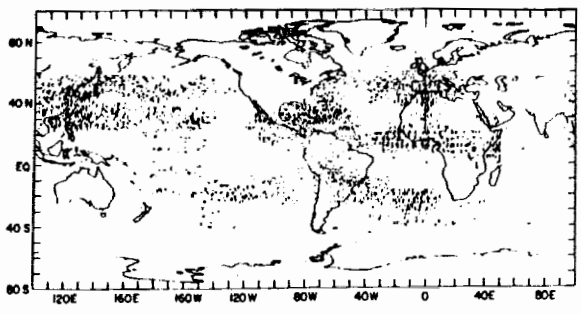

Figure 5. High level cloud motion vectors received on a typical day during March 1984 at NMC. The lack of cloud winds over Indian Ocean is conspicuous.

3. THE COMPOSITE OBSERVING SYSTEM

It is apparent that an analysis system that makes use of all the observing systems is the best hope for the tropics. However, the Post-FGGE operational analysis over the tropics still leaves much to be desired. As is apparent from figure 6, the data gaps between 900 mb and 300 mb are very large over the tropics.

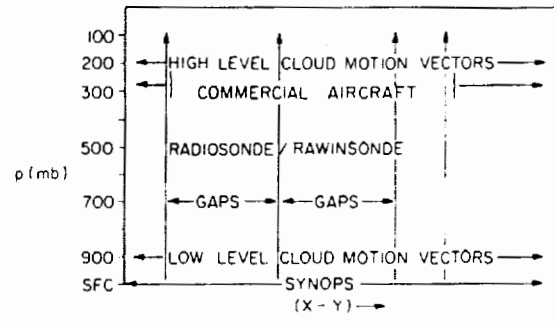

Figure 6. Vertical and lateral data gaps in present observing system.

In this sparse data region of the middle troposphere, the use of climatology as a first guess field is not very desirable since a vertical discontinuity in the analysis usually appears between the data-rich lower troposphere and the upper troposphere. The use of vertical interpolation to provide a first guess appears to be superior to climatology for these middle levels.

In the tropics a number of salient disturbances such as easterly waves, tropical depressions, tropical storms, hurricanes, the intertropical convergence zones, the trades and the broad-scale monsoons are usually described from very few observations. In many instances, there may be almost no upper air soundings within a depression or a tropical storm. In these instances, vertical interpolation between the lower and upper troposphere does not provide a reasonable vertical structure for these tropical disturbances. Most of our present knowledge of these disturbances is largely based on our previous experience from an analysis of data sets from field experiments (ATEX, AMTEX, BOMEX, GATE, MONEX) and from some data-dense regions over the tropics (Caribbean, Marshall Islands, India). Based on the lower troposphere and the upper troposphere data sets and the satellite radiance data sets (visible as well as IR), it should be possible for a computer to recognize the identity and location of major disturbances over a global tropical belt. Such softwares are currently not in existence; however, they can be developed. Synoptic structures can be inserted over these data-sparse regions where the presence of typical disturbances have been identified.

Based on past experience from the tropical field experiments (AMTEX, ATEX, BOMEX, GATE, WAMEX, MONEX) and from studies over the tropical denser data networks (Caribbean, Marshall Islands, India), it should be possible tó construct a number of 3-dimensional grids of data that describe the life cycle of typical tropical disturbances during the formative, mature, and decay stages. These would be anomalies with respect to a local basic state. The parameters that describe the atmosphere may include the winds, temperature, pressure, and the humidity anomalies. This suggestion may seem preposterous; however, if one looks at the aforementioned data gaps, the situation for defining the initial states for numerical weather prediction seems hopeless otherwise!

The broad-scale basic state, however, can be analyzed by using currently available surface and upper air data. Figure 7 shows an example of the data distribution and an analysis of the basic state at the 200-mb level. In this example the broadscale flow was analysed by utilizing a truncated series of spherical harmonies and utilizing a least square fit to determine the coefficients of the expansion.

(a) 200 mb ten-year mean streamlines for February

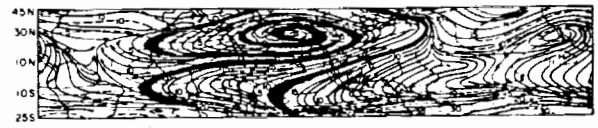

(b) 200 mb ten-year mean streamlines for August

Figure 7. 200-mb monthly mean flow field for February and August. The upper monsoonal outflow regions are darkened.

4. TROPICAL UPPER TROPOSPHERIC MOTION FIELD

These new data sets have become increasingly available for research in the last 15 years. The peak in these data sets was achieved during the global experiment in 1979. Some of the major results based on these data are discussed.

Tropical upper tropospheric climatology. Based on a decade of data sets Pan (1979) and Krishnamurti et al. (1985) have determined the climatology of the flow field at the 200 mb. Figure 7 illustrates these fields for the months of February and August. The winter and summer monsoon outflow layers at the 200 mb are the prominent features here. It has become possible to examine the interannual variability of the motion field from such analysis of monthly mean flows covering several years. This analysis has provided a distinction among various circulation features during El Nino and Non El Nino years. That distinction is most prominent in the composite structure of the divergent circulations. An equatorward and eastward shift of the primary divergent circulation, associated with the planetary scale monsoon, has been well documented for the El Nino years.

Another area of current research is in the studies of low-frequency modes on the time scale of 30 to 50 days. The currently available 200-mb data sets seem to be quite adequate to map the planetary scale eastward propagating divergent circulations on this time scale (Lorenc, 1984; Krishnamurti et al., 1985).

These data sets have been useful in providing estimates of a number of other derived quantities. However, it should be noted that there are some major differences among the analyses performed by different groups. That was apparent in the FGGE analyses produced by the ECMWF, GLAS, GFDL and the U.K. Meteorological office. The analyses, being functions of the model and its physics, contribute to most of the aforementioned differences. This effect can also be attributed to the slight differences in the data sets. It is inevitable that these differences would lead to different forecasts made with several of these analyses. We have noted that the post-FGGE operational analyses, made by different groups, show much large differences over the tropics compared with those made during the FGGE.

Studies by Julian (1982) and Krishnamurti et al. (1983, 1984) show that the operational as well as FGGE tropical data sets are not quite adequate to resolve divergent motion on the scales of individual tropical disturbances. The use of satellite radiance data has been useful in defining such local storm scale divergent motion. However, reasonable amplitudes of such are hard to define from such indirect procedures. Use of structure functions and high resolution cloud winds can provide a useful calibration for the use of the satellite radiance data.

5. SOME RECOMMENDATIONS AND REQUIREMENTS

The determination of high resolution cloud wind providing a global coverage from roughly 45S to 45N is essential for the description of the tropical motion field.

The assignment of proper height for the cloud winds requires further detailed studies. The current error estimtaes are too high.

Much further enhancement of the operational collection of the commercial aircraft wind reports is necessary. The coverage of ASDAR and current AIREP collection appear to be adequate only over the northern Pacific and the northern Atlantic Ocean.

More detailed evaluation of the vertical soundings derived from polar orbital and geostationary satellites is recommended. This could form a very useful supplemental data set for defining the vertical structure of the tropical atmosphere.

The impact of satellite radiance data sets for the definition of the initial divergent motions in tropical disturbances deserves to be explored by numerical experimentation.

ACKNOWLEDGMENTS

The manuscript was ably prepared by Cindy Rothenbach, to whom we are very grateful.

The computations reported here were carried out at the National Center for atmospheric Research, which is sponsored by the National Science Foundation.

REFERENCES

Johnson, D.S., 1984: Meteorological parameters derived from space-based observing systems FGGE and after. Proceedings of the seminar on data assimilation systems and observing system experiments with particular emphasis on FGGE. ECWMF (Shinfield Park, England) pp. 47-108.

Julian, P., 1982: The tropical observing systems in FGGE: an analysis of results. Proceedings of the conference on early results of FGGE and large scale aspects of its monsoon experiments. WMO, pp. 2.2-2.9.

Krishnamurti, T.N., R. Pasch, H. Pau, S. Chu, and K. Ingles, 1983: Details of low latitude numerical weather prediction using a global spectral model I. J. Met. Soc. Japan, 61, 188-207.

Krishnamurti, T.N., K. Ingles, S. Cocke, R. Pasch, and T. Kitade, 1984: Details of low latitude medium range numerical weather prediction using a global spectral model II. J. Met. Soc. Japan, Vol. 62, #4, 613-649.

Krishnamurti, T.N., P.K. Jayakumar, J. Sheng, N. Surgi, and Arun Kumar, 1985: Divergent Circulation on the 30 to 50 day time scale. J. Atmos. Sci., 42, 364-375.

Lorenc, A.C., 1984: The evolution of planetary scale 200 mb divergences during the FGGE year. Meteorological Office Tech. Note II/210, 1-23. (Available from Dynamical Climatology Branch, Meteorological Office, London Road, Bracknell, Berkshire, England.)

Pan, H.L., 1979: Upper tropospheric tropical circulations during a recent decade. Report No. 79-1, Department of Meteorology, Florida State University, Tallahasse, Florida, 1-141.

TABLE 1

ACRONYMS

ASDAR	Aircraft Satellite Data Acquisition Relay
GMS	Geostationary Meteorological Satellite
GOES	Geostationary Operational Equatorial Satellite
METEOSAT	Meteorological Satellite
SYNOPS	Surface Synoptic Data
ECMWF	European Center for Medium Range Weather Forecast
TEMPS	Radiosonde Thermal Data
PILOT	Pilot Balloon Data
AIREP	Commercial Aircraft Pilot Report
SATOBS	Satellite Observations
SATEMS	Satellite-Temperature Observations
GTS	Global Telecommunication System
INSAT	Indian Geostationary Satellite
NMC	National Meteorological Center
VAS	Vertical Atmospheric Sounding
FGGE	First GARP Global Experiment
ATEX	Atlantic Tropical Experiment
AMTEX	Airmass Tropical Experiment
BOMEX	Barbados Oceanic Meteorological Experiment
GATE	GARP Atlantic Tropical Experiment
MONEX	Monsoon Experiment
IR	Infrared Radiation
WAMEX	West African Monsoon Experiment
GLAS	Goddard Laboratory for Atmospheric Science
GFDL	Geophysical Fluid Dynamics Laboratory

OBSERVATIONAL REQUIREMENTS FOR THE REGIONAL SCALE

Louis W. Uccellini
Laboratory for Atmospheres
NASA/Goddard Space Flight Center
Greenbelt, MD 20771

1. INTRODUCTION

The purpose of this paper is to provide observational requirements for the "regional scale" (10^2 to 10^3 km space scale; 3 to 24 h time scale). Given this range, the regional scale represents a spatial and temporal domain in which important scale-interactive processes occur that act to concentrate large vertical wind shears, significant horizontal thermal gradients, and vertical motion patterns into narrow regions.

The evolution of jet streaks[1] represents an important regional-scale phenomenon which is marked by noticeable ageostrophic wind components, significant energy conversions, strong horizontal temperature gradients, associated vertical wind shears, and vertical motion patterns. The secondary, transverse, vertical circulations associated with straight jet streaks have been discussed widely in the literature (e.g., Namias and Clapp, 1949; Bjerknes, 1951; Riehl et al., 1952; Murray and Daniels, 1953; Cahir, 1971). The vertical motion patterns associated with jet streaks are usually embedded in larger scale trough/ridge systems, making the diagnosis of these circulations more difficult (Newton, 1954; Uccellini and Johnson, 1979; Keyser and Shapiro, 1985). However, separating the different mechanisms that contribute to distinct vertical motion patterns provides physical insight into processes which act to focus ascent/descent patterns into smaller regions approaching the meso-α scale domain (Keyser and Shapiro, 1985). The vertical circulations have been related to cyclogenesis and synoptic-scale cloud patterns (Reiter, 1969; Sechrist and Whittaker, 1979). The patterns of divergence associated with the transverse circulation patterns have also been related to the development of severe convection (e.g., Beebe and Bates, 1955; Cahir, 1971; Danielsen, 1974; McNulty, 1978; Uccellini and Johnson, 1979; Bluestein and Thomas, 1984). Cahir (1971) by using a two-dimensional numerical model, showed that vertical motion patterns associated with jet streaks could account not only for the severe weather events but also for the banded structure of many of the more common rain and snow events. Therefore, an accurate specification and simulation of secondary circulations within jet/front systems is an important factor in weather analysis, model initialization/numerical forecasts, and diagnostic studies of scale-interactive processes that dominate the regional scale.

A short review on the mass and momentum adjustments associated with jet streak-induced circulations is discussed in Section 2. Evidence for the need to specify the wind field in the upper troposphere to accurately simulate forcing for the transverse circulations is presented in Section 3.1. The importance of specifying temperature tendency to resolve the lower tropopsheric portion of the transverse circulations is highlighted in Section 3.2. The observational requirements are then discussed in Section 4, along with possible approaches for meeting the requirements on the regional scale.

2. BACKGROUND ON JET STREAKS

Uccellini and Johnson (1979) show how the ageostrophic components in the exit and entrance regions of jet streaks can be studied using the equation of motion in a form (listed in Table 1) that relates isallobaric and inertial-advective contributions to the ageostrophic wind component to the horizontal branches of the secondary circulation associated with jet streaks (Fig. 1). In the exit and entrance regions of the jet streak, where the along-stream variations of the wind and mass

TABLE 1

$$\underset{\sim}{V}_{ag} = \hat{k} \times \frac{d\underset{\sim}{V}}{dt} - \hat{k} \times \frac{d\underset{\sim}{V}_g}{dt}$$

$$= \hat{k} \times \left(\frac{\partial \underset{\sim}{V}_g}{\partial t} + \underset{\sim}{V} \cdot \nabla_\theta \underset{\sim}{V}_g\right)$$

$$\simeq -f^{-2} \nabla_\theta \frac{\partial \psi}{\partial t} + f^{-1} \underset{\sim}{V} \cdot \nabla_\theta (\hat{k} \times \underset{\sim}{V}_g)$$

ISALLOBARIC	INERTIAL-ADVECTIVE
DOMINATES IN LOWER TROPOSPHERE	DOMINATES IN UPPER TROPOSPHERE

[1] Palmén and Newton (1969, p. 199) define jet streaks as the regions of isotach maxima embedded within jet streams.

UPPER TROPOSPHERE: INERTIAL-ADVECTIVE

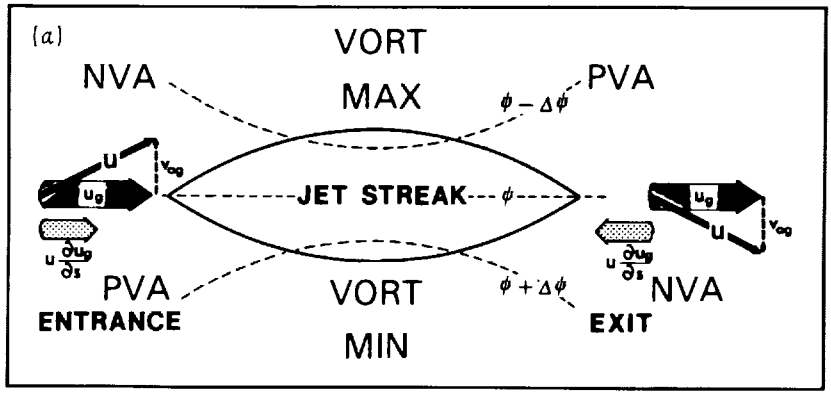

LOWER TROPOSPHERE: ISALLOBARIC

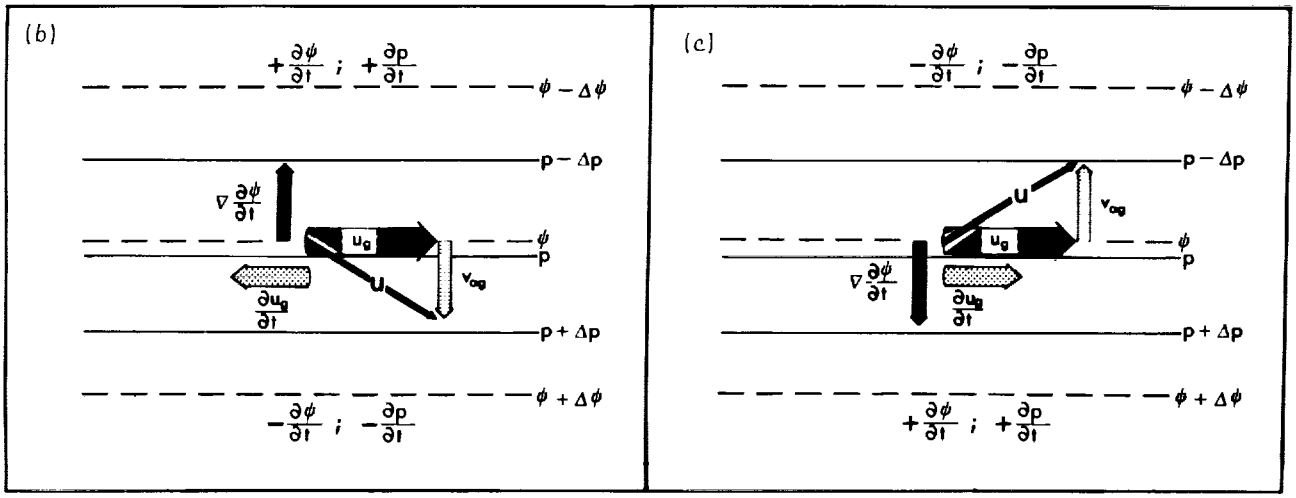

Fig. 1. *(a) Schematic of transverse ageostrophic component (v_{ag}) associated with along-stream variation in the wind and pressure gradient force on isentropic surface at jet streak level. Vorticity maximum and minimum and advection patterns [positive vorticity advection (PVA); negative vorticity advection (NVA)] indicated on cyclonic and anticyclonic sides of jet streak. Montgomery stream function (ψ), along-stream coordinate (s), geostrophic wind (u_g), and total wind (u). (b) Isallobaric component on lower tropospheric isentropic surface beneath entrance region of jet streak; symbols same as in (a), pressure on isentropic surface (p). (c) Isallobaric component for isentropic surface beneath exit region of jet streak.*

distribution are large, the inertial-advective term dominates (Bjerknes, 1951; Uccellini and Johnson, 1979). In the entrance region, the increasing gradients in the Montgomery stream function (ψ_m) and increasing wind speed are associated with an ageostrophic component directed toward the cyclonic side of the jet (Fig. 1a). This ageostrophic component represents the upper branch of a direct circulation which converts available potential energy into kinetic energy as parcels accelerate into a jet. The opposite occurs in the exit region with the ageostrophic component directed toward the anticyclonic side of the jet streak. This ageostrophic component represents the upper branch of an indirect circulation which converts kinetic into available potential energy as parcels decelerate upon exiting the jet streak.

In the lower troposphere, the isallobaric contribution dominates the inertial-advective term (Uccellini and Johnson,

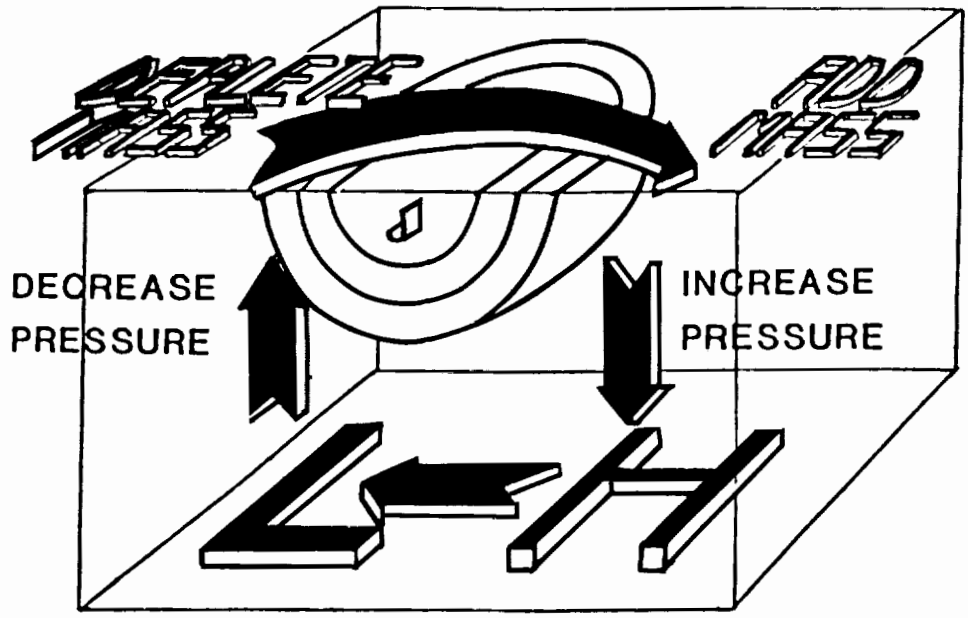

Fig. 2. *Schematic depicting the transverse indirect circulation in the exit region of an upper level jet streak.*

1979; Brill et al., 1985). Beneath the entrance region of the jet streak, the isallobaric component is directed toward the anticyclonic side, opposite to the direction of the inertial-advective component at the level of the jet streak (Fig. 1b). This lower tropospheric ageostrophic component represents the lower branch of the direct circulation in the entrance region. The reverse pattern is found in the exit region, the isallobaric component directed toward the cyclonic side representing the lower branch of the indirect circulation (Fig. 1c). The divergence/convergence patterns associated with these transverse branches yield the vertical motion patterns [ascent in the right entrance and left exit region and descent in the left entrance and right exit region (looking downstream)] which complete the transverse circulations near the jets. [See also Riehl et al. (1952); Beebe and Bates (1955).]

A schematic illustration of the exit region (Fig. 2) shows that the coupling between the various lateral components of the transverse circulations is related to the mass adjustments throughout the troposphere and is based on the more detailed findings of Uccellini and Johnson (1979), Uccellini et al. (1984), Brill et al. (1985), and Kocin et al. (1985). As parcels exit the jet streak and become supergeostrophic (inertial-advective contribution becomes large), they turn toward the anticyclonic side of the jet, depleting (adding) mass on the cyclonic (anticyclonic) side of the jet. The upper level mass divergence on the cyclonic side contributes to ascent, whereas the upper level mass convergence on the anticyclonic side contributes to descent. The decreasing (increasing) pressure on the cyclonic (anticyclonic) side of the jet related to the mass adjustment (temperature change) contributes to the strengthening of the ψ_m gradient and associated increased pressure gradient force beneath the axis of the jet. The isallobaric contribution to the ageostrophic flow (related to this increased pressure gradient force) dominates in the lower troposphere because the low wind speeds usually found there (1) yield a longer time interval for parcels to be affected by the region of changing pressure gradient force (as compared with the upper troposphere, where the parcels rapidly traverse these regions) and (2) also yield a smaller contribution from the inertial-advective term (which generally tends to offset the isallobaric contribution).

This perspective is consistent with other approximations to vertical motion patterns which rely on diagnosing vorticity and temperature advections. The maximum (minimum) relative vorticity patterns located on the cyclonic (anticyclonic) side of the jet streak (Fig. 1a) yield vorticity advection patterns with positive vorticity advection (PVA) and negative vorticity advection (NVA) located in regions marked by ascent and descent, respectively. Furthermore, the isallobaric component in the entrance region (Fig. 1b) is

directed down the slope (from p-Δp toward p+Δp) on the isentropic surface, yielding a total wind (U) that is also directed down the sloping isentropic surface. This condition is equivalent to cold-air advection in the low levels which is typically related to the sinking motion found beneath the entrance region of jets. The cold air advection could act to displace the transverse circulation toward the anticyclonic side of the streak (Shapiro, 1981; Keyser and Pecnick, 1985) such that maximum descent is located nearer to the axis of the jet. The reverse is found in the exit region (Fig. 1c), where the isallobaric contribution to the ageostrophic wind and the resultant total wind is directed up the sloping isentropic surface (from p+Δp to p-Δp). This is equivalent to warm-air advection which also appears to displace the region of ascent associated with the indirect circulation toward a position beneath the axis of the upper-level jet [see, e.g., Uccellini et al. (1984), Brill et al. (1985)] rather than being located only on the cyclonic side of the jet.

It is a general practice to consider the effects of PVA and warm air advection separately as independent "upper-" and "lower-" level forcing [see, e.g., Maddox (1983), Pagnotti and Bosart (1984)]. However, with the configuration presented in Fig. 2, it appears that these separate advective quantities are linked when superimposed in the exit region of jet streaks. The PVA represents a manifestation of the processes contributing to the nature of the upper branch of the circulations and the warm air advection represents a manifestation of the lower branch of the transverse circulation directed up sloping isentropic surfaces.

In summary, with respect to specifying observational requirements for the regional scale, the adjustment process described for jet streaks indicates that the distribution of winds (especially the along-stream variations) near jets is important in the upper troposphere. This finding is consistent with the concept that winds will force mass to adjust on the regional to mesoscale (Rossby, 1938; Washington, 1964). However, the dominance of the isallobaric term for the lower branch of the transverse circulations indicates that the mass tendency (temperature change) is important in the lower troposphere in forcing the wind to adjust to the mass; this result is also consistent with adjustment theory even on the regional to mesoscale (Bolin, 1953).

3. EVIDENCE FOR THE IMPORTANCE OF SPECIFYING UPPER LEVEL WIND STRUCTURE AND LOWER LEVEL MASS TENDENCY FOR RESOLVING JET-RELATED CIRCULATIONS

Numerical experiments conducted by Brill et al. (1985) are now summarized that show that the transverse circulations are driven by the along-stream wind variation that constitutes the basic structure of jet streaks. Evidence is then presented from the 10-11 April case study (Kocin et al., 1982, 1985) which demonstrates that the lower branch of the transverse circulation is dominated by isallobaric effects which could only be resolved by an enhanced radiosonde data set that included 3-h soundings.

3.1 10-11 May 1973 Numerical Experiment

The 10-11 May 1973 case, where severe storms developed in Ohio within the exit region of an upper level jet, was used by Uccellini and Johnson (1979) to describe the coupling concept of upper and lower level jets. The development of the low-level jet (LLJ) represented an enhancement of the lower branch of the indirect circulation in the exit region of the upper level jet. The LLJ is coupled to the upper level jet through the tropospheric mass adjustments. Brill et al. (1985) discuss numerical simulations of this process in detail. The purpose of the numerical experiment was (1) to determine whether the indirect circulation can be identified in numerical simulations, and (2) to determine whether the indirect circulation is sensitive to the initial structure of the upper level jet. Since the results have been published recently, only a summary of the experiment is discussed here.

Two simulations were conducted: (1) experiment E1 that used an enhanced initial data set and maintained a significant along-stream wind variation in the exit region of a jet streak in the central United States (Fig. 3a), and (2) experiment E2 that used a smoothed nondivergent initialized wind field where the along-stream variation in the exit region of the upper level jet is weakened (Fig. 3b). The inertial-advective (IA) term (based on total wind without use of the geostrophic momentum approximation) was used as a measure of the along-stream variation. In the exit region, a 30 m s^{-1} maximum IA component was diagnosed at the initial time for E1 (Fig. 3a) and a 21 m s^{-1} maximum IA component was diagnosed for E2 (Fig. 3b). The jet streak propagated eastward during the 12-h simulation for both E1 and E2, the exit region being located over the Ohio Valley by 9 h into the simulations (Fig. 4).

Cross sections constructed orthogonal to the axis of the upper level jet (see Fig. 4 for line of cross section) reveal that the difference in the initial structure of the jet persisted throughout both model simulations. For E1, an indirect circulation was diagnosed in the exit region of the jet with transverse components greater than 10 m s^{-1} in the upper and lower troposphere and ascent (-4 μb s^{-1}) and descent (8 μb s^{-1}) located along and to right of the jet axis, respectively (Fig. 5). In E2, the indirect circulation was noticeably weaker and the transverse component was only slightly larger than 5 m s^{-1}. The vertical components were decreased by 50% to -2 μb s^{-1} in the ascending branch and 3 μb s^{-1} in the descending branch (Fig. 6).

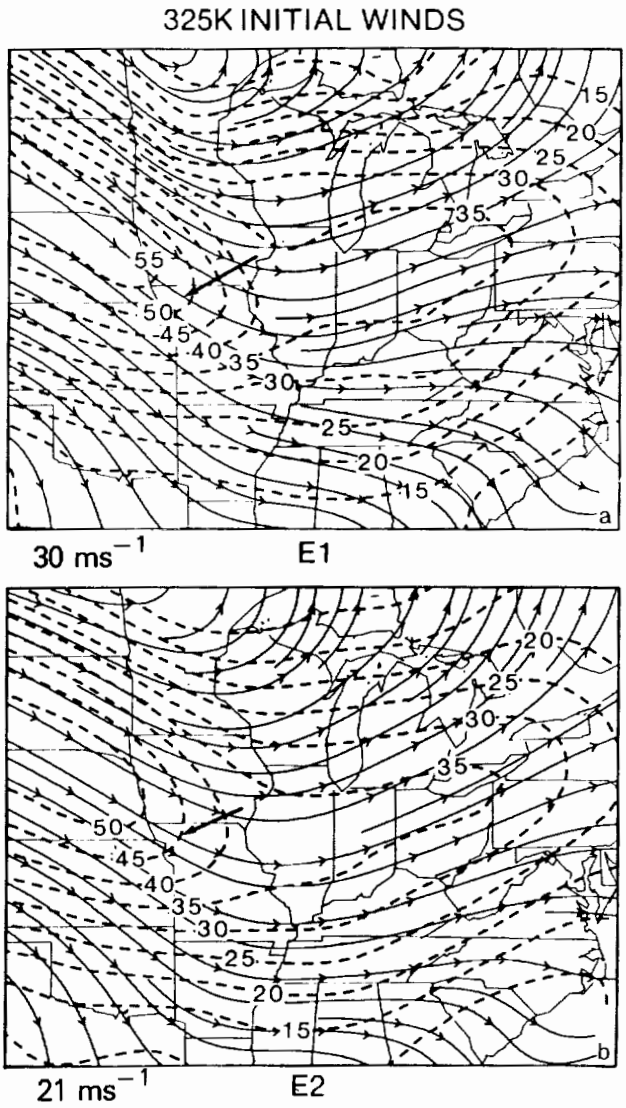

Fig. 3. *Initial winds (1200 GMT 10 May 1973) on 325 K surface for numerical experiments described by Brill et al. (1985). Experiment 1 (E1) where initial analysis yields stronger along-stream variation in exit region of jet streak, with 30 m s^{-1} inertial-advective component indicated in Iowa. Experiment 2 (E2) where smoothed nondivergent analysis yields weaker along-stream variation, with 21 m s^{-1} inertial-advective component. Streamlines (solid) and isotachs (dashed) at 5 m s^{-1} interval [from Brill et al. (1985)].*

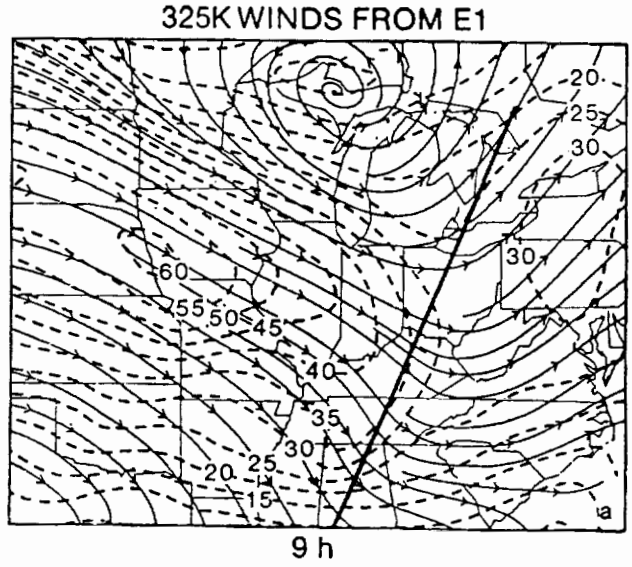

Fig. 4. *Streamlines (solid) and isotachs (dashed) at 5 m s^{-1} interval on 325 K surface from 9 h forecast (2100 GMT 10 May) for E1. The heavy solid line marks position of cross sections shown in Figs. 5 and 6 [from Brill et al. (1985)].*

To summarize the numerical experiments for the 10 May 1973 case:

(1) Differences in initial upper level wind structure in the exit region of the jet streak persisted through the 12-h simulation

(2) The difference in the initial upper level wind analysis had significant impact on the resultant transverse circulations. The strength of the lateral branch is affected when the lateral along-stream wind gradient is weakened. Furthermore, the strength of the vertical branch is also reduced.

Brill et al. (1985) show that the difference in the strength of the lateral branches of the indirect circulation had a significant impact on the differential temperature and moisture advections (forced by the vertical ageostrophic wind shears associated with the indirect circulation) and subsequent convective destabilization. The decreased magnitude of the vertical branches also reduced the model's ability to release the convective instability. Thus, the differences in the basic wind structure between E1 and E2 had significant impact on the model's ability to produce a viable weather forecast for this case.

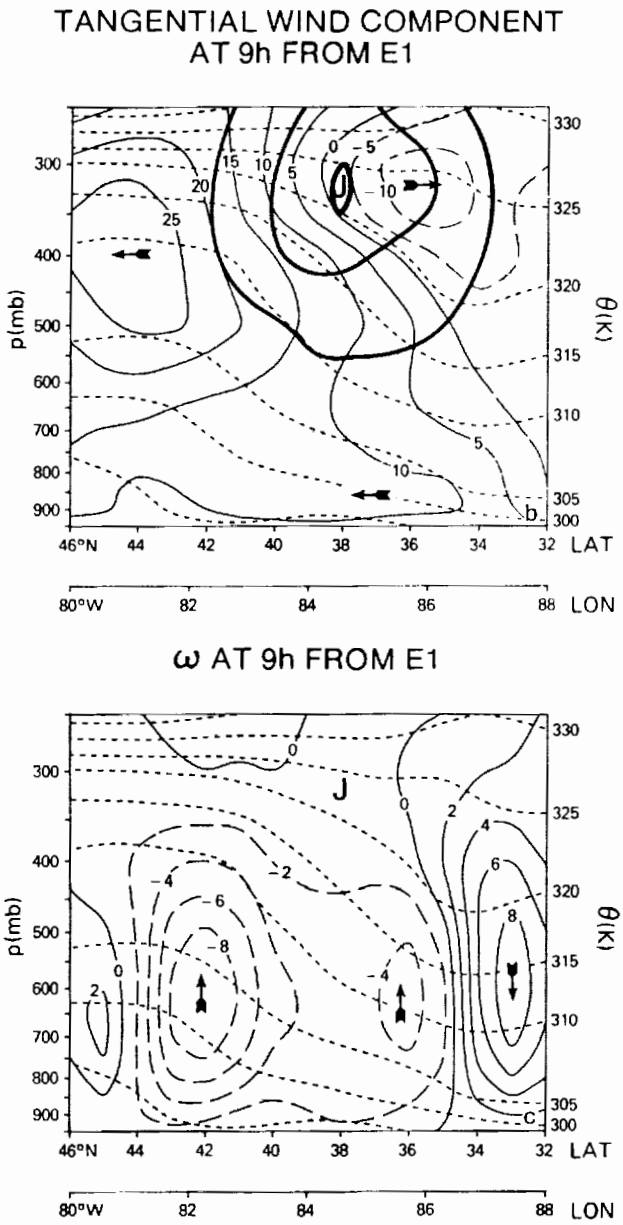

Fig. 5. *Cross sections extending along a rumb line from 46°N, 80°W (left) to 32°N, 88°W (right) taken from 9 h of E1 (see line on Fig. 4). Top is the tangential horizontal wind component (contour interval 5 m s^{-1}, positive right to left), with position of jet (directed into plane of cross section) marked by a J and selected isotachs. Bottom is ω (contour interval 2 μb s^{-1}). Short-dashed contours of potential temperature (K) are shown in the background of each cross section. Latitude and longitude positions (deg) are given at the bottom of each cross section. Long-dashed contours indicate negative values. Arrows indicate direction of motion [from Brill et al. (1985)].*

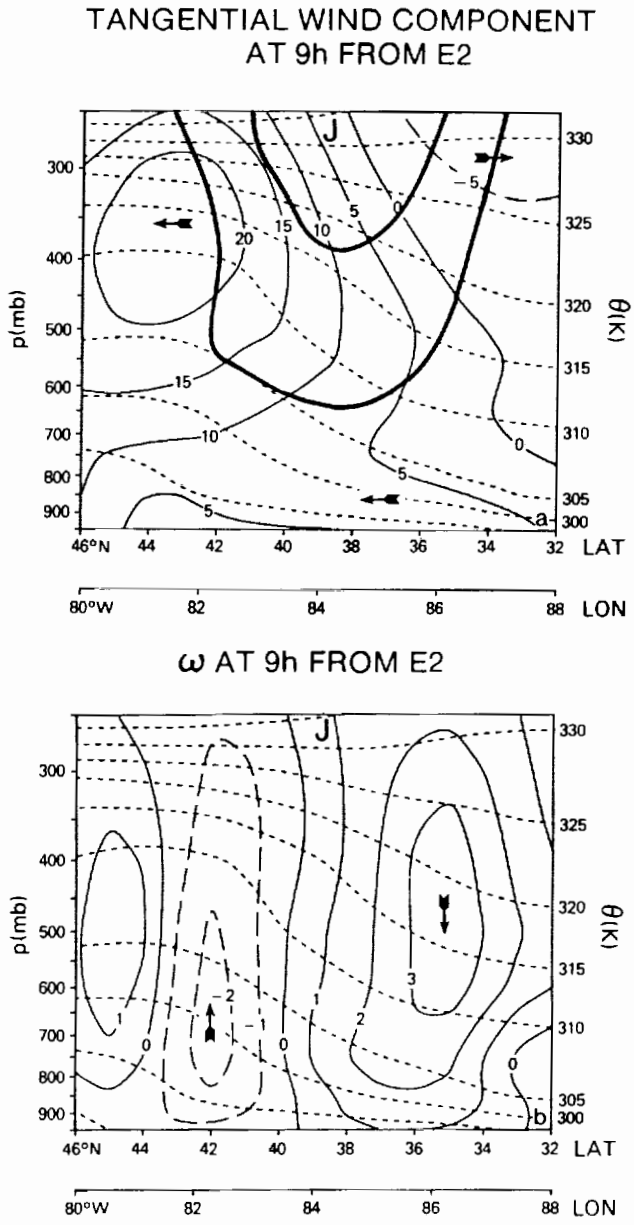

Fig. 6. *Same as Fig. 5 but for E2 [from Brill et al. (1985)].*

3.2 Isallobaric Contribution to Low-Level Jet Formation for the 10-11 April 1979 Severe Weather Outbreak

In this section, results from a recent case study of the Wichita Falls tornado outbreak on 10-11 April 1979 are summarized which highlight the importance of the isallobaric effects in the lower troposphere. A more detailed analysis of the jet streak processes for this case can be found in Kocin et al. (1982, 1985).

At 1200 GMT 10 April 1979, an intense low pressure sytem was developing over Colorado and Wyoming with a cold front extending southward into New Mexico and a warm front restricted to southern Texas and the Gulf Coast (Fig. 7). An amplifying, deep tropospheric wave was located over the southwestern United States and an upper tropospheric jet streak was analyzed by the National Weather Service to extend from northern Baja California toward southwestern Texas. By 0000 11 April 1979 (Fig. 7), the surface low was located in central Colorado with a warm front advancing to the Texas-Oklahoma border. A LLJ is evident at the 850 mb level over Oklahoma beneath the exit region of the upper level jet located in northern Mexico and southwestern Texas. These conditions fit the classic pattern required for the outbreak of severe storms, the LLJ being an important factor in the rapid moisture transport into the storm system (Newton, 1963). The severe weather outbreak for this case devastated the Texas-Oklahoma border region, just south of the warm front, by 0000 GMT 11 April.

Analyses by Zack et al. (1985) and Kocin et al. (1985) and energy diagnostics by Fuelberg and Jedlovec (1982) confirm the existence of an indirect circulation within the exit region of the jet streak in Texas at least through 1800 GMT 10 April. The existence of a LLJ within the exit region of an upper level jet, directed toward the cyclonic side of the flow, is consistent with the coupled jet concept. However, this case differs from the 10 May 1973 study (Uccellini and Johnson, 1979) which involved nearly straight jet flow and no cyclogenesis. Kocin et al. (1985) discuss the impact of the cyclonic curvature in modifying the structure of the transverse circulations.

An important aspect of this case is that 3-h radiosonde data were collected as part of the Severe Environmental Storm And Mesoscale Experiment (SESAME). The 3-h data are now applied to illustrate the rapid evolution of the LLJ which could not be resolved with the 12-h operational network. The development of the LLJ is illustrated on the 305 K isentropic which extends from the planetary boundary layer over southern Texas to the 500 mb level over New Mexico (Fig. 8). Between 1200 and 1500 GMT, only minor wind speed changes occurred over south-central Texas, the wind direction becoming more southerly. At 1800 GMT, wind speeds increase to near 20 m s^{-1} in central Texas. The most dramatic changes, however, occur by 2100 and 0000 GMT 11 April as wind speeds increase to near 25 m s^{-1} in central Texas and then to greater than 30 m s^{-1} in Oklahoma. It thus appears that the development of the LLJ and associated rapid moisture transport occurred within a 6-h period in this case.

Fig. 9 illustrates the ψ_m tendencies and resultant isallobaric winds on the 305 K surface during the period in which the LLJ formed. The 12-h ψ_m tendencies (between 1200 GMT 10 April and 0000 GMT 11 April) indicate only a weakly convergent 1 to 3 m s^{-1} isallobaric wind field during this period. Computing the isallobaric wind with 6-h ψ_m tendencies shows that a stronger isallobaric contribution (greater than 10 m s^{-1}) can be isolated for the second half of the period during the same time the LLJ formed. Computing the isallobaric wind with the 3-h data sets reveals that the convergent nature of the isallobaric wind as well as the largest magnitude (greater than 30 m s^{-1}) amplified between 1800 and 2100 GMT. Furthermore, a complete reversal occurred between 2100 and 0000 GMT as the thunderstorm system developed in northern and north-central Texas. Fig. 9 clearly reveals that 3-h data are necessary to properly resolve these mass adjustments [which Zack et al. (1985) showed, by numerical simulations, to be influenced by jet streak and boundary layer processes]. Trajectories computed by using the explicit approach developed by Petersen and Uccellini (1979) and the 3-h SESAME data show that parcels accelerated dramatically during the period in which the isallobaric forcing was large (Fig. 10). Kocin et al. (1985) found that nearly 85% of the ageostrophic flow that is associated with the parcel accelerations was related to the increase in the isallobaric wind vector between 1800 and 2100 GMT. Fig. 10 also shows trajectories computed by using only the 12-h data which did not resolve the rapid ψ_m changes in Texas (Fig. 9). These parcels (1) did not experience as large an acceleration as that experienced by parcels using the 3-h data, (2) turned more to the right, and (3) did not compare favorably with observations. The difference between the trajectories with and without the 3 h data sets is a measure of the impact that the change in the pressure gradient force (as measured using the SESAME data set) has on the development of the LLJ. This comparison between sets of trajectories confirms the importance of accurately specifying the mass tendency in the lower troposphere by using the 3-h data sets.

To summarize the 10 April 1979 case study:

(1) The LLJ developed rapidly within a 6-h period and was important for the heat and moisture transport into a region in which tornadic storms occurred.

(2) The development of the LLJ was enhanced by the isallobaric contribution to the ageostrophic

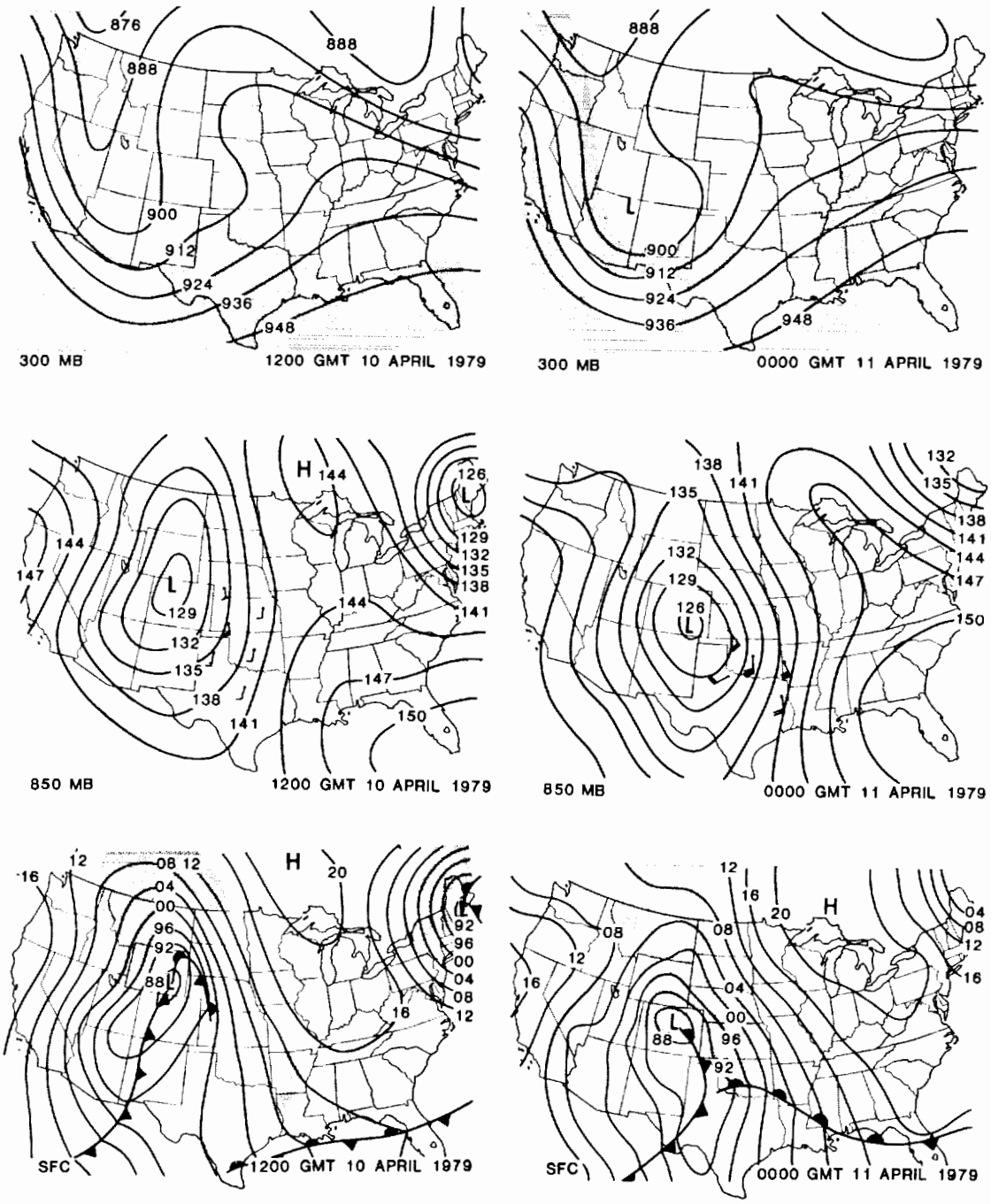

Fig. 7. *Isobaric and surface analyses for 1200 GMT 10 April 1979 (left) and 0000 GMT 11 April 1979 (right). The 300 mb analyses (top) with geopotential height and wind speed (shading for speed >35 m s^{-1}; embedded region of no shading is speed >55 m s^{-1}). The 850 mb analyses (middle) for geopotential height with selected wind barbs (m s^{-1}) indicated. Surface frontal and pressure analyses (bottom).*

wind (i.e., the changing pressure gradient force in the lower troposphere).

(3) The development of the LLJ could not be resolved with the operational 12-h radiosonde network. Twelve-hour data sets were not adequate to represent either the temporal evolution of the wind fields or the changing ψ_m gradient. Three-hour radiosonde data and accurate surface pressure measurements were needed to resolve the forcing of the LLJ for this case.

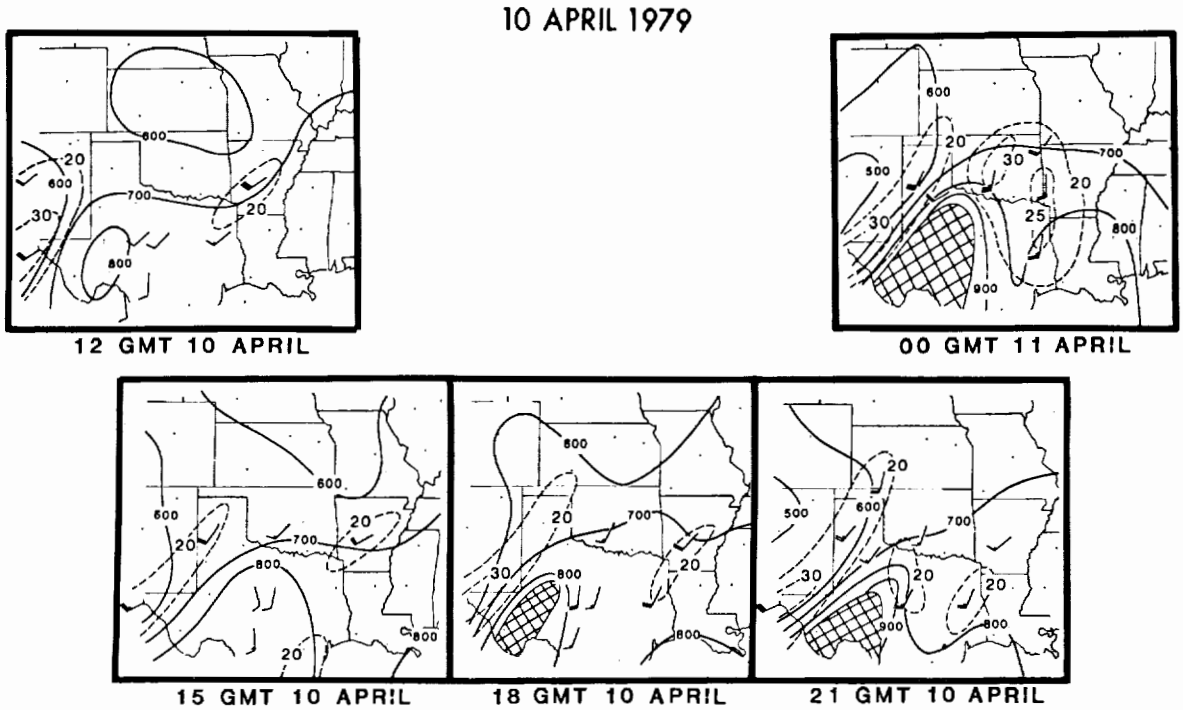

Fig. 8. *The 305 K pressure (solid: 700 = 700 mb) and wind (dashed; m s^{-1}) analyses for 10 April 1979 with times indicated for each panel. Selected wind barbs plotted with standard notation. Shading represents regions where 305 K surface remains beneath the ground.*

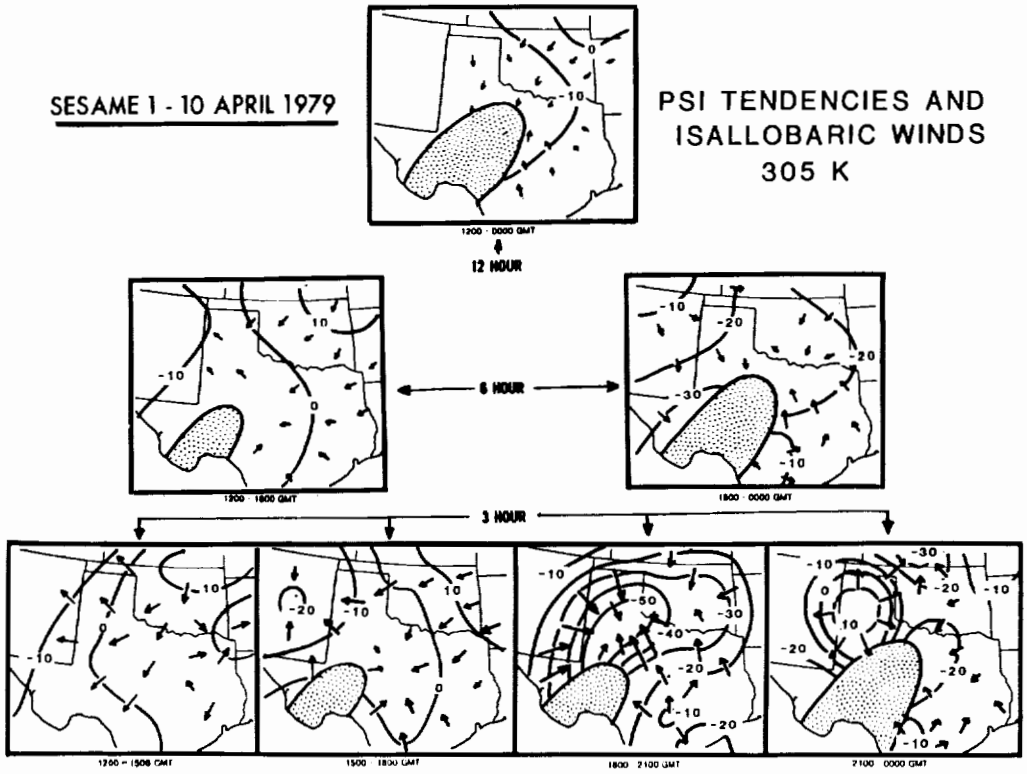

Fig. 9. *Isallobaric wind analysis for 305 K isentopic surface for period between 1200 GMT 10 April and 0000 GMT 11 April 1979. Top: 12-h tendency of Montgomery stream function (ψ) and resultant isallobaric wind vectors. Middle: 6-h ψ tendencies and resultant isallobaric wind vectors. Bottom: 3-h ψ tendencies and resultant isallobaric wind vectors. Times indicated on bottom of each panel. Shading represents regions where 305 K surface remains beneath the ground.*

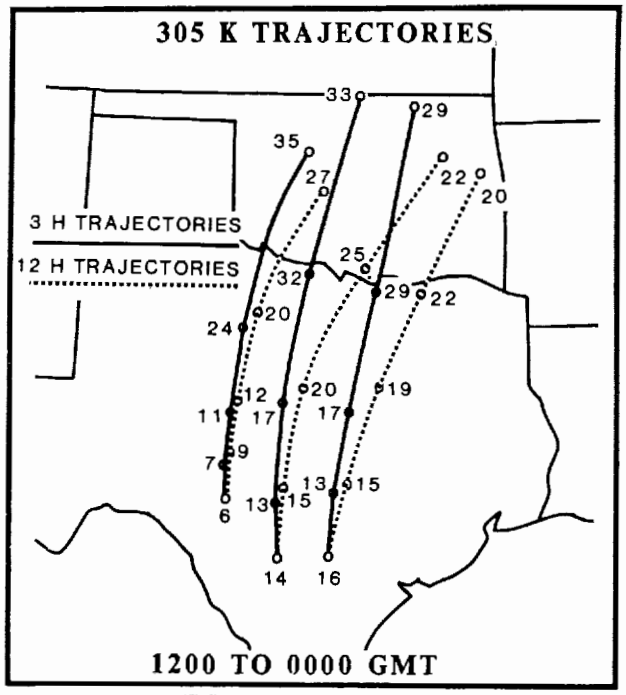

Fig. 10. *Trajectories computed using Petersen and Uccellini's (1979) explicit technique for 305 K surface for 12-h period (1200 GMT 10 April to 0000 GMT 11 April 1979). Solid trajectories using 3-h SESAME data. Dashed trajectories using only 12-h operational radiosonde data. Wind speeds (m s^{-1}) indicated every 3 h.*

4. SUMMARY OF RESULTS

The results of recent numerical simulations and several case studies of transverse circulations show that jet streaks have an important effect upon regional- to mesoscale weather systems. The analyses highlighted in this paper indicate that in terms of geostrophic adjustment concepts, winds are the primary factor in the upper tropospheric adjustment on the regional to mesoscale. However, the mass tendency is of equal importance in the lower tropospheric adjustment. The observational requirements for properly resolving these adjustments are

(1) A spatially uniform data base (100 to 200 km horizontal resolution, 25 mb vertical resolution) that includes accurate wind, temperature, and moisture measurements[2] at the same point and same time and the accurate measurement of surface pressure

(2) An increase in the temporal frequency of data for regional- to mesoscale analysis to a minimum of a 3-h cycle.

These requirements could be met with an enhanced radiosonde network since it is still the only observing system that provides measurements of moisture, temperature, and winds at nearly the same point and same time. Meeting these requirements would make a cheaper radiosonde system a necessity. Nevertheless, this approach would not solve the problem of collecting data over the ocean for the study and prediction of hurricanes and coastal cyclogenesis. The data requirements, therefore, will probably only be met through a careful combination of different observing systems based on remote sensing which supplement the radiosonde network (rather than replace it). The problem in relying on remote sensing to meet all of our requirements is not only a question of accuracy of each measurement; more important is the probability that we will have to rely on a wide range of different observing systems, each with its own strengths, weaknesses, and error characteristics, to provide a data set that spans the entire troposphere with the necessary accuracy for all the parameters. Given these prospects, numerical models will have to be utilized as a basis for the data assimilation on the regional scale to mesoscale much as is now done on the global scale. Therefore, as part of the effort in developing observing systems to meet the data requirements, much research and model development will be required as these observing systems are designed, developed, and applied to the study of regional to mesoscale processes.

[2] Barnes and Lilly (1975) have shown that nearly two-thirds of the variance in water vapor exists at scales less than 200 km for a preconvective environment. In recent numerical experiments, significant differences in the amount and spatial distribution of precipitation produced by a mesoscale model were related directly to the inclusion of detailed mesoscale structure in the initial moisture fields (Perkey, 1980).

ACKNOWLEDGMENTS

This work represents a review, in part, of past work with Paul J. Kocin, Keith F. Brill, and Ralph A. Petersen. The numerous discussions with Daniel Keyser on this topic have also been influential. Thanks to Lafayette Long for his aid in preparing the figures and to Miss Kelly Wilson for typing the manuscript.

REFERENCES

Barnes, S. L., and D. K. Lilly, 1975: Covariance analysis of severe storm environments. Preprints, 9th Conf. on Severe Local Storms, Amer. Meteor. Soc., 301-306.

Beebe, R. G., and F. C. Bates, 1955: A mechanism for assisting in the release of convective instability. Mon. Wea. Rev., 83, 1-10.

Bjerknes, J., 1951: Extratropical cyclones. Compendium of Meteorology, T. F. Malone, Ed., Amer. Meteor. Soc., 577-598.

Bluestein, H., and K. Thomas, 1984: Diagnosis of a jet streak in the vicinity of a severe weather outbreak in the Texas panhandle. Mon. Wea. Rev., 112, 2499-2520.

Bolin, B., 1953: The adjustment of a non-balanced velocity field towards geostrophic equilibrium in a stratified fluid. Tellus, 5, 373-385.

Brill, K. F., L. W. Uccellini, R. P. Burkhart, T. T. Warner, and R. A. Anthes, 1985: Numerical simulations of a transverse indirect circulation and low-level jet in the exit region of an upper-level jet. J. Atmos. Sci., 42, 1306-1320.

Cahir, J. J., 1971: Implications of circulations in the vicinity of jet streaks at subsynoptic scales. Ph.D. thesis, The Pennsylvania State University, 170 pp.

Danielsen, E. F., 1974: The relationship between severe weather, major dust storms and rapid cyclogenesis. Synoptic Extratropical Weather Systems, M. Shapiro, Ed., National Center for Atmospheric Research, 215-241.

Fuelberg, H. E., and G. J. Jedlovec, 1982: A subsynoptic-scale kinetic energy analysis of the Red River Valley tornado outbreak (AVE-SESAME I). Mon. Wea. Rev., 110, 2005-2024.

Keyser, D., and M. J. Pecnick, 1985: Diagnosis of ageostrophic circulations in a two-dimensional primitive equation model of frontogenesis. J. Atmos. Sci., 42, 1283-1305.

_____, and M. A. Shapiro, 1985: A review of the structure and dynamics of upper-level frontal zones. Mon. Wea. Rev. (accepted).

Kocin, P. J., L. W. Uccellini, and R. A. Petersen, 1982: The role of jet streak "coupling" in the development of the 10-11 April 1979 Wichita Falls tornado outbreak. Preprints, 12th Conf. on Severe Local Storms, Amer. Meteor. Soc., 560-563.

_____, L. W. Uccellini, and R. A. Petersen, 1985: Mesoscale aspects of jet streak evolution for a preconvective environment. Archiv. Meteor. Geophy. Bioklim. (submitted).

Maddox, R. A., 1983: Large-scale meteorological conditions associated with midlatitude, mesoscale convective complexes. Mon. Wea. Rev., 111, 1475-1493.

McNulty, R. P., 1978: On upper tropospheric kinematics and severe weather occurrence. Mon. Wea. Rev., 106, 662-672.

Murray, R., and S. M. Daniels, 1953: Transverse flow at entrance and exit to jet streams. Quart. J. Roy. Meteor. Soc., 79, 236-241.

Namias, J., and P. F. Clapp, 1949: Confluence theory of the high tropospheric jet stream. J. Meteor., 6, 330-336.

Newton, C. W., 1954: Frontogenesis and frontolysis as a three-dimensional process. J. Meteor., 6, 330-336.

_____, 1963: Dynamics of severe convective storms. Meteor. Monographs, 5, No. 27, D. Atlas, Ed., Amer. Meteor. Soc., 33-55.

Pagnotti, V., and L. F. Bosart, 1984: Comparative diagnostic case study of East Coast secondary cyclogenesis under weak versus strong synoptic-scale forcing. Mon. Wea. Rev., 112, 5-30.

Palmen, E., and C. W. Newton, 1969: Atmospheric Circulation Systems. Academic Press, New York.

Perkey, D. J., 1980: Impact of moisture on regional scale numerical model simulations. Atmospheric Water Vapor, A. Deepak, T. D. Wilkerson, and L. H. Ruhnke, eds., Academic Press, 513-526.

Petersen, R. A., and L. W. Uccellini, 1979: The computation of isentropic atmospheric trajectories using a "discrete model" approach. Mon. Wea. Rev., 107, 566-574.

Reiter, 1969: Tropopause circulation and jet streams. World Survey of Climatology, Vol. 4: Climate of the Free Atmosphere, D. F. Rex, ed., Publisher, 85-193.

Riehl, H., et al., 1952: Forecasting in the middle latitudes. Meteor. Monogr., No. 5, Amer. Meteor. Soc., 80 pp.

Rossby, C. G., 1938: On the mutual adjustment of pressure and velocity distributions in certain simple current systems II. J. Mar. Res., 7, 239-263.

Sechrist, F. S., and T. M. Whittaker, 1979: Evidence of jet streak vertical circulations. Mon. Wea. Rev., 107, 1014-1021.

Shapiro, M. A., 1981: Frontogenesis and geostrophically forced secondary circulations in the vicinity of jet stream-frontal zone systems. J. Atmos. Sci., 38, 954-973.

Uccellini, L. W., and D. R. Johnson, 1979: The coupling of upper and lower tropospheric jet streaks and implications for the development of severe storms. Mon. Wea. Rev., 107, 682-703.

_____, P. J. Kocin, C. H. Wash, and K. F. Brill, 1984: The Presidents' Day cyclone of 18-19 February 1979: Synoptic overview and analysis of the subtropical jet streak influencing the pre-cyclogenetic period. Mon. Wea. Rev., 112, 31-55.

Washington, W., 1964: A note on the adjustment towards geostrophic equilibrium in a simple fluid system. Tellus, 16, 530-534.

Zack, J. W., M. L. Kaplan, and V. C. Wong, 1985: Numerical simulations of the subsynoptic features associated with the AVE-SESAME I case. Part I: The preconvective environment. Mon. Wea. Rev. (accepted).

THE IMPACT OF MESOSCALE DATA ON THE SIMULATION OF A MESOSCALE CONVECTIVE WEATHER SYSTEM

J. M. Fritsch and D.-L. Zhang

Department of Meteorology
The Pennsylvania State University
University Park, PA 16802

1. INTRODUCTION

Since the advent of numerical weather prediction in the 50's, numerical models have evolved from simple, quasi-geostrophic barotropic systems for limited domains to highly sophisticated, primitive-equation models that include numerous additional physical processes and make predictions for the entire globe. (See Anthes, 1983, for a recent review of numerical models.) During this evolutionary time period, the predictive skills of operational models and their derivative products have increased considerably (Fawcett, 1977; Sanders, 1979; Charba and Klein, 1980; Ramage, 1982). Increases in model skill are, to a large degree, dependent upon improvements in three factors:

1. Model physics
2. Computer power, and
3. Initial conditions.

Of these three, the first two have progressed fairly rapidly whereas, on the other hand, progress in obtaining better initial conditions has been relatively slow. It is almost paradoxical that this is true since there have been great strides in observational technology during the same period that numerical modeling has progressed so quickly. (See Decker et al., 1978; Phillips et al., 1979; Smith et al., 1979; 1981; Little, 1982; Gage and Green, 1982; Hogg et al., 1983; Westwater, et al., 1985.) The difficulty seems to be that each new observing system has one or more of the following problems:

1. Data are generated in a form not readily useable in numerical models

2. Vertical resolution is inadequate

3. Data are not always available and

4. The observing system only covers a fraction of the required area and it is prohibitively expensive to establish a dense network.

Nevertheless, as numerical models become more sophisticated, evidence continues to mount that a substantial improvement in forecasting skill would result if better initial data were available.

The objectives of this paper are (1) to demonstrate the sensitivity of a numerical simulation of a mesoscale convective weather system to the initial conditions, and (2) to provide further evidence of the need for a high resolution observing system that is compatible with numerical-model initial data requirements. To this end, a series of nine numerical-model sensitivity experiments were conducted in which one or more variables from one or more observations (soundings) were omitted and/or adjusted in the model initialization. Two types of soundings were available for manipulation in the sensitivity experiments. Specifically, for the particular event being simulated (the 1977 Johnstown flash flood), an independent mesoanalysis was available from Bosart and Sanders (1981). In his analysis, Bosart produced a fine-resolution three-dimensional array of data from which soundings that helped to define mesoscale features could be extracted. These "nonconventional" soundings were added to the conventional sounding data routinely available for model initialization.

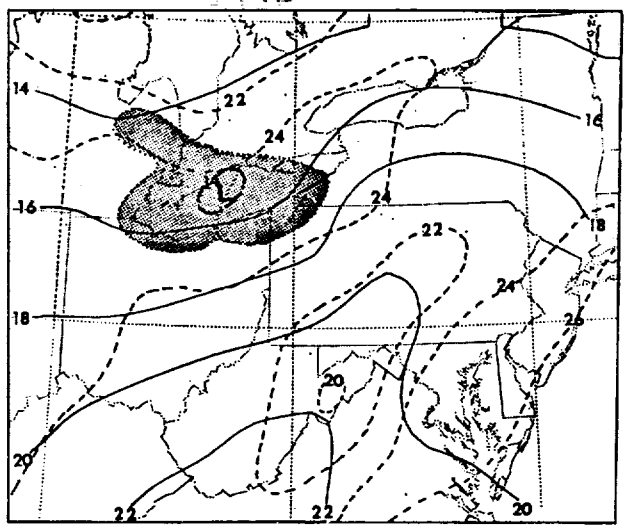

Fig. 1 Analysis of sea-level pressure (solid lines, mb) and surface temperature (dashed lines, °C) at 1200 GMT 19 July 1977. Shading denotes the area of active convection. Dot-dashed line over Lake Erie indicates isobar from Bosart and Sanders' (1981) analysis.

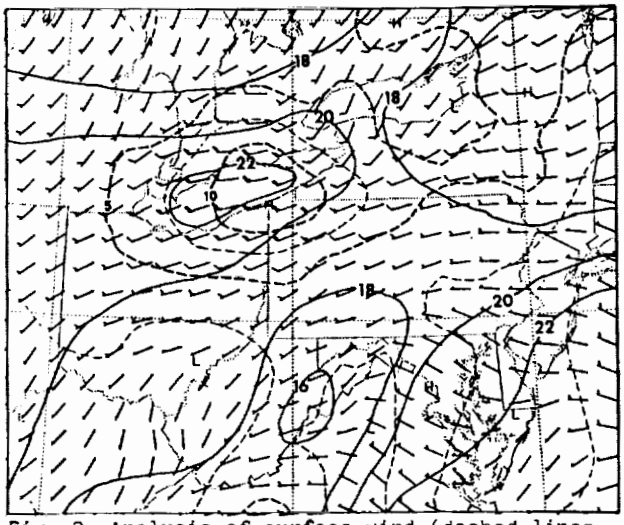

Fig. 2 Analysis of surface wind (dashed lines are isotachs, m s^{-1}) and surface dewpoint (solid lines, ^{o}C) at 1200 GMT 19 July 1977. A full barb is 5 m/s.

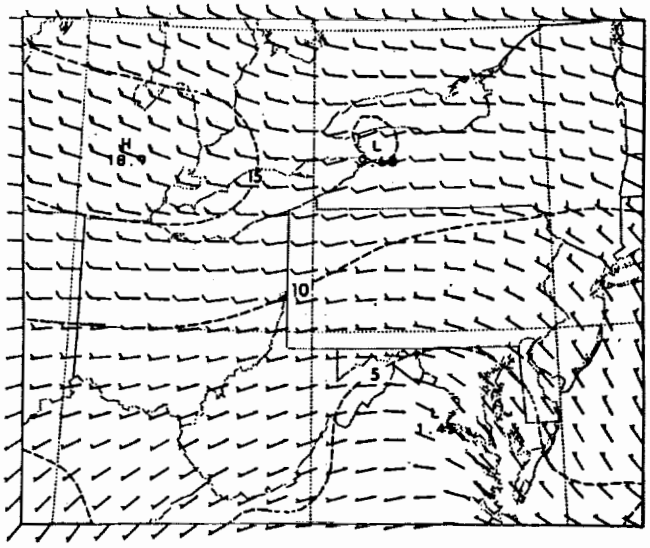

Fig. 3 Analysis of 900 mb wind field (m s^{-1}) at 1200 GMT 19 July 1977. All soundings, conventional and nonconventional, are included in the analysis.

Only the results of two of the experiments will be presented here. Specifically, the sensitivity of the evolution of the convective system to the resolution of the mesoscale moisture and wind fields is examined. A modified version of the Anthes and Warner (1978) model is used for all the experiments; see Zhang (1985) for a description of the modifications.

2. INITIAL CONDITIONS

Figures 1 and 2 show the initial surface conditions for the "control" simulation. In this simulation, all the conventional and nonconventional soundings were used to initialize the model. Figure 3 shows the initial 900 mb wind field for the control simulation while Fig. 4 shows the same field when the wind information

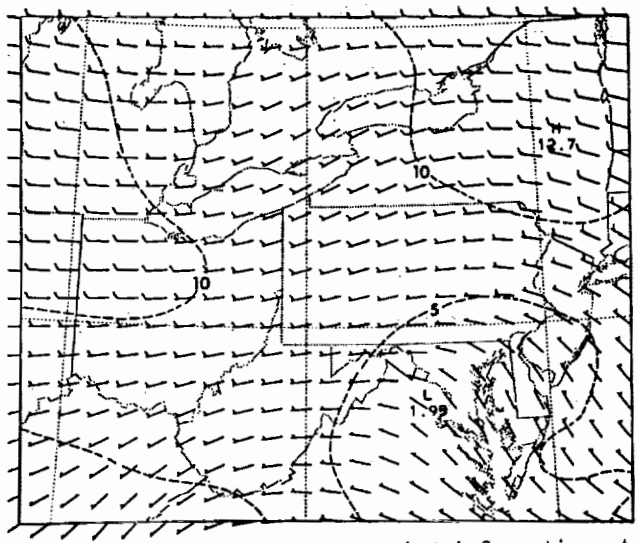

Fig. 4 Same as Fig. 3 except wind information at all nonconventional soundings and at Flint, Michigan sounding is excluded.

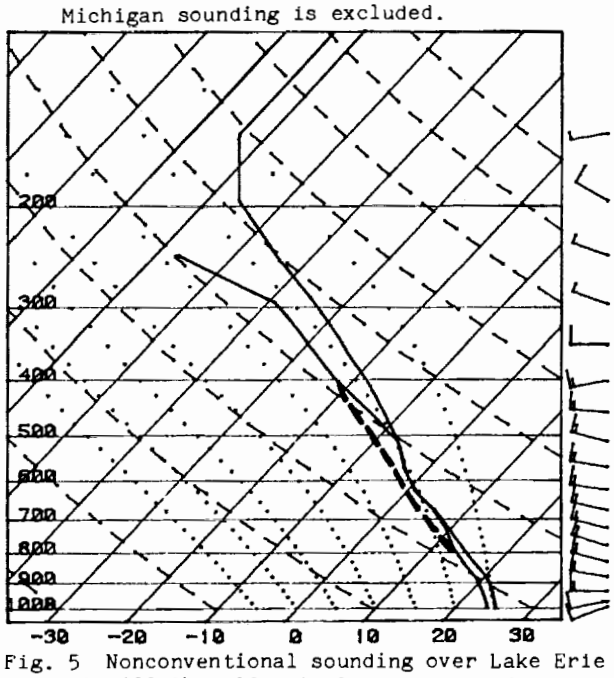

Fig. 5 Nonconventional sounding over Lake Erie at 1200 GMT, 19 July 1977. Heavy dashed line indicates slight drying artificially imposed on sounding for moisture sensitivity experiment.

from all the nonconventional soundings and the Flint, Michigan sounding is omitted. Note the substantial weakening and southward shift of the low-level jet that was over Michigan and the eastern Great Lakes. Sections 3.1 and 3.2 describe the results of simulating the convective event by using these two sets of initial conditions.

Figure 5 shows the nonconventional sounding that was available for over Lake Erie. Section 3.3 describes the results of simulating the convective event when the moisture in this single sounding is reduced slightly in the 700-500 mb layer (see dashed line in Fig. 5). All other conditions were kept the same as in the control simulation.

3. RESULTS OF SENSITIVITY EXPERIMENTS

3.1 Control Simulation

The control simulation is described in detail in Zhang (1985) and Zhang and Fritsch (1985). For lack of space, only a portion of the evolution of the surface features and the convection is presented here (see Figs. 6-9). However, these few figures are sufficient as a basis for comparison with the results obtained from the runs with adjusted initial conditions. In this control simulation, note that the area of deep convection initially over Lake Erie (Fig. 1) elongates into a NE-SW-oriented line and propagates eastward across Pennsylvania. At 0000 GMT (Fig. 9), only the northeastern portion of the line remains active. Note also that by 1800 GMT (Fig. 7), convection has redeveloped over northwestern Pennsylvania and that a distinct mesolow has formed in the same region. This mesolow and associated area of deep convection also propagates eastward as yet a third region of deep convection develops over western Pennsylvania (see Figs. 7, 8 and 9). The total precipitation (i.e., from both convective and stratiform clouds) for the 12-h period is shown in Fig. 10.

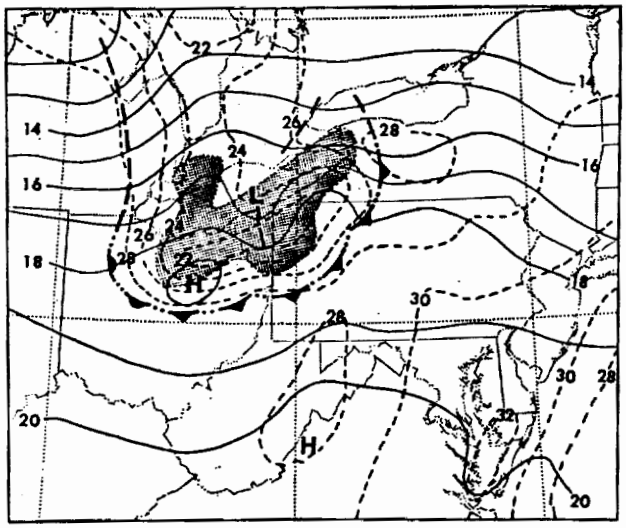

Fig. 6 Analysis of sea-level pressure (solid lines, mb) and surface temperature (dashed lines, °C) for 3 h forecast verifying at 1500 GMT 19 July 1977. Heavy dashed lines indicate troughs. Cold and warm-frontal symbols alternated with double dots indicate moist-downdraft outflow boundaries.

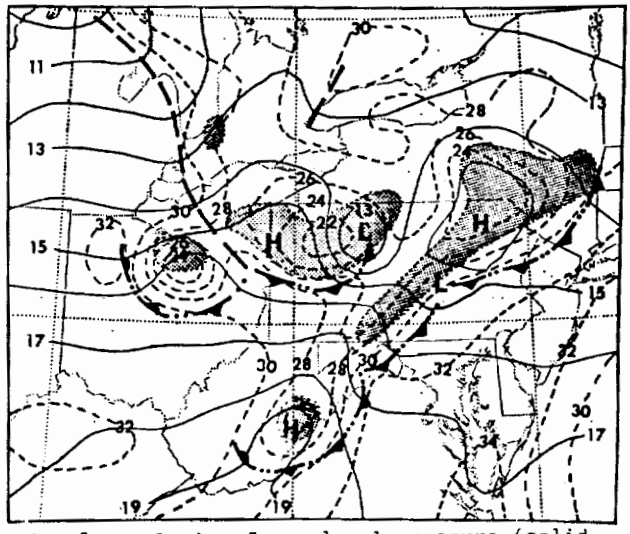

Fig. 8 Analysis of sea-level pressure (solid lines, mb) and surface temperature (dashed lines, °C) for 9 h forecast verifying at 2100 GMT 19 July 1977.

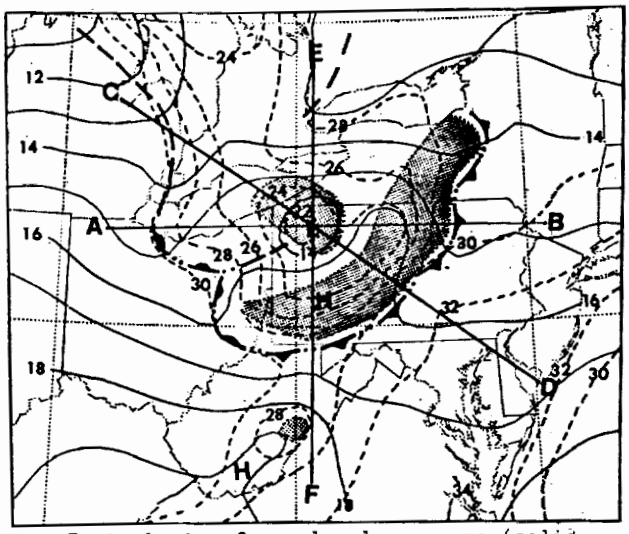

Fig. 7 Analysis of sea-level pressure (solid lines, mb) and surface temperature (dashed lines, °C) for 6 h forecast verifying at 1800 GMT 19 July 1977.

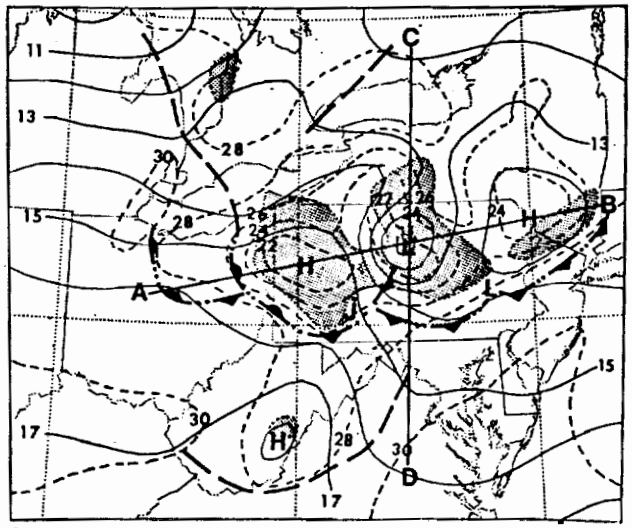

Fig. 9 Analysis of sea-level pressure (solid lines, mb) and surface temperature (dashed lines, °C) for 12 h forecast verifying at 0000 GMT 20 July 1977.

3.2 Sensitivity to Wind Data

In this experiment, the wind information from all the nonconventional soundings and the Flint, Michigan sounding was omitted from the model initial conditions. Figures 11 and 12 show the evolution of the surface pressure and temperature fields, along with the locations of active convection. Note that at six h into the simulation (Fig. 11), the pressure, temperature and convective patterns are more "chaotic" than in the control run (Fig. 7), and that the area of convection over West Virginia is considerably larger. In general though, the pattern of deep convection is basically the same. By 0000 GMT, the general pattern is still very similar to the control run (compare Figs. 9 and 12); however, it is also apparent that there are significant differences as well. Specifically, the weakening and southward shift of the low-level jet seems to have slowed the entire evolution of events and also shifted the main area of convection from western Pennsylvania westward into Ohio. Notice also that the area of convection over West Virginia continues to be significantly larger than in the control run and that the active convection in the SW-NE line is farther south. Finally, it is evident from comparing Figs. 10 and 13 that the general precipitation patterns are very similar; the slowing of the system and the southward shift of the convection have produced only minor changes in the pattern.

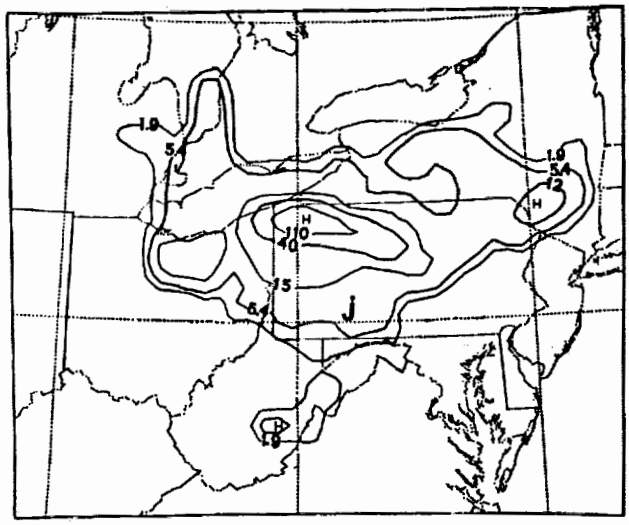

Fig. 10 Predicted accumulated rainfall (mm) for 1200 GMT 19 July 1977 to 0000 GMT 20 July 1977.

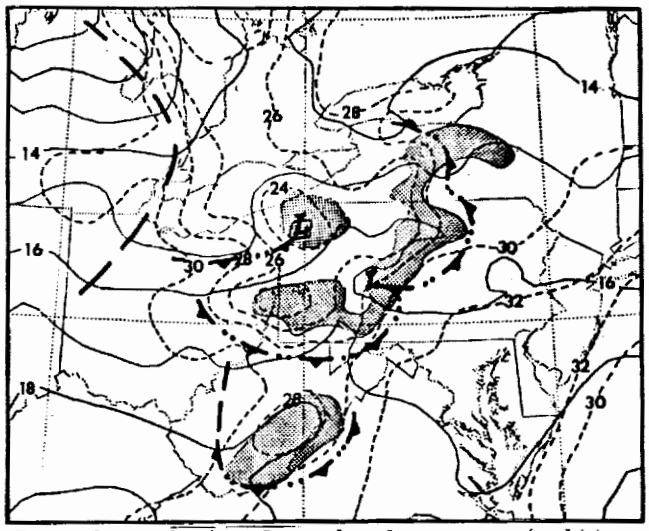

Fig. 11 Analysis of sea-level pressure (solid lines, mb) and surface temperature (dashed lines, ^{o}C) for 6 h forecast. Wind information in the model initialization was eliminated from all nonconventional soundings and the Flint, Michigan sounding.

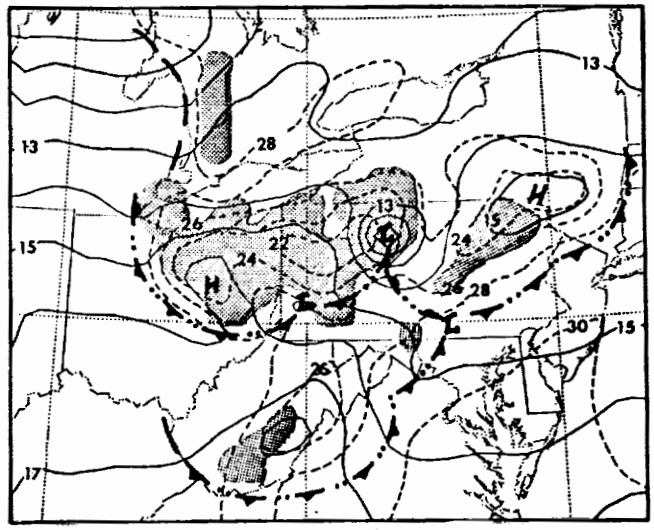

Fig. 12 Analysis of sea-level pressure (solid lines, mb) and surface temperature (dashed lines, ^{o}C) for 12 h forecast. Wind information in the model initialization was eliminated from all nonconventional soundings and the Flint, Michigan sounding.

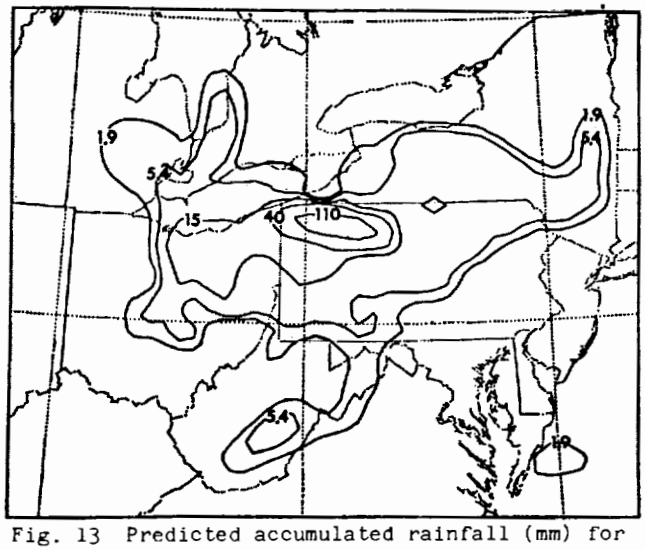

Fig. 13 Predicted accumulated rainfall (mm) for 1200 GMT 19 July 1977 to 0000 GMT 20 July 1977, for simulation where wind information is excluded from initial conditions.

3.3 Sensitivity to Moisture

In this experiment, the impact of drying slightly the 700-500 mb layer at a crucial location (with respect to the area of initial convection) is considered (see Fig. 5). Figures 14 and 15 show the evolution of the surface temperature and pressure and the areas of active convection. In this simulation, the mesolow and associated area of deep convection did not develop as they did in the control run. In place of the mesolow, a strong mesohigh dominates all of western Pennsylvania. The pool of cool moist-downdraft air is more extensive than in the control run, and the temperature gradient behind the outflow boundary is stronger. By 0000 GMT (Fig. 15), the line of convection has moved rapidly eastward, faster than in the control run, and the deep mesolow of the control run is replaced by a very minor low pressure center located considerably farther to the east. Instead of the convection persisting in western Pennsylvania, it redevelops over Ohio along the northwestern flank of the mesohigh outflow boundary. Figure 16 shows the precipitation for this simulation. Although the general pattern is similar to the control run in some respects, it is extremely significant that the very heavy rainfall over western Pennsylvania is absent and the heaviest rainfall is now in Ohio.

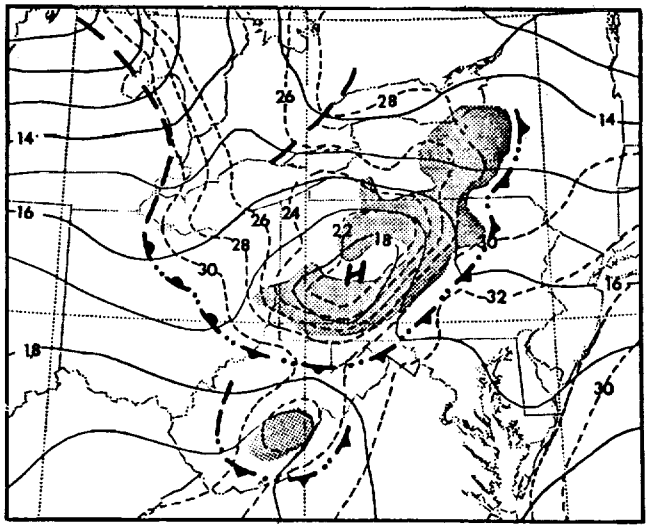

Fig. 14 Analysis of sea-level pressure (solid lines, mb) and surface temperature (dashed lines, °C) for 6 h forecast. Moisture in the nonconventional sounding over Lake Erie is reduced slightly in the 700-500 mb layer.

4. CONCLUSIONS AND DISCUSSION

Based upon numerical model sensitivity experiments on the Johnstown flood event, it appears that numerical prediction of the evolution of mesoscale convective systems is very sensitive to "mesoscale" information about the initial moisture field but only moderately sensitive to omission of information about the mesoscale wind field. It is important to point out that the extreme sensitivity to the moisture field is probably very "event dependent". Specifically, the large differences that occurred when the moisture was adjusted in the nonconventional sounding over Lake Erie primarily resulted from the occurrence or non-occurrence of a warm core vortex (see

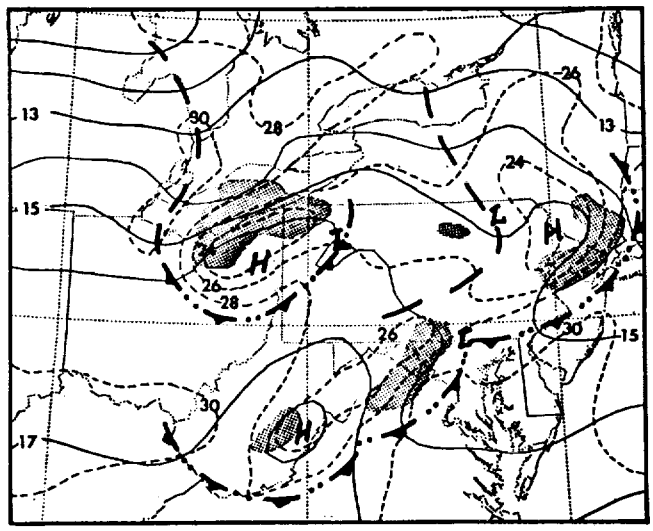

Fig. 15 Analysis of sea-level pressure (solid lines, mb) and surface temperature (dashed lines, °C) for 12 h forecast. Moisture in the nonconventional sounding over Lake Erie is reduced slightly in the 700-500 mb layer.

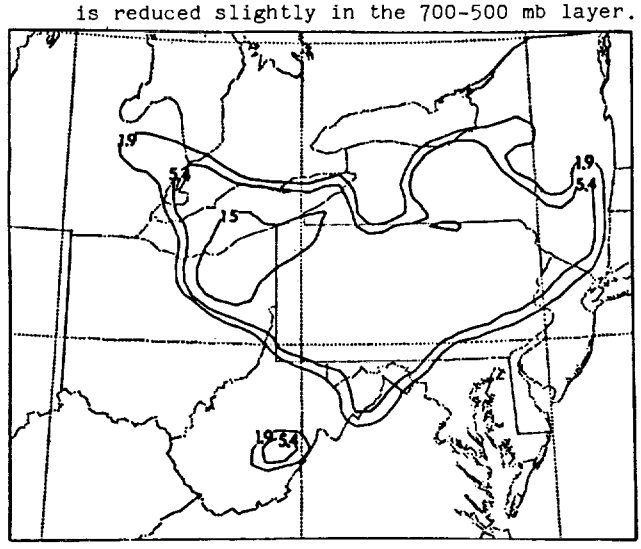

Fig. 16 Predicted accumulated rainfall (mm) for 1200 GMT 19 July to 0000 GMT 20 July 1977 for the simulation where the moisture in the Lake Erie sounding is slightly reduced in the 700-500 mb layer.

Zhang, 1985; Zhang and Fritsch, 1985b). There apparently is a "threshold moisture structure" in this case which after it is reached, warm-core mesocyclogenesis ensues. Since the vortex becomes quite strong, whether it occurs has a large impact on the evolution of events. Johnston (1981) noted the relatively frequent development of such vortices in conjunction with mesoscale convective complexes. In the case of the Johnstown flood, the convective system drifted off the East Coast and developed into a tropical storm (Bosart and Sanders, 1981). This condition

suggests that the observed and simulated mesolow probably was a warm core vortex. Moreover, in the recently conducted Pre-STORM Experiment, an aircraft penetration of such a vortex (over land) confirmed that these vortices are indeed warm core (D. Rodgers, contributing scientist, Pre-STORM Experiment, 1985; personal communication). Therefore, successful prediction of the evolution of mesoscale convective weather systems may hinge upon a model's ability to determine whether warm-core mesocyclogenesis will occur, and this condition seems to depend strongly upon resolving (or predicting) the mesoscale structure of the moisture field.

As mentioned above, the simulation was only moderately sensitive to alterations in the wind field. In fact, based upon the results of sensitivity experiments not presented here, the omission of wind data from any particular sounding did not have an appreciable effect on the evolution of the convection. Only when the wind data was omitted at many soundings so as to substantially alter an entire mesoscale feature (as shown in Figs. 3 and 4), did a significant effect result. This is probably because the mass field acts to restore the basic wind pattern when only wind information is left out. If the mass field were unavailable, and only wind information could be used in the initialization (i.e., the mass field is estimated from the wind field), then omission of wind information would likely have a much more substantial impact. The relative insensitivity of the wind field is in sharp contrast to the moisture field where no such balancing or restoring effect exists. It is noteworthy that Carpenter and Lowther (1982) found a similar result in their studies of the sensitivity of sea-breeze circulations to changes in the initial wind and temperature fields. Alteration of the wind field had little effect on the outcome of their simulations whereas temperature changes had a substantial impact on the results. Perhaps, for convective circulations, the thermodynamics are more important than the dynamics.

ACKNOWLEDGMENTS

This work was supported by USAF Grant AFOSR-83-0064; NSF Grants ATM-8218208, ATM-8113223 and NOAA Cooperative Agreement No. NA82AA-H-00027. Ms. Sue Frandsen quickly and skillfully prepared the manuscript. The authors are grateful to Lance Bosart for providing the mesoscale data set used in the initialization of the model.

REFERENCES

Anthes, R.A., 1983: Regional models of the atmosphere in middle latitudes. Mon. Wea. Rev., 111, 1306-1335.

_____ and T.T. Warner, 1978: Development of hydrodynamic models suitable for air pollution and other mesometeorological studies. Mon. Wea. Rev., 106, 1045-1078.

Bosart, L.F. and F. Sanders, 1981: The Johnstown flood of July 1977: A long-lived convective storm. J. Atmos. Sci., 36, 1616-1642.

Carpenter, K.M. and L.R. Lowther, 1982: An experiment on the initial conditions for a mesoscale forecast. Q. J. R. Meteor. Soc., 108, 643-660.

Charba, J.P. and W.H. Klein, 1980: Skill in precipitation forecasting in the National Weather Service. Bull. Amer. Meteor. Soc., 61, 1546-1555.

Decker, MT., E.R. Westwater and F.O. Guiraud, 1978: Experimental evaluation of ground-based microwave radiometric sensing of atmospheric temperature and water vapor profiles. J. Appl. Meteor., 17, 1788-1795.

Fawcett, E.B., 1977: Current capabilities in prediction at the National Weather Service National Meteorological Center. Bull. Amer. Meteor. Soc., 58, 143-149.

Gage, K.S. and J.L. Green, 1982: A technique for determining the temperature profile from VHF radar observations. J. Appl. Meteor., 21, 1146-1149.

Hogg, D.C., M.T. Decker, F.O. Guiraud, K.B. Earnshaw, D.A. Merritt, K.P. Moran, W.B. Sweezy, R.G. Strauch, E.R. Westwater and C.G. Little, 1983: An automatic profiler of the temperature, wind, and humidity in the troposphere. J. Climate Appl. Meteor., 22, 807-831.

Johnston, E.C., 1981: Mesoscale vorticity centers induced by mesoscale convective complexes. M.S. Thesis, Univ. of Wisconsin, 54 pp.

Little, C.G., 1982: Ground-based remote sensing for meteorological nowcasting. Nowcasting. K.A. Browning, Ed., Academic Press, 65-85.

Phillips, N.A., L.M. McMillin, D.Q. Wark and A. Gruber, 1979: An evaluation of early operational temperature soundings from TIROS-N. Bull. Amer. Meteor. Soc., 60, 1188-1197.

Ramage, C.S., 1982: Have precipitation forecasts improved? Bull. Amer. Meteor. Soc., 63, 739-743.

Sanders, F., 1979: Trends in skill of daily forecasts of temperature and precipitation 1966-78. Bull. Amer. Meteor. Soc., 60, 763-769.

Smith, W.L., M. Woolf, C.M. Hayden, D.Q. Wark and L.M. McMillin, 1979: The TIROS-N operatioal vertical sounder. Bull. Amer. Meteor. Soc., 60, 1177-1187.

_____, V.E. Suomi, W.P. Menzel, H.M. Woolf, L.A. Sromovsky, H.E. Revercomb, C.M. Hayden, D.N. Erickson and F.R. Mosher, 1981: First sounding results from VAS-D. Bull. Amer. Meteor. Soc., 62, 232-236.

Westwater, E.R., W. Zhenhui, N.C. Grody and L.M. McMillin, 1985: Remote sensing of temperature profiles from a combination of observations from the satellite-based microwave sounding unit and the ground-based profiler. J. Atmos. and Oceanic Tech., 2, 97-109.

Zhang, D.-L., 1985: Nested-grid simulation of the mesoscale structure and evolution of the Johnstown flood of July 1977. Ph.D. Dissertation. The Pennsylvania State Univ., 270 pp.

_____ and J.M. Fritsch, 1985: Numerical simulation of a meso- scale warm-core vortex over land. AMS Preprints, 14th Conf. on Severe Local Storms, Oct. 29-Nov. 1, Indianapolis, Ind., J29-32.

DEPARTMENT OF DEFENSE OPERATIONAL APPLICATIONS OF WIND MEASUREMENTS

Allan C. Ramsay, Colonel, USAF

Office of the Under Secretary of Defense for
Research and Engineering, Washington, D.C., USA

1. INTRODUCTION

A stated objective for this symposium is to identify requirements for global wind measurements. This paper will draw from recent reports which considered the impact of over 100 environmental factors known to affect military operations. A conclusion that can be drawn from those analyses is that one environmental factor, ATMOSPHERIC WIND, has an operational impact on each of the 48 mission areas examined. This paper will characterize the impact of WIND on the various mission areas and will define and summarize both "technical" and "operational" requirements for WIND intelligence.

2. ENVIRONMENTAL FACTORS IMPACTING THE DEPARTMENT OF DEFENSE

Military operations are affected by a wide range of environmental elements. Analyses conducted by Army, Navy, and Air Force agencies in 1984 and 1985 (Abrams, et. al., 1984; Brown and McCandless, 1985) considered the impacts of some 19 atmospheric and oceanographic factors on Navy mission areas, some 52 atmospheric/topographic and 61 solar/space-environmental factors on Army and Air Force operations. The atmospheric environmental factors are listed in Table 1. The impact of "wind" was carefully considered by all three Services, and it is, therefore, possible to report qualitative estimates of the sensitivity of various military activities to that particular environmental element.

3. APPLICATIONS OF WIND OBSERVATIONS

3.1 Meteorological Uses

The Department of Defense (DoD) has no meteorological uses for global wind measurements. This is hardly an assertion with which to begin a paper on DoD requirements for global wind measurements - it is technically true because, within the DoD, meteorology is a support activity, and ALL applications of global wind measurements must finally be traceable to an operational mission; and every activity of DoD environmental-support specialists must finally be traceable directly to a formal military mission area.

3.2 Operational Uses of Wind Intelligence

Environmental intelligence is a part - sometimes a small part, but frequently the critical part - of the decision process in virtually every military operation. Mission-area studies have shown that WIND has operational impacts of varying degree on virtually every activity of the DoD. For the purposes of this paper, the obvious impact of severe weather (damaging winds associated with tropical storms, thunderstorms, and tornadoes) will not be discussed; it is sufficient to say that resource protection is an extremely important aspect of every mission area, and is a serious responsibility of all levels of military command - wind measurements on LOCAL, REGIONAL, and GLOBAL scales are required to assess and to forecast damaging weather conditions. The list of truly "all-weather" weapons systems has yet to receive its first entry, because neither ships nor planes operate effectively in tornadoes or typhoons, and because tanks still cannot operate in floods.

Table 1.Atmospheric Factors Impacting Military Operations

Temperature	Ceiling Height	Precipitation Phase	Airframe Icing
Moisture	Cloud Type	Precipitation Rate	
Pressure	Cloud Phase	Precipitation Accumulation	Aerosol Character
Horizontal Wind Velocity	Cloud Liquid Water Content		Aerosol Concentration
Vertical Wind Velocity	Cloud Drop-Size Distribution	Visibility	
Boundary-Layer Wind Variability	Height of Cloud Base	Visible Attenuation	
Boundary-Layer Wind Gusts	Height of Cloud Top	IR Attenuation	Atmospheric Chemistry
	Cloud-Free-Line-of-Sight	Radio Attenuation	
		Visible Effective Range	Synoptic/Air Mass Character
Lightning	Inversion Height	IR Effective Range	Synoptic/Frontal Position
Severe Weather	Mixing Depth	Refractive Index	
Tropical Storm Location		Scintillation	
Tropical Storm Intensity	Contrails		
	Airframe Turbulence		

Table 2 presents a consolidated listing of some 32 DoD mission areas. This listing is a composite of the original 48 mission areas reported in the reference documents. The table indicates a subjective assessment of the relative sensitivity of that mission area to the effects of wind. (Although the mission areas listed refer specifically to Army, Navy, and Air Force, the sensitivities also apply to analogous and operationally identical Marine Corps operations.) There are cases where all Services perform operations in a specific mission area; for example; Tactical Air Strike Warfare includes Navy and Marine operations under that name, Army "aviation" operations, and Air Force "close air support" and "interdiction" operations. Where more than one Service reported a sensitivity to WIND in a given mission area, the highest sensitivity is listed in the table.

Table 2. Sensitivity of DoD Mission Areas to Atmospheric Wind

H = HIGH M = MODERATE L = LOW

MISSION AREA	SENSITIVITY TO WIND:		
	H	M	L
Aerial Refueling		M	
Air Defense		M	
Amphibious Warfare	H		
Anti-Air Warfare			L
Anti-Submarine Warfare		M	
Anti-Surface Ship Warfare	H		
Ballistic Missile Warning			L
Close Combat - Light		M	
Close Combat - Heavy			L
Combat Support, Engineering			L
Command and Control	H		
Communications			L
Electronic Warfare		M	
Fire Support (Artillery)		M	
Flying Training		M	
Intelligence/Surveillance		M	
Inter-theater Airlift		M	
Intra-theater Airlift		M	
Logistics: resupply, repair	H		
Mine Warfare (Land)			L
Mine Warfare (Sea)		M	
Nuclear, Biological, Chemical	H		
Rescue and Recovery	H		
Research, Development, Test & Evaluation		M	
Space Launch and Orbital Support	H		
Space Negation			L
Space Surveillance and Protection	H		
Special Operations	H		
Strategic Strike: Airborne		M	
Strategic Strike: Land-based	H		
Strategic Strike: Sea-based		M	
Tactical Air Strike Warfare	H		

4. DEPARTMENT OF DEFENSE TECHNICAL REQUIREMENTS

A typical description of a "requirement" for meteorological data would include:

- **The atmospheric element ("wind", ... or perhaps, horizontal wind vector, . . .or perhaps vertical wind component, etc.)**
- **The minimum-necessary horizontal and vertical granularity of data values**
- **The minimum-necessary temporal granularity of data values**
- **The minimum-necessary accuracy of the data values.**

We recognize a close relationship between the spatial and temporal scales of measurement: it is clear that we would have little operational use for wind measurements taken with 2000-kilometer horizontal spacing over the northern hemisphere every 20 seconds, or for measurements taken with 100-meter horizontal spacing once a month. Some understanding of the representativeness of individual observations is important in evaluating their usefulness for operations. One of our greatest continuing difficulties lies in specifying accurate "technical" requirements, because we have only a poor understanding of the natural variability of the elements we are concerned with. A typical (un-answerable) question that may be asked of a military meteorologist is, "You say you've measured the wind at point X,Y,and Z and time TTTT. What is the wind at point X1,Y1, and Z1 at the same time - and what was the wind at point X,Y, Z two-and-a-half hours before you measured it?

Regardless of such difficulties, we are able to specify many of our needs for measurements as they relate to specific operational applications.

4.1 Tactical Requirements

Typical requirements for wind measurements, provided in-theater, either directly to a system operator, or to a directly assigned environmental support specialist, or to a regional analysis-and-forecasting center, are listed below Exceptions to these requirements exist for extremely small-scale operations associated with toxic chemical spills, chemical-defense actions, or, perhaps, laser operations.

Element:	Horizontal Wind Component
Horizontal Resolution:	1 km, surface to 10 km over land
	10 km, surface over oceans
	50 km, above 10 km
Vertical Resolution:	30 m, surface to 1 km
	300 m, 1 km to 10 km
	600 m, 10 km to 20 km
Accuracy:	2 m/sec or 5% of true speed
	5 degrees of true direction
Frequency	15 min 1 hr, surface to 10 km
	3 hr, 10 km to 20 km

4.2 Centralized Requirements

Requirements for information delivered routinely to weather centrals are similar, but somewhat less stringent in horizontal resolution and frequency.

Element:	Horizontal Wind Component
Horizontal Resolution:	25 km, surface wind only, over ocean 100 km
Vertical Resolution:	30 m, surface to 1 km 300 m, 1 km to 10 km 600 m, 10 km to 60 km
Accuracy:	2 m/sec or 5% of true speed, 0-15 km 3 degrees of true direction, 0-15 km 10% of true speed, 15-60 km 5 degrees of true direction, >15 km
Frequency:	3 hr

5. DEPARTMENT OF DEFENSE OPERATIONAL REQUIREMENTS

5.1. Definition

The "technical" descriptors of an environmental-support requirement include many of the characteristics being discussed in this conference: an atmospheric observable (wind), spatial and temporal scales of measurement, accuracy and precision of observations. However, because environmental intelligence is an important support tool for operational decisions, the Department of Defense finds that the descriptors of a "requirement" go far beyond the purely technical aspects: a support requirement must be described in terms relevant to the OPERATIONAL DECISION to which the intelligence will be applied. In fact, the "scale size" to which we refer is more appropriately thought of as the scale size of the OPERATIONS rather than the scale size of the measurements.

Environmental intelligence is used in an operational sense as an input to command decisions: when to launch a satellite, which weapon systems to employ, where and how to move troops and equipment. Indeed, in the list of descriptors given below, the "operational" characteristics out-weigh the "technical" characteristics to the extent that, if a compromise is necessary, we must first compromise the technical characteristics: DoD environmental-support agencies and operational decision-makers recognize that even degraded environmental intelligence - delivered at the right place and at the right time- is of far more value than the world's finest data set which first becomes available after the planes or ship or tanks have been launched on a mission. So, while we carefully calculate the necessary spatial and temporal resolution, and the accuracy and precision we need in our observations, we are continually aware of the overriding need to deliver a product (albeit of degraded quality) to the right place, in operationally-significant terms, and in a timely manner.

The primary "operational" descriptors of the DoD requirements are the location of the measurement, the point of delivery of the observations, and the urgency of delivery.

5.2 Location

Department of Defense organizations have global missions; they may be called on to act at any point on the globe, and with very short notice. The most demanding requirement we have for environmental measurements is that they be available from literally anywhere, at any time, most often, the locations from which we need measurements are either REMOTE or are in DENIED territory. Throughout modern history, combatant nations have gone to great lengths to deny weather intelligence to their enemies; the Department of Defense must, therefore, have the capability to acquire the necessary measurements in a distant, or hostile, or distant-and-hostile environment.

5.3 Point of Delivery

The DoD employs environmental intelligence in different ways, usually dependent on the time-sensitivity of the data.

Intelligence on small-scale, short-lived (LOCAL) phenomena - applied to short-lived military actions which are accomplished on a relatively small scale - must be delivered directly to a system operator or to an on-site commander; for example, a pilot on final approach must be immediately aware of a downburst/wind-shear problem; a tank gunner must make immediate crosswind corrections in order to hit his target.

Many DoD operations are supported by directly assigned environmental specialists; examples include oceanographers on board ship or meteorologists stationed at airfields or command posts. Observations provided to these facilities are usually evaluated and interpreted by the environmental-support personnel before being passed on to the decision makers; for example, after initial emergency evacuations are completed, boundary-layer wind observations for toxic-chemical spills or for chemical-warfare-defense operations would typically be evaluated, analyzed, and considered relevant to local topography by a trained meteorologist before being relayed to the on-scene commander. Other examples are found with ship-board oceanographers supporting carrier flight operations, or with directly assigned meteorologists supporting both ground and air operations from a division or brigade operations center.

In other cases, less-perishable wind observations (on both LOCAL and REGIONAL scales) may be collected at regional centers for integration with other data, for inclusion in analysis or forecast products, and for subsequent presentation to decision makers. Examples of regional analysis centers are found at joint task force headquarters, naval regional oceanography centers, or at tactical air control centers, where operations covering many hundreds or thousands of kilometers are planned and controlled.

In still other cases, data on all scales may be relayed to global analysis-and-forecast centers (specifically, the Navy Fleet Numerical Oceanography Center at Monterey, California, or the Air Force Global Weather Central at Omaha, Nebraska) for incorporation in global-scale analyses and forecasts (In exceptional cases, the global centrals may

be called upon to provide REGIONAL or even LOCAL-scale support for short periods of time.)

Finally, observations on all scales may be stored for post-analysis and for climatological evaluation. Although the Department of Defense environmental-support organizations do not truly "archive" data, they must retain selected operationally relevant data sets (or gain access to needed data sets) in order to advise military analysts on details of the environment for past events (aircraft accidents, for example), or to advise planners on the probable conditions that may be encountered for the full spectrum of military activities - ranging from construction of communications towers to para-dropping supplies in disaster-relief missions.

5.4 Urgency

There is a correlation between the urgency of delivery and the required scale size of the observation. The operational value of environmental intelligence decays with time in direct relation to the scale size of the information: small-scale information must be delivered to a decision-maker within a time interval that is compatible with the natural (temporal) variability of the element within the relevant spatial dimension. Typically, observations required on a spatial scale, of, say, less than a few kilometers must be in the hands of a decison-maker within minutes; observations on a scale of a few tens of kilometers must be used within a few hours, and observations on a scale of a few hundred kilometers retain a significant operational value of perhaps 12 hours.

Table 3 summarizes required delivery times of measurements to the various environmental-support echelons in the DoD. Time urgencies for both raw (essentially un-processed) wind measurements and for measurements which have been evaluated, analyzed, correlated, and perhaps incorporated in tailored forecast products are shown. Note that the scale sizes here refer to the military operation being supported, which, in general, is representative of the required spatial and temporal scales of the wind measurements.

Table 3. Urgency of Delivery of Wind Intelligence to Specified Locations (Urgency of delivery of PROCESSED wind intelligence, e.g., incorporated in analyses or forecasts - is shown in parentheses ( )).

DELIVERY LOCATION:	SCALES: LOCAL	REGIONAL	GLOBAL
System Operator or Decision-Maker	minutes (<1hr)	(1-3 hr)	(9-12 hrs)
Direct Envmntl Support Facility	minutes (<1 hr)	<1 hr (1 hr)	(6-9 hrs)
Regional Analysis & Forecast Ctr	minutes	<1hr (<3 hrs)	(6-9 hrs)
Global Analysis & Forecast Ctr	minutes	1 hr	3 hrs
Event Analysis/ Climate Ctr	>day	>day	>day

6. CONCLUDING REMARKS

Looking to the future, we must continue to recognize the guidance given to the individual Services by the Department of Defense: the United States must maintain qualitative versus quantitative military superiority over potential enemies. The employment of the complex and expensive weapon systems critical to that qualitative superiority can be optimized by accurate and timely environmental intelligence. As military operational concepts evolve, we find that our spatial and temporal scales of interest are also evolving - military decisions in future combat situations will be made more quickly than ever before; a commander's objective will be to decide and to act well inside the enemy's decision cycle. In order to make INTELLIGENCE decisions, the intelligent commander will need detailed and accurate knowledge of the impact of the environment on his proposed actions, whether they be the rescue of a seaman from the North Atlantic or the landing of a military force on a beach. ENVIRONMENTAL INTELLIGENCE will become increasingly important, even vital, for effective military command and control.

To summarize the conclusions of interest to this symposium:

* Wind impacts all Department of Defense mission areas.

* Wind intelligence is needed on ALL scale sizes.

* Department of Defense needs and actions are driven more by "operational" requirements than by "technical" requirements: location, delivery point, and urgency of delivery often override the scientific requirements of resolution, accuracy, and frequency of measurement.

Regardless of the compromises that we may be forced to make to insure some level of operational support to commanders, we recognize the importance of WIND, and will continue to address its impact across the full spectrum of our operations.

REFERENCES:

Abrams, I., W.J. Dean, E. Leonard, D. Luke, V. Patterson, A. Ramsay, J. Saccone, 1984: WX 2000 Technical Report, (ESD-TR-84-198). Information Systems and Networks Corporation, Lexington, Mass. (Available only to U.S. Government agencies and their contractors: Electronic Systems Division/XRC, Hanscom AFB, MA 01731.)

Brown, D.N., and S. W. McCandless, Jr., 1985: Environmental Satellite Program for Naval Oceanography. Office of the Chief of Naval Operations, Naval Oceanography Division (NOP 952) Washington, D.C. (FOR OFFICIAL USE ONLY)

57-47
84467

USE OF GROUND-BASED WIND PROFILES IN MESOSCALE FORECASTING

N93-79305

Thomas W. Schlatter

Program for Regional Observing and Forecasting Services
NOAA Environmental Research Laboratories
Boulder, Colorado

1. INTRODUCTION

This paper is a brief review of recent uses of ground-based wind profile data in mesoscale forecasting. Some of the applications are in real time, and some are after the fact. Not all of the work mentioned here has been published yet, but references are given wherever possible.

As Gage and Balsley (1978) point out, sensitive Doppler radars have been used to examine tropospheric wind profiles since the 1970s. It was not until the early 1980s, however, that the potential contribution of these instruments to operational forecasting and numerical weather prediction became apparent. Profiler winds and radiosonde winds compare favorably, usually within a few m s^{-1} in speed and 10° in direction (see Hogg et al., 1983, p. 818, for an example), but the obvious advantage of the profiler is its frequent (hourly or more often) sampling of the same volume. The rawinsonde balloon is launched only twice a day and drifts with the wind.

In this paper, I will (1) mention two operational uses of data from a wind profiling system developed jointly by the Wave Propagation and Aeronomy Laboratories of NOAA, (2) describe a number of displays of these same data on a workstation for mesoscale forecasting developed by the Program for Regional Observing and Forecasting Services (PROFS), and (3) explain some interesting diagnostic calculations performed by meteorologists of the Wave Propagation Laboratory.

2. OPERATIONAL USES OF PROFILER DATA

The Air Route Traffic Control Center (ARTCC) in Longmont, Colorado, has been using data from a wind profiling system at the Denver Airport in conjunction with data from the PROFS surface mesonet (22 stations with an average spacing of about 30 km) since the spring of 1982, primarily for vectoring arriving and departing aircraft. The profiler data have been particularly useful in assessing the severity of lee wave turbulence over the Front Range of the Rocky Mountains west of Denver (Foss and Hinkelman, 1984).

The Denver National Weather Service Forecast Office (WSFO) also receives wind profiles, via AFOS (Automation of Field Operations and Services), the standard communications and display system at forecast offices around the country. The tropospheric winds, transmitted once hourly, have proven useful for tracking short waves, for indicating the strength of mountaintop winds and the potential for lee waves, and for monitoring the depth of low-level upslope winds, which bring more than half of the annual precipitation to Front Range cities.

Because data from the wind profilers are still experimental, they have been provided to the ARTCC and the WSFO with the understanding that quality control is still minimal and occasional bad winds appear. Bad data arise for a number of reasons, including ionized trails of gas left by meteors, aircraft flying through the radar beam or in the side lobes, or faulty operation of one of the beams (the pulses are always aimed in at least two directions, toward the north and east at 15° off the vertical, and sometimes also straight up). Even highway traffic has been detected in the side lobes. Bad data are usually easy to spot in a time-height cross section of winds from a given site; nonetheless, efforts are underway to perform comprehensive quality control automatically, and thus make numerical computations on the data less risky.

3. USE OF THE WIND PROFILER DATA IN REAL TIME ON THE PROFS WORKSTATION

PROFS has developed a workstation for the display and manipulation of detailed meteorological data (Reynolds, 1983). The workstation has been used in several real-time forecasting exercises: in the summers of 1982, 1983, and 1985 (emphasis on detection or severe convective weather and issuance of experimental warnings--see Schlatter et al., 1985) and during late winter and early spring of 1984 (emphasis on public and aviation forecasts--see Schultz et al., 1985).

The displays which incorporate wind profile data include:

- Time-height cross section of winds--a separate product for each profiling site;
- Sounding update--the morning Denver raob sounding is updated by adding on the temperature and dew point changes as recorded by the radiometric profiler (Decker et al., 1978); The updated sounding and current wind profile are plotted on a Skew-T diagram;
- Kinematic analysis of profiler winds--plots relative vorticity, divergence, and vertical velocity as calculated from a triangle of profilers;
- Wind plots from all sites at a given elevation above sea level for overlay on a satellite image of clouds.

The time-height cross section of winds has proven valuable before and during winter storms (Gage and Schlatter, 1984) for tracking the movement of short waves and their occasional amplification into closed cyclonic circulations. When such storms pass through southern Colorado or northern New Mexico, they often cause deep upslope flow off the Great Plains and heavy snowfall along the eastern slopes of the Colorado Rockies.

Participants in the PROFS Cool-Season Forecasting Exercise of late winter and early spring 1984 (Schultz et al., 1985) appreciated data from the five profiling sites in Colorado, located as in Fig. 1. Numerical models run at the National

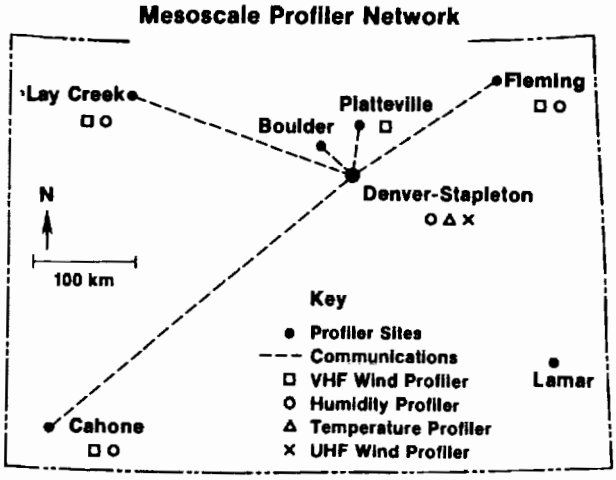

Figure 1. The Colorado wind profiling network as it existed in 1983-1984. Data from all sites were relayed to Boulder for processing.

Meteorological Center (NMC) occasionally have problems when a tropospheric disturbance crosses the Rocky Mountains. Especially troublesome are closed lows aloft that begin to move east from the southwest deserts. Sometimes the circulation maintains itself, but sometimes it collapses in southwest Colorado and a new circulation forms in the Texas Panhandle. The former event is notorious for heavy snow in the Denver area. The latter event often closes highways on the eastern plains of Colorado but spares Denver. More than once during the exercise, the profiler data indicated a sudden shift of winds aloft from southerly to northerly over Denver without a gradual backing through SE, E, and NE as predicted by NMC's Limited Area Fine Mesh model. The cutoff low in southwest Colorado had thus jumped discontinuously eastward, and Denver avoided deep upslope flow and the heavy snow.

Profiler data shed light on a mesoscale phenomenon only recently noticed during winter storms in northeast Colorado. As a surface low develops south or southeast of Denver, a pool of air will often slip southward near the foothills to a point just beyond Denver, where it stalls. This air is slightly cooler (1-2°C) than the air it displaces. Winds in the cooler air are northerly; to the south and east on the plains, winds are southeasterly.

A good example of this feature is shown in Fig. 2, a plot of the surface mesonet stations in northeast Colorado. Precipitation tends to fall to the north and west of the convergence line. Profiler data from two locations verified that the southeasterlies on the plains were overrunning the

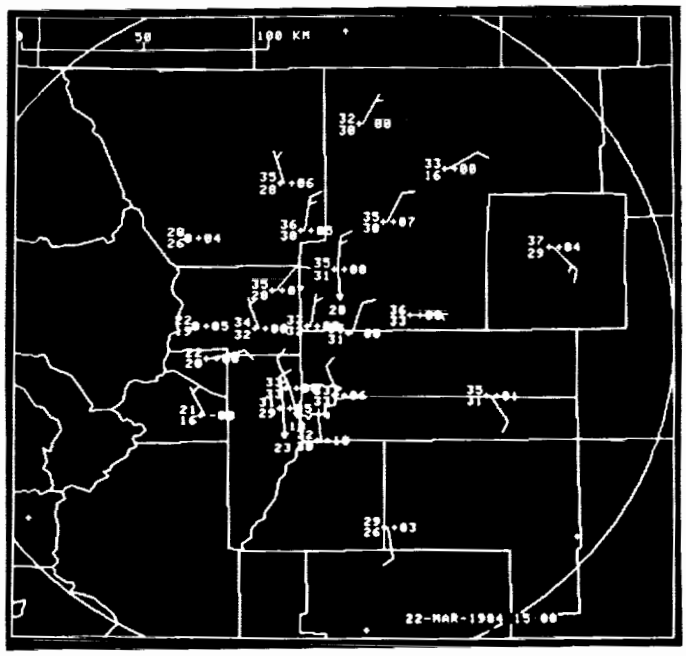

Figure 2. A plot of surface data from the PROFS mesonet in northeast Colorado. Temperature and dew point are plotted in °F. A full wind barb counts for 10 knots; a half wind bard counts for 5 knots. The pressure change in the preceding hour in tenths of millibars is plotted to the right of the station location, which is marked by a cross. A distance scale is at upper left. Note the convergence zone separating the northerly winds close to the foothills (mountains occupy the western one-third of the map) and the southerly winds out on the plains.

wedge of cooler air near the foothills. In Fig. 3, for Denver, one can see clearly the northerly winds close to the surface overrun by southeast winds aloft, especially between 1500 and 2000 GMT. Denver is just below the center of Fig. 2, where the plotted data are crowded. Well to the northeast, off the map in Fig. 2, lies Fleming, Colorado, another profiler site. Figure 4 shows the winds over Fleming, from the southeast at the surface and aloft, from 1500 through 2000 GMT. Evidently, Fleming is east of the overrunning zone. The conceptual model inspired by these data is shown in Fig. 5. We do not yet know how often this event occurs, but we have observed that snowfall tends to decrease once the convergence line southeast of Denver weakens or moves away.

In the spring of 1985, Colorado wind profilers were relocated to the northeastern plains, as shown in Fig. 6, for the purpose of assessing vertical motions during the convective season. As mentioned above, vertical profiles of relative vorticity, divergence, and vertical velocity are

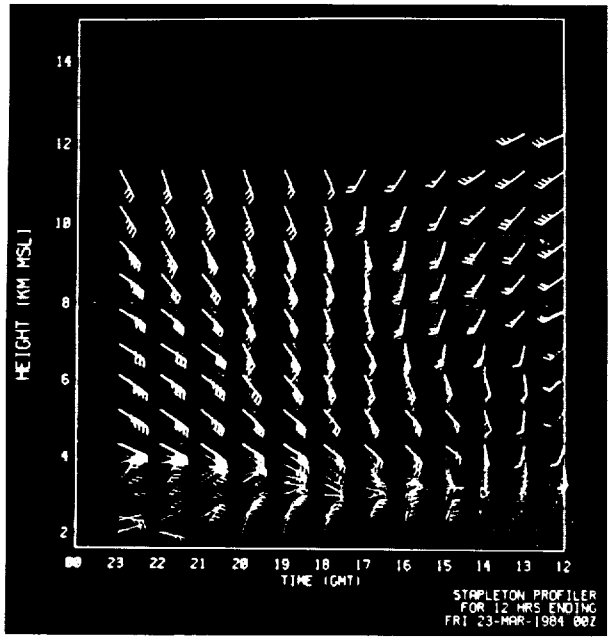

Figure 3. A time-height cross section of winds from the Denver profiler located at Stapleton Airport. Note that time increases toward the left. Substantial snow fell in the Denver area between 1500 and 2300 GMT, over 20 cm in some places, while the southeast winds overran the low-level northerlies.

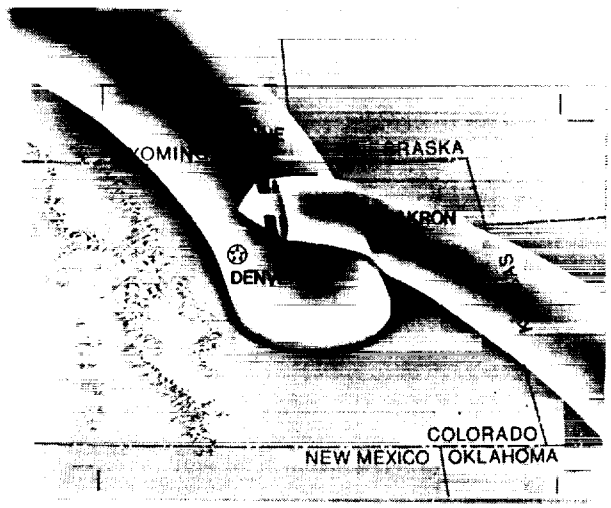

Figure 5. A conceptual model showing southeast winds on the plains of Colorado overrunning slightly cooler northerly flow near the foothills (from Schultz et al., 1985)

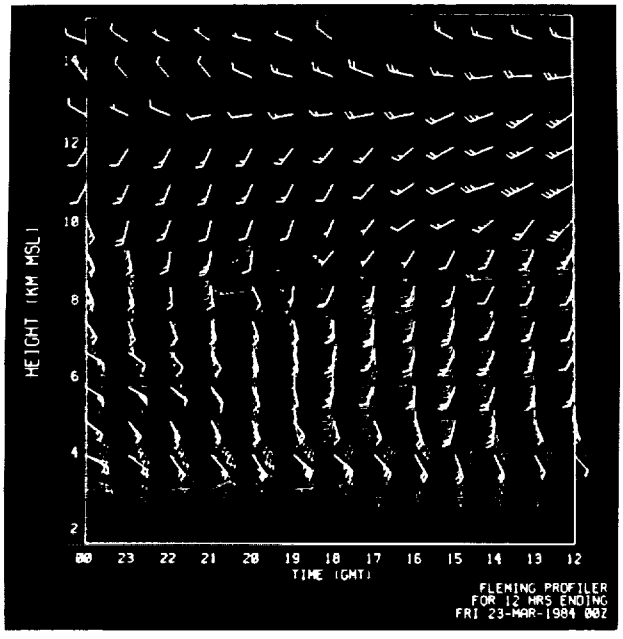

Figure 4. A time-height cross section of winds from the Fleming profiler. No overrunning is evident here.

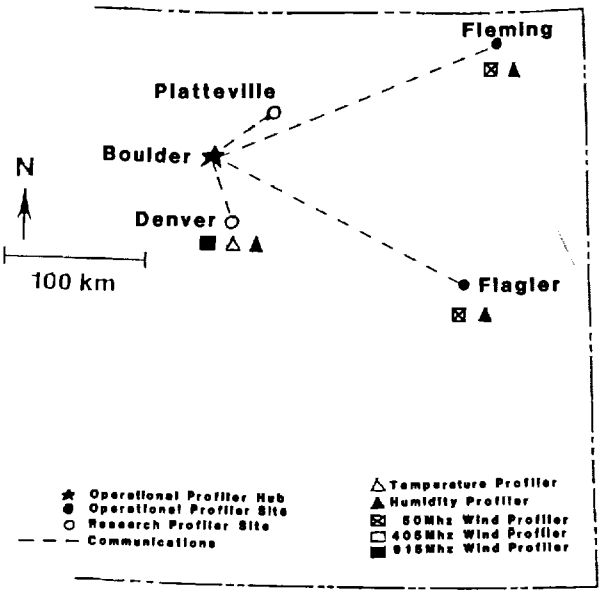

Figure 6. Colorado profiler locations for 1985.

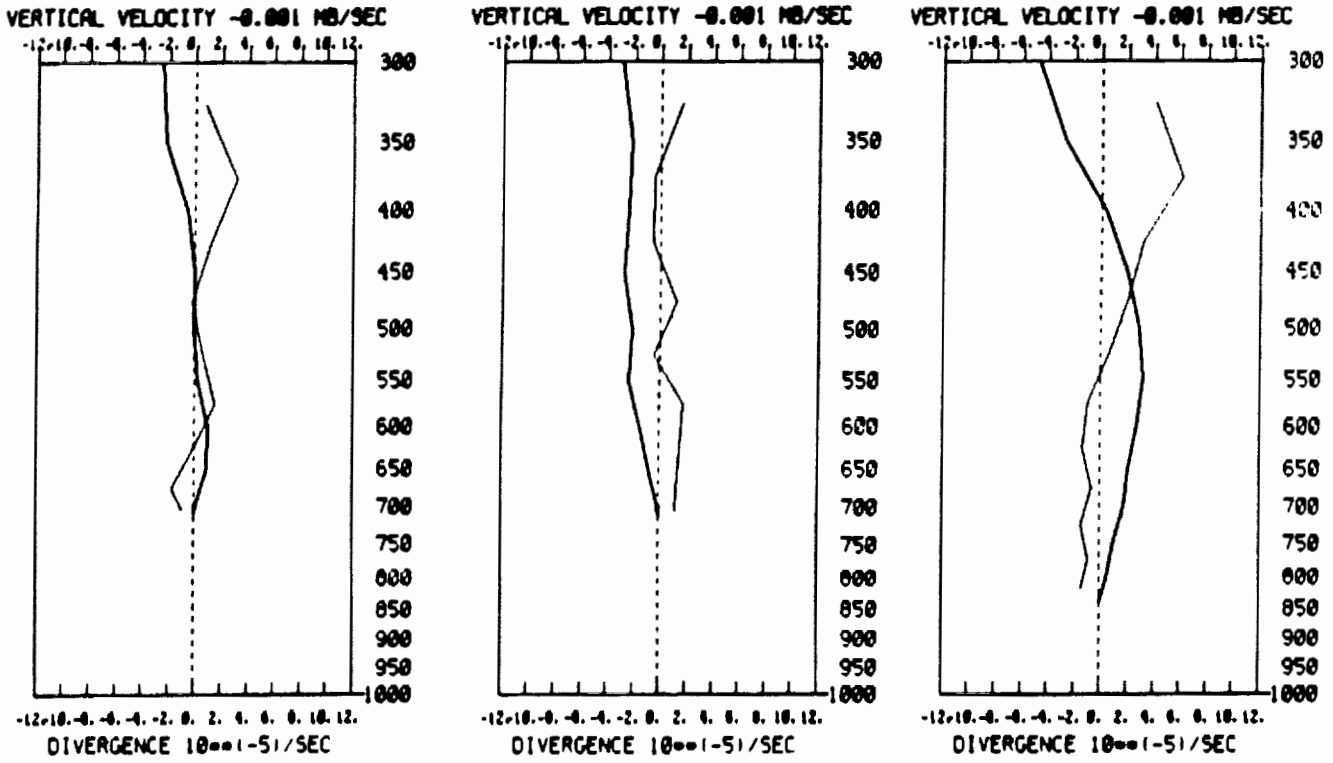

Figure 7. Divergence and vertical velocity profiles for (a) the Platteville-Fleming-Flagler triangle at 1820 GMT 24 July 1985, (b) the same triangle but at 0020 GMT 25 July 1985, and (c) for the triangle of rawinsonde stations: Denver, Colorado, North Platte, Nebraska, and Dodge City, Kansas at 0000 GMT 25 July 1985. The lighter curve is for divergence. The darker curve is for vertical velocity, plotted so that values to the right of the zero line indicate rising motion.

computed hourly. Profiles of divergence (thin line) and vertical velocity (bold line) are shown in Fig. 7 for 1820 GMT (1220 MDT) and 0020 GMT on 24 July 1985. On the afternoon of this day, a weak short-wave trough moved southeast across the triangle, and set off a line of moderate thundershowers, but no severe weather.

In advance of the trough at midday, weak convergence existed near the surface, with divergence of 3×10^{-5} s^{-1} between 350 and 400 mb. Upward motion ($-2 \mu bar\ s^{-1}$) prevailed in the lower troposphere with slightly stronger sinking motion at 350 mb and above. By evening (0020 GMT), the line of showers had moved southeast of the triangle. Divergence in the lower troposphere prompted sinking all the way to 300 mb. Skies were clearing rapidly. It is interesting to note that a similar calculation based upon radiosonde data at Denver, Colorado, North Platte, Nebraska, and Dodge City, Kansas, at 0000 GMT clearly shows low-level convergence surmounted by high-level divergence and moderate lifting in mid-troposphere--stronger signatures of a short-wave passage on the synoptic scale than appeared at the mesoscale. There is no good explanation of this effect, but the diurnal heating cycle on the sloping terrain of NE Colorado could influence the vertical velocity profile when summer winds aloft are light.

Unfortunately, the first level at which profiler winds are available is about 1500 m above the surface. The vertical velocity is assumed to be zero at this level, a bad assumption when boundary-layer convergence sets the stage for thunderstorms. At the very least, surface observations are needed at the three profiling sites forming the triangle. Those observations, along with other surface observations near the legs of the triangle, could be used to compute surface convergence.

4. ANALYSIS OF WIND PROFILER DATA AT WPL

4.1 Determining the Jet Stream Position More Precisely

On 13 June 1983, the jet stream made an unusually late southward foray into Colorado. The NMC analysis based upon U.S. rawinsonde data (Fig. 8) shows the axis of maximum wind stretching from SW Idaho to northern New Mexico. A reanalysis by M.A. Shapiro of NOAA's Wave Propagation Laboratory (Fig. 9) incorporates profiler data from the SW, NW, and NE corners of Colorado. The 110-knot NW wind at Cahone in SW Colorado and the 10-knot SW wind at Lay Creek in NW Colorado led to changes. In the reanalysis, the cyclonic shear north and east of the jet is stronger, and the jet core crosses SW Colorado. These are minor adjustments unless one happens to be flying by commercial jet from Albuquerque, New Mexico, to Salt Lake City, Utah. Minor variations in the routing would cause substantial variations in the headwind experienced.

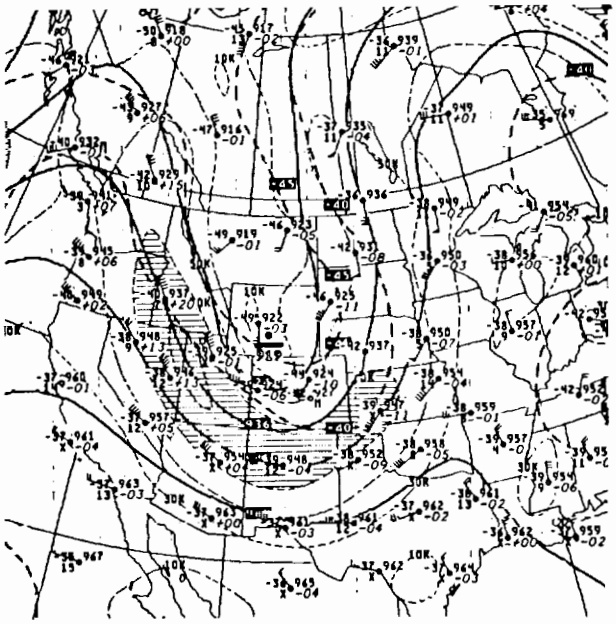

Figure 8. The NMC 300-mb analysis for 1200 GMT, 13 June 1983. Winds exceed 70 knots in the hatched area.

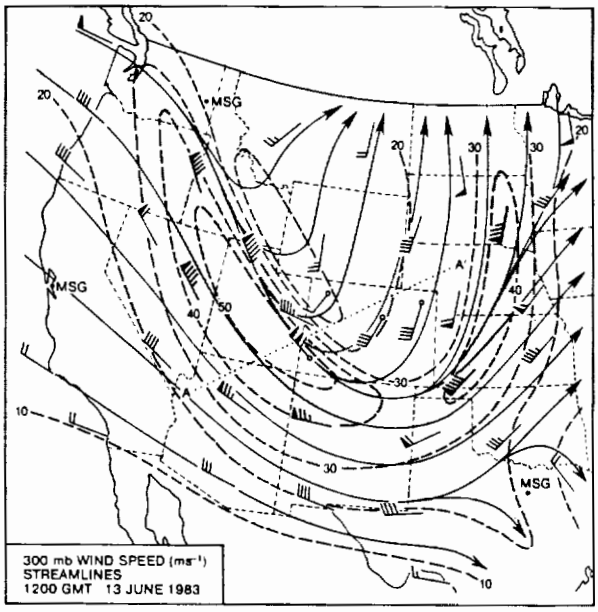

Figure 9. A reanalysis of 300-mb data by M.A. Shapiro, which accounts for winds measured by the Colorado wind profiling network. In comparison with Fig. 8, note the subtle shift of the jet axis into southwest Colorado (from Shapiro et al., 1984).

4.2 Time Variation of Divergence at Different Levels

Zamora and Shapiro (1984) examined the time variation of divergence at 3 and 9 km based upon data from the profilers at Cahone, Lay Creek, and Fleming (refer again to Fig. 1 for locations) on 12 and 13 June 1983. The solid and dashed curves in Fig. 10 give the time-smoothed history of divergence at 9 km and 3 km, respectively. The dots and crosses give the unsmoothed values for the profiler, whereas the triangles and asterisks give the 12-h values obtained from rawinsonde data.

The NMC radar summary for 2035 GMT, 12 June (Fig. 11), shows vigorous thunderstorms in the east part of the triangle: hook echo southeast of Fleming, radar echo tops above 16 km, and hail near the Colorado-Nebraska border. Divergence at 9 km was substantial at this time, although decreasing. Convergence existed at 3 km. Because of mountainous terrain within the triangle, it is impossible to compute divergence below 3 km MSL.

As Fig. 10 shows, divergence at 9 km increased markedly early on 13 June, and was accompanied by convergence at 3 km. Although the consequent upward motion in mid-troposphere was out of phase with the diurnal heating cycle, deep convection developed anyway. A thunderstorm with 0.5 cm hail crossed over Boulder at 1500 GMT, a most unusual event in an area where the diurnal cycle virtually controls convection.

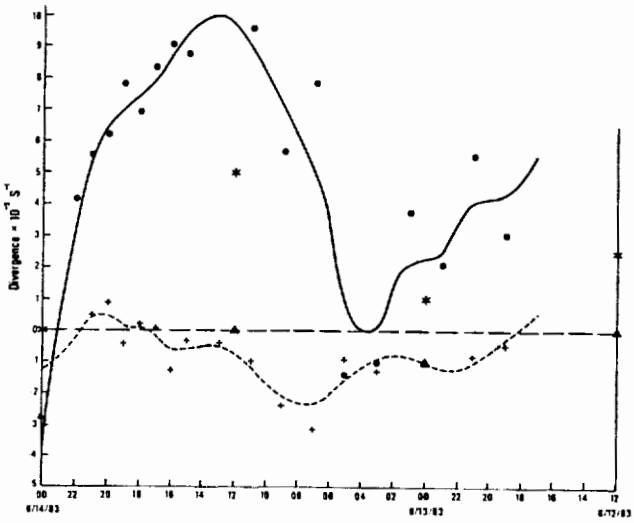

Figure 10. The time-smoothed variation of divergence, 12-13 June 1983, computed at two levels, 9 km (solid line) and 3 km (dashed line) from profilers in the SW, NW, and SE corners of Colorado. Time increases from left to right. The dots and crosses are the unsmoothed values for the profiler. The triangles and asterisks give values computed from rawinsonde data twice a day.

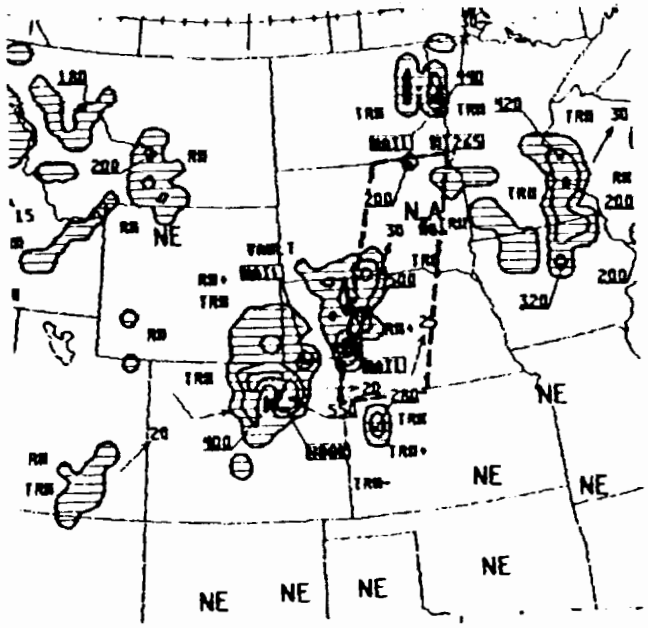

Figure 11. A portion of the NMC national radar summary for 2035 GMT, 12 June 1983.

4.3 Calculation of the Ageostrophic Wind Directly From the Equation of Motion

Zamora et al. (private conversation)[1] have developed a method for computing the ageostrophic wind from profiler wind measurements. He begins with the equation for horizontal, frictionless flow expressed as

$$\frac{d\underline{V}}{dt} = f\underline{V}_{ag} \times \underline{k} \qquad (1)$$

where f is the Coriolis parameter, t is time, $\underline{V}$ is the horizontal wind vector, $\underline{V}_{ag}$ is the ageostrophic component of the horizontal wind, and $\underline{k}$ is a unit vector which points vertically. With expansion of the total derivative, this equation can be written in component form:

$$\left.\begin{aligned} v_{ag} &= \frac{1}{f}\left(\frac{\partial v}{\partial t} + u\frac{\partial u}{\partial x} + v\frac{\partial u}{\partial y}\right) \\ u_{ag} &= \frac{1}{f}\left(\frac{\partial u}{\partial t} + u\frac{\partial v}{\partial x} + v\frac{\partial v}{\partial y}\right) \end{aligned}\right\} \qquad (2)$$

If one assumes that the vector field is linear within the triangle formed by three profiling sites, that is, if

$$\left.\begin{aligned} u(x,y) &= u(x_0,y_0) + \frac{\partial u}{\partial x}(x-x_0) + \frac{\partial u}{\partial y}(y-y_0) \\ v(x,y) &= v(x_0,y_0) + \frac{\partial v}{\partial x}(x-x_0) + \frac{\partial v}{\partial y}(y-y_0) \end{aligned}\right\} \qquad (3)$$

where, for convenience, (x_0,y_0) is chosen to be the center of the triangle, then it is possible to compute each of the horizontal derivatives in Eq. (2) from the wind components measured at the vertices. For u and v in the advection terms, one uses u_0 and v_0. The time derivatives are estimated from the 1-h changes in u_0 and v_0. The estimates of u_{ag} and v_{ag} apply at the center of the triangle.

Zamora and his colleagues have examined the evolution of the ageostrophic wind during two vigorous spring storms which passed over Colorado. With moderate time smoothing, the 1-h values exhibit excellent continuity and match expectations about ageostrophic winds in troughs. Moreover, geostrophic components calculated from rawinsonde heights and winds match those inferred from the profiler data to within a few m s^{-1}.

4.4 Analysis and Model Initialization

Wind profiling systems are capable of up to 100 m vertical resolution. Comparable resolution in temperature is not obtainable from radiometric measurements of the atmosphere either from the ground or from satellites. Several years ago researchers began asking whether detailed wind profiles could be used to build structure back into the smooth temperature profiles retrieved from radiometric data.

The answer seems to be yes. Kuo and Anthes (1985) used simulated wind observations to solve the full divergence equation for the temperature field. They had to prescribe geopotential heights along the boundary of their computational grid in order to obtain a solution. The accuracy of the solution was sensitive to the accuracy of the boundary conditions. When wind observations with random errors of 1 m s^{-1} (standard deviation) were made available on a 350-km grid and the boundary values of geopotential height contained errors typical of a 12-h model forecast, the rms temperature error averaged over all levels was 1.5°C.

Brümmer et al. (1984) devised a variational technique in isentropic coordinates which used detailed wind profiles to add structure to smoothed temperature profiles. The balance equation was used as a weak constraint. All input data were simulated by a high-resolution isentropic model. This technique put realistic gradients back into upper tropospheric frontal zones poorly resolved by temperature data alone. Since the 1984 paper, Brümmer has generalized the variational technique to satisfy the full divergence equation and obtained improved results. She is also conducting experiments to find out whether the temperature and wind fields, as related by the variational technique, can lead to better short-range forecasts.

5. CONCLUDING REMARKS

This paper has examined the use of ground-based wind profiles for mesoscale forecasting. Recognizing that sophisticated automatic quality control procedures are not yet implemented, the Denver WSFO and the Longmont ARTCC have still profited from frequent tropospheric wind data. In various forms, the profiler data have helped forecasters monitor the progress of winter storms hour by hour. Vertical velocity profiles, inferred from winds measured at three profiling sites in northeast Colorado, seem to be correlated with the vigor of summertime convection, but the

[1] Zamora, R.J., M.A. Shapiro, and C.A. Doswell, III, 1985: The diagnosis of upper tropospheric divergence and ageostrophic winds from profiler-network derived wind fields. Manuscript in preparation. NOAA Wave Propagation Laboratory, Boulder, Colorado.

diurnal heating cycle may be masking the synoptic-scale effects on vertical motion.

The new wind data at profiling sites already allow more accurate positioning of jet streams. The frequency of wind profiles (at least hourly) allows direct computation of the ageostrophic wind component from the equation of motion. The detail in the wind profiles adds definition to the much smoother temperature fields derived from radiometric observations.

Forecasters and numerical modelers alike look forward to the deployment of a network of wind profilers in the U.S. Midwest late in this decade.

ACKNOWLEDGMENTS

I wish to thank the NOAA Wave Propagation Laboratory for supplying PROFS with data from the profiling system. Without the cooperation of WPL, few forecasters would have been exposed to these data. Tracy Smith (PROFS) and Bob Zamora (WPL) contributed several figures. Nita Fullerton and Susan Carsten helped prepared the manuscript. Stan Benjamin and Ron Alberty assisted with critical reviews.

REFERENCES

Brümmer, R., R. Bleck, and M.A. Shapiro, 1984: The potential use of atmospheric profilers in short-range prediction. Proceedings of the Second International Symposium on Nowcasting, 3-7 September, Norrköping, Sweden, ESA SP-208, European Space Agency, Paris, 209-212.

Decker, M.T., E.R. Westwater, and F.O. Guiraud, 1978: Experimental evaluation of ground-based microwave sensing of atmospheric temperature and water vapor profiles. J. Appl. Meteor., 17, 1788-1795.

Foss, F., and J.W. Hinkelman, Jr., 1984: Denver ARTCC evaluation of PROFS mesoscale weather products. Joint report, Program for Regional Observing and Forecasting Services and Denver Air Route Traffic Control Center, Longmont, Colorado, 23 pp., 4 appendices. (Available from PROFS R/E23, 325 Broadway, Boulder, CO 80303).

Gage, K.S., and B.B. Balsley, 1978: Doppler radar probing of the clear atmosphere. Bull. Amer. Meteor. Soc., 59, 1074-1093.

Gage, K.S., and T.W. Schlatter, 1984: VHF/UHF radar and its application to nowcasting. Proceedings of the Second International Symposium on Nowcasting, 3-7 September, Norrkoping, Sweden, ESA SP-208, European Space Agency, Paris, 193-200.

Hogg, D.C., M.T. Decker, F.O. Guiraud, K.B. Earnshaw, D.A. Merritt, K.P. Moran, W.B. Sweezy, R.G. Strauch, E.R. Westwater, and C.G. Little, 1983: An automatic profiler of the temperature, wind, and humidity in the troposphere. J. Climate Appl. Meteor., 22, 807-831.

Kuo, Y.-H., and R.A. Anthes, 1985: Calculation of geopotential and temperature fields from an array of nearly continuous wind observations. J. Atmos. Oceanic Tech., 2, 22-34.

Reynolds, D.W., 1983: Prototype workstation for mesoscale forecasting. Bull. Amer. Meteor. Soc., 64, 264-273.

Schlatter, T.W., P. Schultz, and J.M. Brown, 1985: Forecasting convection with the PROFS system: Comments on the summer 1983 experiment. Bull. Amer. Meteor. Soc., 66, 802-809.

Schultz, P., M.C. McCoy, R.E. McGowan, T.W. Schlatter, and J.W. Wakefield, 1985: The first experiment in forecasting cool-season weather with the PROFS system. NOAA Technical Memorandum ERL ESG-16, Environmental Sciences Group, Boulder, Colorado, 25 pp. (Available from PROFS R/E23, 325 Broadway, Boulder CO 80303).

Shapiro, M.A., T. Hample, and D.W. van de Kamp, 1984: Radar wind profiler observations of fronts and jet streams. Mon. Wea. Rev., 112, 1263-1266.

Zamora, R.J., and M.A. Shapiro, 1984: Diagnostic divergence and vorticity calculations using a network of mesoscale wind profilers. Preprints, 10th Conference on Weather Forecasting and Analysis, 25-29 June, Clearwater Beach, Florida, American Meteorological Society, Boston MA, 386-391.

SEVERE WIND FLOW OF SMALL SPATIAL AND TEMPORAL SCALES: THE MICROBURST AND RELATED PHENOMENA

Rita D. Roberts and John McCarthy

National Center for Atmospheric Research*
Boulder, CO 80307

1. INTRODUCTION

Low-altitude winds on the meso- and microscale are the primary focus of study for the Research Applications Program (RAP) of NCAR. Local weather features such as microbursts, microburst lines, gust fronts, and convergent wind boundaries have been observed and documented extensively. A microburst is a strong, small-scale convective storm outflow which diverges horizontally in all directions upon impact with the ground (Fujita, 1981). A microburst line is composed of two or more microbursts which occur either simultaneously or consecutively, and subsequently form a diverging line of outflow. The temporal and spatial scales of these phenomena are shown in Fig. 1. Microbursts and microburst lines generally occur on both the miso- and microscale, while gust fronts and convergent wind boundaries overlap into the mesoscale. Microbursts, in particular, not only are small spatially but are also a short-lived phenomenon. Clearly, some of these features are on a much smaller spatial and temporal scale than can be resolved by a global wind measurement system.

During the past three years, three experiments were held in the Denver, Colorado, area to observe boundary-layer winds. Their main objectives were observation and documentation of those weather features discussed above. The Joint Airport Weather Studies (JAWS) Project, which ran in the summer of 1982, was set up to study microbursts. The Convective Initiation Project (1984) was designed to document clear-air convergent wind boundaries, including gust fronts, and their role in convective storm initiation. This project was immediately followed by the Classify, Locate, and Avoid Wind Shear experiment that expanded upon the work done in JAWS. Details on the scales of these weather features are presented in Section 2. The wind sensors used to detect these phenomena are discussed in Section 3. Concluding comments address the usefulness of a global wind measurement system as it pertains to our local scale of interest.

*The National Center for Atmospheric Research (NCAR) is sponsored by the National Science Foundation.

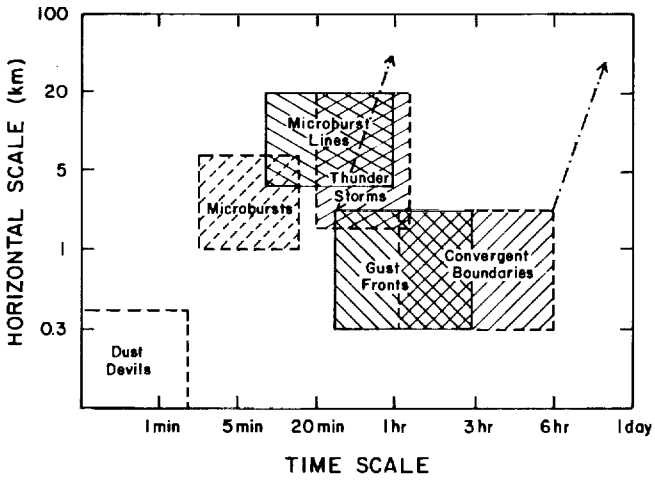

Figure 1. Temporal and spatial scales of local weather phenomena. The boxes designate the limits in horizontal width and time of a particular feature. Cross-hatched regions represent areas of overlap of two features. The dashed-dot lines with arrowheads denote the horizontal length for two of the weather phenomena.

2. LOCAL SCALES OF MOTION

2.1 Mesoscale

It has often been observed that regions of converging flow, initiated by gust fronts or arising from the collision of two different air mass boundaries, have great potential for initiating or enhancing convection. For this reason, the Convective Initiation Project (CIP) was proposed to study mesoscale convergent wind/air mass boundaries and gust fronts and to determine their corresponding roles in the initiation of convective storms. During the project, which ran from 15 May - 30 June 1984, such wind shift lines were frequently detected by Doppler radar and surface wind sensors. Preliminary statistics indicate that 60% of these convergent wind lines initiated convective storms. Numerous other boundaries enhanced growth in pre-existing storms. These boundaries are typically 500 m to 3 km in width and 30 to 120 km long (as denoted by the dashed-dot lines with arrowheads in Fig. 1). They typically last

anywhere from 1 hr to 6 hr. Although gust fronts can often be discerned on satellite photographs as cloud arc lines (Purdom, 1982), it is not evident whether a satellite can detect smaller scale boundaries on a local scale. Certainly, those boundaries and gust fronts which are of short duration are difficult to resolve.

2.2 Microscale to Misoscale

RAP scientists were major participants in the JAWS experiment (McCarthy et al., 1982), which ran from 15 May - 13 August 1982. The main objective of JAWS was to study microbursts and their effect upon aircraft. Fujita has classified a microburst as a misoscale downdraft with horizontal dimensions between 0.4 and 4.0 km. A large number of microbursts were detected by Doppler radar (70 events) and surface wind sensors (160 events). Figure 2 displays a vertical cross section of the winds within a microburst that occurred on 14 July 1982. The winds were derived from radar data by using a dual Doppler radar analysis package (Kessinger et al., 1983). Note that the downdraft, located 14 km west of the CP-2 radar, is only 1 km across, and that the outflow spreads horizontally in both directions. Results from JAWS (Wilson et al., 1984) showed that initially, as the downdraft reaches the surface, a velocity differential of 12 m s^{-1} occurs between peak opposing regions of outflow that are only 1 to 2 km across. Within 5 min, however, the microburst has typically attained its maximum shear, the peak velocity differential (within the range of 22 to 48 m s^{-1}) spanning a distance of 5 km, as is shown here.

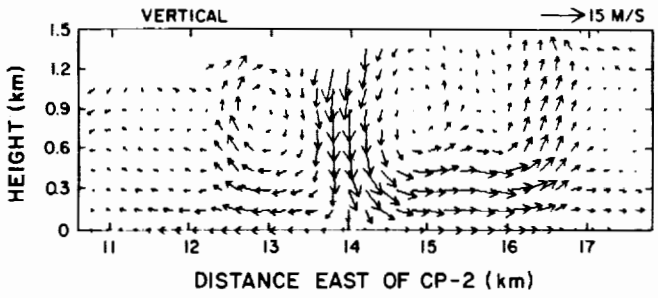

Figure 2. Vertical cross section of the winds within a microburst on 14 July 1982, at 2052 GMT. The center of the microburst was located 14 km east of NCAR's CP-2 radar. The scale vector is located in the upper right-hand corner.

Another feature discovered during JAWS was the microburst line. Microburst lines are generally larger than individual microbursts in horizontal dimension and average 60 min in duration (Hjelmfelt and Roberts, 1985). (See Fig. 1.) The reconstructed radar wind field of a microburst line is shown in Fig. 3. Four distinct microburst outflows are apparent and numbered in this plot; they form essentially a line orientation. Although an individual microburst on the line may last only 10 min, the line itself can persist for over an hour.

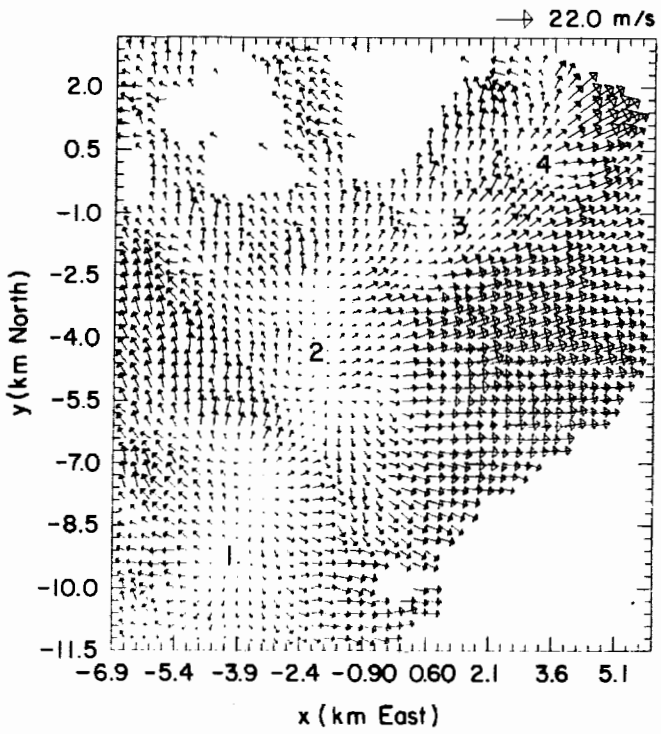

Figure 3. Low altitude (10-100 m) horizontal wind field of a microburst line on 13 July 1982, at 2102 GMT. The line is composed of four microbursts which are numbered here. The scale vector is in the upper right-hand corner.

Both microbursts and microburst lines present a hazard to aircraft. The danger lies in the brevity of dimension and time over which the shear occurs. An aircraft's response as it attempts to land during a microburst occurrence is depicted in Fig. 4 (Elmore et al., 1985). The dashed and solid contours represent velocities parallel to the aircraft's motion. Negative (positive) values correspond to flow toward (away from) the aircraft. The winds were derived by using a dual Doppler radar analysis package. Since this condition is such a small-scale phenomenon, the aircraft has little time to react. As the aircraft descends (solid, sloped line), it encounters the headwind, downdraft, and tailwind components of the microburst in a matter of seconds. Unable to maintain the appropriate airspeed, it crashes 1.2 km short of the runway. With a microburst line centered over a runway, the problems are magnified for arriving and departing aircraft (Hjelmfelt and Roberts, 1985; Stevenson, 1985). Pilots have described flight through a microburst line as being similar to a roller coaster ride. This is definitely not an ideal situation when attempting to maintain the appropriate glide path for an aircraft landing.

On 31 May 1984, a wind-shear-related aircraft accident occurred at Denver's Stapleton International Airport (NTSB, 1985). A microburst was cited as the probable cause. Upon request by the Federal Aviation Administration

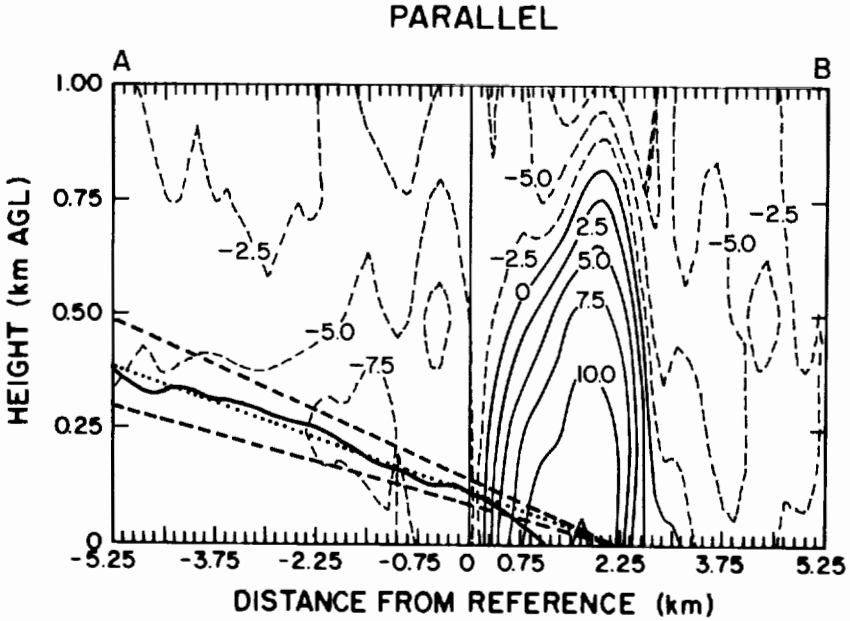

Figure 4. Simulation of an aircraft's approach through a microburst. The solid and dashed contours represent flow parallel to the aircraft's motion. Negative (positive) values correspond to flow toward (away from) the aircraft. The desired approach path is represented by the center dotted line. The heavy dashed lines to either side represent 0.7 degree deviations from the desired glide path, at which point a go-around (escape) is attempted. The heavy solid line depicts the modeled aircraft track.

(FAA), an experiment called the Classify, Locate, and Avoid Wind Shear (CLAWS) Project was held from 2 July - 15 August 1984. Its purpose was to detect and warn of harmful, low-altitude wind shear within 5 n mi of Stapleton Airport (McCarthy and Wilson, 1985). Specifically, if a microburst was detected in the airport vicinity, an advisory was then issued to the air traffic controller. Attempts were made to forecast a microburst occurrence based on Doppler radar signatures of increased convergence with time or the presence of rotation within a given cloud. Obviously, if the microburst was already on the ground, little warning time could be given, since the microburst would soon be at its maximum strength. However, knowing the nature of the wind shear hazard and its location proved to be a valuable aid to pilots. Advisories were issued for microburst lines, also. During one event at Stapleton, a microburst line interrupted operations for 45 min.

Movement of gust fronts and convergent wind boundaries was also noted. Advanced warning of an approaching gust front enabled the air traffic controllers to switch the designated arrival and departure runways prior to the front's passage, and thus allow for more efficient airport operations. Additionally, if two gust fronts or air mass boundaries were forecast to collide over the airport, an advisory indicating the development of thunderstorms was made. Then air traffic controllers at the tower and Air Route Traffic Control Center were prepared for routing traffic around storms and for possible delays. Obviously, local detection of wind shear is of interest to the research community as well as to the public. A detailed analysis of CLAWS from an air traffic perspective can be found in Stevenson (1985).

3. SENSORS FOR PBL OBSERVATION

3.1 Doppler Radar

Doppler radar is a very adept tool for detecting gust fronts and microbursts. NCAR's three Doppler radars, CP-2 (S-Band), CP-3 (C-Band), and CP-4 (C-Band), have very high sensitivities, and result in strong clear-air return. This is important for detection of clear-air boundaries. They can also resolve individual data points down to 150 m spatial resolution. For example, the spacing of the data in Fig. 3 is 300 m, the microbursts being easily discernible. Reflectivity thin lines, associated with gust fronts and convergent boundary regions, generally on the order of 10 to 25 dBZ_e, are often detectable on radar (Wilson, 1985). For incoherent radars, these thin lines are a useful tool in determining the direction and speed of propagation of the associated wind shift lines.

3.2 Surface Mesonet Stations

Surface mesonet information was available for all three experiments from the Program for Regional Observing and Forecasting Services (PROFS) at the National Oceanic and Atmospheric Administration (NOAA). PROFS' mesonet of surface wind and thermodynamic sensors is permanently located in eastern Colorado, extending

from the foothills of the Rocky Mountains out to the plains. Sensors are spaced approximately 40 km apart. This spacing was obviously too large for effective detection of microbursts during JAWS. However, for CIP and CLAWS, the mesonet provided additional information on the location of boundaries and gust fronts and estimates of their strengths. In the context of CLAWS, it was a valuable resource, and gave reinforcement to the wind-shear advisories issued.

The ability to transport surface weather stations to any locale and at any desired spacing provides a very powerful tool for observing winds and thermodynamics on any scale. NCAR's Portable Automated Mesonet (PAM) is such an instrument (Brock and Govind, 1977). In Fig. 5, PAM winds from two separate experiments are displayed. Figure 5(a) is from the PRE-STORM experiment this summer (1985) in Kansas and Oklahoma. Fig. 5(b) is from JAWS. At a glance, it appears that both sites are detecting thunderstorm outflow diverging at the surface. However, PAM spacing in PRE-STORM was 50 km, whereas JAWS required a much smaller spacing of approximately 4 km for detecting microbursts. Clearly, two totally different processes were occurring in these plots. One outflow was on the sub-synoptic scale and the other was on the local mesoscale, respectively. It is interesting to realize that the atmosphere is organized in amazingly similar ways, but with fundamentally different physics on different scales. There are strong implications in these two wind plots on the ability of a global wind measurement system to measure all types of weather phenomena. Certainly, a satellite-based system should at least be able to resolve winds on the scale of 1 degree latitude and longitude (approx. 2500 km^2). The question is whether winds on the scale in Fig. 5(b) will ever be resolved from space.

Even during JAWS, it was discovered that a 4-km station separation was often too coarse for locating microbursts after their initial surface impact within the mesonetwork. Sometimes, a delay of a few minutes between radar detection and PAM detection would occur, at which time a microburst is typically reaching its maximum intensity.

This was also true of the Low-Level Wind Shear Alert System (LLWAS) located at Stapleton Airport. The winds were recorded during the JAWS operations and later analyzed for the FAA (Bedard et al., 1984). The six LLWAS stations, spaced 3.5 km apart, are shown in

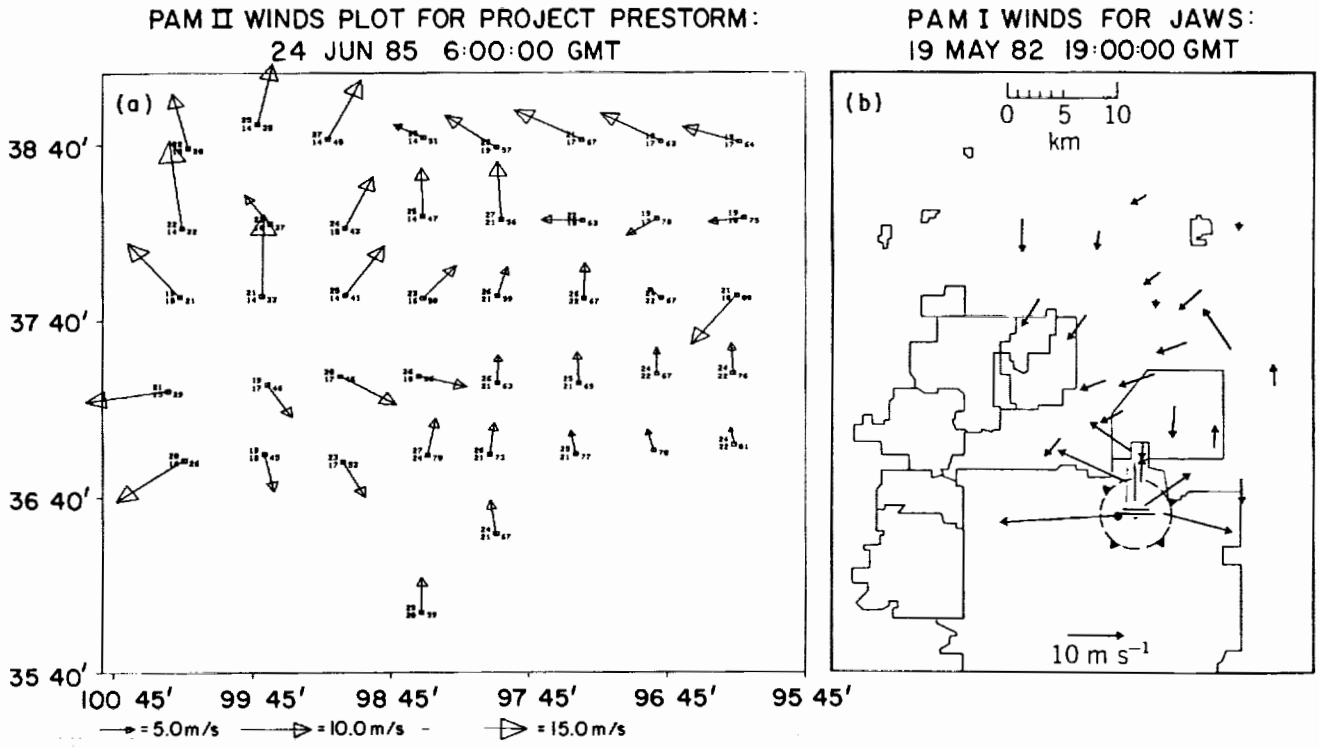

Figure 5. PAM surface winds representing two different scales of motion. (a) Large-scale thunderstorm outflow during PRE-STORM on 24 June 1985, at 6:00 GMT. Axes units are in degrees and minutes of latitude and longitude. PAM stations denoted by the small boxes are located 50 km apart. The numbers to the left of each box are the station temperature (upper) and dewpoint temperature (lower) in degrees C. The station pressure, in millibars, is listed on the right and should be prefixed with a 9. (b) Microburst outflow during JAWS on 19 May 1982 at 18:58 GMT. Average station spacing is 4 km. The horizontal scale is located at the top of the plot. Scale vectors are shown at the bottom of each plot.

Fig. 6. The winds are from a gust front propagating from the south. In general, the ability of LLWAS to detect microbursts was hampered more by the algorithm used to identify wind shear in the network than by the spacing of the anemometers. Nevertheless, CLAWS results showed it was at least 90% effective in warning of gust fronts in the airport vicinity which, after all, was primarily what LLWAS and its algorithm were designed to do. Wilson and Flueck (1985) have recently recommended a finer station spacing of 2.25 km for an improved LLWAS, including the addition of at least five more stations for resolving microburst and gust front events. They have also developed a new set of algorithms that will detect and distinguish various types of wind shear at an airport.

4. UTILITY OF GLOBAL WIND MEASUREMENTS

RAP scientists are interested in winds on a very localized scale. Specifically, this study is of the winds generated by microbursts. Their small horizontal dimensions and brief duration cannot be emphasized enough in the context of detection by wind sensing instruments. The ability to detect a microburst requires instruments capable of high spatial and temporal resolution. Surface remote and in situ instruments such as Doppler radar and surface mesonet stations closely spaced have proven to be adequate for the job. Although a global wind sensor system would be an asset for observing and tracking certain large-scale convective outflows, current satellite instruments do not have the high resolution in space and time required for detection of thunderstorm outflows on the misoscale. Those who address the depth and breadth of a global, satellite-based wind measurement system must recognize the limits of such a system with respect to microbursts and related phenomena on the scale of 0.4 to 4.0 km and temporal scales of 1 to 7 min.

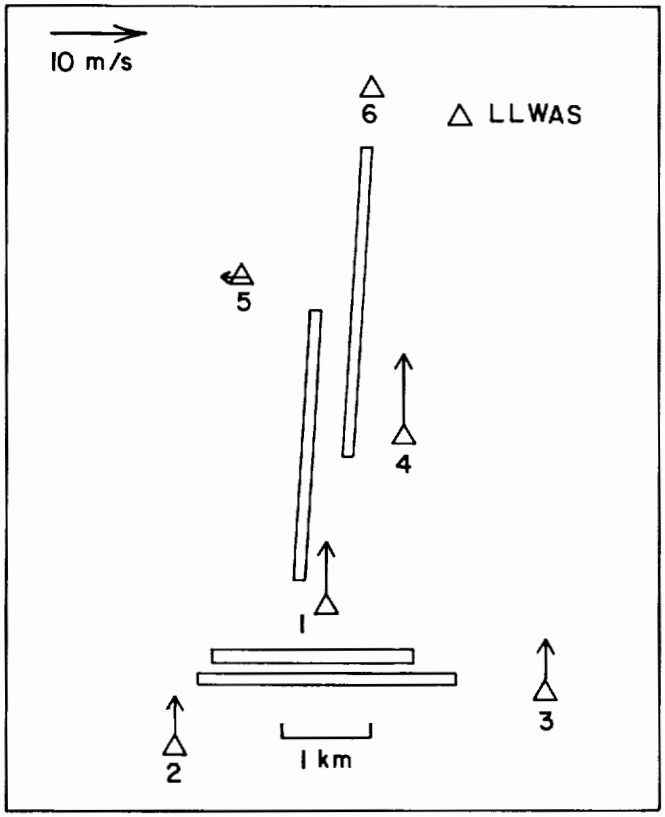

Figure 6. Gust front propagating from the south through LLWAS on 22 June 1982, at 2144 GMT. Average station spacing is 3.5 km. Stations are denoted by triangles and are numbered. The two sets of lines, approximately perpendicular to each other, represent runways at Denver's Stapleton International Airport. The scale vector is located at the top of the plot.

ACKNOWLEDGMENTS

RAP is funded partially by NCAR; the National Science Foundation; the FAA, through Interagency Agreement DTFA01-82-Y-10513; the National Aeronautics and Space Administration, through Interagency Agreement H-59314b; and NOAA, through a cooperative agreement with PROFS of NOAA's Environmental Research Laboratories.

REFERENCES

Bedard, A.J., Jr., J. McCarthy, and T. Lefebvre, 1984: Statistics from the operation of the Low-Level Wind Shear Alert System (LLWAS) during the Joint Airport Weather Studies (JAWS) Project. DOT/FAA/PM-84/32, 76 pp.

Brock, F., and P.K. Govind, 1977: Portable Automated Mesonet in operation. J. Appl. Meteor. 16, 299-310.

Elmore, K.L., J. McCarthy, W. Frost, and H.P. Chang, 1985: A high resolution spatial and temporal multiple Doppler analysis of a microburst and its application to aircraft flight simulation. RAP/FAA Final Report No. 01-86 (in press). The document is available through RAP/NCAR, P.O. Box 3000, Boulder, CO 80307.

Fujita, T.T., 1981: Tornadoes and downbursts in the context of generalized planetary scales. J. Atmos. Sci. 38, 1511-1534.

Hjelmfelt, M.R., and R.D. Roberts, 1985: Microburst lines. Preprint: 14th Conf. on Severe Local Storms, Indianapolis, Ind., Amer. Meteor. Soc., 297-300.

Kessinger, C., M. Hjelmfelt, and J. Wilson, 1983 Low-level microburst wind shear structure using Doppler radar and PAM data. Preprints: 21st Radar Meteor. Conf., Edmonton, Amer. Meteor. Soc., 609-615.

McCarthy, J., J.W. Wilson, and T.T. Fujita, 1982: The Joint Airport Weather Studies Project. Bull. Amer. Meteor. Soc. 63, No. 1, 15-22.

McCarthy, J., and J.W. Wilson, 1985: The Classify, Locate, and Avoid Wind Shear (CLAWS) Project at Denver's Stapleton International Airport: Operational testing of terminal weather hazard warnings with an emphasis on microburst wind shear. Preprint Vol.: 2nd International Conf. on the Aviation Weather System, June 19-21, 1985, Montreal, P.Q., 247-256.

National Transportation Safety Board Aircraft Accident Report, 1985: United Airlines Flight 663, Boeing 727-222, N7647U, Denver, Colorado, May 31, 1984. NTSB/AAR-85/05.

Purdom, J.F.W., 1982: Subjective interpretations of geostationary satellite data for nowcasting. Nowcasting, K. Browning, editor, Academic Press, London, 149-166.

Stevenson, L., 1985: The Stapleton microburst advisory service experiment (an operational viewpoint). DOT-TSC-FAA-85-8. This document is available to the public through the National Technical Information Service, Springfield, VA 22161.

Wilson, F.W., and J.A. Flueck, 1985: A study of the methodology of low-altitude wind shear detection with special emphasis on the LLWAS concept. RAP/FAA Final Report No. 02-85 (in press). This document is available through RAP/NCAR, P.O. Box 3000, Boulder, CO 80307.

Wilson, J., 1985: Tornadogenesis by nonprecipitation-induced wind shear lines. To be published in MWR, January 1986.

Wilson, J.W., C. Kessinger, R.D. Roberts, and J. McCarthy, 1984: Microburst wind structure and evaluation of Doppler radar for wind shear detection. J. of Clim. and Appl. Meteor. 23, 898-915.

CURRENT ISSUES CONCERNING THE REPRESENTATIVENESS AND UTILITY OF CLOUD DRIFT WINDS IN MESOSCALE METEOROLOGY

Steven E. Koch
Laboratory for Atmospheres
NASA Goddard Space Flight Center
Greenbelt, MD 20771

1. INTRODUCTION

High-resolution cloud motion wind (CMW) data sets obtained from geostationary satellites for approximately the past decade have been used for the purpose of estimating mesoscale wind fields in various research studies. Yet there remains much controversy surrounding the proper interpretation and use of the resultant wind vector and kinematic fields. This paper is concerned with (1) how representative are cloud drift winds of actual ambient air motions and (2) what is the degree of practical usefulness of CMW fields for both mesoscale analysis and as input to numerical weather prediction models. The representativeness of CMW data may vary according to the desired application of the data and may further depend upon the nature and space-time variance of the mesoscale atmosphere (Nappo et al., 1982). Other factors that affect the practical utility of these wind measurements must also be understood, but first let us consider just how CMW fields have been used in mesoscale research.

2. APPLICATIONS OF CLOUD DRIFT WIND DATA TO MESOSCALE ANALYSIS AND MODELING

The representativeness of CMW data in tropical and subtropical oceanic environments (characterized by weak vertical wind shear) has been established by intercomparisons with rawinsonde and aircraft wind measurements, as summarized by Shenk (1985) and Peslen et al. (1985). These studies confirm the reliability of CMW winds to an accuracy of 1-3 m s^{-1} in such situations. Verification of mesoscale CMW data sets, particularly those obtained in strongly sheared environments like those of the tropical cyclone and severe thunderstorm, remains much less certain because of the absence of in situ aircraft measurements and, with the exception of one study (Peslen et al., 1985), inadequate rawinsonde coverage. Instead, the mesoscale representativeness of CMW data has been primarily determined by using a utilitarian approach. For example, lower tropospheric convergence fields derived from CMW data have

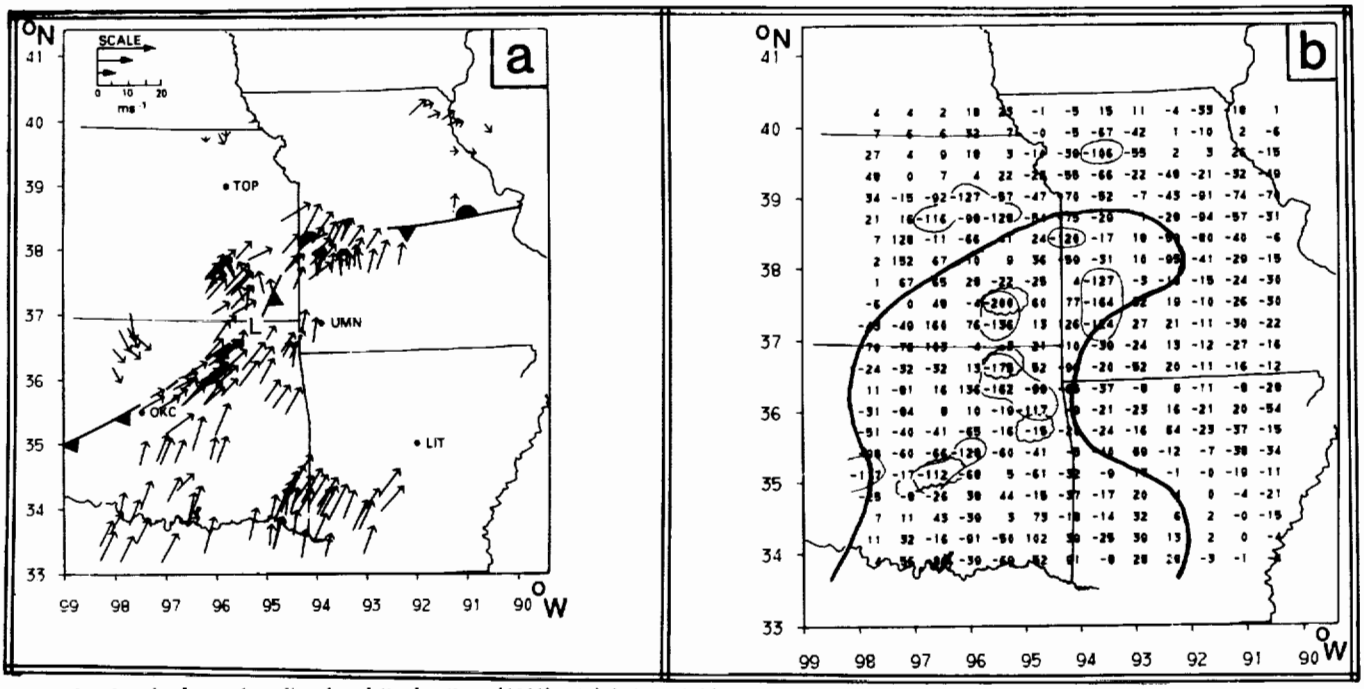

Fig. 1. Analyses from Negri and Vonder Haar (1980) of (a) CMW field at 2105 GMT 24 April 1975 and surface data at 0000 GMT 25 April 1975; (b) moisture divergence field derived from CMW data (values of convergence > 10^{-3} g kg^{-1} s^{-1} are stippled, only alternative grid-point values plotted in x direction), severe storm genesis areas (cloud outlines), and zone of confidence (dark line).

been found to correlate well with the locations of subsequent severe thunderstorm generation by Wilson and Houghton (1979), Peslen (1980), and Negri and Vonder Haar (1980). An illustration of this "proof is in the pudding" approach appears in Fig. 1, which shows excellent correspondence between most of the centers of moisture convergence and subsequent areas of thunderstorm genesis, at least within the "zone of confidence" outlined in Fig. 1b.

The same utilitarian approach to establishing the representativeness of mesoscale CMW has been taken in tropical cyclone studies. Rodgers and Gentry (1983) have shown that tropical cyclone intensity can be monitored by calculating time tendencies of net relative angular momentum derived from upper (cirrus) and lower (cumulus) level CMW data, even though there were areas where dense cirrus clouds prevented tracking of cumulus clouds. Thus, useful cyclone budget information can be extracted from cloud drift winds, although the validity of smaller scale details remains indeterminate.

Customarily, clouds have not been tracked wherever there is the likelihood that cloud motions may be influenced by the presence of gravity or lee waves. However, Pecnick and Young (1984) successfully related CMW-derived divergence fields at cloud top level to surface divergence fields in order to infer the structure and energetics of ∿100-200 km wavelength gravity waves. Such waves have been shown to be responsible for the generation of strong winds and severe convection.

One of the very few attempts at deriving meaningful three-dimensional fields of vertical motion from cloud drift winds was made by Wilson and Houghton (1979). In that study, each cloud motion vector was assigned to one of three layers based upon its cloud top temperature. The continuity equation was integrated within each layer to obtain the vertical motions at 720, 530, and 350 mb (shown in Fig. 2). The surface winds alone were used to obtain vertical motions at 910 mb, which bore little resemblance

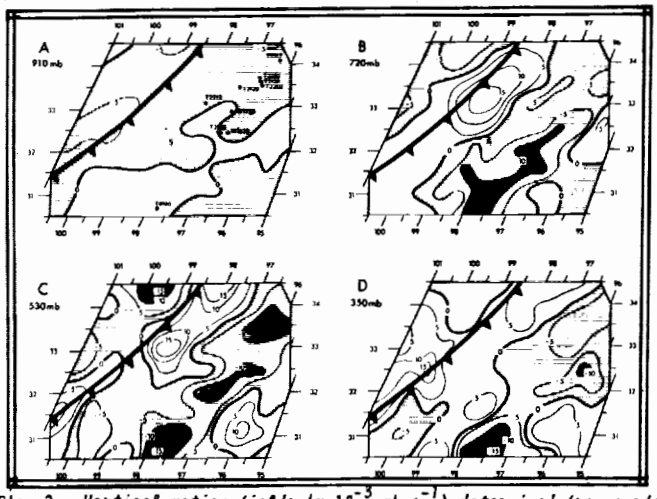

Fig. 2. *Vertical motion fields (x 10^{-3} mb s^{-1}) determined from surface and CMW data, surface position of cold front, and location of severe weather events. Shading indicates the areas where vertical motion is upward. Ordinate and abscissa are degrees north latitude and longitude, respectively [Wilson and Houghton, 1979].*

to the locations of the severe weather events. Inclusion of CMW data above that level resulted in an organized pattern of uplift (width 150 km) ahead of a surface cold front which correlated well with the subsequent severe convection.

A similar approach was used by Lee and Houghton (1984a,b) to insert cumulus CMW data into a mesoscale numerical weather prediction model; in that case, the vectors were assumed to be representative of a 200 mb-deep layer. The cloud wind fields generated perturbations of various scales in the initial kinematic fields, and also effected some noticeable changes in the precipitation forecast during the first 3 h of model integration. However, systematic errors introduced by factors considered below and the lack of mesoscale verification leaves some doubt about whether any useful information was actually provided by the cloud drift winds.

3. ERRORS ARISING FROM NONADVECTIVE CLOUD MOTIONS

Most researchers choose to track cumulus clouds with 1-5 km diameters using 1 km-resolution VISSR imagery at intervals of 3.0-7.5 min. This is done in order to achieve a sufficient number of "representative" tracers of the flow below 700 mb. However, there seems to be a great difference of opinion over which part of the cumulus cloud should be traced to obtain the most representative motions: either its leading edge (Wilson and Houghton, 1979) or its upshear edge (Negri and Vonder Haar, 1980) or the brightness or geometric centroid (Peslen et al., 1985). Furthermore, because of viewing angle problems, the cloud side or base may at times be mistaken for the cloud top (Purdom et al., 1984). A summary of the cloud dynamics factors that cause nonadvective cloud motions is given in Peslen et al. (1985). Peslen (1980) and Wilson and Houghton (1979) assessed cloud tracking errors to be 2.5-2.8 m s^{-1}; the latter study also estimated that errors arising from nonrepresentative cloud motions increased the total error to 4.7 m s^{-1}. However, it is unknown at what level, if any, continental cumulus in baroclinic (strongly sheared) conditions best represent the ambient air motion.

4. UNCERTAINTIES IN CMW HEIGHT MEASUREMENT AND LEVEL ASSIGNMENT

The uncertainty in whether cloud motions in a strongly baroclinic atmosphere represent the winds at any level (or in a layer) has resulted in confusion over which method of cloud height assignment is optimum. Cloud base heights are best determined from surface reports and nearby rawinsondes. Cloud top heights can presently be measured to an accuracy of ±50 mb (100 mb for thin cirrus clouds) in ideal (high emissivity, excellent navigation, etc.) situations by any of three methods:

(1) The bispectral satellite method (Suomi, 1975), which uses visible and infrared data and a local sounding to estimate heights.

(2) The stereographic method (Hasler, 1981), whereby heights can be determined in the stereo overlap area between two geosynchronous satellites.

(3) The VAS method (Menzel et al., 1983), whereby multiple-channel infrared data can be used to assign cloud top heights.

Because of the infrequent availability of stereo data, most researchers have relied upon the bispectral method to separate clouds into "low, medium, or high" levels. The low clouds are then either (a) assigned to a "low layer" ∿200 mb thick (Wilson and Houghton, 1979; Peslen, 1980; Lee and Houghton, 1984a), or (b) assigned to pressure (p) or sigma (σ) surfaces [where σ = cloud base pressure/surface pressure] by using surface and rawinsonde estimates of cloud base levels (Peslen et al., 1985), or (c) assigned to the "level of best fit," which is that level at which the difference between the CMW vector and a nearby rawinsonde wind vector is minimal (Hubert and Whitney, 1971; Negri and Vonder Haar, 1980).

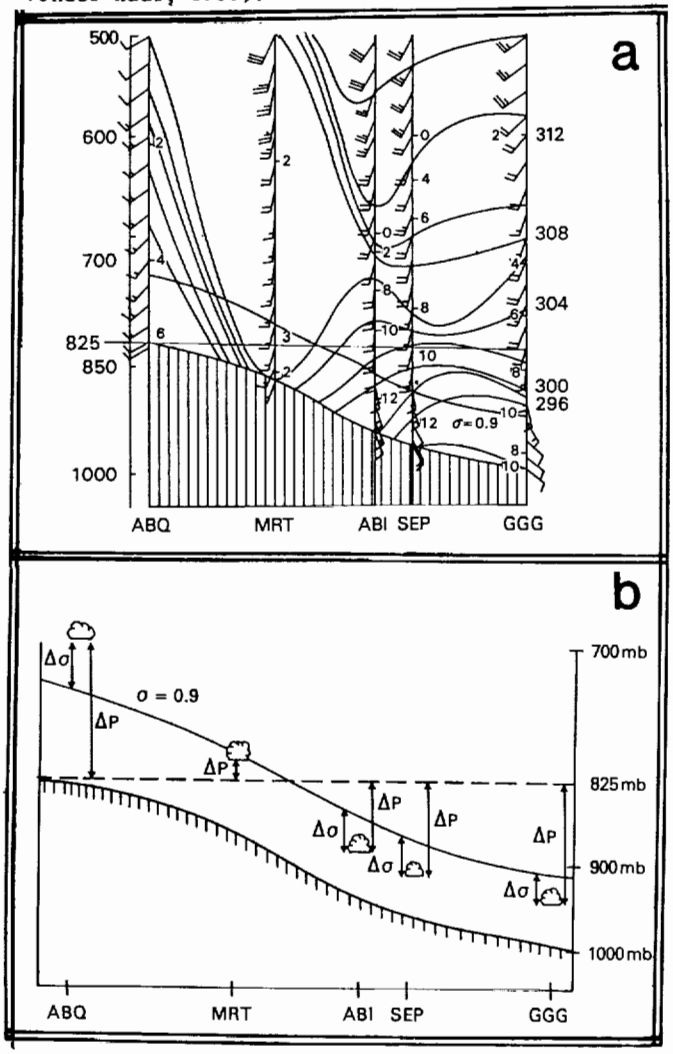

Fig. 3. *Rawinsonde and CMW analyses for the 10 April 1979 SESAME case (Peslen et al., 1985): (a) Vertical cross section from Albuquerque (ABQ), NM to Longview (GGG), TX (solid lines = isentropes in °K, small numbers = mixing ratios in g kg⁻¹, wind barbs in m s⁻¹); and (b) Schematic diagram showing calculated cloud base levels and their vertical separations from the p = 825 mb and σ = 0.9 coordinate surfaces (Δp and Δσ, respectively).*

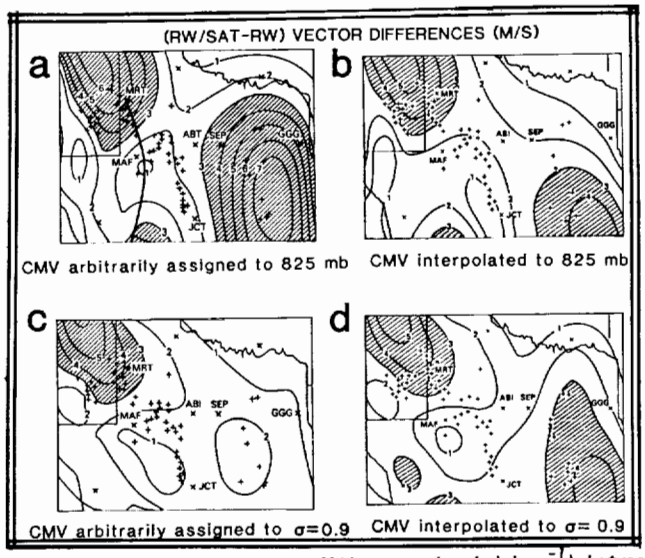

Fig. 4. *Magnitude of the vector differences in wind (m s⁻¹) between the combined (CMW + RW) and RW winds for various methods of CMW level assignment (see subtitles). Vector differences greater than 3 m s⁻¹ are shaded. The (+) and (x) markers are the CMW and rawinsonde (RW) data locations. Heavy line denotes dryline location.*

4.1 Effects Upon Mesoscale Analyses

The combined errors due to nonadvective cloud motions, inaccuracies in determining cloud height, and misassignment of CMW data to a nonrepresentative level contribute more to the total CMW computational error than any other source of error (Lee, 1979). The effect of these combined height assignment errors becomes important whenever there is a substantial vertical wind shear, for then erroneous divergence fields will be created at the assignment level. For a given vertical wind shear ($\Delta V/\Delta z$) and combined height assignment error ($\Delta z_\varepsilon/\Delta x$)$_s$, where s = p, , etc., is the assigned ε coordinate surface, the anomalous divergence is

$$\left(\frac{\Delta V}{\Delta x}\right)_s = \left(\frac{\Delta V}{\Delta z}\right)\left(\frac{\Delta z_\varepsilon}{\Delta x}\right)_s . \qquad (1)$$

An illustration of this effect is presented in Fig. 3, which shows (a) a vertical cross section perpendicular to a strong dryline located near MRT, and (b) the vertical separation of the cloud bases (calculated with surface and rawinsonde data) from the p = 825 mb and σ = 0.9 surfaces. Cloud bases increase in elevation and tend to parallel the sigma surface in going westward from the moist air in eastern Texas. Vector difference magnitudes $\Delta V > 6$ m s^{-1} result from arbitrarily assigning the CMW to the 825 mb pressure surface (Fig. 4a) in regions where vertical separations Δp are largest (Fig. 3b). This method of assignment to a pressure surface is the customary practice, and yet this analysis from Peslen et al. (1985) shows that very significant differences (and, by implication, errors) can arise from using it. The errors are noticeably reduced by assigning the CMW data to the σ = 0.9 surface. Peslen et al. (1985) further show that the arbitrary assignment to the 825 mb surface deteriorates the derived

divergence fields, particularly in eastern Texas where Δp is the greatest.

There is no reason why assignment errors could not also adversely affect the derived divergence fields at even smaller scales. Notice that there is nearly 90^{o} of wind direction variability between some of the CMW vectors due north of the low pressure system in Fig. 1. The sounding taken at Monnett, Mo. (UMN) also showed nearly 90^{o} of wind veering with height in the 950-800 mb layer. Erroneous convergence of 1×10^{-4} s^{-1} could result from the effect of this vertical wind shear over a $\Delta z_{\varepsilon} = \pm 0.5$ km layer and a scale of only twice the grid spacing ($2\Delta x = 80$ km) according to equation (1), or equivalently 50% of the maximum moisture convergence in Fig. 1. Similar concerns can be raised against the representativeness of some of the small-scale convergence centers found in Wilson and Houghton (1979) and Peslen (1980). The fact that some of these centers exhibit temporal persistence has been offered as evidence in support of their realism. However, persistence can be obtained simply by continuously tracking clouds over the same small area, and then assigning the CMW to a single isobaric surface, when in actuality they may be 50-100 mb above or below that level. On the other hand, the agreement between such zones of convergence ahead of cold fronts or drylines and the subsequent locations of convective development does indirectly suggest that the principal zones may be realistic. Similar errors due to vertical wind shear exist when tracking cirrus clouds in the upper troposphere near jet streams and in the anvil outflow layer of tropical cyclones.

4.2 Effects Upon Model Forecasts

A clear illustration of the degrading effects of level misassignment in the presence of shear comes from a numerical experiment in which insertion of cirrus-level CMW into a global weather forecast model produced a deterioration in the forecast of a rapidly developing maritime cyclone (Ebersole, 1984). The bispectral method of height assignment resulted in cloud drift winds nearly 25 m s^{-1} slower than nearby aircraft winds at the assignment level! Since the jet streak intensity was underestimated, a poor forecast of cyclogenesis resulted.

Another numerical study, in which cumulus-level CMW were inserted into a mesoscale model, failed to show persistence of CMW-induced divergence features with wavelengths of 300-800 km (Lee and Houghton, 1984b). This condition suggests that the CMW information was rejected by the model, perhaps because the data were assumed to be representative of an entire ~200 mb layer. This assumption introduced systematic errors due to the vertical wind shear effect "comparable to the horizontal variations estimated for typical mesoscale features" (Lee and Houghton, 1984a, p. 994).

5. THE UTILITY OF CMW FIELDS

This section discusses several problems that limit the practical usefulness of CMW data for mesoscale research.

5.1 Inadequate Coverage

It is not possible to accurately measure cloud motions at more than three levels because clouds at too many levels will hide useful tracers. This limitation has serious ramifications for both the retrieval of three-dimensional fields of mesoscale vertical motion, and for the development of insertion techniques for model initialization. The lack of vertical coverage may also help to explain the rapid loss of mesoscale divergence in the Lee and Houghton (1984b) model study. This behavior is consistent with the predictions from geostrophic adjustment theory, namely, that single insertion of data into a model at only one or two levels will result in the generation of inertial gravity waves (because of the geostrophic imbalance thus created). These waves are quite dispersive and effect the rapid loss of the satellite information.

The horizontal coverage of clouds is also very inadequate for mapping the total wind field: cirrus clouds are evident only in the disturbed flow near jet streaks and convective regions, whereas cumulus clouds are often totally lacking behind drylines and in the immediate post-frontal environment. In fact, the almost total lack of tracers behind the cold front in Oklahoma in Fig. 1 adds to the earlier concerns about the meaningfulness of the derived convergence centers ahead of this front [similarly for the dryline study of Peslen (1980)].

5.2 Objective Map Analysis Problems

The highly nonuniform distribution of most CMW data sets presents formidable problems for the interpolation of the data to a uniform array of grid points. Unfortunately, this objective analysis step is a necessary requirement for both diagnostic analysis and model initialization. Simple techniques for addressing this problem include (1) an elliptical weighting scheme designed to fill in long data-void strips (Lipton and Hillger, 1982) and (2) a Gaussian weighting scheme which gives the analyst information on the degree of "data clustering" (Koch et al., 1983). However, much more sophisticated objective analysis techniques that consider the particular statistical structure of CMW data need to be developed.

Very little is actually known about the nature and variability of CMW data. Structure function analysis of the Negri and Vonder Haar (1980) case (Fig. 1) by Maddox and Vonder Haar (1979) has revealed the highly anisotropic nature of this one data set (compare the u and v wind component curves in Fig. 5). Note also the rapid decrease in correlation of the u wind component at 40 km radius. Although the authors attribute this to the presence of horizontal wind shear, the effects discussed in Section 4.1

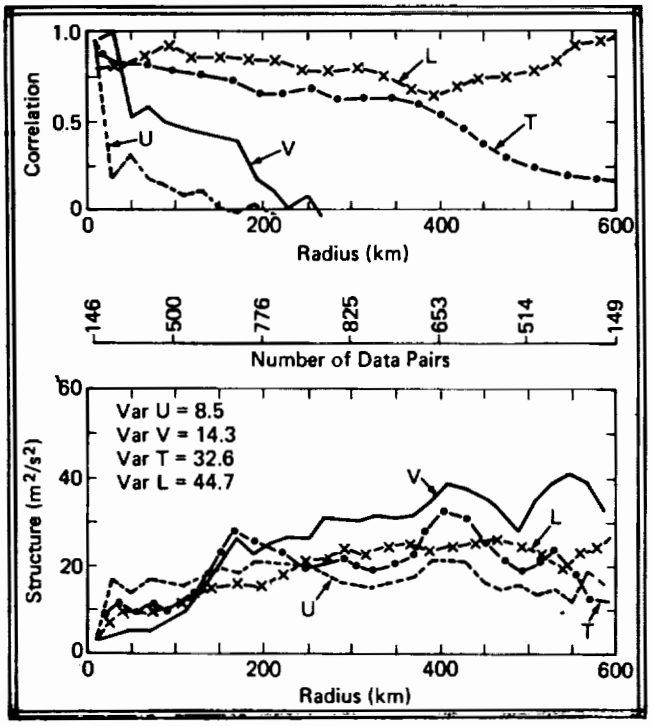

Fig. 5. *Plots of normalized correlation function (top) and structure function (bottom) for the u, v, transverse (T), and longitudinal (L) wind components at 2105 GMT 24 April 1975 (see Fig. 1) [from Maddox and Vonder Haar (1979)].*

could easily have contributed to this effect. Lee and Houghton (1984a) have computed rms and bias differences between low-level CMW and rawinsonde data. The results (Fig. 6) do not provide an optimum area (radius) for objectively analyzing (averaging) CMW data so as to obtain the best agreement with the rawinsonde reports. Thus, it appears that additional studies of the statistical structure of CMW data need to be performed before objective analysis methods tailored to these data can be developed.

Lee and Houghton (1984a) also systematically examined the effects caused by the choice of objective analysis method. They showed that the analysis schemes all reproduced essentially the same patterns in the fields, although differences between the divergence analyses were about half of the typical magnitude of divergence ($\sim 2 \times 10^{-5}$ s^{-1}). The velocity field differences were also comparable to the "natural horizontal variations expected in mesoscale features of 100 km scale." Clearly, these differences are unacceptably large. This study also showed the difficulty of choosing a representative grid size because of the highly irregular spacing of the CMW data. Amplitude changes and phase shifts of patterns in regions of sparse data coverage and near edges of the analysis area were the result of this non-uniform data coverage.

5.3 Coordinate Level Assignment Difficulties

Once the heights of the CMW vectors are determined, one must still assign the entire set of vectors to a coordinate surface before the data can be used either in diagnostic studies or for model initialization. The Peslen et al. (1985) study concluded that if one is forced to arbitrarily assign the CMW to a surface, vector speed differences from rawinsonde values could be appreciably reduced by using a sigma surface instead of a pressure surface. However, limitations are imposed on the sigma surface in areas displaying strong moisture gradients and vertical wind shears, at least when an arbitrary assignment method is used (as over New Mexico in Fig. 4c). The most meaningful kinematic fields resulted when the CMW were vertically interpolated to a coordinate surface by using the actual shear from mesoscale rawinsonde observations. Thus, real-time mesoscale observations (or realistic predictions) appear to be necessary in order to obtain highly accurate assignment of CMW to coordinate surfaces. This information is not readily available.

6. CONCLUDING REMARKS AND RECOMMENDATIONS

The technique of deriving winds from cloud drift motions appears to provide information for mesoscale diagnostic analysis, at least for scales larger than 100 km. However, there are many unsolved problems. Comparisons of CMW with in situ aircraft or ground-based remote sensors (like NOAA's wind profiler) need to be made to ascertain the actual representativeness of CMW data in continental, vertically sheared situations. A continuing problem is that the accuracy of cloud height estimation seems to be no better than ± 0.5 km, enough to produce significant wind errors of ~ 5 m s^{-1} due to the effects of vertical shear. New objective analysis techniques tailored to the specific characteristics of CMW data, namely, their highly non-uniform coverage and their (presently inadequately understood) unique statistical structure, are urgently needed.

It seems that cloud drift wind data are, in isolation, ill suited as input to mesoscale models when forecasts are made in strongly sheared, pre-convective environments. The lack of a truly three-dimensional wind field from cloud drift winds and the related need to assign the data to just a couple of coordinate surfaces

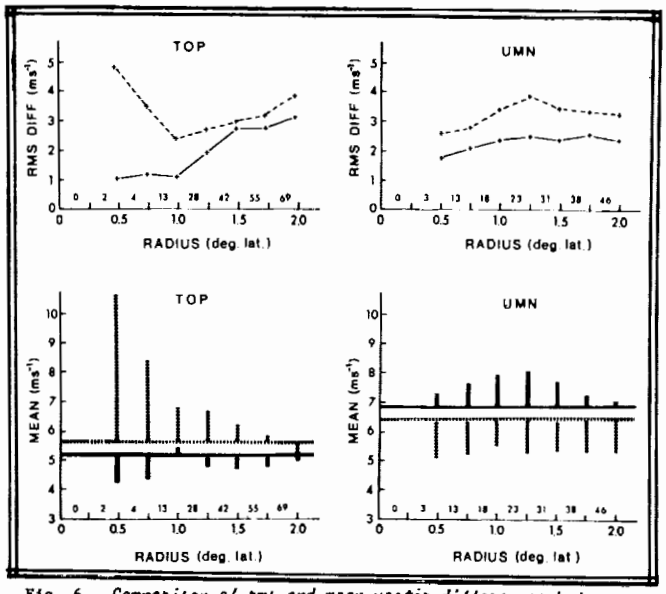

Fig. 6. *Comparison of rms and mean vector differences between satellite wind and rawinsonde wind within a circular region about rawinsonde stations TOP and UMN. Mean differences (biases) are given by length of vertical lines [from Lee and Houghton (1984a)].*

implies that CMW data may not produce a sustained impact in such model forecasts. Another problem that needs addressing is the likelihood that multiple-coordinate surfaces would need to be used whenever strong moisture and wind gradients exist. These conditions are more likely to be encountered in large domains. Unfortunately, the domain size must be "large" for model impacts to be even possible.

Finally, it is suggested that experiments be performed to find means of merging or synthesizing CMW data with other wind measurement systems, such as the wind profiler, Doppler lidar, and mesoscale rawinsondes.

REFERENCES

Ebersole, K. A., 1984: Diagnostic verification of the GLAS general circulation model as applied to a case of extratropical maritime explosive cyclogenesis. M.S. Thesis, Naval Postgraduate School, Monterey, CA, 110 pp.

Hasler, A. F., 1981: Stereographic observations from geosynchronous satellites: An important new tool for the atmospheric sciences. Bull. Amer. Meteor. Soc., 62, 194-212.

Hubert, L., and L. Whitney, 1971: Wind estimation from geostationary satellite pictures. Mon. Wea. Rev., 99, 665-672.

Koch, S. E., M. desJardins, and P. J. Kocin, 1983: An interactive Barnes objective map analysis scheme for use with satellite and conventional data. J. Clim. Appl. Meteor., 22, 1487-1503.

Lee, D., 1979: Level assignment in the assimilation of cloud motion vectors. Mon. Wea. Rev., 107, 1055-1073.

Lee, K. L., and D. D. Houghton, 1984a: A quantitative study of satellite winds for mesoscale meteorology. Mon. Wea. Rev., 112, 990-1004.

_____, and D. D. Houghton, 1984b: Impact of mesoscale satellite wind data on numerical model simulations: A case study. Mon. Wea. Rev., 112, 1005-1016.

Lipton, A. E., and D. W. Hillger, 1982: Objective analysis of discontinuous satellite-derived data fields for grid point interpolation. J. Appl. Meteor., 21, 1571-1581.

Maddox, R. A., and T. H. Vonder Haar, 1979: Covariance analysis of satellite-derived mesoscale wind fields. J. Appl. Meteor., 18, 1327-1334.

Menzel, W. P., W. L. Smith, and T. R. Stewart, 1983: Improved cloud motion wind vector and altitude assignment using VAS. J. Clim. Appl. Meteor., 22, 377-384.

Nappo, C. J., et al., 1982: The Workshop on the Representativeness of Meteorological Observations, June 1981, Boulder, Colo. Bull. Amer. Meteor. Soc., 63, 761-764.

Negri, A. J., and T. H. Vonder Haar, 1980: Moisture convergence using satellite-derived wind fields: A severe local storm case study. Mon. Wea. Rev., 108, 1170-1182.

Pecnick, M. J., and J. A. Young, 1984: Mechanics of a strong subsynoptic gravity wave deduced from satellite and surface observations. J. Atmos. Sci., 41, 1850-1862.

Peslen, C. A., 1980: Short-interval SMS wind vector determinations for a severe local storms area. Mon. Wea. Rev., 108, 1407-1418.

_____, S. E. Koch, and L. W. Uccellini, 1985: The effect of the arbitrary level assignment of satellite cloud motion wind vectors on wind analyses for a pre-thunderstorm environment. J. Clim. Appl. Meteor. (accepted).

Purdom, J. F. W., T. H. Vonder Haar, J. K. Stewart, and N. E. Leary, 1984: Diagnosing the severe thunderstorm environment by mesoscale cloud tracing--a new approach and new information. Preprints, Conf. on Satellite Meteorology/Remote Sensing and Applications, Amer. Meteor. Soc., Tampa, FL, 100-105.

Rodgers, E., and R. C. Gentry, 1983: Monitoring tropical-cyclone intensity using environmental wind fields derived from short-interval satellite images. Mon. Wea. Rev., 111, 979-996.

Shenk, W. E., 1985: Cloud motion derived winds: Their accuracy, coverage, and suggestions for future improvement. Symposium on Global Wind Measurements, Columbia, MD (this proceedings volume).

Suomi, V. E., 1975: Man computer interactive data access system (McIDAS). NASA Contract NAS5-23296, University of Wisconsin, Madison, WI. [NTIS 75N28733.]

Wilson, T. A., and D. D. Houghton, 1979: Mesoscale wind fields for a severe storm situation determined from SMS cloud observations. Mon. Wea. Rev., 107, 1198-1208.

OBSERVING SYSTEM SIMULATION EXPERIMENTS AT GFSC

R. Atlas, E. Kalnay, W. E. Baker, J. Susskind, D. Reuter, and M. Halem

Laboratory for Atmospheres
NASA/Goddard Space Flight Center
Greenbelt, MD 20771

1. INTRODUCTION

A series of realistic simulation studies is being conducted as a cooperative effort between the European Centre for Medium Range Weather Forecasts (ECMWF), the National Meteorological Center (NMC), and the Goddard Laboratory for Atmospheres (GLA), to provide a quantitative assessment of the potential impact of future observing systems on large scale numerical weather prediction. A special objective of this project is to avoid the unrealistic character of earlier simulation studies. Following a brief review of previous simulation studies and real data impact tests, the methodology for the current simulation system will be described. Results from an assessment of the realism of the simulation system and of the potential impact of advanced observing systems on numerical weather prediction and preliminary results utilizing this system will be presented at the conference.

2. EARLY SIMULATION STUDIES

Since the advent of meteorological satellites in the 1960s, a considerable research effort has been directed toward the design of space-borne meteorological sensors, the development of optimal methods for the utilization of satellite soundings and winds in global-scale models, and an assessment of the influence of existing satellite data and the potential influence of future satellite data on numerical weather prediction. Observing system simulation experiments have played an important role in this research and in the planning of Data Systems Tests (DST) and the First GARP Global Experiment (FGGE). Such studies have aided in the design of the global observing system, the testing of different methods of assimilating satellite data, and in assessing the potential impact of satellite data on weather forecasting.

The earliest simulation studies proceeded according to the following sequence of steps: First, an artificial history of the atmosphere is created by numerical integration of a model. Second, simulated "data" are created from the history by addition of random variations to the history values for temperature, wind, and pressure. Third, the numerical integration that created the history is repeated, but with the meteorological variables in the model replaced by the simulated data at locations and times corresponding to the assumed pattern of observations.

For example, if the observing subsystem under study is designed to produce wind data, the winds in the history are replaced by simulated wind "data" at locations, heights, and times corresponding to the coverage expected from the observing system. If the study is directed at the performance of an observing subsystem design to yield temperature or pressure information, the temperature or pressure values in the history are replaced by the respective simulated "data" in a similar fashion.

If the data had no errors, and therefore were identical with the history values, and were inserted at all grid points, the new integration would be identical with the history. However, when errors are present, the inserted data perturb the computed circulation, and cause it to depart from the history. The difference between the history and the perturbed circulation resulting from the data insertion is a measure of the effect of the errors in the simulated data. The effect of the errors usually is expressed in terms of differences of the meteorological variables such as wind components, averaged over all points of the computing grid. These differences are considered to represent the errors in the determination of the global atmospheric states, resulting from the assumed errors in the observing system.

In order to simulate different types of data and data coverage and assess their impact on forecasting skill, a somewhat different approach has been utilized (Cane et al., 1981). In this procedure a forecast model is integrated for a long period, such as one or two months. This long run is then assumed to be "nature." "Observations" are then extracted from the nature run, following a suitable geographical and temporal distribution, and random "observational" errors are added. These simulated observations are then assimilated with an analysis cycle, and the same model is used as a "forecast model" from the analyzed fields.

Simulation studies conducted by Charney et al., (1969), Halem and Jastrow (1970), Jastrow and Halem (1970, 1973), Williamson and Kasahara (1971), Kasahara (1972), Gordon et al. (1972),

and others indicated that all three of the primary meteorological variables--wind, pressure, and temperature--could be determined if a continuous tinuous time history of any one of these variables were inserted into a general circulation model. In addition, these studies provided an analysis of the GARP data requirements, the "useful" range of predictability, the need for reference level data, and the relative usefulness of asynoptic versus synoptic measurements and analysis. From the results, it was concluded that the assimilation of satellite-derived temperature profiles meeting the GARP data specifications should yield a substantial improvement to the accuracy of numerical weather forecasts.

An examination of the underlying rationale for the simulation studies as previously conducted (Jastrow and Halem, 1973), as well as a comparison of the results of the above studies with the results of subsequent real data impact tests indicates several important limitations. The most important weakness stems from the fact that the same numerical model has been used both to generate the simulated observations and to test the effectiveness of these observations. Other weaknesses relate to the model-dependence of the studies and the specification of observational errors as random.

3. REAL DATA IMPACT TESTS

In recent real data impact studies, most of the qualitative conclusions of the preceeding observing system simulation experiments have been confirmed, although in some respects the results appear to be overly optimistic. In particular, it was clear from estimates of the quality of satellite temperature soundings and cloud-track wind data obtained during the NASA Data Systems Test (DST), (Desmarais et al., 1978) that the accuracies of the FGGE satellite observing systems would be considerably poorer than were needed to infer wind profiles of the accuracy specified in the GARP data requirements. Moreover, as a result of these DST studies, expectations that the FGGE observing system would significantly improve the forecast skill and range of useful predictability also were questionable. For example, a forecast impact test by Ghil et al. (1979) with a coarse resolution second-order model showed only a modest beneficial impact of the DST-6 satellite sounding data, whereas a similar study by Tracton et al. (1980) revealed a slight negative impact for DST-5 and a slight positive impact for DST-6, both of which were meteorologically insignificant.

More recently, however, when the same DST-6 temperature-sounding impact test was repeated with a more accurate forecast model employing higher resolution, Atlas (1979, 1982) and Atlas et al. (1979, 1982) showed that the DST data were in certain cases capable of making modifications to the analyzed atmospheric states that produce meteorologically significant improvements in the 72 h forecasts over North America. Also, the first FGGE case studies reported by Bengtsson (1981a,b) with the ECMWF model indicated improvements in short- and extended-range forecasts with the FGGE data. Similarly, Gustaffson (1979), employing the Swedish operational forecast/analysis system (i.e., a 300 km, quasi-geostrophic model), showed periods during the first Special Observing Period (SOP-1) in which the satellite information had a positive impact on the objective analysis and also resulted in improved numerical forecasts.

These results are supported by our recent investigation of the FGGE satellite observing system for the SOP-1 period (Halem et al., 1982). Utilizing the GLAS Fourth Order Global Atmospheric Model, an extensive series of data assimilation/forecast impact experiments have been conducted. These experiments show that although the GARP data accuracy requirements for the satellite observing systems were not met, assimilation of FGGE satellite data is capable of providing a reasonable determination of the complete atmospheric state. In general, a small improvement to forecast skill in the Northern Hemisphere and a larger improvement in the Southern Hemisphere results from the assimilation of sattellite soundings and cloud-track winds.

4. REMAINING PROBLEMS AND THE PRESENT STUDY

The results of the real data impact studies indicate that major deficiencies in the global observing system still exist and that the FGGE satellite sounders are far from optimal. Advanced passive infrared and microwave sounders and active scatterometer and lidar sounders in a variety of combinations have recently been proposed to improve the accuracy of satellite observations and extend the useful range of numerical weather prediction. Realistic observing system simulation experiments are required to determine which of the proposed instruments will provide the greatest improvements as well as the optimal design of the future global observing system.

As indicated before, previous simulation studies have been characterized by the use of the same model to simulate "nature" and observations and to produce forecasts. This "identical twin" problem may distort the conclusions derived from such studies, as discussed in the following section.

In the present study, we attempt to avoid these limitations by designing a more realistic simulation system and calibrating its results by comparison with real data experiments performed with a similar system, and by accurately simulating the expected accuracy and characteristics of observational systems. The simulation system will then be used to study the potential impact of advanced passive sounders and lidar temperature, pressure, humidity, and wind observing systems.

5. DESIGN OF THE SIMULATION SYSTEM

The analysis/forecast simulation system consists of four elements: (1) An atmospheric model integration to provide a complete record of the "true" state of the atmosphere (called nature). This record is then used to fabricate observational reports and to evaluate analyses and forecasts. (2) A conventional data assimilation cycle that is used as the "control experiment." The control experiment is like an operational

forecast-analysis cycle based on conventional observations except that it makes use of fabricated conventional data obtained from the nature run to produce the analyzed fields. (3) A satellite data assimilation that differs from the control in also including fabricated satellite data incorporated in an intermittent or time-continuous manner, in the forecast-analysis cycle. (4) Forecasts produced from both control and satellite initial conditions. Comparison of these forecasts with nature provides an assessment of the impact of satellite data.

Two important considerations are involved in the design of the control assimilation run: the nature of the initial conditions, and the forecast model used. In reality, short-range forecasts have errors stemming from three different sources: (1) inaccuracy of the initial state; (2) model errors that can be ascribed to numerical truncation (horizontal and vertical truncation errors due to insufficient resolution); and (3) model errors that can be ascribed to the "physics" of the model. The latter include parameterization of subgrid processes like radiation, cumulus convection, and friction, as well as sources of external forcing, like orography, sea/land contrast, and even the use of an artificial rigid top boundary condition, common to all numerical models. Numerical and "physical" deficiencies introduce systematic errors in the model integrations which are most evident in the differences between model and observed climatological averages. A striking example of these climatological errors is apparent in the stationary, forced planetary waves. Even though these large-scale waves are numerically well resolved, they are not well simulated by numerical models. In a numerical forecast, a model tends to drift toward its own climatology, so that serious errors in the stationary waves are apparent after even a short time. For realistic simulation studies, all three sources of errors should be simulated. In previous simulation experiments, the same model was used to produce the "true" state and "forecasts." Therefore, the errors in the for casts were due only to errors in the initial conditions. This method ("identical twin experiment") has the apparent advantage that it isolates the effect of initial data errors and avoids both numerical and "physical" errors. On the other hand, it has a very important shortcoming: since the model and "nature" have the same climatology, the accuracy of the simulated forecasts may be far superior to the accuracy of real forecasts. As a result, the external error growth due to the fact that current models are only approximations of the atmosphere is not present in the "identical twin" experiments. This has the effect of increasing the skill of conventional forecasts at low levels of data coverage, because the perfect forecast model is able to "fill up" data gaps. Consequently, at low levels of data, the impact of an observing system is overestimated, whereas the impact of high levels of data, such as provided by satellites can be underestimated. In addition, if the "nature" and "forecast" models are not realistic enough, i.e., don't possess a realistic model climatology, the data impact may be distorted. For example, a forecast model that cannot simulate the "roaring forties" regime in the Southern Hemisphere will not be helped by better low level winds in the Southern Hemisphere. The forecast model used should be sufficiently accurate that error growth should be dominated by initial data errors rather than by model-dominated errors such as truncation errors. Otherwise, the experiment may overestimate the skill of the forecast and underestimate the influence of the data on the analysis.

Finally, if simulation studies are to provide an accurate indication of how simulated data will influence forecasts in the real world, it is crucial that their error characteristics be realistic. For simulated observational errors to be representative of real observational errors they should be introduced at actual observing locations and should not be just white noise. Random errors with a standard deviation of the order of GARP errors saturate the spectrum at high frequencies and their effect is mostly averaged out. Bias and horizontal and vertical correlations of errors with each other and with the synoptic situation should be introduced appropriately.

In the current simulation studies, we attempt to minimize difficulties of earlier studies discussed previously. In order to avoid the "identical twin" character of previous studies, the high resolution (1.875° x 1.875° x 15 levels) ECMWF model will be used as nature, and the 4° x 5° x 9 levels GLA (previously known as GLAS) model for assimilation and forecasting. Special care will be taken to simulate realistically observational errors.

6. GLA SIMULATION OF OBSERVATIONS OF SPACE-BASED SOUNDING SYSTEMS

In this study, we will be simulating forecast impacts using the current passive HIRS2/MSU sounding system as well as other passive systems using the Advanced AMTS and AMSU infra-red and microwave sounders alone and in various combinations. In addition, we will simulate active lidar systems which measure pressure profile, temperature profile, and winds. The location and times of the passive soundings will be identical to those produced operationally in November 1979. In the case of the operational HIRS2/MSU sounding system, one could simulate atmospheric soundings in a manner analogous to those of the conventional observing system by using actual statistics relating accuracies of retrieved atmospheric soundings with colocated radiosonde reports. This approach has two important drawbacks. First, this procedure can not be used with future sounders, for which there are no error statistics. Secondly, and much more significantly, the errors of temperature profiles retrieved from passive sounders are not random, but are highly correlated in the horizontal and vertical and are dependent on the nature of the synoptic situation, including the interrelationship between atmospheric temperature-humidity profile, ground temperature, and cloud fields.

To simulate atmospheric temperatures determined from passive sounders, we therefore take the more fundamental approach of first simulating

radiance observations seen by the satellite and then retrieving temperature pr files from the observations. The simulations are performed using the radiative transfer model described in Susskind et al. (1983) and temperature retrievals as in Susskind et al. (1984). In order to simulate radiances for the channels for a given observation, one needs the surface pressure, atmospheric temperature-humidity-ozone profile, the ground temperature and emissivity as a function of frequency, and the multi-layer cloud field together with the spectral properties of the clouds. In addition, one needs the viewing angle of the satellite and location of the sun. In order to simulate a sounding reported at a given time and location, the atmospheric temperature-humidity profile is taken from the "nature" run, as obtained from ECMWF, interpolated in space and time to the satellite coordinates. The surface pressure is obtained using interpolated sea level pressure values, again given by "nature," and topographical fields. The fields obtained from ECMWF however did not contain information about ozone, ground temperature and emissivity, and clouds. Of these, ozone is the least significant and was fixed as a function of latitude according to climatological values. The ground temperatures and surface emissivities were simulated according to reasonable values determined from analysis of HIRS2/MSU data for November 1979 as in Susskind et al. (1984).

In the case of ground temperature, we generated fields of $T_G - T_A$, that is ground temperature minus surface air temperature, and examined their mean and standard deviation over a 2°x2° grid for the month. Ground temperatures for a given location were then defined as $T_G = T_A + \overline{T_G - T_A} + \delta$ where T_A is the interpolated surface air temperature as above, $\overline{T_G - T_A}$ is the mean ground-surface air temperature difference for the location as determined from real HIRS2/MSU data for the month, and δ is a random component consistent with the observed standard deviation. Surface emissivity, ε, at 50.3 GHz, which is an important factor affecting MSU and AMSU observations, was determined in an analogous manner, using mean and standard deviation values of ε determined for November 1979 from the real HIRS2/MSU data. It was interesting to note, looking at these maps, that the standard deviations of ε were in general small, except for those areas where the ice edge was changing during the month or in regions of variable snow cover. Surface emissivity for the infra-red channels was taken as fixed as described in Susskind et al. (1983).

Perhaps the single most important factor affecting the observations and accuracy of passive retrievals is clouds. In order to get the proper spatial correlations of errors as a function of synoptic situation, the cloud fields must be very realistically related to the synoptic situation. We used the relative humidity fields, r_j, to produce up to four levels of broken clouds at each sounding location, with pressures at 850 mb, 700 mb, 500 mb, and 300 mb. The cloud fraction α_j at a given level j is simulated according to

$$\alpha_j = \frac{r_j - r_{cj}}{1 - r_{cj}}$$

where r_{cj} is a pressure dependent relative humidity cutoff value whose values were provided by NMC.

The radiances for channel i observed by the satellite are computed as

$$R_i = \sum \alpha_j^* R_{ij} + (1 - \sum \alpha_j^*) R_{i,CR}$$

where R_{ij} is the radiance which would be observed in channel i if the field of view were completely covered by clouds at level j. $R_{i,CLR}$ is the radiance which would be observed if there were no clouds, and α_j^* is the fraction of the sky covered by clouds at layer j as seen from above. Clearly, while α_j can be as large as 1, $\sum \alpha_j^*$, can only be between 0 and 1. To insure this, we assume the clouds in each layer are totally correlated in space and fix $\alpha_j^* = \alpha_j - \sum_k \alpha_k^*$ for layer j where α_j^* represents all layers above j, but constrain α_j^* to be no less than zero. In other words, α_j^* equals zero if α_j is less than the cloudiness above, and α_j^* is the difference between α_j and the largest cloudiness above otherwise All cloud radiances are simulated assuming the clouds are opaque at infrared frequencies and transparent at microwave frequencies.

The GLA retrieval method uses two field of view to perform a cloud correction to be used on the observed infrared radiances. In the simulation of radiances, observations in two fields of view were simulated for each sounding. The radiances are simulated assuming only the cloud fractions α_j^* differ in the two fields of view. For a given level, $\alpha_{j,1}^*$ and $\alpha_{j,2}^*$, are simulated from α_j^* in the following way. At $\alpha_j = 0$ or 100, both cloud fractions are set at 0 to 100. Otherwise $\alpha_{j,1}^*$ is less than α varying linearly between the following points (0, 0), (20, 10), (90, 60) and (100, 100), and $\alpha_{j,2}^*$ is greater than α_j^* varying linearly between the points (0, 0), (20,30) and (100,100). This allows for reasonable discrimination between the cloud fraction and radiances in both fields of view. In analysis of actual data, this discrimination, which is necessary for performing the cloud correction, is obtained by separating and then averaging observations in the warmest and coldest individual spots in an area.

As in the analysis of real HIRS2/MSU data, soundings are rejected if the radiances indicate too much cloudiness in the field of view (typically more than 70% in a sounding area) or if no atmospheric solution can be found from which computed radiances match the cloud corrected radiances to within 1°K. AMTS and AMSU observations and retrieved temperatures are produced in an analogous way.

In the case of active sounders, the errors obtained from analysis of the data are more nearly random and uncorrelated with each other. Therefore, the approach of generating random uncorrelated errors will be used in simulating retrieved quantities. To begin with, the coverage of sounding data will be taken as in the passive sounders for comparison purposes. Later, more

realitic scan patterns for the active sounders will be used. Studies will be made as a function of assumed noise level and scan pattern. In all cases, signal to noise values will be attenuated at given levels according to the effective cloud cover, α_f, as defined above.

7. PRELIMINARY RESULTS

For all the experiments which have been completed to date, the nature run is a twenty-day integration from 0000 GMT 10 November 1979 using the 15 level, 1.875° resolution, ECMWF model. All types of FGGE and conventional data were simulated by NMC by interpolating the nature fields to observation locations and adding assumed random or systematic errors to the interpolated values (C. Dey, personal communication). Only satellite temperature soundings were assumed to have systematic errors. These were generated using the first approach described in Section 6. GLA simulated retrievals using the second approach described in Section 6 are currently being generated but have not yet been used in our experiments. LIDAR wind profiles were simulated at TIROS observation locations with 1-3m sec^{-1} accuracy. Wind profiles were not generated at levels below which the integrated cloud amount exceeded 90%.

Experiments have been conducted to calibrate the simulation system and determine its realism, and to begin to assess the relative impact of temperature and wind profile observing systems. To this end, two real data assimilation cycles, a control and FGGE (see Halem et al., 1982 for descriptions), and five simulated data assimilation cycles, control, FGGE, control plus TIROS, control plus perfect temperatures, and control plus wind profiles were performed for the period 0000 GMT 10 November to 0000 GMT 25 November 1979.

The NMC analysis for 0000 GMT 10 November was used as initial conditions for the real data assimilation cycles. Initial conditions for the simulated data assimilations were provided by a real data control assimilation from 0000 GMT 4 November to 10 November. Eight five-day forecasts were generated from each assimilation at 48 h intervals beginning on 11 November. In addition, a twelve-day integration from the ECMWF analysis at 0000 GMT 10 November was generated with the GLA model. This forecast was then compared to the nature run as a measure of the differences between the two models.

Fig. 1 shows that there are substantial differences between the GLA and ECMWF sea level pressure forecasts from 10 November as verified over North America. For the first four days the differences between the two model forecasts are about as large as the differences between the ECMWF forecast and its analysis. However, from five to eight days the two model forecasts resemble each other more closely than either forecast represents the analysis. In addition an examination of global difference fields between the forecasts and between each forecast and the analysis (not shown) reveals that in the Northern Hemisphere, the model forecast differences are of a larger scale than the forecast versus analysis differences. These results indicate that the simulation system is significantly more realistic

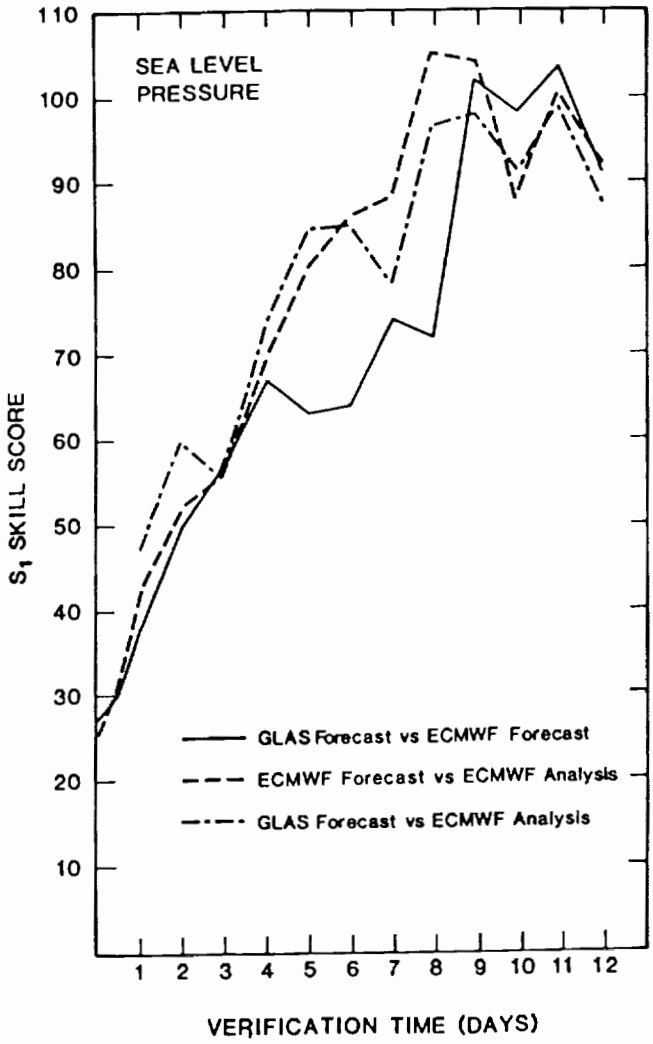

Fig. 1 Sea level pressure S_1 scores for North America for the ECMWF Nature run verified against the ECMWF analysis, and the corresponding GLAS model forecast from the ECMWF analysis at 0000 GMT 10 Nov 79 verified against the ECMWF analysis and the ECMEF Nature run.

than the identical twin systems described previously. But the differences between the models still may not be large enough to represent the differences between models and the real atmosphere.

Fig. 2 summarizes the initial results of our simulation experiments. S_1 skill scores averaged for eight forecast cases are presented for the control, control plus TIROS and control plus wind profiles for the Northern Hemisphere, and for the control, control plus TIROS and control plus wind profiles and FGGE experiments for the Southern Hemisphere. The FGGE results were nearly identical to the control plus TIROS in the Northern Hemisphere and are not shown. Similarly the control plus perfect temperatures were on the average similar to the control plus TIROS and are not presented.

From Fig. 2, it can be seen that the use of simulated wind profile data shows a significant improvement over the TIROS or FGGE experiments in

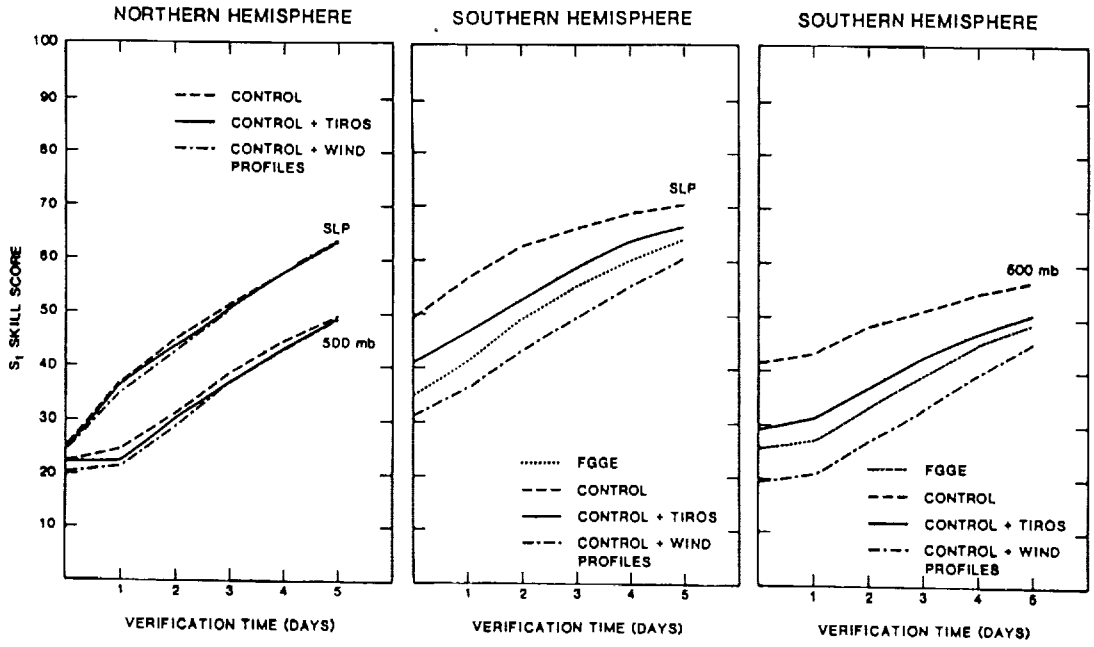

Fig. 2 Simulated data S_1 score verification.

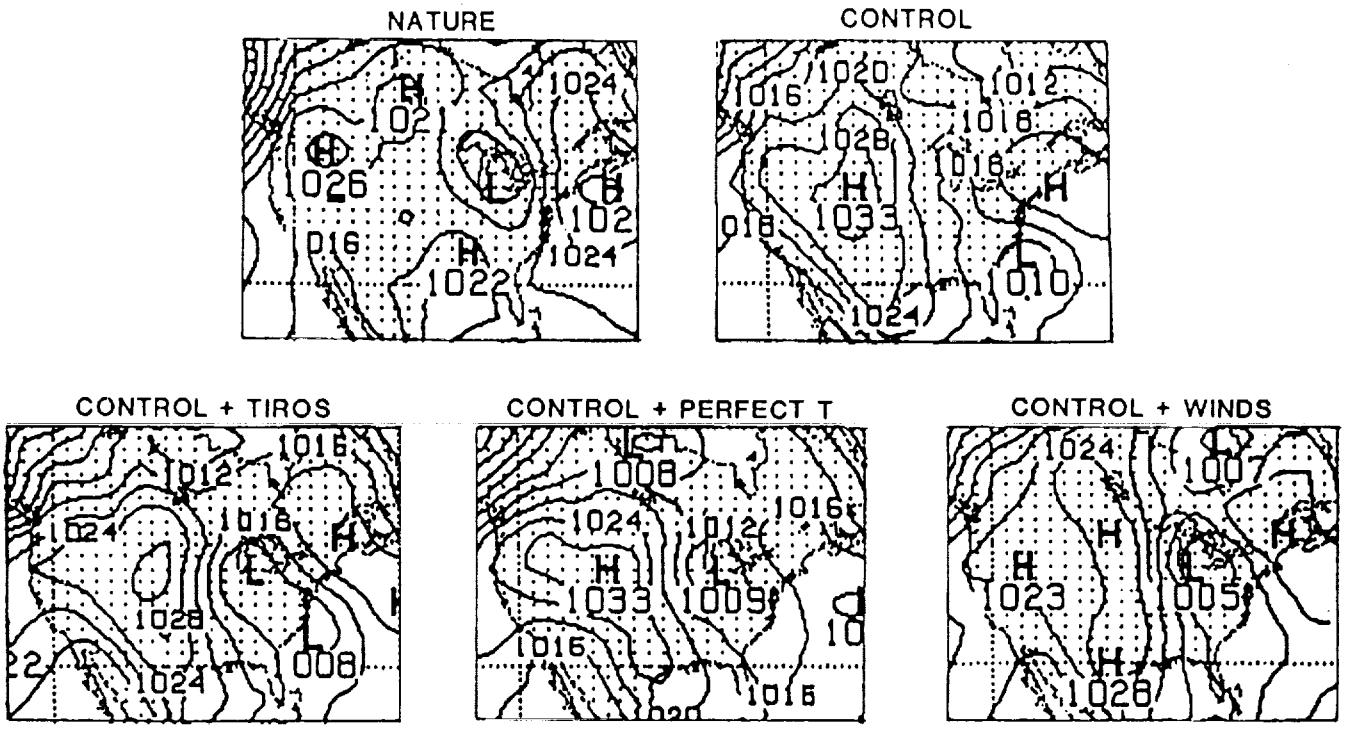

Fig. 3 Simulated 5 day sea level pressure forecasts from 23 Nov 79 and verification.

the Southern Hemisphere. For the Northern Hemisphere the impact of both simulated TIROS and wind profiles is only very slightly beneficial on the average. However, in specific cases, significant forecast improvements occur for smaller regions. Fig. 3 shows a case of major improvement in the prediction of a storm over the United States which was poorly forecasted with the simulated control system. The use of TIROS data improved the prediction of the low near the Great Lakes. Significant further improvement resulted from either perfect temperatures or wind profiles.

To measure the realism of the simulation results, comparisons were made between the real and simulated data verifications for the same regions. These comparisons showed that the simulated control experiment was unrealistically accurate in the Northern Hemisphere but realistic in the Southern Hemisphere. In addition, the impact of TIROS and FGGE data appears to be slightly overestimated requiring a small calibration to the simulation impact results.

8. CONCLUSIONS

The general conclusions from these studies are that (i) the use of wind profile data produces more accurate 1-5 day forecasts than temperature data and (ii) if the proposed accuracies and coverage for a LIDAR wind profiler can be achieved, then Southern Hemisphere analyses and forecasts should become as accurate as those for the Northern Hemisphere.

ACKNOWLEDGMENTS

The authors wish to acknowledge D. Edelmann, J. Pfaendtner, G. Avesian, A. Pursch, J. Terry, J. Ardizzone, D. Jones, and D. Wallace for their contributions to this project, L. Rumburg for drafting the figures, and M. Wells for typing the manuscript.

REFERENCES

Atlas, R., 1979: A comparison of GLAS SAT and NMC high resolution NOSAT forecasts from 19 and 11 February 1976. NASA Tech. Memo. 80591. Goddard Space Flight Center, Greenbelt, Maryland 20771, (NTIS N80-17638), 6 pp.

_____, 1982: The growth of prognostic differences between GLAS model forecasts from SAT and NOSAT initial conditions. Mon. Wea. Rev., 110, 877-882.

_____, M. Halem, M. Ghil, 1979: Subjective evaluation of the combined influence of satellite temperature sounding data and increased model resolution on numerical weather forecasting. Preprints Fourth Conf. on Numerical Weather Prediction, Silver Spring, Maryland, Amer. Meteor. Soc., 319-328.

_____, 1982: The effect of model resolution and satellite sounding data on GLAS model forecasts. Mon. Wea. Rev., 110, 662-682.

Bengtsson, L., 1981a: Numerical prediction of atmospheric blocking--a case study. Tellus, 33, 19-42.

_____, 1981b: The impact of FGGE on global medium range forecasts. Characteristics of atmospheric planetary circulations and associated model forecast skill during FGGE case studies selected by WGNE. Proceedings of the International Conference on Early Results of FGGE and Large-Scale Aspects of its Monsoon Experiments, Tallahassee, Florida, 12-17 January, 1981.

Cane, M. A., V. J. Cardone, M. Halem, and I. Halberstam, 1981: On the sensitivity of numerical weather prediction to remotely sensed marine surface wind data: A simulation study. J. Geophys. Res., 86, 8093-8106.

Charney, J., M. Halem, and R. Jastrow, 1969: Use of incomplete historical data to infer the present state of the atmosphere. J. Atmos. Sci., 26, 1160-1163.

Desmarais, A., S. Tracton, R. McPherson, R. Van Haaren, 1978: The NMC report on the Data Systems Test. (NASA Contract S-70252-AG), U.S. Dept. of Commerce, NOAA, NWS.

Ghil, M., M. Halem, R. Atlas, 1979: Time-continuous assimilation of remote-sounding data and its effect on weather forecasting. Mon. Wea. Rev., 107, 140-171.

Gordon, C. T., L. Umscheid, Jr., and K. Miyakoda, 1972: Simulation experiments for determining wind data requirements in the tropics. J. Atmos. Sci., 29, 1064-1075.

Gustaffson, N., 1979: Use of Data from Meteorological Satellites. The Impact of Satellite Information on Short-Range Numerical Forecasts. Lannior, France, 17-21 Sept., 1979 (ESA SP-143 Oct. 1979), 113-127.

Halem, M., E. Kalnay-Rivas, W. Baker, and R. Atlas, 1982: An assessment of the state of the atmosphere as inferred from the FGGE satellite observing systems during SOP-1. Bull. Amer. Meteor. Soc., 63, 407-426.

_____, R. Jastrow, 1970: Analysis of GARP data requirements. J. Atmos. Sci., 27, 177.

Jastrow, R., and M. Halem, 1970: Simulation studies related to GARP. Bull. Amer. Meteor. Soc., 51, 490-513.

_____, 1973: Simulation studies and the design of the first GARP Global Experiment. Bull. Amer. Meteorol. Soc., 54, 13-21

Kasahara, A., 1972: Simulation experiments for meteorological observing systems for GARP. Bull. Amer. Meteorol. Soc., 53, 252-264.

Susskind, J., J. Rosenfield, and D. Reuter, 1983: An accurate radiative transfer model for use in the direct physical inversion of HIRS2 and MSU temperature sounding data. J. Geophys. Res., 88C, 8550-8568.

_____, and M. T. Chahine, 1984: Remote sensing of weather and climate parameters from HIRS2/MSU on TIROS-N. J. Geophys. Res., in press.

Tracton, M. S., A. J. Desmarais, R. D. McPherson and R. J. van Haaren, 1980: The impact of satellite soundings upon the National Meteorological Centers Analysis and Forecast Systems - The Data Tests results. Mon. Wea. Rev., 10

Williamson, D., and A. Kasahara, 1971: Adaptation of meteorological variables forced by updating. J. Atmos. Sci., 28, 1313-1324.

511-47

84471

N93-70310

DESIGN OF A WINDSAT OBSERVING SYSTEM SIMULATION EXPERIMENT

Clifford H. Dey and William J. Bostelman

National Meteorological Center, NWS, NOAA
Washington, DC 20233

Charles P. Arnold, Jr.

USAF, Assigned to NESDIS, NOAA
Washington, DC 20233

1. MOTIVATION FOR THE NMC SIMULATION PROJECT

The concept of an observing system simulation experiment (OSSE) was apparently first conceived by Newton (1954), who suggested that variations of fictitious (simulated) observations could be used to evaluate the effect of variations of the observational network on numerical forecasts. Several investigations followed -- Best (1955), Bristor (1958), and Jess (1959). Bristor's work is of particular interest, because it was the first actual OSSE we have found. In his experiment, Bristor created simulated observations from a hypothetically correct actual analysis (the reference atmosphere), and examined the effect of network density and observational error on both analyses made with the simulated data and the ensuing numerical predictions. Many of the concepts used in OSSEs to this day were pioneered by Bristor in his paper. However, neither fundamental alterations of nor significant additions to the observational network in which OSSEs could play a role were under consideration at that time, so interest in these experiments waned.

With the exception of an interesting theoretical paper by Alaka and Lewis (1967), the hiatus of activity in this area continued through almost all the 1960's, and OSSE remained a solution looking for a problem. However, motivation for a rebirth of interest was provided by the initiation of the Global Atmospheric Research Program (GARP) in 1967. One of the stated objectives of GARP was to determine acceptable compromise solutions to the data requirement problem. In order to meet this objective, the U.S. Committee for GARP proposed a national effort to study the predictive consequences of proposed observation systems, to be known as "Observing System Simulation Experiments" (Charney et al., 1969). A practical problem to which the concept of OSSE could be applied existed at last.

A landmark paper by Charney, Halem, and Jastrow (1969) ushered in the period of intense activity in OSSEs. Their approach was to use a model forecast to provide a 4-dimensional reference atmosphere. Starting from a perturbed initial state, a second forecast was then made with the same prediction model (the assimilation run). Simulated observations taken from the reference atmosphere were inserted into the assimilation run, and the degree to which the assimilation run approached the reference atmosphere was examined. Because the same numerical prediction model that was used to generate the reference atmosphere was also used to make the assimilation run, this type of experiment is referred to as an identical twin experiment. A number of identical twin experiments followed -- for example, Halem and Jastrow (1970), Jastrow and Halem (1970), Williamson and Karahara (1971), Bengtsson and Gustafsson (1971), Kasahara and Williamson (1972), and Gordon et al. (1972).

Williamson and Kasahara's 1971 paper was the first to question use of identical twin experiments. They proposed instead an alternative which we have chosen to call fraternal twin experiments. In this approach, the numerical prediction model used in the assimilation run has lower resolution and less sophisticated physics than the model used to generate the reference atmosphere. It soon became apparent that identical twin experiments gave unrealistically optimistic results, and the fraternal twin approach gained favor. By 1974, the Joint Organizing Committee for GARP specifically ruled out use of identical twin experiments to determine which of the possible special observing networks would be most effective during GARP. A number of fraternal twin experiments were run, notably those of Williamson (1975), Lorenc (1975), and Bromley (1978).

Nitta (1975) summarized the OSSEs made up to that time. He reviewed both identical twin and fraternal twin experiments and found neither gave completely satisfactory results. He suggested that use of a time series of analyses might be an improvement. However, once the GARP observational array had been agreed upon, much of the motivation to run OSSEs was gone, and interest diminished once again.

Since the advent of satellite-observed vertical temperature profiles, the lack of vertical wind profiles on a global scale has been viewed as perhaps the major deficiency in our observational network. By the end of the 1970's, technical developments suggested that active laser radar (lidar) methods might be able to fill this need. By mid-1980, the U.S. Air Force's Meteorological Satellite Program was considering such an approach, and the U.S. Air Force supported a feasibility study by the National Oceanic and Atmospheric Administration's Wave Propagation Laboratory (WPL). It was concluded from the feasibility study that the idea had merit, but that it was likely to be extremely expensive. Whereas a passive radiometer might cost the federal government three million dollars or so, it is likely that an active lidar instrument (WINDSAT) might cost as much as half a billion dollars to develop and place into orbit a single prototype unit. This extremely high cost led the feasibility study to recommend, among other things, that the benefits such data might be expected to produce be thoroughly examined through OSSEs. WPL asked the National Meteorological Center (NMC) to help by making such studies. NMC responded by establishing the Simulation Project in the summer of 1980. Motivation for OSSEs had been reestablished, this time directly involving NMC.

2. HISTORY OF THE NMC SIMULATION PROJECT

The NMC Simulation Project was originally staffed by three persons; C. H. Dey and W. J. Bostelman of NMC and then Major J. D. Warburton, the AFGWC*/NMC Liaison at that time. At the outset, two goals were established for the project:

1. To develop an understanding of the data requirements for NMC's analysis and prediction systems.

2. To develop a means of evaluating the potential usefulness of proposed new observation systems and changes to existing ones in meeting these requirements.

The approach of OSSEs was chosen to pursue these goals. It was planned from the very beginning for calibration of the simulation system to be the first objective and execution of a WINDSAT OSSE to be the second.

A plan was formulated to create the reference atmosphere by time interpolating a series of objective analyses using cubic splines. It was our feeling that this approach would (a) provide a reference atmosphere with the most realistic evolution of meteorological features possible, and (b) minimize (but not remove) the influence of a numerical prediction model on the reference atmosphere. There was some precedence for this choice for both Bristor (1958) and Bengtsson and Gustavsson (1972) based their reference atmosphere on objective analyses, and Nitta (1975) had alluded to it as a more realistic choice. However, it had not been widely tested. The development of the computer codes to perform the cubic spline interpolation and to create the simulated observations began in late 1980. By the end of 1981, however, both Warburton and Dey had been forced by circumstances to spend most of their time on other more pressing issues. This lack of human resources, coupled with the woefully inadequate computational capabilities that existed at NMC at the time, caused the project to lag. By the end of 1982, it was evident that NMC alone could not afford to devote sufficient personnel and computer time to complete the project as originally planned. For this reason, NMC decided to seek help.

To this end, a workshop on the design of credible simulation experiments was held at NMC in February 1983. A wide range of investigators attended, most of whom had practical experience running OSSEs. All participants agreed that although serious deficiencies existed and careful interpretation was required, OSSE's offered the only available method for providing decision makers with information necessary to determine whether a proposed observing system would be worth the investment. The consensus of the workshop participants was that OSSEs should concentrate on two systems -- the next generation of satellite temperature sounders and the proposed WINDSAT instrument. Two candidates were considered for use as the reference atmosphere for such experiments -- the NMC proposal of a time series of real atmospheric analyses and the more conventional approach of using a long run of a general circulation model. The latter was recommended, again as the consensus of the workshop.

As a result of the workshop, the Goddard Laboratory for Atmospheric Sciences (GLAS)* and the European Center for Medium Range Weather Forecasts (ECMWF) agreed to join NMC in a new cooperative program for conducting and evaluating OSSEs. The ECMWF agreed to generate the reference atmosphere by making a 20-day prediction with a 15 level, N48 resolution version of their grid point global model. In addition to the existing physics contained in the model, it would also include a diurnal cycle. NMC's role in the effort was to generate a data base of simulated observations from the reference atmosphere. Once available, GLAS and ECMWF (as well as anyone else who might be interested) were to conduct a series of fraternal twin experiments with the simulated observations by using their own assimilation/forecast systems. The time period for the experiment was chosen to be 10-30 November 1979, for both

*Air Force Global Weather Center.

*Presently Goddard Laboratory for Atmospheres (GLA).

GLAS and ECMWF had already conducted real data impact tests with FGGE level IIb data for that period.

ECMWF delivered the 20-day forecast to NMC in the spring of 1983. NMC then simulated all FGGE level IIb data available during 10-30 November 1979, the period with which the forecast coincided. In addition, they simulated observations from the proposed WINDSAT instrument. The entire set of simulated observations was completed in late fall 1983. GLAS agreed to convert the simulated observations from NMC to FGGE format. They completed this task early in 1984 and sent a copy of the simulated observations in FGGE level IIb format to ECMWF. Since that time, GLAS has run OSSEs with the simulated data, but ECMWF has not.

In the original plan prepared at the 1983 workshop, it was not envisioned that NMC would run any OSSEs with the simulated data because of the severe lack of human and computational resources mentioned previously. By early 1984, however, two changes had occurred that led NMC to reestablish their plans for OSSEs. The first was the significantly increased computational capabilities because of NMC's purchase of a CYBER 205 computer in the summer of 1983. The second was the reavailability of the AFGWC/NMC liaison, by then Lt. Col. C. P. Arnold, Jr., to the project on a nearly full time basis. It was therefore decided to fulfill the original plan to run a WINDSAT OSSE. The renewed effort was facilitated by the fact that NMC already possessed the entire set of simulated observations in its own internal format. The design of the experiment run is described in the next section, and the calculation of the simulated observations in the fourth section. A discussion of some of the strengths and weaknesses of this experimental design are discussed in the final section.

3. EXPERIMENTAL DESIGN OF THE WINDSAT OSSE

The simulated observations used for the WINDSAT OSSE were those already produced by NMC as part of the inter-agency agreement made at the 1983 OSSE workshop. Therefore, this OSSE falls under the category of fraternal twin experiments. In that data set, simulated observations had been created at the location and time of nearly all FGGE IIb (main) data during the period 10-30 November 1979 (COBAL and LIMS data were not simulated, nor were significant-level RAOB data). The global data assimilation system (GDAS) used in the experiment was the version then operational at NMC. It featured a multivariate optimum interpolation analysis in isobaric coordinates coupled with a 30-wave, 12-layer version of the NMC global spectral prediction model. This prediction model had slightly less resolution and significantly less sophisticated physics than did the ECMWF model used to create the reference atmosphere. The NMC global spectral prediction model is described in Sela (1980), while details of the NMC GDAS used may be found in Dey and Morone (1985).

The experiment consisted of five runs. Each run featured a five-day data assimilation period beginning on 10 November 1979, followed by a single five-day forecast from the last analysis in the data assimilation period. The five-day forecast was made with the same prediction model that was used in the GDAS. The first guess for the first analysis in the data assimilation segment of each run was a 6-hour forecast from 1984. This was done so the first guess used to begin each run would be meteorologically realistic, but uncorrelated with the actual meteorological situation existing at 0000 GMT on November 10. In order to insure the analysis did not simply reject all the observations, the gross error check on the data was removed for the first few analyses of each run. Despite this, the comparative quality control procedure (the buddy check), which was not disabled, rejected a normal quantity of observations. The five runs differed only in the observations made available to the analyses. The data used in each run were the following:

Run 1: All real FGGE IIb data

Run 2: All real FGGE IIb data except RAOB winds

Run 3: All simulated FGGE IIb data

Run 4: All simulated FGGE IIb data except RAOB winds

Run 5: All simulated FGGE IIb data plus simulated WINDSAT observations between 30°N and 30°S

Runs 1, 2, 3, and 4 were used to calibrate the experiment, and Runs 3 and 5 were used to evaluate the effect of WINDSAT observations. For the purposes of calibration, yet a sixth 5-day forecast was made, one that began from the reference atmosphere itself at 0000 GMT on November 15. This forecast is the "best" one can do, in context of this experiment, from simulated data. It therefore provides limiting values on the accuracy of the 5-day forecasts from Runs 3, 4, and 5.

Most of the comparisons we considered in this OSSE were based on the 6-hour forecasts made in the data assimilation segment of the runs. We anticipated a spin-up period due to our choice of the first guess used to start each run. This spin-up period proved to be 36 hours. We furthermore restricted our comparisons to those 6-hour forecasts that were valid at either 0600 GMT or 1800 GMT. This was done because only the 0000 GMT and 1200 GMT analyses had access to a significant number of RAOB observations. However, it restricted the number of 6-hour forecasts available for compari-

son in each run to 7; those valid at 1800 GMT on November 11, 12, 13, and 14 and at 0600 GMT on November 12, 13, and 14. Because the number of forecasts available for comparison was so limited, we tested the results for statistical significance. The 5-day forecasts were used only to suggest how the effects noted in the 6-hour forecasts might have evolved if those forecasts had continued. Since there was only one 5-day forecast in each run, statistical significance is naturally not claimed for any results involving them.

Each forecast was verified by comparing it with a verifying field. For Runs 1 and 2, the verifying fields for the 6-hour forecasts were provided by the appropriate analysis from Run 1. The 5-day forecasts from Runs 1 and 2, on the other hand, were compared with the ECMWF FGGE Level IIIb analyses. Verifying fields for both the 6-hour and 5-day forecasts from Runs 3, 4, and 5 were taken from the reference atmosphere at the time the forecast was valid. The verifications were done in the form of both root-mean-square errors (RMSE) and anomaly correlations for a number of variables and pressure levels. The verification scores were broken down into 4 wave number groups; zonal, waves 1-3, waves 4-9, waves 10-20 and waves 1-20.

Given, for example, RMSE values for some variable at some pressure level and wave number group from Runs 1, 2, 3, and 4, a ratio (R) was formed, where

$$R = \frac{RMSE(1)-RMSE(2)}{RMSE(3)-RMSE(4)}.$$

R is the calibration factor for this variable, pressure level, and wave number group. We then took the corresponding RMSE value from Run 5 and hypothesized that if we really had been able to make a run with WINDSAT data (call it Run X), we would have found

$$\frac{RMSE(1)-RMSE(X)}{RMSE(3)-RMSE(5)} = R$$

as well, which can be rewritten as

$$RMSE(1)-RMSE(X) = R[RMSE(3)-RMSE(5)].$$

Thus, the calibration factor R along with the RMSE values from Runs 3 and 5 allow us to estimate the change in RMSE values we could expect if we really did have WINDSAT data. This procedure was applied to anomaly correlation values as well. The test for statistical significance was applied to the 7 values of R available for each parameter, pressure level, and wave number group examined. Fundamentally, very consistent values of R tend to demonstrate statistical significance and may therefore be used with some confidence. Very erratic values of R, on the other hand, show no such statistical significance and may be considered to be unreliable.

The actual results from the WINDSAT OSSE are discussed in the companion paper in this volume (Arnold, Dey, and Bostelman, 1985). The remainder of this note is devoted to a discussion of the procedures we used to generate the simulated observations and some questions left open by the experimental design we chose.

4. PREPARATION OF THE SIMULATED OBSERVATIONS

The basic information used to create the simulated observations was provided by the 20-day ECMWF forecast that served as the reference atmosphere and the FGGE level IIb (main) data set. This information was used to create simulated observations at the locations in time and space of most FGGE IIb data available for the period 10-30 November 1979. The exceptions were COBAL, LIMS, surface wind, and significant level RAOB reports. In addition, a simulated WINDSAT data set was created. For this purpose, it was assumed that the WINDSAT instrument would be on the same satellite platform that contained the passive radiometer. Therefore, the WINDSAT data set was produced by creating vertical profiles of wind observations at the locations of all TIROS data during the 20-day period.

For any given time, the first step in the process was to extract station identification information from all FGGE IIb data valid within $\pm$ 3 hours of the nominal observation time. The information extracted was

(1) Station identification

(2) Station latitude, longitude, and elevation

(3) Observation time

(4) Report type

(5) Instrument type

(6) Number of reported levels (Any levels missing from the FGGE IIb data were also designated as missing in the simulated data.)

This information was used to create the station identification record of the simulated observations. A special station identification record was created for WINDSAT data, in which the report location and observation time was extracted from the TIROS data.

Although simulated TIROS reports were created as the time and location of the actual TIROS reports by using the information from the TIROS identification record, the retrieval type of the simulated TIROS reports were changed. A statistical cloudiness algorithm originally developed by the Air Force was tuned to the

ECMWF forecast and used to estimate the cloudiness of the reference atmosphere. Our version of the algorithm produced estimated cloudiness at 3 levels -- 850 mb, 700 mb, and 500 mb -- as well as a total integrated cloudiness value. (Note that we did not estimate high cirrus clouds.) The retrieval type of the simulated TIROS reports was determined by the estimated total cloudiness of the reference atmosphere at the time and location of the report as follows:

0%-60% cloud cover - path A retrieval

61%-90% cloud cover - path B retrieval

91%-100% cloud cover - path C retrieval

These values were chosen because they resulted in approximately the same portion of simulated A, B, and C retrievals as actually existed in the FGGE data at day 2 of the period (12 November 1979). This cloudiness information was also used to determine the reported levels of WINDSAT data. Upon a suggestion of Dr. Milton Huffaker, we did not allow the WINDSAT instrument to produce any winds reports below the level at which the total integrated (from above) cloudiness exceeded 90%.

After establishing the station identification records for all simulated observations for some time period, the next step was to interpolate the observed variables from the reference atmosphere to the observation locations. Reference atmosphere fields of h, u, v, T, and rh were available every 6 hours at the 15 mandatory pressure levels from 1000 mb to 10 mb (only to 300 mb for rh). The interpolation from the archived reference atmosphere 1.875° latitude-longitude gridded fields to the observation locations was biquadratic in the horizontal (bilinear for rh) and linear with the natural logarithm of pressure in the vertical.

The simulated observations were then created by adding observational errors to the interpolated values. Random observational errors were added for all types of observations, and systematic errors (from Schlatter, 1981) were added for TIROS reports. The random errors were produced by providing a random number generator a standard deviation appropriate for the particular type and level of observation. The standard deviations used are given in Table 1. The systematic errors added for the TIROS reports are given in Table 2.

This procedure was used to produce a set of simulated observations for every 6-hour period from 10 November 1979 through 30 November 1979.

5. STRENGTHS AND WEAKNESSES OF THE EXPERIMENTAL DESIGN

This experiment has a number of important strengths. First of all, realistic distributions of the complete current observational data base (as well as a potentially valuable

Table 1 - OBSERVATIONAL ERROR STANDARD DEVIATIONS

Surface Reports

SFCLT	SFCST	SFCBT	SFCLP	SCFSP	SFCBP	SFCLW	SFCSW	SFCBW
1.0	1.0	1.5	1.0	1.0	2.0	0.0	2.5	0.0

Upper Air Reports

Pressure	1000	890	700	500	400	300	250	200	150	100	70	50	30	20	10
RADT	1.1	1.1	1.1	1.3	1.5	1.7	1.9	2.0	2.1	2.2	2.5	3.0	3.5	4.1	4.5
DRPT	1.1	1.1	1.1	1.3	1.5	1.7	1.9	2.0	2.1	2.2	2.5	3.0	3.5	4.1	4.5
RADW	2.0	2.0	3.0	4.0	5.0	6.0	6.0	6.0	6.0	6.0	6.0	6.0	6.0	6.0	6.0
DRPW	2.0	2.0	3.0	4.0	5.0	6.0	6.0	6.0	6.0	6.0	6.0	6.0	6.0	6.0	6.0
PIBW	1.8	2.6	3.5	5.0	6.0	8.2	10.0	10.0	10.0	9.2	8.0	6.0	6.0	6.0	6.0
AIRT	3.0	3.0	3.0	3.0	3.0	3.0	3.0	3.0	3.0	3.0	3.0	3.0	3.0	3.0	3.0
ASDT	3.0	3.0	3.0	3.0	3.0	3.0	3.0	3.0	3.0	3.0	3.0	3.0	3.0	3.0	3.0
AIRW	7.0	7.0	8.0	8.0	8.0	8.0	8.0	8.0	8.0	8.0	8.0	8.0	8.0	8.0	8.0
ASDW	2.0	2.0	3.0	4.0	5.0	6.0	6.0	6.0	6.0	6.0	6.0	6.0	6.0	6.0	6.0
COBW	5.0	5.0	5.0	5.0	5.0	5.0	5.0	5.0	5.0	5.0	5.0	5.0	5.0	5.0	5.0
SATN	4.0	4.0	5.0	7.0	7.0	8.0	8.0	8.0	8.0	8.0	8.0	8.0	8.0	8.0	8.0
SATJ	6.0	6.0	6.0	10.0	10.0	13.0	13.0	13.0	13.0	13.0	13.0	13.0	13.0	13.0	13.0
SATE	7.0	7.0	8.0	8.0	8.0	8.0	8.0	8.0	8.0	8.0	8.0	8.0	8.0	8.0	8.0
SATI	4.0	4.0	5.0	7.0	7.0	8.0	8.0	8.0	8.0	8.0	8.0	8.0	8.0	8.0	8.0
SATT	4.0	4.0	5.0	7.0	7.0	8.0	8.0	8.0	8.0	8.0	8.0	8.0	8.0	8.0	8.0
SATF	7.0	7.0	8.0	8.0	8.0	8.0	8.0	8.0	8.0	8.0	8.0	8.0	8.0	8.0	8.0
SATG	7.0	7.0	8.0	8.0	8.0	8.0	8.0	8.0	8.0	8.0	8.0	8.0	8.0	8.0	8.0

TIROS Soundings and WINDSAT

TIRAB	2.0	1.8	1.7	1.8	1.8	1.9	1.9	2.0	2.0	2.2	2.4	2.5	2.6	2.8	2.8
TIRC	3.9	2.5	2.2	2.2	2.0	1.9	1.8	1.7	1.6	1.4	2.5	2.6	2.7	2.8	2.8
WSAT	1.0	1.3	1.6	2.0	2.3	2.5	2.6	2.7	2.8	2.9	2.9	3.0	3.0	3.0	3.0

Legend:
SFCL - Surface land
SFCS - Surface ship
SFCB - Surface buoy
RAD - Radiosonde
DRP - Dropsonde
PIB - PIBAL
AIR - Aircraft
ASD - ASDAR
COB - COBAL
SAT - Satellite cloud tracked winds
TIRAB - TIROS A&B retrievals
TIRC - TIROS C retreivals
WSAT - WINDSAT
T - temperature (in °K)
W - wind (in ms^{-1})
P - pressure (in mb)

Table 2 - TIROS SYSTEMATIC TEMPERATURE ERRORS (°K)

Pressure Layer	Retrieval Method A	B	C
50-70	0.0	0.0	0.0
70-100	-0.7	-0.7	-0.5
100-150	-0.5	0.15	-0.1
150-200	-0.1	0.3	0.4
200-250	0.5	0.6	1.2
250-300	0.6	0.5	0.9
300-400	0.1	-0.05	-0.15
400-500	-0.4	-0.3	-1.1
500-700	-0.5	-0.35	-1.2
700-850	-0.5	+0.35	-0.6
850-1000	-0.35	+0.3	+1.65

new one) were created for an extended period of time. The simulated observations possess realistic instrument error and a normal quantity of missing values. Despite its limitations, it is probably (in our biased opinion) the most extensive and realistic simulated data base currently available. Second, the number of 6-hour forecasts made during the assimilation runs was adequate to apply tests of statistical significance. In fact, as described in the companion paper in this volume, most comparisons involving the 6-hour forecasts did turn out to be statistically significant. Finally, comparisons of our results with those of GLAS run on the same set of simulated observations should allow for the first time some assessment of the system dependency of OSSE results.

However, this experimental design has several weaknesses as well. The most important was that only one 5-day forecast was integrated from each data assimilation run. As a result, we can attach no statistical significance to any result involving the 5-day forecasts. Another weakness was that since only one time period was examined, we cannot dismiss the possibility that different time periods would have given different results. Not only would we have liked to have made a 5-day forecast from the 0000 GMT and 1200 GMT analyses from each data assimilation run (beginning at 1200 GMT on 11 November), we also wanted to run a number of experiments like this one, perhaps as many as seven, from different time periods. Such extensive testing was beyond the resources available for this study. However, it should be done for any OSSE that would be used to determine the future of a potentially important and certainly expensive observing system such as WINDSAT.

Although these two limitations were due to a lack of resources, another weakness -- inadequate observational errors in the simulated observations -- was not. We feel the random observational errors we added to the interpolated values to create the simulated observations are realistic. These random errors, along with the systematic TIROS temperature errors, essentially represent instrument error. However, random errors are relatively easy for current objective analysis procedures to remove. On the other hand, a significant proportion of what is, from the point of view of the analysis system, "observational error" is not random. Rather, it is due to the instrument responding to scales of motion that are not adequately resolved by the resolution of either the data base or our numerical analyses. This part of the observational error is correlated rather than random, and is much more difficult for objective analysis techniques to remove.

In theory, the fraternal twin experimental design accounts for precisely this type of observational error by using a forecast model whose resolution is greater than that of the assimilation system to generate the reference atmosphere. In practice, however, numerical prediction models contain numerical noise control techniques in order to make the prediction appear "meteorological," i.e., smooth. It is our feeling that forecasts made even with high resolution global prediction models therefore contain significantly less energy in scales of motion beyond the resolution of the observational network than does the atmosphere. The result is that this part of the observational error is badly underestimated in fraternal twin as well as in identical twin OSSEs. We not believe that numerical prediction models used to provide the reference atmosphere should have these numerical noise controls removed. This procedure would provide a reference atmosphere with a more realistic energy spectrum and lead to more believable OSSEs.

It is important to point out a special aspect of running OSSEs at an operational numerical weather prediction center such as NMC. As long as the question of system dependency of OSSE results remains an open one, OSSEs must be run on the analysis/prediction systems that would actually use the proposed observations, i.e., those in use at operational centers. However, a thorough OSSE requires a very considerable allocation of people and computational resources. As noted in section 2, we at NMC have not always found it possible to allocate the necessary level of resources. The result has been an ebb and flow of progress in the Simulation Project as the availability of these resources has changed. We suspect that our experience is not unique. Therefore, the meteorological community is faced with several choices if OSSE research is considered valuable enough to continue. One is to find the means to provide several operational centers with the resources necessary to run thorough OSSE programs. A second is for research centers

that can afford to run OSSEs to use operational versions of data assimilation systems in their experiments. The third is to prove beyond doubt that OSSE results are not system dependent. The choice is not clear, but it is clear that a choice must be made.

ACKNOWLEDGMENT

The authors wish to thank Dr. Ronald D. McPherson for his unfailing encouragement and support in the early stages of this project. We also wish to thank Joyce Peters for typing and editing the manuscript.

REFERENCES

Alaka, M. A., and F. Lewis, 1967: Numerical Experiments Lending to the Design of Optimum Global Meteorological Networks. Technical Memorandum WBTM TDL-7, Environmental Science Services Administration, Weather Bureau, Washington, DC, USA.

Arnold, C. P., C. H. Dey, and W. J. Bostelman, 1985: Results of an Observing System Simulation Experiment Based on the Proposed WINDSAT Instrument. In Global Wind Measurements, W. E. Baker and R. J. Curran (Eds.), A. Deepak Publishing, Hampton, Virginia, 81-88.

Bengtsson, L., and N. Gustavsson, 1972: Assimilation of Non-synoptic Observations. Tellus, 24, 383-398.

Best, W. H., 1955: Differences in numerical prognoses resulting from differences in analyses. Tellus, 8, No. 3, 351-356.

Bristor, C. L., 1958: Effect of data coverage on the accuracy of 500 mb forecasts. Mon. Wea. Rev., 86, 299-308.

Bromley, R. A., 1978: Simulation Experiments to Assess the Effectiveness of the Observing System for FGGE. GARP Working Group on Numerical Experimentation, Report 16, 54 pp. Can be obtained from WMO Secretariat, Geneva, Switzerland.

Charney, J., et al., 1969: Plan for United States Participation in the Global Atmospheric Research Program. National Academy of Sciences, Washington, DC 20069.

Charney, J., M. Halem, and R. Jastrow, 1969: Use of incomplete historical data to infer the present state of the atmosphere. J. Atmos. Sci., 26, 1160-1163.

Dey, C. H., and L. L. Morone, 1985: Evolution of the National Meteorological Center global data assimilation system: January 1982-December 1983. Mon. Wea. Rev., 113, 304-318.

Gordon, C. T., L. Umscheid, and K. Miyakoda, 1972: Simulation experiments for determining wind data requirements in the tropics. J. Atmos. Sci., 29, 1064-1075.

Halem, M., and R. Jastrow, 1970: Analysis of GARP data requirements. J. Atmos. Sci., 27, No. 1, 177.

Jastrow, R., and M. Halem, 1970: Simulation studies related to GARP. Bull. Amer. Meteor. Soc., 51, No. 6, 490-513.

Jess, E. O., 1959: A numerical prediction experiment involving data paucity and random errors. Tellus, 12, No. 1, 21-30.

Kasahara, A., and D. Williamson, 1972: Evaluation of tropical wind and reference pressure measurements: numerical experiments for observing systems. Tellus, 24, No. 2, 100-115.

Lorenc, A. C., 1975: Results of Observing Systems Simulation Experiments for the First GARP Global Experiment. Contained in the GARP Working Group on Numerical Experimentation, Report 10, 37-68. Can be obtained from WMO Secretariat, Geneva, Switzerland.

Newton, C. W., 1954: Analysis and data problems in relation to numerical prediction. Bull. Amer. Meteor. Soc., 35, No. 7, 287-294.

Nitta, T., 1975: Some Analyses of Observing Systems Simulation Experiments in Relation to the First GARP Global Experiment. Contained in the GARP Working Group on Numerical Experimentation, Report 10, pp. 1-35. Can be obtained from WMO Secretariat, Geneva, Switzerland.

Schlatter, T. W., 1981: An assessment of operational TIROS-N temperature retrievals over the United States. Mon. Wea. Rev., 109, 110-119.

Sela, J. G., 1980: Spectral modeling at the National Meteorological Center. Mon. Wea. Rev., 108, 1279-1292.

Williamson, D. L., 1975: Observing Systems Simulation Experiments for the First GARP Global Experiment. Contained in the GARP Working Group on Numerical Experimentation, Report No. 10, 97-124.

Williamson, D. L., and A. Kasahara, 1971: Adaption of meteorological variables forced by updating. J. Atmos. Sci., 28, No. 8, 1313-1324.

RESULTS OF AN OBSERVING SYSTEM SIMULATION EXPERIMENT BASED ON THE PROPOSED WINDSAT INSTRUMENT

Charles P. Arnold, Jr.
Lt. Col., USAF, Assigned to NESDIS, NOAA
Washington, DC 20233

Clifford H. Dey and William J. Bostelman
National Meteorological Center, NWS, NOAA
Washington, DC 20233

1. INTRODUCTION

The motivation for the research described in this paper derives from a suggested solution to a perceived shortfall in numerical weather analysis and prediction. The shortfall stems from the limited amount of wind observations available to the analysis. The proposed solution, considered in this paper, is a space-based active remote wind sensing instrument called 'Windsat'.

In order that numerical weather prediction models accurately portray or simulate the future state of the atmosphere, an accurate and complete initial description of the atmosphere is considered necessary. This initial state, the analysis, depends upon measurements, or estimates, of all dependent variables in the prognostic equations. These variables include the mass field variables of temperature and moisture and the momentum field specified by the wind vector. Furthermore, this information is needed globally and throughout the atmosphere.

Together with 'conventional' meteorological measurements provided by such instrumented platforms as rawinsondes and aircraft, satellites have helped create a more global 3-dimensional description of the atmosphere. However, this observing system is not complete in the sense that each platform does not provide all the necessary measurements. Satellites, although they provide critical temperature measurements, lack the capability at present to provide wind and moisture measurements. As a result, both the analysis and the forecast are degraded.

There are, of course, many possible candidate solutions to the lack of global wind data such as the use of constant level balloons, cloud track winds, and various satellite instruments. One of the most innovative space-based proposals was made by Huffaker (1978). By measuring the Doppler shift of radiation back-scattered from atmospheric aerosols, the wind vector can be deduced. A laser radar (lidar) generates the highly coherent signal. The instrument is call a Windsat.

Unfortunately, lidar is a costly solution. Estimates for a shuttle-compatible research version have been as high as 0.5 billion dollars. However, because of its estimated cost, it becomes a very good candidate for a simulation experiment requiring super-computer speed. The reason being that if the cost of the experiment greatly exceeds the cost of the instrument, it is better to fly the instrument and perform after-the-fact data impact studies with real data. This was clearly not considered to be the case in our experiment even when considering the relatively high cost of the experiment.

Since the idea of an active wind 'sounder' is a relatively recent concept and since most attention has been paid to either existing or planned temperature 'sounders', it is not surprising then that very little simulation research has been directed at wind measurements. Halem and Dlouhy (1984) have been among the few to do so. Their results, however, were unrealistic in the sense that only perfect or errorless winds were simulated, and the simulated data were not assimilated together with all the other simulated conventional and satellite observations which would be available.

This paper provides first, an abbreviated description of the experiment which is more fully described by Dey, Arnold and Bostelman (1985). The results are then discussed and a summary and concluding remarks follow.

2. DESCRIPTION OF THE EXPERIMENT

This experiment was designed to evaluate the contribution to an assimilation and forecast model from a complete, global wind field. In order that the experiment be as realistic as possible, it considered the experience and recommendations of researchers over the past 30 years (Arnold and Dey, 1985).

A reference atmosphere was provided by the European Center for Medium Range Weather Forecasting (ECMWF) which consisted of a 20-day prediction for the FGGE period 10-29 November 1979. The model used was the ECMWF 15-level N48 resolution version of their grid point

model. From this reference atmosphere, simulated data were also available for the same period.

In the past there have been objections to assimilating the simulated data directly back into the same model used to generate it in the first place, the so-called 'identical twin' experiment. These objections are generally known as questions of model dependency, the central question being 'to what extent will data and model which share the same or similar physical heritage influence the results of the experiment?' It has generally been believed that simulation experiments have been too optimistic as a result of this inherent compatibility (Kasahara, 1972). Another aspect of this same question is that identical twin experiments do not simulate the relationship which is known to exist between model and reality, i.e., the model is only a poor reflection of reality. To avoid these pitfalls, we chose a second model for the assimilation and forecast, which we have termed a 'fraternal twin' experiment, acknowledging that the models, although not identical, are still more similar to one another than they are to the real world. The NMC 12-level 30-mode spectral model was chosen also because of its poorer resolution and physics than the ECMWF model and thereby satisfied the second objection mentioned above.

In addition to the issue of model dependency, we considered the questions of data dependency, 'to what extent can we assure independence among the data?'; statistical significance, 'to what extent can we determine the significance of our results?'; calibration, 'to what extent can we translate results from the simulated to the real world?'; and interpretation, 'to what extent can we interpret our results into a realistic measure of forecast improvement?'. In our companion paper (Dey, Arnold and Bostelman, 1985) these questions will be discussed in greater detail. It is necessary, however, to describe briefly the calibration procedure we used, but before doing so we need to describe the five computer runs that were generated.

Computer Runs 1 and 2 were used to perform a data impact experiment. Run 1 was a 5-day assimilation run using all available real FGGE data and a six hourly update frequency. Each 6 hours the integration was halted and data no older than 6 hours was assimilated into an optimum interpolation (OI) analysis by using the models' forecast field as the first guess. After initialization, based on a nonlinear normal mode formulation, the next 6 hour cycle was begun. Computer Run 2 was identical to Run 1 except that all rawin wind data were withheld in the assimilation.

Runs 3-5, based on simulated data, were used to complete an Observing System Simulation Experiment (OSSE) based on Windsat. Similated observations were generated by selecting values of the desired meteorological variables at both the desired locations and observation times from the reference atmosphere. To each element in this set of 'perfect observations' were added representative observational errors in a manner described in Dey, Arnold and Bostelman (1985). This final set of simulated data was then assimilated as described above.

Run 3 was in every sense similar to the real data run, Run 1, except that all available real data was substituted with simulated data at the same times and locations. Run 4 was identical to Run 3 except all simulated rawin wind data were withheld. Run 5 was identical to Run 3 except that simulated Windsat data were added to form a more complete data set.

Windsat winds were simulated only in the tropics (30N-30S), only where there were satellite soundings, assuming that the Windsat would be on a satellite with other remote sensing instrumentation; and only down to cloud top if clouds were present. There was no account made for a variable aerosol distribution. Winds were generated from the surface to 50 mb with 1 km vertical resolution and the observational error was assumed to be 1.0 m sec^{-1} based on Huffaker (1978).

The meteorological variables considered in the evaluation of the experiment were the zonal and meridional wind components (u,v) and the geopotential height (z). The forecast values of these variables were extracted at 850, 500, 250, and 100 mb. The primary statistical parameter selected was the root mean square error (rmse) between these forecast values and the verifying analysis values taken from the reference atmosphere. The anomaly correlation, a measure of skill, was also used. Evaluations were made over an entire hemisphere (southern or northern) and could be examined by one of four wave groups-short waves, wavenumbers 10-20; long waves, wavenumbers 1-3; medium waves, wavenumbers 4-9; and all waves, wavenumbers 1-20.

Various comparisons could then be made from the 5 runs. From the real data runs (1,2), which formed a data impact experiment in itself, the results of the 5-day assimilation and a single 5-day forecast, generated from the last cycle of the assimilation, could be compared. These comparisons show the impact real rawin wind observations contribute to the 6-hour and 5-day forecasts. When similar comparisons are made from runs 3 and 4, the impact of simulated rawin wind observations can be determined.

A very simple calibration procedure was developed on the basis of the comparisons between the two sets of runs (1 with 2 and 3 with 4). It was assumed that the average difference of the rmse's in the simulated runs (3,4) would be linearly related to the same in the real runs (1,2). It was further assumed that this relationship could then be used to obtain a first-guess impact in the real world from the impact observed in the simulated world when Windsat winds were added to the simulated data base.

The final set of comparisons, from runs 3 and 5 were used to determine the impact resulting from the addition of Windsat winds to the assimilation, and the calibration technique was then used to provide an estimate of what that impact might be in the real world. As with the other runs, a 5-day assimilation cycle along with a single 5-day forecast were made from Run 5.

3. RESULTS

Figure 1 shows the rms errors of the 100 mb zonal wind 5-day assimilation for runs 1 and 2. The errors fall rapidly from an initial arbitrary first guess and level off after only 18 to 24 hours to an asymptotic value which is characteristic of the particular model used.

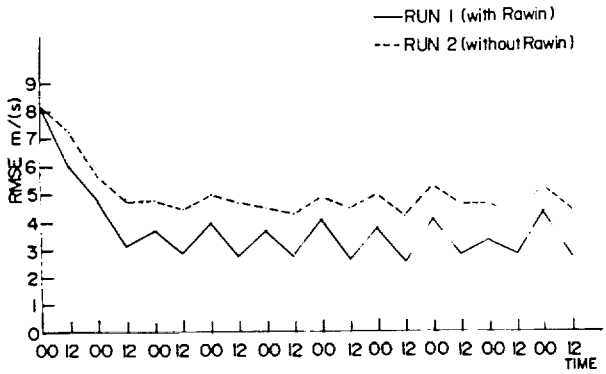

Figure 1. Root mean square error (rmse) vs time for a 5-day assimilation of run 1 vs run 2, zonal wind, 100 mb level, northern hemisphere, all wave numbers.

The average difference between runs 1 and 2 after this asymptotic state is reached is 1.7 m sec^{-1} which corresponds to a 38% reduction in the errors of u when rawin winds are added to the assimilation. The sawtooth pattern common to an assimilation run such as these is a result of varying data available to the forecast with greater amounts normally available at the data on-times of 00Z and 12Z which result in lower rms errors at the following off-times. Table 1 shows statistics for each of the other levels, hemisphere, and geopotential height. Statistics were only compiled for the composited off-times (06Z and 18Z) because there was little or no statistically significant difference between rms errors at the on-times. At the off-times, rms error differences were significant at all levels and in both hemispheres. The zonal wind statistics show a larger positive impact, as a result of adding global rawin winds, in the northern hemisphere than in the southern hemisphere. This result is felt to be a direct consequence of having 10 times as many rawins in the northern hemisphere. Surprisingly, the geopotential statistics show little differences between hemispheres.

Overall there is a consistent positive impact at all levels, both hemispheres, and for both geopotential height and zonal wind component. The meridional wind component was not examined. There was, in the northern hemisphere, for example, an average 3-m improvement

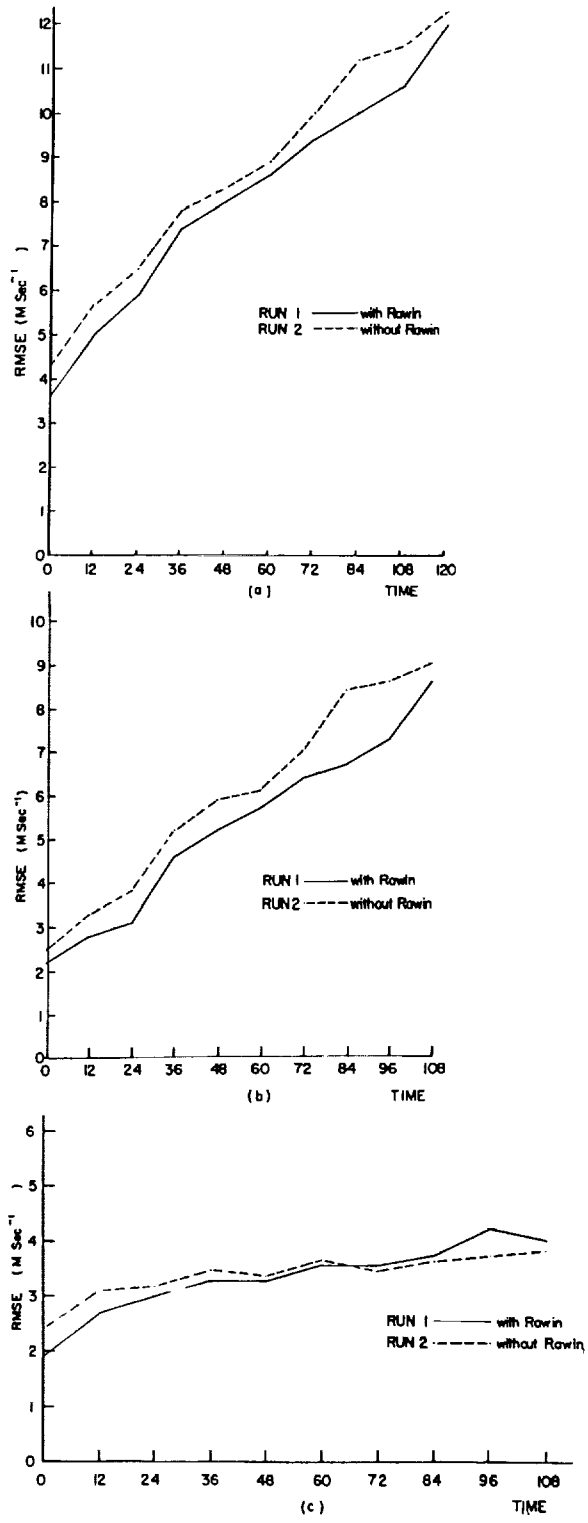

Figure 2. Root mean square error (rmse) vs time for a 5-day forecast of Run 1 vs Run 2, zonal wind, 250 mb level, northern hemisphere. (a) all wavenumbers (b) long waves only (c) short waves only.

in the 6-hour forecast of geopotential when winds were added to run 2. The zonal wind forecast was improved by 1.0 m sec^{-1} which represented an average improvement over all 4 levels of 28%.

Figure 2 shows the error growth of the 250 mb zonal wind during the 5-day forecast for runs 1 and 2. The overall (all waves) small positive improvement in the 5-day forecast appears to have been carried by the much greater improvement in the long waves. This was true even though the initial 6-hour improvement was about equal between wave groups (long waves vs short waves). This result was characteristic of all levels. If this result is found to be true in general, it would imply that the Windsat instrument should be designed so that its spatial resolution matches the intended forecast range. It would not be useful in other words to obtain wind observations on a meso-scale, corresponding to the shorter waves, if the observations are to be used for medium range forecasts. Although not shown, the average improvement in the 5-day forecast of the zonal wind was found to be greater in the northern hemisphere. This result follows from the differences observed in the assimilation runs mentioned above.

The simulated runs, runs 3 and 4, corresponding to the real data cases described above, agree very well with the latter. The assimilation results for the 100-mb zonal wind are shown in Figure 3. As in the real data cases, the errors drop off rapidly, reaching their asymptotic level within 18-24 hours. The average difference in rms errors beyond that point are approximately 0.7 m sec^{-1}, which corresponds to a 16% reduction in the errors when simulated rawin winds are assimilated along with the remaining simulated data set.

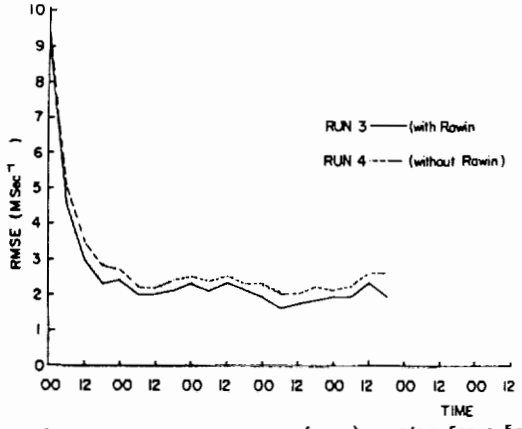

Figure 3. Root mean square error (rmse) vs time for a 5-day assimilation of run 3 vs run 4, zonal wind, 100 mb level, northern hemisphere, long waves only.

A set of calibration coefficients could be calculated after determining the average difference in rms errors associated with the real and simulated data runs. These values could then be used in subsequent simulation runs to arrive at an estimate of the expected contribution of a proposed data source once it became available. The calibrated values are enclosed by parentheses in Tables 2, 3, and 4.

When Windsat winds are added to the assimilation, very reasonable reductions in the rms errors are observed. Consistent positive improvements in the reduction of errors are observed at all levels for both hemispheres and for both zonal wind and geopotential height. In Figure 4, the errors in the 100-mb zonal wind are reduced by 0.8 m sec^{-1} on the average, and correspond to nearly 25% improvement. The average reduction for all levels, as seen in Table 2, is 17%. When the calibration coefficient is applied, it can be seen that nearly a 50% overall improvement in the 6-hour wind forecasts could be expected through the troposphere, the greatest improvements being found at and above 500 mb.

The results of the 5-day forecast made from run 5 are compared with those from both runs 3 and 4 in Figures 5 and 6. The average improvments over the 5 day period are summarized for the northern and southern hemispheres in Tables 3 and 4, respectively. With the addition of Windsat winds, the forecast of the zonal wind component is seen to be improved at all levels but with increasing magnitude with height. At 100 mb, there is a calibrated improvement of 43% whereas the average improvement at all levels is seen to be 31%. As expected, the shorter range 6-hour forecasts in the assimilation show considerably greater improvements than the 5-day forecast, in the northern hemisphere (Table 3). Although the same is true in the southern hemisphere (Table 4), the magnitudes are less. This result cannot be explained on the basis of unequal hemispheric distribution of the Windsat winds since an equal number of winds were assimilated in both hemispheres. One possible explanation is that this was a period of stronger weather activity in the northern hemisphere; hence, the observations were able to make a greater contribution in this hemisphere.

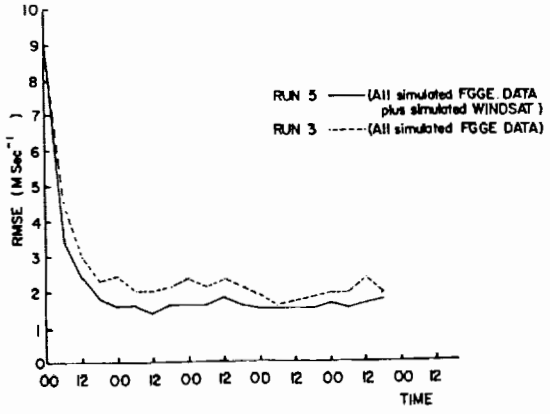

Figure 4. Root mean square error (rmse) vs time for a 5-day assimilation of run 3 vs run 5, zonal wind, 100 mb level, northern hemisphere, long waves only.

Table 1. Data impact results from assimilation runs 1 and 2. All waves, off-time data times (06,18Z) only, NH/SH.

Level (mb)	Avg. Diff. Between RMS Errors (2-1) Z(m)	Avg. % Red. in RMSE of Z	Avg. Diff. Between RMS Errors (2-1)u(m sec^{-1})	Avg. % Red. in RMSE of U
850	1.7/2.6	15%/21%	0.5/0.5	21%/22%
500	2.1/2.7	16%/17%	0.7/0.6	29%/21%
250	2.6/2.8	14%/13%	0.9/0.7	22%/18%
100	5.5/4.5	19%/16%	1.7/0.8	38%/21%
Avg. All levels	3.0/3.2	16%/17%	1.0/0.7	28%/21%

STATISTICAL SIGNIFICANCE (ALL WAVES, 24 HR. SEP. OF FCSTS)

Level (mb)	Z FCST Valid On-Time	Z FCST Valid Off-Time	U FCST Valid On-Time	U FCST Valid Off-Time
850	No/Yes	Yes/Yes	No/Prob.	Yes/Yes
500	No/No	Yes/Yes	Prob./No	Yes/Yes
250	No/No	Yes/Yes	Yes/No	Yes/Yes
100	No/No	Yes/Yes	Yes/No	Yes/Yes

Table 2. Composite statistics, all assimilation runs (1-5). All waves, off-time data times (06,18Z) only, N.H. only, calibrated values in parentheses.

Level (mb)	Avg. Diff. Between RMS Errors Z (m)			Avg. % Red. in RMSE of Z			Avg. Diff. Between RMS Errors U (m sec^{-1})			Avg. % Red. in RMSE of U		
	1 vs 2	3 vs 4	5 vs 3	1 vs 2	3 vs 4	5 vs 3	1 vs 2	3 vs 4	5 vs 3	1 vs 2	3 vs 4	5 vs 3
850	1.7	1.0	0.1(0.2)	15	8	1(2)	0.5	0.3	0.2(0.3)	21	11	8(15)
500	2.1	1.4	0.2(0.3)	16	11	2(3)	0.7	0.2	0.6(2.1)	29	6	19(90)
250	2.6	1.7	0.5(0.8)	14	12	4(5)	0.9	0.3	0.6(1.8)	22	7	17(53)
100	5.5	3.2	1.7(2.9)	19	15	9(11)	1.7	0.7	0.8(1.9)	38	16	24(57)
Avg. All levels	3.0	1.8	0.6(1.0)	16	12	4(5)	1.0	0.4	0.6(1.5)	28	10	17(48)

Table 3. Percent reduction in rmae zonal wind, run 5 vs 3, all waves, N.H., assimilation cycle and 5-day forecast.

	Assimilation	5-Day FCST (Avg. Improvement)
850	8% (15)	7% (13)
500	19% (90)	7% (34)
250	17% (53)	11% (35)
100	24% (57)	18% (43)
Avg. All Levels	17% (54)	11% (31)

Table 4. Percent reduction in rmse zonal wind, run 5 vs 3, all waves, S.H., assimilation cycle and 5-day forecast.

	Assimilation	5-Day FCST (Avg. Improvement)
850	6% (11)	4% (8)
500	16% (77)	3% (14)
250	15% (47)	6% (19)
100	20% (48)	11% (26)
Avg. All Levels	14% (46)	6% (17)

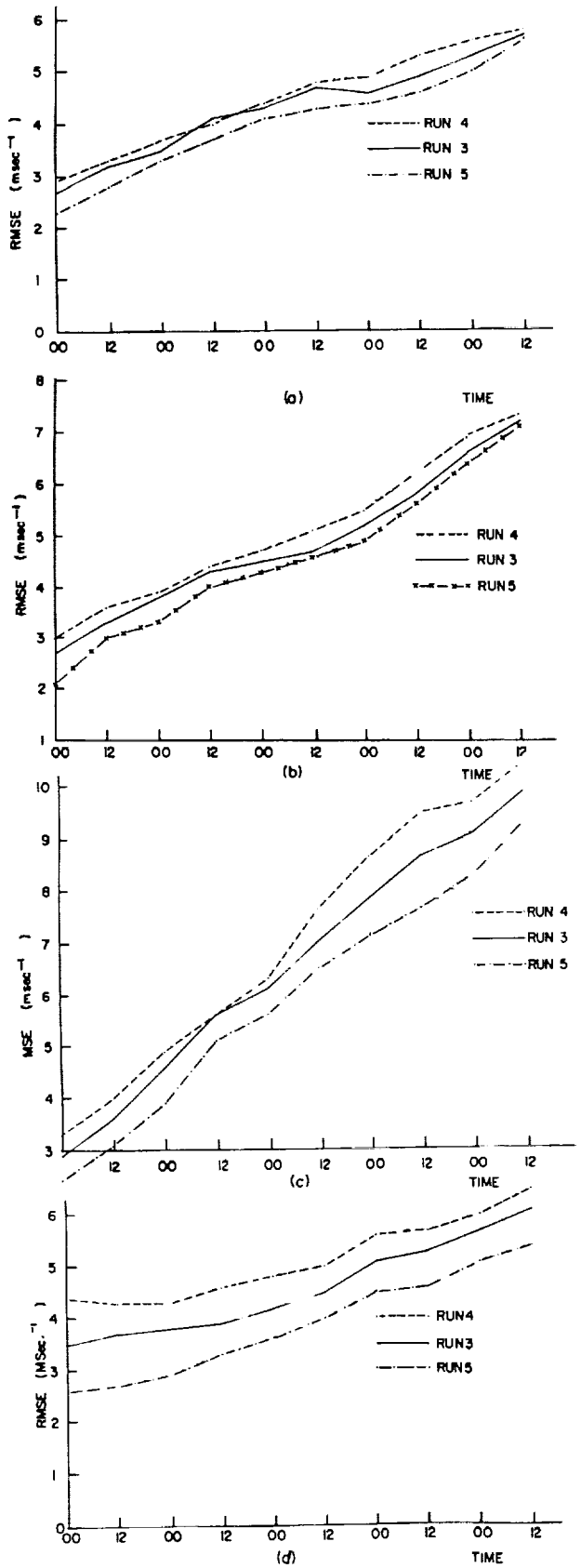

Figure 5. Root mean error (rmse) vs time for a 5-day forecast of runs 3, 4, and 5, zonal wind, northern hemisphere all waves. (a) 850 mb (b) 500 mb (c) 250 mb (d) 100 mb.

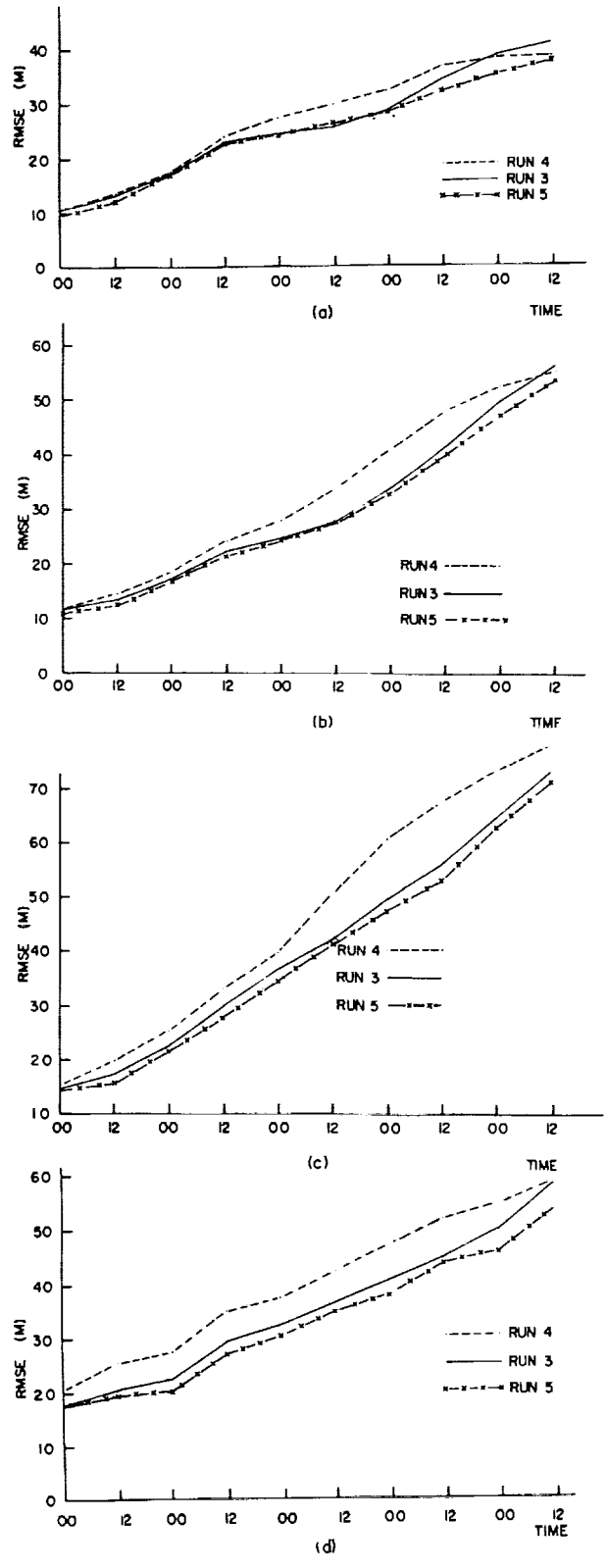

Figure 6. Same as Figure 5 except for geopotential height.

The 5-day height forecasts are compared in Figure 6. At 850 mb, where the influence of short waves dominate that of the long waves, there is no significant difference to the forecast with the addition of Windsat winds. There is, however, a very small but steady increase in forecast improvements with height. These results are consistent with the overall 5% reduction in the rmse of height reported in Table 2 for the 6-hour forecast period.

Figures 7 and 8 portray the anomaly correlation for the 500- and 100-mb 5-day forecast. Values above 60% represent skillful forecasts. In both figures, it can be seen that the addition of Windsat winds in the tropical region (30N - 30S) improves the forecast as much as the addition of global rawin winds does. At 100 mb (Figure 8), an extrapolation of the three curves down to an anomaly correlation value of 60% reveals that a 'skillful' forecast of u can be extended by 18-24 hours with the addition of Windsat winds.

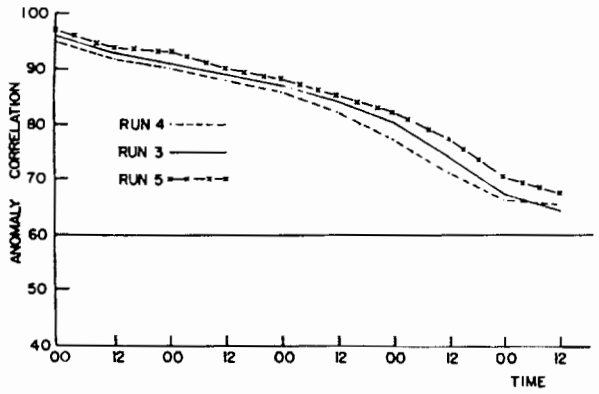

Figure 7. Anomaly Correlation vs time for a 5-day forecast of runs 3, 4, and 5, zonal wind, 500 mb level, northern hemisphere, all waves.

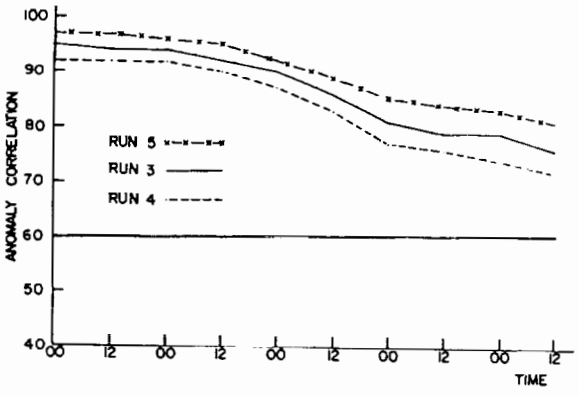

Figure 8. Same as Figure 7, except for 100 mb level.

4. SUMMARY AND CONCLUDING REMARKS

Two fraternal twin experiments were conducted as part of this study. A data impact experiment using real data (runs 1 and 2) was conducted to assess the impact that rawin wind observations have on both a 5-day assimilation and a single 5-day forecast generated at the end of each assimilation. An observing system simulation experiment (OSSE) using simulated observations (runs 3, 4, and 5) was conducted in order to first calibrate the OSSE results and second to use this calibration to estimate the 'real world' impact from the contribution of global 3-dimensional wind profiles generated from a space-based lidar system known as Windsat. Each of the three runs in the second experiment were also 5-day assimilation runs with a 5-day forecast initialized from the last 6-hour update cycle of the assimilation.

The data impact study revealed a consistent positive impact when rawin winds were added back into an otherwise complete FGGE data set. Both the 6-hour and 5-day forecasts were improved at all levels, in both hemispheres, and for both the wind and the geopotential height fields. Similar results were obtained from the two parallel simulation runs 3 and 4. Together with the results from runs 1 and 2, calibration coefficients were generated so as to 'correct' the results determined from the addition of Windsat winds (run 5).

The Windsat simulation showed a positive improvement in all cases studied. Even though only the tropics were enhanced with these wind observations, hemispheric rms errors were decreased in both the assimilation and 5-day forecast. The 6 hour forecasts of zonal wind from the assimilation run were improved by as much as 50% on the average, and the single forecast showed an average improvement of near 30%. Even though these calibrated values are considered too optimistic, the skill of the forecast generated from this run extended the useful forecast period by 18-24 hours.

Among the limitations of this study were the calibration method used and the fact that ony a single forecast could be obtained. The latter is considered to be more of a limiting factor than the former.

ACKNOWLEDGMENTS

The authors wish to thank Ms. Mary Chapman for typing and editing the manuscript.

REFERENCES

Arnold, C. P. and C. Dey, 1985a: Observing systems simulation experiments: past, present, and future. Submitted for publication to the Bull. Amer. Meteor. Soc.

Dey, C., C. P. Arnold, and W. Bostelman, 1985: Design of a windsat observing system simulation experiment. In Global Wind Measurements, W. E. Baker and R. J. Curran (Eds.), A. Deepak Publishing, Hampton, Virginia, 73-79.

Halem, M. and R. Dlouhy, 1984: Observing system simulation experiments related to space-borne lidar winds profiling. Part 1: Forecast impacts of highly idealized observing systems. Preprint volume: Conference on Satellite Meteorology/Remote Sensing and Applications of the American Meteorological Society, 25-29 June, Clearwater, FL.

Huffaker, R. M., 1978: Feasibility study of satellite-borne lidar global wind monitoring system. NOAA Tech. Memo., ERL WPL-37, 276 pp.

Kasahara, A., 1972: Simulation experiments for meteorological observing system for GARP. Bull. Amer. Meteo. Soc., Vol 53, 252-264.

USE OF WIND DATA IN GLOBAL MODELLING

J. Pailleux

European Centre for Medium Range Weather Forecasts
Shinfield Park, Reading, Berkshire, U.K.

1. INTRODUCTION

The European Centre for Medium Range Weather Forecasts (ECMWF) is producing operational global analyses every 6 hours and operational global forecasts every day from the 12Z analysis.

The first purpose of this paper is to describe how the wind data are used in the ECMWF global analysis. For each current wind observing system, its ability to provide initial conditions for the forecast model is discussed as well as its weaknesses. An assessment of the impact of each individual system on the quality of the analysis and the forecast is given each time it is possible (section 2). Sometimes the deficiencies which are pointed out are related not only to the observing system itself but also to the optimum interpolation (OI) analysis scheme; then some improvements are generally possible through ad hoc modifications of the analysis scheme and especially tunings of the structure functions. Examples are given in section 3.

Section 4 deals with the future observing network over the North Atlantic. Several countries, coordinated by WMO, are working to set up an "Operational WWW System Evaluation" (OWSE), in order to evaluate the operational aspects of the deployment of new systems (ASDAR, ASAP). Most of the new systems are expected to be deployed before January 1987, and in order to make the best use of the available resources during the deployment phase, some network studies are carried out at the present time, by using simulated data for ASDAR and ASAP systems. They are summarised at the end of section 4.

2. WIND DATA USED IN THE ECMWF GLOBAL ANALYSES

All wind data available on the GTS are used in the ECMWF analaysis scheme, which is a global 3-dimensional multivariate statistical scheme described in Lorenc (1981). One important feature of the present system regarding the use of data is the following: the data are used at 15 standard p levels from 1000 to 10 hPa, and the observations which are reporting on non standard levels are first moved to the nearest standard level (by using the first guess gradient) before the computation of the increment "observation-guess". For the future it is planned to use all the observations at the reported level, which is expected to increase the analysis resolution in the vertical, especially in the boundary layer (sondes - Part B) and near the tropopause (aircraft reports). All details about the data selection and the quality control in the ECMWF analysis system are given in Lönnberg (1984).

2.1 Surface wind observations

The multivariate scheme is processing the mass and the wind field at the same time with a geostrophic assumption between the wind increments and the height increments. As far as the surface wind data are concerned, the increments are evaluated by subtracting the post-processed 10m wind (coming from the 6-hour forecast) from the observed value. Then the major problem in the use of the data comes from the validity of the geostrophic assumption itself which is questionable because of the roughness. To cope with this problem the surface wind observations are discarded over land and used only over sea (SHIP messages). No experiment has been carried out at ECMWF to assess the impact of surface wind data on the analysis and the forecast.

2.2 Radiosonde observations (TEMP, PILOT)

Radiosonde is the only observing system which provides the analysis with a direct description of the vertical wind profile, this description being very important when fast baroclinic waves are developing. Two obvious drawbacks of the radiosonde network are

1. Most of the radiosonde stations report only twice a day (00 and 12Z)
2. For a global model the data coverage is much too poor in the Southern Hemisphere, in the tropics, and even over the oceans of the Northern Hemisphere.

Although several Observing System Experiments (OSE) have been carried out in the past to assess the impact of the radiosonde data, no experiment has been concentrated on the usefulness of wind data only.

2.3 Aircraft data (AIREP, ASDAR, AIDS)

Automatic aircraft wind measurements (ASDAR, AIDS) have been made for the first time during the FGGE year, and these data have been used in addition to the conventional AIREPS in the ECMWF analysis system for the FGGE III-b analysis production, as well as for operations. At the moment, the number of automatic aircraft

reports is very limited in the daily operations, but this number is expected to increase soon (see section 4). The main problem with manual reports seems to be related to coding mistakes (bad geographical locations, incorrect times, measurements expressed in the wrong units, etc.). However, several studies have shown (see Pierrard (1985)) that the aircraft data are quite accurate and well in agreement with the radiosonde data. The major weakness, which will be difficult to overcome, is again related to the data coverage which is poor for a global model, even if the horizontal resolution of an ASDAR system is very high along the aircraft route.

An evaluation of the impact of aircraft data on the ECMWF analyses and forecasts has been made with the FGGE data sets and the results are gathered in Baede (1985). The main conclusion is that the aircraft data are very helpful for the analyses, especially in the tropics, and that they have a small but significant positive impact on the numerical forecasts.

2.4 Cloud track wind data (SATOBS)

The cloud wind data are used in the ECMWF analysis system in exactly the same way as AIREPS, except that over land they are used only in the equatorial belt (20S - 20N) for the following reason:

Several OSEs have been carried out on cloud track winds by using the ECMWF analysis and forecast systems, and the FGGE data set (Källberg et al., 1982, and Uppala et al., 1984). This observing system seems to be very useful for the quality of the analysis and short range forecasts inside the tropics, and also in the Southern Hemisphere, because of its good data coverage. A positive impact on the forecast was also found in the Northern Hemisphere in specific cases. But at the same time a specific weakness of the system has been pointed out, namely its inability to measure strong winds. In other words, a clear underestimation of high winds results and leads, for example, to a bad description of the sub-tropical jet stream.

As this problem was more apparent over land than over sea (perhaps partly because of the orography), as usually there are conventional data over land in mid-latitudes, the SATOB data have been discarded from the operational analysis over land between 20N and 90N and between 20S and 90S.

Recent studies carried out at ECMWF, and also, for example, in France by Pierrard (1985), show that this weakness still exists in the present operations. The basic problem is probably related to the fact that it is wrong to assume that the wind speed is equal to the cloud speed in the jet streams. Some assimilation tests are now being performed in which the SATOB winds are "recalibrated" after an evaluation of their bias by comparison with other wind data (radiosonde -AIREP). The following diagram (Fig. 1), taken from Pierrard (1985), shows an example of the evaluation of the Meteosat winds against the radiosondes: on the horizontal axis the RS wind (in knots) is plotted whereas the speed difference Vsatob - Vrs is plotted on the vertical axis. When the RS wind is larger than 100 knots, the mean difference Vsatob - Vrs is around -50 knots!

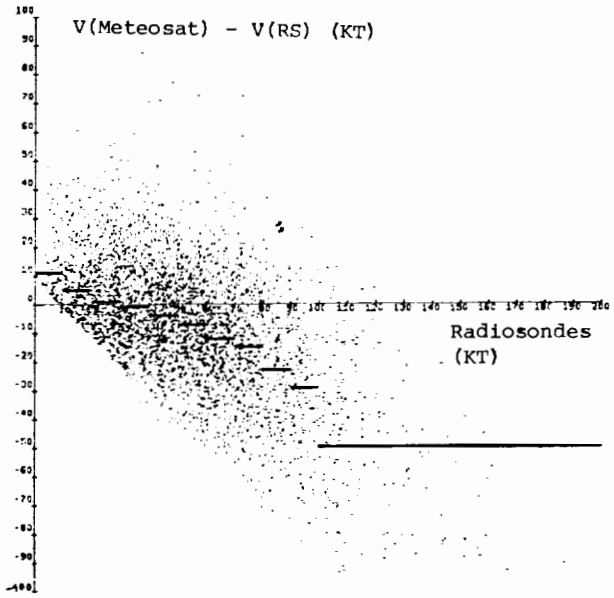

Figure 1: 9476 comparisons RS/Meteosat

3. MAIN WEAKNESSES IN THE USE OF WIND DATA STRUCTURE FUNCTIONS

Except the radiosonde network which gives a description of the vertical wind profiles, all the other wind observing systems are providing only single level data. This condition means that the 06Z and 18Z analyses (in the 6-hour analysis cycles) are carried out with wind observations at the surface (SHIPS) and near the tropopause (AIREPS and SATOBS) only. These wind observations are extrapolated in the vertical by using the structure functions which are assumed for the 3-D OI scheme. As the structure functions are not flow-dependent, they are accurate in a mean sense, but they are unable to catch some specific features such as strong shears or other extreme cases. In Hollingsworth and Lönnberg (1984), the difficulties of representing the wind shear correctly in the structure functions of an OI scheme is pointed out. But it is also shown that significant improvements can be obtained in this area by a better mathematical approximation of the structure functions and appropriate tunings.

As far as the horizontal correlation of the forecast error is concerned, up to May 1984, the ECMWF OI analysis system had used an approximation by a gaussian function:

$$r_h = C^{-\frac{r^2}{2a^2}} \qquad (a = \text{length scale})$$

to represent to geopotential height forecast error. Then the horizontal correlations for the wind components are derived through the

geostrophic assumption. The correlations r^{uu} and r^{vv} derived from the gaussian correlation r_h are anisotropic, and a strong negative correlation is found for r^{uu} in the transverse direction, as indicated on the following diagrams (Fig. 2).

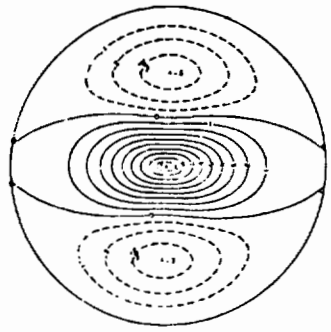

Correlation U-U

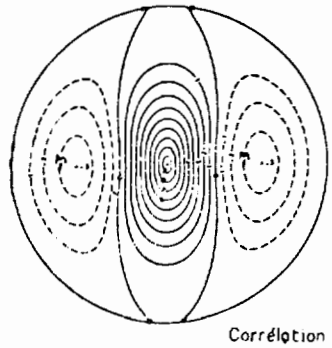

Corrélation V-V

Figure 2: Horizontal correlation for wind forecast errors derived from a gaussian height correlation

Such a shape in the structure function r^{uu} derived from a gaussian function is unrealistic and can lead to serious drawbacks in the analysis, as shown in the following case extracted from Gustafsson and Pailleux (1981): the spurious North-eastern flow in the analysis by (10N, 25W) is due to the large amount of South-western observed winds near the African coast (Fig. 3).

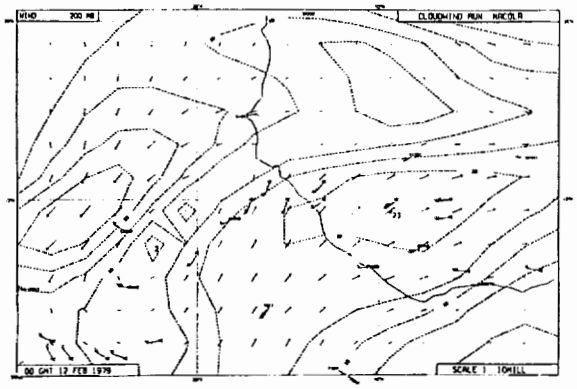

Figure 3: 200-mb wind analysis near the African coast

If the function r_h is now replaced by a development in Bessel functions which gives a more accurate representation of the spectrum of the forecast errors (modification made in the operations in May 1984), then the negative values become less important and the problem mentioned before, much less serious.

4. FUTURE NORTH ATLANTIC NETWORK AND RELATED STUDIES

Since the FGGE year a lot of work has been carried out by several institutions coordinated by WMO in order to work out an optimised Global Observing System (GOS) for the analysis and forecast requirements. An OWSE will take place along these lines over the North Atlantic from January 1987. The purpose is to test the operational aspects of the deployment of new systems on that area: buoys, ASAP and ASDAR, before deploying them in other areas of the world. Most of the evaluation will take place after the deployment of the systems in 1987-88 (parallel runs with and without the deployed systems), but before that some studies have been carried out in order to prepare the deployment itself.

4.1 Available Resources for the OWSE-NA

Forty to fifty drifting buoys are expected to be deployed at one time, most of them measuring surface pressure only (no wind measurement).

The ASDAR data coverage should be at least as good as at the end of the FGGE year. If a high level of development of the ASDAR system is assumed, the typical data coverage map for a 00Z analysis in 1987/88 could be the one represented in Fig. 4: the map shows the routes which should be covered by ASDAR observations for a 6-hour period around 00Z.

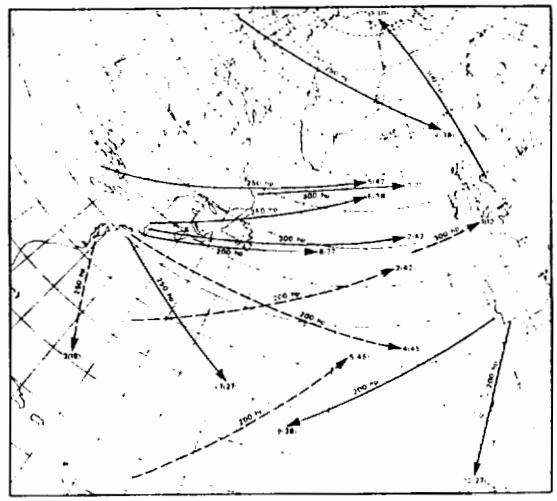

Figure 4: ASDAR distribution assumed for 00Z. The number of observations along a track is in parenthesis

If the level of development is just equal to what was available during FGGE, then only the full lines should be taken into account in the data coverage map. For 12Z, a similar map is obtained with simulated ASDAR observations, except that most of the ASDAR observations are in the eastern part of the Atlantic instead of the western part, because of the usual plane timetables. These ASDAR observations are expected to be made in addition to the conventional AIREPS which are already available.

The most important improvement over the North Atlantic is expected to come from the development of the ASAP systems which will provide several additional soundings (mass and wind-field). Nine ASAP ships are likely to be available at the beginning of 1987 and their mean number during the OWSE-NA will be around thirteen. On the other hand, the fixed weather ship R will disappear (L, C and M will be kept). The routes have already been decided for several of the ships to be equipped with the ASAP system, but there are still different possible scenarios which can be envisaged for the total deployment of the systems.

4.2 Network Studies Already Carried Out

Some network studies were carried out in 1984 to test some potential configurations for the future North Atlantic network. See Pailleux (1984). The principal objectives of these studies are as follows:

- To introduce some simulated data (in addition to other real data in an OI analysis scheme
- To calculate the analysis error standard deviation σ_a over the North Atlantic area. The ratio σ_a/σ_p can be computed as well
- To use these quantities in order to work out some objective scores which are measuring the efficiency of all the envisaged configurations in order to choose the best configuration each time it is possible.

Most studies carried out in 1984 were made with a reduced number of ASAP systems (between 4 and 8). The main result is that a fixed weather ship could be as efficient as 4 ASAP systems put on 4 ships travelling between Europe and North America.

4.3 Present Status of North Atlantic Network Studies

Some new configurations which have not been tested in Pailleux (1984) have been defined by taking into account all practical information given in section 4.1. They include the 2 ASDAR scenarios which are described in that section and the number of ASAP systems varies between 9 and 17. The geographical location files have been derived for the simulated ASDAR and ASAP data: the ASAP data have been put on the correct routes wherever possible, the locations have been produced on a 15-day period, and some reasonable assumptions have been made about the time when each ASAP system is useless (ship in port, or outside the Atlantic area).

Fig. 5 shows two typical examples of ASAP data coverage maps. The squares are the fixed R S stations which will be available during the OWSE-NA. By adding the dots we get an ASAP scenario which is the "mean OWSE-NA" scenario with 13 ships and by adding the crosses a more optimistic assumption about the development of the ASAP system is made.

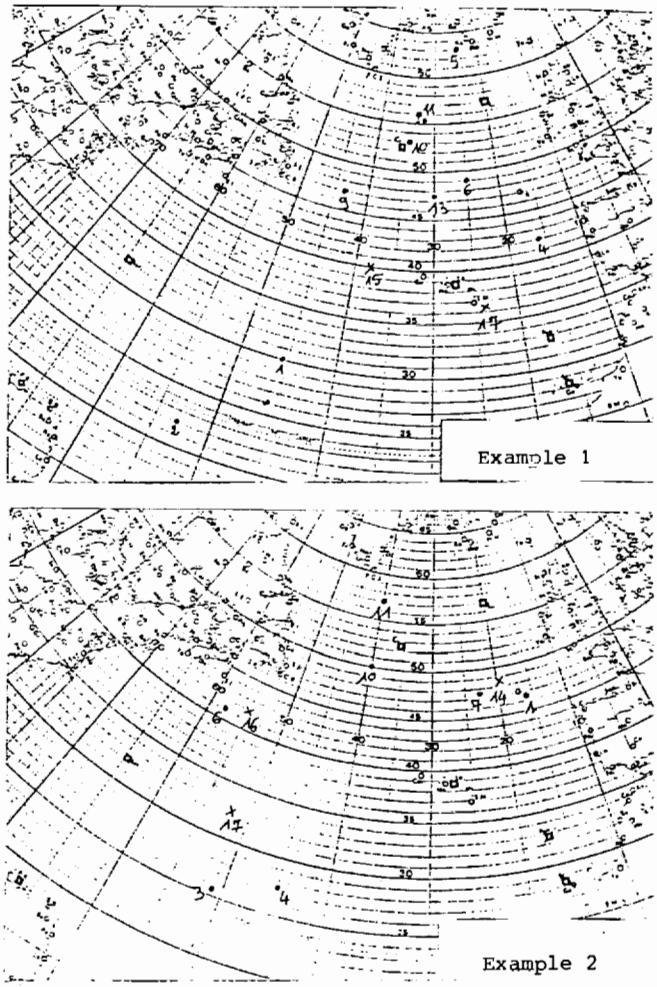

Figure 5: Examples of simulated ASAP data coverage maps with up to 17 ships. (Ships numbers from 1 to 17.

The calculations of σ_a and σ_a/σ_p have not yet been completed, but they will be done on different configurations by several centres: ECMWF, Paris, Offenbach etc. However, the following remarks can be made:

It is difficult to separate the impact of wind measurements and the impact of mass measurements, as all the variables are measured by the ASAP system and processed at the same time in the OI analysis and in the network studies.

It is also difficult to assess the different levels of development of the ASDAR system in that context, partly because they are single-level data. See section 3. However, it seems

reasonable to assume that the impact which has been assessed in Baede et al. (1985) or in Barwell and Lorenc (1985) with FGGE data is still valid for the future OWSE-NA.

An ASAP ship is available a little more than 60% of the time (in a mean sense, depending on the length of the crossing and on the time when the ship is outside the Atlantic area).

With a total number of ships equal to 13, the ASAP data coverage is almost stationary in time. Its quality does not vary too much from one day to another.

Looking at the plans of the different countries, there is a danger of finding a lot of ships in a small area between the Channel and New York/Boston/Saint Laurence, while other areas of the Atlantic are empty. One purpose of the network studies is to find out to what extent it is useful to try to put some ASAP systems on southern routes such as Gibraltar - Boston or Spain - West Indies.

5. CONCLUDING REMARKS

The wind data measurements which are used in current global modelling are: the surface data, the radiosonde data, the AIREPS and the SATOBS. In the future several improvements can be expected, especially over the oceans, from the deployment of ASAP and ASDAR systems, and the OWSE-NA will be the starting point of this important deployment phase.

Other new systems, such as surface winds measured from scatterometers or wave-radars can improve the wind measurements of the Global Observing System, and ECMWF is planning some studies to remove the ambiguity which will affect the ERS1 wind observation.

However, the main shortcoming of the present and future wind observing system seems to be the lack of a global 3-dimensional network: most of the wind observations are single level data and the current OI analysis schemes cannot make the best use of these data.

REFERENCES

1. Baede, A.P.M., Uppala, S. and Källberg, P., 1985: Impact of aircraft wind data on ECMWF analyses and forecasts during the FGGE period, 8-19 November 1979. ECMWF Technical Report No. 47.

2. Barwell, B.R., and Lorenc, A.C., 1985: A study of the impact of aircraft wind observations on a large-scale analysis and numerical weather prediction system. Quart. J. R. Met. Soc., 111, 103 - 129.

3. Gustafsson, N., and Pailleux, J., 1981: On the quality of FGGE data and some remarks on the ECMWF data assimilation system. ECMWF Technical Memorandum No. 37.

4. Hollingsworth, A., and Lönnberg, P., 1984: The statistical structure of short range forecast errors as determined from radiosonde data. Part I: The wind field. Proceedings of the ECMWF seminar on data assimilation systems and observing system experiments (September 1984) - Vol 2, 7-69.

5. Källberg, P., Uppala, S., Gustafsson, N., and Pailleux, J., 1982: The impact of cloud wind data on global analyses and medium range forecasts. ECMWF Technical Report No. 34.

6. Lönnberg, P., and Shaw, D., 1984: Data selection and quality control in the ECMWF analysis system. Proceedings of the ECMWF workshop on data selection and quality control in the analysis (November 1984).

7. Lorenc, A.C., 1981: A global three-dimensional multivariate statistical interpolation scheme. Mon. Wea. Rev., 109, 701 - 721.

8. Pailleux, J., 1984: Testing the North Atlantic observing network using different analysis schemes. Proceedings of the ECMWF seminar on data assimilation systems and observing system experiments (September 1984). Vol 1, 327 - 344.

9. Pierrard, M.C., 1985: Intercomparison between cloud track winds and radiosonde winds. Proceedings of the Meteosat user conference - Rome (May 1985).

10. Uppala, S., Hollingsworth, A., Tibaldi, S., and Källberg, P.: Results from two recent observing system experiments at ECMWF. Proceedings of the ECMWF seminar on data assimilation systems and observing system experiments (September 1984). Vol 1, 165 - 202.

CALCULATION OF GEOPOTENTIAL AND TEMPERATURE FIELDS FROM AN ARRAY OF NEARLY CONTINUOUS WIND OBSERVATIONS

Ying-Hwa Kuo and Richard A. Anthes

National Center for Atmospheric Research*
Boulder, Colorado 80307

1. INTRODUCTION

The recent development of the wind Profiler, a ground-based Doppler radar system that provides high (every few minutes) temporal resolution vertical profiles of the horizontal wind, represents a breakthrough in wind-sounding technology (Hogg *et al.*, 1983; Strauch *et al.*, 1984). The nearly continuous wind soundings, with an accuracy equal to or better than rawinsondes, offer many opportunities in research and operational meteorology (Hovermale, 1983; Shapiro *et al.*, 1983). Data processing and analysis techniques, such as temporal filtering and time-to-space conversions, promise to yield horizontal wind analyses with accuracies much better than possible in the past; in particular, it is likely that meaningful fields of temporally continuous horizontal divergence and derived vertical motion can be estimated in real time. The fields of vertical motion may prove useful in short-range forecasting if, as suggested by previous studies (e.g. Ogura, 1975), low-level mesoscale convergence precedes the outbreak of convective precipitation, as well as in diagnostic research studies which often require accurate, independent estimates of vertical velocity (for example, budget studies of heat, moisture, vorticity, or kinetic energy).

Another potential use of temporally continuous analyses of horizontal divergence is in the initialization of numerical weather prediction models. Not only could the divergent component of the wind be provided directly to numerical models, but the analysis of divergence may also be useful in estimating the temperature structure through the diagnostic divergence equation (Fankhauser, 1974; Bleck *et al.*, 1984). This equation relates the geopotential field to the horizontal wind field and includes terms involving the divergence, its temporal rate of change, and the vertical velocity. After the geopotential has been found, the temperatures may be calculated from the hydrostatic equation. Although it is unlikely that the need for some independent measurements of temperature will be eliminated, the derived temperatures may provide useful supplementary information to improve the temperature analysis.

This paper investigates the accuracy of temperature estimates derived from the divergence equation when wind observations of various spatial and temporal resolutions and accuracies are available. The basic data set used in this study is the high-resolution model data set used by Kuo and Anthes (1984a) in observing systems simulation experiments (OSSE) designed to estimate the errors in heat and moisture budgets (Kuo and Anthes, 1984b) calculated from the AVE-SESAME-1979 spatial observational network. This model data set is modified in ways to simulate wind observations that appear feasible from an operational regional network of wind Profilers. This study has been completed (Kuo and Anthes, 1985). The report presented here is a reduced version of the original paper.

2. THEORY AND COMPUTATIONAL PROCEDURES

2.1. The Divergence Equation

Because the Profiler OSSEs are done on a Lambert Conformal Map Projection, the divergence equation is derived from the equation of motion on that projection,

$$\frac{\partial D}{\partial t} + m^2\left(u\frac{\partial D'}{\partial x} + v\frac{\partial D'}{\partial y}\right) + m^2(D')^2$$

$$+2m^2\left(\frac{\partial v}{\partial x}\frac{\partial u}{\partial y} - \frac{\partial u}{\partial x}\frac{\partial v}{\partial y}\right) + \omega\frac{\partial D}{\partial p}$$

$$+m\left(\frac{\partial \omega}{\partial x}\frac{\partial u}{\partial p} + \frac{\partial \omega}{\partial y}\frac{\partial v}{\partial p}\right) - m\gamma v + m\beta u - f\zeta$$

$$= -m^2\nabla^2\phi + m^2\left(\frac{\partial F_u/m}{\partial x} + \frac{\partial F_v/m}{\partial y}\right) \qquad (1)$$

where

$$D \equiv m^2\nabla \cdot \mathbf{V}/m \qquad (2)$$

* The National Center for Atmospheric Research is sponsored by the National Science Foundation

$$D' \equiv \nabla \bullet \mathbf{V} \tag{3}$$

$$\zeta = m^2 \left(\frac{\partial v/m}{\partial x} - \frac{\partial u/m}{\partial y} \right) \tag{4}$$

$$\gamma = \frac{\partial f}{\partial x}, \beta = \frac{\partial f}{\partial y} \tag{5}$$

where u and v are the horizontal wind components in the west-east and south-north directions respectively, ω is the vertical velocity in pressure coordinates (dp/dt), f the Coriolis parameter, ϕ the geopotential, m the map-scale factor, and F_u and F_v represent frictional and other subgrid-scale effects. In the numerical model used to generate the data set used in OSSE, F_u and F_v are modeled at all levels according to

$$F_u = -K\nabla^4 u \tag{6}$$

$$F_v = -K\nabla^4 v \tag{7}$$

with an additional term representing surface drag in the lowest level of the model.

With analyses of both divergent and rotational wind components available at frequent intervals (e.g., 1 h), all the terms on the left side of Equation (1) may be estimated by finite differences. If the frictional terms on the right side of Equation (1) are neglected, the geopotential ϕ may be solved over a region, if values of ϕ around the lateral boundaries of the domain are known. In the calculations in this paper all frictional terms are ignored.

Neglect of the divergence and vertical velocity terms in Equation (1) yields the balance equation. Anthes and Keyser (1979) used the balance equation to derive temperature in their initialization of a six-layer numerical model. They found root-mean-square (rms) differences between the derived temperatures and independently analyzed temperatures of between 2°C and 4°C in the lower troposphere (1,000-700 mb), about 1.5°C in the middle troposphere (400-700 mb), and between 2°C and 3°C in the upper troposphere (about 200 mb). They attributed the large errors in the lower troposphere to neglect of friction, and in the upper troposphere to the coarse vertical resolution in resolving the high stability. In addition to these effects, the neglect of horizontal divergence, which is usually largest in the lower and upper troposphere, may have contributed to these errors.

2.2. The Data Set

The data set used in this study was produced by a mesoscale model described by Anthes *et al.* (1982) and Kuo and Anthes (1984a). The model consists of ten evenly spaced layers (Figure 1) and has a horizontal resolution of 50 km. The model domain is centered over Oklahoma (Figure 2). Frictional effects in the PBL are considered by the bulk aerodynamic method. Both stable precipitation and convective precipitation are parameterized. The model was initialized at 1200 GMT 10 April 1979 and the simulation carried out for 24 h.

Because the model simulation contains high temporal frequency variations which are not considered realistic, all model data were temporally filtered to eliminate oscillations with periods less than 6 h. This procedure described and illustrated fully by Kuo and Anthes (1984a) yields a slowly varying, dynamically consistent data set. The horizontal wind components from this data set are used to estimate the terms on the left side of Equation (1) to calculate the geopotential. The hydrostatic equation is then used to calculate the temperatures, and these derived temperatures are compared with the temperatures in the model data set, which are assumed to be free of error.

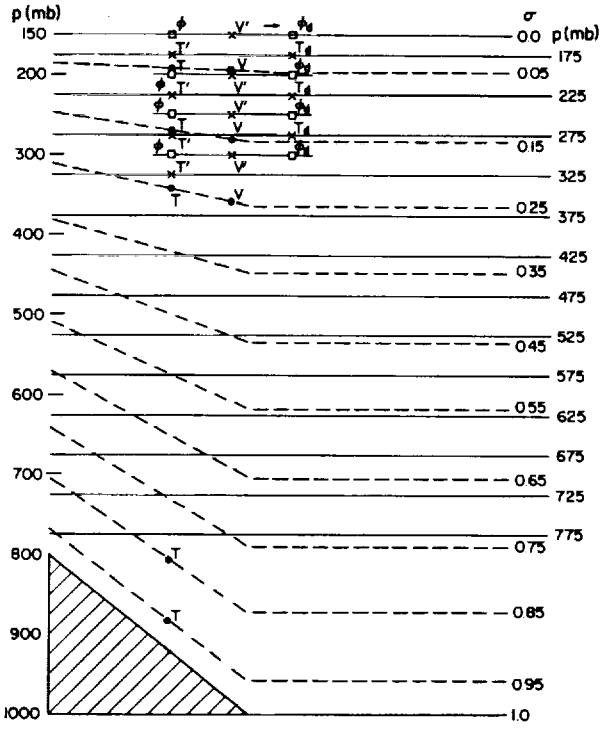

FIG. 1. Vertical grid structure of OSSE. The dashed lines are the model σ-levels at which the temperature T and wind components V are defined. The straight solid lines are constant-pressure levels at which the interpolated model temperatures T' and the temperatures T_d derived from the divergence equation are defined (175, 225, ... 775 mb). The interpolated velocity components V' and the derived geopotentials ϕ_d are defined on the constant-pressure surfaces 150, 200, 250, ... mb.

2.3. Computational Procedure

The computational procedure is summarized by the following steps.

(1) The model wind components from the ten model σ−levels are interpolated to constant pressure surfaces spaced 50 mb apart (150, 200, ... 1,000 mb; see Figure 1). The wind components at 150 mb are obtained by extrapolation. The wind components below ground are set to zero.

(2) Two passes of a 1-2-1 smoothing operator are applied in the horizontal to eliminate any 2 Δs noises, where Δs is the grid size (50 km).

(3) The vertical motion ω is calculated from the horizontal divergence by using the kinematic method with $\omega = 0$ at the upper and lower boundaries (150 and 1,000 mb) following O'Brien's (1970) technique.

(4) All terms on the left side of Equation (1) are calculated by using centered differences.

(5) The model temperatures are interpolated from the ten model σ−levels to constant pressure levels located halfway between the levels at which winds are defined (175, 225, ... 975 mb) and smoothed lightly in the horizontal. The temperatures at 175 mb are obtained by extrapolation (Figure 1). The temperatures below ground are extrapolated from the lower model level by using the standard lapse rate (6.5 K km^{-1}).

(6) The geopotential ϕ is calculated on the lateral boundaries at each constant pressure level (150, 200, ... 1,000 mb) from the interpolated temperatures T′ by integrating the hydrostatic equation downward from 150 mb, the top σ−level in the model (Figure 1).

(7) The ϕ_d on the interior is calculated from Equation (1) by using the forcing function (step 4) and the values of ϕ on the lateral boundaries.

(8) The derived temperatures T_d are calculated from the derived values of ϕ_d by using the hydrostatic equation.

(9) The rms differences between derived and true temperatures and geopotentials are computed.

There are three sources of error in the above procedure. The first is the neglect of the frictional terms F_u and F_v in the diagnostic calculation. Presumably, these terms are most important in the PBL of the model and on the smallest scales, where the ∇^4 terms are large. The second source of error is the vertical interpolation of the model data from σ to pressure levels, as well as the several interpolations necessary to obtain derived and true estimates of temperature and geopotential at the same levels (for verification). Finally, truncation errors are introduced in the calculations of the spatial and temporal derivatives on the left side of Equation (1).

3. RESULTS

The results from 11 OSSEs are summarized in Table 1. The calculations are carried out at 12 h of the model simulation. The rms errors of temperature and height are computed over 13 pressure levels (175, 225, ... 775 mb for temperature, and 200, 250, ... 800 mb for height). The lower levels are not included because of higher uncertainties associated with extrapolation below ground. Experiment 1 is the control; it utilizes the full data set at highest resolution in time and space with perfect values of ϕ specified as the boundary condition. The errors in this case result only from the three sources discussed in Section 2.3. They represent the inherent errors associated with this retrieval technique with the resolution shown in Figure 1. If perfect observations were available on isobaric surfaces so that vertical interpolations were not necessary, these errors could be reduced. It is noteworthy that the rms temperature errors of 0.64°C are considerably less than those reported by Anthes and Keyser (1979) and are comparable to instrument errors associated with radiosondes (Kuo and Anthes, 1984a). The rms height errors of $\approx$ 4 m are considerably smaller than the differences between operational analyses of geopotential height, which is $\approx$ 20 m at 500 mb (Baumhefner, 1984; Hollingsworth *et al.*, 1985). With the high vertical resolution of the actual Profiler data, the errors associated with vertical interpolation will be minimal; hence, one should regard the errors of Experiment 1 as the upper bound of the errors associated with the retrieval technique.

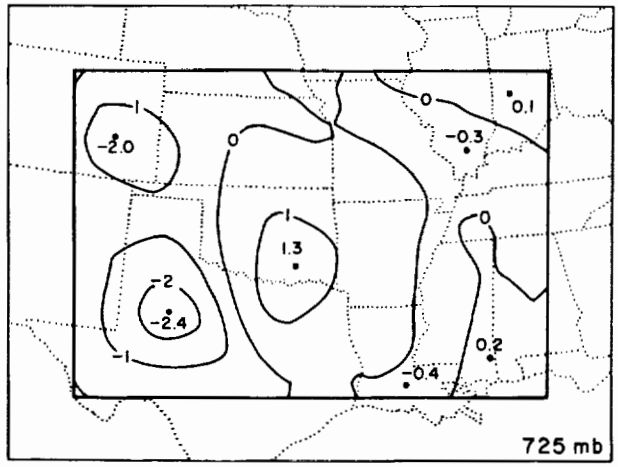

FIG. 2. Difference between derived and model temperatures (°C) for Experiment 1 at 725 mb.

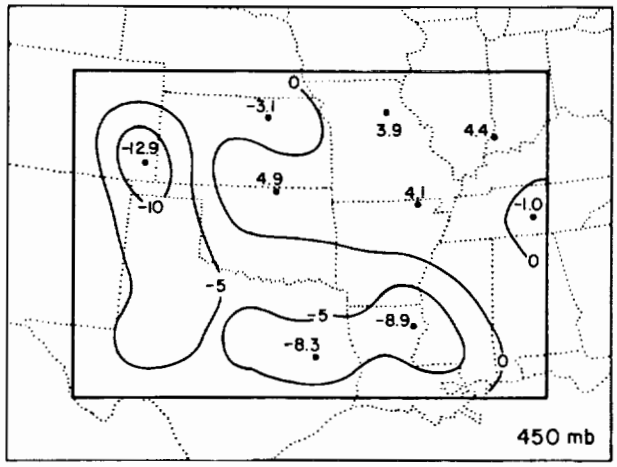

FIG. 3. Difference between derived and model height (m) for Experiment 1 at 450 mb.

Figures 2 and 3 show the differences between the derived temperatures from the true temperature at 725 mb and the differences between the derived geopotential height from the true geopotential height at 450 mb. As suggested by the rms errors, the errors at most points are less than 1°C. However, systematic errors of greater than 1°C exist over western Texas, Oklahoma, and parts of Colorado and Kansas. These temperature errors and the associated errors in static stability could be important in numerical forecasts of convective systems. The height errors are generally less than 10 m.

The results from Experiment 1 indicate that useful height and temperature data can be derived from high-resolution wind data. The subsequent experiments (Table 1) indicate the way in which a degradation in temporal and horizontal resolution and superposition of errors on the wind observations contribute to increases in height and temperature errors. In addition, a comparison of Experiment 3, in which the balance equation is used rather than the full divergence equation, with Experiment 2 gives an estimate of the value of including the divergence and vertical motion terms in the diagnostic calculation.

TABLE 1. Summary of Observing Systems Simulation Experiments.

Experiment	Horizontal resolution	Temporal resolution (h)	Superimposed error ($m\ s^{-1}$)	Equation	rms errors: Temperature (°C)	rms errors: Height (m)
1	50	0.17	0	divergence	0.64	4.0
2	50	1	0	divergence	0.65	4.1
3	50	1	0	balance	1.22	6.4
4	200	1	0	divergence	0.59	4.0
5	350	1	0	divergence	0.79	4.5
6	250*	1	0	divergence	1.62	6.0
7	200	1	1	divergence	0.86	4.2
8	350	1	1	divergence	0.96	4.8
9	250*	1	1	divergence	1.97	6.9
10	350	1	1 (plus errors on boundary values of geopotential)	divergence	1.00	11.1
11	350	1	1 (plus systematic errors of geopotential on boundaries)	divergence	1.55	18.8

* Irregular grid.

Experiment 2, in which data at a time interval of 1 h rather than 10 min are used in the calculation, gives results almost identical to those of Experiment 1. This result is not surprising because the model data set was filtered to remove temporal scales less than 6 h.

The neglect of the divergence and vertical motion terms in Experiment 3 produces a significant increase in rms temperature and height errors. The rms temperature errors double and the rms height errors increase by about 56%. The smaller percentage increase in the height errors indicates that some of the temperature errors cancel in the vertical integration. To understand better the errors associated with the balance equation, we calculate the mean absolute value of each term. The results indicate that all the terms associated with divergence and vertical motion have the same order of magnitude as the major terms in the divergence equation. Most importantly, the mean absolute value of the sum of all the divergence and vertical motion terms is 2/3 of the mean absolute value of the sum of all the other terms. This result indicates that the balance equation is not a suitable approximation for mesoscale circulations.

Experiments 4 and 5 investigate the effects of decreased horizontal resolution. In these experiments, the wind data are extracted on a regular grid with separations of 200 or 350 km, and then analyzed by a cubic-spline technique to the original 50 km grid. The small increase in rms errors in these two experiments indicates that, for this case, the calculations are not sensitive to horizontal resolution when the observations are on a regular mesh.

Observation points are generally spaced irregularly, and objective analysis is needed to obtain estimates of the variables on a regular grid. Ogura and Chen (1977) have shown that even though the variable itself is well analyzed, derived quantities (such as divergence and vorticity) can be very sensitive to the analysis procedure. Experiment 6 investigates the effect of irregularly spaced observations and the necessary objective analysis. In Experiment 6, the model wind components are extracted at the points of the AVE-SESAME-1979 network (Alberty *et al.*, 1980) which have an average station separation of 250 km. These data are then analyzed by the Cressman (1959) objective analysis scheme by using Experiment 8 as the first guess. The rms errors for Experiment 6 are 1.62°C for temperature and 6.0 m for the geopotential height. The rms temperature errors are twice as large as those of Experiment 5. Figure 4 shows the temperature error at 725 mb for this experiment. Over the area of strong convection in Oklahoma, the temperature error is 5.3°C. These results suggest that accurate divergence and vertical motions are much more difficult to estimate when wind observations are placed irregularly.

Experiments 7 and 8 investigate the effect of adding random errors (rms errors of 1 $m\ s^{-1}$) to the wind observations at 200 and 350 km resolutions. As expected, the greatest errors occur for the coarse resolution (Experiment 8). In spite of the wind errors, it is apparent that useful temperature information can still be derived from the divergence equation. However, a somewhat worse situation exists at 425 mb (not shown) where temperature errors exceed 3.5°C over eastern Oklahoma and over parts of Arkansas, Louisiana, and Mississippi. These are regions of strong moist convection and latent heating in the numerical simulation, and the divergent wind components and vertical motion are large here. Therefore, the errors due to vertical interpolation of these quantities are probably larger here than in other parts of the domain.

The effects of adding random errors to the wind observations on the irregular mesh of Experiment 6 were investigated in Experiment 9. The rms errors in temperature and geopotential height are increased, compared with the errors in Experiment 6, to 1.97°C and 6.9 m, respectively. The general pattern and magnitude of the temperature errors for Experiment 9 (not shown) are similar to those of Experiment 6 (Figure 4). A comparison of the results of Experiments 7, 8, and 9 indicates that the effects of random wind errors are larger when observations are available at irregular points than when they are available on a regular mesh.

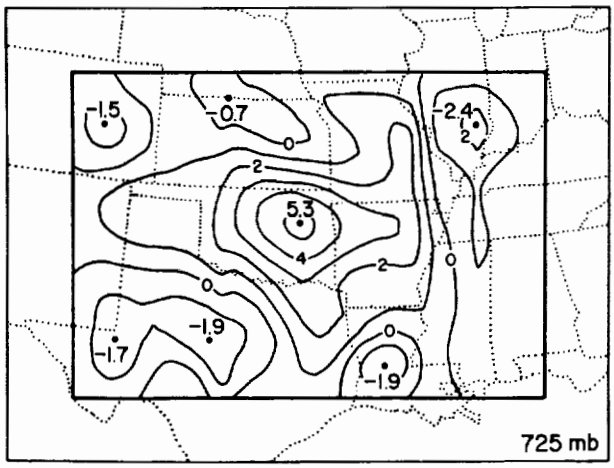

FIG. 4. Difference between derived and model temperatures (°C) at 725 mb for Experiment 6.

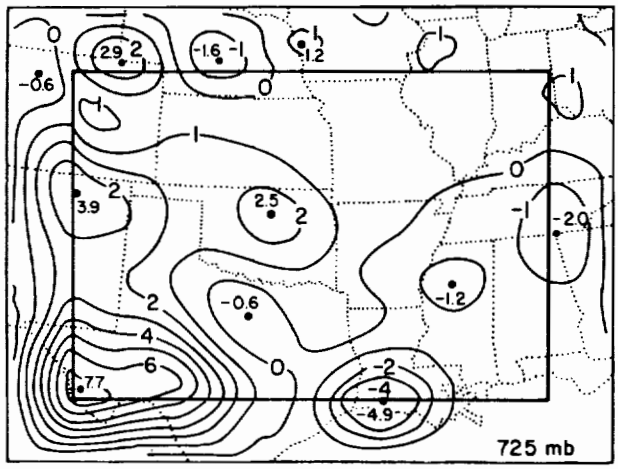

FIG. 5. Difference between model and derived temperatures (°C) at 725 mb for Experiment 11. The differences outside the interior region represent the systematic error in temperature; the differences over the interior region illustrate the effect of systematic errors in the boundary conditions plus random errors in the wind observations.

In the above calculations, the true values of the geopotentials serve as the boundary conditions in the solution of the divergence equation. In an operational configuration, the boundary conditions have to be estimated from either radiosonde and satellite observations or from a numerical model forecast, and they are likely to contain a certain amount of systematic and random errors. To test the sensitivity of the derived temperature and geopotential fields to errors on the lateral boundaries, a degraded temperature field is first created by adding 0.5°C (in an rms sense) temperature with 350 km spacing. The contaminated observations are then analyzed and integrated to obtain a degraded geopotential field. When averaged over 13 levels, the degraded geopotentials contain an rms error of 8.0 m. Experiment 10 is then carried out with conditions identical to those of Experiment 8, except that the boundary conditions are specified from the degraded geopotential field. The rms errors of Experiment 10 are 1.0°C in temperature and 11.1 m in geopotential height (Table 1). The rms differences between Experiments 10 and 8, which are a measure of the errors introduced by errors in the lateral boundary conditions, are 0.47°C in temperature and 8.8 m in geopotential height. The differences of temperature and geopotential fields between Experiments 10 and 8 are maximized near the boundaries (not shown). However, these differences decrease rapidly away from boundaries, in agreement with the theoretical analysis of Anthes and Keyser (1979). This condition suggests that useful estimates of temperature and geopotential can still be obtained despite the existence of random errors in geopotential height at the boundary.

In an operational system, the boundary conditions in geopotential height could be obtained from a large-scale model's forecast temperatures. The forecast temperatures are likely to be more highly correlated in the vertical than are the random errors superimposed in Experiment 10. Experiment 11 investigates the effects of such systematic errors in the boundary values of geopotential height. In this experiment, an analysis of geopotential height is obtained from the AVE-SESAME-1979 temperature observations (Kuo and Anthes, 1984a). The rms differences of observed compared with model heights and temperatures are 25.6 m and 1.93°C, respectively, averaged over the 13 levels. These values represent the forecast errors of this particular simulation and are slightly less than the typical errors of regional-scale models as reviewed by Anthes (1983). Experiment 11 is then carried out with conditions identical to those of Experiment 8, except that the boundary conditions are specified from the observed rather than from the model geopotential heights. The results of Experiment 11 are shown in Figure 5. Owing to the forecast temperature errors, the model geopotential heights on the boundary may be systematically higher (or lower) than the observed heights, and this error results in a positive (or negative) bias error over the whole domain. The rms errors for Experiment 11 are 1.55°C and 18.8 m, compared with 0.96°C and 4.8 m for Experiment 8. These results indicate that systematic errors in the boundary conditions contribute significant errors to the derived temperatures on the interior. Independent temperature observations from radiosondes, satellite, or from temperature profilers are needed to provide accurate estimates of geopotential height for the boundary conditions.

Some of the temperature errors are not correlated in the vertical; they can be suppressed by a light vertical smoothing. To illustrate the effect of vertical smoothing, a simple 1-2-1 smoother is applied to the derived temperature field of Experiment 11. The results showed slight improvement. The rms error averaged over 13 levels was reduced from 1.55°C to 1.36° C.

4. CONCLUDING REMARKS

Observing systems simulation experiments indicate that useful estimates of temperature can be derived from high-resolution wind observations such as those that might be obtainable from a regional network of wind Profilers. Adding the divergence and vertical motion terms to the balance equation to form the complete divergence equation reduces the errors in derived temperatures and heights. This result suggests that the balance equation is not a suitable approximation for mesoscale circulations. Observations on an irregularly spaced grid

lead to greater errors than those on a regularly spaced one. Significant errors are introduced when systematic errors in geopotential are provided as lateral boundary conditions. Vertical smoothing is effective in suppressing some of the temperature errors.

These results probably depend somewhat on the vertical resolution of the model (10 layers in this study). Further studies should employ a higher resolution model with the retrieval technique directly applied on the constant $\sigma-$levels to avoid vertical interpolations. Further model simulations should also be carried out to test the usefulness of the derived temperature fields in initializing numerical models along with the wind fields obtained from a wind Profiler system.

REFERENCES

Alberty, R. L., D. W. Burgess and T. T. Fujita, 1980: Severe weather events of 10 April 1979. *Bull. Amer. Meteor. Soc.*, **61**, 1033-1034.

Anthes, R. A., 1983: Regional models of the atmosphere in middle latitudes. *Mon. Wea. Rev.*, **111**, 1306-1335.

Anthes, R. A. and D. Keyser, 1979: Tests of a fine-mesh model over Europe and the United States. *Mon. Wea. Rev.*, **107**, 963-984.

Anthes, R. A., Y.-H. Kuo, S. G. Benjamin and Y.-F. Li, 1982: The evolution of the mesoscale environment of severe local storms: Preliminary modeling results. *Mon. Wea. Rev.*, **110**, 1187-1213.

Baumhefner, D. P., 1984: Analysis and forecast intercomparisons using the FGGE SOP1 data base. Paper presented at the NAS FGGE Workshop. Available from author at National Center for Atmospheric Research, Boulder, Colorado 80307.

Bleck, R., R. Brummer and M. A. Shapiro, 1984: Enhancement of remotely sensed temperature fields by wind observations from a VHF radar network. *Mon. Wea. Rev.*, **112**, 1795-1803.

Cressman, G. P., 1959: An operational objective analysis system. *Mon. Wea. Rev.*, **87**, 367-381.

Fankhauser, J. C., 1974: The derivation of consistent fields of wind and geopotential height from mesoscale rawinsonde data. *J. Appl. Meteor.*, **13**, 637-646.

Hogg, D. C., M. T. Decker, F. O. Guiraud, K. B. Garnshaw, D. A. Merritt, K. P. Moran, W. B. Sweezy, R. G. Strauch, E. R. Westwater and C. G. Little, 1983: An automatic profiler of the temperature, wind and humidity in the troposphere, *J. Climate Appl. Meteor.*, **22**, 807-831.

Hollingsworth, A., A. C. Lorec, M. S. Tracton, K. Arpe, G. Cats, S. Uppala and P. Kallberg, 1985: The response of numerical weather prediction systems to FGGE level II-b data. Part I: Analysis. *Quart. J. Roy. Meteor. Soc.*, **111**(No. 467), 1-66.

Hovermale, J. B., 1983: Summary of a workshop on atmospheric profiling, 3-4 March, Boulder, CO. *Bull. Amer. Meteor. Soc.*, **64**, 1062-1066.

Kuo, Y.-H. and R. A. Anthes, 1984a: Accuracy of diagnostic heat and moisture budgets using SESAME-79 field data as revealed by the observing system simulation experiments. *Mon. Wea. Rev.*, **112**, 1465-1481.

Kuo, Y.-H. and R. A. Anthes, 1984b: Mesoscale budgets of heat and moisture in a convective system over the central United States. *Mon. Wea. Rev.*, **112**, 1482-1497.

Kuo, Y.-H. and R. A. Anthes, 1985: Calculation of geopotential and temperature fields from an array of nearly continuous wind observations. *J. Atmos. Oceanic Technol.*, **2**, 22-34.

O'Brien, J. J., 1970: Alternative solutions to the classical vertical velocity problem. *J. Appl. Meteor.*, **9**, 197-203.

Ogura, Y., 1975: On the interaction between cumulus clouds and the large-scale environment. *Pure Appl. Geophy.*, **113**, 869-889.

Ogura, Y. and Y.-L. Chen, 1977: A life history of an intense mesoscale convective storm in Oklahoma. *J. Atmos. Sci.*, **34**, 1458-1476.

Shapiro, M. A., D. C. Hogg and C. G. Little, 1983: The wave propagation laboratory profiler system and its applications. *Proc. Fifth Symposium on Meteorological Observations and Instrumentation*, Toronto, Amer. Meteor. Soc., 174-182.

Strauch, R. G., D. A. Merritt, K. P. Moran, K. B. Earnshaw and D. van de Kamp, 1984: The Colorado wind-profiling network. *J. Atmos. Oceanic Technol.*, **1**, 37-49.

MEASUREMENT OF WIND NEAR THE SURFACE

Fred V. Brock*
National Center for Atmospheric Research
Boulder, Colorado

1. INTRODUCTION

This paper is a survey of instrumentation suitable for measurement of wind near the surface of the earth by using in-situ techniques and further restricted to sensors that are operational. In this case, a sensor is deemed to be operational if it is commercially available. There is no discussion here of the systems that might be used to acquire, process, display, and store the sensor data. It is assumed that some sort of automatic data logging equipment would be used. Without special requirements such as need for high frequency response, low power consumption, etc., this treatment must be quite general and provides little detail. Also, without special restrictions, emphasis must be placed on conventional sensors that provide the bulk of wind data today.

2. CUP ANEMOMETERS

The cup anemometer consists of a cup wheel with three or four cups designed to rotate in response to the horizontal component of the wind vector. The cup wheel turns a transducer, usually either a voltage generator or a light chopper, to produce an electrical signal, a voltage or a frequency, proportional to the wind speed. (See Busch et al., 1980).

Because of bearing friction there is a starting speed called the threshold which is typically 0.3 to 1.0 m/s. In wind speeds well above this region, cup anemometers are linear and accurate to within 1% of the reading. Ideally, a cup anemometer would respond to a non-horizontal component of the wind vector as the cosine of the angle from the horizontal.* Actually, the response function is usually greater than the cosine of the angle, and this causes overestimation of the horizontal component in turbulent flow or when the flow is not horizontal as may occur on hillsides. This type of error is a function of anemometer design and can be a major source of error in some anemometers.

*Currently at the University of Oklahoma, Norman, Oklahoma

In a steady wind, as in a wind tunnel, the cup anemometer dynamic performance can be reasonably approximated by a first-order linear differential equation

$$\tau \frac{dV}{dt} + V = Vi \qquad (1)$$

where Vi is the wind speed, V is the speed indicated by the anemometer after calibration, t is the time and τ is the time constant. The time constant is inversely proportional to the wind speed so another parameter called the distance constant

$$\lambda = \tau V \qquad (2)$$

is used to characterize the dynamic performance. The distance constant typically ranges from 1 to 20 m, the shorter values being associated with lighter, less rugged cup wheels. Since the time constant is a function of the wind speed, substitution of equation (2) into equation (1) makes that equation nonlinear. The response to increasing wind speed is faster than that for decreasing wind speed so it follows that all cup anemometers must overestimate the mean wind speed to some extent. The amount of overestimation is proportional to the distance constant and to the turbulence intensity squared ($\sigma v^2/V^2$).

Deformation of the cup wheel changes the calibration so light cup wheels are sensitive to birds and bullets and strong winds. Icing can coat the cups and cause a temporary calibration change and even stop it altogether.

Bearing friction will increase with use especially when the anemometer is exposed to dust or salt spray. From zero wind speed to speeds several times the nominal threshold, the anemometer performance is quite nonlinear and presents special problems for measurement of light winds.

Cup anemometers are simple, reliable, can be made rugged, are easy to maintain, do not need alignment to the wind direction, and are ideal for continuous wind measurement. They have very limited frequency response, can overestimate the mean wind, and are quite nonlinear at low wind speeds.

3. WIND VANES

Wind vanes rotate about a vertical axis, two axes for the bivane, to indicate the wind direction. The shaft of the vane turns a transducer to produce an electrical signal. This is usually a single potentiometer for automatic weather stations that with a reference voltage, produces a voltage proportional to wind direction. Alternatively, a shaft digitizer can be used to generate a digital signal. See Busch, et al., 1980.

The static errors of wind vanes arise from misalignment and from the transducer. A single potentiometer has a dead zone of 3 to 5 degrees, usually at north, and may have some small nonlinearity. Bearing friction, unless it becomes excessive, is not usually a problem.

The wind vane is usually represented as a second-order linear system

$$\frac{1}{\omega n^2}\frac{d^2\theta}{dt^2} + \frac{2\zeta}{\omega n}\frac{d\theta}{dt} + \theta = \theta_1 \qquad (3)$$

where θ_1 is the wind direction, θ is the indicated direction, ωn is the natural frequency and ζ is the damping ratio. As with cup anemometers the natural frequency is a function of the wind speed

$$\lambda n = \frac{2\pi V_1}{\omega n} \qquad (4)$$

while the damping ratio is independent of wind speed. The damping ratio ranges from 0.1 to 0.7. The vane amplifies some gust frequencies when the damping ratio is less than 0.6. The dynamic performance of wind vanes is not critical to most applications. One exception is the measurement of the standard deviation of wind direction for atmospheric dispersion studies.

Wind vanes are free from bias, proper alignment being assumed. However, deformation of the vane could cause a bias. They are susceptible to damage from birds and from icing. Potentiometer wear is a more serious problem than bearing wear.

4. PROPELLER ANEMOMETERS

Propeller anemometers are similar to cup anemometers in many respects. They have similar static and dynamic characteristics but the propeller responds (imperfectly) only to the axial component of the wind speed. There are several configurations of propeller anemometers in common use. A single propeller can be mounted on a vertical axis to measure the vertical component of the wind speed, two or three can be mounted on orthogonal axes to measure the horizontal or total wind vector, and a single propeller in the propeller-vane (propeller-bivane) combination can measure the horizontal (total) wind vector. (See Busch et al., 1980 and Michelena and Holmes, 1983).

As noted, the static characteristics of a propeller are similar to those of a cup anemometer, the major difference being that the propeller response to an off-axis wind vector is considerably less than the ideal cosine response. If the propeller axis is fixed as in the two- or three-axis configuration, it is necessary to correct the outputs by using a polynomial expansion or table look-up. Thus, for real time display, a microprocessor is required. Such corrections are not required in the propeller-vane combination.

The dynamic performance can be approximated using equations (1) and (2) with a correction for the distance constant based on the angle of attack, θ, for fixed-axis propellers,

$$\lambda(\theta) = \lambda(\theta)\ \cos^{1/2}\theta \qquad (5)$$

where $\lambda(\theta)$ is the distance constant for a given angle of attack.

Propeller blades are designed to be mechanically interchangeable and can be changed without affecting the calibration unless they have been damaged. Depending on the materials used in the construction of the blades, propellers can be quite rugged and suitable for use in harsh marine environments (see Michelena and Holmes, 1983). Propeller anemometers have the same bearing sensitivity as cup anemometers and similar threshold characteristics.

Like cup anemometers, propeller anemometers are simple and reliable; they can be rugged; they are easy to maintain but they do require alignment. The propeller-vane combination is comparable to a cup anemometer and wind vane with similar performance characteristics. Unless there are special requirements, as in Brock and Saum, 1983, a cup anemometer and wind vane or propeller-vane would be preferable to two orthogonally mounted propellers used to measure the horizontal wind vector. This preference is because the cosine characteristics of the propellers require correction which must be done in real time in many cases. However, three orthogonal propellers for measurement of the total wind vector are preferable to the propeller-bivane since the latter is awkward to use and generally is not as reliable.

5. DYNAMIC ANEMOMETERS

The dynamic or drag force anemometer is a sensor which measures wind velocity by detecting the drag force on an object in the flow. This object is a cylinder for detecting two-dimensional or a sphere for detecting three-dimensional flow. Motion of the cylinder or sphere in response to the wind force is opposed by a restoring spring and is sensed by transducers. Some examples of this type of anemometer are described in Doeblin, 1975, Smith, 1980 and Van Cauwenberghe et al., 1983.

The static calibration equation is given by

$$F = \frac{\rho A C\rho \; IVI \; V}{2} \qquad (6)$$

where ρ is the air density, A is the cross-sectional area, C_d is the drag coefficient, V is the wind vector, and F is the force vector. It is very nonlinear since the absolute magnitude of the wind vector term causes determination of each velocity component to depend on all three force components.

The dynamic response is determined by the spring torque used to hold the object in position and it is limited by the size of the cylinder or sphere. The frequency bandwidth is proportional to the square root of the spring constant. Increasing the stiffness of the spring increases the bandwidth. But, since this condition decreases the range of motion, it increases the required sensitivity of the transducers.

The drag force anemometer has no moving parts which would seem to make it an ideal mechanical anemometer. The calibration could be affected by freezing rain or snow accumulation which would change the aerodynamics. This condition could be prevented by using heaters. However, the spring stiffness changes with time and temperature and is the most serious disadvantage of this device.

6. TETHERED KITES

A tethered kite called a Tethered Aerodynamically Lifting Anemometer (TALA) has been used to make spot measurements in winds from 3 to 50 m/s and at elevations up to 300 m. It is a special kite design that has been tested in wind tunnels and in the vicinity of a 300 m tower (Kaimal, et al., 1980).

Although each kite must be calibrated, the general performance equation is

$$F = \frac{\rho \; V^{1.967}}{2} \qquad (7)$$

where V is the wind speed, ρ is the air density and F is the force on the kite. The speed is inferred from the drag on the string, the direction from the string azimuth, and the elevation from the string elevation angle.

The dynamic performance has not been well established but response to 10Hz in a 10 m/s wind has been claimed. One model requires manual readout and another has automatic data recording but, in either case, the kite must be attended since it will fall in light winds. It is a relatively inexpensive means to make spot measurements to 300 m.

7. HOT WIRE AND HOT FILM ANEMOMETERS

Hot wire and hot film anemometers are used to infer the wind speed from the cooling of a heated wire or film, which is dependent on the speed and density of flow past the sensing element. The response speed of wires and films is a function of the thermal mass of the element. Hot wires are the fastest conventional wind sensors available since they use very fine platinum wires, typically 5 m in diameter. These sensors are well suited to measurement of atmospheric turbulence or for use on an aircraft. Film sensors are made by depositing a thin film of platinum on a cylindrical quartz or glass core and then insulted with a very thin quartz or ceramic coating. The rod diameter may be 50 m in diameter or more; thus, the frequency response is inhibited somewhat. For a general treatment, see Doeblin, 1975, Hasse and Dunckel, 1980, and Perry, 1982.

In a wire operated in the constant temperature mode, the current, I, through the sensor is related to the wind speed by King's law

$$I^2 = A + B \; V^{1/2} \qquad (8)$$

which is applicable above 1 m/s. The calibration is a function of the air density and of the wire (or film) characteristics including possible atmospheric contamination. It is not uncommon to monitor the mean air speed simultaneously with a cup anemometer to provide an on-going calibration check.

The dynamic response characteristics can be quite complex but it is relatively easy to increase the frequency response by decreasing

the probe size so that the details of the frequency response are seldom needed. However, a hot film anemometer with a large probe may have rather poor frequency response in the 10 to 100 Hz range.

Probe configurations are available to sense the three-dimensional wind vector but they must be oriented into the mean wind to avoid probe obstruction effects. They are susceptible to atmospheric contamination which does affect the calibration. Larger hot film probes are less susceptible and can be cleaned to restore the calibration. Also, larger probes are more rugged than the small hot wire probes. Rain produces spikes in the data which can be readily edited out.

8. SONIC ANEMOMETERS

The sonic anemometer measures the time required to transmit an acoustic signal across a fixed path to determine the wind velocity component along that path. It's frequency response is limited by the spatial averaging along the path. It is an absolute instrument and responds linearly to the wind speed. See Coppin and Taylor, 1983, Kaimal, 1980 and Kaimal, et al., 1980.

The calibration equation for a single-axis, dual-path sonic anemometer, from Kaimal, 1980, is

$$Vd = \frac{201.5\ T\ \Delta t}{d} \qquad (9)$$

where d is the path length, T is the absolute air temperature, Δt is the difference in transit time for both directions over the path, and V_d is the average wind speed over the path. Three-dimensional anemometers are available.

The bandwidth of a sonic anemometer is a function of the wind speed and is approximately $V/2\pi d$.

The sonic anemometer is fairly expensive, compared with simple mechanical sensors, and requires considerably more power. There can be signal loss due to heavy rain or wet snow. It has somewhat greater bandwidth than the mechanical anemometers but considerably less than hot wire or hot film anemometers.

REFERENCES

Brock, F.V. and G.H. Saum, 1983: Portable automated mesonet II. In Preprints of the Fifth Symposium on Meteorological Observations and Instrumentation, AMS, 314-320.

Busch, N.E., O. Christensen, L. Kristensen, L. Lading, and S.E. Larsen, 1980: Cups, vanes, propellers, and laser anemometers. In Air-Sea Interaction: Instruments and Methods. Edited by F. Dobson, L. Hasse and R. Davis, Plenum Press, New York, 801 pp.

Coppin, P.A. and K.J. Taylor, 1983: A three-component sonic anemometer/thermometer system for general micrometeorological research. Bound.-Layer Meteor., 27, 27-42.

Doeblin, E.O., 1975: Measurement Systems: Application and Design. McGraw-Hill, New York, 882 pp.

Hasse, L. and M. Dunckel, 1980: Hot wire and hot file anemometers. In Air-Sea Interaction: Instruments and Methods, F. Dobson, L. Hasse and R. Davis, (eds), Plenum Press, New York, 801 pp.

Kaimal, J.C., 1980: Sonic anemometers. In Air-Sea Interaction: Instruments and Methods , F. Dobson, L. Hasse and R. Davis, (eds), Plenum Press, New York, 801 pp.

Kaimal, J.C., H.W. Baynton and J.E. Gaynor (eds), 1980: Low-level intercomparison experiment, WMO Instruments and Observing Methods, Report No. 3.

Michelena, E.D. and J.F. Holmes, 1983: A rugged, sensitive, and light-weight anemometer used by NDBC for marine meteorology. In Preprints of the Fifth Symposium on Meteorological Observations and Instrumentation, AMS.

Perry, A.E., 1982: Hot-Wire Anemometry. Clarendon Press, Oxford, 184 pp.

Smith, S.D., 1980: Dynamic anemometers. In Air-Sea Interaction: Instruments and Methods, F. Dobson, L. Hasse and R. Davis, (eds.), Plenum Press, New York, 801 pp.

Van Cauwenberghe, R., F. Kuja, and J. Motycka, 1983: De-iceable drag anemometer. In Preprints of the Fifth Symposium on Meteorological Observations and Instrumentation, AMS, 11-15.

REFERENCE LEVEL WINDS FROM BALLOON PLATFORMS

Vincent E. Lally

National Center for Atmospheric Research*
Boulder, Colorado

1. INTRODUCTION

The superpressure balloon was developed to provide a method of obtaining global winds at all altitudes from 5 km to 30 km. If a balloon could be made to fly for several weeks at a constant altitude, and if it could be tracked accurately on its global circuits, the balloon would provide a tag for the air parcel in which it was embedded. The Lagrangian data on the atmospheric circulation would provide a superior data input to the numerical model.

The Global Atmospheric Research Program (GARP) was initiated in large part based on the promise of this technique coupled with free-floating ocean buoys and satellite radiometers. The initial name proposed by Charney for GARP was SABABURA -- satellite - balloon - buoy - radiometric system (Charney, 1966). Unfortunately, although the superpressure balloon exceeded its designers' expectations for flight duration in the stratosphere (longest flight duration of 744 days), flight duration below 10 km was limited by icing in super-cooled clouds to a few days. The balloon was relegated to a secondary role during the GARP Special Observing Periods.

The several major superpressure balloon programs for global wind measurement are described below as well as those new developments which make the balloon once again an attractive vehicle for measurement of global winds as a reference and bench-mark system for future satellite systems.

2. MAJOR WIND MEASUREMENT BALLOON SYSTEMS

2.1 GHOST

The concept of a global wind-measurement system based on satellite tracking of superpressure balloons was first proposed in 1959 (Lally, 1960). The Global HOrizontal Sounding Technique (GHOST) was the generic name for a series of Southern Hemisphere flights at altitudes from 1 km to 30 km to test the ability of superpressure balloons to fly for several weeks. Location was determined by H.F. telemetry of the elevation angle of the sun to a number of receiving sites located around the globe. At the same time NASA initiated a program to provide balloon location from orbiting satellites. During this period, from 1966 to 1970, hundreds of flights were made in the Southern Hemisphere with average duration of 3 months at 24 km, improving to 9 months at 15 km, and dropping to 5 days at 5 km. Fig. 1 indicates a typical trajectory for a 200 mb flight.

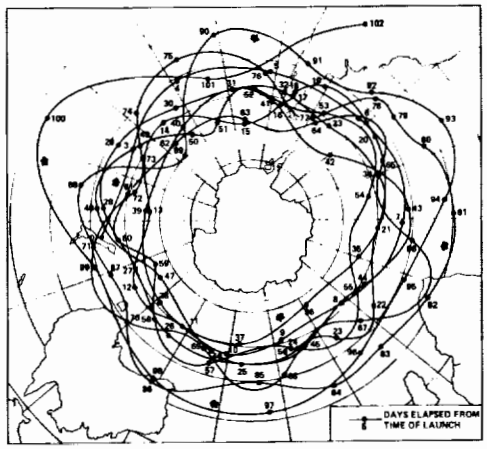

Fig. 1 Complete flight trajectory for balloon No 79R launched from Christchurch, New Zealand. Flight level was 200 mb

2.2 Nimbus-4/IRLS

The first successful satellite system for tracking-balloons was flown on the Nimbus-4 satellite in 1970. Between June and November of 1970, 26 large superpressure balloons were flown from Ascension Island at altitudes of 20 and 24 km.

This program provided considerable improvement in the understanding of the air motion in the tropical stratosphere (Angell, 1972). Longest flight was 155 days with 7 flights exceeding 3 months. The high cost of the Interrogation, Recording & Location System (IRLS) precluded any further balloon experiments.

2.3 EOLE

France undertook the first major superpressure balloon program (EOLE) by using the balloon techniques developed in the GHOST program and a satellite transponder system for balloon location and telemetry. Four hundred

*The National Center for Atmospheric Research is sponsored by the National Science Foundation.

seventy-nine balloons were launched from 3 sites in South America in 1971 and flew at an altitude of 12 km. The results were most successful: 280 balloons were simultaneously in flight at the peak of the experiment. The cost of the electronic expendables ($25,000 per platform) precluded an operational follow-on to this pioneering program.

2.4 TWERLE

The Tropical Wind Energy Conversion and Reference-Level Experiment (TWERLE) was a program to test a new low-cost location and telemetry system. The Random Access Measurement System (RAMS) was designed by the Goddard Space Flight Center specifically for superpressure balloon location. Guest investigators were welcomed on the experiment which was flown on the Nimbus-6 spacecraft. The TWERLE experiment was a great success and the 430 balloons launched from 4 Southern Hemisphere sites resulted in a number of significant advances in our understanding of atmospheric circulation (The TWERLE Team, 1977). The guest investigator programs were even more successful -- culminating now in the ARGOS and air-sea rescue systems with tracking of free-floating buoys, animals, adventurers, and the location of aircraft and ships in distress.

2.5 The Carrier-Balloon System

The Nimbus-4/IRLS test demonstrated that superpressure balloons flown in the tropical stratosphere will remain in the tropics for periods of 2 to 3 months. Since wind data in the tropics were needed for the Global Weather Experiment, a system was proposed and designed consisting of up to 100 balloons flying at 24 km, each equipped with 100 dropsondes. The dropsondes, when released on command, translated the OMEGA navigation signals to a ground computer via the balloon and the GOES satellite. The system was successfully demonstrated on 12 flights from French Guiana, but was not used in the GARP program since an aircraft-based dropsonde system permitted drops in the most active areas rather than random drops throughout the tropics (Passi and Olson, 1974).

2.6 The Tropical Constant-Level Balloon System

After the successful demonstration of the RAMS system with TWERLE, France agreed to take over the responsibility for the development and operation of a similar system (ARGOS) to be flown on the NOAA polar-orbiting satellites. The first of these systems was made operational prior to the Global Weather Experiment special observing periods of January and June 1979. Three hundred thirteen balloons were flown during these periods from Ascension Island, Canton Island, and Guam. The wind data from these flights at an altitude of 14 km provided an invaluable addition to the GARP archives since aircraft drop windsonde measurements were at lower altitudes and the radiometric data from the polar orbits cannot be translated into wind data in the deep tropics. The balloon trajectories provide additional insight into the circulation patterns since we can consider the balloon as a Lagrangian tracer. (A film of balloon trajectories was shown at the workshop at this time.)

The expendable costs for this program were reduced to $1500 for the electronic system and $1000 for the balloon -- a major reduction from EOLE costs, but still too high for a continuing operational program (Julian and Lichfield, 1978).

2.7 The Radiation-Controlled Balloon (RACOON)

For operational flights, superpressure balloons may prove to be too costly at stratospheric altitudes and (unless releasing dropsondes) provide data at only one altitude. An intriguing concept is to use a low-cost zero-pressure balloon flying at an altitude of 35 to 40 km during the daytime in the tropics or summer mid-latitude. At night the gas in the balloon cools and the balloon sinks. As the balloon drops through increasingly colder temperatures it reaches an altitude at which it again is neutrally buoyant. The excursion is typically 10 to 15 km. At the next sunrise the balloon ascends to its original altitude. If the balloon is equipped with an OMEGA navigator and appropriate sensors, it is possible to take 2 soundings a day of wind, pressure, temperature, gases, and aerosols in the altitude range of 20 to 40 km.

The technique has been demonstrated in two flights from French Guiana which circumnavigated the globe without ballast in 1980. The technique is now being tested to carry large scientific payloads (1000-2000 kg) around the world with recovery near the launch site. Only a scientific interest and modest funds are needed to make the technique operational for global wind measurements in the tropical stratosphere.

3. MICROGHOST

On the assumption that an operational superpressure balloon system would have to be inexpensive and nonhazardous to aircraft, NASA sponsored a study program with NCAR to design such a system which could be used as a reference level for winds in the mid-latitudes. Pressure data from free-floating ocean buoys together with the wind and temperature data from balloons flying at 12 km would provide the basis for improvement of the accuracy of winds derived from radiometric techniques. The balloon-based winds would also serve as a bench-mark for calibration of winds derived by satellite-based laser or other new techniques.

Initial studies were concerned with adding interferometric measurements to the satellite doppler frequency measurement, so that the severe requirement of frequency stability on the

platform transmitter could be removed. A more pragmatic approach was later adopted and assumed that the ARGOS location system would not be changed; however, an oscillator could be used with modest stability over the severe temperature range which the balloon platform experiences, but with a well-behaved calibration as a function of temperature. Telemetry of the temperature of the crystal then obviates the need for oven control. Several balloon flights were made from New Zealand to document this low-cost approach.

For the last several years, the goal of tracking whales and other mammals at sea as well as animals and birds has driven a number of researchers. There is now available (as a result of collaboration between oceanographers, bird-trackers, NASA, industry, and NCAR engineers) a new ARGOS platform which ideally suits the needs for the MICROGHOST program. It weighs 100 grams, plus a few grams of foam packaging, plus 250 grams of Lithium batteries which provide day-night power for four months. It operates over the range of -40°C to +70°C. It is certified for ARGOS use. Cost will be less than $500 in large quantities.

A spherical superpressure balloon capable of carrying a 500-gram payload at 200 millibars is 3 meters in diameter. Cost of the balloon is approximately $1000. A much simpler design, the tetrahedron, can be manufactured for $200 or less. This is not an efficient design. However, by stressing the tetrahedron at high temperatures for 12 or more hours, it assumes a nearly spherical shape and is able to take stresses equivalent to those of the spherical balloon. This "tetrasphere" concept was developed as part of the MICROGHOST program. It has been successfully tested and flown.

The two elements of an operational super-pressure balloon flight program are now at hand. At a cost of less than $1000 per flight, balloons can be flown for periods up to 4 months at the 12 km (200 millibar) level with wind determinations made 8 times per day by using the two ARGOS-equipped polar-orbiting satellites. The flight history of the past 20 years indicates that adequate coverage of the mid-latitudes of the Southern Hemisphere can be achieved from a single launch site located at any latitude from 35° to 45° S. Only a source of funding of 500K per year is needed to make such a system operational.

4. SUMMARY OF RESULTS

Superpressure balloons provide a proven technique for obtaining global winds at any altitude from 12 km to 24 km. As a reference level for use with other technologies, a system providing at all times 100 or more platforms flying at 200 mb can be readily implemented for the middle latitudes of the Southern Hemisphere.

A system for measuring global winds in the tropical stratosphere can be achieved by using zero-pressure balloons which make twice-daily excursions from 20 km to 35-40 km.

REFERENCES

Angell, J.K., 1972: Air motions in the tropical stratosphere deducted from satellite tracking of horizontally floating balloons. J. Atmos. Sci., 29(3), 570-582.

Charney, J.G. (Ed.), 1966: The Feasibility of a Global Observation and Analysis Experiment. National Academy of Sciences/National Research Council, Washington, DC, 172 pp.

Julian, P. and E. Lichfield, 1978-1979: Systems and techniques for synoptic windfinding. Atmospheric Technology, 10. National Center for Atmospheric Research, Boulder, Colorado, 75 pp.

Lally, V.E., 1960: Satellite satellites--a conjecture on future atmospheric sounding systems. Bull. Amer. Meteor. Soc., 41(8), 429-432.

Passi, R.M. and M.L. Olson, 1974: Carrier balloon windfinding subsystem evaluation. Bull. Amer. Meteor. Soc., 55(12), 1463-1469.

The TWERLE Team, 1977: The TWERLE experiment. Bull. Amer. Meteor. Soc., 58(9), 1936-1948.

BALLOON-BASED INTERFEROMETRIC TECHNIQUES

David Rees

Department of Physics and Astronomy,
University College London, Gower Street, London, WC1E 6BT, UK

1. INTRODUCTION

A balloon-borne triple-etalon Fabry-Perot Interferometer, observing the Doppler shifts of absorption lines caused by molecular oxygen and water vapour in the far red/near infra-red spectrum of back-scattered sunlight, has been used to evaluate a passive space-borne remote-sensing technique for measuring winds in the trophosphere and stratosphere. There have been two successful high-altitude balloon flights of the prototype UCL instrument from the National Scientific Balloon Facility at Palestine, Texas (May 1980, Oct. 1983). The results from these flights have demonstrated that an interferometer with adequate resolution, stability and sensitivity can be built. The wind data are of comparable quality to those obtained from operational techniques (balloon and rocket sonde, cloud-top drift analysis, and from the gradient wind analysis of satellite radiance measurements). However, the interferometric data can provide a regular global grid, over a height range from 5 to 50 km in regions of clear air. Between the middle troposphere (5 km) and the upper stratosphere (40 to 50 km), an optimised instrument can make wind measurements over the daylit hemisphere with an accuracy of about 3-5 m/sec (2 sigma). It is possible to obtain full height profiles between altitudes of 5 and 50 km, with 4 km height resolution, and a spatial resolution of about 200 km, along the orbit track. Below an altitude of about 10 km, Fraunhofer lines of solar origin are possible targets of the Doppler wind analysis. Above an altitude of 50 km, the weakness of the back-scattered solar spectrum (decreasing air density) is coupled with the low absorption crosssection of all atmospheric species in the spectral region up to 800 nm (where imaging photon detectors can be used, causing the along-the-track resolution (or error) to increase beyond values useful for operational purposes. Within the region of optimum performance (5 to 50km), however, the technique is a valuable potential complement to existing wind-measuring systems and can provide a low cost addition to powerful active (LIDAR) wind measuring systems now under development.

2. BACKGROUND

Major advances in the description and understanding of the behaviour of the earth's atmosphere have followed the development and wide exploitation of novel techniques for the measurement of key parameters such as temperature, density, wind velocity and the concentration of minor active species such as water vapour, ozone and nitrogen/chlorine compounds. At present, there are a number of operational spaceborne sensors recording temperature, humidity, and the distribution of important minor atmospheric species on a regular global basis. One outstanding objective is an operational global multi-level wind-measuring system, providing data from the boundary layer to the upper stratosphere, in a grid form suitable for use in operational meteorology. No single affordable instrument, active or passive, may be able to provide the total range of requirements: an altitude resolution of 100 to 200 metres in the boundary layer, and a half scale height (3-4 km) in the middle and upper stratosphere; a two sigma error of 5 m/sec or less. Larger errors would render the wind data irrelevant to the majority of objectives in weather reporting, forecasting, or climatology.

The wind inputs to present operational meteorological systems are from a combination of sources: cloud top drifts (continental-scale satelitte imagery from sun synchronous or geostationary orbit); winds derived from the gradient wind equation applied to satellite infra-red radiance data; rocket/balloon-sonde observations and aircraft inertial navigation data (true air speed/heading minus derived ground track velocity). Future systems will be augmented by powerful and expensive space-borne Doppler Lidar systems. Lidar systems can provide uniquely accurate and high resolution wind measurements, particularly in the boundary layer and the trophosphere. Passive interferometric wind measurements provide a relatively cheap technique for mapping, with 2 to 4 km vertical resolution, wind structures of the middle and upper trophosphere (in clear air regions), and the stratosphere. The combination of Doppler Lidar systems and passive interferometers should be complementary, and their combination should greatly augment the present data.

Doppler spectroscopy/interferometry of upper atmospheric emissions in the visible and near-visible parts of the spectrum has been widely exploited for many years (Armstrong, 1958, 1968; Hernandez, 1976).

Below an altitude of about 80 km, however, atoms and molecules are collisionally deactivated from excited states generating emissions in the visible/near IR spectrum. Since emission spectroscopy/interferometry cannot be used for Doppler wind measurements in the atmosphere below 50 or 60 km, a series of theoretical and empirical studies of the properties of absorption lines, generated by various atmospheric species in the back-scattered solar spectrum, was commenced in the mid 1970's (Hays et al., 1978;

Rees et al., 1978, 1979). In parallel with theoretical studies (Hays, 1982), an instrument capable of observing such absorption lines in the back-scattered solar spectrum, with the necessary combination of sensitivity, spectral resolution and stability was also developed for balloon-borne experiments (Rees et al., 1982).

The back-scattered solar spectrum contains many (Fraunhofer) absorption lines throughout the UV, visible and infra-red parts of the spectrum. These absorption lines are mainly of solar origin, however, many are of Telluric origin, such as the Chappius bands of Ozone. The near IR spectrum contains many strong absorption bands due to molecular oxygen (680 and 760 nm) and water vapour.

Many of the individual absorption lines, as observed from ground level, are optically thick and are pressure broadened in the troposphere. Such lines have limited usefulness for Doppler wind measurements, since the wind error from a Doppler analysis is roughly inversely proportional to the width of the target line (other factors, instrumental and intensity, being constant).

Observed from space, however, many of the absorption lines in the band sequences of molecular oxygen and water vapour are narrow and optically thin when observed at the earth's limb, over a wide range of altitudes. Only in the lower troposphere are such absorption lines severely pressure broadened and usually optically thick. Within the lower troposphere, Fraunhofer lines of solar origin offer altervative spectral targets for Doppler wind measurements. In sunlight reflected from cloud tops, Doppler shifts record the true bulk motion of the winds at cloud top level, even when the development of cloud features (from space imagery) are dominated by orographic or frontal system processes. Back-scattered sunlight from 'clear' air in the troposphere due to Mie and Rayleigh scattering is significantly weaker than that reflected from cloud tops; however, absorption lines in the back-scattered spectrum still carry the Doppler wind information.

Obtaining a good height resolution is the major difficulty with a passive observing technique. Height resolution is limited by the limb-scanning geometry and by the weighting of the atmospheric absorption and scattering. Half the scale height of the absorbing or scattering/reflecting species is a realistic limit. For molecular oxygen, the best height resolution is about 4 km within the troposphere and the stratosphere.

Water vapour is a useful additional spectral target, its scale height being about half that of the atmosphere and 2 km height resolution should be possible with water vapour targets. This does not quite meet the most critical meteorological objectives but such data would be a major improvement over the presently available global wind data.

3. THEORETICAL TREATMENT

Extensive work during the past two decades has provided a theoretical foundation for the generation of absorption lines within the earth's atmosphere, and an understanding of the performance of the instrumentation developed for Doppler wind measurements by using atmospheric absorption lines. The general theory has been described by Hays (1982), Rees et al. (1981) and in references within these papers.

Simulations of the instrumental performance, and of the spectra which a spaceborne instrument would observe, will be used to illustrate the data obtained from two high altitude balloon flights of the UCL triple etalon interferometer.

4. INSTRUMENTATION

The Fabry-Perot interferometer has long been used in applications requiring high spectral resolution. Recently, the powerful technique has been tamed for space applications for thermospheric wind measurements (Hays et al., 1981, Rees et al. 1982, Killeen et al., 1982). The rugged FP interferometer has high resolution and stability, and has an intrinsic high throughput (aperture* solid angle) when used with a multiplexed detector of low noise such as an imaging photon detector. This makes the FPI a first choice for a possible spaceborne interferometer for lower atmospheric wind observations.

Single etalon interferometers have, however, inadequate spectral discrimination for absorption line studies, since many free spectral ranges of the high resolution etalon will be transmitted by the narrowest usable bandwidth interference filters. Multiple etalon instruments (PEPSIOS, Mack et al., 1965) have been used with high intensity absorption line sources (solar spectroscopy). However, the weakness of back-scattered sunlight from the upper troposphere and stratosphere makes the PEPSIOS, which cannot be multiplexed, inherently unsuitable.

The triple etalon interferometer (Figure 1) has been specially adapted for absorption line Doppler interferometry, for use with a two-dimensional imaging photon detector, essential to obtain maximum instrument throughput and sensitivity:

I. The three etalons (High Resolution Etalon, HRE; Medium Resolution Etalon, MRE; Low Resolution Etalon, LRE) have relatively large, noncommensurate ratios between their plate spacings and thus free spectral ranges, not the close vernier ratios used by PEPSIOS. Each etalon, in sequence strongly suppresses the unwanted adjacent free spectral ranges of the next higher resolution etalon and blend to the transmission profile of the narrow band-pass interference filter. The MRE and LRE have to minimise vignetting the transmission of off-axis light to the HRE and detector. All three etalons will be capacitance stabilised (Rees et al., 1980) for fine tuning their transmission, permitting the

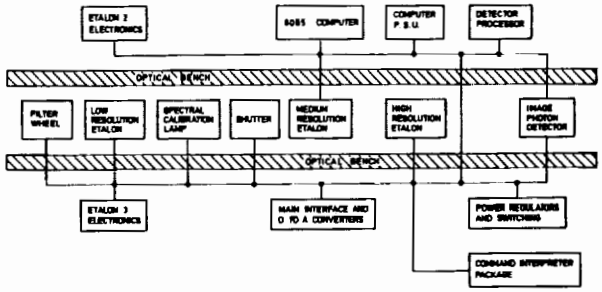

FIGURE 1. Schematic configuration of the optical and electronic systems of the UCL balloon-borne, triple etalon interferometer. A 40 cm diameter telescope feeds light into the filter wheel unit The light is then re-collimated through the three 95 mm clear aperture etalons before the distant field (0.2 degrees FOV and the Fabry-Perot fringes are imaged onto the detector.

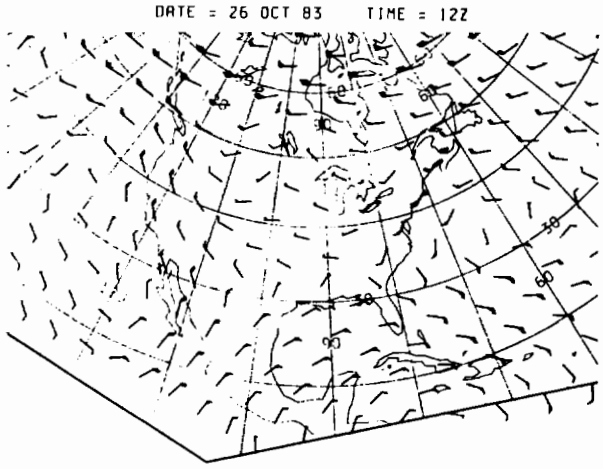

FIGURE 2. Winds derived from satellite radiance measurements over the continental USA 26 October 1983, 12 Z. 20 mB, or about 26 km.

rapid sequential observation of a variety of different absorption lines, and optimising the detector/signal processing.

II. PEPSIOS is able to take advantage of modest angles between the optical axes of each of the three etalons. This greatly reduces the effects of unwanted mutual interference fringe patterns generated between the many internal and external surfaces of the three etalons. However, in the imaging triple etalon interferometer, the three etalons have to be mounted very accurately with a common optical axis.

Many special design features are incorporated into the etalons, their coatings and mountings, to make this rather special arrangment work. A detailed review of the major design features can be found in Rees et al. (1986).* Critical features are summarised in Table 1.

* Unpublished Paper

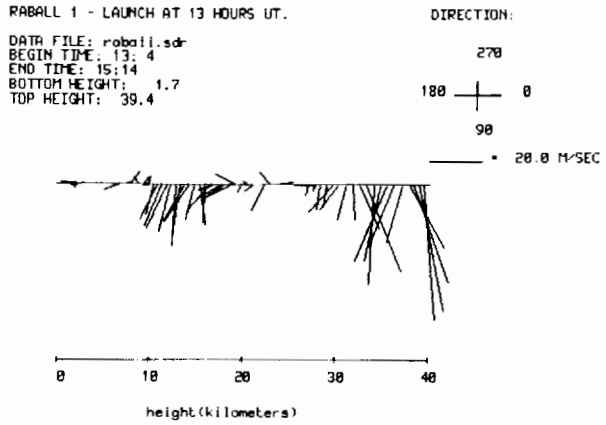

FIGURE 3. Wind profile to 40 km altitude, derived from one of the RABALLS flown from Palestine, Texas, for wind intercomparison with the data from the flight of the Fabry-Perot interferometer.

TABLE 1.

Instrument Float Altitude, km	38.0
Line-of-sight/Tangent angle, deg	-3.6 and -5.0
Angle of view, deg	0.2
Scale height, km	7.0
Wavelength for tuning, nm	688.4
Natural line wavelength, nm	688.4
Absorption cross section, M^2	0.3×10^{-27}
Aperture of optical system, M^2	0.01
E-width of prefilter, nm	0.10
Central wavelength of filter, nm	688.4
Prefilter peak transmission, nm	0.30
HRE plate spacing, mm	10.0
HRE finesse	20.0
MRE plate spacing, mm	1.82
MRE finesse	15.0
LRE plate spacing, mm	0.215
LRE finesse	15.0
Number of detector pixels	64
Detector quantum efficiency	
etalons are auto-tuned	0.030

RESULTS

For -3.6			For -5.0
0.577		Filtrage	0.577
29	km	Median Altitude	24
0.024	HRE	Free Spectral Range	0.024
402.4	km	Distance to tangent point	558.6
25.4	km	Altitude of tangent point	13.6
0.18	sec	Integration time to 100 counts	0.033

5. LOGISTICS OF THE OCTOBER 27, 1983 UCL BALLOON FLIGHT

During late October 1983, the prevailing winds between 35 and 40 km over the southern USA were eastward, 25 to 30 m/sec, with fluctuations of 10 - 15 m/sec. Winds over the continental USA, derived from satellite radiance data for 20 mB level are shown in Figure 2. On 27 October, the drift velocities of two balloons with similar

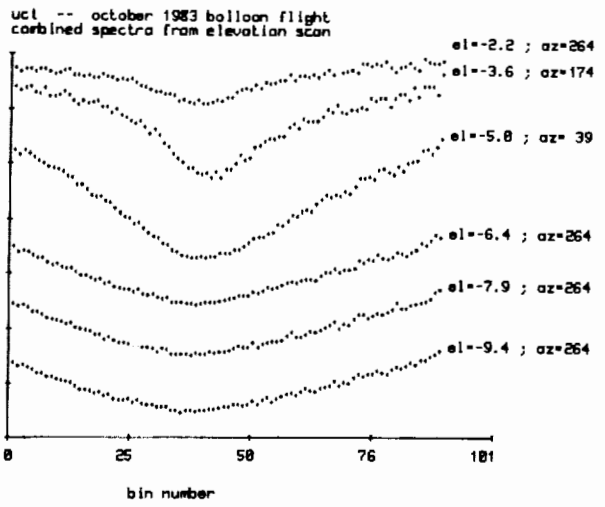

FIGURE 4. Spectra obtained over the elevation range -2.2 degrees to -5.0 degrees. Depth at the centre of the -3.6 and -5.0 degrees spectra is about 40% of the adjacent contiuum. The -6.4 degree spectrum is a view of the geometrical horizon from 38 km, but at that and lower angles, there is little contribution from below about 10 to 12 km altitude.

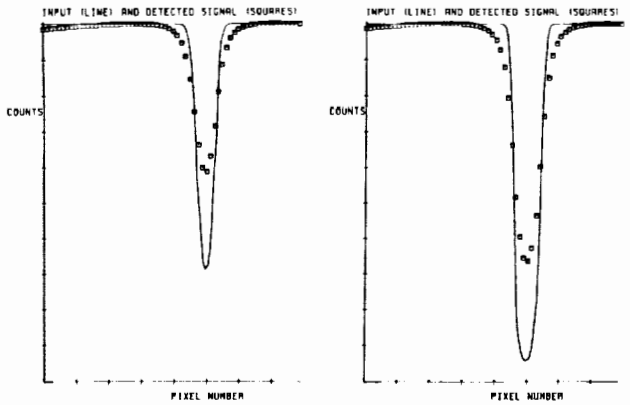

(a) (b)

FIGURE 5. Simulation of the performance of the balloon borne interferometer viewing the 688.4 nm line of molecular oxygen. Limb-viewing angles of -3.6° (a) and -5.0° (b) have been assumed.

ascent and float characteristics (UCL 0600 CST, GSFC 0930 CST (both 38 km)), differed by 15 degrees and 10 m/sec. The wind data from one of four comparative RABALL flights are shown in Figure 3.

A 90 min loss of OMEGA tracking and radar identification of the UCL balloon about 6 hours into the flight, requiring a temporary shut down of the instrument and platform was the only problem during the flight, and 10 hours of useful scientific experiments were carried out (Rees et al., 1986).*

*Unpublished paper

6. WIND MEASUREMENTS FROM THE OCTOBER 1983 FLIGHT

The Doppler data to be discussed here are derived from one of several complete elevation scans, and from two of the many complete azimuthal scan sequences carried out during the flight, observing the 688.4 nm rotational line of molecular oxygen beta band, $b^1\Sigma_g^+ - X^3\Sigma_g^-$.

6.1 Observing Sequence 1

A sequence of scans were obtained (Figure 4) over a range of elevation angles, scanning from 2.2 degrees above the tangent plane to a maximum depression angle of-9.5 degrees. This sequence of spectra are shown in Figure 4. In Figure 5 a comparable set of simulations are shown for the viewing conditions and performance of the balloon instrument.

This band of molecular oxygen only appears in absorption, with no resonance-fluorescence emission. The line becomes broader and deeper with a decreasing altitude at the limb. The centre of the line is optically thick below an altitude of the order of 10 to 12 km. Below 10 km, the effects of Mie scattering are important.

In 'earth-scans', at depression angles of -6.5, -7.9 and -9.5 degrees, for which the interferometer views the earth's surface, the line remains broad. Except for signals reflected from cloud tops, absorption lines of Telluric origin, such as the one observed here, cannot provide accurate wind measurements in the lowest troposphere.

At limb scan altitudes above about 34 km (-2 degrees), the intensity of the back-scattered solar spectrum at 688.4 nm is too low for high quality interferograms to be obtained in a period of ten seconds using the low noise and relatively low red-sensitivity IPD chosen for this flight (operating temperature of 30 C, no cooler).

6.2 Observing Sequence 2

The Doppler analysis of one of several sequences limb-scan observations at a constant depression angle of -5 degrees, corresponding to a limb altitude of about 13 km, is shown in Figure 6. The geometric altitude uncertainty is about 1-2 km, and simulations indicate that the median altitude uncertainty is about 1-2 km, and simulations indicate that the median altitude of the signal in this absorption line is about 24 km.

The wavelength of the absorption line changes with viewing azimuth as the gondola was rotated in azimuth, at pre-set intervals of 45 degrees. The values do not, however, accurately fit a sine wave.

Comparing observations to the east and to the west from the moving balloon platform, a wind value of about 30 m/sec is obtained, with the atmosphere moving toward the balloon in the east and away from the balloon in the west. Comparing

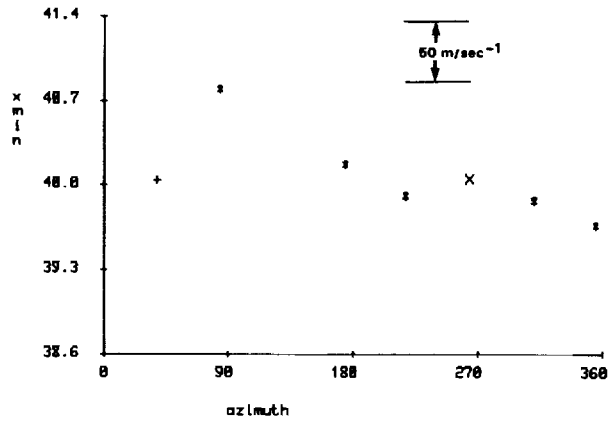

FIGURE 6. Calculated Doppler shifts as a function of azimuth for a limb scan at 5.0 degrees. The altitude at the tangent point is about 13 km, but the median altitude at the bottom of the line is about 24 km (+/- 3 km). The maximum blue Doppler shift is when the balloon is viewing eastward, and this corresponds to a 20 m/sec relative wind. Since the balloon was drifting about 30 m/sec eastward, the actual wind speed was approximately 10 m/sec (eastward). The data do not fit an exact sine curve, indicating wind structures (5 to 10 m/sec) within the 800 km diameter region viewed from 38 km altitude.

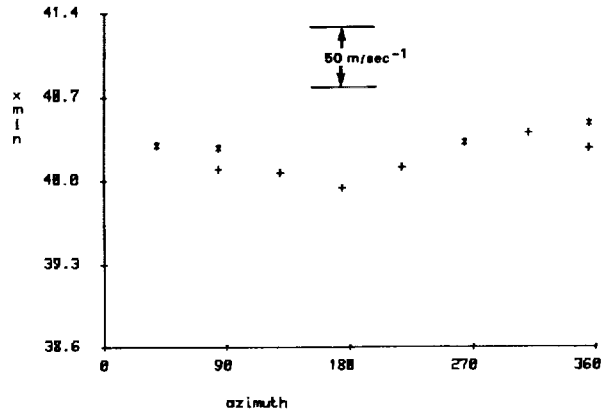

FIGURE 7. Similar data to that in Figure 6, except for an elevation angle of 3.6 degrees. The tangent altitude is about 25 km and the mean altitude at the bottom of the line is about 29 km. This time the Doppler data fit a sine curve as a function of azimuth, and the mean wind, relative to the balloon is from the north, 10 to 15 m/sec amplitude. This particular pattern was reproduced in a number of scan sequences at this elevation angle, and may be a result of the relatively strong wind disturbances south and north of the balloon track, which can be seen in the satellite wind data of Figure 2.

the observations to the north and to the south, the atmosphere in the north appears to be moving away from the balloon, whereas that in the south is moving toward the platform (velocity of about 10 m/sec). These 'relative' winds agree with the available meteorological wind data between 20 and 25 km altitude, and with the known movement of the UCL gondola at 38 km, which is the 'restframe' for the wind velocity measurements.

6.3 Observing Sequence 3

Figure 7 shows the Doppler fits to an azimuthal scan sequence obtained at a depression angle of -3.6 degrees (tangent altitude about 24 km, a mean sampled altitude of about 29 km). The individual measurements fit a sine wave reasonably well. A mean wind direction, relative to the balloon, is from an azimuth of about 350 degrees, with a velocity of about 20 m/sec.

The departure of the individual Doppler measurements at -5 degrees depression angle from a pure sine wave reflects several contributing factors. The statistical error is small, less then 5 m/sec, for both sets of limb-scan data. The statistical Doppler wind error at -5 degrees (similar line shape, higher signal levels). There is a true variation of wind velocity within the region (800 km diameter) observed as the instrument and gondola are rotated (at this depression angle) through 360 degrees in azimuth angle.

Comparable spatial variability is shown in the available satellite radiance derived winds for both 26 and 28 October, which probably underestimate the true spatial variaility of the wind on the scale size of 400 to 800 km. Individual RABALL wind data also show considerable variability on a time scale of several hours.

7. INTERCOMPARISON OF THE INTERFEROMETRIC WIND DATA WITH METEOROLOGICAL RESULTS

At about the depression angle of -5.0 degrees, corresponding to a mean altitude of about 24 km, the Doppler winds are consistent with the difference between the low velocity eastward winds at 24 km, shown by the satellite radiance and RABALL wind data, and the faster eastward winds at the float altitude of 38 km. This wind flow is not purely zonal. Larger scale wind structures, over the region of up to 800 km scanned by the FPI, are illustrated by the departures of the individual FPI measurements from a fit to a pure sine wave as a function of azimuth and by the satellite radiance winds.

The Doppler wind data from the -3.6 degree azimuth scan indicate a faster southward flow, relative to the velocity of the gondola, than that shown in the data from the RABALL's released from Palestine. However, the satellite radiance wind data show considerable structure in the wind flow at the 29 km (about 10 mB), within 400 km of the gondola. Winds in the regions sampled by the interferometer were apparently moving southward and eastward, in a surface frame of reference, each component being about 20 m/sec.

This particular set of data was obtained during the period when OMEGA tracking failed. This caused uncertainty in the drift velocity of the gondola relative to the ground for a short period The gondola drift is, essentially, the base-line for the wind velocity measurements.

There is another inherent difficulty in obtaining an absolute base-line for the balloon Doppler wind data. It was not practical to generate an on-board spectral reference for the absorption lines used, although they can be generated in the laboratory. For a satellite-borne instrument, an absolute velocity reference is generated by sequentially observing regions of the atmosphere from distinct directions. This is not possible with the uncontrolled drift of a short duration balloon flight.

The available wind data from four sources has been compared:

RABALLS and High Altitude Scientific Flights from Palestine (27 October); Rocket sondes from White Sands and from Wallops Island (26, 28 October only); Conventional and routine balloon sondes from the meteorological system; Winds derived from satellite radiances (26, 28 October only).

These data are all in general agreement with the prevailing eastward winds at 38 km, but they also show both spatial and temporal variations (data from specific stations) of the order of 5 to 10 m/sec, at various times and altitudes during the 48 hour period. Detailed comparisons between the satellite radiance data and the discrete local measurements also show variations of 5 to 10 m/sec. This data sample is quite unsuitable for a full statistical analysis of the intercomparison of the distinct techniques. However, the Doppler wind measurements from the UCL FPI are generally consistent with the available comparative data, and such differences which exist lie within the range of temporal and spatial structures observed by the different techniques. The Doppler data also lie within the range of differences between the distinct data sources.

8. SUMMARY AND PROGNOSIS FOR FUTURE OPERATIONAL SCHEMES

The performances of a prototype triple etalon interferometer from a balloon-borne platform has demonstrated that, with further modest instrumental refinements, a space-borne instrument can prov de a global pattern of winds in the upper tropospehre and stratosphere with the typical coverage, height and grid resolution of operational meteorological satellites measuring temperature. The modest payload support requirements of such an instrument, in comparison with future Doppler Lidar systems, make the inclusion of the passive interferometer in a wind measuring system an excellent prospect for providing good coverage in the upper troposphere and throughout the stratosphere. In the middle and upper stratosphere, the data provided by a passive interferometer will be much more cost effective than that from a Doppler Lidar, although there is little doubt that the prospective space-borne Doppler Lidar system are uniquely capable of providing the high resolution wind measurements which are essential in the boundary layer, troposphere and lower stratosphere (up to 20 km).

ACKNOWLEDGEMENTS

The instrument development and balloon flights were partly supported by grants from the UK Science and Engineering Research Council. Additional support for the comparative balloon sonde flights, together with the acquisition of complementary wind data, was obtained from the Gassiot Committee of the UK Meteorological Office and NASA. The staff of NSBF provided invaluable operational support for the preparations prior to the flight and for the flights. The US Air Force contributed to the UK/USA freight transportation.

REFERENCES

Armstrong, E.B., 1958: J.Phys. Radium, 19, 358
Armstrong, E.B., 1968: Planet. Spac. Sci., 16, 211
Hays, P.B., 1982: Applied Optics, 21, 1136
Hays, P.B., Hernandez, G., Rees, D.,Roble, R.G: 1978: Proposal to NASA - High Resolution Doppler Imager, Part I & II
Hays, P.B., Killeen, T.L., Kennedy, B.C., 1981: Space Sci. Instrum., 5, 395
Hernandez, G., 1976: J. Geophys. Res., 81, 5165
Killeen, T.K., Hays, P.B., Kennedy, B., Rees,D. 1982: Applied Optics, 21, 3903
Mack, J.E., McNutt, D.P., Roesler, F.L., Chabbal, R.J. 1965: Applied Optics, 2, 873
Rees, D., 1979: COSPAR, Scientific Ballooning, 207
Rees, D., 1979: Published in proceedings of the ESA Special Symposium at Ajaccio, Corsica
Rees, D., Fuller-Rowell, T.J., Lyons, A., Killeen, T.L., Hays, P.B., 1982: Applied Optics, 21, 3896
Rees, D., McWirther, I., Hays, P.B., Dines, T., 1981: J. Phys. E: Sci. Instrum., 14, 1320
Rees, D., Rounce, P.A., McWirther, I., 1980: Proceedings of EAS Conference SP-152, 89
Rees, D., Rounce, P.A., McWirther, I., Scott, A.F.D., Greenaway, A.H., Towlson, W., 1982: J. Phys. E: Sci. Instrum., 15, 191
Rees, D. et al., 1986: Balloon borne wind observations of the stratosphere using a triple etalon Fabry-Perot interferometer. To be submitted.

AN OPERATIONAL ASDAR SYSTEM

James K. Sparkman, Jr.

National Environmental Satellite,
Data, and Information Service

George J. Smidt

National Weather Service

National Oceanic and Atmospheric Administration
Washington, D.C., 20233, USA

1. INTRODUCTION

The story of the Aircraft to Satellite Data Relay (ASDAR) program began when airline meteorologists realized that Boeing B-747s and other "wide-bodied" commercial jets provided cockpit displays of digital values for outside air temperature and winds. Somewhat later, when a few B-747s were used to carry portable air quality monitoring equipment for the Global Air Sampling Program (GASP), scientists at the National Aeronautics and Space Administration's Lewis Research Center, in Cleveland, Ohio, explored ways in which these digital values could be used to label data collected during the GASP flights. Digital values of GASP analyses were recorded on cassettes, along with digital values of location and altitude, time, winds, and temperature, obtained by micro-processors from within the host aircraft's avionics. Cassettes were removed at intervals and forwarded to Lewis for analysis. These tapes suggested a way in which manually recorded in-flight meteorological reports could be replaced by an automatic system, which could record winds and air temperatures as often as desired.

Although meteorological data, tape recorded in flight, were used to great advantage in several research programs, satellite data relay of in-flight reports, in near real-time, appeared to be the only method in which data collected during long overseas flights could reach meteorological data users in time for full data utilization for operational weather analysis and forecasting.

Data relay from aircraft was a technical possibility only because of the foresight of the planners of the geostationary meteorological satellites eventually launched by the U.S., Europe, and Japan. Working together, satellite system designers sought to minimize radio frequency bandwidth requirements, to permit emergency interchangeability of satellites (which is now taking place), and to permit ships or other moving "sensor platforms" to address all satellites through a common uplink radio frequency (402 MHz). (By contrast, in the world of commercial communications satellites, a given frequency on one spacecraft has a different use aboard an adjacent satellite. This condition requires radio uplinks to use narrow-beam antennas and to point only to a single satellite.)

As a part of the First GARP Global Experiment (FGGE 1978-79), NASA proposed to NOAA a cooperative program in which prototype ASDAR units would be designed and fabricated, and offered for worldwide test deployment by other airlines and meteorological services participating in The Global Weather Experiment (FGGE). Seventeen ASDAR boxes were built under NASA's guidance, were approved for flight aboard U.S.-built commercial B-747 aircraft, and were deployed aboard several airlines during the FGGE. (Carriers included Pan Am, Scandanavian Air Lines, British Airways, KLM, Lufthansa, Qantas, South African Airways, and Singapore Air Lines. A single ASDAR was also carried aboard a USAF C-141 cargo carrier. Several units are still in operation.) ASDAR data were applauded for their quality, timeliness, and as a new source of data from regions heretofore unreported for weather analysis. The nature of the data from any given overseas flight, since it derives from a single suite of sensors during the aircraft's passage through space and time, permitted flight reports to be treated as a line integral. Thus geometric heights of temperatures and winds could be calculated from ASDAR reports spaced 7.5 minutes apart and containing only barometric altitude values. The impact on a regional weather analysis of transit of an ASDAR-carrying aircraft, following days or weeks of data-less analyses by weather computers, was remarkable to see. For the next several days, fine detail would replace large smooth curves.

2. PROTOTYPE ASDAR

NASA's prototype ASDAR demonstrated successfully that automated data relay by meteorological geostationary satellites could be accomplished from an aircraft. This procedure required development of a sufficiently powerful transmitter at 402 MHz, a low-profile, omni-directional

antenna to be placed atop an aircraft, and a micro-processor to select values for altitude, latitude and longitude, wind direction and speed, time and temperature from appropriate sources. These values are assembled into a correctly formatted message for transmission to any meteorological geostationary satellite within radio range. Four metsats now operate around the Earth; thus data relay is permitted from virtually all locations equatorward of 80° latitude.

Special design features included fail-safe isolation between the ASDAR package and its data sources aboard the host aircraft, and a microprocessor design such that any processor malfunction would lead to a full shut down. (No data are a more obvious failure mode than bad data, and a record of no bad data soon allows users to give ASDAR data a high ranking value in their data utilization schemes.) Designers also sought to compress ASDAR messages toward a goal of a 30-second time slot per report (based on eight timed reports) and so to maximize use of satellite relay channels. (No effort was made to achieve additional reports during aircraft altitude changes.)

3. PRODUCTION ASDAR UNIT

A production model ASDAR unit is now nearing completion and certification for flight aboard several aircraft models, including B-747s, DC-10s, L-1011s, and more recent aircraft models including B-757s and B-767s and A-300s. Design goals stressed are for collection of more data, and more accurate data, than was achieved by the prototype ASDAR. The unit is being built by GEC-McMichael Ltd., Slough, England, under a contract with the World Meteorological Organization supported by a consortium of nations. Participants include Saudi Arabia, United Kingdom, Australia, West Germany, Sweden, Spain, Netherlands, U.S.A., Canada, and New Zealand.

3.1 Data Volume

Wide body jets, industry wide, average 13 hours flight per day, for a 12,000 km flight path. Eight ASDAR reports per hour yields 104 reports per day per aircraft, timed reports being assumed, with reports spaced about 110 km apart. Reports in batches are radioed once per hour, for relay through a satellite transponder.

The new ASDAR unit has built-in flexibility, to permit the box to match differing aircraft models, and differing components found within each aircraft type.

In addition to timed reports made during level flight, reports will be made during ascents and descents, spaced at 10 mb (i.e., 10 hPa) pressure-height intervals at altitudes below approximately 850 mb, and at 50 mb intervals above 850 mb. Surface pressure based on altimeter readings at ground level is reported.

Still additional measurements may be reported, if wind values are encountered which are (a) stronger than 60 knots and (b) are greater than 10 knots more than the last value read, or the last timed value.

3.2 Data Accuracy

If the prototype ASDAR produced data of excellent quality, the reader may ask, why seek to improve it? The answer is simple. For lack of resources (e.g., dollars), the prototype ASDAR did not seek to accommodate itself either to several different aircraft types, or still less, to various configurations of navigation systems and avionics installations. The authors were intimately involved in selecting host aircraft for the 17 prototype ASDAR units. Telephoned conversation with airlines would establish first whether their navigation and avionics arrays were compatiable with the already-fixed ASDAR prototype design, based on equipment used then by Pan American Airways' 747s. If the first answer was negative, a question of an airline's willingness to participate in the program was left unasked. Pan Am's equipment (as well as that of several other major airlines) included units which produced quality calculations of air temperatures and winds.

But even Pan Am's winds and temperatures could have been improved, and the new ASDAR design seeks to achieve this. The weak link is temperature. Although B-747s almost universally carry a high quality platinum resistance wire temperature probe suitably mounted to protect it from dust, hail, or rain, its values are always increased by "Mach effects," that is, the adiabatic warming of air impinging on the sensor. At the time of the FGGE, corrections for Mach effects were made in each aircraft by mechanical computers. These units are analog slide rules with nonlinear transfer functions, based on the reported "Total Air Temperature," indicated altitude (pressure), and indicated air speed. Although approximately correct, these units are not optimum.

True air speed, in turn, is determined using "static air temperature," (i.e., outside air temperature free of Mach effects.) Hence, to the degree that static air temperature is poorly calculated, an error is fed into true air speed calculations. True air speed and aircraft heading are known vectors, along with ground speed and direction (the "course made good" of mariners), which permits calculation of the third side of the vector triangle, the wind speed and direction. Static air temperature is now computed in newer aircraft by microprocessors, but generally to accuracy specifications that are little better than those achieveable by the older servo-computers; many mechanical systems (each costing about $30,000) will remain in use for years to come.

In the new ASDAR unit, aircraft roll angle will also be read and used as a quality control check for wind values. Provisions are made for insertion into ASDAR reports of "turbulence" information, relative humidity or dew point. "Turbulence" is deduced from any unexpected accelerometer data values. Moisture values must await the development of a suitable sensor. Suitable, in this case, means a sensor that can operate unattended without deterioration, for at least the months that separate major aircraft overhauls.

Details of the new ASDAR's algorithms for computation of air temperature and winds are considered to be proprietary by the ASDAR manufacturer. However, much of this information is available through the manufacturers of temperature probes for aircraft, and of air data computers. In comparing the prototype and new ASDAR's, a key fact to note is that ASDAR had access only to temperature values no more precise than 1°C, since cockpit displays, following tradition, report only whole degrees. New ASDARs calculate and report air temperature to 0.1°C, with accuracies on the order of 1°C. Wind accuracies vary with the type and manufacture of the navigation system. Quality wind navigation systems can be expected to calculate winds, and compensate flight headings for these winds, so as to guide aircraft across the Atlantic with errors of 50 nautical miles or less. New inertial systems, using lasers for internal measurements of components, should surpass this accuracy. Current "high accuracy" systems are reported to have wind errors of 1.5 ft/sec, based on a sample rate of 40 samples/sec.

4. DATA TRANSMISSION

ASDAR transmissions from aircraft in flight often are received by more than one meteorological geostationary satellite, since the service fields of view of the four data relay spacecraft overlap. Participating are the U.S. GOES-East nominally at 75° West longitude, GOES-West at 135° West, Japan's GMS at 140° East, and Europe's Meteosat at 0° East/West. With "footprints" reaching 80° out from a satellite sub-point, large FOV overlaps occur except in the Indian Ocean. Coverage agreements among satellite operators eliminate duplication of ASDAR reports forwarded over the WMO's Global Telecommunications System trunk lines between continents.

ASDAR transmissions will include both an aircraft identifier and an ASDAR unit I.D. This will allow data users to amass statistics regarding the accuracy of wind and temperature measurements from each aircraft. Box I.D.'s will help ASDAR system monitors appraise the status of each unit deployed: whether its transmissions are on time, broadcast at correct radio frequency, and at suitable power levels. The latter parameters are complicated by the Doppler effects occurring between aircraft and spacecraft, maximum as an aircraft approaches or leaves a satellite at the horizon of its radio range, zero when a flight track overflies a satellite's sub-point.

Two-minute transmission windows per aircraft will permit some tolerance for time gained or lost by ASDAR's internal clock, as well as provide time for messages derived from ascents, descents, or strong wind shear. In instances where not all reports can be transmitted during the first assigned transmission time, they may be held for transmission an hour later, if not crowded out of the buffer memory by new reports.

The output of satellite data relay transponders (at 1694 MHz) is nominally received by satellite data processing centers in the U.S., Japan, and Germany, for processing and retransmission to users. However, reports are broadcast in clear and can be received by anyone who wishes to assemble a receiving station and data processors. (In the U.S., the same data downlink includes reports from thousands of river, tide, and rainfall gauges, snowfall, earthquake sensor outputs, etc. ASDAR users must have micro-processors to select out desired values from the larger data stream.)

5. PROGRAM STATUS

Engineers at GEC-McMichael Ltd. expect the new ASDAR unit to reach completion and certification in time for test deployment early in 1986. Certification involves approval by aviation officials that the unit may be carried aboard commercial (i.e., passenger carrying) jets, and by satellite personnel that the box may use assigned time-and-frequency slots within the satellites Data Relay Transponder. Each group focusses on such questions as frequency, stability, and freedom from unwanted radio frequency transmissions. Aviation personnel look as well to determine that any ASDAR failure mode cannot endanger other avionics within the host aircraft, or that an ASDAR failure cannot release toxic fumes, etc. Since these requirements are available to the designer before an ASDAR unit is begun, certification is largely a matter of demonstrating a clean radio signal, and a review of design features. For a first unit, the ASDAR unit will be turned on and off, while air crews test all their communications and a navigation gear to observe any cross effects between units. Several hours flight are involved, usually at a time when the aircraft in is under test for other problems.

Cost of the new ASDAR unit, including an installation kit (a nontrivial array of cables, mounting brackets -- which may cost $1000 each -- and coaxial cable) is now estimated at about $50,000 each. Four years' maintenance may well exceed this figure.

6. ASDAR POTENTIAL

6.1 ASDAR Fleet Selection

The deployment of only 17 prototype units led to some unexpected results. Despite a goal of placing boxes on airlines with routes optimum for collection of "met" data from remote regions, ASDAR data distribution analysis shows that the route between London, the Persian Gulf, Singapore and Melbourne was oversampled. Africa was far undersampled, since only KLM occasionally flew down the eastern third of the continent to Johannesburg. (SAA's flights skirt the continent over water, en route to London or New York.) Qantas' and British Airways' routes from Australia to California were the only frequent Pacific Ocean coverage. Rio de Janeiro to Johannesburg to Australia was the only South Atlantic and Indian Ocean crossing predictable.

From this analysis, it may be speculated that a fleet of 200 ASDAR units, as currently envisioned, will likely lead to still greater data redundancies over heavily traveled routes. Fortunately, the new ASDAR's features should allow greater diversity, if diversity of routes can be established as a priority goal. The new ASDAR will be compatible with the avionics of B-757 and 767 aircraft, in addition to the larger 747s and DC-10s. This compatibility should permit ASDAR coverage along routes which today do not support a jumbo jet. Routes from South America westward, and flights among Pacific Islands come to mind, routes now flown by 707s and even smaller aircraft. (Even 707s will, in many instances, be retrofitted with newer generation avionics in the years ahead, which will add them to the potential ASDAR fleet.)

Since the prototype ASDAR was, in some instances, deployed through the transfer of funds between WMO members, (called then the Voluntary Assistance Program), the means are established for optimizing an operational ASDAR fleet.

6.2 Technical Outlook

Despite the growing success of "satellite cloud motion winds," and its progenies, "satellite-observed moisture advection of moisture winds" and "ozone winds," meteorologists expect that in situ measurements from ASDAR will continue to be desirable through the present century. After that, an "active" (i.e., radar-like) wind-satellite may reduce the need for in situ measurements at flight levels. However, this condition is not yet certain.

In the near period, it appears probable that technological changes will enhance ASDAR's ability to measure winds. Inertial Navigation Systems appear to be growing less costly and more sensitive. And, despite the onset of new satellite global navigation systems reporting location to 10's of meters, it appears probable that the needs of automatic piloting will dictate that a mini-inertial navigation system will be retained, to re-position aircraft headings in regimes of changing wind velocities. Although this mini-nav system perhaps need not calculate winds numerically, it would have to "evaluate the wind vector" as part of its appraisal of required new headings. Data read-out would cost little. Should economic distress force the use of aircraft without automatic pilot assistance, modern nav aids, including OMEGA radio navigation and nascent satellite navigation systems, would permit such a mode. Winds would no longer be machine calculated. However, this condition eventually appears unlikely. Given the cost of airframes and fuel, a "saving" incurred by increasing air crew labors while opening a possibility of less efficient flight seems a choice few managers would select.

The economic payoff for ASDAR is the more efficient flight of aircraft through a time and space domain with both present and future uncertainty of wind fields. The promise of ASDAR remains: A more precise monitoring of the meandering river of air called the Jet Stream should permit a more precise forecast of its future position -- later today, and all day tomorrow -- with an economic saving of fuel for all aircraft. At present, over oceanic regions, the present position of the jet and its eddies are not sufficiently known for optimum flight planning (especially in areas in which assigned "tracks" do not lock an aircraft into an unchangeable route). Resulting from a poor knowledge of today's flow -- and a poor history of meanders -- we are still unable to avoid occasional embarrassing forecasts for tomorrow's jet, especially during the changes of seasons. A history of jet stream movement, over years and decades, is also the key to analysis as to whether climate, on a global basis, is changing. The jet stream brings weather to the mid latitudes; the habits of the jet stream deliver climate.

The strategies for the new ASDAR deployment will thus determine what gains accrue to airlines, to meteorology, and to all of mankind from the potential to make high quality meteorological measurements over wide areas of the Earth, and deliver these data promptly to users worldwide.

S19-47
84479

A FGGE WATER VAPOR WIND DATA SET

N93-70318

Tod R. Stewart

Cooperative Institute for Meteorological Satellite Studies
Madison, Wisconsin, USA

Christopher M. Hayden

NOAA/NESDIS Applications Laboratory
Madison, Wisconsin, USA

1. INTRODUCTION

It has been recognized for some time that water vapor structure visible in infrared imagery offers a potential for obtaining motion vectors when several images are considered in sequence (Fischer et al., 1981). A study evaluating water vapor winds obtained from the VISSR atmospheric sounder (Stewart et al., 1985) has confirmed the viability of the approach. More recently, 20 data sets have been produced from METEOSAT water vapor imagery for the FGGE period of 10-25 November 1979. Where possible, two data sets were prepared for each day at 0000 and 1200 GMT and compared with rawinsondes over Europe, Africa, and aircraft observations over the oceans. Procedures for obtaining winds were, in general, similar to the earlier study. Motions were detected both by a single pixel tracking and a cross correlation method by using three images individually separated by one hour. A height assignment was determined by matching the measured brightness temperature to the temperature structure represented by the FGGE-IIIB analyses. Results of this study show that the METEOSAT water vapor winds provide uniform horizontal coverage of mid-level flow over the globe with good accuracy.

2. MEASUREMENT TECHNIQUE

The tracking of water vapor structure to obtain wind vectors is an extension of the technology developed to obtain winds from cloud motions on geostationary satellite images. Three images separated in time are loaded in the McIDAS computer with geometric fidelity ensured by navigation algorithms implicit in the system (Suomi et al., 1983). The three images used for tracking yield two estimates of the wind which are objectively compared and rejected if they differ by greater than 5 mps. Changes in the cloud (water vapor) field are followed in time, either by a direct, operator controlled tracking or by a cross correlation method which matches small patterns in the successive images. In this study, approximately 60% of the winds were determined by single pixel tracking and 40% used the cross correlation. This result contrasts with the earlier study using GOES VAS data where the cross correlation technique could not be used. The difference appears to be in the resolution of the data which in the case of METEOSAT is 5 km as compared with the 16 km available from GOES.

To be a valid tracer of the wind, a feature must be a quasi-passive, shallow body drifting with the wind throughout the series of images being used. Clouds have been shown to be suitable tracers even though there is some shape evolution during the tracking period. Water vapor inhomogeneities also prove to be valid tracers. The "trackability" depends on the operator's distinguishing features which are small enough to represent a uniform flow of air and yet large enough to have a lifetime sufficient for identification over the interval of several images. The lifetime depends on their dissipation by atmospheric turbulence and is therefore a function of the size of the tracer and the eddy diffusivity of the atmosphere. Bauer (1974) in a review of experimental data on the horizontal spreading of inert tracers shows that a tracer with 100 km width will have, on the average, a lifetime of one day. However, depending on the eddy diffusivity, this feature can have a lifetime from three hours to more than three days. By contrast, a 10 km feature will have an average lifetime of only one hour. This latter fact explains, perhaps, the success of the correlation method with the METEOSAT data and the failure with GOES.

An example of the imagery used to generate water vapor winds in this study is given in Fig. 1(a). This picture is taken from the McIDAS television screen with the 6.7 micrometer image enhanced to delineate the moisture features. Bright white represents cloud. Gray features are areas of high water vapor concentration which give way to the dark or dry areas associated with mid-level subsidence. Winds derived from this (and two subsequent images) are shown in Fig. 1(b). Note that uniform coverage is obtained even in the areas which appear dark and featureless in the image. It should be mentioned that the dense coverage featured in Fig. 1(b) was produced for only the earliest third of the data sets. Economic factors dictated a reduced coverage for the

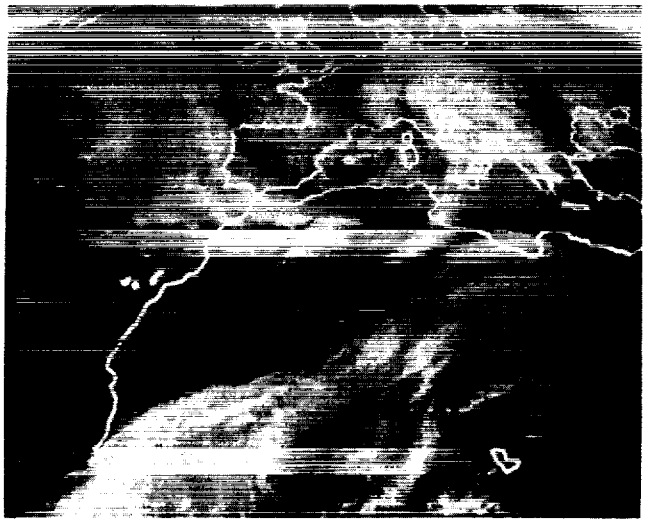

(a). METEOSAT 6.7 micrometer imagery for 1130 15 November 1979.

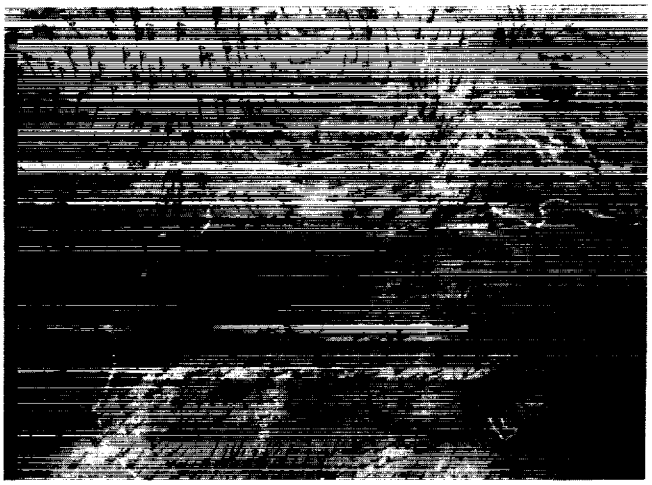

(b). Water vapor winds tracked from METEOSAT 6.7 micrometer measurements at 1130, 1230, and 1330 GMT 15 November 1979.

Figure 1. Examples of Imagery

later sets and winds were produced on a regular grid of 2.5 degrees for both latitude and longitude. An example of such a data set is shown in Fig. 2. The reduced coverage is actually more commensurate with FGGE objectives and follows the recommendation of modelers who will be using the data.

3. HEIGHT ASSIGNMENT

The only quantity available for distinguishing the altitude of the tracers is the brightness temperature of the scene. Fortunately, this has proven to be quite effective, and there are supporting physical arguments. The radiance sensed by the 6.7 micrometer water vapor channel corresponds to a layer-averaged Planck radiance emerging from a portion of the atmosphere whose location is determined by two factors: (1) the profile of

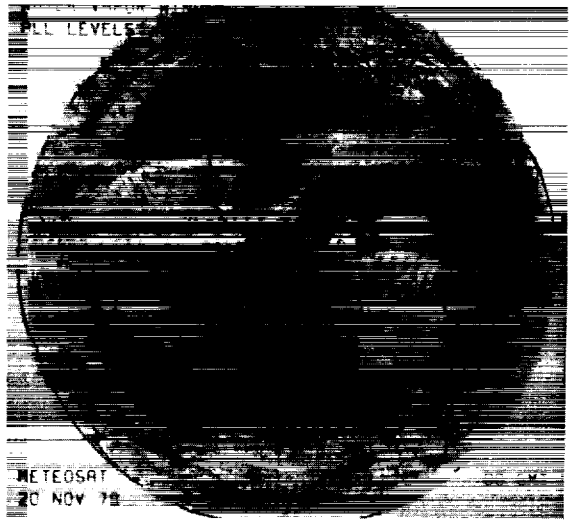

Figure 2. Water vapor winds tracked from METEOSAT 6.7 micrometer measurements at regular grid spacing of 2.5 degrees in latitude and longitude.

the emissivity of the radiating water vapor, and (2) the profile of the transmissivity of the entire depth of water vapor above each radiating level. The emissivity profile varies with the profile of water vapor mixing ratio whereas the transmissivity profile varies with the profile of integrated precipitable water vapor. The 6.7 micrometer channel saturates rather quickly, which is to say that a relatively modest amount of water vapor will mask all radiation emanating from below. Thus, radiation measured from space is primarily representative of the uppermost moist region (high emissivity) with dry air (high transmissivity) above. Variation in this relationship will occur as the profile of the mixing ratio through the radiating layer becomes less uniform. The relationship will break down completely when there is insufficient moisture to radiatively saturate the measurement or when the lapse rate becomes isothermal.

The magnitude of the radiance observed is proportional, through Planck's law, to the mean temperature of the atmosphere as weighted by the product of the emissivity and transmissivity profiles (the temperature profile weighting function). The 6.7-micrometer weighting function is gaussian with a half-width of about 300 mb and a peak ranging in pressure altitude between 200 and 500 mb levels, depending on the water vapor profile characteristics. Water vapor tracers will be sensed in this pressure range.

It was shown in the GOES VAS study that an excellent empirical relationship exists between brightness temperature (x) and the radiosonde measured temperature (y) at the level where water vapor tracers and rawinsonde best fit. A similar study has been conducted with the METEOSAT data, the result of which is shown in Fig. 3. The regression relationship for METEOSAT

$$y = 0.714x + 65.6 \quad (1)$$

can be compared with the previous VAS result of

$$y = 0.734x + 61.0 \quad (2)$$

The close agreement is rather remarkable in view of the different instruments, locations, and seasons involved.

It was stated in the earlier study that uncertainties associated with the matching of radiosonde and brightness temperature did not justify applying the regression relationship and a direct 1:1 correspondence was used to supply pressure heights. Two things have caused us to revise this opinion. First, in extensive application of the water vapor wind measurement at CIMSS during the 1984/85 winter, we noted that upper level winds were consistently too fast; this condition implied that the assigned heights were too high. Application of equation (2) in place of the direct relationship alleviated the error. Second, the confirmation afforded by equation (1) is convincing.

The slope of the regression relationship conveys that the brightness temperature is warmer than the ambient temperature at lower levels and colder at higher levels in the atmosphere. It is not immediately obvious why this, and not the exact opposite, should be so. One might reasonably argue that the air at low temperature cannot hold much moisture; therefore, radiative saturation might be difficult to achieve, warmer radiation from below would transmit to the sensor, and the brightness temperature of the cold tracer would be relatively warmer than the radiosonde at high levels. Furthermore, for warm tracers, more moisture could be expected to exist in the atmosphere above to attenuate transmission, so the brightness temperature of the warm tracer would be relatively colder than the radiosonde at low levels. This is not so. The physical reason for the result of equations (1) and (2) is not simple. A likely explanation is nonuniformity in the profile of mixing ratio through the sensed layer. In general, the mixing ratio becomes increasingly less uniform through a layer as pressure and temperature increase. The relative effect on the brightness temperature is to increase values at the warmer end and thus reduce the slope of the temperature/brightness temperature relationship as observed in Fig. 3.

The temperature provided by equations (1) or (2) is converted to a pressure altitude by finding its equivalent in a profile from a separate source. The latter is obviously a contributing factor in the accuracy of the data, and one generally seeks the best information available. As mentioned earlier, for this study the FGGE-IIIB analyses, interpolated to the location of the tracer, were used.

4. RESULTS

Typically, 3500 water vapor winds were generated for each case over the geographical area shown in Fig. 1(a). From the total data set, approximately 2800 winds were matched and compared with radiosondes and aircraft measurements. Any water vapor wind within a two degree

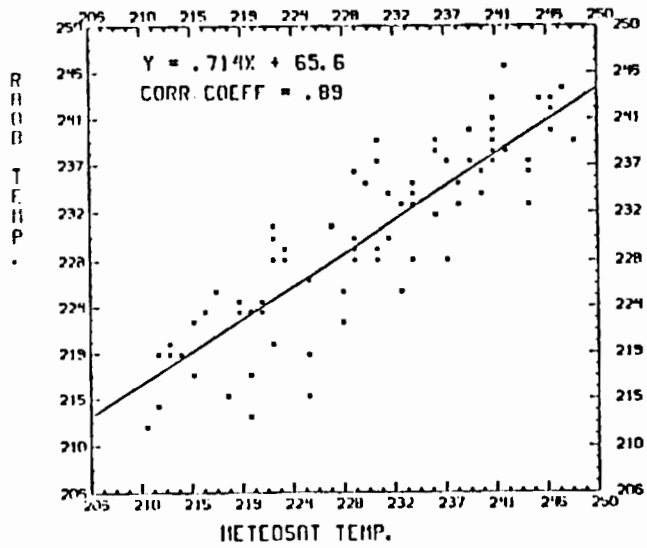

Figure 3: Scatter diagram of radiosonde temperatures plotted against METEOSAT 6.7 micrometer brightness temperature measurements for matched samples of water vapor tracked and rawinsonde measured winds.

(latitude) radius of a rawinsonde or aircraft measurement is a candidate for verification. It is compared with the rawin/aircraft measurement at the assigned level of the water vapor wind. Thus, vapor winds from 226-274 mb are compared with the 250 mb rawinsonde, 275-350 mb are compared with the 300 mb, etc.

Tables 1 and 2 present statistics for water vapor winds obtained from GOES VAS and those obtained from METEOSAT. Comparisons are given for both speed and vector differences. The RMS difference for speed is 4.4 mps for GOES and 7.0 mps for METEOSAT; the vector difference is 7.9 for GOES and 8.8 for METEOSAT. The observation that METEOSAT winds are somewhat less accurate than those from GOES is possibly due to

Table 1. Water-vapor winds (WV) compared with rawinsondes (R); speed RMS differences.

GOES water vapor winds compared with nearest mandatory level

Day	Number of Comparisons	WV-R RMS(m/s)	WV-R corr coeff	Signs WV	Signs R
83228 (12 Z)	282	3.69	0.871	7.40	6.68
84192 (12 Z)	153	4.60	0.935	12.37	11.46
84193 (12 Z)	148	4.23	0.838	7.62	6.47
84194 (12 Z)	159	4.64	0.808	7.60	6.74
84198 (12 Z)	169	5.32	0.884	11.15	9.18
84199 (12 Z)	226	6.61	0.815	9.21	10.91
84201 (12 Z)	164	4.15	0.901	9.44	8.08
84202 (00 Z)	170	3.25	0.882	6.62	6.66
84202 (12 Z)	179	3.13	0.889	6.72	6.52
84208 (00 Z)	181	4.58	0.896	10.30	9.47
84208 (12 Z)	275	4.67	0.855	8.97	7.88
Total number of comparisons		2106			
Avg. Speed Diff. RMS (m/s)		4.44			

METEOSAT water vapor winds compared with nearest mandatory level

Day	Number of Comparisons	WV-R RMS(m/s)	WV-R corr coeff	Signs WV	Signs R
79316 (00 Z)	348	7.21	0.737	9.63	7.60
79316 (12 Z)	269	7.52	0.744	9.11	7.77
79317 (00 Z)	292	6.28	0.794	9.37	7.81
79317 (12 Z)	198	6.85	0.778	9.26	6.87
79319 (00 Z)	322	6.36	0.833	11.19	10.44
79319 (12 Z)	234	7.26	0.916	16.51	13.59
79321 (00 Z)	216	7.11	0.899	16.77	16.34
79321 (12 Z)	195	7.38	0.909	17.35	15.20
79324 (00 Z)	427	7.20	0.765	9.85	8.57
79325 (00 Z)	435	6.44	0.714	8.85	7.95
79328 (00 Z)	567	7.38	0.641	8.07	6.45
Total number of comparisons		3503			
Avg. Speed Diff. RMS (m/s)		7.00			

Table 2. Water-vapor winds (WV) compared with rawinsondes (R); vector differences.

GOES water vapor winds compared with nearest mandatory level

Day	Number of Comparisons	WV-R RMS(m/s)	WV-R corr coeff	Sigma WV	Sigma R
83228 (12 Z)	269	6.84	0.858	12.45	12.65
84192 (12 Z)	147	7.79	0.926	17.40	18.23
84193 (12 Z)	144	7.22	0.866	13.81	13.89
84194 (12 Z)	155	6.45	0.873	12.63	11.94
84198 (12 Z)	165	9.10	0.860	16.87	16.31
84199 (12 Z)	225	9.22	0.862	15.20	16.90
84201 (12 Z)	152	9.01	0.831	15.74	15.17
84202 (00 Z)	159	5.59	0.874	10.53	10.97
84202 (12 Z)	174	6.27	0.869	11.65	12.02
84208 (00 Z)	177	7.26	0.910	16.15	15.97
84208 (12 Z)	256	6.94	0.872	13.52	13.36
Total number of comparisons		2023			
Avg. Vector Diff. (m/s)		7.88			

METEOSAT water vapor winds compared with nearest mandatory level

Day	Number of Comparisons	WV-R RMS(m/s)	WV-R corr coeff	Sigma WV	Sigma R
79316 (00 Z)	295	8.91	0.813	14.97	12.08
79316 (12 Z)	208	9.74	0.861	17.31	14.69
79317 (00 Z)	246	8.11	0.830	14.34	11.61
79317 (12 Z)	166	8.25	0.851	15.07	11.88
79319 (00 Z)	277	8.24	0.874	16.76	15.69
79319 (12 Z)	191	9.12	0.939	25.15	23.04
79321 (00 Z)	118	8.88	0.911	21.44	20.76
79321 (12 Z)	113	9.20	0.922	22.77	21.63
79324 (00 Z)	341	8.60	0.884	18.01	15.62
79325 (00 Z)	380	8.85	0.843	15.93	15.05
79328 (00 Z)	429	8.80	0.859	12.87	11.35
Total number of comparisons		2764			
Avg. Vector Diff. RMS (m/s)		8.79			

navigation differences. METEOSAT navigation involves remapping of the earth into a polynomial fit navigation which assumes that the earth is a perfect sphere. This assumption makes the navigation for METEOSAT inherently less accurate than the navigation used with GOES which is based on a simple two-body model. Another possible source of the decreased accuracy is the inclusion of automatic (cross correlation method) winds in the METEOSAT data.

Table 3. Comparison of water-vapor winds with cloud drift winds.

Data Set		Avg. Vector Mag. Diff. RMS(m/s) Altitude Low	Mid	High	No. Comparisons Altitude Low	Mid	High
15 January 1983 - 13 February 1983							
GMS	(Japan)	4.3	-	15.2	263	-	332
GOES	(NESDIS)	5.3	-	16.0	604	-	92
METEOSAT	(ESA)	9.6	11.1	12.4	516	389	411
July 1983							
GMS	(Japan)	3.8	-	11.3	196	-	860
GOES	(NESDIS)	5.5	-	9.2	571	-	166
METEOSAT	(ESA)	7.1	10.8	10.3	184	180	631
21 January 1984 - 13 February 1984							
GMS	(Japan)	4.9	-	10.7	339	-	171
GOES	(NESDIS)	4.9	-	11.5	428	-	90
METEOSAT	(ESA)	6.2	10.3	10.6	370	328	534
July 1984							
GMS	(Japan)	-	-	-	-	-	-
GOES	(NESDIS)	5.5	-	9.2	554	-	169
METEOSAT	(ESA)	5.9	-	10.3	292	328	534
Water Vapor (GOES)		-	-	7.9	-	-	2023
Water Vapor (METEOSAT)		-	-	8.8	-	-	2764

In terms of absolute accuracy, the water vapor winds appear to be equivalent to cloud drift winds which have received wide acceptance in operational application. Table 3 gives some of the recent verification statistics gathered for cloud drift winds over the last two years (Whitney, 1983). In general, the vector difference for the cloud drift winds is given as 10 mps or greater whereas that for the water vapor winds studied here is approximately 9 mps.

5. CONCLUDING REMARKS

The main purpose of this note is to publish the availability of a FGGE water vapor wind data set. In addition, however, several important features of water vapor wind derivation have been brought to light. First, the winds derived from METEOSAT as well as those from GOES appear to have an accuracy at least equivalent to that of cloud drift winds. Second, the relationship between brightness temperature and the temperature of the level of best fit for the winds appears to be stable and can be expressed by a simple linear regression. Third, the 5 km resolution of METEOSAT imagery offers promise for automatic processing of the data as opposed to operator tracking.

REFERENCES

Bauer, E., 1974: Dispersion of tracers in the atmosphere and ocean: Survey and comparison of experimental data. J. Geo. Res., Vol. 79, No. 6, 789-795.

Fischer, H., N. Eigenwillig, and H. Maller, 1981: Information content of METEOSAT and NIMBUS/THIR water vapor channel data; altitude association of observed phenomena. J. Appl. Meteor., 20, 1334-1352.

Stewart, T. R., C. M. Hayden, and W. L. Smith, 1985: A note on water vapor wind tracking using VAS data on McIDAS. Bull. Amer. Meteor. Soc., Vol. 66, No. 9, 1111-1115.

Suomi, V. E., R. Fox, S. S. Limaye, and W. L. Smith, 1983: McIDAS III: A modern interactive data access and analysis system. J. Climate Appl. Meteor., 22, 765-778.

Whitney, L. F., 1983: International comparison of satellite winds--an update. Advances in Space Research, 2, 73-77.

CLOUD MOTION DERIVED WINDS: THEIR ACCURACY, COVERAGE AND SUGGESTIONS FOR FUTURE IMPROVEMENT

William E. Shenk

Goddard Space Flight Center
Greenbelt, Maryland, USA

1. INTRODUCTION

Nature has provided us with a natural and easily visible method of tracing atmospheric motion through the measurement of cloud velocities. This source of wind information has been available from geosynchronous satellites since the launch of the ATS-1 Spin Scan camera in 1966. This sensor provided adequate spatial and temporal resolution views of individual cloud systems that could represent the wind with useful accuracy. Subsequent satellites (e.g. the GOES series) have had higher spatial and temporal resolution and improved other characteristics (e.g. spacecraft stability) that have yielded better results. With the later satellites, even smaller clouds (more representative tracers of atmospheric motion, Fujita et al, 1975) and more clouds (better coverage) could be followed. During the last decade, cloud motion derived winds have become part of the operational system as they are routinely provided to the National Meteorological Center (NMC) as input to the global numerical models.

The last 10 years have also seen the development of much improved ground-based wind measuring systems (e.g. Little, 1982) and plans outlined for new space wind measurement approaches (e.g. Doppler lidar). Therefore, the future wind measurement system that will serve all scales of meteorology will come from several sources, each of which has strengths and limitations. The cloud motion winds should be able to complement the other sources and be one of the primary data sources for mesoscale systems where (1) high spatial and temporal resolution are needed, (2) in cloudy areas where other techniques have more difficulties, and (3) over water where ground based systems are difficult and/or expensive to install and maintain.

The principal limitations of cloud motion winds (CMW's) are that they (1) can be measured within the limits that cloud motions can represent the wind only where trackable clouds exist, (2) require knowledge of the cloud height, (3) require high spatial and temporal resolution geosynchronous satellite systems with high attitude determination accuracy, and (4) need sophisticated interactive computer systems for the calculation of high resolution fields. This paper will examine these limitations and make suggestions for how this valuable product could be improved. Also, major uses of the data for mesoscale purposes will be discussed.

2. HOW ACCURATE ARE CLOUD MOTION WINDS?

This question was asked from the time the first ATS-1 image sequences were seen. Most of the verification has been done by comparing radiosonde releases within a few hours and hundreds of km of the cloud motions (e.g. Hubert and Whitney, 1971). In general, these results indicated that low level cumulus CMW's were within 3-4 m/sec of the 850-mb winds and that the differences between cirrus CMW's and upper troposphere winds were around 8-10 m/sec. There were two major sources of error in this approach which are the cloud height uncertainty and the difference in time and space between the CMW's and the radiosondes. Since the true accuracy of the CMW's would affect (1) the quality of the derived fields that start with the wind data (e.g. vorticity, convergence), (2) how these data could be used in numerical models, and (3) the impact of satellite design parameters, Hasler et al. (1979) conducted an aircraft verification program to virtually eliminate these two major error sources and re-evaluate cloud motion-wind relationships.

The aircraft experiment examined extensively the cloud motion-wind relationship for cumuliform clouds over the tropical and subtropical oceans, which is the predominant cloud type viewed from a geosynchronous satellite. Some cirrus clouds were also tracked although the sample was small and the upper tropospheric flow relatively weak for the tropical and subtropical regimes that were observed. An expedition to the Azores in the winter was included to obtain high wind speed conditions as part of the overall sample and a wintertime Bermuda experiment was also included for pre and post frontal situations.

Table 1 is a summary of the comparison between the CMW's and the inertial navigation system derived winds from the aircraft (accuracy of about 1 m/sec.). The results are presented

TABLE 1.

CLOUD MOTION VERSUS IN-SITU AIRCRAFT WIND*

Cloud Type	Oceanic Weather Regimes	Date	Location	Number of cloud tracks	Average Cloud Speed ($m\ s^{-1}$)	$\overline{V_{cloud} - V_{wind}}$ / $V_{cloud} - V_{wind}$ 67%** ($m\ s^{-1}$) 150 m	Cloud Base	Mid Cloud	Cloud Top	Mean in Cloud Layer
Low-level cumulus	Trade Wind	Dec 72 Apr 74 Jul 74	NW Caribbean SW Caribbean Gulf of Mexico	40	8.7	1.6/1.9	1.5/1.5	2.9/3.4	6.2/6.8	2.8/3.2
	Subtropical High	Feb 77	NE Atlantic	6	17.8	3.5/3.7	1.8/1.9	5.4/4.6	9.6/9.1	5.1/4.8
	Frontal	Feb 76	NW Atlantic	18	15.3	3.6/3.8	3.2/3.8	2.8/3.3	5.6/6.9	2.5/2.9
Cirrus	Subtropics	Dec 72	W Caribbean	5	11.0	--	2.2/1.7	2.0/1.8	2.9/2.2	1.7/2.0

* All measurements were made in-situ by aircraft equipped with Inertial Navigation Systems.

** The 67% subscript means that two-thirds of the differences have this value or less.

TABLE 2.

SATELLITE CLOUD WIND SYSTEMATIC BIAS ERRORS FOR OCEANIC CUMULUS CLOUDS

Weather Regimes	Location	Satellite Cloud Motion Versus Cloud-Base Wind: Number of cloud tracks	V_{cloud} ($m\ s^{-1}$)	V_{CBW} ($m\ s^{-1}$)	Systematic Bias (cloud - CBW): Speed ($m\ s^{-1}$)	direction (deg)
Trade Winds	NW Caribbean	6	12.2	12.3	-0.1	0.5
	Gulf of Mexico	10	5.3	5.3	0.0	5.0
Subtropical High	NE Atlantic	7	19.0	18.0	1.0	1.6
Frontal	NW Atlantic	19	15.7	16.2	-0.5	5.1

as a function of meteorological regime and for four levels with respect to the cloud layer as well as for the mean wind in the cloud layer. Table 1 shows that the best relationship between CMW and the wind for the trade wind and subtropical cumulus is at the cloud base which was usually very close to 500 m and that the vector difference is 1.5 m/sec which is considerably better than the 3-4 m/sec reported by other investigators and not much different than the accuracy of the aircraft measuring system. The CMW-wind relationship is considerably degraded at the cloud top than at the base. For the case of the wintertime frontal cumulus, the cloud base relationship is not as good (∿3 m/sec) and the relationship is slightly better (∿2.5 m/sec) for the mean wind in the cloud layer. The cloud top relationship is still worse by almost a factor of 2. The convective forcing at the base is probably not as strong for the frontal case as for the other tropical cumulus situations which is why the cloud base level for the CMW-wind relationship is best for the tropical cumulus.

The results for the cirrus clouds in Table 1 are also much better than reported earlier which could be in part caused by the relatively low (11 m/sec average speed) of the sample. However, the largest part of the difference in the results is believed to be the result of the proper comparison between the aircraft winds and cloud motion at the cloud level. The approximately 2 m/sec comparison is most encouraging for using these winds as a high quality data source for the upper troposphere.

Table 2 shows the systematic bias for low level clouds. All the speed bias was ≤1 m/sec. and direction bias was within 5°. These values are at approximately the limit of the experimental measurement system.

These results, although not comprehensive for all cloud types and meteorological regimes, are most encouraging and indicate that cloud motions are a high quality and resolution data source. These results have also been invaluable in designing future geosynchronous satellite imaging systems to specify the correct spatial and temporal resolutions and operating scenarios to extract the optimum value from CMW's.

3. CMW COVERAGE

The experience with CMW's has been that their coverage over oceans for low level clouds is nearly complete and that ≤100 km wind resolution would be possible over more than 50% of the area. Over land the coverage is about the same in the tropical daytime when convection is in its earlier stages, but is much more localized at night or when extensive cirrus is present associated with strong convection in the late afternoon and evening. Cirrus coverage is good where extratropical storm systems, large tropical clusters, or jet streams are present and infrequent elsewhere. There are often large clear areas in between. These are the areas where water-vapor pattern derived winds or other methods (e.g. lidar) would be especially valuable. The use of middle clouds is less predictable and they are often associated with complex cloud systems related to storms. As a result, satellite radiometric methods often have problems locating and tracking these clouds. There is a good possibility that other satellite cloud height and tracking methods (i.e. stereo) will be able to locate these clouds much more effectively. The full range of stereo possibilities will be discussed below.

4. CLOUD HEIGHT MEASUREMENT

As noted earlier, cloud height is a crucial parameter and probably is the dominant source of error for the cirrus CMW's. The best solution is stereo from two geosynchronous satellites looking simultaneously at the same area (Minzner et al., 1978; Hasler, 1981). This height accuracy of this temperature independent method is 500 m for clouds at any altitude using the visible channel from the GOES satellites. Since the 1 km resolution visible channel is used, the small clouds can be resolved as well as details in the structure of cirrus. This combination of high spatial and height resolution is excellent for resolving the levels of clouds that, by appearance, might be placed at the same level. This is an especially important consideration over land areas where the cloud base and top altitude can change substantially for cumulus in a relatively short distance due to a change in the meteorological regime. Another meteorological situation where the stereo helps to resolve height differences that are not visually apparent is in tropical cyclones where it has been found that the cirrus top altitude can vary by several km in different parts of the cyclone circulation that was not obvious by looking at a series of time lapse images.

In the absence of stereo, there are several radiometric techniques that can be used that are improvements over simply taking the cloud top temperature directly from the satellite infrared radiance measurements. Desbois, et al. (1982) and Shenk and Curran (1973) have developed multispectral techniques for improving cirrus cloud height estimates. The Desbois et al. technique can be used all day since two infrared (6.7 and 11 μm) channels are used whereas the Shenk and Curran method can be used during daylight where visible and 11 μm channels are employed. Another infrared method has been developed by Menzel et al. (1983) which utilizes three channels on the short wavelength side of the 15 μm CO_2 absorption region. All these multispectral methods are temperature-dependent and yield accuracies in the 50-mb range which is 1.5-2 km for cirrus.

5. SATELLITE REQUIREMENTS

The combination of the Hasler et al. (1979) accuracy results, the development of the stereo technique and other height measuring algorithms, and the basic properties of the clouds (e.g. size, lifetime, etc.) lead to a set of optimum satellite requirements for measuring CMW's to the accuracy limits found by Hasler, et al. (1979). For mesoscale analysis (areas of about

1000 x 1000 km), they are discussed below. The spatial resolution of the channels for tracking low cloud motions over land should be 200 m. The cumuliform clouds typically last about 5 minutes (Fujita et al., 1975) and this high resolution will be able to locate them with sufficient precision to provide 1-2 m/sec CMW accuracy. The measurements should be made every 1 minute to insure that adequate surveillance continuity of the cloud field is maintained since they change shape, merge, etc. so frequently. Over water, these low cloud parameters can be relaxed to 500 m resolution, 15 minutes total tracking time, and a 3-5 minute image interval. For middle clouds and cirrus, the spatial resolution can be 1-4 km, the total tracking time 15-60 minutes, and the image interval 5-10 minutes.

For CMW's as input to synoptic and global analysis, the spatial resolution could be lowered to 1 km. However, the temporal resolution should be no less than 3 minutes for low clouds over land with a total tracking time of about 15 minutes. Over water the total tracking time can be 30 minutes for all clouds, with an image interval of 10 minutes for low clouds. The image interval and tracking time should remain the same for middle and high clouds.

The 200-m spatial resolution is achievable in the visible with moderate sized (30-40 cm optics) telescopes in geosynchronous orbit. This is the size we fly now on the GOES series and plan to fly in the next GOES series starting around 1990. At night we will have to accept much lower infrared spatial resolutions ($\sim$2-4 km) with the same size telescope. Instruments with 1-1.5 m optics could deliver 500-1000 m infrared resolutions to do accurate tracking at night. There are no known difficulties in designing the sensors to meet the temporal frequency requirements and the total tracking time requirements are met simply by scanning the same area a sufficient number of times at the correct temporal resolution.

The future GOES series will have 1 km visible and 4 km infrared resolution with extensive periods of 5-minute temporal resolution over 3000 × 3000 km areas. Thus, all the resolution and tracking time requirements for middle and high cloud motion during the day will have been fully met when the satellite is in the 3000 × 3000 km sector mode. A high percentage of the low cloud motion requirements over water will also be realized with the satellite operating in the same sector mode during the day. There will be some loss of accuracy since the spatial resolution is 1000 m instead of 500 m. The greatest compromise will be in the accuracy of the low clouds over land. What will probably happen for these clouds is about 3 m/sec accuracy for some of the trackable cumulus. This value should still be good enough to define large mesoscale convergence zones that precede extensive thunderstorm development.

At night it will still be possible to determine middle and high cloud motions for long tracking periods (i.e. 60 minutes) with 2-3 m/sec. accuracy. Some over-water mesoscale low cloud tracking should be possible although it will be sharply reduced with the 4-km resolution. Mesoscale low cloud tracking over land at night would be essentially eliminated with suitable accuracy.

The last set of sensor requirements concern cloud height measurement. Simultaneous stereo is needed to obtain the most accurate cloud top heights and is especially critical for middle and high clouds. The image synchronization should be $\leq$10 sec to minimize false parallax caused by cloud motion. Two km or higher infrared resolution could provide effective stereo at night to complement the already successfully demonstrated daytime GOES stereo. High resolution visible and infrared channels ($\leq$8 km resolution) should be flown to implement the multispectral techniques described earlier.

Besides adequate sensor characteristics, the movements of the spacecraft must be known and removed such that the 1-2 m/sec total cloud tracking system accuracy can be achieved. This means that unknown attitude motions must be less than a few hundred meters over the tracking interval of a few hundred seconds for the low clouds. Therefore, the spacecraft attitude determination must be close to the spatial resolution of the highest resolution channel over the shortest cloud tracking interval. Within an image, the line-to-line stability should be within 10-20% of the highest resolution channel and the stability of the entire image should be within one pixel of the highest resolution channel.

6. DATA ANALYSIS APPROACH

Experience has shown that interactive systems under computer control yield the highest quality resolution CMW results (Suomi, 1975; Billingsley, 1976). The capability of a meteorologist to select which targets are the most useful is unequalled by any known automated method. There are situations where automated methods can yield excellent results where cloud fields are homogeneous and techniques like cross correlation can be used (Wilson, 1984). These areas can be selected by an operator who can determine the suitability of an area. Finally, the operator can decide if the final CMW product is within acceptable limits. An operator is also important in the calculation of stereo cloud heights. Selection of targets is still needed since we have not yet developed an automated cloud height contouring approach. However, once the cloud selection is made, algorithms exist which automatically calculate the height.

7. MESOSCALE ANALYSIS

As mentioned before, the operational emphasis on utilizing CMW's has been on analyzing winds for the NMC models. However, there has been a considerable amount of research done showing how CMW's from GOES can be used for improving mesoscale analysis.

Several investigations have shown how CMW's contribute to defining the lower tropospheric convergence field a few hours prior to the

development of intense convection. (See Negri and Vonder Haar, 1980, Maddox et al., 1977; Peslen, 1980; and Peslen et al., 1985.) These convergence zones can be established by upper tropospheric imbalances produced by jet streaks (Uccellini and Johnson, 1979). All these studies show, by using 3-5 minute interval GOES visible data, that the principal mesoscale convergence areas can be detected by tracking the small cumulus that develop before the major thunderstorms. In general, the CMW's can provide higher resolution wind fields than the surface networks and do not have the influence of local surface effects on the measurements. However, considerable care must be given to the vertical placement of the CMW since strong low-level vertical shear is often present in severe local storm cases. Peslen et al. (1985) have demonstrated that placing the CMW's on a sigma surface yielded better results than assigning the winds to a constant pressure surface. The CMW's in these cases were calculated across the portions of the Great Plains (mostly Oklahoma and Texas) where there were very strong east-west moisture and cloud base height gradients.

A major advantage of using CMW's is that it is possible to calculate a field in a very few minutes and check the consistency with the prior field. Peslen (1980) did this and found that the major mesoscale convergence zone ahead of a dry line (which later produced the famous Omaha, Nebraska tornado of May 6, 1975) was consistently reproduced in each of the analyses. This consistency increases the confidence in the analysis. The next generation GOES satellite, with the designed capability to take frequent ($\leq$5 minute) stereo imagery over regional areas for hours could have a major impact in defining these important convergence areas. If a 1-2 minute temporal resolution mode is used, which would increase the number of tracked CMW's and provide continuity of the time history of each tracked cloud, then perhaps the scale of the convergence areas can be reduced since the confidence factor in the analysis has been raised.

Another mesoscale analysis area that shows considerable promise for CMW's is tropical cyclones. Short interval ($\leq$7.5 minute) GOES data have produced high density CMW generated lower and upper tropospheric wind analyses (See Rodgers and Gentry, 1983; Rodgers et al., 1979.) These data could be valuable inputs for tropical cyclone modeling, for investigating theories of tropical cyclone strengthing, and for the operational meteorologist in defining the radii of various speeds of damaging winds. The upper tropospheric circulation is especially useful for determining the potential for early tropical cyclone formation and intensification, and for assessing the interaction between the cyclone and its surrounding environment. This interaction is a new arena of study and is not well understood and could lead to new ideas for predicting cyclone movement and intensification. The next generation GOES imager, with the greater emphasis on frequent interval data with more channels and stereo for better cloud height measurement, should provide even higher density and quality tropical cyclone CMW mesoscale fields.

8. CONCLUSIONS

The cloud motion-wind relationship is considerably better than the accuracy being achieved with the current satellite measuring system. Therefore, improvement is needed in the use of the current observing system and the accompanying data analysis techniques and better future observing systems must be flown to take advantage of the CMW quality that is there. The CMW data complement the other major wind measuring systems that are in place and are planned.

REFERENCES

Billingsley, J. B., 1976: "Interactive Image Processing for Meteorological Applications at NASA/GSFC," Preprints, AMS 7th Conf. Aerospace and Aeronautical Meteorology and Symposium on Remote Sensing from Satellites, Melbourne, Florida, 268-275.

Desbois, M., G. Seze, and G. Szejwach, 1982: "Automatic Classification of Clouds on METEOSAT Imagery: Application to High Level Clouds," J. of Appl. Met., 21, 401-412.

Fujita, T. T., E. W. Pearl, and W. E. Shenk, 1975: "Satellite-Tracked Cumulus Velocities," J. of Appl. Met., 14, 407-413.

Hasler, A. F., 1981: "Stereographic Observations from Geosynchronous Satellites: An Important New Tool for the Atmospheric Sciences," Bull. of the Amer. Meteor. Soc., 62, 194-212.

Hasler, A. F., W. C. Skillman, and W. E. Shenk, 1979: "In Situ Aircraft Verification of the Quality of Satellite Cloud Winds Over Oceanic Regions," J. of Appl. Meteor., 18, 1481-1489.

Hubert, L. F. and L. Whitney, 1971: "Wind Estimation from Geostationary Satellite Pictures, Mon. Wea. Rev., 99, 665-672.

Little, C. G., 1982: "Ground Based Remote Sensing for Meteorological Nowcasting," Chapter in Nowcasting, K. A. Browning, ed., Academic Press, 65-85.

Maddox, R. A., A. J. Negri, and T. H. VonderHaar, 1977: "Analysis of Satellite-Derived Winds for April 22, 1975," Preprint volume, AMS 10th Conf. on Severe Local Storms, Omaha, Nebraska, Oct. 18-21, 1977, 54-50.

Menzel, W. P., W. L. Smith, and T. R. Stewart, 1983: "Improved Cloud Motion Wind Vector and Altitude Assignment Using VAS," J. of Clim. and Appl. Meteor., 22, 372-384.

Minzner, R. A., W. E. Shenk, R. D. Teagle, and J. Steranka, 1978: "Stereographic Cloud Heights from Imagery of SMS/GOES Satellites," Geophys. Res. Lett., 5, 21-24.

Negri, A. J. and T. H. VonderHaar, 1980: "Moisture Convergence Using Satellite-Derived Wind Fields: A Severe Local Storm Case Study," Mon. Wea. Rev., 108, 1170-1182.

Peslen, C. A., 1980: "Short-Interval SMS Wind Vector Determinations for a Severe Local Storm Area," Mon. Wea. Rev., 108, 1407-1418.

Peslen, C. A., S. E. Koch, and L. W. Uccellini, 1985: "The Effect of the Arbitrary Level Assignment of Satellite Cloud Motion Wind Vectors on Wind Analyses in the Pre-Thunderstorm Environment," NASA Tech. Memo. 86186, Goddard Space Flight Center, Greenbelt, MD, 56 p.

Rodgers, E., R. C. Gentry, W. E. Shenk, and V. Oliver, 1979: "The Benefits of Short Interval Satellite Images to Derive Winds for Tropical Cyclones," Mon. Wea. Rev., 107, 577-584.

Rodgers, E. B. and R. C. Gentry, 1983: "Monitoring Tropical Cyclone Intensity Using Environmental Wind Fields Derived from Short Interval Satellite Images," Mon. Wea. Rev., 111, 979-996.

Shenk, W. E. and R. J. Curran, 1973: "A Multi-spectral Method for Estimating Cirrus Cloud Top Heights," J. of Appl. Met., 12, 1213-1216.

Suomi, V. E., 1975: "Man Computer Interactive Data Access System (McIDAS)," NASA Contract NAS5-23296, Univ. of Wisconsin.

Uccellini, L. W. and D. R. Johnson, 1979: "The Coupling of Upper and Lower Tropospheric Jet Streaks and Implications for the Development of Severe Convective Storms," Mon. Wea. Rev., 107, 682-703.

Wilson, G. S., 1984: "Automated Mesoscale Wind Fields Derived from GOES Satellite Imagery," Preprint Volume, AMS 10th Conf. on Satellite/Remote Sensing and Applications, Clearwater Beach, Florida.

S21-47
84481

N93-10320

WIND MEASUREMENTS WITH THE HIGH RESOLUTION DOPPLER IMAGER (HRDI)

W.R. Skinner, P.B. Hays, and V.J. Abreu

Department of Atmospheric & Oceanic Science
Space Physics Research Laboratory
The University of Michigan
Ann Arbor, Michigan 48109-2143

1. INTRODUCTION

The Upper Atmosphere Research Satellite (UARS), to be launched in 1989, is to provide a global data set required to understand the mechanisms controlling upper atmosphere structure and processes, as well as the response of the upper atmosphere to natural and human perturbations.

The High Resolution Doppler Imager (HRDI) is the primary instrument for measuring the dynamics of the stratosphere and mesosphere. The goal of HRDI is to measure wind velocities in the stratosphere and mesosphere during the day and the mesosphere and thermosphere at night with an accuracy of 5m/sec. HRDI will determine winds by measuring Doppler shifts of atmosphere absorption and emission features. Line of sight winds will be taken in two directions, thus allowing the wind vector to be formed.

This paper overviews the HRDI instrument. The basis of the measurement is explained, as is an outline of the instrument. Since neither instrument or observational techniques is fully mature, only a brief sketch is presented here.

2. DESCRIPTION OF MEASUREMENT

The spectrum of red and near IR light scattered from the Earth's atmosphere is largely dominated by rotational lines of the molecular oxygen atmospheric bands. The O_2 atmospheric ($b^1\Sigma g^+ - X^3\Sigma g^-$) bands can be observed both in emission and absorption. This can be explained in the following qualitative argument (see Figure 1): solar radiation incident on the atmosphere is absorbed and causes the molecules in the ground state ($X^3\Sigma g^-$) of molecular oxygen to enter the excited ($b^1\Sigma g^+$) state. This can either occur directly through resonance or through photochemical reactions (Wallace and Hunten, 1968). This state is weakly quenched at mesospheric altitudes, where O_2 emission lines in the A(0,0) band are observable. Emission in the B(1,0) and γ(2,0) bands is much weaker due to the fact that excited vibrational states are quenched into the v'=0 state before the electronic transition takes place. Emission in the B and γ bands thus can be ignored. Below ~50 km quenching rather than emission dominates the loss process. In this instance the photons absorbed

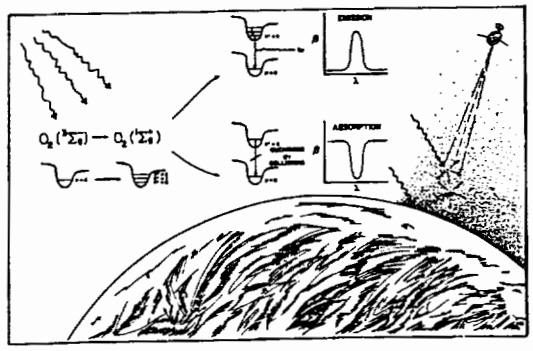

Figure 1. Qualitative illustration of the behavior of the O_2 atmospheric band showing emission at high altitudes and absorption at low altitudes.

are not re-emitted and absorption lines develop in the spectrum. Absorption features in the A, B, and γ bands can be observed when solar radiation is elastically scattered by molecules (Rayleigh) and aerosols (Mie) into the field of view of the observer. This scattering may be direct, or be reflected from the surface and then scattered. Figure 2 shows the development of an absorption line in the B band. This line (P15)is of moderate strength (0.6852 cm^{-1}/km-atm) and is calculated using a multiple scattering simulation. Lines of weaker or stronger intensity will show less or more absorption. The line shapes are shown as being viewed from a satellite at 600 km and with line of sight tangent heights of 45 to 5 km in 10 km increments. They are normalized to the same asymtpotic values for ease of comparison. The actual signal levels vary by several orders of magnitude, from 2.5×10^5 Rayleigh/Angstrom at 45 km to 4.6×10^7 Rayleigh/Angstroms at 5 km. At tangent heights of 5 and 15 km, the lines are the result of scattering from low altitudes where pressure broadening effects dominate and consequently the lines are very broad. Notice that in going from 5 to 15 to 25 km major changes occur in the wings of the line. When the tangent height is 25 km or above the wings of the lines resemble those at low altitudes. The center of the line, however, has developed a nipple, and the whole line shape appears as a superposition of two components: a narrow one which is contributed by the scattering taking place at

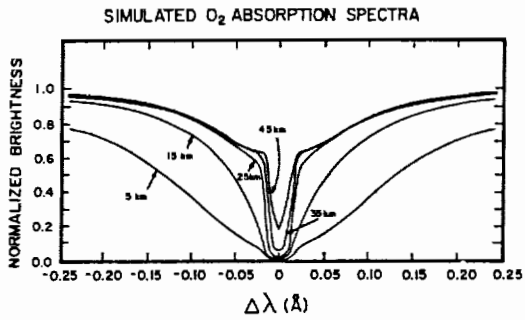

Figure 2. Simulated absorption line spectra using a multiscattering model with low levels of stratospheric aerosols. Data have been simulated for a viewing platform on a satellite at 600 km. Data for tangent heights of 45, 35, 25, 15, and 5 km are shown. Data are normalized to make the asymoptic values agree. Asymoptic values are 2.7×10^5 for 45 km, 1.1×10^6 for 35 km, 4.8×10^6 for 25 km, 2.2×10^7 for 15 km, 4.6×10^7 for 5 km, with units in Rayleighs/Angstrom.

altitudes near the tangent point and a much broader component which is sensitive to parameters of the lower atmosphere and the ground. At higher tangent heights ( ) 25 km), the absolute value of the asymptote changes, but the general shape of the lines remains the same.

Emission spectra of atoms and molecules have been used to measure the Doppler shifts and Doppler widths of emission lines from which winds and temperatures have been inferred. HRDI will analyze the emission lines of the O_2 atmospheric A band in a very similar fashion as its predecessor, the Dynamics Explorer Fabry-Perot Interferometer (Hays et al., 1981; Killeen and Hays, 1984). At altitudes where it is necessary to use absorption, lines in the A, B and γ bands will be used. The lines observed in each band will be chosen to optimize the wind measurement. The effect of winds on absorption lines is quite similar to that observed with emission. Hays (1982) discusses the problem in some detail.

In order to determine vector winds it is necessary to look at the same volume of space from nearly orthogonal directions. A possible data collection scheme in limb viewing mode is shown in Figure 3. It should be emphasized that this figure is only conceptual and does not necessarily reflect actual operating procedure. The satellite is moving at a rate of 7.5 km/s and provides a translation of the observing platform. Desired look directions are provided by the instrument telescope. An observing sequence could commence with four vertical scans through the atmosphere. The number of points taken in a vertical scan is programmable and will depend on the scientific requirements. The telescope is slewed backward and four additional

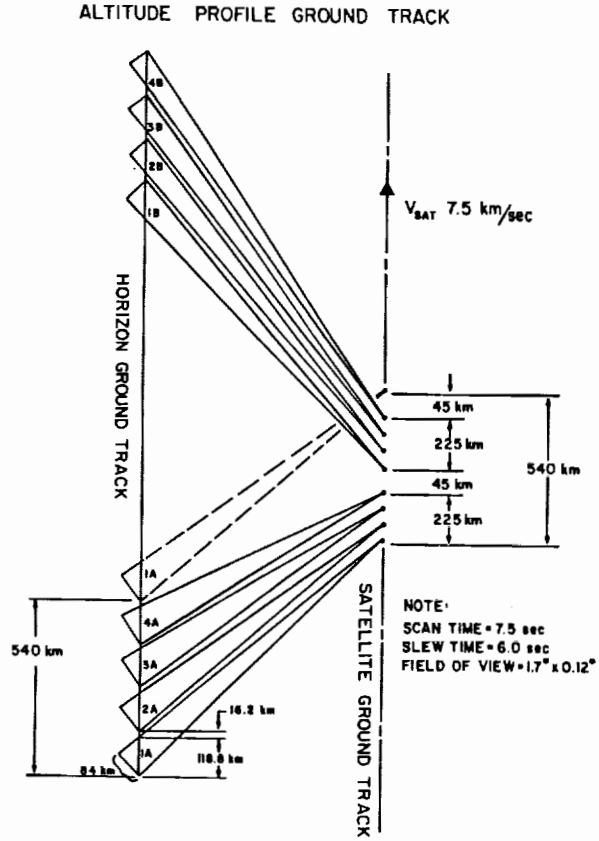

Figure 3. HRDI viewing Geometry.

scans are taken. By this time the satellite has moved enough so that by looking back at the same volume as initially, the line of sight varies by nearly 90 degrees. In this manner data are obtained that allow wind vectors to be formed. The pattern is then repeated to form the next sequence of vectors.

3. INSTRUMENTATION

The HRDI instrument is designed to view the Doppler shifts of absorption or emission lines in the same volume of air from two different directions. This procedure allows vector winds to be determined. HRDI is basically a limb viewer, although the possibility exists for direct viewing of the atmosphere. A summary of the instrument is shown in Table 1.

The HRDI instrument is designed around the Fabry-Perot interferometer. The latter was chosen because of its large light gathering power and high resolution. The HRDI instrument is a logical extension of the Dynamics Explorer Fabry-Perot Interferometer (DE-FPI) (Hays et al., 1981). The present instrument includes three etalons in tandem to reduce the amount of unwanted light that would otherwise be

Table 1. HRDI instrument summary

Item	Description
Type of measurement	Doppler shift and line broadening of scattered sunlight and atmospheric emissions in the visible
Type of instrument	Triple etalon Fabry-Perot interferometer
Geophysical parameters determined	Horizonal vector wind and atmospheric temperature
Azimuth viewing geometry	45^0, 135^0, 225^0, and 315^0 $\pm 5^0$ to spacecraft velocity vector
Zenith viewing geometry	horizonal to nadir
Maximum latitude sampled	74^0
Wavelength coverage	6000 to 8000 Å
Spectral resolution	0.015 Å
Number of wavelengths sampled simoultaneously	32
Integration time	0.1 second
Vertical resolution	6.0 km at limb (0.12^0 field of view)
Horizonal resolution	128 km at limb (1.7^0 field of view)
Time for one vertical scan	programmable, typically 7 to 10 seconds
Distance along spacecraft track	55 km for 7.3 second scan potential of four vertical scans in 500 km track
Instrument mass	150 kg
Average power	86 Watts
Data rate	4750 bps

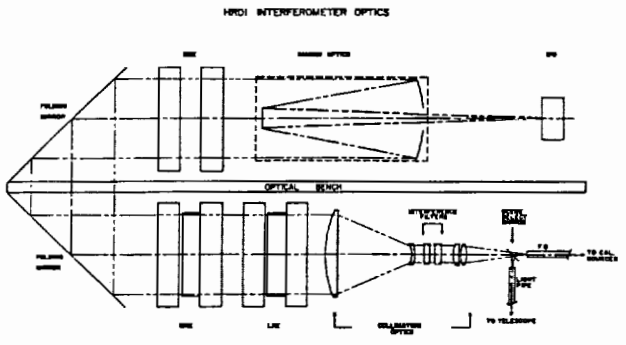

Figure 4. Optical layout of the HRDI instrument. F.O. = fiber optic, LRE = low resolution etalon, MRE = medium resolution etalon, HRE = high resolution etalon, and IPD = image plane detector.

transmitted through a single etalon. The multi-interferometer concept is discussed in works such as Mack et al., 1963 and McNutt, 1965. Figure 4 shows the schematic for the HRDI instrument incorporating the three etalons in series. Light from the atmosphere is collected by a fully gimballed telescope that allows observation of the atmosphere on either side of the spacecraft. Light enters the instrument either from the telescope or from calibration sources by positioning a scene selection mirror. The light beam is expanded and passes through a dual filter wheel. Each filter wheel can hold eight filters. These filters allow the instrument to isolate a spectral region about 10 Angstroms wide. The light beam is then expanded again and goes through two of the etalons. Two corner mirrors are used to direct the light through the third interferometer. Finally, the beam is focussed by the telescope onto the detector. The detector is a multiple anode concentric ring detector that spatially scans the highest resolution interferometer in wavelength. It does this by means of an anode pattern that mimics the interference pattern produced by the interferometers. This device, known as an Image Plane Detector (IPD), allows several points in a wavelength region to be monitored simultaneously. HRDI will collect 32 samples over approximately a 0.2 Angstroms region. The IPD has been used earlier on the Dynamics Explorer Fabry-Perot Interferometer, and a discussion of the device and its usage can be found in Hays et al., 1981, Killeen et al., 1983, and Killeen and Hays, 1984. The detector for HRDI differs from the DE-FPI detector mainly in the number of channels, 32 for HRDI compared to 12 for DE-FPI. The interferometers are scanned in wavelength by using piezoelectric devices to control the spacing of the etalon gap in two of the three Fabry-Perot devices. The third is spatially scanned by the multiple anode detector mentioned above. The resolution of the instrument is approximately 0.015 Angstroms.

The instrument is controlled by a dedicated microcomputer. The computer is necessary to properly control the spacing of the interferometer gaps, compensate for thermal drifts, and to point the telescope.

An engineering model version of this instrument has been built and an example of the instrumental function is shown in Figure 5. This shows the transmittance of the triple etalon system as a function of wavelength. This figure illustrates that the goal of using three etalons to reduce sideband transmittance has largely been achieved. The large sidebands at about ±4 Angstroms are removed by an interference filter. Figure 6 shows a comparison of a measured and simulated instrument function. The simulation allows for defects of the etalons, and shows that good agreement with the measured instrument is

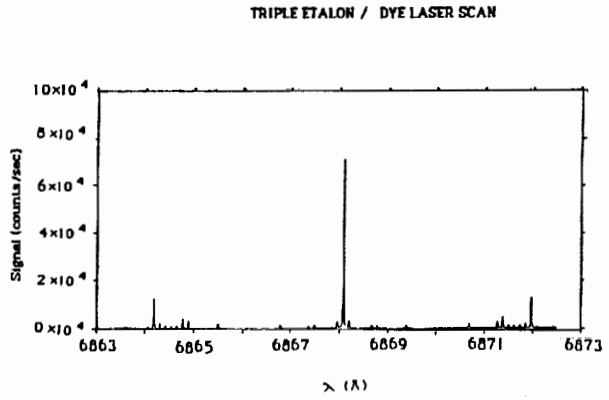

Figure 5. Engineering model triple etalon scan.

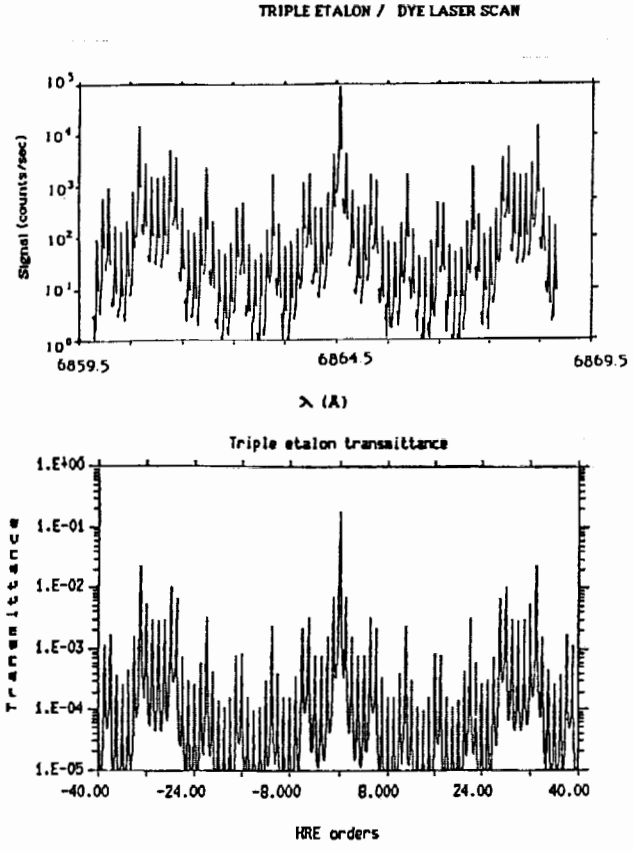

Figure 6. Comparison of measured triple etalon scan (top) and simulated (bottom).

attainable. Each peak shown in the figure is a resonance of the high resolution etalon (HRE). If the medium (MRE) and low (LRE) etalons were not present, all the peaks would have the same value. It is seen that the addition of the MRE and LRE reduces the transmitted light by several orders of magnitude. The maximum of the HRE peaks varies with the resonance conditions in the MRE and LRE. The MRE has a resonance every 5.5 orders of the HRE and this is clearly observed. This pattern is in turn modulated by the LRE. The LRE has a peak about every 30 orders of the HRE and only one sideband on each side of the central peak is apparent.

4. REFERENCES

Hays, P.B., T.L. Killeen and B.C. Kennedy, The Fabry-Perot Interferometer on Dynamics Explorer, Space Science Instrumentation, 5, 395, 1981

Hays, P.B., High-resolution optical measurements of atmospheric winds from space. 1: Lower atmosphere molecular absorption, Appl. Opt., 21, 1136, 1982.

Killeen, T.L., B.C. Kennedy, P.B. Hays. D.A. Symanow and D.H. Ceckowski, An Image Plane Detector for the Fabry-Perot Interferometer on Dynamics Explorer, Appl. Opt., 22, 3503, 1983.

Killeen, T.L. and P.B. Hays, Doppler line profile analysis for a multichannel Fabry-Perot Interferometer, Appl. Opt., 23, 612, 1984.

Mack, J.E., D.P. McNutt, F.L. Roesler and R. Chabbal, The PEPSIOS Purely Interferometric High-Resolution Scanning Spectrometer. I. The Pilot Model, Appl. Opt., 2, 873, 1963.

McNutt, D.P., PEPSIOS Purely Interferometric High-Resolution Scanning Spectrometer. II. Theory of Spacer Ratios, J. Opt. Soc. Am., 55, 288, 1965.

Wallace, L. and D.M. Hunten, Dayglow of the Oxygen A Band, J. Geophys. Res., 23, 4813, 1968.

RADAR WIND PROFILERS

R. G. Strauch

NOAA/ERL/Wave Propagation Laboratory
Boulder, Colorado 80303

1. INTRODUCTION

Vertical profiles of horizontal and vertical wind can be measured throughout the troposphere and into the lower stratosphere in nearly all weather conditions with VHF and UHF Doppler radars. The radars used for this application are less sensitive versions of research radar facilities developed to study the middle atmosphere. Many of these MST (Mesosphere-Stratosphere-Troposphere) research systems are in operation worldwide; others are under development. Doppler radars for wind profiling in the cloud-free and precipitation-laden troposphere and lower stratosphere have evolved from the MST technology. The critical component of the radar is the antenna; the rest of the radar hardware can be very basic. Table 1 lists some radars developed for wind profiling; 10-cm wavelength "meteorological" Doppler radars have limited clear-air capability but provide excellent winds during stratiform precipitation. A network of meteorological Doppler radars (about 100 systems) is planned for the continental United States by the early 1990's. Although only a few longer wavelength radars have been built and operated as wind profilers, others (Penn. State University, France) are under construction and many more of these systems will be built in the very near future. Procurement plans have already been made for an evaluation network of 30 UHF and VHF wind profilers to be deployed in the central United States by 1990. A United States national network would be the logical extension if the evaluation network proves valuable. The evaluation network will serve both research and operational users.

Table 1. Radar Wind Profilers

Location	Wavelength (m)	Maximum average power (W)	Antenna aperture (m^2)
Fleming, CO	6.02	400	2500
Flagler, CO	6.02	400	2500
Norman, OK	6.02	400	2500
Platteville, CO	6.02	400	10,000
Platteville, CO	0.74	800	54
Denver, CO	0.33	450	100

It should be noted that although wind profiling radars are now in operation, there are many questions that remain to be answered before the "optimum" system can be built. These questions include choice of wavelength, data processing and averaging algorithms, and antenna pointing strategy. It is doubtful that one system will satisfy all requirements or be optimum for all the applications that are envisioned. There are also advocates for radar wind measurement systems that do not use the Doppler shift of the scattered signal to measure velocity, but rather measure the wind by the correlation of echo fluctuations on spaced receiving antennas that receive radiation scattered from the atmosphere illuminated by a zenith-pointing transmitting antenna.

Another point to be noted is that the radar wind profilers are "nearly" all-weather devices. What are the weather conditions that degrade or preclude wind profile measurements with Doppler radar? First, there is the obvious situation of strong convection where no single Doppler device can measure the winds because the assumptions that must be made regarding the flow field will not be valid. The assumptions required depend on the number of antenna pointing positions and the dwell time at each position. For 2 antenna pointing positions the main assumptions are that horizontal winds vary only with height and vertical wind is negligible; with 3 antenna pointing positions the horizontal and vertical winds are assumed to vary only with height. Seven antenna pointing positions are needed if the wind field is assumed linear (uniform gradients). In strong convection the spatial and temporal scales of motion cannot be measured by a single Doppler radar. The other weather situations that prevent the radar profiler from obtaining good wind information are related to weak scattering where the signal-to-noise ratio is inadequate. This sometimes occurs just below the tropopause in a height interval of 1-3 km; the signal is strong enough to obtain good wind data below the interval and also may be sufficient to measure winds above this dropout region. Another type of signal dropout that occurs also depends on the refractive turbulence in the upper troposphere; the radar will obtain data to some height (say 7-9 km MSL for UHF and 11-13 km MSL for VHF) with a very abrupt upper height cutoff. The maximum height can change by 4-6 km in 3 hours or less as the atmosphere changes over the radar. The

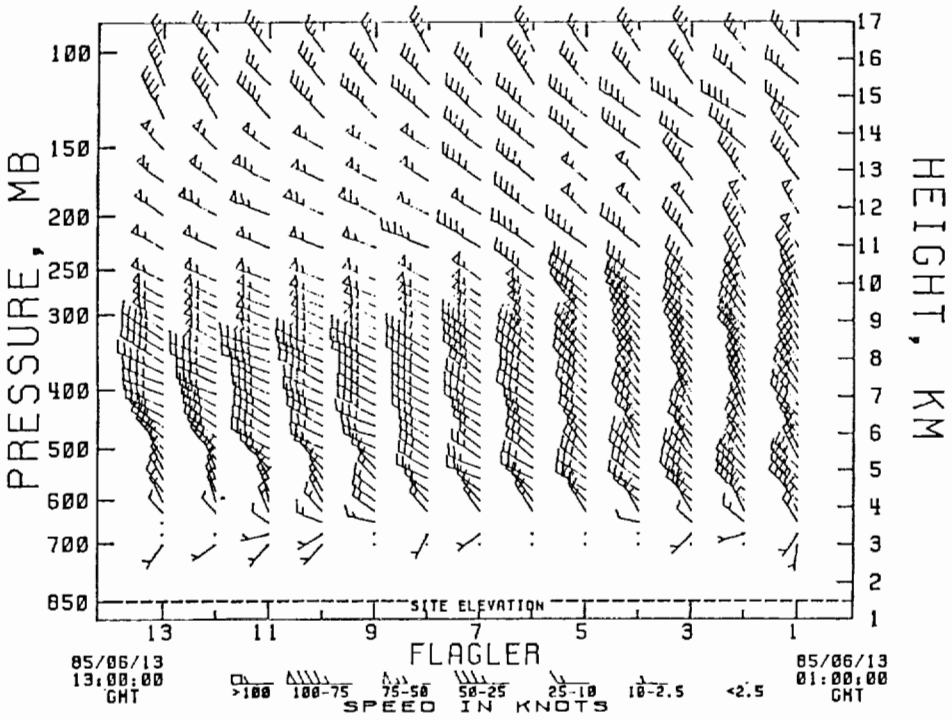

Figure 1. Hourly-averaged wind profiles measured with a 50-MHz radar. Data below 10 km MSL are obtained with a 3-μs pulse; data above 10 km MSL are obtained with a 9-μs pulse. Site is located about 150 km SE of Denver.

atmospheric characteristics that determine clear air radar performance are being characterized by using a 2-year data base obtained with the Colorado wind profiler network.

2. COLORADO WIND PROFILING NETWORK

A network of UHF and VHF radars has been operated in Colorado to test the effectiveness of various wavelengths for radar wind profiling. The first radar operated in this network was a 50 MHz radar at Platteville, originally developed by NOAA's Aeronomy Laboratory (Ecklund et al., 1979). In 1983 a 915-MHz radar and 3 new 50-MHz systems were placed in operation. In 1984 a 405 MHz radar was added and in 1985 one of the 50-MHz systems was moved to Oklahoma. These 6 radars operate continuously and unattended; their data are sent by telephone to a central computer every hour. The radars, their data processing, and automated operation are described by Strauch et al. (1984). The wind data are being used by research meteorologists and on an experimental basis by operational meteorologists for air traffic control and weather forecasting. This small research network has provided the background for the procurement of the 30-station evaluation network.

Figure 1 shows a sample of the hourly wind data provided by the VHF radars. There is no filtering from hour-to-hour (horizontal axis) or in height (vertical axis). Each data point is the radar-estimated wind averaged for 1 hour. There is some correlation in the vertical because the sample height spacing is 2/3 of the pulse

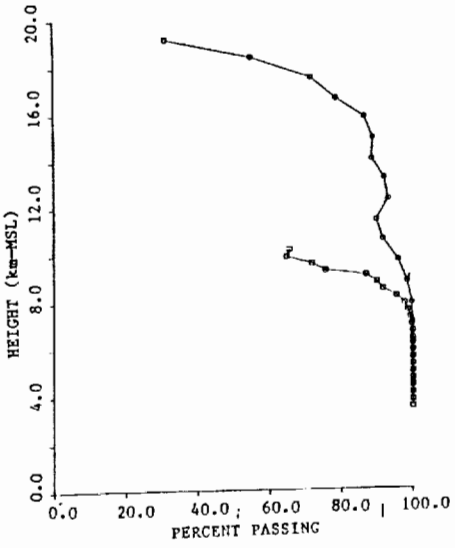

Figure 2. Percentage of time the 6-m radar was able to measure wind profiles with a 3-μs pulse (squares) and a 9-μs pulse (circles). Power aperture product is the same for both modes. Data shown are from 450 profiles measured from Nov. 12 to Dec. 12, 1983. Twelve profiles are measured during each hour; 4 or more must pass a consistency test to produce a wind profile. Site is located about 240 km NW of Denver, CO.

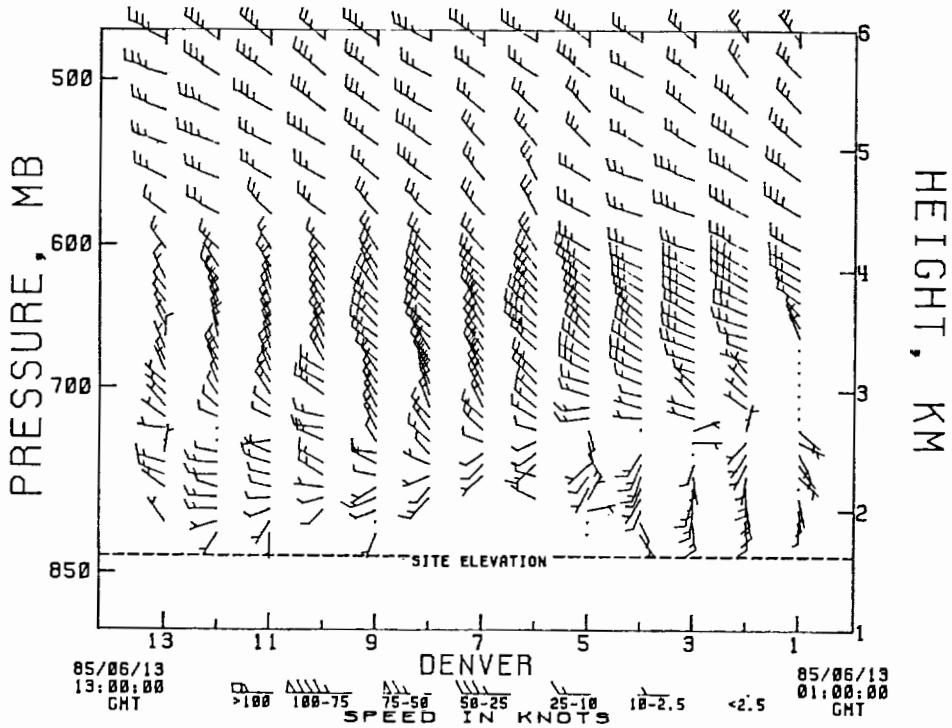

Figure 3. Hourly-averaged wind profiles measured with a 915-MHz radar. Data from 1.6 km to 4 km are obtained with a 1-μs pulse; data from 4 km to 6 km are obtained with a 3-μs pulse. Data are shown only to 6-km altitude to illustrate resolution.

length. The VHF radar data in Figure 1 are from a 2-beam system; vertical motion is assumed negligible when averaged for an hour. The VHF radars have a minimum height coverage of about 1.5 km above ground. This limitation is related to the allowed bandwidth (0.4 MHz), transmit/receive switch recovery and transients, turn-off time of the transmitter, and antenna reflections. Figure 2 illustrates the height coverage of one of the VHF radars using 3- and 9-μs pulse widths and about 400 watts of rf power. The data shown are for winter operation; summer data show a similar trend but the decreased coverage at upper altitudes starts at about 13-14 km instead of at 16 km as in Figure 2.

Figure 3 illustrates low-altitude data obtained with the 915-MHz radar. The minimum height for this radar is about 200 m AGL. The UHF radars use 1-, 3-, and 9-μs pulses and therefore have better height resolution. However, their upper altitude performance is not as good as the VHF radars. Winds are almost always measured to 4 km MSL with the 1-μs pulse (the highest altitude sampled with this mode), but the height coverage of the 3- and 9-μs data depends strongly on the properties of the particular air mass above the radar. In the summer months the 9-μs data extend only 1-3 km above the 3-μs data whereas the VHF data (Fig. 2) show a substantial height increase. The performance of short wavelength clear-air radars is limited at upper altitudes because the inner scale of turbulence can exceed half the radar wavelength and greatly reduce radar reflectivity.

Figure 4 illustrates the wind data obtained with the 405-MHz radar. Its performance characteristics lie between those of the 50- and 915-MHz systems in most respects. These data samples illustrate what can be achieved with automated radar wind profilers. The absolute accuracy of the data cannot be inferred from these samples but the internal consistency indicates a precision better than 1 m/s for orthogonal wind components. In most cases the precision is much better than 1 m/s. Note the consistency of wind direction when the wind speed is low. The accuracy of the radar-measured winds has been verified by comparisons with laser radar data, radiosondes, and with microwave radar during precipitation but we do not have a satisfactory method for comparison that can establish the absolute accuracy or find biases caused by improper antenna pointing.

3. FUTURE DEVELOPMENTS

The radar wind profilers developed for the Colorado network were designed to obtain hourly-averaged winds suitable for observing weather systems for synoptic meteorology and to aid in air traffic control problems such as fuel-efficient flight planning. Radars similar to these will be procured for the 30 station evaluation network; site spacing will be about 200 km. These radar systems will be widely used in weather research and operations in the next decade.

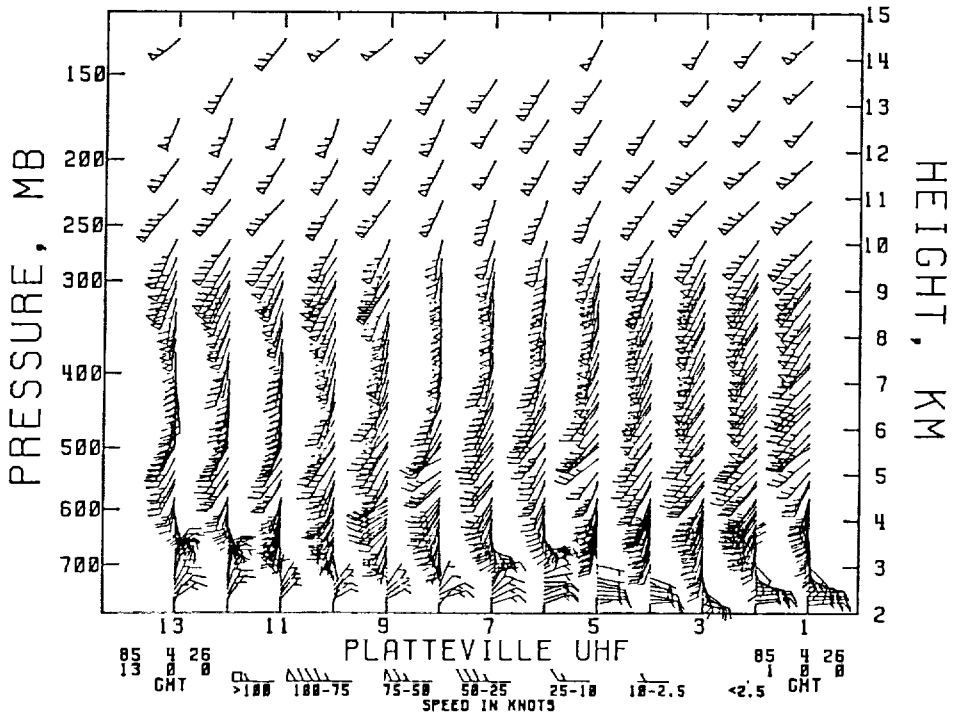

Figure 4. Hourly-averaged wind profiles measured with a 405 MHz radar. Data from 2 to 4.4 km are obtained with a 1-μs pulse; from 4.4 km to 10 km with a 3-μs pulse, and above 10 km with a 9-μs pulse. Site is located about 50 km NE of Denver.

There are many potential operational and research applications for a wind profiler suitable for observing winds on smaller spatial and shorter temporal scales, a "mesoscale" rather than "synoptic" scale profiler. These applications include airport traffic control and safety, artillery corrections, tracer mapping related to operations with potentially hazardous materials (nuclear power plants and chemical plants) and transport of conventional power plant emissions. Such a profiler would obtain wind profiles every few minutes with 100-m height resolution to 6-8 km altitude. For this application a UHF radar (400 MHz) with multiple beam steering or fully scannable antenna would be the logical choice. Plans are under way to develop such a system.

The microwave FM-CW Doppler radar with its very high resolution and very low minimum height coverage is an excellent boundary-layer wind profiler. It has been used for research for 15 years but has not impacted operational meteorology. The FM-CW radars operated to date have been 10-cm-wavelength systems. The experience with the Colorado network indicates that a longer wavelength system (30 cm) could be a much better wind profiler than acoustic systems, for low-altitude/high-resolution applications.

Finally, a research radar system that would greatly aid the understanding of the atmosphere and how wind profilers should be designed would be a high-resolution radar with a maximum height coverage of about 12 km. Present wind profiling radars have resolution that is too coarse at mid- and upper-tropospheric levels to resolve the structure of radar reflectivity that is used as a wind tracer. At lower altitudes the acoustic sounders and 10-cm FM-CW radar show the complex structure of reflectivity; at upper altitudes there is little available data (no continental United States data) on the scattering layers, their height distribution, and their scattering intensity relative to the background. These data are important for wind profiling because the structure of reflectivity determines the spatial and temporal averaging that should be used with radars with limited resolution. In addition, when signal properties other than mean Doppler shift are used to infer atmospheric parameters, it is essential to understand the actual structure of radar reflectivity. A 200-MHz radar with 20-MHz bandwidth would provide the resolution and upper tropospheric coverage desired.

4. THE ROLE OF PROFILER IN GLOBAL WIND MEASUREMENTS

The radar wind profiler, as described in this paper, is not envisioned as a space-borne remote sensor. The role of radar profilers will be to provide high-resolution wind data that will complement measurements from space and serve as a calibration for a global system. There will also be radar wind profilers operating unattended on islands and possibly on ships and buoys that will provide some data over water.

The question of a space-borne UHF radar wind profiler as a competitor to WINDSAT has arisen.

The infrared laser is by no means a perfect answer for global winds. The technology will be difficult; there will be serious problems with clouds in some important meteorological situations; and the resolution will not be satisfactory for all users. Nevertheless, studies show that the infrared Doppler system is feasible (Huffaker et al., 1984). Although no formal study of UHF radar has been made (to the author's knowledge), there are practical problems that make radar a less attractive candidate for a space-borne wind profiler.

Practical problems include the antenna size and average transmitted power needed to achieve the required sensitivity and resolution, compensation for vehicle motion on a pulse-to-pulse basis, and limited dwell time because of antenna motion. The average power-antenna aperture product needed for a 300-km altitude system would be about 30 dB greater than the 10^5 w-m^2 used for ground-based systems. The antenna diameter needed for a 3-km resolution would be about 100 λ, or about 75 m at the shortest wavelength suitable for tropospheric wind profiling. The phase center of the antenna would have to be shifted from pulse to pulse to compensate for the motion of the antenna (or else a much larger antenna would be needed). Ground-based systems use about 1 min of total dwell time to obtain radial velocity estimates; a space-borne system would have to operate with much less dwell time, further increasing the power-aperture product needed. A space-borne radar for global precipitation presents formidable technical problems; a space-borne clear-air Doppler radar would be much more difficult to realize. For these reasons the infrared Doppler system is a better choice for a space-borne wind profiler.

5. CONCLUDING REMARKS

Continuous, automated measurement of tropospheric wind profiles with UHF and VHF Doppler radars has been demonstrated. Ground-based networks of these radars will be available as part of a global wind measurement system, and remote single stations could be built to further complement a space-borne measurement device. A number of ground-based wind profilers will be in place by the time a space system is tested so the global wind measurement system should be designed with these ground-based profilers providing part of the picture.

REFERENCES

Ecklund, W. L., D. A. Carter, and B. B. Balsley, 1979: Continuous measurement of upper atmospheric winds and turbulence using a VHF Doppler radar: Preliminary results. J. Atmos. Terr. Phys., 41, 983-994.

Huffaker, M. R., T. R. Lawrence, M. J. Post, J. T. Priestly, F. H. Hall, R. A. Richter, and R. J. Keeler, 1984: Feasibility studies for a global wind measuring satellite system (WINDSAT): analysis of simulated performance. Appl. Opt., 23, 2523-2536.

Strauch, R. G., D. A. Merritt, K. P. Moran, K. B. Earnshaw, and D. Van de Kamp, 1984: The Colorado wind profiling network. J. Atmos. Oceanic Technol., 1, 37-49.

PASSIVE REMOTE SENSING OF STRATOSPHERIC AND MESOSPHERIC WINDS

Daniel J. McCleese and Jack S. Margolis

Jet Propulsion Laboratory
California Institute of Technology
Pasadena, California 91109

1. INTRODUCTION

This paper describes a passive infrared sensor for remote sounding of the wind field in the stratosphere and mesosphere from near Earth orbital spacecraft. The instrument employs gas correlation spectroscopy together with electro-optic phase-modulation techniques to measure winds in the 20- to 120-km altitude range globally, both in the day and at night, and with a vertical resolution of better than the atmospheric scale height. Measurements of temperature and the amounts of key atmospheric species may also be made simultaneously and in coincident fields of view with the wind observations. The sensor is currently being developed at the Jet Propulsion Laboratory as a candidate for the upcoming NASA Earth Observation System.

Specification of the upper atmospheric winds is a crucial step toward an understanding of the physics and chemistry of the upper atmosphere as well as of its susceptibility to change. Direct wind measurements up to an altitude of at least 100 km are required to examine the dynamics of the upper atmospheric circulation in general and to determine, in particular, the accuracy of using the geostrophic approximation in deriving winds in extratropical latitudes from observed temperature fields. This is the conventional approach used to obtain upper atmospheric winds from satellite data. In regions where ageostrophic components of the wind are strong, direct measurements of the wind are the only reliable means of determining wind fields. Such regions include the equatorial atmosphere, much of the mesosphere since atmospheric tidal components are important there, and any region of strong acceleration/deceleration. Not only is it important to understand the physical processes operating in such areas, but direct wind measurements could provide the coverage and resolution required to diagnose the full impact of such events on the general circulation of the upper atmosphere.

2. MEASUREMENT APPROACH

The direct measurement of wind is made through the detection of wind-induced Doppler shifts in the thermal emission spectra of selected atmospheric species. An important advantage of gas correlation spectroscopy is that the energy grasp of the instrument is high since all the spectral lines of the gas which fall within the bandpass of the instrument contribute to the measured signal. Measurements are made by viewing the limb of the atmosphere. In this viewing geometry the atmospheric spectrum appears as a series of thermal emission lines formed against the cold background of space.

The principle of operation of the wind sensor is the correlation of spectral absorption lines of a gas in a cell within the instrument with the thermal emission lines of the same gas in the atmosphere. The exact correlation of the two sets of spectral lines is destroyed by relative motion between the instrument and atmosphere, and the radiant power incident on the detector is a function of the degree of correlation between the two sets of lines. The measurement of the wind induced Doppler shift between the two spectra, as well as that induced by the motion of the spacecraft, is made by determining the frequency shift required to re-establish exact correlation between the lines in the cell and the lines from the atmosphere. This condition is accomplished by the phase modulation of the incoming radiation by using an electro-optically active crystal.

Figure 1 shows a schematic of the sensor. To resolve both horizontal components of the wind vector at a point in the atmosphere, the instrument views the limb both ahead of and behind the spacecraft at angles of $\pm 45^{o}$ with respect to the subspacecraft track. Two fixed telescopes are used, each feeds an optical arm comprising a telescope, an electro-optic phase modulator (EOPM), reference gas cell, spectral bandpass filter, and detector array. The optical arms view the limb alternately through the two telescopes by means of a beam-switch. Three gas cells are required for wind measurements over the full 20 to 120 km altitude range. The reference gas cells used are: N_2O with a filter bandpass of 1280-1300 cm^{-1} for the 20 to 56 km altitude interval, CO_2 between 695-715 cm^{-1} for 56 to 76 km, and CO_2 at 670-690 cm^{-1} for 76 to 120 km.

Figure 2 illustrates the operation of the EOPM in measuring winds. The top part of Fig. 2a shows the unmodulated atmospheric emission spectrum and the reference cell spectrum with no relative velocity. In the lower part of Fig. 2a the atmospheric spectrum is modulated at frequency ω_m with EOPM modulation index chosen to produce zero carrier amplitude. The spectra shown in Fig. 2a are Doppler-shifted by a relative velocity between the atmosphere and reference cell in Fig 2b. The modulation

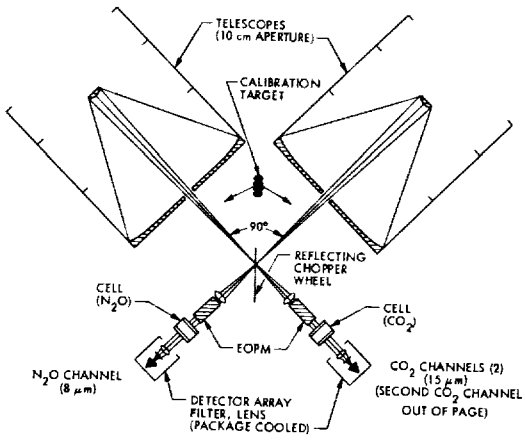

Figure 1. Schematic diagram of the flight wind sensor.

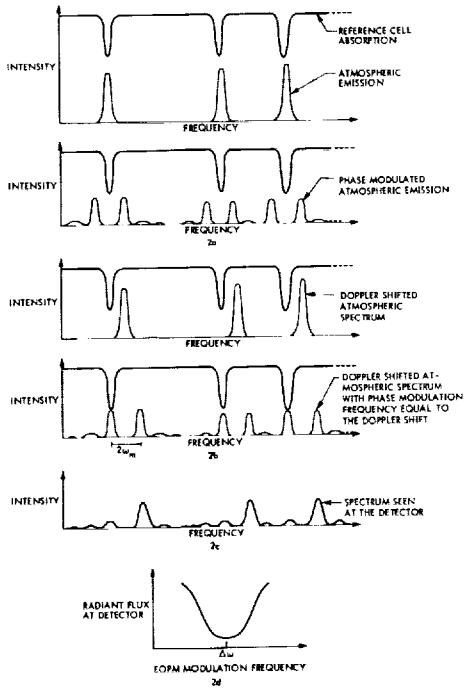

Figure 2. The principle of operation of the EOPM for measuring winds is shown.

frequency ω_m in this figure corresponds to the Doppler shift produced by the relative velocity. Figure 2c is the spectrum of the radiant flux from the atmosphere as seen at the detector for the conditions shown in Fig. 2b. In Fig. 2d the variation of the radiant flux, for a fixed relative velocity, is shown as a function of EOPM modulation frequency. The minimum measured flux occurs at the modulation frequency which is equal to the Doppler shift of the spectrum.

3. LABORATORY SIMULATION OF WIND MEASUREMENT

In an early phase of the development of the wind sensor, a laboratory test was undertaken. A test facility was built with which we have examined the sensitivity of the sensor to small Doppler shifts in an observed spectrum.

The experimental apparatus is shown schematically in Fig. 3. A rotating 25-cm-diameter disk with 360 mirrored facets cut into its periphery was used to simulate wind induced Doppler shifts between the spectral lines of a volume of gas and the lines of the same gas in a reference cell. For convenience, the laboratory experiment was performed in absorption. A pressure modulation cell was used in the laboratory rather than a static reference cell to improve the rejection of undesirable sources of modulation.

Figure 4 shows the responsivity of the breadboard sensor to simulated relative velocities in the range 300 to 360 m/s, corresponding to Doppler shifts of 1.3×10^{-3} to 1.6×10^{-3} cm^{-1} at 1300 cm^{-1} by using the ν_1 band of N_2O. In the example shown in Fig. 4 the (2σ) noise-equivalent wind (NEW), defined as the minimum detectable radiance change and the corresponding Doppler shift, is 3 m/s in each measurement. Also shown in Fig. 4 is the theoretical responsivity of the breadboard sensor for the laboratory conditions (solid line).

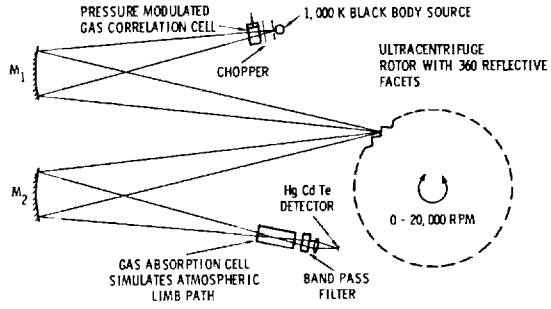

Figure 3. Functional diagram of the laboratory wind sensor test facility.

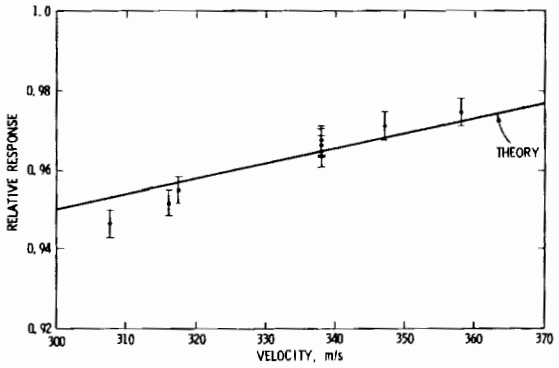

Figure 4. The responsivity of the laboratory wind sensor (using N_2O in the 1250 to 1310 cm^{-1} spectral interval) for simulated winds in the range 300 to 360 m/s. The experimental results are shown in 2σ error bars. The theoretical responsivity of the sensor for the laboratory conditions is also shown (solid line).

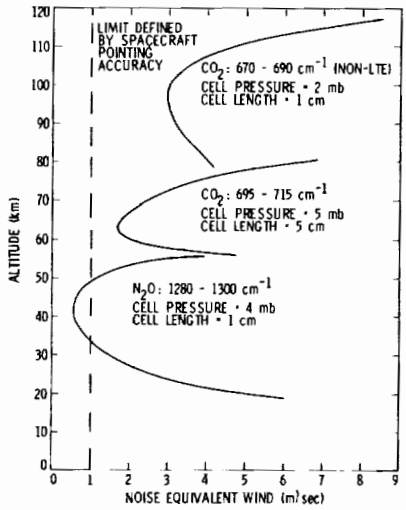

Figure 5. Estimated noise-equivalent-wind (NEW) for the wind sensor over the 20 to 120 km altitude interval. The vertical dashed line is the limit to measurement accuracy due to spacecraft pointing accuracy 1 m/s.

4. ANTICIPATED PERFORMANCE OF A FLIGHT WIND SENSOR

The performance of the wind sensor has been estimated by using a computer simulation of the instrument and its observations. The simulation is based on the U.S. Standard atmosphere and trace species distribution as given by Logan et al. (1978). The instrument instantaneous field of view for each of its detectors are S_1:B_1 operated at 15 K, with the entire instrument cooled to 220 K to reduce background radiation. The measurement dwell time for each sample is 20 sec. This time gives a horizontal spatial smear due to spacecraft motion of 150 km. The NEW for the wind sensor deduced from the simulations is presented in Fig. 5. The lack of local thermodynamic equilibrium for CO_2 in the region above 80 km was approximately accounted for by reducing the population of the ν_2 band of CO_2.

5. CONCLUDING REMARKS

An upper atmospheric wind sensor is under development which uses electro-optic gas correlation spectroscopy to determine the global wind field in the 20 to 120 km altitude interval. Laboratory tests and numerical modelling indicate that a spacecraft-borne sensor will be capable of making wind measurements with an accuracy of better than 5 m/s and a 5 km vertical by $\approx$ 150 km horizontal spatial resolution.

ACKNOWLEDGMENT

The research described in this paper was carried out at the Jet Propulsion Laboratory, California Institute of Technology, under contract with the National Aeronautics and Space Administration.

REFERENCE

Logan, J. A., Prather, M. J., Wofsy, S. C., and McElroy, M. B., 1978: Atmospheric Chemistry: Response to Human Influence, Philos. Trans. R. Soc. London Ser. A290, 187.

NASA SCATTEROMETER OCEANIC WIND MEASUREMENT SYSTEM

M. Freilich, F. Li, P. Callahan, and C. Winn

Jet Propulsion Laboratory
California Institute of Technology
Pasadena, California, USA

1. INTRODUCTION

Satellite scatterometers are active microwave radars designed to yield measurements of near-surface horizontal wind velocity over the ocean. Scatterometers are unique in that they are the only existing microwave remote-sensing instruments that allow measurements of both wind speed and wind direction. NASA will fly a scatterometer, NSCAT, aboard the NAVY Remote Ocean Sensing System (N-ROSS) mission starting in late 1990. N-ROSS is a spaceborne ocean remote sensing system with a planned mission life of three years (Honhart, 1984). In addition to the NSCAT, N-ROSS will have three other microwave instruments mounted on a single satellite flying in a near polar orbit: an altimeter, a special sensor microwave/imager (SSM/I), and a low frequency microwave radiometer. This paper describes the NSCAT to be flown on N-ROSS.

NSCAT will obtain frequent, accurate, high-resolution measurements of near-surface vector winds over the global oceans. NSCAT measurements will be applied to a variety of oceanographic and meteorological research studies, as well as to near-real-time operational weather and wave predictions for the Navy and other users. (See Freilich, 1985, for a more detailed review of the N-ROSS mission, the NSCAT systems, and potential scientific uses of scatterometer data.) Although similar in design to the Seasat scatterometer (SASS), NSCAT will have enhanced capabilities leading to more accurate and higher resolution measurements and greater coverage than was possible with SASS. The three-year lifetime of the N-ROSS mission will allow studies of important geophysical phenomena with time scales longer than could be resolved by the three months of SASS data.

NSCAT will measure normalized radar cross-section (NRCS), σ_o, by illuminating the ocean's surface with microwave pulses and measuring the power of the return signal. The NRCS is computed by using the radar return signal and the radar equation (Johnson et al., 1980). Backscatter at moderate incidence angles ($25° < \theta < 70°$) is primarily due to Bragg scattering of the incident radar signal from sea-surface roughness elements having scales comparable with the radar wavelength. (For NCSAT, Bragg wavelengths will range from 2 to 5.5 cm.) Although an accurate, dynamically based analytic model relating the two-dimensional wavenumber spectrum of these short gravity-capillary water waves to local wind parameters does not presently exist, considerable empirical evidence and simple physical models suggest that the Bragg waves, and hence the radar cross-section, are in fact sensitive functions of the local wind velocity.

A wind retrieval algorithm, utilizing the empirically determined geophysical model relating σ_o to wind velocity, is used to compute wind speed and direction from the measured NRCS. (See, for example, Jones et al., 1982; Schroeder et al., 1982.) Because of the nearly cos(2X) azimuthal dependence of the σ_o (X is the angle between the wind direction and the antenna illumination, see Jones et al., 1982; Schroeder et al., 1982), a limited set of σ_o measurements does not, in general, allow a unique wind direction to be retrieved. The resulting multiple vector wind solutions are called directional ambiguities. Most of the wind vectors retrieved by SASS had four directional ambiguities. Direct application of SASS data for geophysical studies was thus limited because most studies require unique vector winds as inputs. NSCAT is designed to alleviate the directional ambiguity problems that plagued SASS.

2. NSCAT REQUIREMENTS

Performance requirements for NSCAT were established by the NASA Satellite Surface Stress working group, S^3, and by the Navy (O'Brien, 1982; JPL, 1983). NSCAT is required to measure vector winds over at least 90% of the global, ice-free oceans at least once within every two-day period. Wind speed measurements for NASA research users must have an rms accuracy of the greater of 2 m/s or 10% for wind speeds ranging from 3-30 m/s. The dynamic range of the instrument must not preclude measurements of wind speeds up to 100 m/s, assuming that the geophysical model function remains valid at such wind speeds. At least 90% of the vector winds retrieved must have no more than two ambiguities approximately 180° apart. Wind direction rms accuracy must be 20° or better for the ambiguity closest to the true wind direction. Winds must be retrieved with a resolution of 50 km. The absolute location of the center of each vector wind cell must be known to better than 50 km (rms), and the relative locations of the centers of adjacent vector wind cells must be known to better than 10 km (rms). Since the absorption due to liquid atmospheric water can alter the

Table 1
A Comparison of the Nominal System Parameters for the NSCAT and SASS Scatterometers

	NSCAT	SASS
Orbit Altitude	830 km	800 km
Orbit Inclination	98.7°	108°
Operation Frequency	13.995 GHz	14.599 GHz
Receiver Noise Figure	4.0 dB	5.7 dB
Transmitter Pulse Length	5.0 ms	4.8 ms
Transmitter Duty Cycle	31 %	17 %
Peak RF Power Output	110 W	110 W
Antennas	6	4
Number of σ_o Measurement Cells	25	12
σ_o Measurement Cell Resolution	25 km	50 km
Doppler Filtering	Digital	Fixed-Frequency

observed σ_o and, therefore, can degrade the vector wind measurements beyond specifications, a rain flag is necessary to identify those σ_o and vector wind cells retrieved from regions of excessive atmospheric absorption. Data derived from the SSM/I will be used to set the rain flag. For near-real time operational use, the Navy requirement for speed rms accuracy is 4 m/s at a spatial resolution of 25 km or less.

In order to ensure that useful data are available in a timely fashion for NASA research studies, S^3 has also put forth requirements on data processing throughput and data distribution. Vector wind data from NSCAT must be processed to wind field maps and be made available to research users within 2-3 weeks of data acquisition. Raw as well as selected volumes of the processed data will be archived for later use.

3. NSCAT INSTRUMENT DESCRIPTION

The design of the NSCAT flight instrument is based heavily on the SASS design and the results from several previous studies of spaceborne scatterometers (Grantham et al., 1982). Table 1 provides a comparison of the nominal system parameters of NSCAT and SASS. A block diagram of the NSCAT instrument is shown in Figure 1.

The nominal NSCAT operation frequency will be 13.995 GHz, compared to the SASS frequency of 14.599 GHz. This change in frequency is in response to a reallocation of the frequency spectrum available for remote sensing.

NSCAT will use six fan-beam antennas with surface illumination patterns shown in Figure 2. The SASS illumination pattern was similar, but without the center antenna beams. The measurements of σ_o by NSCAT at a third azimuthal angle, made possible by the center antenna beams, greatly increase the instrument's skill in removing directional ambiguities, with the result that more than 90% of the retrieved winds will consist of two ambiguities which are nearly 180° apart.

In the baseline design, two of the six antennas will be dual-polarized while the other four will be singly polarized. Thus, there will be eight antenna beams. (See Fig. 1.) The baseline antenna configuration and polarization was

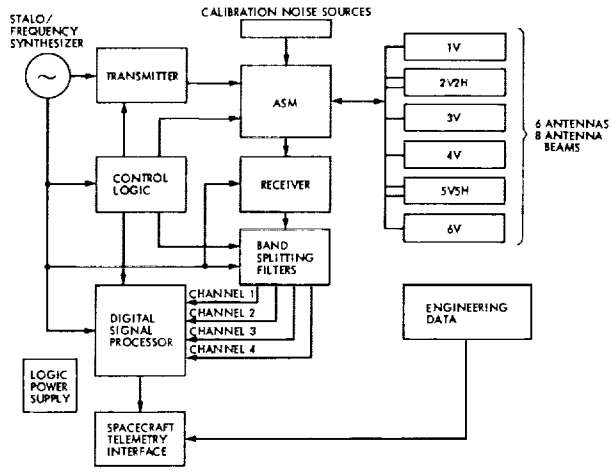

Figure 1. Block Diagram for the NSCAT Instrument

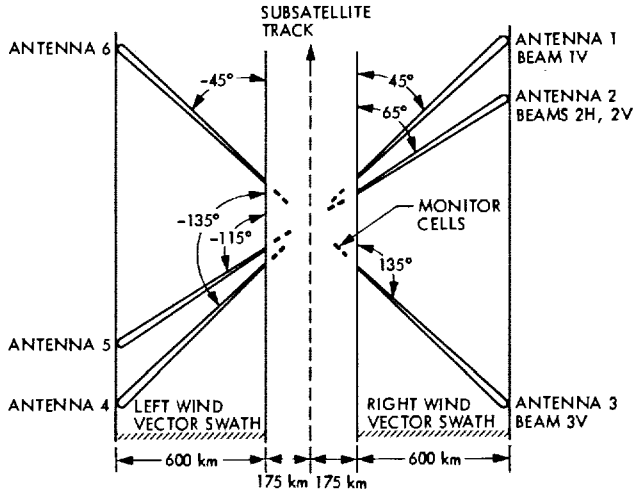

Figure 2. Antenna Illumination Patterns

selected based on the results of an extensive series of system performance simulation studies.

Spatial resolution of σ_o measurements is achieved by subdividing each illumination pattern in the along-beam dimension by Doppler filtering. NSCAT will have 25 σ_o cells, each with a characteristic area of $(25\ km)^2$. It is envisioned that 16 σ_o cells will be combined in retrieving winds at 50-km resolution for the NASA users, whereas four cells will be used to retrieve winds at 25-km resolution for Navy applications.

One of the measurement cells from each of the antenna beams will be at an incidence angle of approximately 11°. The data obtained from these cells will be used for monitoring the instrument performance, since at these incidence angles, σ_o is relatively insensitive to wind velocity (Schroeder et al., 1982).

A stable local oscillator (STALO in Figure 1) will provide reference frequencies for the transmitter, receiver, and digital processor. The transmitter subassembly is designed with redundant travelling wave tube amplifier units in order to enhance the system reliability. The transmitter will provide pulses with 110 W peak power at a 31% duty cycle. The antenna switching matrix (ASM) will sequentially cycle through the eight antenna beams in approximately 3.75 s to achieve the desired along-track resolution of 25 km. In the baseline design, for each antenna beam, 25 pulses will be transmitted and the return signal powers will be averaged. An additional set of four "listen only" measurement intervals for each antenna beam, during which pulse transmission is inhibited, will be used to estimate system noise and the natural emmissivity of the ocean.

A GaAsFET receiver will be used to amplify the return signal. This improvement in receiver technology provides a lower overall system noise temperature relative to SASS. (Refer to Table 1.) The receiver output will be split into four channels of different, partially overlapping bandwidths by the band-split filters. The channel splitting will be used to reduce the amount of computation required in the digital signal processor (DSP).

In SASS the Doppler filtering for along-beam resolution was achieved through the use of fixed-frequency band-pass filters (Johnson et al., 1980). As the frequencies and bandwidths of the analog filters were fixed, the latitude-dependent Doppler shift caused by the Earth's rotation distorted the pattern and size of the σ_o measurement cells from the fore and aft beams. Except at the extreme latitudes of the orbit, one pattern was compressed while the other was expanded, leading to misregistrations between the fore and aft beams and a reduction in effective vector wind measurement swath width.

For NSCAT, Doppler filtering and associated data windowing and power detection will be performed by using an onboard Fast Fourier Transform digital signal processor. A closed-form analytic expression describing the normalized standard deviation of σ_o estimates from a digital filter system (such as that in the baseline design) has been derived and used in the detailed design of the DSP (Chi et al., 1985). The DSP compensates for latitude-dependent Doppler shifts due to the Earth's rotation by adjusting the frequency ranges of the band-pass Doppler filters. Both the orbital period and a set of parameters for the filters will be stored onboard the spacecraft in RAM and may be modified as the orbital parameters are varied. The orbital position computation in the DSP will be synchronized with equator crossing times. This compensation for the Earth's rotation will ensure that the measurement cells from the different beams will be nearly coregistered and thus will maximize the swath width over which vector wind measurements can be made. Details of the system are described in Long et al. (1984) and Chi et al. (1985).

4. NASA RESEARCH-MODE GROUND DATA PROCESSING SYSTEM FOR NSCAT

A research-mode NSCAT Ground Data Processing System (NGDPS) will be established at JPL to reduce the raw NSCAT data and to distribute NSCAT data products to NASA investigators in a timely manner. Figure 3 shows a schematic diagram of the data flown through this system. The input to the NGDPS will consist of NSCAT telemetry (radar return data calibration data, and engineering data) orbit and attitude data, and partially processed SSM/I brightness temperatures. The NGDPS will first convert all NSCAT telemetry to engineering units. Earth locations for the σ_o measurement cells will be calculated using the orbit and attitude information. Scatterometer radar return data will then be converted to σ_o estimates by using the radar equation. At this stage any σ_o cells containing land or ice will be removed from further pro-

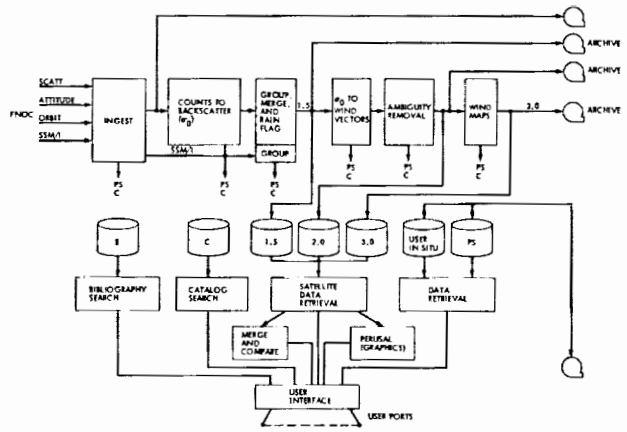

Figure 3. Schematic Diagram of the NSCAT Ground Data Processing System

cessing. SSM/I brightness temperatures, where available, will be used to detect excessive atmospheric absorption due to the presence of rain and corresponding σ_o cells will be flagged. Ambiguous vector winds will then be retrieved by binning σ_o estimates from various antenna beams into 50 km wind cells.

An additional processing step will be used to select a unique vector wind from among the (nominally two) ambiguities. The ambiguity removal process will utilize the intrinsic skill provided by the instrument as well as correlations between neighboring vector wind cells. Examples of such techniques are discussed in Schroeder et al. (1983).

Wind field maps will be constructed by spatially and temporally averaging the unique wind vectors. Maps with 1° x 1° x 2-day resolution will be produced. It is expected that the maps will be used by research investigators to assess data availability and to identify regions of space and time containing large-scale phenomena of interest. The maps and associated statistical information may also be used directly for the construction of even larger scale spatially and/or temporally averaged data sets for the study of large-scale air-sea interactions.

The raw data set, as well as selected volumes of the processed sets, will be archived and distributed to the research users by a data management subsystem. The data system is designed to complete the above data processing and distribution tasks within two weeks of data acquisition from the N-ROSS project. More detailed discussions of the NGDPS and its data products can be found in Benada et al. (1984) and Freilich (1985).

5. SYSTEM PERFORMANCE VERIFICATION

The performance of the NSCAT system will be verified in the year following launch. The accuracies of σ_o measurements, cell locations, rain flags, and retrieved vector winds will be evaluated based on comparison data collected in the six months after launch. Aircraft underflight measurements of σ_o, rain, and winds data from mobile ground receiving stations and *in situ* wind velocity measurements from buoys and ships of opportunity will be compared with NSCAT data. Within the first six months following launch, data from the mobile ground receiving stations and NSCAT σ_o measurements over isotropic scattering regions (such as the Amazon forest, see Johnson et al., 1980) will be used to establish antenna pattern corrections and to verify the accuracy of σ_o cell locations. Rain flag and σ_o accuracy will be assessed at this time by comparing NSCAT data with suitably averaged aircraft underflight measurements of σ_o and liquid atmospheric water. Interim sensor data records will be produced during the six months of this instrument verification.

Wind measurements from ships, buoys, and aircraft will be compared with retrieved NSCAT vector winds in order to verify the accuracies of the retrieval algorithm and the geophysical model function relating σ_o to wind velocity. High resolution *in situ* wind measurements are planned to be acquired in two special validation field experiments. Each experiment will collect comparision data for two months, with both experiments being conducted during the first six months following launch. Spot (instantaneous) comparisons, indirect comparisons between NSCAT data and high resolution regional weather maps, and comparisons between spatially and temporally averaged *in situ* and NSCAT data will be used to assess the accuracy of NSCAT vector wind products. Appropriate changes to the geophysical model function, if necessary, will be made within the first year of the mission. Interim geophysical data records produced in the first year of the mission will be succeeded by final geophysical data records for the following years.

The internal calibration sources, ground receiving stations, data from isotropic land scatterers, and the σ_o cells at ~11° incidence angle will be used to monitor the long-term stability of the NSCAT flight instrument. Periodic status reports and updates to the instrument parameters used in the NGDPS will be produced during the lifetime of the mission.

6. CONCLUDING REMARKS

Satellite scatterometers are active microwave instruments that can provide all-weather measurements of surface wind velocity over the oceans. This paper provides a brief description of the NSCAT flight instrument and ground data processing systems. It is expected that NSCAT will provide accurate, global observations of oceanic winds for a period of three years. These wind data will have significant impact on many studies in marine forecasting of weather and waves, in ocean circulation studies, and potentially in climatological studies of the ocean-atmosphere feedback system.

ACKNOWLEDGMENTS

The authors would like to acknowledge the assistance given by B. Martin and the Scatterometer Project Team at JPL. We would also like to acknowledge the help provided to us by many NASA Langley Research Center personnel who were involved in the scatterometry program, especially E. Bracalente, T. Campbell, and W. Grantham. The research described in this paper was performed by the Jet Propulsion Laboratory, California Institute of Technology, under contract with the National Aeronautics and Space Administration.

REFERENCES

Benada, J.R., P. Callahan, G. Pihos, J. Brown, L. Noon, P. McCabe, and D. Lame, 1984, NASA scatterometer research data processing system - requirements and design, Proceedings of 1984 International Geoscience and Remote Sensing Symposium, Strasbourg, France.

Chi, C., D. Long, and F.K. Li, 1985, Radar backscatter measurement accuracies using digital Doppler processors in spaceborne scatterometers, IEEE Trans. on Geoscience and Remote Sensing, submitted.

Freilich, M.H., 1985, Science Opportunities Using the NASA Scatterometer on N-ROSS, JPL external publication 84-57.

Grantham, W.L., E.M. Bracalente, C.L. Britt, Jr., F.J. Wentz, W.L. Jones, and L.C. Schroeder, 1982, Performance evaluation of an operational spaceborne scatterometer, IEEE Trans. on Geoscience and Remote Sensing, Vol. GE-20, No. 3.

Honhart, D.C., 1984, Navy remote ocean sensing system (N-ROSS), SPIE Proceedings, Washington, DC, May 3-4, 1984.

Johnson, J.W., L.A. Williams, E.M. Bracalente, F.B. Beck, and W.L. Grantham, 1980, SEASAT - A satellite scatterometer instrument evaluation, IEEE Journal of Oceanic Engineering, Vol. OE-5, No. 2, p. 138-144.

Jones, W.L., L.C. Schroeder, and F.J. Wentz, 1982, The SEASAT - A satellite scatterometer: the geophysical evaluation of remotely sensed wind vectors over the oceans, J. Geophys. Res., Vol. 87, p. 3297-3317.

Long, D., C. Chi, and F. Li, 1984, Digital filter processing design for spaceborne scatterometers, Proceedings of the 1984 International Geoscience and Remote Sensing Symposium, Strasbourg, France.

JPL, 1983: N-ROSS scatterometer proposal, internal proposal.

O'Brien, J.J., and the Satellite Surface Stress Working Group, 1982, Scientific Opportunities Using Satellite Surface Wind Stress Measurements Over the Oceans, NOVA University N.Y.I.T. Press, Fort Lauderdale, 153 pp.

Schroeder, L.C., D.H. Boggs, G. Dome, I. Halberstam, W.L. Jones, W.J. Pierson, and F.J. Wentz, 1982, The relationship between wind vector and normalized radar cross section used to derive SEASAT - A satellite scatterometer winds, J. Geophys. Res., Vol. 87, p. 3318-3386.

Schroeder, L.C., W.L. Grantham, E.M. Bracalente, C.L. Britt, Jr., S. Shanmugan, F.J. Wentz, D. Wylie, and B. Hinton, 1983, Study of removal of ambiguous wind direction results from a Ku-band scatterometer wind sensor using measurements at three different azimuth angles, Proceedings of 1983 International Geoscience and Remote Sensing Symposium, San Francisco, CA.

ULTRAVIOLET–EXCIMER LASER–BASED INCOHERENT DOPPLER LIDAR SYSTEM

I. Stuart McDermid and James B. Laudenslager

Jet Propulsion Laboratory
California Institute of Technology
4800 Oak Grove Drive
Pasadena, CA 91109, USA.

David Rees

Department of Physics and Astronomy
University College London
Gower Street
London WC1E 6BT, England, UK.

1. INTRODUCTION

The measurement of accurate temperature and wind velocity profiles throughout the troposphere and lower stratosphere (0 – 40 km), with a height resolution on the order of 100 – 200 m, and a time resolution of 1 – 5 min, has been a long–standing operational requirement for many purposes of the meteorological services and the FAA.

The lidar technique is capable of the simultaneous determination of wind velocity and temperature with accuracy, time, and altitude resolution which are essential for the detailed study of the propagation of tidal and gravity waves in the presence of background prevailing wind systems. Wind measurements in the atmosphere are important for the greater understanding of the dynamics of the atmosphere which is necessary to enable reliable modeling of both chemical and physical processes. In the troposphere the measurement of wind vectors affecting aeronautical activities, such as detection of wind shear and clear air turbulence, could improve the safety of such activities. Weather predictions could be improved with global observations from a space–based system.

To improve weather predictions, especially short range 1 – 2 day forecasts, requires fine–mesh models with fine spatial and temporal resolution. Better horizontal wind information than is currently obtained is needed and the fine–mesh models are also sensitive to the vertical wind components, unlike large scale circulation models. This is especially true in the tropics where the synoptic scale temperature and pressure gradients are weak. In the extratropical regions, nongeostrophic wind components near the tropopause and at lower altitudes are important for the prediction of weather developments and cannot be derived from the temperature field alone. With regard to the vertical wind component, there is currently no satellite method for measuring it. A spaceborne Doppler lidar could provide direct measurements of vertical and horizontal winds to the required accuracy and with the desired spatial and temporal resolution for better weather predictions.

A number of different systems have been designed to measure the Doppler shift with an active lidar configuration. The approaches differ in the manner in which the frequency shift is detected and measured, and in the types and wavelengths of the lasers used. The most frequently used lasers to date have been cw argon ion and CO_2 lasers, and pulsed coherent CO_2 lasers. The frequency shift can be measured in a number of ways: directly by high resolution interferometry, by comparing the the backscattered signal with that from a local oscillator in either a coherent heterodyne or homodyne system, or by splitting the laser beam in such a way that the geometry of the paths to the target volume produces a differential in received frequencies.

Development of active wind sensors to date has been principally concentrated on CO_2 coherent heterodyne systems [Bilbro, 1980]. However, CO_2–based lidar systems can only be used in regions with high aerosol concentrations due to the small backscatter coefficients at these wavelengths; studies of the possibilities of using shorter wavelength lasers are now being made. An instrument which has successfully measured Doppler shifts from clear–air backscattering by using visible wavelengths and a Fabry–Perot interferometer has been described by Benedeti–Michelangeli *et al* [1972]. This system utilized an argon ion laser and measured winds at ranges of 750 m in the troposphere; however, background radiation limited this system to operation at nighttime. An analysis of the possibilities of making wind measurements from an orbital platform with a high–resolution Fabry–Perot interferometer has been made by Abreu [1979]. He has shown that winds in the troposphere and stratosphere could be measured to an accuracy of 2 m s^{-1} using the backscattered radiation from aerosols and cloud tops. These simulations were based on the use of a frequency doubled Nd:YAG laser with a spectral bandwidth of 10^{-4} nm and a pulse energy of 300 mJ. Until recently narrow bandwidth,

moderate energy lasers in the ultraviolet have not been available and therefore have not previously been considered for active wind sensors. Following the recent development at JPL of a single-mode xenon chloride laser [Pacala *et al*, 1984b], an ultraviolet Doppler lidar system is now an attractive possibility. In general, the coherence properties of short pulse lasers render coherent detection methods inappropriate and the optimum choice for an incoherent detector is a multiple Fabry-Perot interferometer using an imaging detector to observe the fringe pattern. Such devices have recently been developed at UCL and successfully applied to the measurement of upper atmosphere winds by passive techniques [Rees *et al*, 1982b]. A similar system is under development for the NASA Dynamics Explorer satellite by Rees *et al*[1982a]. When coupled, the single-mode XeCl laser and the capacitance stabilized triple Fabry-Perot interferometer exceed all of the specifications put forward by Abreu [1979] and by the Shuttle Lidar Working Group [1979] for a system to make measurements of atmospheric winds from space to an accuracy of 2 m s^{-1}.

2. PRINCIPLES OF DOPPLER MEASUREMENTS

The principles of Doppler wind measurements are well understood and are based on the phenomenon that light absorbed, emitted, or scattered by particles having a radial velocity with respect to the line of sight of an observer will appear shifted in frequency. The Doppler shifted frequency, ν_D, is given by

$$\nu_D = \nu_0(1-u/c) \quad (1)$$

where ν_0 is the reference frequency in the rest frame of the particles, u is the line-of-sight velocity, defined as positive if receding from the observer, and c is the speed of light. Passive instruments have been used to measure the shift of absorption lines, of O_2 and H_2O, in the visible spectrum between 590 and 690 nm of sunlight backscattered by Rayleigh or Mie scattering in the Earth's atmosphere. Also, emission from the 630 nm OI line has been observed and used to determine wind fields in the thermosphere. One of the concerns in passive measurements is the lack of certain knowledge of the altitude at which the emission is occurring. In an active system this information is obtained from range-gating the receiver and using the pulse transit time to give the distance to the sampled volume. In the passive experiments the Doppler shift is given by

$$\Delta\nu_D = \nu_0(u/c) \quad (2)$$

which should be compared with an active lidar, where the return signal arises from elastic backscattering of the reference laser radiation, for which

$$\Delta\lambda_D = 2\lambda_0(u/c) \quad (3)$$

In either case the change in wavelength due to line-of-sight wind speeds in the meter per second range are on the order of one part in 10^8. Thus the primary consideration in any Doppler wind instrument is the accuracy to which the wavelength can be determined. The precision with which the wavelength may be determined is dependent on a number of factors such as the received photon flux and the profile of the instrument broadened feature, including broadening effects due to instrument instability. In an active system such instabilities can occur in both the laser transmitter and the etalon receiver. Other factors which impose a limit on the minimum wind velocity that can be measured are the Doppler broadening of the scattered radiation due to random, thermal motion of atmospheric particles and molecules and the spectral bandwidth of the laser. With the advent of properly mounted and evacuated etalons using either Zerodur spacers or capacitance-stabilized designs, problems which have been significant in the past, due to the lack of stability of etalon cavities, are no longer of significance at the level of a few m/s. Progress in increasing the stability and transmission of Fabry-Perot etalons is still being made and these are the most suitable type of dispersive element for use in an incoherent active Doppler lidar system. Similarly, recent improvements in laser technology have produced high energy lasers with spectral bandwidths $\approx 2\times10^{-4}$ Å [Pacala *et al*, 1984a,1984b].

3. LASER BACKSCATTER

The return signal in the Doppler lidar experiment is derived from elastic backscattering by molecules, Rayleigh scattering, and by aerosols, Mie scattering. The backscatter coefficients for both modes of scattering show an exponential wavelength dependence. While the Rayleigh scattering cross-section follows the well known λ^{-4} dependence, the wavelength dependence of the aerosol scattering cross section is also influenced by the particle size distribution and there is no simple function that adequately describes atmospheric aerosol scattering. Experimental measurements of these cross sections are sparse and theoretical estimates are strongly model dependent. The ratio of backscatter coefficient at ruby (694 nm) to that at CO_2 (10.6 μm) has been modeled as 20 to 40 [Fitzgerald, 1984] but was measured in one study as 400 to 1000 [Schwiesow *et al*, 1981]. It would appear that a variation of 2 – 3 orders of magnitude between 300 nm and 10.6 μm is a reasonable estimate [Megie & Menzies, 1980]. Under all conditions the use of near-UV wavelengths results in greater return signals and under certain clean conditions, ie. essentially no aerosols such as in the upper atmosphere, UV wavelengths provide the only means of obtaining measurable returns with reasonable laser energies.

4. EYE SAFETY

A factor of particular concern is that of eye safety, especially if the lidar is being operated in a nadir viewing mode from an aloft platform or is in use near air traffic corridors. The American National Standards Institute (ANSI) has recommended limits for direct ocular exposures from a laser beam. For the excimer laser wavelengths being considered for this demonstration, 308 and 353 nm, the exposure limits for a 100 ns duration pulse is 5.6×10^{-3} J cm^{-2}. This

can be compared to the maximum permitted exposure (MPE) for Nd:YAG wavelengths, for example, which is 5×10^{-7} J cm^{-2} at 530 nm and 5×10^{-6} J cm^{-2} at 1060 nm. Therefore, greater laser energies (by 3–4 orders of magnitude) can be used in the UV with a corresponding increase in signal levels. The safety limits in the far infrared, for example at 10.6 μm, are similar to those in the UV.

5. DEMONSTRATION CONCEPT

A demonstration experiment is being readied at JPL and the first results should be available by the end of 1985. This demonstration experiment relies on the coupling of two independently developed and state-of-the-art technologies to prove the feasibility and applicability of UV excimer lasers together with a multiple Fabry–Perot direct detection scheme for the remote measurement of atmospheric wind velocities. The instrumentation to be used in this collaborative project is based on Fabry–Perot interferometer techniques which have been developed at UCL, including appropriate time–resolving detectors and the necessary electronic and signal processing hardware and software systems. The UV excimer lasers have been developed exclusively at JPL for remote sensing applications which require precise control of the wavelength and spectral bandwidth of the laser output. This project is being carried out at the JPL–Table Mountain Laser Remote Sensing Facility.

During the past 14 years there has been a development program involving Fabry–Perot interferometers at UCL. This program has lead to the space–qualification of various etalon and detector systems which have since been used in satellite, rocket and balloon flight programs [Rees *et al*, 1982a]. The techniques have also been used to create a successful series of ground–based Fabry–Perot interferometers which have been used for thermospheric wind and temperature measurements on a routine basis from several high–latitude stations, particularly at Kiruna (Sweden), Kilpisjarvi (Finland), Svalbard (Spitzbergen) and Halley Bay (Antartica) [Rees and Greenaway, 1983].

In addition a balloon–borne triple–etalon interferometer has been flown successfully on two occasions from Palestine, Texas (May 1980, Oct 1983) [Rees *et al*, 1982b] for the development of stratospheric and tropospheric wind measurement techniques that will be exploited on the HRDI instrument of the NASA UARS satellite which will be flown in 1989.

During the past two years, a precision wavelength–meter has been developed and built for the calibration of a tunable dye laser lidar which the University of Bonn (West Germany) has been using for mesospheric temperature measurements. An upgrade of this wavelength–meter will be used for the wavelength calibration of the JPL UV excimer laser lidar system. The major upgrade will be the monitoring of the complete spectrum of the lidar output on a pulse–by–pulse basis.

Photon–counting imaging detectors with fast time resolution have also been developed at UCL for use in laser spectroscopy, imaging, and interferometry. These multi–channel photon–counting detectors will be adapted for use with an optimized FP interferometer, which will be matched to the optical output of the JPL lidar detector system. This interferometer detector will measure the time–of–flight resolved spectrum of the backscattered signal from the atmosphere, which will be cross–referenced to the calibrated spectrum transmitted by the lidar, to produce the corrected Doppler shifts and winds due to the atmospheric layers sampled by the lidar.

6. THE WAVELENGTH–METER

A schematic illustration of the wavelength–meter, and of its interfaces with the transmitting lidar and signal processing equipment is shown in figure 1 and is described fully by Rees and Wells [1985]. Since the tuning range of the xenon chloride laser is only about 15 Å, this unit will be designed as a single channel device whereas an earlier version was designed to be able to take a second channel to provide a greater free spectral range. Also, compared with the earlier device, the signal processing electronics have to be modified to transfer the complete laser spectrum, pulse–by–pulse, to the data analysis equipment. This procedure does not involve additional signal processing in the wavelength–meter, but does require a faster data transfer rate, via a parallel line, interface.

7. THE INTERFEROMETER DETECTOR

Figure 2 shows schematically the interferometer detector and associated electronics systems which will be used for Doppler analysis of the signal backscattered by the atmosphere from the transmitted lidar pulses. Not shown is the feed back from the wavelength–meter which is required to calibrate the output lidar spectrum in order to obtain slant range wind data. The actual detector type which will be used is essentially a 20–channel photomultiplier, based on a micro–channel plate intensifier and a multi–element anode fabricated to match the wavelength output of a Fabry–Perot interferometer. This device can be used as a photon counting system at modest photon rates, but it will be used as an analog detector (current mode) for the JPL lidar time–of–flight application to comply with the fast sampling rate and high photon detection rate for the duration of the returned lidar pulses.

The optical interface of this system to the lidar receiving telescope has to be optimized carefully, and the transmitting telescope of the lidar as well as the spectral shape and linewidth of the laser itself must also be optimized carefully in order to obtain the best possible performance from the integrated Doppler Interferometer / Lidar system.

8. RETURN SIGNAL MODEL

The intensity of backscattered laser radiation can be calculated by using a simple model. The U.S. Standard Atmosphere [1976] and a continental haze type aerosol distribution has been used to compute the atmospheric backscatter, β, and attenuation, æ,

coefficients. For example, for the horizontal range at the altitude of the Table Mountain Lidar Facility (2 km), and for the two wavelengths 308 and 353 nm, the calculated local coefficients are as follows

$$\left.\begin{array}{ll} 308\ \text{nm} & \beta_R = 1.16 \times 10^{-2}\ \text{km}^{-1}\ \text{sr}^{-1} \\ & \beta_A = 3.38 \times 10^{-4}\ \text{km}^{-1}\ \text{sr}^{-1} \\ & æ_R = 9.75 \times 10^{-2}\ \text{km}^{-1} \\ & æ_A = 1.25 \times 10^{-2}\ \text{km}^{-1} \\ & æ_{O3} = 8.7 \times 10^{-3}\ \text{km}^{-1} \end{array}\right\} \quad (4)$$

$$\left.\begin{array}{ll} 353\ \text{nm} & \beta_R = 6.72 \times 10^{-3}\ \text{km}^{-1}\ \text{sr}^{-1} \\ & \beta_A = 2.75 \times 10^{-4}\ \text{km}^{-1}\ \text{sr}^{-1} \\ & æ_R = 5.65 \times 10^{-2}\ \text{km}^{-1} \\ & æ_A = 1.22 \times 10^{-2}\ \text{km}^{-1} \\ & æ_{O3} = 1.36 \times 10^{-5}\ \text{km}^{-1} \end{array}\right\} \quad (5)$$

The lidar equation can then be used to calculate the range dependence of the return signal S

$$S = E \times (\beta_R+\beta_A) \times \$(R) \times \$(\lambda) \times A \times \Delta R \times \exp\{-2\int^R (æ_R+æ_A+æ_{O3})\} / R^2 \quad (6)$$

where E is the laser energy, $\$(R)$ is the overlap function of the transmitter and receiver optics, $\$(\lambda)$ is the telescope–receiver efficiency at wavelength λ, A is the receiver aperture, and R is the range. To evaluate this equation we use the backscatter and attenuation coefficients listed above, the laser energy is assumed to be 100 mJ pulse^{-1}, the aperture of the receiver is 40 cm, the overall quantum efficiency of the receiver and filter is 0.5%, and the transmitter/receiver overlap is 80% over the entire range. The results show that for horizontal ranges up to 2 km, greater than 10^5 photons per pulse are counted, while this count falls to 10^4 at 5 km and 10^3 at 10 km. While the backscattering coefficients for the longer 353 nm wavelength are lower than those at 308 nm, the ozone attenuation is lower at this wavelength and thus the signals from long ranges are slightly increased at 353 nm. Similar calculations can be made for a vertically oriented lidar in which case the backscatter falls off more rapidly with increasing range due to the decreasing aerosol density but this effect is somewhat compensated by the increased atmospheric transmission.

While these calculations give the magnitude of the total return signal, it is the spectral distribution of the backscattered radiation that is of primary importance for the wind measurement. The spectral distribution of initially monochromatic radiation backscattered by air molecules in random motion is given by

$$\frac{1}{S}\frac{dS(\sigma)}{d} = \sqrt{\frac{mc^2}{8\pi\sigma^2 kT}} \exp\left[\frac{-mc^2\ (\sigma-\sigma_0)^2}{8\sigma^2 kT}\right] \quad (7)$$

where m is the mean molecular mass, k is Boltzmann's constant, T is the absolute temperature, σ_0 and σ are the wavenumbers (1/wavelength) of the incident and scattered radiation, respectively. The spectral distribution of the laser light backscattered by molecules (Rayleigh) is therefore the convolution of the laser spectral distribution with equation (7). However, for laser bandwidths narrow compared with the Doppler width, the laser can be assumed to be monochromatic. The spectral distribution of the radiation scattered by aerosols follows that of the laser due to the low thermal velocity of the aerosol particles. The lidar equation can easily be separated into aerosol and Rayleigh components and it can be shown that for the particular model used (characterized by a relatively low aerosol loading), 3% of the total signal at 308 nm and 4% at 353 nm is due to aerosol scattering. The backscatter spectrum is the superposition of the aerosol and molecular backscatter spectra and it can be simulated. By assuming a Gaussian profile for the laser output spectrum, the intensity distribution of the laser spectrum, and hence also the aerosol backscatter spectrum, is given by

$$I = I_0 \exp\{-(\sigma-\sigma_0)^2 / 0.36\ (\Delta\sigma_{0.5})^2\} \quad (8)$$

where $\Delta\sigma_{0.5}$ is the laser bandwidth (FWHM). For the XeCl laser operating on a single longitudinal mode the FWHM is $\approx 1 \times 10^{-5}$ nm (0.1 mÅ). Evaluating equations (7) and (8) and normalizing for the relative magnitudes of the aerosol and Rayleigh signal returns gives the simulated backscatter spectrum. Figure 3 shows a number of these spectra for different laser bandwidths. While the intensity units on these plots are arbitrary, they are consistent between plots and can be used to compare relative intensities. It is clear from these plots that it is advantageous to operate at the minimum possible laser bandwidth in order to enhance the narrow aerosol return compared with the broadened molecular signal.

In operation, a very small fraction of the laser beam will be deflected into the wavelength–meter as the pulse is transmitted. This provides a measurement of the output wavelength and establishes a reference for that particular pulse. After a small delay the backscattered, Doppler–shifted radiation is sampled by the detector and the wavelength of the aerosol return is compared with the reference wavelength. By following this procedure for each pulse individually, any mode hops between laser pulses will not affect the determination of the wind speed. The differential measurements can still be averaged in order to increase the measurement accuracy.

9. COMPARISON OF INCOHERENT AND COHERENT LIDARS

Comparison of the UV or visible incoherent Doppler Lidar to the coherent infrared Lidars using either pulsed CO_2 TEA lasers at 9 μm or pulsed Nd:YAG at 1.06 μm is based on three primary factors: (1) the ability to measure wind speeds in the troposphere from space with a resolution of 1–2 m/s, (2) the ability to measure the wind speed at this resolution with adequate S/N from orbital heights, and 3) the capability of the Lidar technology to operate in space for two

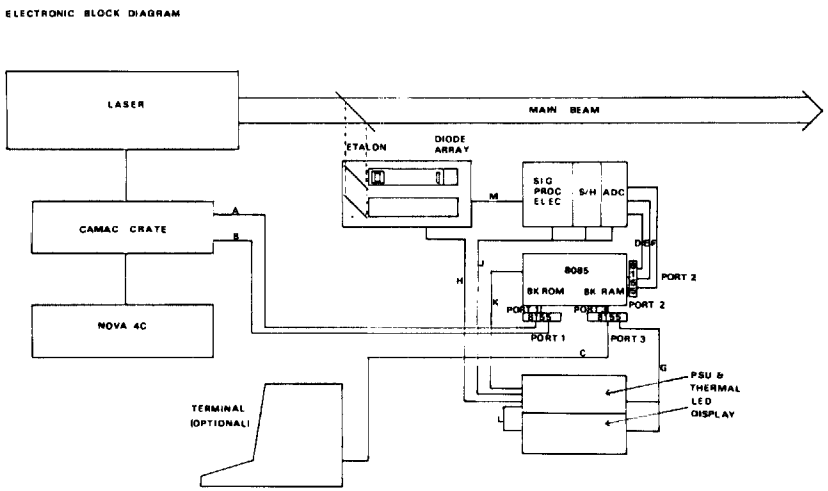

Figure 1. Wavemeter Electronics Block Diagram

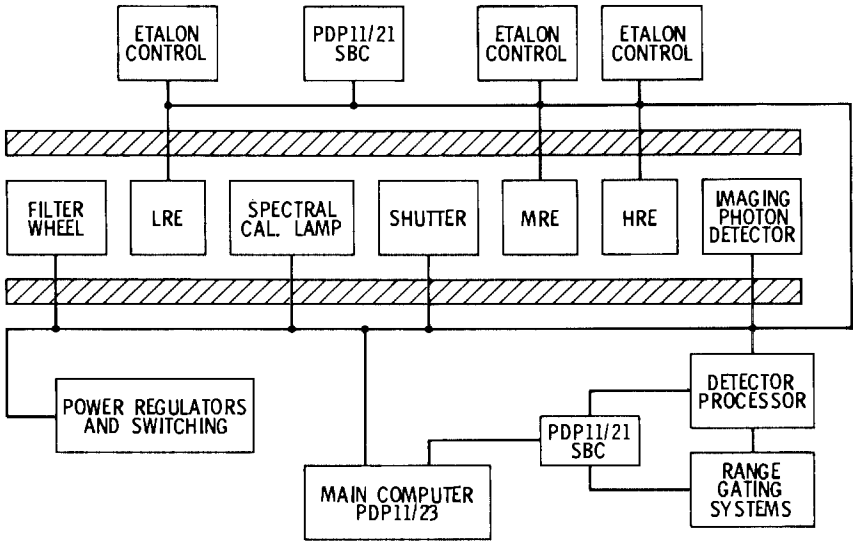

Figure 2. Interferometer Control Schematic

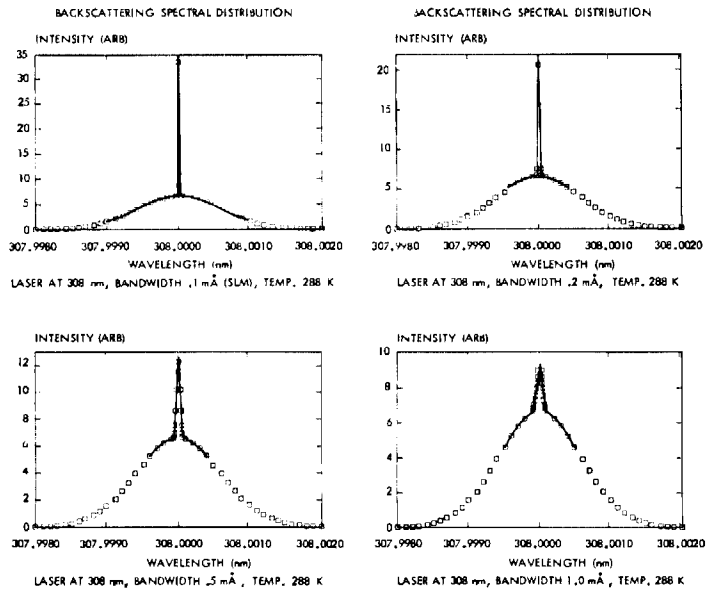

Figure 3. Atmospheric Backscatter Spectra

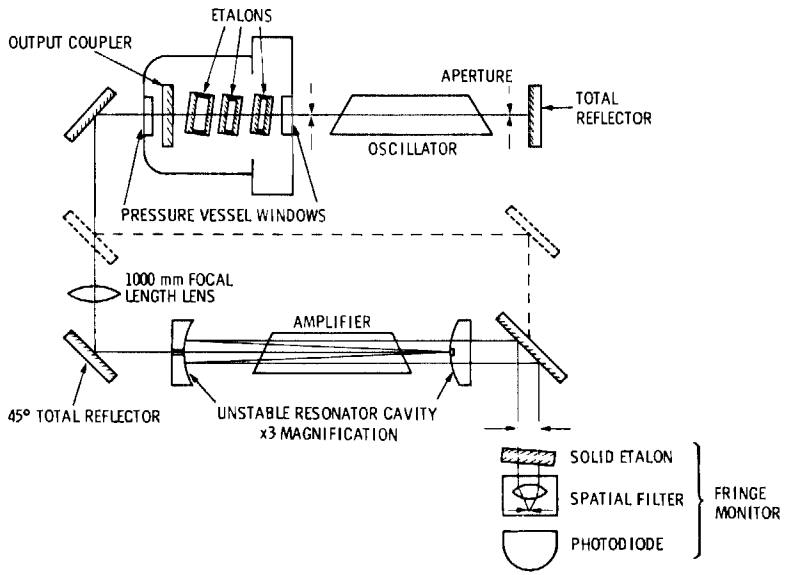

Figure 4. Narrow-Linewidth XeCl Oscillator-Amplifier System

years and still provide adequate operational wind measurements. Based on laboratory demonstrated laser and receiver technology, both the shorter wavelength incoherent Lidar and the CO_2 laser coherent Lidar are capable of achieving wind speed measurements with resolution in the 1–2 m/s range. For comparison of S/N, the efficiency of the heterodyne detection at CO_2 laser frequencies for coherent measurements is superior to that of the incoherent multiple Fabry–Perot imaging detector. However, this advantage is compensated by the larger backscatter coefficient at the shorter UV/visible wavelengths used for the incoherent Lidar. Therefore, until more field measurement data are obtained from the two types of Lidars, there does not appear to be a distinct advantage of one Lidar over the other for either resolution or achievable S/N when the same size collector and the same laser pulse energy are considered. The real choice between the two types of Lidars, at least for space applications, will depend on Lidar technology issues, specifically that of the laser transmitter.

The CO_2 laser technology for both the local oscillator and the pulsed amplifier are well developed systems which have been field tested for wind measurements and have been commercialized in a variety of industrial applications. Because this laser system has been functional for many years, its technical limitations for a space–borne Doppler Lidar are fully identified. These limitations are primarily the short lifetime , $< 10^7$ discharge cycles, of the isotopic gas mixture and electrical components and control of the frequency chirp for a high power laser amplifier as is required from space. Typical operating specifications for a space–borne laser transmitter are 5–10 J per pulse at 10 Hz, a lifetime of $> 10^8$ pulses and good electrical efficiency, at least 1%. Although pulsed CO_2 lasers can be designed to produce the required pulse energy, repetition rate, and efficiency, these features have not as yet been demonstrated collectively in a frequency–controlled high energy device and the lifetime has never been demonstrated. The coherent Lidar also has to deal with the problem of speckle and atmospheric turbulence which is not a problem for the incoherent method. While there is not an eye safety problem for coherent Doppler Lidars at 10.6 μm there is one at 1.06 μm.

Incoherent Lidars based on the flashlamp pumped, frequency doubled, Nd:YAG laser have low efficiency, <1%, have poor operational lifetime due to flashlamp pumping, and must consider eye safety limits especially for daytime measurements where a narrow field of view Lidar configuration is required.

The excimer laser Lidar is a more recent technology but one that is undergoing rapid development in both government and commercial sectors. A XeCl excimer laser operating at 3.5 J per pulse, with efficiency of ≥1% and repetition rates exceeding 25 Hz is being constructed at JPL for a DIAL measurement of stratospheric ozone. A high power, 100 W, 1 J per pulse 100 Hz XeCl laser was run at 1% efficiency for over 10^8 shots for a DARPA funded lifetime test program and in a separate DoD program a XeCl laser amplifier was demonstrated at 4.2% efficiency and >4 J/pulse at 100 Hz. The frequency bandwidth control of a directly tuned XeCl oscillator and injection–locking of a XeCl amplifier has already been demonstrated at JPL in the device shown in figure 4. Therefore, the technology to put a XeCl excimer based Doppler Lidar in space is further along in demonstrated technology than that for the CO_2 laser system. However, some of the excimer laser technology such as X–ray preionization and magnetic switching [Laudenslager *et al* , 1984] could be incorporated into the CO_2 pulsed power amplifier to improve its component lifetime, but the gas lifetime and chirp control still need to be improved. A distinct advantage for incoherent Doppler Lidar is that the absolute frequency of the excimer laser transmitter does not have to be controlled, only narrow bandwidth, because the laser wavelength transmitted is compared with the Doppler–shifted backscattered return signal on each pulse and therefore the laser can alternate among different modes in the optical cavity. This procedure puts the frequency control and stabilization problem on the passive wavemeter and multiple Fabry–Perot filter where the technology is easier to control instead of on the laser transmitter.

In conclusion, the operational capabilities for a space–borne Doppler Lidar may not be too different for incoherent and coherent systems based on physics of measuring the Doppler shift with laboratory laser systems and detectors. The real difference will depend on the development of space–qualified laser technology to operate for the required time period with control of the laser frequency at the higher powers and efficiencies required from a satellite.

ACKNOWLEDGEMENT

This work is funded by a grant from the California Institute of Technology President's Fund and is being carried out at the Jet Propulsion Laboratory, through an agreement with the National Aeronautics and Space Administration, and at the University College London.

REFERENCES

Abreu, V. J., 1979: Wind Measurements from an Orbital Platform Using a Lidar System With Incoherent Detection: An Analysis. Applied Optics, 18, 2992.

Benedetti–Michelangeli, G., F. Congeduti and G. Fiocco, 1972: Measurement of Aerosol Motion and Wind Velocity in the Lower Troposphere by Doppler Optical Radar. J. Atmospheric Sciences, 29, 906.

Bilbro, J. W., 1980: Atmospheric Laser Doppler Velocimetry: An Overview. Optical Engineering, 19, 533.

Fitzgerald, J. W., 1984: Effect of relative humidity on the aerosol backscattering coefficient at 0.694 and 10.6 μm wavelengths. Applied Optics, 23, 411.

Hays, P. B., V. J. Abreu, J. Sroga and A Rosenberg, 1984: Analysis of a 0.5 Micron Spaceborne Wind Sensor. Poceedings of the Conference on Satellite Remote Sensing and Applications, Florida.

Laudenslager, J. B., T. J. Pacala, I. S. McDermid and D. M. Rider, 1984: Applications of excimer lasers for atmospheric species measurements. Proc. SPIE, 461, 34.

Megie, G., and R. T. Menzies, 1980: Complementarity of UV and IR differential absorption lidar for global measurements of atmospheric species. Applied Optics, 19, 1173.

Pacala, T. J., I. S. McDermid and J. B. Laudenslager, 1984a: Ultranarrow linewidth, magnetically switched, long pulse, xenon chloride laser. Appl. Phys. Lett., 44, 658.

Pacala, T. J., I. S. McDermid and J. B. Laudenslager, 1984b: Single longitudinal mode operation of a XeCl laser. Appl. Phys. Lett., 45, 507.

Rees, D., T. J. Fuller–Rowell, A. Lyons, T. L. Killeen and P. B. Hays, 1982a: Stable and Rugged Etalon for the Dynamics Explorer Fabry–Perot Interferometer. Applied Optics, 21, 3896.

Rees, D., P. A. Rounce, I. McWhirter, A. F. D. Scott, A. H. Greenaway and W. Towlson, 1982b: Observations of atmospheric absorption lines from a stabilized balloon platform and measurements of stratospheric winds. J. Phys. E: Sci. Instrum., 15, 191.

Rees, D., and A. H. Greenaway, 1983: Doppler imaging system: an optical device for measuring vector winds. Applied Optics, 22, 1078.

Rees, D., and M. Wells, 1985: A Precision Wavelength Meter for a Pulsed Laser. J. Phys .E: Sci, Instrum., In Press.

Shuttle Atmospheric Lidar Research Program, 1979: Final Report of the Atmospheric Lidar Working Group. NASA SP–433.

Schwiesow, R. L., R. E. Cupp, V. E. Derr, E. W. Barrett, R. F. Pueschel and P. C. Sinclair, 1981: Aerosol backscatter coefficient profiles measured at 10.6 μm. J. Appl. Meteor., 20, 184.

S26-47
84486
N93-70325

DEVELOPMENT OF A 0.5 μM INCOHERENT DOPPLER LIDAR FOR SPACE APPLICATION

A. Rosenberg and J. Sroga

RCA Astro-Electronics
P. O. Box 800
Princeton, NJ 08540

1. INTRODUCTION

Weather forecasts are generated by numerical models of the atmosphere which require the initial state to be known before extrapolating the model to the future. The quality of these numerical weather forecasts is limited by not only the physical principles which are incorporated into numerical models, but also the accuracy in determining the initial state of the atmosphere. The initial state is determined from measurements of atmospheric pressure, temperature, moisture and wind fields; therefore, forecast accuracies are limited by the quality and quantity of these measurements. Global measurement systems from spaceborne platforms are under development to complement the current groundbased radiosonde systems for improved atmospheric measurement capabilities not only over areas where the current measurements exist but also to provide measurements over regions where data are sparse such as the oceans. Recent studies aimed at assessing the impact of proposed global measurement systems have indicated that proposed wind profile measurements are effective in reducing forecast errors (Atlas, et al., 1985).

Spaceborne lidar systems have been proposed to achieve the wind profile measurement capabilities indicated by the numerical studies. Two different principles are under consideration for a global wind measuring system. One technique requires measuring the Doppler shift between the atmosphere and the satellite to derive the wind vectors, and the other technique derives the wind vectors from the displacement of aerosol backscatter patterns between successive scans through the atmosphere. This latter technique has been used as an effective tracer for boundary-layer winds (Eloranta et al., 1975) and such a conceptual design has been proposed for a spaceborne system by Atlas and Korb, 1981.

There are several lidar systems being proposed which use either heterodyne (coherent) or direct (incoherent) detection techniques to measure the Doppler shift. CO_2 Doppler lidar systems have demonstrated Doppler wind measurements with the required accuracies from both ground-based (Hall et al., 1984) and airborne systems (Bilbro et al., 1984) and have been the primary candidates for a global wind sensor (Windsat). Feasibility studies have been undertaken by Huffaker et al., 1984, to analyze the theoretical performance and to determine system specifications of a spaceborne CO_2 Doppler lidar. Alternatives to the CO_2 system which operate at shorter wavelengths to increase the system signal to noise by utilizing the increased aerosol backscatter at these wavelengths have also been proposed. A heterodyne Doppler lidar operating at 1.06 μm is currently under development at Stanford (Kane et al., 1984) which has the additional advantages of compactness and solid-state laser technology. Doppler wind measurements have also been demonstrated by using a scanning interferometric technique in the visible portion of the spectrum (Benedetti-Michelangeli et al., 1972 and Congeduti et al., 1981). A spaceborne lidar system utilizing this interferometric technique has been described by Abreu, 1979.

This paper describes the current status of a prototype 0.53 μm Doppler lidar system under development at RCA. This system consists of a frequency doubled Nd:YAG laser constrained to yield a narrow bandwidth, single frequency pulse, a Fabry-Perot Interferometer (FPI) utilizing an Image Plane Detector (IPD) to measure the backscattered spectrum for each pulse and a Data Acquisition System (DAS) to sample, store, and analyze the backscattered signal. These individual subsystem components have been assembled and preliminary atmospheric testing has recently begun. Atmospheric backscatter spectra are presented which demonstrate the capabilities of this system to distinguish between return signals from aerosols, molecules, and clouds.

2. ANALYSIS OF AN INCOHERENT DOPPLER LIDAR

The technology developed for the Dynamics Explorer satellite program to measure the temperature and wind in the thermosphere (Hays et al., 1981) is the basis for the incoherent Doppler lidar detection technique described here. The principal difference between the Doppler lidar technique and that for the Dynamics Explorer is the transmitted laser pulse for the spectral source, the higher spectral resolution

of the interferometer and higher speed data system required for Doppler lidar wind measurements in the troposphere. Figure 1 schematically illustrates the incoherent Doppler lidar technique. The left hand panels show the spectral distribution of the laser transmitter and atmospheric backscatter which consists of a narrow aerosol spike superimposed upon a broader Rayleigh or molecular return. The central panels show the image of the Fabry-Perot transmission fringe pattern where the change in the diameter of the central fringe is related to the Doppler shift between the transmitted laser spectrum and the peak aerosol backscatter spectrum. The Image Plane Detector has 12 segmented, equal area, concentric ring anodes which are designed to imitate the Fabry-Perot fringe pattern and allow the input spectrum to be sampled, simultaneously, over equal wavelength intervals of that portion of the etalon's free spectral range imaged onto the detector. A schematic of the IPD anode is also shown in the central panel. The signal intensity measured by the 12 IPD channels are schematically shown in the right hand panels. The Doppler shift and the differences between the laser and backscatter spectra are evident.

A theoretical description of the incoherent Doppler lidar is given in a paper by Hays, et al., 1984. The signal intensity measured in each of the 12 IPD channels is modeled as a function of the system design parameters such as the etalon plate spacing, reflectivity, number of anode rings, fraction of the fringe-patterned imaged, optical and detector quantum efficiencies, which are known, and the desired quantities such as the Doppler shift and the spectral characteristics of the transmitter laser source and the scattering media. These unknown quantities (Doppler shift velocity, molecular scatter or background signal, scattering source width and intensity) are derived by a least squares regression procedure to fit the theoretical model to the measured data. The uncertainty in these curve-fitting parameters can be developed from the regression equations and the statistical uncertainty in the measurements. An equation for the statistical error $(\delta V^2)^{1/2}$ in the Doppler shift velocity is (Hays, et al., 1984):

$$(\delta V^2)^{1/2} = \Delta V_{l+s} \cdot c \cdot (C_{ph})^{-1/2}$$

where ΔV_{l+s} is the width (FWHM) of the combined source and laser signal in velocity units, C_{ph} is the total photometric aerosol signal detected without the high resolution element and c is a function of the instrument design parameters along with the aerosol to molecular backscatter ratio. Optimizing the incoherent Doppler lidar design is achieved by minimizing the statistical Doppler wind errors by using this equation. The value of c varies from approximately 1.3 for aerosol to backscatter ratio typical of the boundary layer to about 3.0 for typical values at 10 km. A pulsed Nd:YAG laser has a value of 30 m/s for ΔV_{l+s}. Preliminary calculations of a spaceborne system were presented (Hays, et al., 1984) that indicate a 10 watt laser output power would meet wind measurement requirements in the troposphere.

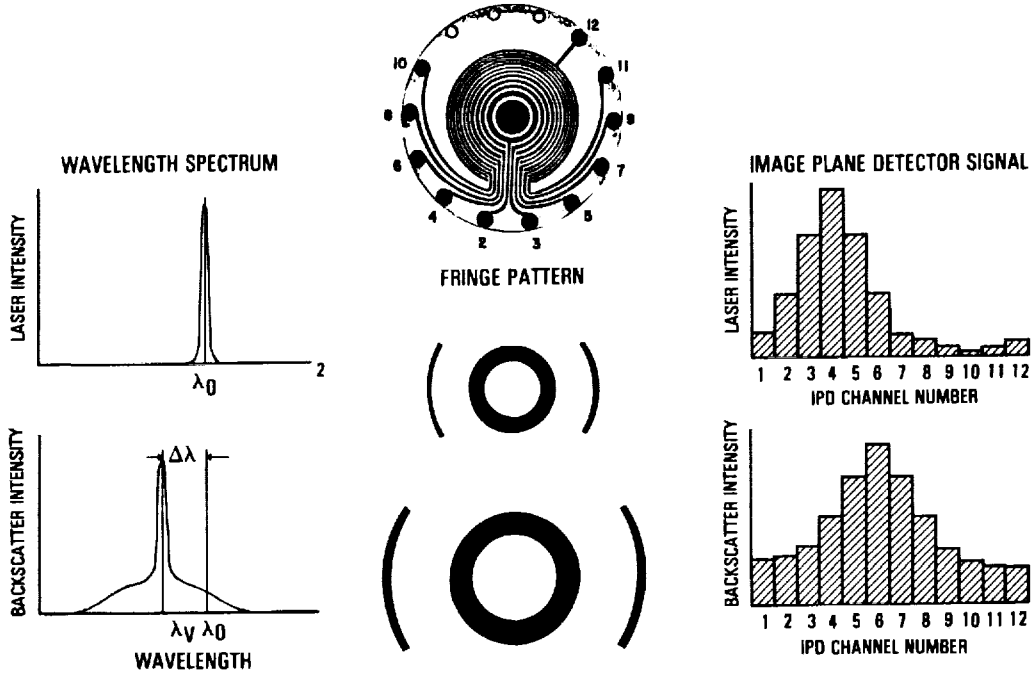

Fig. 1: 0.53 μm Incoherent Doppler Lidar Detection Schematic (see text).

3. PROTOTYPE INCOHERENT DOPPLER LIDAR SYSTEM

Based upon these theoretical calculations, an experimental program was started with the following goals. A groundbased, interferometric Doppler lidar was to be designed and constructed as a prototype spaceborne sensor using a solid-state laser and the Fabry-Perot interferometer technology demonstrated by the Dynamics Explorer satellite. The capabilities of this system under a variety of atmospheric conditions is to be evaluated and comparisons made with theoretical calculations in order to accurately assess the capabilities of a spaceborne incoherent Doppler lidar. A block diagram of the prototype system is shown in Figure 2.

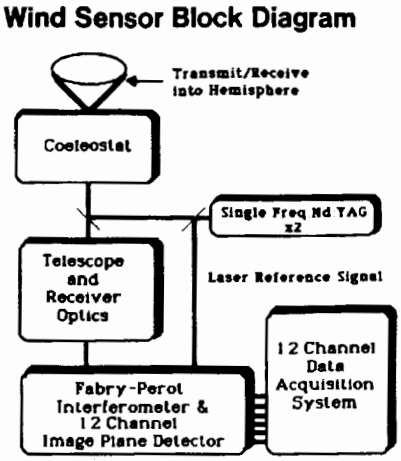

Fig. 2: Wind Sensor Block Diagram.

3.1 Transmitter

The 0.53 μm Doppler Wind Sensor transmitter is a frequency doubled, Nd:YAG laser constrained for narrow bandwidth, single frequency operation utilizing a telescopic resonator configuration (Hanna et al., 1981) to extract a large energy TEM_{oo} pulse from the oscillator. Two techniques are employed to constrain the oscillator output to a single frequency. A solid, 15 mm intracavity etalon is used to reduce the number of lasing frequencies (longitudinal modes) which experience gain and a prelase detection technique (Hanna et al., 1972, Berry et al., 1981) preferentially selects the single longitudinal mode which experiences the greatest gain. The energy of the oscillator pulse is greatly increased by two Nd:YAG amplifiers and a KD*P crystal converts the 1.064 μm pulse to 0.53 μm radiation. The output beam is expanded by a 5X telescope and directed into the atmosphere by steering optics. The operating characteristics of the Nd:YAG laser are listed in Table 1.

TABLE 1. TRANSMITTER CHARACTERISTICS

Operating Wavelength	0.53 μm (SHG of 1.064 μm)
Pulse Energy: Oscillator	40 mj @ 1.064 μm
Amplifiers	375 mj @ 1.064 μm
	30-35 mj @ 0.53 μm
Pulse Width	35-40 ns (FWHM)
Bandwidth (Transform Limit)	25-30 MHz
Single Mode Operation	90-95% of Pulses
Beam Divergence	0.50 mrad

3.2 Receiver

The operating characteristics of the receiver system are given in Table 2. A fiber optic cable simplifies the coupling of the backscattered light collected by the telescope into the Fabry-Perot interferometer and eliminates any systematic angular dependence of the backscattered light. The design of the etalon is similar to the one flown on the Dynamics Explorer satellite (Hays et al., 1981) with a thermally compensating and bonded construction producing a very stable interferometer. The combination of etalon gap spacer with low plate reflectivity is a result of optimizing the design of the interferometer for minimum Doppler shift measurement error. The Image Plane Detector for the 0.53 μm Doppler lidar is the same design as that used on Dynamics Explorer (Killeen et al., 1983). The Fabry-Perot interferometer with the associated IPD electronics were designed and constructed by Professor P. B. Hays and his associates at the University of Michigan Space Physics Research Laboratory.

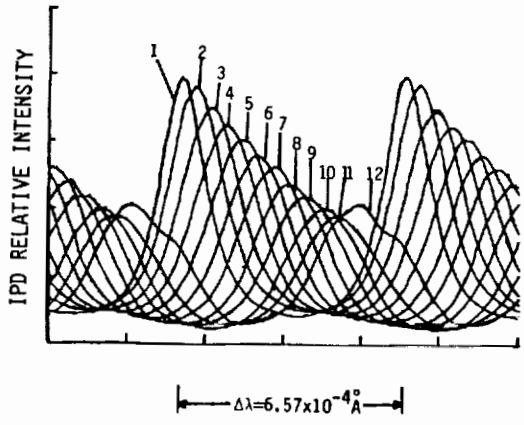

Fig. 3: Relative Transmission Intensity of the FPI-IPD system as a function of wavelength for each of the 12 channels. These distributions were obtained by pressure scanning the etalon chamber while using a stabilized single frequency helium neon laser as the illuminating source.

TABLE 2. RECEIVER CHARACTERISTICS

Telescope	31.75 cm dia. f/16 Cassegrain
Fiber Optic Coupling	f/6 Final System
Fabry-Perot	
Interference Filter	7.5 nm (FWHM)
Etalon Spacer (Zerodur)	30.48 cm
Etalon Plate Reflectivity	~73% @ 0.53 μm
Coated Plate Area	5 cm dia.
Image Plane Detector	ITT Model F4151
Photocathode	S20 1.2 cm dia.
Quantum Efficiency	10% @ 0.53 μm (typical)
Anode	12 Concentric Equal Area Rings ($0.077 cm^2$)
Amplification	3 Microchannel Plates (MCP) Z Configuration 10^6 Maximum Gain

3.3 Data Acquisition System

The backscattered photoelectrons detected by the FPI-IPD system are converted into a voltage signal and interfaced to a Data Acquisition System (DAS). Digital conversion of the IPD analog signals are accomplished either by one of two systems depending on the required sampling rate. For slow sampling rates such as continuous calibration sources, a LeCroy model 8212A data logger is used to sample the twelve IPD signals along with system monitoring parameters. The high speed data system which is used for sampling pulsed sources such as the Nd:YAG laser and atmospheric backscatter, consists of two identical Transiac TRAQ 1 multichannel A/D systems, each system sampling six IPD signal outputs. Both the data logger and the TRAQ 1 systems have 12 bit resolution and simultaneously sample all channels. The current sampling rate of the TRAQ 1 system is 500 KHz that yields a 300 m spatial resolution in the lidar return.

The digitized signals from the data systems are transmitted to a LeCroy System 3500 microcomputer through a CAMAC control interface. The LeCroy system has a printer, two floppy disk drives for storage of data and built-in graphics capabilities. A Tektronix model 4632 is used to obtain a hard copy, graphical representation of the data.

3.4 System Performance

The multispectral capabilities of the FPI-IPD detector system are shown in Figure 3 which illustrates the FPI transmission intensity of a stabilized, single frequency helium-neon laser source as a function of the pressure difference between the etalon chamber and a pressure reference. The corresponding wavelength increment derived from the interference criteria is also shown. All 12 channels were sampled simultaneously along with the pressure transducer output and stored onto a disk. These data are used to calibrate the FPI-IPD system in a similar manner as that described by Killeen and Hays (1984). Figure 4 illustrates the response of the receiver system to a spectrally narrow (a, single frequency HeNe laser) and a spectrally broad (b, white light) illuminating source and is indicative of the difference in the Doppler lidar system response to aerosol backscatter, which has a bandwidth much smaller than the instrumental free spectral range, from that of molecular backscatter, which has a bandwidth larger than the free spectral range.

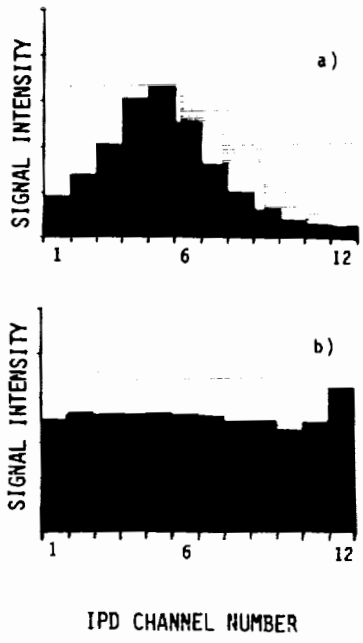

Fig. 4: IPD signal intensity as a function of the channel number for a narrow spectral line source. (a) Stabilized, single frequency HeNe laser and a broad spectral source. (b) White light input.

Preliminary experiments to measure the atmospheric backscatter with the 0.53 μm Doppler lidar system were conducted on June 4, 1985 since overcast sky conditions would illustrate the difference between the backscatter spectra from clear air and clouds. The lidar system was pointing vertically during this experiment since only the difference in the spectra was desired. The total 0.53 μm backscatter detected by a photomultiplier indicated multiple thin cloud layers between 1.0 and 2.4 km (ASL) with sufficient signal from the clear atmosphere below. The data system had ten channels operational at that time and sampled the backscatter at 300 m intervals starting at

approximately 150 m. The IPD was operated at low gain as a precaution since these devices can be damaged by intense light pulses at high gain. The atmospheric spectra shown here have not been corrected for the range square attenuation, geometrical overlap, or for variations in the sensitivity of the IPD channels.

Figure 5 shows an example of the atmospheric backscatter spectra sampled for a single laser pulse. Height intervals labeled 4, 5 and 6 (1050,1350,1650 m ASL) clearly show a narrow spectral line which is indicative of the strong, narrow bandwidth backscatter from clouds with the Rayleigh scatter component being much smaller than the cloud signal. The narrow spectral distribution is also evidence of single mode operation of the laser transmitter. The backscatter spectra sampled at heights 1, 2, and 3 (150 m, 250 m, and 750 m) are from the clear atmosphere and illustrate both the narrow band aerosol signal superimposed upon the broadband Rayleigh return. This effect is easily seen by noticing that the ratio of the peak to the minimum signal is less for the backscatter from the clear atmosphere than that from the clouds. These spectra are evidence of the capability of the 0.53 μm Doppler lidar to distinguish between aerosol, cloud, and molecular backscatter.

4. CONCLUDING REMARKS

This paper has presented a brief description of the 0.53 μm incoherent Doppler lidar technique and the current status of the groundbased, prototype system under development. The capabilities of the individual subsystem components (laser transmitter, receiver and data systems) have been demonstrated and atmospheric testing of the combined system has begun. Preliminary results show the ability of the 0.53 μm Doppler lidar to differentiate the narrow backscatter spectrum from atmospheric aerosols and clouds from that of the spectrally broader molecular return.

A number of tasks need completion before comparing the 0.53 μm Doppler lidar wind measurements with ground truth. System improvements, such as optimizing the IPD electronics design to increase the useful dynamic range of the detector system, increasing the data system sampling speed to improve range resolution and sampling the transmitted laser spectrum are planned. The instrument calibration and analysis techniques are similar to those described by Killeen and Hays, 1984 for the Dynamics Explorer FPI and are currently being developed for this system. Completion of these items will allow demonstration of the Doppler wind measurement capabilities of this system.

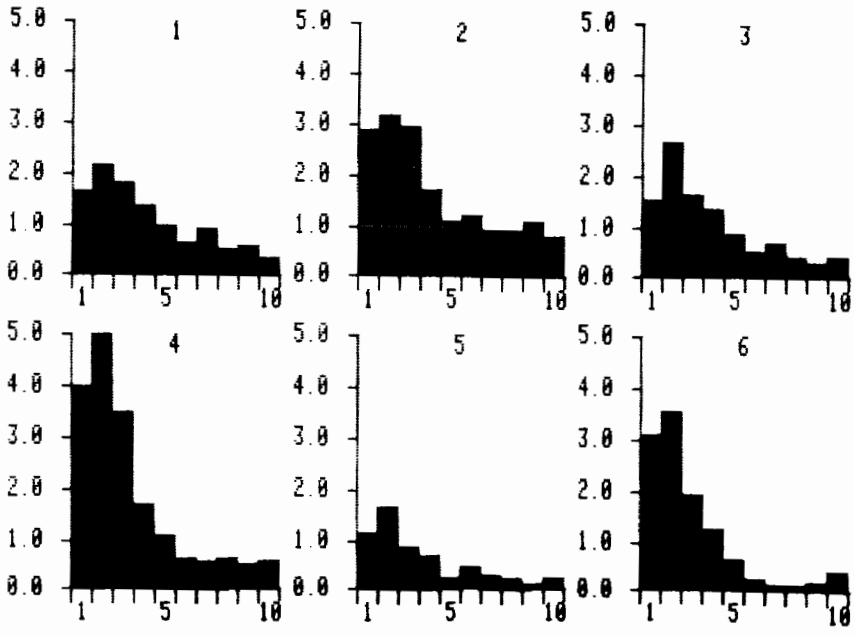

Fig. 5: Atmospheric backscatter obtained with the 0.53 μm Doppler lidar on June 4, 1985. Spectra are sampled at heights (1) 150 m, (2) 450 m, (3) 750 m, (4) 1050 m, (5) 1350 m, and (6) 1650 m (see text for explanation).

REFERENCES

Abreu, V. J., 1979: Wind Measurements from an Orbital Platform using a Lidar System with Incoherent Detection: An Analysis. Appl. Opt., v18, pp. 2992-2997.

Atlas, D. and C. L. Korb, 1981: Weather and Climate Needs for Lidar Observations from Space and Concepts for Their Realization. Bull. Am. Meteor. Soc., v62 pp. 1270-1285.

Atlas, R., E. Kalnay, W. E. Baker, J. Susskind, D. Reuter and M. Halem, 1985: Doppler Lidar Impact Study. Third NASA/NOAA Infrared Lidar Backscatter Workshop, Incline Village, Nevada, Jan. 14, 1985.

Benedetti-Michelangeli, G., F. Congeduti and G. Fiocco, 1972: Measurement of Aerosol Motion and Wind Velocity in the Lower Troposphere by Doppler Optical Radar. J. Atmos. Sci., v29, pp. 906-910.

Berry, A. J., D. C. Hanna and C. G. Sawyer, 1981: High Power, Single Frequency Operation of a Q-Switched TEM_{oo} Mode Nd:YAG laser. Opt. Comm., v40, pp. 54-58.

Bilbro, J., G. Fichtl, D. Fitzjarrald, M. Krause and R. Lee, 1984: Airborne Doppler Lidar Wind Field Measurements. Bull. Am. Meteor. Soc., v65, pp. 348-359.

Congeduti, F., G. Fiocco, A. Adriani and C. Guarrella, 1981: Vertical Wind Velocity Measurements by a Doppler Lidar and Comparisons with Doppler Sodar. Appl. Opt., v20, pp. 2048-2054.

Eloranta, E. W., J. M. King and J. A. Weinman, 1975: Determination of Wind Speeds in the Boundary Layer by Monostatic Lidar. J. Appl. Meteor., v14, pp. 1485-1489.

Hall, F. F. Jr., M. Huffaker, R. M. Hardesty, M. E. Jackson, T. R. Lawrence, M. J. Post, R. A. Richter and B. F. Weber, 1984: Wind Measurement Accuracy of the NOAA Pulsed Infrared Doppler Lidar. Appl. Opt., v23, pp. 2503-2506.

Hanna, D. C., B. Luther-Davis and R. C. Smith, 1972: Active Q-Switching Technique for Producing High Laser Power in a Single Longitudinal Mode. Elect. Lett., v8, pp. 369-370.

Hanna, D. C., C. G. Sawyer and M. A. Yuratich, 1981: Large Volume TEM_{oo} Mode Operation of Nd:YAG Lasers, Opt. Comm., v37, pp. 359-362.

Hays, P. B., T. L. Killeen and B. C. Kennedy, 1981: The Fabry-Perot Interferometer on Dynamics Explorer. Space Sci. Intrum.,v5, pp. 395-416.

Hays, P. B., V. J. Abreu, J. T. Sroga and A. Rosenberg, 1984: Analysis of a 0.5 μm Spaceborne Wind Sensor. Preprints from Conference on Satellite/Remote Sensing and Applications, Clearwater Beach, Florida, June 25-29, 1984.

Huffaker, M., T. R. Lawrence, M. J. Post, J. T. Priestly, F. F. Hall, Jr., R. A. Richter and R. J. Keeler, 1984: Feasibility Studies for a Global Wind Measuring Satellite System (Windsat): Analysis of Simulated Performance. Appl. Opt., v23, pp. 2533-2536.

Kane, T. J., B. Zhou and R. L. Beyer, 1984: Potential for Coherent Doppler Wind Velocity Lidar using Neodymiun Lasers. Appl. Opt., v23, pp. 2477-2481.

Killeen, T. L., B. C. Kennedy, P. B. Hays, D. A. Symanow and D. H. Ceckowski, 1983: Image Plane Detector for the Dynamics Explorer Fabry-Perot Interferometer. Appl. Opt., v22, pp. 3503-3513.

Killeen, T. L. and P. B. Hays, 1984: Doppler Line Profile Analysis for a Multichannel Fabry-Perot Interferometer. Appl. Opt., v23, pp. 612-620.

AEROSOL PATTERN CORRELATION TECHNIQUES OF WIND MEASUREMENT

Edwin W. Eloranta

Department of Meteorology
University of Wisconsin
Madison, Wisconsin 53706

1. INTRODUCTION

This paper reviews the current status of lidar image correlation techniques of remote wind measurement. It also examines the potential use of satellite borne lidar global wind measurements using this approach.

Lidar systems can easily detect spatial variations in the volume scattering cross section of naturally occurring aerosols. Lidar derived RHI, PPI and range-time displays of aerosol backscatter have been extensively employed in the study of atmospheric structure. Descriptions of this type of data can be obtained in many references including: Kunkel et al. (1977), Kunkel et al. (1980), Boers et al. (1984), Uthe et al. (1980), Melfi et al. (1985) and Browell et al. (1983). It is likely that the first space-borne lidars for atmospheric studies will observe aerosol backscatter to measure parameters such as boundary layer depth and cloud height. This paper examines the potential application of these relatively simple aerosol backscatter lidars to global wind measurements.

2. DISCUSSION

Lidar displays depicting the same atmospheric volume at closely spaced time intervals clearly show that aerosol inhomogeneities are advected with the wind. This has led a number of investigators to study the use of aerosol backscatter structure correlation techniques to determine wind speed, wind direction and turbulence. Studies of this type have been presented by a number of authors including: Eloranta et al. (1975), Kunkel et al. (1980), Sroga et al. (1980), Zuev et al. (1979), Derr et al. (1972), Sansano et al. (1982), Ferrare (1984). Two general, closely related, approaches are used to extract wind measurements from the lidar backscatter data. In the first, the spatial distribution of scattered intensity is measured at two separate times and the wind is determined from the relative displacement required to most closely match the two distributions. In the second approach, a time history of the backscattered intensity is measured at two points and the time shift required to most closely match the data series is determined. Both techniques require calculation of space-time correlation functions or closely related Fourier transformed quantities to determine the time lag or spatial displacement which best matches the data sets.

The lidar backscatter structure techniques of wind measurement have several attractive features:(1) measurements can be made with simple incoherent backscatter lidar systems; (2) measurements are not limited to the radial component of the wind; two or three spatial wind components can be measured in the same sample volume; (3) the altitude of the wind measurement is precisely known without the uncertainties implicit in passive wind measurement techniques; (4) the structures used for wind tracking are not limited to aerosol scattering; for example advanced lidars might produce wind measurements at the same time as producing detailed maps of water vapor concentration.

In order to derive winds from displacement of lidar observed atmospheric structures, it is necessary that (1) the lidar backscatter signal contain inhomogeneities on the spatial scale of the separation between the observations which exceed noise induced fluctuations in the lidar signal, (2) the coherent lifetime of the inhomogeneity must must exceed the time interval between lidar observations, (3) the inhomogeneities must drift with the wind unlike an orographically anchored cloud or a propagating wave cloud. Both ground and aircraft based lidar observations have shown that these conditions are normally present for aerosol backscatter signals from the convective boundary layer. It is also apparent that the conditions necessary for measurement of winds from the displacement of lidar observed atmospheric structures would be easily satisfied for lidar returns from the types of clouds which are routinely used to obtain cloud track winds from satellite images. Studies of water vapor inhomogeneities observed with the METEOSAT satellite show that these mid-tropospheric features accurately portray the wind field (Eigenwillig,1982). This fact suggests that the aerosol displacement techniques of wind measurement may also be applicable to water vapor measurements provided by future differential absorption or Raman lidar systems.

Observations with the ground-based University of Wisconsin lidar show that measurements of wind speed, wind direction and the intensity of turbulence can usually be obtained inside the convective boundary layer. One of the measurement techniques used involves processing a time series of lidar backscattering profiles obtained by using the geometry shown in Figure 1.

The cross path wind is obtained by measuring the time it takes for aerosol structures to drift from one of the azimuthal directions to the next. The longitudinal component of the wind is determined from the radial displacement which occurs during the cross path drift time. In practice the cross-path drift time and radial displacement are determined by computing two-dimensional lag cross-correlations or from an equivalent, but computationally more efficient, fast Fourier transform technique. The three angle azimuth scan also allows a measurement of the intensity of turbulence. Wind fluctuations which take place on a time scale shorter than the averaging time used for the lidar wind profile measurement make the cross correlations determined from the outside angle of the scan smaller than those computed from the adjacent angles. A detailed description of this measurement procedure is provided by Sroga et al. (1980). (See Fig. 1.)

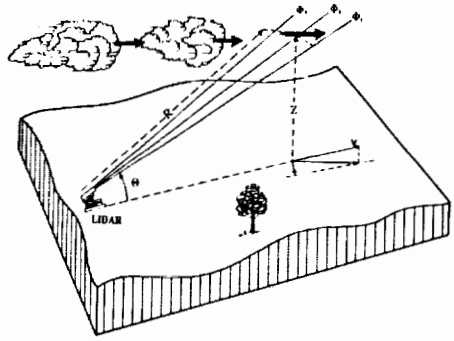

Fig. 1. The geometry used for lidar wind measurements. The lidar is operated at a constant small elevation angle and scanned back and forth between three closely spaced azimuth angles. Range-resolved profiles of backscattered intensity are recorded at ≈1 s intervals for a period of 2-5 min to produce a wind measurement. Wind velocities are calculated in terms of a radial component v and a cross-path component u. Reprinted from Sroga (1980).

The above lidar technique provides vertical profiles of both horizontal components of the wind and the intensity of turbulent wind fluctuations. Profiles are obtained in a period of ≈ 5 minutes and extend from near the ground to the top of the convective boundary layer. Remote wind measurements are routinely obtained at ranges up to 7km in clear air. During one experiment the system acquired approximately 250 wind profiles consisting of nearly 1200 usable wind measurments (Hooper,1982). A comparison of these profiles with concurrent kytoon borne anemometer and dual theodolite track pilot balloon wind measurements yielded root-mean-square differences of 0.7 meters/sec in speed and 7 degrees in direction. It is belived that much of the difference in the measurement is a result of the different volume averagings represented by the measurements.

A separate experiment, where wind measurements were obtained from two-dimensional cross-correlations computed between pairs of PPI sector scans observed approximately three minutes apart, provided the measurements presented in Figure 2 (Ferrare,1984). Each data point in this figure is a statistically independent measurement. The small scatter in the speed measurements implies a precision of roughly 0.2 meters/second; this is considerably better than ± 1 meter/sec variations one expects from balloon tracking or tower mounted anemometers.

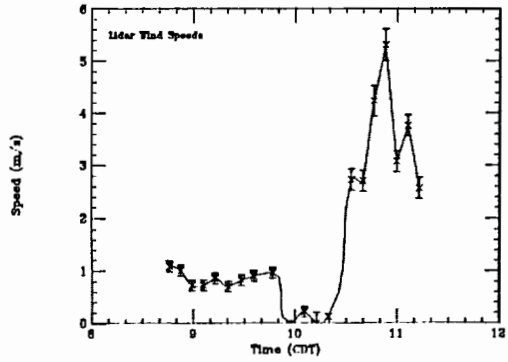

Fig. 2. Lidar measured wind speeds derived from cross-correlation functions computed from PPI scan data. Reprinted from Ferrare (1984).

The PPI sector scan data set used for these wind determinations is similar to data which could be acquired from a space borne lidar system operated in the mode suggested by Atlas and Korb (1981). They propose a lidar located in a 200 km altitude orbit. The lidar would alternately scan across the orbital path directed 45° in front of the satellite and 45° behind the satellite. This geometry, shown in Figure 3, provides two separate three-dimensional maps of the aerosol structure inside each measurement volume. The forward volume would be observed approximately one minute before the aft volume and spatial cross-correlations between the time separated measurements would be used to recover the wind data.

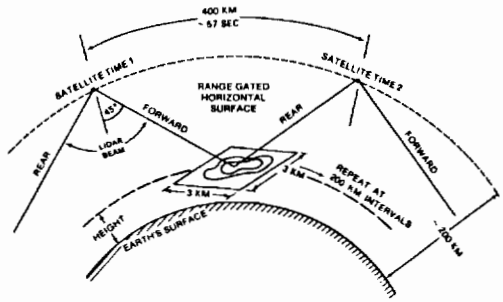

Fig. 3. Conceptual space lidar wind system using aerosol pattern displacement between successive forward and rearward views of same area at constant height. Reprinted from Atlas and Korb (1981).

The conceptual system proposed by Atlas and Korb (1981) provides a sample volume 3 km on a side and 250 meters deep. Each sample consists of two 60 by 60 arrays of backscatter measurements separated by a one minute time interval. These sample arrays are similar to those used in the sector scan data presented by Ferrare (1984): he analyzed data from squares 1 km on a side, consisting of 64 by 64 points, separated by 3-minute time intervals. The similarity of the data sets make it clear that convective boundary-layer wind measurements can be obtained from space-borne aerosol lidar data if the signal to noise ratios are sufficient to allow observation of naturally occurring backscatter inhomogeneities.

In order to estimate signal to noise ratios achieveable from a satellite borne lidar, the following system parameters were assumed:

Transmitted pulse energy	4 Joules
Receiver appeture	1 meter
Recever bandpass	0.1 nanometer
Wavelength	1.06 micron
Beam divergence	0.25 milliradian
Background radiance	$\approx$10 mw $cm^{-1}str^{-1}\mu^{-1}$
Detector quantum efficency	33%
System optical efficiency	$\approx$20%
Backscatter cross section	0.001 km^{-1} str^{-1}
Reciever integration time	300 nanoseconds

These parameters provide a minimum detectable aerosol backscatter fluctuation of 3% to 10% depending critically on the assumed background radiance and the receiver spectral bandpass. Ground based lidar measurements show that fluctuations of this magnitude are nearly always present in the top 20 to 30% of the continental boundary layer. Lower in the boundary layer strong mixed turbulence frequently reduces the fluctuation contrast below this range. Far fewer aerosol fluctuation measurements exist for the free troposphere and inside stable boundary layers; it is expected that the percentage of observations containing aerosol backscatter fluctuations of this magnitude will be considerably reduced under these conditions. A stable atmospheric layer also may support propagating buoyancy waves; under some conditions these wave structures may provide false wind indications. Both the backscatter fluctuation statistics and the influence of wave motions on aerosol displacement wind measurements require further study.

3. CONCLUDING REMARKS

At the present state of knowledge, we believe that satellite borne aerosol backscatter lidar systems could provide global wind measurements in the upper part of convective boundary layer. These measurements should provide accuracies of $\approx$ 1 meter/second and 10 degrees. The measurements would be obtained with horizantal spatial resolutions of a few kilometers and vertical resolutions of 50 to 250 meters. The application of these techniques to the free troposphere, stable boundary layers and other passive tracers (such as water vapor) requires additional study.

REFERENCES

Atlas, D. and C.L. Korb, 1981: Weather and Climate Needs for Lidar Observations from Space and Concepts for Their Realization, Bull. Am. Meteor. Soc., 62, pp. 1270-1285.

Armstrong, R.L., J.B. Mason and T. Barber, 1976: Detection of Atmospheric Aerosol Flow Using a Transit Time Lidar Velocimeter. Appl. Opt., 15, pp. 2891-2895.

Boers, R., E.W. Eloranta and R.L. Coulter, 1984: Lidar Measurements of Mixed Layer Dynamics: Test of parameterized Models of Mixed Layer Growth Rate J. Climate and Appl. Meteor., 23 247-266.

Browell, E.V., A.F. Carter, S.T. Shipley, R.J. Allen, C.F. Butler, M.N. Mayo, J.H. Siviter, Jr., W.M. Hall, 1983: NASA multipurpose airborne DIAL system and measurements of ozone and aerosol profiles, Appl. Opt., 22, No. 4, pp. 522-534.

Derr,V.E., R.E. Cupp, and A. Cohen, 1972: Active wind measurements by lidar. Proceedings of the Fourth Conference on Laser Radar, Tucson, Arizona.

Eigenwillig, E. and H. Fischer, 1982: Determination of Midtropospheric Wind Vectors by Tracking Pure Water Vapour Structures in METEOSAT Water Vapor Image. Bull. Am. Meteor. Soc., Vol. 63, No. 1, pp. 44-58.

Eloranta, E.W., J. King and J.M. Weinman, 1975: The Determination of Wind Speeds in the Boundary Layer by Monostatic Lidar, J. Appl. Meteor., Vol. 14, No. 8, pp. 1485-1489.

Ferrare, R.A., 1984: Lidar Observation of Organized Convection within the Atmospheric Mixed Layer. University of Wisconsin-Madison, Masters Thesis, pp. 204.

Hooper, W.P., 1982: Lidar Observations of the Diurnal Variations of Wind Speeds and Turbulence inside the Planetary Boundary Layer, University of Wisconsin-Madison, Masters Thesis, 160 pp.

Kunkel, K.E., E.W. Eloranta, and S.T. Shipley, 1977: Lidar Observations of the Convective Boundary Layer. J. Appl. Meteor., 16, No. 12, pp. 1306-1311.

Kunkel, K.E., E.W. Eloranta, and J.A. Weinman, 1980: Remote Determination of Boundary Layer Characteristics from Lidar Measurements, J. Atmos. Sci., Vol. 37, No. 5, pp. 978-985.

Melfi, S.H., J. Spinhirne, S-H. Chou and S. Palm, 1985: Lidar Observations of Vertically Organized Convection in the Planetary Boundary Layer, J. Climate and Appl. Meteor., 24, No. 8, pp. 806-821.

Sroga, J.T., E.W. Eloranta and T. Barber, Lidar Measurement of Wind Velocity Profiles in the Boundary Layer, J. Appl. Meteor., 19, No. 5, pp. 598-605.

Sansano, Y., H. Hirohara, T. Yamasaki, H. Shimizu, N. Takeuchi, and T. Kawamra, 1982: Horizontal Wind Vector Determination from the Displacement of Aerosol Distribution Patterns Observed by a Scanning Lidar. J. Appl. Meteor., 21, pp. 1516-1523.

Uthe, E.E., N.B. Nielsen, W.L. Jimison, 1980: Airborne Lidar Plume and Haze Analyzer (ALPHA-1), Bull. Am. Meteor. Soc., 61, No. 9, pp. 1035-1043.

S28-47
84488

COHERENT DOPPLER LIDARS - CURRENT U.S. 9-11 μm SYSTEMS

N93-70327

Freeman F. Hall, Jr.

NOAA/ERL/Wave Propagation Laboratory
Boulder, Colorado 80303

1. INTRODUCTION

To gain a proper perspective of the potential of coherent Doppler lidars for global wind sensing sometime in the future, we need to examine where we are, how we got here, and the expectations for future lidar system development. First we give a brief review of lidar developments leading to our present technology. Next we survey present U.S. infrared systems with particular attention to the pulsed systems since they are the ones that will have sufficient range to operate from satellites. Finally we comment on trends and probable future developments. Only unclassified lidars are considered. The considerable DoD support for classified applications certainly enhances future developments in components and subsystems.

2. BACKGROUND

In an earlier review (Hall, 1983) we pointed out a number of reasons why wind-sensing lidars using CO_2 lasers operating at 10.6 μm are the predominant system type:

(a) Lower spatial coherence losses from turbulence compared with lasers operating at visible or near IR wavelengths

(b) Less bandwidth required to cover the same range of wind velocities

(c) A greater number of photons per watt of transmitted power, thus improving the detection statistics.

(d) High electrical-to-optical power efficiency

(e) Reduced alignment tolerances because of the relatively long infrared wavelengths

(f) Eye safety considerations.

The development and use of pulsed Doppler lidars in the field progressed rather slowly, undoubtedly because there was much pessimism about the effects of turbulence, volume scattering, interferometer alignment feasibility, and data processing. Demonstrations of CW lidars such as those by Huffaker et al. (1967), Bostick (1968), and by Lawrence et al. (1972) helped to remove the lingering doubts of R&D managers/sponsors on wind-measurement feasibility. A number of applications such as measuring wind flow around natural vegetation (Durst et al., 1975), dust devil winds (Schwiesow and Cupp, 1976) and airborne measurements of wind shear (Callan et al., 1980) followed during the late 1970's. These and many other applications were described in the Doppler lidar review paper by Bilbro (1980).

The focused CW Doppler lidars discussed so far are inherently range limited. The backscatter radiation mixes efficiently with the local oscillator radiation only from the volume in the atmosphere on which the transmitting telescope is focused. As the focal distance recedes farther and farther from the telescope, spatial resolution is poorer so that ranges of only several hundred meters are feasible with convenient optical telescope diameters. To overcome this limitation, pulsed lidars were developed.

The system at NASA Marshall Space Flight Center was originally designed to investigate clear-air turbulence some distance in front of aircraft (Huffaker, 1974). This system uses a master oscillator followed by a power amplifier (MOPA) laser chain and with the various modifications and improvements over the years now delivers 14 mJ pulses. This lidar has since been used for many airborne investigations of wind fields such as through mountain passes, in the vicinity of storms, and also from a mobile laboratory trailer (Bilbro et al., 1984).

3. PRESENT STATUS

The next obvious step to improve the pulse power, and thus the range, of Doppler lidars was to progress from the low pressure MOPA configuration to the high gas pressure, transverse excitation, atmospheric pressure or TEA lasers. It remained to be demonstrated that TEA lasers could be made to produce a coherent, chirp-free pulse that could be coupled through a transmit/receive switch without damaging the receiver detector. But after satisfactory chirp was successfully demonstrated at the Canadian Defense Research Establishment (Cruickshank, 1979), the first TEA lidar with a T/R switch for wind measurement was assembled at United Technologies Research Center under contract to NOAA in 1980. The system has since shown a capability for measuring winds within 0.5 m/s at ranges up to 22 km (Hall et al., 1984) and has proved itself a useful atmospheric science research tool.

Interferometer alignment, where the backscattered signal beam must be mixed within diffrac-

tion limits with the local oscillator beam onto the detector, has not been a problem with either the NOAA or the Marshall system. On one occasion the NOAA lidar was trailered from Boulder to Buckley Air National Guard Base, loaded onto the NASA Superguppy aircraft, flown to Edwards Air Force Base, off-loaded (roughly), and trailered on dirt roads for 5 miles. It was found to be in perfect alignment on start-up.

Some of the earlier theoretical treatments of laser beam coherence loss on propagation through atmospheric turbulence overlooked the near compensation of the backscattered radiation returning through the same eddies to the monostatic receiver. We have experienced little signal degradation with the NOAA lidar because of turbulence.

The hybrid laser configuration, where both the low pressure gas, master oscillator and the TEA laser are in the same cavity, is energy limited at some small multiple of the 100 mJ per pulse of the present NOAA lidar. Several laboratories (the Jet Propulsion Laboratory, the NASA Langley Research Center, the Air Force Geophysical Laboratories, and the NOAA Wave Propagation Laboratory) are investigating injection-lock laser configurations to improve the pulse energy. The characteristics of earlier pulsed lidars plus this new breed of coherent CO_2 lidars are summarized in Table 1.

A very real concern for a satellite lidar system is how to handle the wide bandwidth raw data. Almost certainly some onboard data processing will be required. Significant improve-

Table 1. U.S. Pulsed IR Doppler Lidars for Wind/β Measurements

Laboratory	Where housed	Laser type	Energy per pulse	Pulse rep. freq. (Hz)	Data processor/ recorder	Scanner	Wave-length	β cali-bration	Upgrades planned
NASA/MSFC Huntsville, AL	Semi-trailer	Raytheon low pressure MOPA	14 mJ	110	Lassen complex covariance w/vector display	30 cm alt-azi	10.6 μm (P-20)	Ground returns	Injection-locked TEA under study at MSNW
NASA/MSFC Moffett Field, CA	CV990 aircraft	Raytheon low pressure MOPA	14 mJ	110	Lassen complex covariance w/vector display	24 cm fore-aft, or conical 40°	10.6 μm (P-20)	Ground returns	Injection-locked TEA under study at MSNW
NOAA/WPL Boulder, CO	Semi-trailer	UTRC hybrid TEA	100 mJ	10	Lassen complex covariance w/color display	28 cm alt-azi	P-20 R-18 R-20	Sulfur & sandpaper targets	MSNW injection-locked TEA being installed (2 J, 50 Hz)
JPL Pasadena, CA	Lab.	Lumonics TEA injection lock	1-3 J	0.1	HP 1000 model 45	15 cm alt-azi	9.25 μm 10.6 μm	Sulfur, sandpaper, aluminum targets	1 J, 5 Hz planned
AFGL Bedford, MA	Semi-trailer	GE TEA E-beam ionized, injection lock	1 J	50	To be determined	30 cm alt-azi	10.6 μm	Not yet in operation	Balloon-borne system planned
NASA/LaRC Hampton, VA	Lab.	CLS-modified lumonics TEA injection lock	0.75 J	20	To be determined	To be determined	10.6 μm	Not yet in operation	Airborne operation projected

ments have been made in data processing that even now enhance the utility of wind-sensing lidars in field measurement programs. A real-time, pulse pair (really complex covariance) processor was developed for the NASA Marshall lidar in 1980 (Lee, 1981). A similar multilag processor with real-time color display has been used with the NOAA lidar since 1983. Such spectral moment processors reduce the data bandwidth required by a factor of over 1000, demonstrating the future feasibility of satellite telemetry of onboard processed wind field data.

We have found the real-time color displays to be extremely useful in identifying events that warrant more detailed scans or immediate evaluation during field experiments. For example, in an experiment monitoring down-canyon winds the lidar could help position balloon-tethered probes at the proper level to find shear interfaces and to find the times when smoke releases would show the desired wind circulation patterns for photography. On the one earlier occasion when the NOAA and NASA-Marshall lidars performed coordinated scans during the Joint Airport Weather Studies (JAWS) experiment, the real-time processing in both lidars helped identify those time-segments when dual lidar (thus full 2D wind field depiction) data sets were obtained. So far this is the only dual Doppler lidar experiment, but there will undoubtedly be others in the future.

4. TRENDS AND PROBABLE FUTURE DEVELOPMENTS

The present generation of joule-energy level coherent lasers now entering field use points the way to the next step in pulsed coherent lidar system development. Simultaneously, the success of the airborne NASA-Marshall system, and the automatic cavity tuning of the new NOAA lidar, demonstrate the feasibility of removing intensive hands-on control of the systems. WINDSAT analyses (Huffaker et al., 1980) indicate that multi-joule lidars will be required for global wind sensing, but such energy levels are now less than an order of magnitude beyond energies achieved with the newest systems. The NASA Langley Research Center work indicates that catalytic conservation of CO_2 (Hess et al., 1985) may extend the lifetime of lasers to the durations required for satellite application. Over the next few years these "new generation" lidars will undoubtedly be used in cross-calibration and in both surface-based and airborne measurements of the aerosol-scattering characteristics in the 9-11 μm spectral region. The enhanced (x3) backscatter at 9.25 μm as compared with 10.6 μm for 5 km altitude aerosols, as measured at JPL, points to the necessity for β measurements throughout the 9-11 μm band (Menzies et al., 1984). This interesting observation will be supplemented when the Marshall 9.11 μm CW lidar flies on the CV 990 sometime next year. With continued support for the ongoing programs at funding levels at or only slightly beyond those now available, the lidar community will obtain the experience and data required to design and build the next generation of lidars for space shuttle or free-flying satellite experiments. This experience will lead to the possibility of an operational Doppler lidar wind sensor in the foreseeable future.

REFERENCES

Bilbro, J. W., 1980: Atmospheric laser Doppler velocimetry: an overview. Opt. Engr., 19, 533-542.

Bilbro, J., G. Fichtl, D. Fitzjarrald, M. Krause, and R. Lee, 1984: Airborne Doppler lidar wind field measurements. Bull. Amer. Meteorol. Soc., 65, 348-359.

Bostick, H. A., 1968: Experiments with a CO_2 laser radar system. Proc. 13th Annual Tech Symp., SPIE, 351-356.

Callan, R., R. Foord, J. Hill, R. Jones, G. Jones, D. Laycock, A. Parkin, J. M. Vaughan, D. V. Willetts, and A. Woodfield, 1980: Development of an airborne CO_2 laser velocimeter. Coherent Laser Radar for Atmospheric Sensing, Technical Digest, Optical Society of America, Washington, D.C. pp. ThB2-1 - ThB2-3.

Cruickshank, J. M., 1979: Transversely excited atmospheric CO_2 laser radar with heterodyne detection. Appl. Opt., 18, 290-293.

Durst, F., M. Zare, and G. Wigley, 1975: Laser-Doppler anemometry and its application to flow investigations related to the environment of vegetation. Bound.-Layer Meteorol., 8, 281-322.

Hall, F. F., Jr., 1983: Coherent Doppler lidars for wind sensing in the atmosphere. Optical Techniques for Remote Probing of the Atmosphere. Technical Digest, Optical Society of America, Washington, D.D., pp. TuB3-1-TuB3-4.

Hall, F. F., Jr., R. M. Huffaker, R. M. Hardesty, M. E. Jackson, T. R. Lawrence, M. J. Post, R. A. Richter, and B. F. Weber, 1984: Wind measurement accuracy of the NOAA pulsed infrared Doppler lidar. Appl. Opt., 23, 2503-2506.

Hess, R. V., P. Brockman, D. R. Schryer, I. M. Miller, C. H. Bair, B. D. Sidney, G. M. Wood, B. T. Upchurch, and K. G. Brown, 1985: Technology assessment of high pulse energy CO_2 lasers for remote sensing from satellites. NASA Tech. Memo. 86415, Langley Research Center, Hampton, VA, 41 pp.

Huffaker, R. M., E. Rolfe, and A. V. Jelalian, 1967: Laser Doppler techniques for remote wind velocity measurements. NASA TM X-53711, Specialist Conference on Molecular Radiation, MSFC, Huntsville, AL, 328-358.

Huffaker, R. M., 1974: CO_2 laser Doppler systems for the measurement of atmospheric winds and turbulence. Atmospheric Technology, NCAR, Boulder, CO (No. 6), 71-76.

Huffaker, R. M., T. R. Lawrence, R. J. Keeler, M. J. Post, J. T. Priestley, and J. A. Korrell, 1980: Feasibility study of satellite-borne lidar global wind monitoring system. Part II. NOAA Tech. Memo. ERL WPL-63, Boulder, CO, 124 pp.

Lawrence, T. R., D. J. Wilson, C. E. Craven, I. P. Jones, R. M. Huffaker, and J. A. L. Thomson, 1972: A laser velocimeter for remote wind sensing. Rev. Sci. Inst., 43, 512-518.

Lee, R. W., 1981: Digital processor for coherent CO_2 systems. Physics and Technology of Coherent Infrared Radar, SPIE Vol. 300, 196-199.

Menzies, R. T., M. J. Kavaya, P. H. Flamont, and D. A. Haner, 1984: Atmospheric aerosol backscatter measurements using a tunable coherent CO_2 lidar. Appl. Opt., 23, 2510-2517.

Schwiesow, R. L., and R. E. Cupp, 1976: Remote Doppler velocity measurements of atmospheric dust devil vortices. Appl. Opt., 15, 1-2.

COHERENT LASER RADAR - CURRENT EUROPEAN SYSTEMS

J. Michael Vaughan

Royal Signals and Radar Establishment
Malvern, Worcestershire, WR14 3PS, UK

1. INTRODUCTION

Coherent laser radar systems at 10 μm have been investigated in Europe for well over a decade. In the past few years the level of activity has increased rapidly and work is now in progress on systems and components at a large number of research institutions and industrial firms. Some of the principal organisations now involved are shown in Table 1:

Table 1. PRINCIPAL EUROPEAN CENTRES

France:	ONERA: Crouzet, SAT, CGE
	CNES/CNRS
W. Germany:	DFVLR, Siemens, MBB Batelle Institute
Sweden:	NDRI
UK:	RSRE/RAE
	GEC Avionics, Ferranti, Barr & Stroud, Cossor, (Edinburgh Instruments, Plessey, Mullard, MESL/RACAL, EEV) Hull University
Netherlands:	TNO Laboratory

In Table 1 the underlined organisations have had specific involvement with wind and aerosol measuring lidars; those shown in parenthesis are largely concerned with components. The strength of any system technology is very dependent on the underlying device and component technology. Section 2 of this review outlines some of the particular European strong points in device physics and technology.

In addition to wind measurement systems, much work has been done on other applications of coherent laser radar including ranging, imaging and coherent DIAL investigations such as those at Hull University. In order to provide a broad picture, some of these other applications are also outlined briefly in Section 3.

An indication of current European interest may be gauged from the recent 3rd Coherent Laser Radar Meeting (3CLRM) held in Malvern in July 1985. Equipment, both systems and components, was exhibited by 7 industrial firms and of the 135 attendees 103 were from European organisations; 33 of the 61 presenting papers were of European origin. The present brief review draws heavily on a number of the papers recorded in the Proceedings of the 3rd Topical Meeting on Coherent Laser Radar, (1985); more detailed information should be sought directly from the papers themselves or from the authors.

2. DEVICE PHYSICS AND TECHNOLOGY

The following brief notes outline a few of the many devices and components for coherent laser radar either commercially available or under active study in Europe.

2.1 Lasers

Research in CO_2 laser physics of both CW and pulsed has been strongly funded. A wide range of CW lasers, both conventional cavity and waveguide, and RF and DC excited are now available from several manufacturers. Many of these have been designed for severe, high vibration environments with long guaranteed lifetimes. A selection of one manufacturer's range is illustrated in figure 1 - from Paper X.1 in the Proceedings (1985) (See also papers V.1, V.2, V.4, VI.2, X.2 and X.4.)

Fundamental studies of pulse laser physics, in particular laser-induced effects of frequency chirping (LIMP), have been pursued by Willetts and Harris at RSRE. In paper V.6 of the Proceedings (1985) they describe a high energy oscillator design with output pulse energy of 1.1 J and the LIMP effect reduced to less than 200 kHz chirp in a 5 μs pulse. Further detailed accounts of this work may be found in Willetts and Harris (1982, 1984).

Valuable progress in developing CO_2 oxidation catalysts for extending pulse laser life time was also reported by Willetts (paper V.3 of Proceedings 1985). Different techniques have been investigated for preparation of the tin (IV) oxide base and subsequent impregnation with platinum and palladium salts. A selection of different forms derived from the Universal Matthey Produces (UMP) process in shown in figure 2. With this, and material available in monolith form from the AERE Harwell process, activities as high as 3×10^{-2} ℓ sec^{-1} gm^{-1} have been demonstrated. Sealed TEA CO_2 lasers containing these catalysts have operated satisfactorily for up to 2×10^7 pulses.

2.2 Modulators

Considerable progress in improving the

Figure 1. A selection of CO_2 waveguide lasers from 2 to 20 Watts [from Ross and Holt, paper X.1 , Proceedings, 1985]

(a) Extruded UMP CO oxidation catalyst

(b) UMP CO oxidation catalysts, various geometries

(c) 13 mm UMP catalyst wafers cemented to metal plate

(d) 13 mm UMP catalyst wafers indium soldered to metal cups

Figure 2. Forms of oxidation catalysts [from Willetts, paper V.3, Proceedings 1985]

performance of germanium acousto-optic modulators has been achieved by Fox et al. of the Philips Research Laboratories (paper VI.5 of Proceedings 1985). These improvements include (a) increased optical power handling, (b) reduced acoustic back-reflection level and (c) easier optical alignment. Figure 3 shows one of their modulator packages, including focussing lenses and driver amplifier, available at centre frequencies of 60 to 100 MHz.

2.3 Detectors

High sensitivity detectors marketed by SAT (France) and Mullard (UK) for 10 μm heterodyne operation over a large bandwidth have been notably successful. Recent work at Mullard has investigated operation with thermoelectric cooling (paper VI.4, Proceedings 1985). A bandwidth of 100 MHz with a heterodyne NEP of better than 2×10^{-19} W Hz^{-1} has been demonstrated. The p-type CMT photoconductor device is housed in an engineered encapsulation with integral electronics and electromagnetic screening for optimum performance.

3. COHERENT LASER RADAR SYSTEMS

For convenience, the following review is grouped by nation or institution and, in the space available, is necessarily selective. It must be understood that it has not been possible to include much excellent, innovative work from several other centres.

3.1 France

A dual scanning CW system has been built by the Crouzet corporation and flown in a helicopter. Ground and airspeed data are obtained; signal processing is by wideband surface acoustic spectrum analysis. System weight is approximately 200 kg.

A joint program has recently been started by CNES and CNRS for the application of a coherent pulsed CO_2 Lidar to meteorology and described by P. H. Flamant, A. Chedin and E. Megie (paper I.3, Proceedings 1985). A ground-based lidar is now under development as a first step toward an airborne system.

3.2 Netherlands

Work on an AM-coded coherent rangefinder has been conducted at the TNO Laboratories; ranging performance to 5 km has been reported (a useful general account of ranging and imaging instruments worldwide may be found for example in Hulme, 1982).

3.3 Sweden

Extensive investigations (for example, Steinvall et al., 1983; Renhorn et al., 1983) with coherent laser systems at 10 μm have been conducted at the National Defence Research Institute (NDI). In paper I.2 (Proceedings 1985) Steinvall and his colleagues outlined their work including an FMCW laser radar test bed. Figure 4 shows range-gated images obtained with this system. A pulse coherent system has also been studied to give greater range resolution. In other work, target and terrain signatures have been investigated, together with atmospheric effects and theoretical studies of a computer model for an imaging laser radar. A multi-function CO_2 laser radar is presently under construction incorporating a programmable waveguide laser in the transmitter (paper X.2, Proceedings 1985).

3.4 West Germany

A wide ranging programme of measurements with a CW system has been under way at DFVLR for some years (for example, Kopp et al., 1984; Werner et al., 1984). This system incorporates an 8-Watt cavity laser, 30 cm Cassegrain transmitter, and SAW signal processing built by GEC Avionics (Borehamwood). Several technical innovations have been investigated including use of an optical amplifier, and homodyne to heterodyne conversion by use of transverse mode spacing (paper VI.2 and VI.3, Proceedings 1985). The fast data analysis and computing facility developed for the laser radar has been described by Werner (paper VIII.1 Proceedings 1985) and incorporates special pattern recognition procedures (Kopp et al., 1984). These have been extensively applied and include for example measurement of velocity profiles and transport of wake vortices generated by heavy landing aircraft at Frankfurt airport. In an interesting deployment the equipment was set up on a North Sea research platform (paper XII.2, Proceedings 1985). Wind profiles were measured at a range of heights and distances (see figure 5) in order to compare and adjust satellite-borne microwave sensor wind field data derived from wave height and direction.

A notable application of CO_2 coherent laser radar has been developed in a collaborative project by DFVLR and the Battelle Institute (paper IX.2, Proceedings 1985). They found good characterisation of rock and soil samples by comparing the backscatter ratio of 9.2 μm/9.6 μm returns to that of 10.2/10.6 μm returns. In preliminary work a 2-laser system was flown and obtained data for different wavelength pairs. Following this flight a four laser system named LIMES (Lidar Multispectral scanner Earth Observation System) is now under construction. The optical arrangement is shown in figure 6. Since the Doppler shifts at each wavelength differ by more than 5% from each other, signal processing can be carried out in a single frequency selective device such as a surface acoustic wave analyser.

3.5 UK

An account of earlier work on ranging and imaging in the UK may be found for example in Hulme (1982). A high PRF 10-μm pulsed coherent laser rangefinder was described by Martin of GEC Avionics, Borehamwood (paper III.3, Proceedings 1985) and is shown in figure 7. Detailed studies of SNR and signal variance with range have been made. A compact FMCW laser radar build at RSRE for range and velocity measurement was described by Brown et al (paper III.2, Proceedings 1985); imaging and vibration studies with a chirp system were described by Constant et al (paper III.4, Proceedings 1985).

The thrust of the work programme has been to build compact robust and reliable equipments,

Figure 3. Acousto-optic modulator package, type No. AOM100, complete with focussing lenses and driver amplifier
[from Fox, Nicholls and Simmons, paper VI.5 , Proceedings 1985]

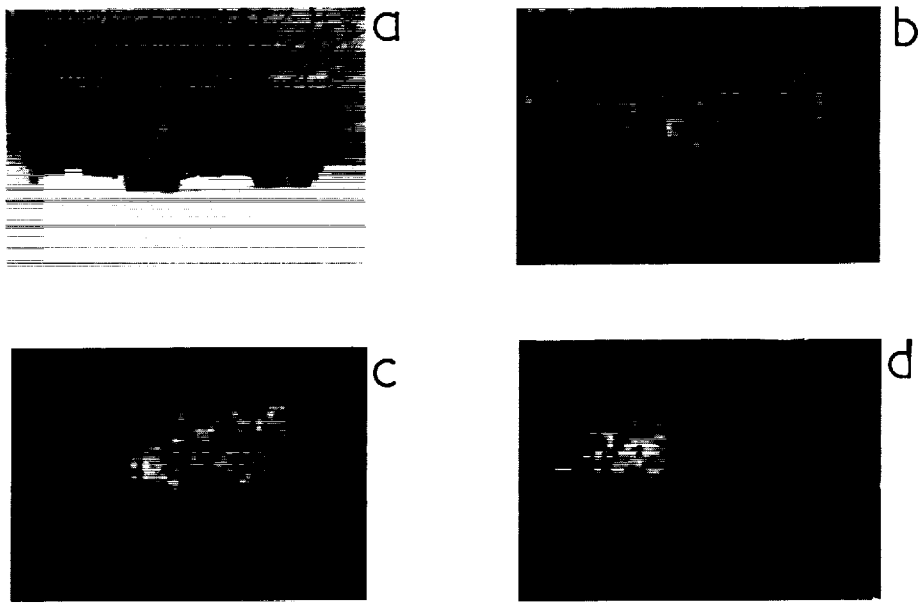

Figure 4. Example of range gated image. Distance 1200 m
(a) Telephoto showing a truck and a jeep
(b) Laser radar intensity image of the scene in (a)
(c) and (d) show range gated images with the range interval containing the truck and the jeep respectively
[from Letalick, Renhorn and Steinvall, paper I.2
Proceedings 1985]

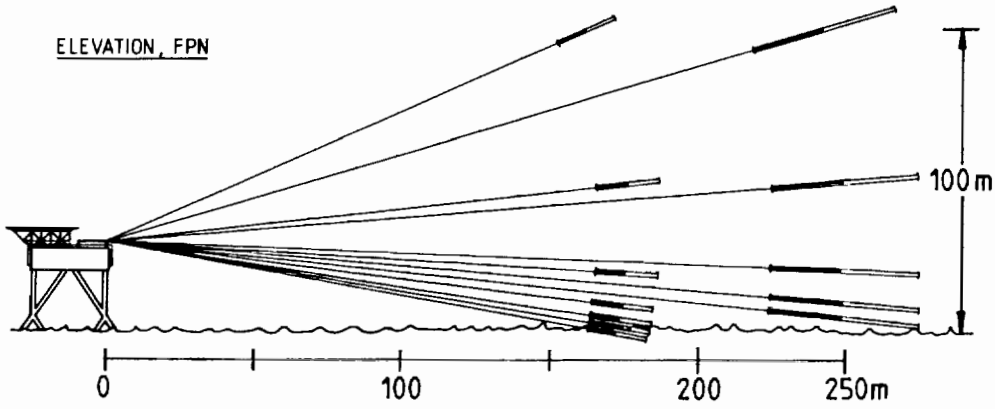

Figure 5.
Installation of laser anemometer on a North Sea platform with indicated probe volumes [from Werner, Kopp and Biselli, paper XII.2 - Proceedings 1985]

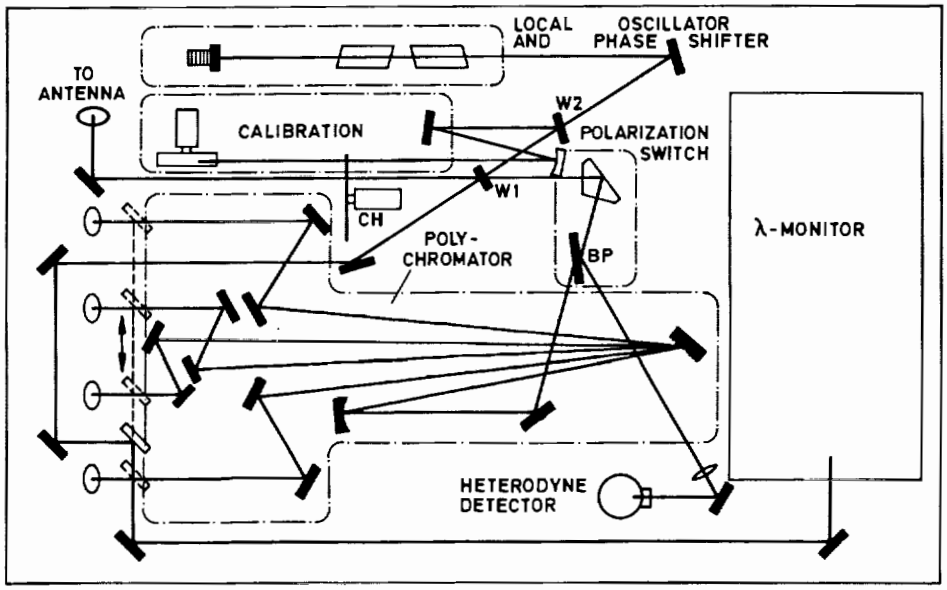

Figure 6.
Optical arrangement of the 4-laser LIMES sensor [from Lehmann and Wieseman, paper IX.2, Proceedings 1985]

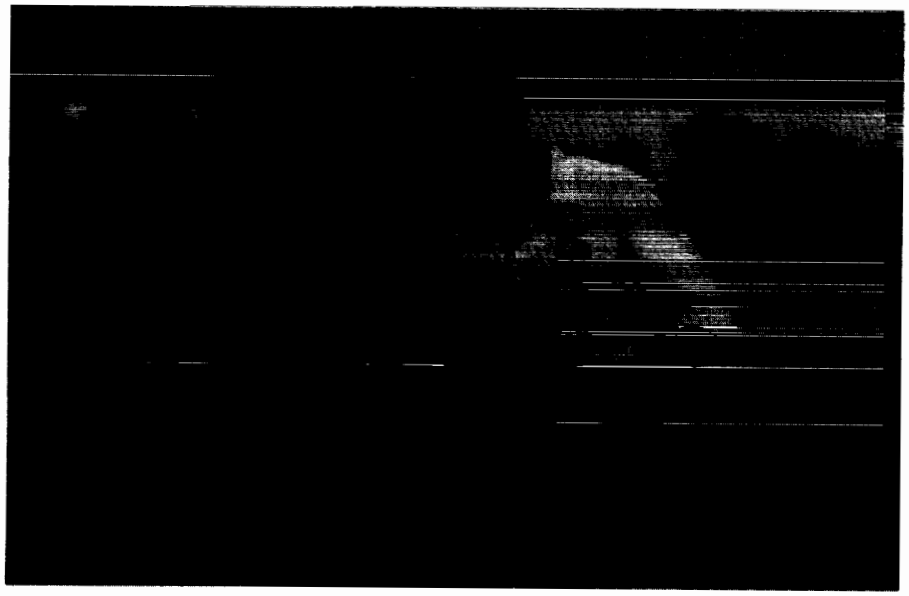

Figure 7.
A high PRF 10 μm pulse coherent laser rangefinder [from Martin, paper III.3 - Proceedings 1985]

operating at optimum sensitivity and to carry out assessment of system performance. This is exemplified in the Laser True Airspeed System (LATAS) built at RSRE and installed in the HS125 research aircraft at RAE (Bedford). Over four years of flight trials experience has now been accumulated. The equipment and performance has been described in several publications (for example Woodfield and Vaughan, 1983, 1984), it incorporates a 4-Watt CW waveguide laser, Joule-Thompson cooled wide band detector, SAW signal processing and digital integration of spectra. A block diagram is shown in figure 8. The optics head is enclosed in the unpressurised nose of the aircraft, the signal processing and recording in the cabin. Test flying has been conducted in a wide variety of conditions in northern Europe at altitudes to 13 km, and also during the Joint Airport Weather Studies (JAWS) project in Colorado in 1982. Figure 9 shows spectra of aerosol return in clear and relatively calm air and figure 10 shows a sequence of recordings selected at 2-second intervals during passage of a thunderstorm microbust. Figure 11 shows the change of airspeed during this passage with a windshear approaching 50 knots in 6 seconds. In addition to airspeed investigation much data has been accumulated on the variation of backscatter in the atmosphere (e.g. fig 12). A brief outline summary of these data are shown in table 2.

Table 2. SUMMARY OF BACKSCATTER MEASUREMENTS [$\beta(\pi)$ in m^{-1} sr^{-1}]

UK	(a) Summer - usually > $10^{-10}m^{-1}$ sr^{-1} to 10 km
	(b) Winter - often remarkably clear above inversions but usually $\gtrsim 10^{-10}$ to 6 km and $\sim 10^{-10}$ above.
COLORADO - JAWS	Summer 1982 $\gtrsim 10^{-10}$ to 13 km
ARCTIC	4 Flights in Summer 1982 - very variable with haze layers at $\sim$ 8 km
GIBRALTAR	(a) Summer - 2 flights: 5-10 x 10^{-10} to 12 km including haze layers $\gtrsim 10^{-8}$ at 11 km and a few thin layers $\sim 10^{-10}$ at 5 km
	(b) Winter - 2 flights: $\gtrsim 10^{-10}$ to 5 km $\gtrsim 4 \times 10^{-11}$ 5-10 km

Perhaps the most encouraging aspect of the LATAS programme has been the reliability and robustness of the equipment. During one period of 22 months, including the JAWS exercise, the optics head in the nose of the aircraft was never opened or removed. Periodic calibration checks showed no loss of performance. On fifteen separate occasions the equipment has been demonstrated in flight to visitors without failure. After four years a recent stand down period has been due to malfunction of power supply and digital electronics in the integrator; the so-called "high risk" optical and laser equipment remains in good order.

4. CONCLUDING REMARKS

European work has for the most part concentrated on the use of CW laser radars. Nevertheless, the performance achieved in many systems establishes the increasing maturity of the field and a degree of reliability that may reasonably be extrapolated to yet more complex and pulsed systems. In summary

(1) European CO_2 laser coherent radar is very active with increasing involvement of firms and institutions.

(2) Particular strengths are evident in component technology including:

   (a) The Range of CW lasers that are available.

   (b) Pulse stabilisation and lifetime (catalyst technology)

   (c) Detectors, modulators and SAW signal processing

(3) Robustness and reliability has been demonstrated in several systems - most notably in the air by the RSRE/RAE LATAS over 4 years of flight trials.

ACKNOWLEDGEMENT

The author is indebted to many colleagues for discussions and information including D.V. Willetts, H.M. Lamberton and P.H. Davies (RSRE), B. Rye and D. Hall (Hull University), C. Lennon (GEC Avionics), I. Ross (Ferranti), P. Flamant (CNRS), Ch. Werner (DFVLR) and O. Steinvall (NDRI). As always any errors or omissions are the responsibility of the author.

REFERENCES

Proceedings 3rd Topical Meeting on Coherent Laser Radar, 1985: Technology and Applications. Held at Malvern, UK July 1985, under auspices of the IOP, CLAS-AMS, IRC; the OSA was a Co-operating Society for the Meeting. (Copies available from the Treasurer, Dr D.V. Willetts, RSRE, Malvern.)

Hulme, K. F. (1982): Infrared Phys. 25, 457-66 (1985): Opt. Laser Tech. 18, 213-5

Kopp, F., Schwiesow, R. L. and Werner, Ch. (1984) J. Climate and Appl. Meteor., 23, 148.

Kopp, F., Bachstein, F. and Werner, CH. (1984). Appl. Opt. 23, 2488.

Renhorn, I., Steinvall, O., Letalick, D., Gullberg, K., Claesson, T. and Widen, A. (1983): SPIE Vol. 415, p39.

Steinvall, O., Bolander, G. and Claesson, T. (1983): Appl. Opt. 22, 1688

Werner, Ch., Kopp, F. and Schwiesow, R. L. (1984) Appl. Opt. 23, 2482

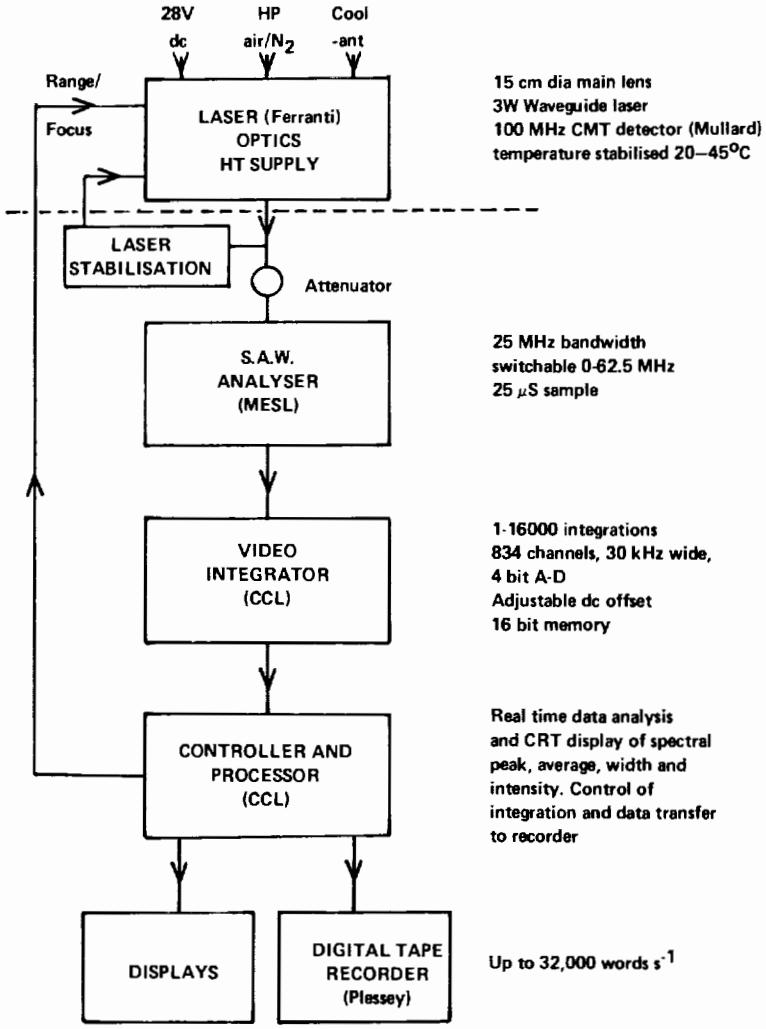

Figure 8.
Block diagram of the RSRE/RAE
LATAS airborne equipment

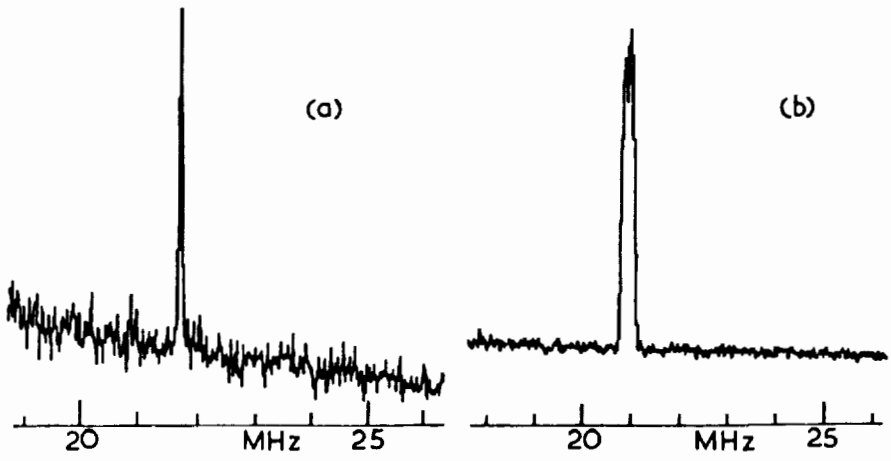

Figure 9. Doppler spectra in the atmosphere recorded with LATAS. Set range 100 m, 25 ms integration
(a) height 5000 ft, the peak frequency corresponds to 225.2 knots
(b) height 960 ft, mean frequency corresponds to 215.0 knots
Note the increased width due to turbulence of ~ 5 knots

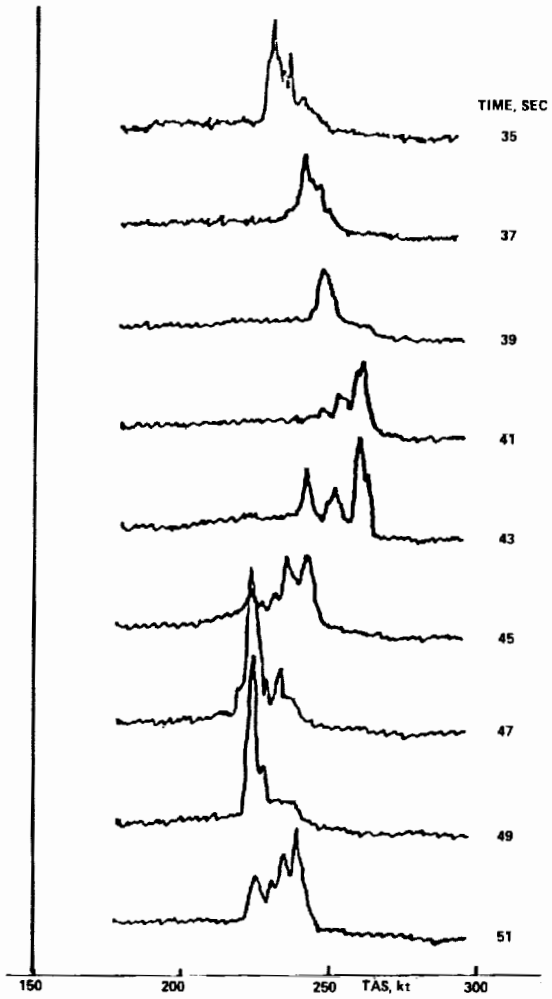

Figure 10. Passage through a thunderstorm microburst showing LATAS spectra at 2 second intervals
[Flt 792, 14 July 1982, JAWS trial]

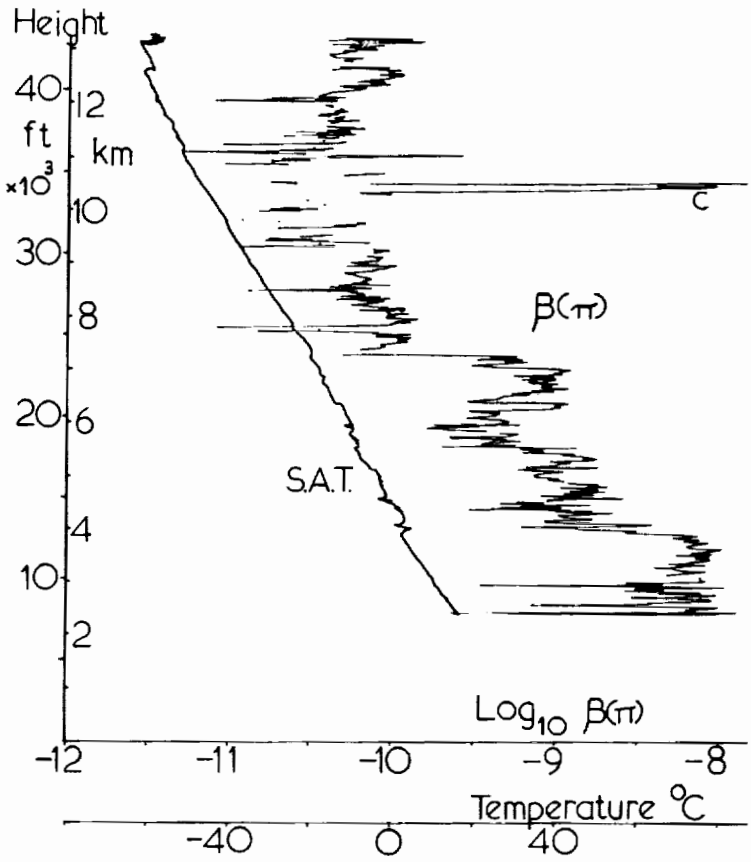

Figure 12. Atmospheric backscattering coefficient $\beta(\pi)$ sr^{-1} m^{-1} and static air temperature SAT versus indicated height in ft and km (ASL). The strong return at (c) at 33000 ft later in the day became a visible layer of cirrus cloud.
[Flt 772, am 1 July 1982, from Jefferson County Airport Colorado, surface visibility > 80 miles]

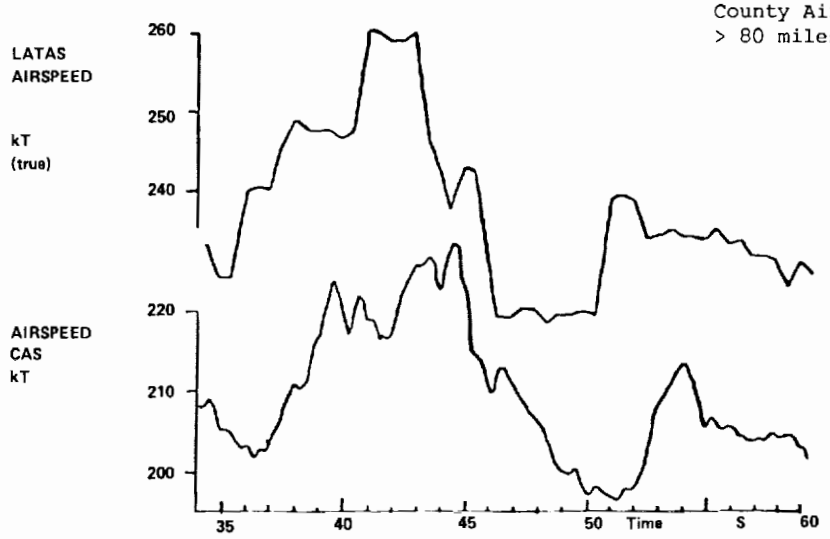

Figure 11.

Passage through a thunderstorm microburst showing the response of LATAS and the subsequent on board airspeed. Note the 2-3 second lead of the LATAS airspeed.
[Flt 792, 14 July 1982 JAWS trial]

Willets, D. V. and Harris, M. R. (1982): J. Phys. D, 15, 51-67.

Willetts, D. V. and Harris, M. R. (1984): Opt. Comm. 49, (2), 151-4.

Woodfield, A. A. and Vaughan, J. M., July (1983): Airspeed and Wind Shear Measurements with an Airborne CO_2 Continuous Wave Laser. RAE Technical Report No. 83061.

Woodfield, A. A. and Vaughan, J. M. (1984): AGARDOGRAPH No. 373, Flight Test Techniques, paper 22.

COHERENT DOPPLER LIDAR AT 1.064 MICRONS

Robert L. Byer and Thomas J. Kane

Ginzton Laboratory
Stanford University
Stanford, California, USA

1. INTRODUCTION

The Nd:YAG laser operating at 1064 nm may offer advantages over the 10.6 micron CO_2 coherent Doppler Lidars which have been extensively developed and applied to atmospheric wind measurements. The velocity and range resolution accuracy are improved at 1064 nm for measurements made at the same signal to noise ratio (Kane and Byer, 1984). However, backscatter from the atmosphere is greater at 1064 nm than at 10.6 microns so that the velocity resolution at a given depth resolution is improved.

The development of coherent Lidar at the 1064 nm wavelength began in 1980 with the initial goal of demonstrating that the solid state laser medium could operate at sub-megahertz line widths for the 5 msec round trip time required for the transmission and detection of a coherent signal from an 800 km altitude orbiting satellite. The research led to the demonstration of a flashlamp-pumped 100 kHz line width Nd:YAG oscillator (Sun and Byer, 1982).

The success of the flashlamp-pumped oscillator led to the understanding that an all solid state oscillator might be possible using laser diodes (LD) as the pump source. Work was initiated along this line and almost immediately led to the successful demonstration of an efficient, stable, all solid state Nd:YAG oscillator (Zhou et al., 1985). The early success has been followed by extension of the concept to the LD pumping of a ring oscillator (Kane and Byer, 1985a) and to the design and development of the Stanford Coherent Lidar System (Kane and Byer, 1985b).

2. THE STANFORD COHERENT LIDAR SYSTEM

The coherent Lidar system that has been designed and is now being tested is shown in Figure 1. The system consists of a LD-pumped master oscillator, a LD-pumped reference oscillator that is offset locked to the master oscillator, a flashlamp pumped linear amplifier with 60 dB of gain, a transmitting telescope, and a single mode fiber receiver and beam combiner prior to the InGaAs detector. The system schematic, illustrated in Figure 1, has all of the components of a traditional coherent Radar system that operates in the microwave region of the spectrum (Skolnik, 1962).

We have initiated testing of the system components. The LD-pumped ring oscillator operates at 25% slope efficiency when pumped by a multistripe Spectra Diode Laboratory diode laser. Up to 25 mW of cw output power has been obtained from this source in a single axial and single spatial mode. Recently, the spectrum of the laser oscillator has been measured by frequency comparison against the LD-pumped local oscillator source. The two oscillators were offset locked at 40 MHz and the beat frequency measured over time. Initial results show that the oscillators are stable to within 40 kHz over minutes of operation. The residual drift is due to temperature changes of the LD-pumped oscillators. Thus, these LD-pumped oscillators have adequate coherence for Doppler measurement of velocity to less than 2 cm per second.

A key component of a Coherent Doppler Radar system is the power amplifier. We have designed and demonstrated the first 60 dB gain linear power amplifier in Nd:YAG (Kane et al., 1985b). The power amplifier uses angular multiplexing in a slab geometry design to implement the high gain without excessive feedback to the oscillator. A permanent magnet Faraday isolator is also used to eliminate feedback to the oscillator. The amplifier uses a single crystal of Nd:YAG 4 mm by 4 mm by 100 mm in length pumped by a single flashlamp. The design does allow the use of LD-pumping in the future when LD-arrays become available at reasonable cost. The power amplifier operates in a linear regime and is not expected to broaden the oscillator spectrum.

For future wind-sensing systems that require greater transmitter power, a power amplifier that boosts the power levels from the present levels of 3-5 kW to levels of 3-5 MW must be added. We expect that such a power amplifier will take advantage of the slab configuration (Eggleston et al., 1984; Kane et al., 1985a) and that it will be, in the future, LD-array pumped.

The operation of the coherent Doppler Lidar system at 1064 nm offers the potential of using single mode fibers for the mixing of the received signal with the local oscillator. We have implemented a fiber mixing circuit. The use of fibers greatly reduces the alignment problems associated with the use of mirrors and beamsplitters in traditional coherent detection approaches.

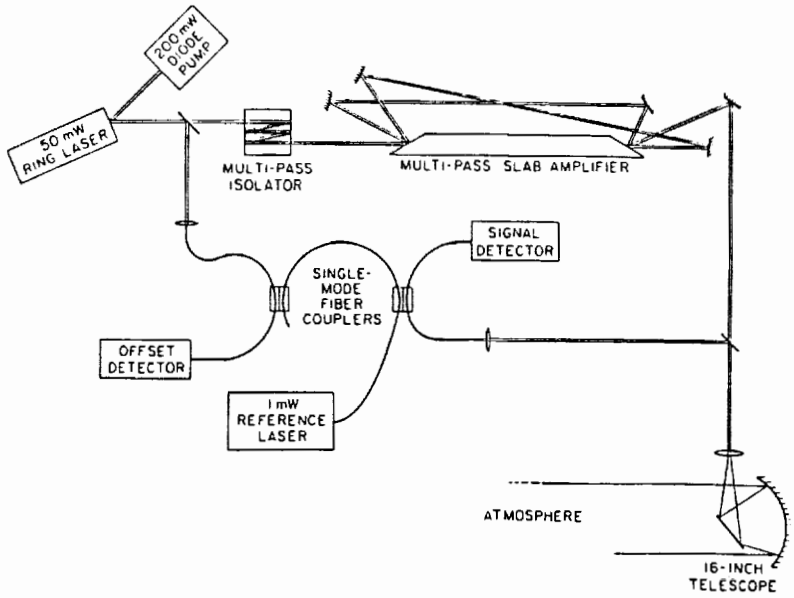

Figure 1. Coherent Lidar anemometer shown schematically.

To date we have detected return signals from local hard targets and have confirmed that the returned signals are coherently mixed with the local oscillator on the detector. The local oscillator power required to achieve shot noise operation of the InGaAs detector is less than 1 microwatt. The system is assembled and undergoing final component testing. To date all the subsystem components have operated as designed. We expect to achieve operation of the entire system as a coherent Doppler Lidar before the end of the year.

3. CONCLUDING REMARKS

The rapid development of laser diodes offers the opportunity to design an all solid state transmitter for coherent Doppler Lidar by using Nd:YAG as the gain medium. We have demonstrated that the components of such a system operate as expected. We believe that LD-pumped solid state laser oscillators and amplifiers offer an approach to space qualified transmitters with coherence, power, efficiency, and operating lifetime necessary to meet satellite platform requirements.

4. REFERENCES

Eggleston, J.M., T.J. Kane, K. Kuhn, J. Unternahrer, and R.L. Byer, 1984: The Slab Glass Laser-Part I: Theory, IEEE J. Quant. Electr.,QE-20, 289.

Kane, T.J., and R.L. Byer, 1984: The Potential for Coherent Doppler Wind Velocity Lidar Using Neodymium Lasers, Appl. Optics, 23, 2477.

Kane, T.J., and R.L. Byer, 1985a: Monolithic, Unidirectional, Single Mode Nd:YAG Ring Laser, Optics Letters, 10, 62.

Kane, T.J., and R.L. Byer, 1985b: Coherent Lidar Anemometry Using Nd:YAG Lasers: System Design and Performance, presented at the 3rd Conference on Coherent Laser/Radar: Technology and Applications, Malvern, Worcs. England.

Kane, T.J., J. Eggleston, and R.L. Byer, 1985a: The Slab Geometry Laser-Part II: Thermal Effects in a Finite Slab, IEEE J. Quant. Electr., QE-21, 1195.

Kane,T.J., W. Kozlovsky, and R.L. Byer, 1985b: High Gain Multi-pass Amplification in a Single Nd:YAG Slab presented at the Conference on Lasers and Electro-optics, Baltimore, Maryland.

Skolnik, M.I., 1962: Introduction to Radar Systems, McGraw-Hill, New York.

Sun, Y.L., and R.L. Byer, 1982: Sub-Megahertz Frequency Stabilized Nd:YAG Oscillator, Optics Letters, 7, 408.

Zhou, B.K., T.J. Kane, G. Dixon, and R.L. Byer, 1985: Efficient Frequency Stable Laser Diode Pumped Nd-YAG Laser, Optics Letters, 10, 62.

THE EFFECTS OF WAVELENGTH ON COHERENT DOPPLER LIDAR PERFORMANCE

T. R. Lawrence

NOAA/ERL/Wave Propagation Laboratory
Boulder, Colorado 80303 USA

1. INTRODUCTION

Hitherto, long-range wind-sensing coherent (heterodyne) lidars have utilized CO_2 lasers (operating at a 10-μm wavelength) since these were the only high-power single-mode (spatial and axial) pulsed sources available. This property ensures temporal coherence over the required spatial resolution, e.g., the pulse length. Recent developments in Nd:Yag lasers makes possible the consideration of a 1.06-μm source (Kane et al., 1984). The relative merit of operation at various wavelengths is a function of system parameter, backscattering cross section, signal processing, beam propagation, and practical and eye safety considerations. These factors are discussed in the context of a global wind-sensing coherent lidar.

2. WAVELENGTH DEPENDENCE OF THE VARIOUS FACTORS

2.1 System Parameters

The sensitivity or signal to noise ratio (SNR) equation of a coherent lidar is given by the expression (Thomson and Dorian, 1967):

$$SNR = \frac{\pi\eta J\beta c D^2 \exp(-2kL)}{8h\nu B[L^2 + (\frac{\pi D^2}{4\lambda})^2 (1 - \frac{L}{f})^2]}$$

where

- η system efficiency including the detector quantum efficiency
- $h\nu$ photon energy
- c velocity of light
- D exp(-2) diameter of the transmitted Gaussian beam
- λ laser wavelength
- J transmitted pulse energy
- β aerosol backscattering coefficient
- L lidar range
- k extinction coefficient
- f range to geometric focus
- B electronic bandwidth

and applies to an untruncated Gaussian apodization of the transmitter telescope. The quantities J/hν (the number of photons emitted by the laser) and 1/B(the inverse of the system electronic bandwidth) are each proportional to the wavelength,the first by virtue of the smaller photon energy and the second because of the smaller Doppler shifts at the longer wavelengths. The product of this wavelength squared dependence and that of the backscattering coefficient is thus a good "Figure of Merit" for assessing the wavelength dependence of coherent lidars and is explored in Section 2.2. Deferring discussion of the beam extinction (the exponential term) until Section 2.4 one is left with the free space antenna gain terms. In a space lidar the target will always be in the far-field of the telescope such that the second term in the denominator is negligible compared with L^2 and thus the antenna gain term becomes independent of wavelength. However, in assessing potential space system capabilities by extrapolating from the demonstrated performance of ground based systems, it should be noted that for ground based systems, a larger wavelength has a considerable SNR and operational advantage because of antenna gain considerations. Figures 1 and 2 summarize this advantage. Plotted in Figure 1 is the gain improvement ratio for 10.6 over 1.06 μm against range for several typical telescope diameter/focal range combinations. It is noted that this gain is considerable except for the focal range (where the gains match) or where the telescope diameter is small. There is a considerable penalty in using small optics, however, as shown in Figure 2 (due to the D^2 factor in the numerator). Accommodation for truncation of the transmitted Gaussian beam reduces this advantage because the gain functions are not as selective about the focus, but the effect remains a factor to be considered.

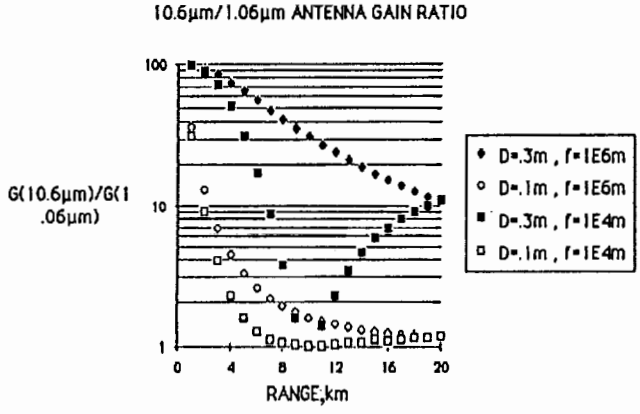

Figure 1. Predicted ratio of 10.6 μm to 1.06 μm antenna gain for some typical ground-based system parameters. (D, telescope diameter; f, geometric focal range.)

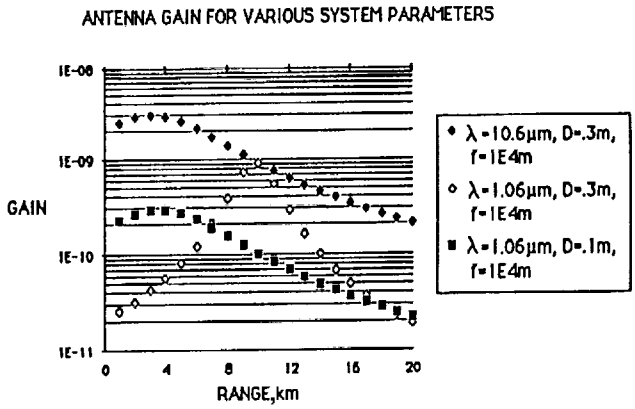

Figure 2. Nonnormalized antenna gain for some typical ground-based system parameters to illustrate the effects of telescope diameter.

2.2 The Backscatter Coefficient

By making the assumption that the aerosol size distribution is of the Deirmendjian "Haze C" or Junge form, Mie theory can be used to calculate the backscatter wavelength dependence for various assumptions regarding the particle's refractive index (a function of the particle material and laser wavelength). Table 1 gives refractive index values for "dust-like" and "water soluble" material (McClatchey and Selby, 1974), and for water (Centeno, 1941).

The radar cross sections calculated by using Mie theory are shown in Figure 3. For the dust-like and water-soluble material the cross-section decreases essentially as the -1.5 power of the wavelength whereas for water there is an approximate inverse square dependence. For wavelengths extending into the millimeter wave region, the negative wavelength dependence becomes much steeper even for water, which has a highly anomalous dielectric constant (n^2) of 81 at the longer wavelengths (see Fig. 4). Thus, extending considerations to the mm wave region would be futile for a device based on aerosol scattering. Such wavelengths are also not optimum for radars based on refractive turbulence scattering. In the visible through the long wavelength infrared, however, there is no distinct advantage in operating at shorter wavelengths based on backscattering considerations.

Simultaneous and co-located data obtained by using the NOAA lidars[1] at 0.69 and 10.6 μm, respectively shows evidence for the above numerically predicted wavelength dependence. The measured ratio of 10.6 to 0.69 μm backscatter (left-hand axis) is plotted against altitude in Figure 5. The right-hand axis indicates the values of the ratio corresponding to various power law exponents. To altitudes of 15 km MSL the data cluster around the -1.5 power value. At higher altitudes the exponent increases to -2, consistent with the expectation that the particle size distribution contains fewer large particles at the upper altitudes. The repetition of this experiment concentrating on the 9.2 μm wavelength would be very meaningful for assessing the relative merits of the wavelength regimes. The latter wavelength is in the dispersion regions of several

[1] Personal communication, M.J. Post and G.T. McNice NOAA/WPL, 1985

Table 1: Aerosol Complex Index of Refraction n-in': n = Real (Scattering) Part and n'= Imaginary (Absorption) Part

Wavelength, micron	Dust-like	Water-soluble	Water
.5145	1.53-i.008	1.53-i.005	1.33-i.00
.6943	1.53-i.008	1.53-i.007	1.33-i.00
1.06	1.52-i.008	1.52-i.017	1.33-i.00
10.6	1.62-i.120	1.76-i.070	1.18-i.08

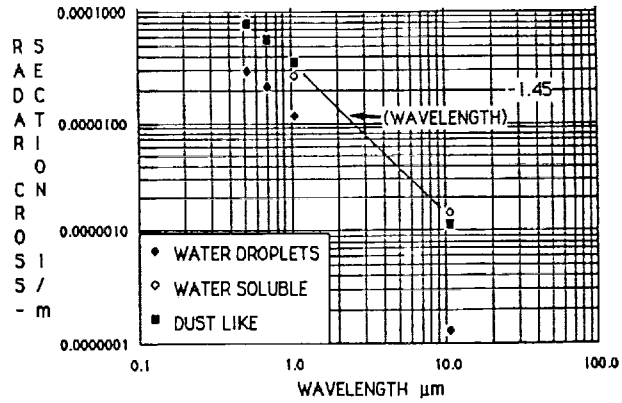

Figure 3. Radar cross section (proportional to backscatter coefficient) plotted against wavelength for a Haze C particle size distribution of water droplets, water soluble and dust-like material.

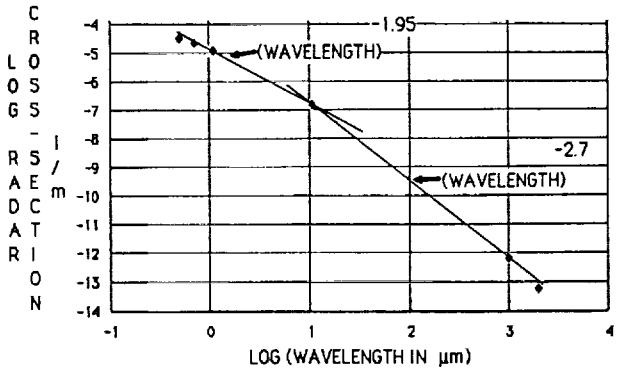

Figure 4. Radar cross section (proportional to backscatter coefficient) plotted against wavelength for a Haze C particle size distribution of water droplets. It demonstrates that the cross section decreases more rapidly with increasing wavelength in the far-infrared.

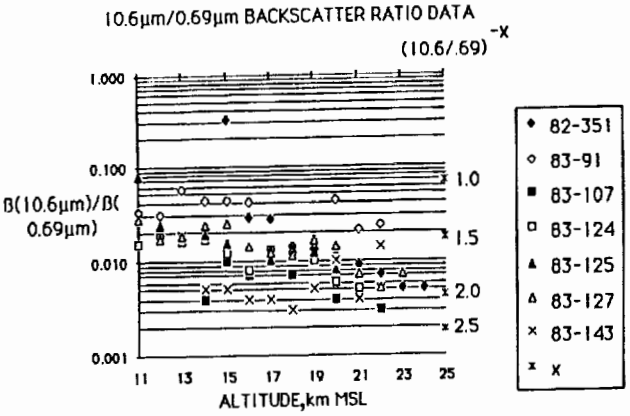

Figure 5. Measured 10.6 μm, 0.69 μm backscatter cross-section ratios for simultaneous co-located experiments are plotted against altitude. Data are evident for (wavelength)$^{-1.5}$ dependence of backscatter cross-section. Information in the legend is the Julian date. Data: Courtesy of M.J. Post and G.T. McNice NOAA/WPL.

atmospheric aerosol constituents, (Huffman, 1981), and the increased backscatter levels have been observed (Menzies et. al., 1984).

2.3 Signal Processing

The velocity estimate standard deviations σ_v, for the complex covariance and FFT Doppler estimators has been given by Zrnic(1977) as

$$\sigma_v = \frac{\lambda}{4\pi\sqrt{2\tau_p T_s}} \left[2\pi^{1.5}\rho + \frac{16\pi^2\rho^2}{SNR} + \frac{X}{SNR^2}\right]^{0.5}$$

where λ the transmitted wavelength
τ_p the coherent integration time
T_s the sampling period ($= \lambda/2V_{max}$)
V_{max} the maximum unaliased velocity
SNR the wideband signal to noise ratio
ρ the signal spectral width normalized by the total bandwidth
X = 1 for complex covariance and $2\pi^2/3$ for FFT.

In the limit of small SNR, the third term dominates and results in (for complex covariance processing)

$$\sigma_v = \frac{1}{4\pi SNR}\left[\frac{\lambda V_{max}}{\tau_p}\right]^{0.5} .$$

Since τ_p (the coherent integration time and thus the optimum pulse duration) is inversely proportional to the wavelength because of the rearrangement within the particle cloud due to turbulence, there is an apparent independence of σ_v on wavelength. However, the increased number of velocity estimates that a reduced pulse duration allows within a given range increment yields an overall square-root wavelength dependence for the standard deviation of the velocity estimate. The equation has been studied in detail by Kane et al. (1984) who show that the advantage for the lower wavelength varies from square root to linear with increasing SNR.

2.4 Beam Propagation

At longer wavelengths "clear air" extinction is due primarily to molecular absorption. For CO_2 laser radiation, it is dominated by water vapor and atmospheric CO_2 attenuation. In Figure 6 are shown two-way space-to-ground absorption profiles for three laser lines for various model atmospheres calculated by using Air Force Geophysical Laboratory codes. A 300-km polar orbit, a plane parallel atmosphere, propagation along an azimuth of 15° and a nadir angle of 62° are assumed, and accommodation is made for the satellite Doppler shift. To minimize attenuation, use of an isotopic gas mix is required and it is observed that for the 9.11-μm example, the total extinction can be kept below 3 dB down to the lower atmosphere. Fortuitously, the latter wave-

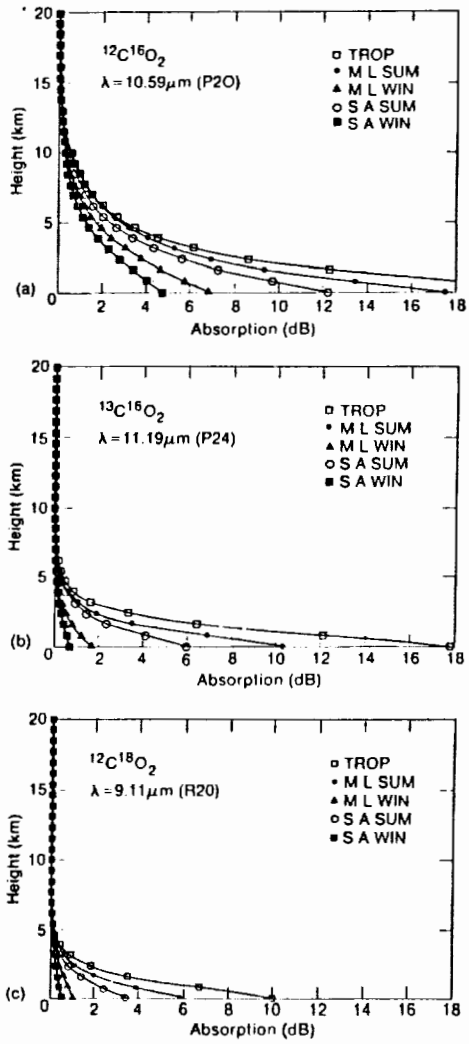

Figure 6. Space to altitude atmospheric extinction for three wavelengths in the CO_2 laser band and for various model atmospheres.

length is also that for which there is a local maximum in the backscatter coefficient for the atmospheric aerosol (see Section 2.2).

At lower wavelengths the extinction is dominated by aerosol and molecular scattering (and consequently is not sensitive to satellite Doppler shift), and farther toward the ultraviolet by molecular attenuation. Two-way transmission losses for several wavelengths through a plane parallel atmosphere (middle-latitude summer conditions) along a 60° nadir angle calculated by using data from McClatchey et al. (1972) are shown in Table 2.

Table 2. Two-way Atmospheric Transmission as a Function of Wavelength (Plane parallel atmosphere and a 60 degree zenith angle)

Wavelength (μm)	Attenuation loss (dB)
0.337	19.08
0.488	7.20
0.5145	6.65
0.6328	4.50
0.6943	5.91
0.86	2.98
1.06	2.37
1.536	1.67
10.6*	23.8

* Not Doppler shift adjusted.

A minimum in the attenuation is evident in the 1- to 2-μm range. It is also apparent that visible systems would have to demonstrate superior system efficiencies in order to overcome the increased transmission losses, particularly in the ultraviolet-visible boundary zone within the eye safe region (see Section 2.6). The table reemphasizes the impracticality of a 10.6-μm space lidar and the need for an isotopic CO_2-based laser to avoid the extinction due to the atmospheric CO_2.

2.5 Practical Considerations

The major system requirements of a Doppler lidar global wind-sensing lidar have been identified elsewhere, e.g., Lawrence (1981).

In favor of larger wavelength are

(1) The lower Doppler shift with the consequent decrease in the processing data rate.

(2) The lower tolerance required of optical components, in particular the meter class diffraction-limited transmitter telescope, the cost impact of which would be significant.

(3) The more relaxed platform jitter specification because of the wider diffraction-limited field of view.

(4) The larger diffraction-limited field of view allowing for easier compensation for lag angle and nadir orientation adjustments during round-trip to Earth's surface and signal reception times.

Most of these advantages apply to coherent lidars only.

On the other hand, the longer wavelength sources tend to be physically large and relatively inefficient and require occasional consumable replenishment, e.g., the transmitter laser gas mixture.

In favor of smaller wavelength systems would be the potential availability of solid-state lasers; thus consideration of reliable, compact components requiring little maintenance is possible.

2.6 Eye Safety Considerations

Since the field of view of a Doppler lidar is diffraction limited, the irradiance at ground level for a given pulse energy varies inversely as the wavelength squared. Thus, for example, over a 1000 km slant path the irradiances generated by a 1 J/pulse, 1 m telescope diameter lidar (scintillation effects, beam inhomogeneities and atmospheric extinction being ignored) would be $2*10^{-5}$ J/cm^2 (1.06 μm) and $2*10^{-7}$ J/cm^2 (10.6 μm). The maximum permissible (ocular) exposure values (ANSI-Z136.1 (1976)) are $5*10^{-6}$ J/cm^2 (1.06 μm) and $2*10^{-2}$ J/cm^2 (>1.4 μm). Thus, although for the longer wavelengths the irradiances are well within eye-safe limits, the irradiance of an operational lidar in the wavelength region 0.4 to 1.4 μm would be in excess of safety limits and thus would have to be eliminated from consideration. An acceptable wavelength region would be below 0.4 μm but above the ozone band cutoff (0.3 μm); however, no coherent source is currently available in this region.

3. CONCLUDING REMARKS AND RECOMMENDATIONS

The sensitivity of a coherent lidar is relatively independent of the wavelength. However, for a given output signal-to-noise ratio (SNR), the variance of the velocity estimate decreases as the square root of the wavelength in the limit of small SNR. With proper choice of wavelength total atmospheric propagation losses can be low (2-3 dB) in the region 0.8 to 2 μm and around 9 μm. In the visible region, Rayleigh scattering ensures >7 dB of attenuation, which would require a system operating in this region to have superior properties, e.g., overall system efficiencies, to overcome this penalty. Practical considerations currently heavily favor the longer wavelength but technology development could change this. Eye-safety considerations essentially eliminate consideration of wavelengths in the 0.4 to 1.4 μm region. The wavelength span 1.4 to 2 μm seems a particularly promising region for a candidate system because of low atmospheric extinction, the velocity accuracy advantage of lower wavelengths and mainly because Nd laser technology may be readily extrapolated to this region.

There is a need for a measurement program to verify the wavelength dependence of the atmospheric aerosol backscatter coefficient, to determine backscatter coefficient climatology at promising wavelengths over data-sparse regions of the Earth (particularly in the vicinity of 9.1 μm). Technology development of sources at promising wavelengths is needed so that systems can be used to generate a data base and a realistic assessment of their capabilities can be made. In the meantime, the CO_2 laser will remain the prime candidate for the wind sensing mission.

Since the driving requirement is for a highly efficient and long lifetime laser, in the final analysis, future laser developments will have a big impact on the choice of wavelength.

REFERENCES

American National Standard for the safe use of lasers. ANSI-Z136•1-1976. Published by the American National Standards Institute, New York, NY 1976.

Centeno, M., 1941: Refractive index of liquid water in the near infrared spectrum. JOSA, 31, 245.

Huffman, D. R., 1981: A survey of optical constants in the 5-25 micron spectral region. Final Technical Report to Naval Air Systems Command, Contract No. N00019-79-C-0557 from Univ. of Arizona.

Kane, T. J., B. Zhou, and R. L. Byer, 1984: Potential for coherent Doppler wind velocity lidar using neodymium lasers. Appl. Opt., 23.

Lawrence, T. R., R. M. Huffaker, R. J. Keeler, M J. Post, R. A. Richter, and F. F. Hall, Jr., 1981: Feasibility and design considerations of a global wind sensing coherent infrared radar (WINDSAT). SPIE Vol. 300 Physics and Technology of Coherent Infrared Radar.

Menzies, R. T., M. J. Kavaya, P. H. Flamant, and D. A. Haner, 1984: Atmospheric aerosol backscatter measurements using a tunable coherent CO_2 lidar. Appl. Opt., 23, 2510.

McClatchey, R. A., R. W. Fenn, J. E. A. Selby, F. E. Volz, and J. S. Garing 1972: Optical properties of the atmosphere (Third Edition). AFCRL-72-0497, Environmental Research Papers No. 411, Air Force Cambridge Research Laboratories, Bedford, MA.

McClatchey, R. A., and J. E. A. Selby, 1974: Atmospheric attenuation of laser radiation from 0.76 to 31.25 microns. AFCRL-TR-74-003, Environmental Research Papers No. 460, Air Force Cambridge Research Laboratories, Bedford, MA.

Thomson, J. A. L., and M. F. Dorian, 1967: Heterodyne detection of monochromatic light scattered from a cloud of moving particles. Technical Report CDC-ERR-AN-1090, General Dynamics/Convair, San Diego, CA.

Zrnic, D. S. 1977: Spectral moment estimators from correlated pulse pairs. IEEE Trans. Aerosp. Electron. Syst., AES-13, 344-354.

A COMPARISON OF DOPPLER LIDAR WIND SENSORS FOR EARTH-ORBIT GLOBAL MEASUREMENT APPLICATIONS

Robert T. Menzies

Jet Propulsion Laboratory
California Institute of Technology
Pasadena, CA 91109

1. INTRODUCTION

At the present time there are four Doppler Lidar configurations which are being promoted for the measurement of tropospheric winds: (1) the coherent CO_2 Lidar, operating in the 9-μm region, using a pulsed, atmospheric-pressure (TEA) CO_2 gas discharge laser transmitter, and heterodyne detection; (2) the coherent Neodymium-doped YAG or Glass Lidar, operating at 1.06-μm, using flashlamp or diode laser optical pumping of the solid-state laser medium, and heterodyne detection; (3) the Neodymium-doped YAG/Glass Lidar, operating at the doubled frequency (at 530 nm wavelength), again using flashlamp or diode laser pumping of the laser transmitter, and employing a high-resolution tandem Fabry-Perot filter and direct detection; and (4) the Raman-shifted Xenon Chloride Lidar, operating at 350 nm wavelength, using a pulsed, atmospheric pressure XeCl gas discharge laser transmitter at 308 nm, Raman-shifted in a high-pressure hydrogen cell to 350 nm in order to avoid strong stratospheric ozone absorption, also employing a high-resolution tandem Fabry-Perot filter and direct detection.

Comparisons of these four systems can include many factors and tradeoffs, e.g., efficiency, maturity of technology, reliability and lifetime, compactness, etc. Although many statements can be made regarding the relative capabilities and drawbacks of the technology required for each system, the major portion of this comparison is devoted to the topic of efficiency. Efficiency comparisons are made by estimating the number of transmitted photons required for a single-pulse wind velocity estimate of ± 1 m/s accuracy in the middle troposphere, from an altitude of 800 km, which is assumed to be reasonable for a polar-orbiting platform of multi-year lifetime. The Earth-orbiting Doppler Lidar measurement requirement is assumed to be driven by the forecast improvement application - an application which places an emphasis on ± 1 m/s measurement accuracy per pulse, with a range gate corresponding to 1 km vertical resolution, and a scanning capability and pulse repetition frequency consistent with twice daily global coverage and horizontal averaging over 300 km by 300 km cells.

The requirement for measurement of the two components of the horizontal wind field (for a vector wind determination), combined with the desirability of daily global coverage, has resulted in studies of various scan concepts, the conical scan concept being the least demanding when consideration is given to the effects of time-dependent accelerations on pointing stability, power required to effect the scan, etc. (Huffaker, 1978; Lockheed Missiles and Space Co., 1981; RCA Astro-Electronics, 1983). The scanning results in large Doppler shifts of backscattered signals due to the orbiting spacecraft velocity. Maximum shifts for a 55° nadir angle are given for each Doppler Lidar system in Table 1. (The 55° nadir angle results in global coverage at the equator when a platform altitude of 800 km is assumed.) Table 1 summarizes the characteristics of each of the four Doppler Lidar systems considered. A 1-m diameter telescope is assumed in each case.

For the purpose of the overall efficiency calculations and comparison, it is assumed that the predominant electrical power consumer is the pulsed laser transmitter. The power draw for other components in each lidar system, with the possible exception of the scanning telescope assembly, is much smaller than that required for the class of laser transmitter required to make sufficiently accurate Doppler measurements (i.e., a pulse energy in the 2-20 Joule range, and a pulse repetition rate of several Hz). It is assumed that the scanning telescope power requirement, although possibly not negligible when compared with that of the transmitter, is the same for each of the four lidar systems considered.

2. EFFICIENCY CALCULATIONS

The calculation of overall efficiency can proceed by considering for each system: (1) the number of photons per joule of transmitted energy, per unit area of the receiver telescope (1 m.), which are backscattered from a 1-km aerosol column as a function of altitude; (2) the number of photons needed at the telescope primary mirror in order to measure a (single-shot) Doppler shift with ± 1 m/s accuracy from a 1-km aerosol column; and (3) the electrical efficiency of each transmitter (i.e., the power draw required for the ± 1 m/s single-shot measurement accuracy).

The results of the computation of the first factor, the aerosol backscattered photon number, per Joule of transmitted energy per m^2 of receiver telescope area, are plotted in Figure 1.

Table 1. DOPPLER LIDAR SYSTEM DESCRIPTIONS

9-μm CO_2

- Transmitter: Single-Frequency Pulsed TEA-CO_2, λ = 9.11 μm, 0-18 isotope of CO_2
- Transmitter Est. Electrical Efficiency: 6%
- Receiver: Coherent Detection, Matched Filter Bandwidth in IF Domain, Local Oscillator Required
- Turbulence Effects (Loss of Coherence Due to Propagation Path): No Problem for 1-m Diameter Telescope
- $\Delta\nu_1$ (1 m/s Radial Motion) = 200 kHz*
- τ_{tl} (Equivalent Transform - Limited Pulse Duration) = 5 μs
- $\Delta\nu_{max}$ (S/C Velocity, 55° Nadir Angle) = 1100 MHz†

530-nm Doubled Nd:YAG

- Transmitter: Frequency-Doubled, Single-Frequency, Pulsed Nd:YAG MOPA, Diode Laser Pumped
- Transmitter Est. Electrical Efficiency: 2.5%
- Receiver: Tandem F-P Etalon, High Resolution Etalon Gap = 30 cm (FSR = 500 MHz), IPD with 12-Ring Anode
- Turbulence Effects: No Problem for 1-m Telescope
- $\Delta\nu_1$ (1 m/s Radial Motion) = 4 MHz*
- τ_{tl} (Equivalent Transform-Limited Pulse Duration) = 250 ns
- $\Delta\nu_{max}$ (S/C Velocity, 55° Nadir Angle) = 22 GHz†

1-μm Nd: YAG

- Transmitter: Single-Frequency, Pulsed MOPA, Diode Laser Pumped, λ = 1.06 μm
- Transmitter Est. Electrical Efficiency: 5%
- Receiver: Coherent Detection, Matched Filter Bandwidth in RF Domain, Local Oscillator Required
- Turbulence effects (Loss of Coherence Due to Propagation Path): Marginal Problem for 1-m Diameter Telescope
- $\Delta\nu_1$ (1 m/s Radial Motion) = 2 MHz*
- τ_{tl} (Equivalent Transform-Limited Pulse Duration) = 500 ns
- $\Delta\nu_{max}$ (S/C Velocity, 55° Nadir Angle) = = 11 GHz†

350-nm Raman-shifted XeCl

- Transmitter: Raman-Shifted Single-Frequency XeCl Excimer, Injection-Controlled
- Transmitter Est. Electrical Efficiency: 4%
- Receiver: Tandem F-P Etalon, with High-Resolution Etalon Band Gap = 30 cm (FSR = 500 MHz), IPD with 12-Ring Anode
- Turbulence Effects: No Problem for 1-m Telescope
- $\Delta\nu_1$ (1 m/s Radial Motion) = 6 MHz*
- τ_{tl} (Equivalent Transform-Limited Pulse Duration) = 170 ns
- $\Delta\nu_{max}$ (S/C Velocity, 55° Nadir Angle) = 32 GHz†

---

* The frequency shift for backscatter from aerosol with 1 m/s radial velocity component.

† The frequency shift for backscatter due to the orbiting spacecraft velocity component along the line-of-sight for a conical scan with 55° nadir angle.

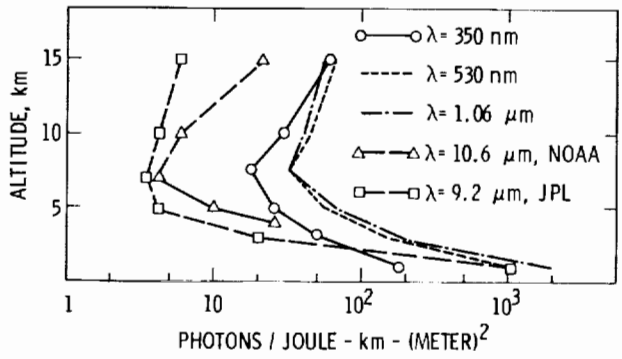

Fig. 1. The number of photons per joule of transmitted energy per unit area of receiver telescope (1 m^2) received from the backscatter of a 1-km aerosol layer as a function of altitude.

This calculation was presented by Abreu (1979) for the λ = 500 nm case, assuming an orbital altitude of 250 km, and a 45° nadir angle. Abreu used an unpublished aerosol backscatter model from Shettle & Fenn for his calculations. We have used the same aerosol backscatter model used by Hays, et al. (1984), which agrees quite closely with model calculations of Kent (1985) for mid-tropospheric altitudes and is within a factor of two of the model used by Abreu. The results of Kent's calculations, using continental aerosol models based on data from Cress (1980) and Patterson, et al., (1980) and marine tropsopheric aerosol models based on data from Patterson, et al. (1980), indicate little difference between the backscatter characteristics of continental and marine free troposphere aerosols at wavelengths of 350 nm, 500 nm, and 1.06 μm. There is a large difference at wavelengths near 10 μm, however. This appears to be validated when comparing aerosol backscatter profiles taken at NOAA over Boulder, CO, and at JPL over Pasadena, Ca. The data taken by the NOAA group are all at λ = 10.6 μm. An enhancement is predicted at wavelengths near 9 μm due to refractive index resonances and has been observed experimentally by the JPL group. After taking averages over many backscatter profile data sets, this enhancement appears to be approximately a factor of three at mid-tropospheric altitudes. Even this enhancement does not completely make up for the larger backscatter coefficients measured by the NOAA group, presumably because their measurements are of a continental aerosol, while the JPL measurements are on aerosols that are more representative of marine aerosol than continental aerosol.

The calculations indicated in Figure 1 include the effects of Rayleigh and aerosol extinction at the 350 nm and 500 nm wavelengths. The Rayleigh scattering loss is most pronounced at the 350 nm wavelength, with a round-trip transmission of only 0.25 resulting for propagation down to 5 km. These sources of extinction are negligible at the 1-μm and 9-μm wavelengths. It is assumed that the operational wavelength for the CO_2 lidar is 9.11 μm, which is the short wavelength band R(20) line of the $^{12}C^{18}O_2$ molecule. The use of the rare isotope laser line eliminates loss due to atmospheric carbon dioxide, so that the only substantial loss is due to the water vapor continuum, which becomes important at altitudes below 2.5 km. However the aerosol backscatter rises by a tremendous factor at these low altitudes when using 9-μm wavelength radiation, which more than compensates for the water vapor absorption loss.

Referring to Figure 1, the large difference in aerosol backscatter coefficients between the near-UV/mid-visible wavelengths and the 9-10 μm wavelengths (e.g., 5 x 10^{-8} m^{-1} sr^{-1} at λ = 500 nm vs 10^{-10} m^{-1} sr^{-1} at λ = 9.25 μm at 5 km altitude is largely compensated, of course, by the fact that a 1-J pulse contains 20 times as many photons at 10-μm wavelength as does a 1-J pulse at 500 nm wavelength. The Rayleigh scattering loss also accounts for a large factor in the near-UV, as mentioned earlier.

Next we address the second factor, the number of photons needed at the telescope mirror in order to measure a (single-shot) Doppler shift corresponding to a 1 m/s accuracy in determination of tne (horizontal) wind. First we address the optical/quantum efficiency factor for each system.

For the CO_2 Doppler lidar receiver, heterodyne detection using photomixers with 0.40 effective quantum efficiency and flat frequency response to greater than 1 GHz exist and can be matched with low-noise RF preamps such that local oscillator induced quantum noise predominates over amplifier noise when the local oscillator power is a few milliwatts. The optical efficiency of the receiver prior to the photomixing process is estimated to be 0.25, due to various factors including beam shape mismatch and pointing jitter. Thus the overall optical/quantum efficiency is 0.1, which is the value used in the NOAA-WPL Feasibility Study (Huffaker, et al., 1980).

The corresponding estimate for the 1-μm Nd:YAG coherent system is fraught with uncertainty, because this technique is so new at 1.06 μm that accurate photomixer quantum efficiencies have not been measured. Several technological hurdles must be overcome. The local oscillator frequency will most likely have to be swept in order to compensate for the large Doppler shifts encountered in the conical scan due to the spacecraft velocity. The eye safety problem associated with a coherent lidar at 1.06 .m is a major obstacle. In a standard coaxial transmit/receive coherent lidar with 1-m diameter telescope, calculations indicate that the maximum permissible exposure level for a night-adaptive eye would limit the transmitted pulse energy to no more than 40 mJ! Clearly the transmitted beam divergence must be increased, and an array of photomixers must must be used to view the transmitted beam "footprint" in the troposphere. The signals from the individual photomixers would then be incoherently added. We assume an array of 100 elements, with a factor of 2 loss due to packing efficiency in the focal plane. The process of independent detection and incoherent adding

causes a factor of 10 loss for a 100 element array when compared with a single element, diffraction limited, coaxial coherent lidar. (Using a 10 times smaller diameter transmitter telescope to spread the beam to a footprint size corresponding to 4J pulse eye-safety threshold, results in a factor of 10^2 reduction in speckle lobe diameter at the receiver primary, making the array necessary.) We assume the array configuration, even though it may be entirely impractical. If we assume each photomixer has 40% effective heterodyne quantum efficiency, and the other optical losses are comparable to those of the coherent CO_2 system, then the overall optical/quantum efficiency is 5×10^{-3}.

The Doppler receiver for the 350 nm and 530 nm lidars are nearly the same. We assume collimating optics, an interference filter and a medium resolution scanning etalon in order to block the scattered solar radiation, and a rigid high resolution etalon made of ultra-low thermal expansion spacer material (e.g., Zerodur), followed by an imaging photon detector (IPD) with a multi-ring anode detector. A small (short gap) Fabry-Perot etalon has flown on Dynamics Explorer (Hays et al., 1981), and a triple-etalon instrument (with a 1 cm gap high-resolution etalon and an imaging photon detector) has flown as a balloon-borne instrument (Rees et al., 1982). This type of receiver has been described in a lidar context by Abreu (1979) and Hays et al. (1984). The overall quantum efficiency for the IPD is assumed to be 10%, based on information supplied by authors of Hays et al., (1984). [The overall quantum efficiency of the balloon-borne instrument IPD, as quoted by Rees, et al. (1982), is 5%.] The etalon throughput is 80%. The optical efficiency, or throughput, of the rest of the optical receiver system is assumed to be 25%. Thus the overall optical/quantum efficiency is 2.0×10^{-2}.

The next issue to be addressed is the necessary SNR for a ±1 m/s measurement accuracy. With the coherent CO_2 and Nd:YAG Doppler lidars the use of matched filters in the IF domain and the complex covariance (pulse pair) algorithm is appropriate. These are standard Doppler radar techniques, and the use of the appropriate expression for expected rms velocity error (Zrnik, 1979; Kane, et al., 1984) leads to a required signal-to-noise ratio (SNR) for a velocity error of 1 m/s:

$$\delta v = \frac{\lambda}{4\pi}\left(\frac{f}{2NLt}\right)^{1/2}\left(2\pi^{3/2}W + \frac{16\pi^2W^2}{SNR} + \frac{1}{(SNR)^2}\right)^{1/2}$$

where λ = 10-μm or 1-μm; f = sampling frequency, which is related to the maximum measurable Doppler shift, or wind velocity, as dictated by the Nyquist criterion ($V_{NY} = f\lambda/2$); t = pulse duration; L = ratio of range gate length to pulse length; N = number of pulses averaged; and W is a measure of the frequency spread of the return signal in the absence of noise ($W = (V_{NY})^{-1}(V_{bw}^2 + V_{atm}^2)^{1/2}$), where V_{bw} is the velocity uncertainty due to the pulse bandwidth, and V_{atm} is the standard deviation of the velocity distribution due to atmospheric effects in the propagation and scattering processes). If we assume the following values for the quantities $V_{bw} = \lambda/4t$ = 2.5 m/s, V_{atm} = 0.3 m/s, then W can be calculated for various Nyquist velocities. At this point it is important to distinguish between the "wide-band" SNR, which is the quantity appearing in Eqn. (1) and is related to the sampling frequency, f, and the "narrow-band" SNR, which is related to the coherent integration time and depends on the pulse length, t. It was recognized in early feasibility studies (Huffaker, 1978) that if a maximum unaliased velocity of 50-100 m/s were desired, a bandwidth reduction technique should be applied. One technique discussed in that study is the use of a bank of overlapping filters, of width approximately 2 MHz (corresponding to a velocity of 10 m/s at λ = 10 μm), each followed by an A/D. Each output could then be processed for the Doppler information in parallel. Assuming this technique is adopted, then $\delta v \simeq 1$ m/s for a "narrow-band" $(SNR)_N > 4$, assuming t = 2 μs, for the CO_2 lidar case. The sampling frequency must be an order of magnitude higher at 1 μm in order to have the same value for V_{NY}. Thus, for equal pulse durations, the difference between the $(SNR)_W$ and $(SNR)_N$ is 10 dB larger in the 1-μm receiver than than in the 10-μm receiver. The overall result, using Eqn (1), is that $\delta v \simeq 1$ m/s for $(SNR)_N > 12$. These results are summarized in Table 2.

Table 2. RECEIVER DOPPLER SHIFT MEASUREMENT EFFICIENCY: COHERENT LIDARS (±1 m/s ACCURACY)

CO_2 Lidar, λ = 9.11 μm

- Telescope Primary Area: 1 m^2
- Pulse Spectral Width: 500 kHz
- Matched Filter Receiver
- Optical and Quantum Efficiency: 0.10
- Processor Minimum $(SNR)_N$ = 4 (6 dB)
- No. Photons Needed at Primary: >40

Nd: YAG Lidar, λ = 1.06 μm

- Telescope Primary Area: 1 m^2
- Pulse Spectral Width: 500 kHz
- Matched Filter Receiver
- Optical and Quantum Efficiency: 5×10^{-3}
- Processor Minimum $(SNR)_N$ = 12
- No. Photons Needed at Primary: > 2.4×10^3

The necessary SNR for a 1 m/s measurement accuracy using the F-P etalon and imaging photon detector combination described earlier is approximately the inverse of the ratio of the frequency shift Δv, to the resolution of the high resolution FP element. We assume the latter is 50 MHz, i.e., a finesse of 10, which closely matches the 12-ring anode configuration of the IPD. Thus the ratio is approximately 0.1. The entire FSR is imaged onto the IPD anode because of the influence of the conical scan on the frequency of the backscattered radiation. The conical scan will cause the frequency to move up and down periodically over many times the FSR (i.e., 22-32 GHz). A scanning medium resolution etalon will be required to scan

in order to maintain the passband in the correct frequency region. The data processing algorithm will be required to identify the order of the HRE into which the backscattered radiation is shifted at any particular time. Because it is equally likely that the backscattered radiation frequency may occupy any portion of the FSR of a particular order, the entire FSR must be imaged at all times.

Assuming photon counting and Poisson statistics, the necessary number of photo-electrons for SNR = 10, for example, is 100. The presence of the Rayleigh signal in several adjacent 50 MHz channels will increase the required number of signal (aerosol backscattered) photons for SNR > 10 in discriminating between resolution elements.

The results for the 350 nm and 530 nm wavelength Doppler lidar Fabry-Perot etalon receivers are summarized in Table 3.

Table 3. Receiver Doppler Shift Measurement Efficiency: Direct Detection F-P Etalon Lidars (± 1 m/s Accuracy)

Nd:YAG (X2) Lidar, λ =530 nm	
- Telescope Primary Area:	1 m^2
- Pulse Spectral Width:	<30 MHz
- High Res. Etalon FSR:	500 MHz
Spectral Resolution:	50 MHz
- Optical and Quantum Efficiency:	0.02
- Total Required Signal Photocounts:	90
No. Photons Needed at Primary:	4.5×10^3
Raman-Shifted XeCl Lidar, λ = 350 nm	
- Telescope Primary Area:	1 m^2
- Pulse Spectral Width:	<30 MHz
- High Res. Etalon FSR:	500 MHz
Spectral Resolution:	50 MHz
- Optical and Quantum Efficiency:	0.02
- Total Required Signal Photocounts:	105
No. Photons Needed at Primary:	5×10^3

3. CONCLUDING REMARKS

The required transmitter pulse energies can now be estimated, and by using the estimated electrical efficiency factors in Table 1, the overall power draw for each lidar instrument can be estimated. Using, e.g., a 5 km altitude for the wind measurement, the required transmitter pulse energies for single-shot velocity measurement with 1 m/s accuracy are as follows (assuming a 1-km vertical resolution, which corresponds to a 1.75 km slant range resolution):

9.11 μm CO_2 Lidar:	6 J
1.06 μm Nd:YAG Lidar:	23 J
530 nm Nd:YAG (X2) Lidar:	40 J
350 nm R.S. XeCl Lidar:	100 J

Clearly single-shot measurement estimates are not feasible for the UV, visible, and near-IR lidars from an orbiting altitude of 800 km with a 55° nadir angle (slant range = 1400 km). Serious eye-safety problems occur for both the 1.06 μm and 530 nm wavelengths at these pulse energy levels also. The above result is in reasonable agreement with the calculations of Abreu (1979), when scaling his estimated pulse energy requirement for a ±2 m/s accuracy at a slant range of 350 km to the requirements of this exercise. Abreu concluded that at 5 km altitude a 10-pulse average would be required from a 0.3 J transmitter for a ±2 m/s accuracy. Recognizing that the received photon number requirement for the F-P Etalon receiver is approximately proportional to the inverse square of the required velocity accuracy for small Doppler shifts (due to photon counting statistics), his result would scale to a 10-pulse average from a 20-J transmitter for the ±1 m/s accuracy from the 800 km, 55° nadir angle platform.

REFERENCES

Abreu, V.J., "Wind Measurements from an Orbiting Platform Using a Lidar System with Incoherent Detection: An Analysis", Appl. Opt. 18, 2992 (1979).

Cress, T.S., "Airborne Measurement of Aerosol Size Distributions Over Northern Europe, Vol. 1. Spring and Fall, 1976, Summer, 1977, AFGL, Environmental Research Paper 702 (May 1980).

Hays, P.B., T.L. Killeen, & B.C. Kennedy, "The Fabry-Perot Interferometer on Dynamics Explorer", Space Science Instr. 5, 395 (1981).

Hays, P.B., V.J. Abreu, J. Sroga, & A. Rosenberg, "Analysis of a 0.5 Micron Spaceborne Wind Sensor", presented at the AMS Conference on Satellite Remote Sensing, Clearwater, FL, June, 1984.

Huffaker, R.M., editor, 1978: Feasibility Study of Satellite-Borne Lidar Global Wind Monitoring System, NOAA TM ERL WPL-37.

Huffaker, R.M., T.R. Lawrence, R.J. Keeler, M.J. Post, J.T. Priestly, and J.A. Korrell, 1980: Feasibility Study of Satellite-Borne Lidar Global Wind Monitoring System, Part II, NOAA TM ERL WPL-63, 1980.

Kane, T.J., B. Zhou, & R.L. Byer, 1984: Potential for Coherent Doppler Wind Velocity Lidar Using Neodymium Lasers, Appl. Opt. 23, 2477-2481.

Kent, G.S., 1985: personal communication.

Lockheed Missiles & Space Company, Inc., with Perkin Elmer and GTE Sylvania, 1981: Global Wind Measuring Satellite System - WINDSAT, Final Report, NOAA Contract NA79RA C00127, April, 1981.

Patterson, E.M., C.S. Kiang, A.C. Delany, A.F. Wartburg, A.C.D. Leslie, and B.J. Heubert, 1980: Global Measurements of Aerosol in Remote Continental & Marine Regions: Concentrations, Size Distributions, & Optical Properties, J. Geophys. Res. 85, 7361-7375.

RCA Government Systems Division, Astro-Electronics, Princeton, NJ, with Perkin-Elmer Corp. and Math. Science Northwest, Inc., 1983: Feasibility Study of a Windsat Free Flyer, Final Report, Contract NA82RAC00141, July, 1983.

Rees, D., P.A. Rounce, I. McWhirter, A.F.D. Scott, A.H. Greenaway, and W. Towlson, 1982: Observations of Atmospheric Absorption Lines from a Stabilized Balloon Platform & Measurements

of Stratospheric Winds", J. Phys. E: Sci. Instrum. 15, 191-206.

Zrnik, D.S., 1979: Estimation of Spectral Moments for Weather Echoes, IEEE Transactions on Geoscience Electronics, GE-17, 113-128.

S33-47

84493

N93-70382

LOCKHEED DESIGN OF A WIND SATELLITE (WINDSAT) EXPERIMENT

John S. Osmundson and Stephen C. Martin
Lockheed Palo Alto Research laboratory
Palo Alto, California, 94304 USA

1. INTRODUCTION

WINDSAT is a proposed space-based global wind-measuring system. A Shuttleborne experiment is proposed as a proof-of-principle demonstration before development of a full operational system. WINDSAT goals are to measure wind speed and direction to ±1 m/s and 10° acuracy over the entire earth from 0- to 20-km altitude with 1-km altitude resolution. The wind-measuring instrument is a coherent lidar incorporating a pulsed CO_2 TEA laser transmitter and a continuously scanning 1.25-m-diameter optical system. The laser fires at an 8-Hz prf and the optics performs a conical scan at 60° to nadir with a 7-s period. Each laser pulse is backscattered by aerosols in the earth's atmosphere with a Doppler shift since the aerosols are moving with the wind. The wind speed is measured by heterodyne detecting the backscattered return laser radiation and measuring this frequency shift. Each wind-speed measurement must be repeated at a different look angle to determine wind direction. The combination of a continuously rotating optical system with heterodyne detection leads to a requirement for active alignment, or image motion compensation, of the return radiation. Short-term pointing stability of 2 μrad and long-term pointing accuracy of 100 μrad is required for efficient detection and accurate wind mapping. A separate attitude determination and control system is required on the Shuttle to meet these WINDSAT accuracies.

Several years ago, the national Oceanic and Atmospheric Administration (NOAA), under the direction of R. Milton Huffaker, performed a Phase A WINDSAT study which showed the feasibility of measuring global winds using a spaceborne coherent lidar(Huffaker 1978, 1979). The ultimate goal of the program was to place coherent lidars in a network of operational satellites to provide continuous mesurements of global winds in order to obtain more accurate long-range weather forecasts.

The NOAA Phase A study showed the conceptual feasibility of an operational wind-measuring lidar and proposed a Shuttleborne experiment as a proof-of-principle demonstration. Lockheed Missiles & Space Company, Inc. (LMSC), with Perkin-Elmer, GTE Sylvania, and Mathematical Sciences Northwest as principal subcontractors, then performed a Phase B hardware feasibility study of a Shuttleborne WINDSAT experiment under contract to NOAA(Osmundson, 1981). The WINDSAT experiment was proposed to fly in 1987.

Measurement goals of both the operational system and the Shuttle experiment were to measure wind speed to ±1 m/s and wind direction to ±10°. Winds would be measured over the entire earth from the earth's surface to an altitude of 15 to 20 km, with 1-km altitude resolution. An operational system would be in an 800-km, circular polar orbit. Results obtained from a 300-km-altitude Shuttle orbit would have to show scalability to the operational system.

2. MEASUREMENT APPROACH

The WINDSAT lidar operation is conceptually simple, as shown in Fig. 1. A laser pulse is directed through a transceiver (consisting of a laser transmitter and transmitting and receiving optics) toward the earth's atmosphere. A small fraction of the incident pulse is sent back as signal into the transceiver due to backscatter from atmospheric aerosols. Since the aerosols are moving with the wind, the signal is Doppler shifted from the transmitted frequency. The signal is heterodyne-detected and the frequency shift measured; thereby the wind component along the transceiver line-of-sight was given. This component is known as the radial wind component.

The transmitted pulse and the return signal are shown in the temporal domain in Fig. 2. The transmitted pulse is nominally 5-μs long. The return pulse is considerable longer because of its long atmospheric interaction path. The mean atmospheric aerosol distribution is largest at the earth's surface and exponentially decreases with altitude. Therefore, the leading edge of the signal has the smallest amplitude and, on the average, increases for lower altitude returns. Large temporal and spatial aerosol variations lead to large signal amplitude variations. Earth's surface and cloud surface returns give sharply discontinuous, high-amplitude returns. The returned signal, shown in Fig. 2, can be time-sampled, or range-gated, to resolve atmospheric layers.

The same transmitted pulse and return signal for one range bin is shown in frequency space (Fig. 3). The transmitted pulse is nominally 200 kHz wide, which is the frequency spread given by the inverse of the pulse width. (This condition is known as a transform limited pulse.) The return signal has a gross Doppler offset of approximately 0 to ±1.5 GHz because of Shuttle-earth relative motion. The Doppler shift component due to winds is typically in the range

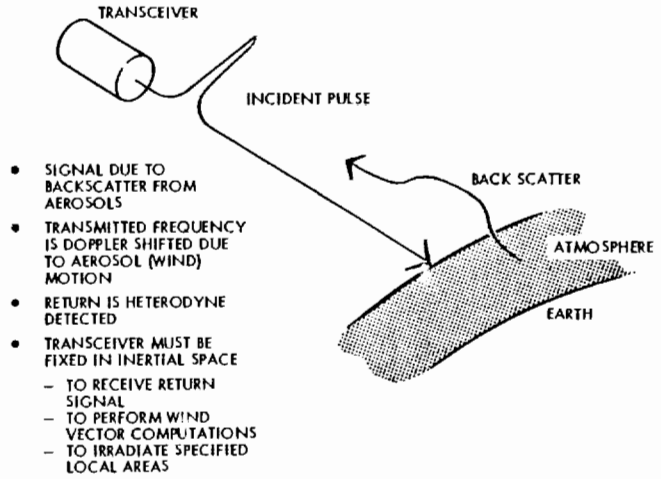

Figure 1. WINDSAT Measurement

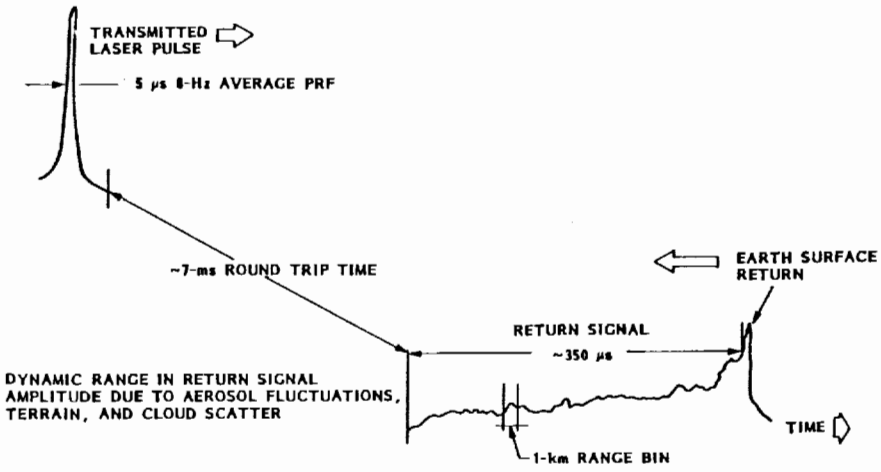

Figure 2. WINDSAT Signal Temporal Characteristics

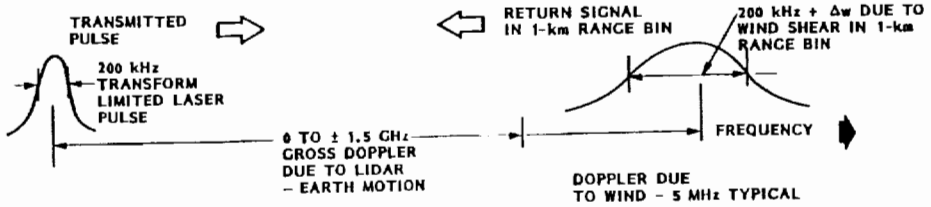

Figure 3. WINDSAT Signal Spectral Characteristics

±22 MHz. In addition, any laser frequency spreading or vertical wind components cause the signal spectrum to be broadened.

Measuring winds over the entire globe with high accuracy levels leads to the following key LIDAR features:

- o Scanning optics
- o Heterodyne detection
- o Highly accurate pointing
- o Highly stabilized laser transmitter

Scanning of the transmitted beam is required to cover the entire earth and to make measurements of the same locale from two different look angles. This is required to convert line-of-sight (radial) wind components into orthogonal components parallel to the earth's surface, thereby obtain wind direction. The scanning system must also provide for pointing at selected local areas such as storm centers and must provide a reasonable sampling density in 300-km by 300-km areas. This is a grid size useful to weather modelers.

Several scanning concepts were considered by Perkin-Elmer during the study and a continuous conical scan approach was finally chosen. By using this technique, the transmitted beam is continuously scanned in a pattern as shown in Fig. 4. Solid dots on the ground track represent laser pulses when the transmitter is operated at 8 pps. Each firing point coincides with a firing point on a later scan and thus allows two different look angles for each measurement point. Details of this scan approach are well covered in the NOAA Phase A report.(Huffaker, 1978)

Figure 4 also shows another scan concept considered, a step-stare scan. Here the laser is fired at a point and the optics stopped to collect the return signal. The optics is then stepped over and the process repeated; thus a raster scan is created. The step-stare approach was rejected because of the perturbations introduced into the system by primary mirror accelerations.

The process of heterodyne detection is shown in Fig. 5. A local oscillator (LO) laser of known frequency f_{LO} is mixed with a return signal of frequency $(f_t + \Delta t)$, where f_t is the transmitted frequency and Δt is the Doppler shift. The two beams are mixed on a heterodyne detector which converts the optical signal to an electrical signal of frequency $\pm[f_{LO} - (f_t + \Delta t)]$. By choosing f_{LO} properly, the electrical signal will be in a convenient microwave domain. A condition for heterodyne detection is that the signal and LO beam be well aligned. In a continuously scanning system, the signal beam returns off-axis to the optics and requires a lag angle compenstor (LAC) to bring the beam back on-axis.

Beam alignment for heterodyne detection requires 2-μrad optics alignment during the 7-ms pulse roundtrip time. Long-term pointing accuracy, required for computing wind vectors and for accurate local targeting, is 100 μrad. In the WINDSAT pointing system, the scanning optics, optical train, laser, and focal plane are referenced to each other and to an attitude sensor through a computation system.(see Osmundson et al., 1980).

System and subsystem requirements were developed by NOAA during Phase A and refined by LMSC during Phase B. The most important of these are:

Laser Transmitter:	CO_2 TEA 9.11 μm 10 J/pulse 8 pps 3- to 10-μs pulse duration (5-μs nominal)
Optics:	1- to 2-m-diameter diffraction limited
Pointing Determination and Control:	100-μrad accuracy long-term 2-μrad short-term (7 ms)

3. WINDSAT DESIGN

A side view of the instrument mounted on the Shuttle pallet is shown in Fig. 6. The transmitter laser, focal plane, and signal processor are mounted on a support structure that is attached to the Shuttle pallet. A torque motor, attached to the top of the support structure, drives a rotating telescope. The telescope fits within the Shuttle payload envelope in any scan orientation. The telescope is a 1.25-m diameter, f/0.95 instrument, diffraction limited with a 0.2 linear obscuration. Lag angle compensation is achieved with two agile mirrors. One mirror is a fast one-dimensional rotating polygon, which performs a first-order linar correction to the return signal. The second mirror, a slower two-axis gimbaled flat one, performs a second-order correction. The second mirror also corrects for laser beam wander and Shuttle perturbations, and thus allows the WINDSAT instrument to be hard mounted to the payload bay(Glenn and McGuirk, 1980; and McGuirk, Glenn, 1980). The choice of 1.25-m, f/0.95 optics was the largest low-risk telescope which would fit in the payload bay without deployment or erection. The instrument was sized to give over 20 dB of excess link margin for clear air returns from 5- to 10-km altitudes under nominal conditions.

The laser is an injection-controlled unstable resonator CO_2 TEA laser. The preferred means of excitation includes E-beam control. The laser is specified to have an end-to-end efficiency of 5.3 percent and a discharge efficiency of 19 percent (Gardner, 1980).

A separate WINDSAT attitude determination system consisting of two star sensors (for redundancy) and an inertial reference unit (IRU) is provided since the Shuttle-provided unit cannot be used due to thermal warping of the payload bay. The attitude determinations are sent to the telescope lag angle control system and to the electronic unit which removes gross Doppler due to

- GLOBAL COVERAGE
- SAMPLING DENSITY SUFFICIENT FOR 300 km x 300 km GRID MEASUREMENTS
- TWO OR MORE LOOK ANGLES FOR EACH MEASUREMENT
- LOCAL AREA TARGETING

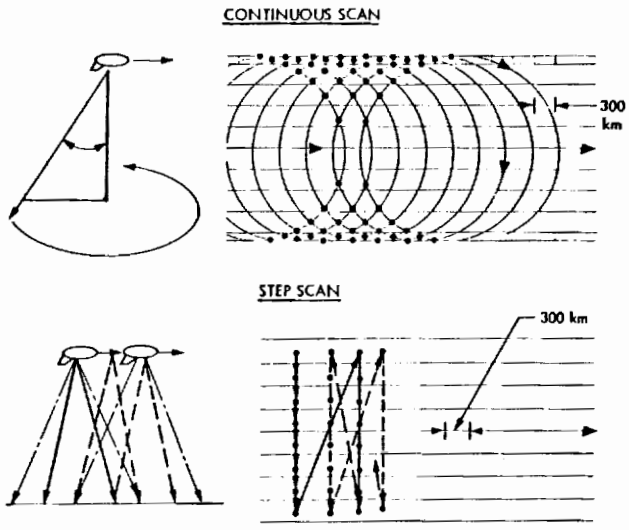

Figure 4. Scanning Options

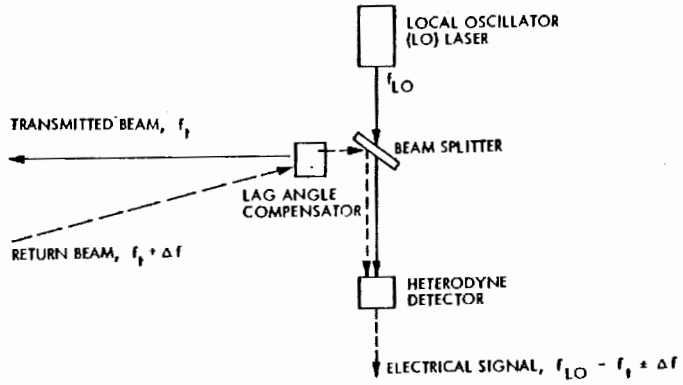

Figure 5. Heterodyne Detection

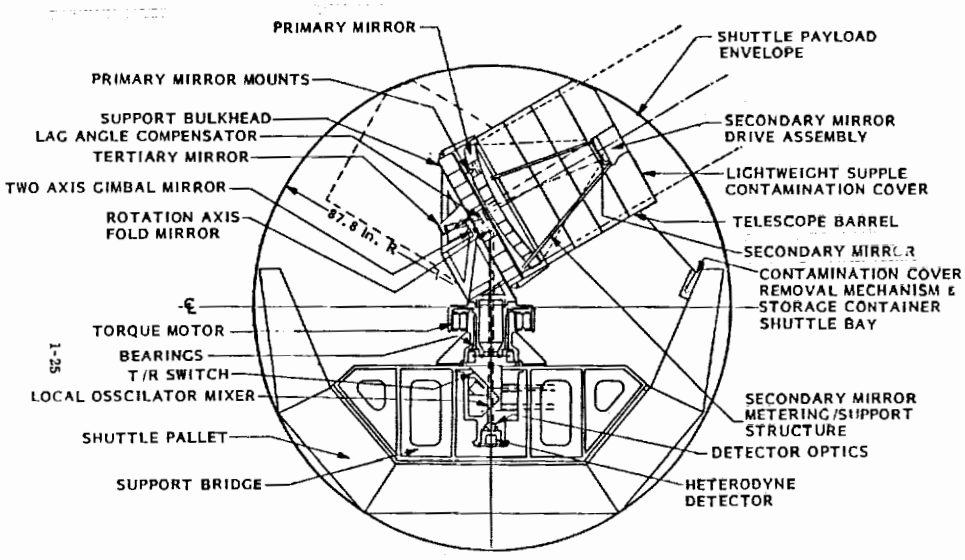

Figure 6. Side View of Lidar Mounted on Shuttle Pallet

Shuttle-earth relative motion. Ephemeris information from the global positioning system (GPS) is also required for pointing determination.

The focal plane consists of a small CW CO_2 local oscillator laser and a single element, cryogenically cooled HgCdTe photodiode.

Signal and data processing provide onboard radial wind estimation in one range bin for every pulse (Parks et al., 1980). All the lidar data are compressed to a 1-Mb rate, then buffered and transmitted to ground through TDRSS for ground processing. Command and control functions are performed by two 16-bit microprocessors and two random access memories.

Total WINDSAT payload weight is 833 kg and total prime power is 1977 W. The optics design includes a moderate amount of lightweighting but the total instrument has not been lightweighted since the Shuttle payload capability is far in excess of WINDSAT requirements. WINDSAT must be flown with the igloo configuration to meet the payload prime power requirements.

A 7-day mission is planned as the baseline flight, with 19 h of "lidar-on" time allotted over 5 on-orbit experiment days. Several experiments could be run, including measurements of radial wind without scanning, plus local, regional, and global wind measurements.

4. SCALABILITY TO AN OPERATIONAL SYSTEM

Scalability of the WINDSAT Shuttle experiment to an operational system is an important feature. The operational WINDSAT lidar would have to fit the satellite payload constraints, have adequate performance from 800-km altitude, and have a 3- to 5-year life. Candidate platforms are existing or upgraded weather satellites or advanced satellites. Payload and power capabilities of these platforms range from 500 kg to over 1000 kg, and from 500 W to more than 2 kW. The Shuttleborne WINDSAT lidar could be scalable to an operational platform by keeping the lidar weight and power within operational platform capabilities. The excess lidar link margin demonstrated in a Shuttle experiment will show that an operational lidar weight and power could be reduced sufficiently to fit a given platform.

Excess link margin can be traded against lower lidar weight and/or power, as shown in Fig. 7. Here the operational link margin is plotted against total lidar weight as a function of lidar prime power. The operational lidar assumed to be further lightweighted from the Shuttle design.

The curve labeled I represents a case of minimum lidar weight, assuming no limit on prime power. Minimum weight is obtained by reducing optics size and increasing laser size and output power. Points on the upper end of Curve I represent laser power levels which stress technology and/or exceed resonable total lidar power budgets. Dashed curves of Fig. 7 correspond to minimum weight systems up to the point where total instrument power requirements equal 1500 W, 1250 W, and 1000 W. The laser power is kept constant above these points and increased S/N is obtained only by increasing the optics diameter.

Figure 7 shows that a reasonably sized system offers substantial link margin. A 1000-lb (455 kg), 1500-W system has a S/N of greater than 7 x 10^2, for example. Further weight savings may be realizable, especially for very small systems. Curve II on Fig. 7 shows weight against S/N assuming that the platform has all the required attitude-sensing capability. This assumption indicates that the platform's control system can be used for some of the lidar control and processing functions, and hence that a lidar-specific attitude sensing system is not needed.

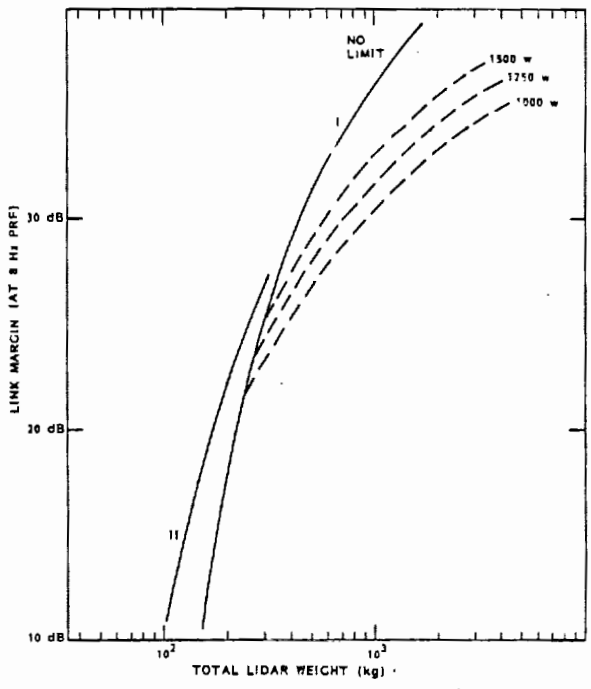

Fig. 7 Lidar Weight as a Function of Link Margin

REFERENCES

Gardner, P. J., 1980: WINDSAT Laser Transmitter Design. Technical Digest - Coherent Laser Radar for Atmospheric Sensing, Opt. Soc. America, 1980.

Glenn, P. and M. McGuirk, 1980: Scanning System Considerations for Coherent Lidar. Technical Digest - Coherent Laser Radar for Atmospheric Sensing, Opt. Soc. America, 1980.

Huffaker, R. M. (Ed)., 1978: Feasibility Study of Satellite-Borne Global Wind Monitoring System. NOAA Technical Memorandum ERL WPL-37, September 1978.

Huffaker, R. M. et al., 1979: Feasibility Study of Satellite-Borne Global Wind Monitoring System, Part II. 10 December 1979.

McGuirk, M., and P. Glenn, 1980: Implementations for a Coherent Lidar Optical Scanner. Technical Digest - Coherent Laser Radar for Atmospheric Sensing, Opt. Soc. America, 1980.

Osmundson, J. S., A. G. Tuffo, J. K. Parks, J. B. Forsyth and L. L. Morgan, 1980: Shuttle-Borne Coherent Lidar Feasibility. Technical Digest - Coherent Laser Radar for Atmospheric Sensing, Opt. Soc. America, 1980.

Osmundson, J. S., 1981: Global Wind Measuring Satellite System. Final Report for NOAA-WPL Contract NA79RAC00127, Lockheed Report No. D767868, April 1981.

Parks, J. S., W. I. Dobrov and J. S. Osmundson, 1980: WINDSAT Signal Processing. Technical Digest - Coherent Laser Radar for Atmospheric Sensing, Opt. Soc. America, 1980.

WINDSAT FREE FLYER USING THE ADVANCED TIROS-N SATELLITE*

Herbert M. Gurk and Paul F. Kaskiewicz

RCA Astro-Electronics Division
Princeton, N.J.

Wolf P. Altman

RCA Advanced Technology Laboratory
Moorestown, N.J.

1. INTRODUCTION AND MISSION REQUIREMENTS

In previous studies of the feasibility of an Earth Orbiting Doppler lidar for global wind measurement, it was found that the instrument accommodations required were so great that the space vehicle necessary was the STS Space Shuttle Vehicle (Lockheed, 1981) or some currently non-existent) large satellite in low Earth orbit. Together with representatives of the National Oceanic and Atmospheric Administration (NOAA), Mathematical Sciences Northwest, Inc. (MSNW) and Perkin-Elmer Corp., however, we have recently shown that this type of lidar could now be built to be accommodated by an existing class of free flying, near-polar orbiting, meteorological satellites, the RCA Advanced TIROS-N (ATN) series. MSNW conceived the laser subsystem, Perkin-Elmer the optical system, and RCA the system design, the spacecraft bus and the on-board data processor.

The guidelines for the Windsat Free-Flyer Study were set by the Wave Propagation Laboratory (WPL) of NOAA. The launch date of the operational spacecraft was assumed to be in the early 1990's, following a development program on the lidar instrument. The free flyer was to be launched using the Space Shuttle. The satellite was to be based on the concepts RCA had proposed (RCA, 1981a,b) for the Shuttle launched versions of the meteorological satellites currently designed and built by RCA.

The performance and operational requirements set by WPL for this study were very similar to those for the Shuttle Windsat study, (Lockheed, 1981), with one major exception. In order to reduce power, the lidar would transmit and process the returns from pulses sent at a 2 pps rate rather than at an 8 pps rate. The other requirements are summarized in Table 1. The lidar transceiver concept is based on an injection-locked CO_2 TEA laser operating at 9.11 μm.

TABLE 1. WINDSAT FREE-FLYER MISSION REQUIREMENTS

- Lidar Wind Sounding from a Sun Synchronous Satellite
- Lidar
  - Aperture: 1.25m
  - Fixed Nadir Look Angle: 52.7°
  - 10 Joules Output per Pulse
  - 2 Pulses per Second
  - 3 to 4 Microsecond Pulse Duration
- Operational Modes
  - Continuous Conical Scan, Rotation Period = 19.04s
  - Stop and Stare
  - High Spatial Resolution Intermittent Observation, $\geq$15° from Subtract Normal
- On-Board Doppler Processing
- Real Time and Stored Data Transmission
- 2 Year Operations Goal
- STS Launch to Shuttle Parking Orbit, followed by Direct or Indirect Ascent to Operational, Near-Polar Orbit

The orbit for the Windsat Free Flyer would be sun-synchronous and circular at 833 kilometers altitude, i.e., at an inclination of 98.7 degrees and with a period of approximately 102 minutes. The corresponding satellite subtract velocity is 6.576 km/sec, and the separation of consecutive tracks is 25.5° along the equator. Since the geocentric angular width of the coverage swath is approximately 22.8°, there is less than a 300 km gap between the zones covered on consecutive swaths. Since the horizontal resolution is to be nominally 300 km, two full global coverages are obtained each day. The on-orbit mission goal is for a two-year life.

Doppler processing is to take place on-board the spacecraft, and the derived backscatter power, mean frequency, and variance of the frequency are to be transmitted to the ground for each altitude cell for each pulse. There are to be twenty 1 km attitude cells, covering the lowest 20 km of the troposphere. Data transmission is to be both in real time (so that ground stations in view may obtain it immediately) as well as after storage (so that all data around the orbit may be recovered). Auxiliary data, defining spacecraft and telescope position, orientation,

*An expanded version of this paper appeared in Applied Optics, 1 August 1984, Vol. 23, No. 15

†This work was supported by the Defense Meteorological Program of the United States Air Force and by the National Oceanic and Atmospheric Administration under contract number NA82RAC00141. The contract monitor was R. Milton Huffaker of the Wave Propagation Laboratory of the NOAA Environmental Research Laboratory, Boulder, Colorado 80303.

and calibration parameters, are to be transmitted along with the lidar outputs.

2. LIDAR INSTRUMENT

The development of the telescope system from that of the earlier Shuttle based concept has been described by McHugh of Perkin Elmer (McHugh, 1983). The overall lidar instrument package for this satellite will be mounted at the end of the Equipment Support Module (ESM). The telescope, switch and detector assembly, and the laser subsystem are integrated and aligned on an optical bench on which they are mounted. The bench is a key part of the optical system; it simplifies the definition of the optical interfaces between the three major elements and provides the support for the integrated lidar to be mounted to the spacecraft.

The key result of the telescope and optical system study was the reduction of its weight to 285 kg, including an estimated 91 kg for the optical bench. The optical subsystem concept is basically identical to the one developed for the study of the Shuttle-based lidar (Lockheed, 1981). In order to reduce the weight, however, the chief structural elements of the system (including the primary mirror) are to be constructed of honeycombed beryllium, manufactured by means of Perkin-Elmer's proprietary HIP (Hot Isostatic Press) process. Through use of this process, the mass of the optical subsystem is reduced by 40% below that of the design developed during the Shuttle study.

The development of the laser system from that of the earlier Shuttle based concept is described by Mathematical Sciences Northwest as part of the RCA Windsat Study (Byron, 1983 and RCA, 1983). On the basis of these results, a UV-preionized laser can be incorporated in the design and achieve high efficiency and low frequency-chirp, obviating the requirement for high voltages (80 to 100 kV) necessary for the e-beam preionization scheme which had been recommended in the previous studies (Lockheed, 1981). A single CW laser is utilized as both the local oscillator and the injection source. This reduces the weight and power by 14 kg and 30 W below those of the previous designs. The required laser lifetime is achieved by judicious selection of a combination of gas composition and catalytic converters.

The resultant laser system for the Free-Flyer lidar requires 448 watts, weighs 155 kg and fits in a total package 1.5m x 1m x 0.5m. The laser transmitter efficiency is 5.3%. Laser cooling is provided by a liquid coolant which passes through the cavity and is pumped through a large area passive radiator mounted on the spacecraft to face cold space. The HgCdTe detector on this system uses a radiative cooler of the same type as is currently used for many spaceborne infrared radiometers.

The third major element of the lidar is the signal processor. The primary purpose of this processor is to digitize the analog output from the transceiver, perform on-board Doppler processing, and compress the high data rate of 242 kbps to a more manageable rate in real time. The date to be transmitted are the first three moments of the Doppler-processed return signal for each range (i.e., altitude) cell for each transmitted pulse. These moments are (1) the total detected power, (2) the mean frequency (which is indicative of the radial wind velocity) and (3) the variance of the spectral energy distribution. The total data rate for 20 range cells per pulse and 2 pulses per second is 960 bps (assuming 10, 8, and 6 bits, respectively, for the three moments).

The processing techniques proposed for the Windsat Free Flyer are basically the same as for the Shuttle study, in particular the use of Fast Fourier Techniques for spectral estimation. Estimates have been developed for the power, weight, and size of the signal processor and are traceable to actual hardware under construction. The processor has four major elements. First, a variable frequency synthesizer removes the background Doppler shift due to satellite motion and Earth rotation from the total Doppler shift of the signal. An electronically tunable synthesizer using a Yttrium Iron Garnet (YIG) oscillator, YIG bandpass filter, and comb generator under development at RCA are recommended for the synthesizer. Secondly, a high speed digitizer using currently available chips is proposed. Thirdly, a high speed memory using a combination of Emitter Coupled Logic (ECL) and CMOS logic in a sequence of ping-pong and serial buffers is recommended. Finally, the spectral estimator using FFT processing uses two parallel ATMAC II microprocessors, developed by RCA's Advanced Technology Laboratories, for the generation of the three moments.

Auxiliary processing functions are performed by the spacecraft computer. The overall signal processor is packaged in three boxes to spread the thermal dissipation in order to simplify its mounting beneath spacecraft louver radiators. The resulting signal processor power and weight have been reduced from 186 watts and 51 kg for the Shuttle hardware to 85 watts and 12 kg for the Free-Flyer subsystem.

For the lidar as a whole, the weight has been reduced from 831 kg to 470 kg and the power from 2123 watts to 559 watts.

3. SPACECRAFT ACCOMMODATIONS FOR WINDSAT

3.1 Orbit Achievement

The requirements for spacecraft subsystem capabilities - payload weight, fields-of-view, power, thermal control, attitude determination and control, data handling, communications and command - were primarily determined from the on-orbit mission requirements. However, the capabilities of the on-board propulsion system (assumed to use 703 kg of hydrazine) and the STS launch constraints determine how much the total spacecraft can weigh. Unless one is willing to pay the high price of a dedicated Shuttle launch, it is expected that the Shuttle will have to be shared

between at least two payload spacecraft on any launch. Since the two spacecrafts are not likely to require the same operational inclination and orbit nodal crossing, a compromise Shuttle parking orbit may be required. For the SAATN and Block 5D-3 proposals (RCA, 1981a,b, the worst case Shuttle parking orbit was assumed to have an inclination of 104° and a nodal crossing 5 hours from that desired. In order to change the nodal crossing, the satellite was to be transferred to an intermediate "drift" orbit at 460-480 km altitude where it was to stay for up to 90 days while the orbit plane precessed to the desired node. Assuming the same procedure is used for Windsat and that 658 kg of the 703 kg of hydrazine is available for transfers to the drift orbit and from there to the mission orbit (including necessary inclination changes), then the maximum dry weight for Windsat using this "worst-case" indirect ascent and the SAATN size hydrazine and nitrogen tanks is 1369 kg.

3.2 Spacecraft Configuration

The overall configuration for the Windsat lidar and the ATN-based spacecraft bus was developed to satisfy the constraints imposed by stowage within the Space Shuttle Vehicle for launch and also the field-of-view requirements of the lidar and the spacecraft subsystems for all phases of the mission. An artist's conception of the final configuration of the Windsat spacecraft is shown in Figure 1.

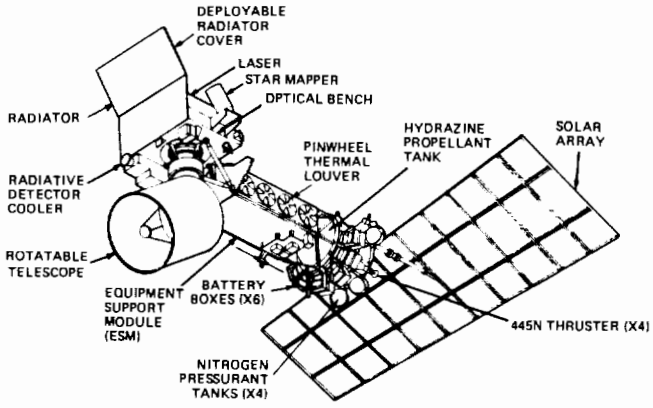

Figure 1 Windsat Free Flyer Operational Configuration

The lidar is mounted on the cold space end of the Equipment Support Module (ESM) of the ATN spacecraft in the location occupied by the Instrument Mounting Platform (IMP) on current ATN's. This location permits a view of cold space for the cone-shaped HgCdTe detector cooler and for the large, 1.5 m^2, radiator used to cool the laser.

The cooler cover is shown open for the spacecraft in its operational orbit. The spacecraft velocity is normal to the long dimension of the ESM (i.e., in or out of the paper) with the lidar end of the spacecraft furthest from the Sun. The 10-panel solar array rotates about the array boom, keeping the Sun on the solar cell side of the array as the spacecraft orbits the Earth.

There were three specific drivers in developing this ATN concept for Windsat:

- Payload - the weight, physical size, and view factors required for the lidar instrument and its coolers
- Cradle - the need to provide the structural interface with the Shuttle (assumed to be similar to that for SAATN)
- Cocoon - the desirability of a contamination shield to protect the payload while in the Shuttle, but which in turn severely limits the envelope of the spacecraft in its stowed position within the Shuttle bay

Figure 2 shows an orthographic projection within the Shuttle with the array fully deployed (which does not occur until the operational orbit is attained) to give the reader a clearer view. The major configuration changes from existing ATN spacecraft include:

- A larger solar array (25% area increase)
- The use of the unique optical bench of the integrated lidar instrument as the mounting interface instead of an Instrument Mounting Platform (IMP) which on ATN is part of the spacecraft structure
- Lowering the total instrument package to fit within the Shuttle
- The mounting of all attitude sensors on the optical bench
- Changing of the direction of the thrusters to fire through the average position of the center of gravity
- Strengthening of the structure to carry the 485 kg lidar load at the end of the spacecraft.

Table 2 summarizes the weight of Windsat. As can be seen, the required liftoff weight is 187 kg less than the capability of the propulsion system (in the assumed indirect ascent scenario described earlier). Thus, there is considerable margin to allow for uncertainties of early design and/or growth.

3.3 Electrical Power

Windsat requires electrical power not only during its operational phase at 833 km altitude, but also during the ascent phases which may be as long as 200 minutes each (between Shuttle and drift orbits and between drift and operational orbits) and during the drift phase (for up to 90 days). The principal initial concern was to support the requirements of the mission phase continuously, if possible, for two years. Table 3 indicates the operational on-orbit power for the bus and payload (in the continuous scan mode) as just under 800 watts. This load can be supported through a two year operational life by increasing the ATN array size to 14.6 m^2, using 10 instead of 8 standard ATN solar panels and limiting the range of Sun angles (i.e., the angle between the

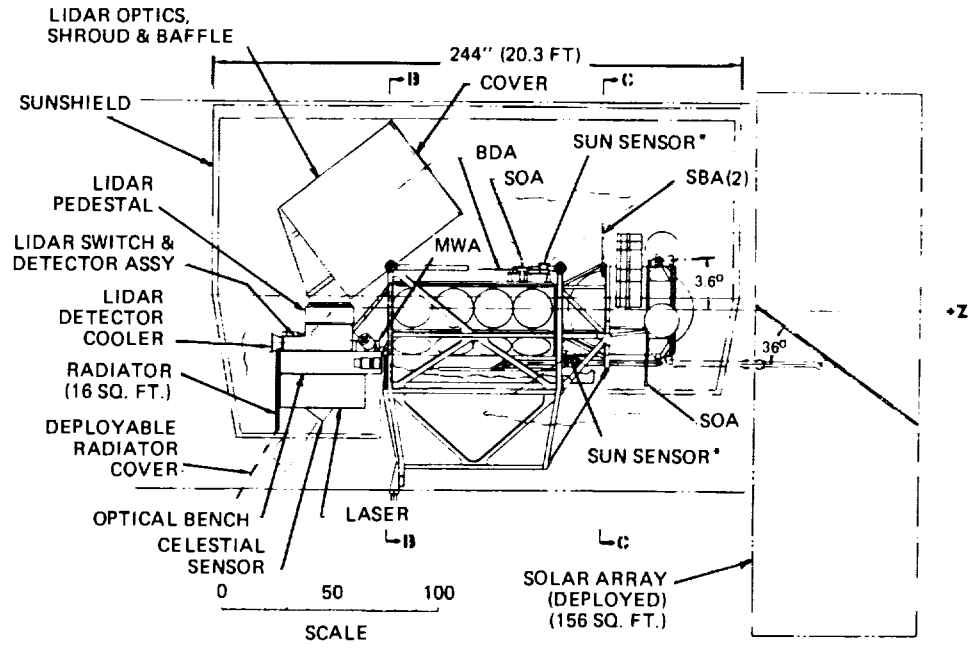

Figure 2. Windsat Spacecraft Configuration

TABLE 2. WINDSAT SYSTEM WEIGHT

Subsystem	Weight (kg)
Structure	196
Thermal	32
Attitude Determination and Control	58
Power	172
Communications	9
Command/Control	30
Data Handling	42
Harness	69
Propulsion (Dry)	104
Payload	470
S/C Dry Weight	1182
N_2H_4 (603 kg) + GN_2 (30 kg)	773
Liftoff Weight	1915
Liftoff Capability	2102
Margin	187

Sun-line and the orbit normal) to 5° - 40° which correspond to early morning or late afternoon local times for the nodes of the orbit. With this limitation, the solar illumination remains closer to the array normal and can provide the necessary output for spacecraft loads including battery charging.

Three nickel cadmium batteries, of 26.5 amp-hr capacity each, provide power during eclipses and for peak short-term loads. The ATN power distribution system which normally has a +28V regulated bus and a +28V pulse load bus will be modified to have the +28V regulated bus and an unregulated bus in the range of +17 to +30V. The latter provides power to the laser which contains its own conditioner to increase the voltage to 30-40 kV.

Power requirements for the ascent and drift phases are slightly greater than 200 watts for the bus functions plus the heater requirements for the laser. In order to reduce the latter to approximately 25 watts, a cover is kept on the laser radiator during these phases to limit the heat loss (and keep the coolant from freezing). Even with this limitation, the batteries are insufficient to provide the necessary power for even the 200 minute ascent phases, let alone the potential 90-day drift. To provide sufficient power, the solar array (but not the solar array boom) is opened so that its full 14.6 m^2 area of cells is exposed. During 35-50 minutes of ascent, the spacecraft is available for an orientation (in roll) to expose the cells sufficiently to charge the batteries. Likewise, during the full drift period, the spacecraft is oriented so as to provide solar illumination on the array. In this way, sufficient power is also available during these phases. The solar array boom is deployed upon achievement of the operational orbit.

TABLE 3. WINDSAT ORBIT-AVERAGE OPERATIONAL POWER REQUIREMENTS

	Orbit-Average Power (Watts)
LIDAR	
Optical Subsystem (Telescope, Scan Mechanism, Structure, Optical Bench)	20
Lidar Tranceiver (CO^2 Laser, Local Oscillator, Detector Cooler Power Conditioner)	448
Laser Cooling Array	0
Signal Processing/Data Handling	85
Attitude Sensing	Included in spacecraft allocation
Momentum Compensation	6
Total Lidar	559
SPACECRAFT BUS	
Attitude Determination and Control	85
Thermal	80/54 (5°/40° Sun angle)
Command/Control	30
Communications	11
Power	6
Data Handling	17
Total Spacecraft Bus	229/203 (5°/40° Sun angle)
TOTAL	788/762 (5°/40° Sun angle)

3.4 Thermal Control

The major changes to the ATN thermal subsystem arise because of the need to accommodate the lidar. Three items are of most significance for thermal control of this instrument. The major requirement is to dump approximately 400 W of heat from the laser. The recommended scheme is to pump the laser coolant from the laser into tubing running through the back of a 1.5 m^2 radiator which faces cold space. With the coolant entering at 330 K and the radiator at 320 K, the heat from the laser can be dissipated.

The other two items of interest are the HgCdTe detector and the signal processor. The detector must be cooled to approximately 105 K. A multistage passive radiator of the type used on ATN for the Advanced Very High Resolution Radiometer (AVHRR) instrument or on Block 5D-2 for the OLS instrument can be used to cool the detector by radiating heat to cold space. This cooler is also mounted on the anti-Sun edge of the optical bench. The signal processor generates approximately 85 watts to be dissipated. By packaging the processor into three boxes of proper dimensions, they can be mounted under four louver radiators in the ESM, each of which can dissipate approximately 25 watts.

3.5 Guidance and Control

The Guidance and Control subsystem for Windsat uses a combination of the techniques proposed for the SAATN and the Block 5D-3 spacecraft, most of which are currently used on the ATN and Block 5D-2 spacecraft. Guidance and thrust control is provided during ascent for the hydrazine liquid propulsion system under computer control using an automatic velocity metering technique and the uplinking of targeting parameters from the ground. The three active gyros of the inertial measurement unit (IMU) are used for 3-axis sensing during ascent. The nitrogen thrusters are used for reorientation of the spacecraft for thruster burns and solar array illumination, and for other attitude maneuvers.

Operational attitude control uses a star mapper, for precision attitude determination updates and IMU gyros for continuous sensing. The system is a zero-momentum 3-axis control system with control actuation using three orthogonal reaction wheel assemblies (RWA's) plus a skewed fourth RWA for redundancy, and magnetic torquing for momentum control. This precision attitude determination and control system provides attitude determination to 0.003 degree (1σ) and pointing control to 0.1 degree (1σ) which are two to four times better than the Windsat requirements. Short term jitter is also controlled to better than the 0.011 degree per second required.

3.6 Data Handling, Communications, and Command

The data handling, communications, and command subsystems for Windsat use the corresponding subsystem equipment from the SAATN spacecraft with some eliminations of unnecessary equipment. Table 4 summarizes the estimated lidar data rate. The TIROS Information Processor (TIP) is used to format payload instrument data as well as spacecraft and payload health-and-status telemetry for storage and downlink transmission. The TIP format can accommodate 6160 bits per second of payload data and, hence, is more than adequate for the Windsat lidar data.

TABLE 4. ESTIMATED LIDAR DATA RATE

Type	Rate (bps)
Doppler Data	960
Support Measurements	1063
Housekeeping	670
Total Sensor Rate	2693

Three NASA standard, dual-transport tape recorders are required for Windsat; one for around-the-orbit recording, a second to play back the data from the previous orbit, and a third as a spare. Each transport on each recorder can store over two orbits of data. The TIP input is at 8.32 kbps; recorder playback is increased 40:1 to 332.8 kbps.

Windsat downlink communications are both real time and for playback of the recorders, using a VHF beacon link for the former and two S-band links for recorder playbacks.

Command requirements for Windsat are also not yet determined because of the lack of a detailed design. However, as was the case for health and status telemetry, there is considerable margin for lidar commands after the command requirements for the bus have been satisfied. The bus only uses about 40% of the available command capability for pulse and level commands.

4. CONCLUDING REMARKS

The results of this study show the feasibility of carrying a wind measuring lidar on an ATN-derivative free flying spacecraft. The overall configuration fits within the Shuttle bay and uses the same techniques for STS Launch as the proposed SAATN spacecraft. The lidar can be made light enough that the total weight of the satellite is well within the capability of the on-board propulsion system for transfers to a Sun synchronous orbit at 833 km attitude. The principal techniques for weight minimization are the use of the Perkin Elmer proprietary HIP process for the telescope, new packaging concepts for the laser and for the optics-laser interface, and the application of current technology to the signal processing hardware. Power minimization is achieved for the lidar primarily by use of a low pulse repetition frequency, i.e., 2pps, and again by the use of current processor technology. The power capability of the spacecraft is enhanced by increasing the ATN array size 25%, through the addition of two more solar array panels of the present size, and by limiting the range of Sun angles over which the spacecraft is operated. The same basic concept for the lidar as proposed in the Shuttle Windsat study is recommended here, but there are some changes in details to improve weight and power. No major technology breakthroughs are required for the lidar, but some technology experiments are recommended for the laser subsystem to verify isotopic gas lifetime and performance, modulator life and weight, and for space qualification. Spacecraft changes are all natural modifications or growth to accommodate the payload. Overall, the proposed system provides substantial margin for the uncertainties for the future and for potential payload change, and also demonstrates the reasonableness of the Windsat Free Flyer concept.

REFERENCES

Byron, S.R., S.E. Moody and T.A. Znotins, 1983: Definition Study of Windsat Laser Subsystem, Technical Digest, 2nd Topical Meeting on Coherent Laser Radar, Technology and Applications, Optical Society of America, Paper TUC4.

Lockheed Missiles and Space Company, 1981: Report LMSC-D767868, "Global Wind Measuring Satellite System - Windsat", Final Report, NOAA contract #NA79RSC00127, Prepared for National Oceanic and Atmospheric Administration, Wave Propagation Laboratory, April 1981.

McHugh, T., and K. Hancock, 1983: Windsat Free-Flyer Telescope Concept Using Ultralight Weight Beryllium Technology, Technical Digest, 2nd Topical Meeting on Coherent Laser Radar, Technology and Applications, Optical Society of America, Paper TUC5.

RCA Astro-Electronics, 1981a: Proposal No. 102983-A, NOAA-H, -I, and -J Satellite Program Technical Proposal, Prepared for National Aeronautics and Space Administration, Goddard Space Flight Center, Request for Proposal No. 5-65316/42, February 26, 1981.

RCA Astro-Electronics, 1981b: Proposal No. 102932-A, prepared for Space and Missile Systems Organization, United States Air Force, Request for Proposal No. F04701-81-R-0017, 5 June 1981.

RCA Astro-Electronics, 1983: Feasibility Study of a Windsat Free Flyer, Final Report, with subcontractors Mathematical Sciences Northwest, Inc. and Perkin Elmer Corporation, prepared for National Oceanic and Atmospheric Administration, Environmental Research Laboratories, Contract NA82RAC00141, 21 July 1983.

PRELIMINARY PLAN FOR A SHUTTLE COHERENT ATMOSPHERIC LIDAR EXPERIMENT (SCALE)

D. Fitzjarrald, R. Beranek, J. Bilbro, J. Mabry

NASA Marshall Space Flight Center
MSFC, Alabama USA

1. INTRODUCTION

A study has been completed to define a Shuttle experiment that solves the most crucial scientific and engineering problems involved in building a satellite Doppler wind profiler for making global wind measurements. The study includes: 1) a laser study to determine the feasibility of using the existing NOAA Windvan laser in the Space Shuttle spacecraft, 2) a preliminary optics and telescope design, 3) an accommodations study including power, weight, thermal, and control system requirements, and 4) a flight trajectory and operations plan designed to accomplish the required scientific and engineering goals. The experiment will provide much-needed data on the global distribution of atmospheric aerosols and demonstrate the technique of making wind measurements from space, including scanning the laser beam and interpreting the data. Engineering accomplishments will include space qualification of the laser, development of signal processing and lag angle compensation hardware and software, and telescope and optics design. All of the results of this limited Spacelab experiment will be directly applicable to a complete satellite wind profiler for the Earth Observation System/Space Station or other free-flying satellite.

2. STUDY GOALS AND LIMITATIONS

The experiment described herein is intended to answer questions standing in the way of development of a satellite Doppler Lidar wind profiler that can only be answered by a space flight experiment. The design philosophy is to keep the experiment simple, so that it remains a relatively cheap, Spacelab operation. For this reason we have chosen to use an existing and proven laser design with 2 J pulse energy, which is somewhat smaller than the 10 J laser required for a free-flyer. Technology development of the larger laser and its attendant lifetime requirements can be pursued in earthbound laboratories. We have chosen to use a telescope that is fixed in the Shuttle bay to eliminate the complexity and expense of scanning optics. Scanning the beam to make wind measurements will be done by movement of the entire Shuttle vehicle. The design study was carried out in all relevant areas far enough to determine that the system could be built using existing technology.

3. SCIENCE

The most crucial atmospheric science question that must be answered before adequate performance and feasibility analyses can be made for CO_2 lidars concerns the amount and distribution of aerosols that contribute to backscatter in the 10 micron spectral range. The latest data analyses indicate that there is a global background of aerosol backscatter at or below approximately 10^{-10} m^{-1} sr^{-1}. Superimposed on the low background level are regions of higher backscatter, including all of the planetary boundary layer, much of the mid-troposphere over land, the lower and middle troposphere during remote ocean dust events, subvisible cirrus in the upper troposphere, and volcanic events in the upper tropospher and lower statosphere. The SCALE experiment is designed to provide global backscatter distribution with the best possible sensitivity using current technology by using the lowest Shuttle altitude and the largest practical optics aperture.

Figure 1a shows the system sensitivity at various altitudes for three AFGL standard atmospheres using the nominal design values of 185 km altitude, 2 J laser energy, 1.25 m aperture, a signal to noise ratio of 5 db, and operation at the 9.11 micron isotope laser wavelength. The laser feasibility study indicates that the additional cost for operation at 9.11 micron wavelength will be modest. Included for comparison in figure 1b are the results of the same calculation for a normal isotope operation at 10.6 microns. The differences are entirely due to the effects of absorption by atmospheric CO_2. With this performance all of the enhanced backscatter events will be covered, and the sensitivity is close enough to the expected background level to delineate the worldwide distribution of very low backscatter areas. The low altitude of the Shuttle compensates for the lower laser pulse energy, so that the sensitivity is nearly that of a free-flying wind profiler.

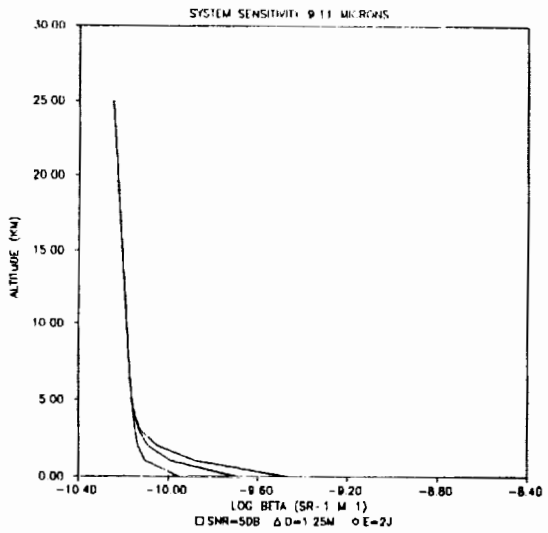

Figure 1a System Sensitivity 9.11 Microns

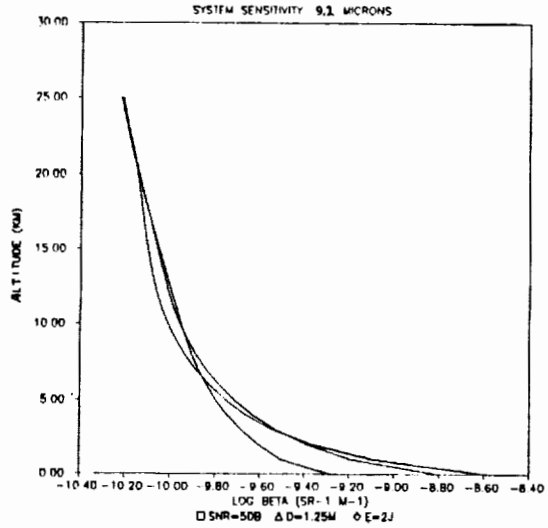

Figure 1b System Sensitivity 9.2 Microns

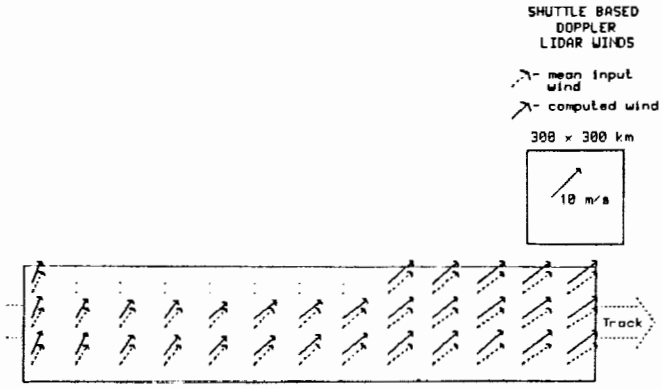

Figure 3 Computer Simulation of SCALE Measured Winds

Figure 2 shows the ground projection every 10 sec of the lidar line of sight in the scanning mode, ie. optics fixed in the Shuttle bay and the orbiter rotating at 2 deg/sec about its yaw axis. At the 25 Hz lidar pulse rate there will be sufficient line of sight estimates to calculate the wind in a 300 km swath along the flight track, as shown in figure 3, which gives the result of a computer simulation using a realistic simulated wind field and random errors. Wind estimates will be calculated for each 1 km of altitude along during the scanning mode. Approximately 2 scans will be made per orbit to allow wind estimates to be compared with selected ground and rawindsonde sources.

Figures 4a and 4b show 24 hour repeating orbits for two possible Shuttle missions. A number of ground target sites for backscatter and wind comparisons are shown on the figure, including the NOAA, JPL, and MSFC ground based lidars. Southern hemisphere remote ocean, and tropical measurement comparisons will be very important, and are shown on the map. A detailed Shuttle trajectory and lidar ground track are shown in figure 5 over the southern US showing the area for a detailed rawindsonde comparison in the MSFC area. This area is substantially the same as that of the radiosonde network for the planned 1986 NASA Satellite Precipitation And Cloud Experiment (SPACE), which will provide some valuable data for simulations and planning for a comparison experiment with the Shuttle Lidar.

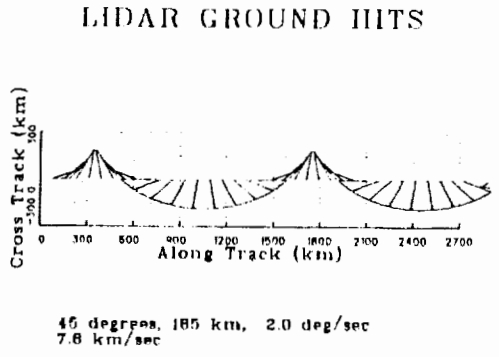

Figure 2 Ground Projection of Lidar Beam

4. LASER TRANSMITTER, OPTICS, AND TELESCOPE

The results of the laser study are summarized in figure 6. The conclusions are that the conversion to Space Shuttle operation is feasible, with some design modifications, principally to the pulse forming and power components. Pulse repetition will be reduced from the 50 Hz of the Windvan design to 25 Hz, to conform with the Shuttle power limitations. The laser transmitter and pulse forming modules will be housed inside an enclosure to provide acoustic and EMI protection for the Shuttle and to provide the transmitter with the proper environment.

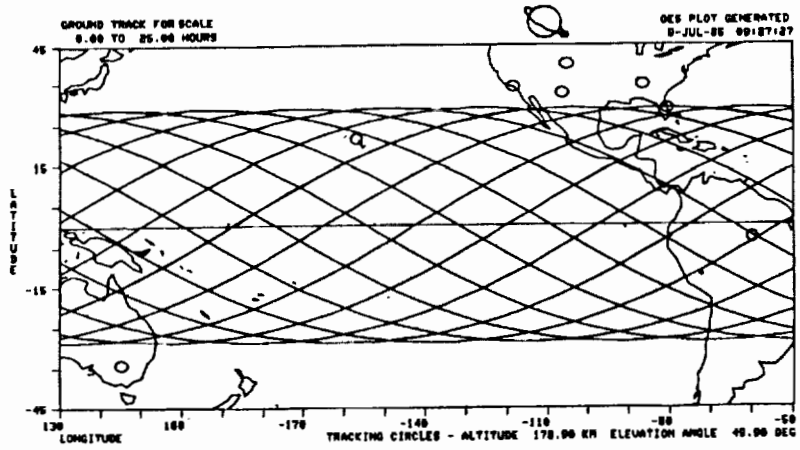

24 HOUR REPEATING ORBIT

INCLINATION 28.5 DEG

ALTITUDE 178 KM

TARGETS AVAILABLE (SHOWN BY - O)

	SITE	LATITUDE	LONGITUDE
	BOULDER, CO	40.0	-156.26
	HUNTSVILLE, AL	34.7	-86.6
K	KSC, FL	28.5	-80.7
K	MANAUS, BRAZIL	-3.06	-60.0
K	MAUNA LOA, HA	21.2	-157.2
	MELBOURNE, AUSTRALIA	-34.2	145.0
	PASADENA, CA	34.1	-118.52
	WHITE SANDS, NM	32,4	-106.5

Figure 4a Shuttle Orbit 28.5 deg Inclination

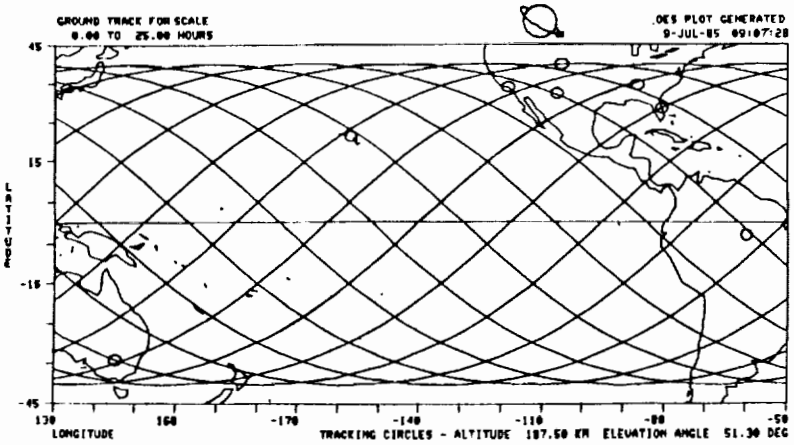

24 HOUR REPEATING ORBIT

INCLINATION 40 DEG

ALTITUDE 187.5 KM

TARGETS AVAILABLE (SHOWN BY - O)

	SITE	LATITUDE	LONGITUDE
K	BOULDER, CO	40.0	-156.26
K	HUNTSVILLE, AL	34.7	-86.6
K	KSC, FL	28.5	-80.7
K	MANAUS, BRAZIL	-3.06	-60.0
K	MAUNA LOA, HA	21.2	-157.2
K	MELBOURNE, AUSTRALIA	-34.2	145.0
K	PASADENA, CA	34.1	-118.52
K	WHITE SANDS, NM	32,4	-106.5

Figure 4b Shuttle Orbit 40 deg Inclination

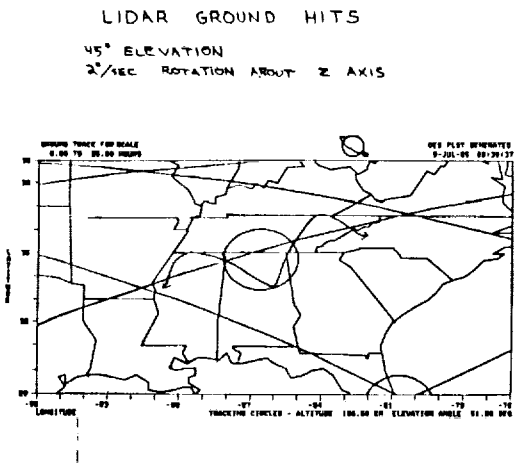

Figure 5 Laser Beam Ground Track During Scan

STI STUDY SHOWS SHUTTLE BASED "WINDVAN" CONVERSION FEASIBLE

- STUDY PREMISE - Take existing design and see if it can be shuttle qualified
- KEY RESULT - STI/NOAA "WINDVAN" CO_2 lidar system can be shuttle compatible
- WEIGHT, VOLUME, POWER REQUIREMENTS REASONABLE
- NO NEW TECHNOLOGY NEEDED
  - Repackaging and qualification engineering would be needed
- PRINCIPAL ENGINEERING/PACKAGING DESIGN MODIFICATIONS
  - Compact pulse power
  - Solid state switch rather than thyratron
  - Launch harden certain components

Figure 6 Laser Study Results

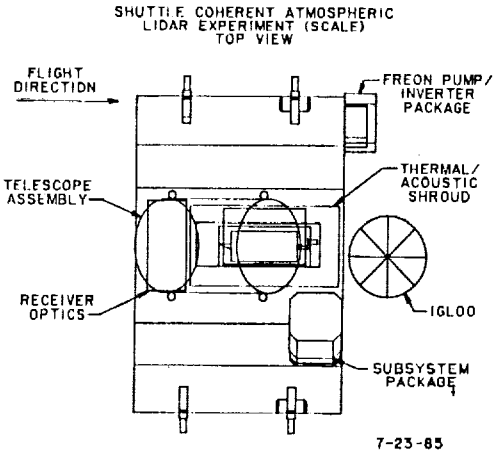

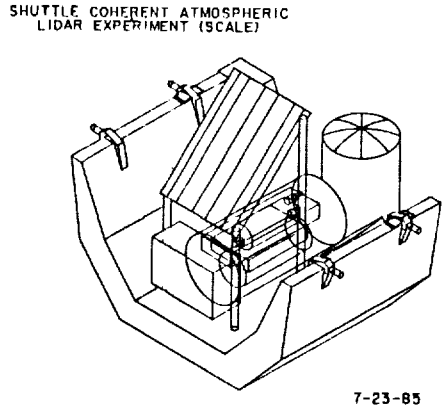

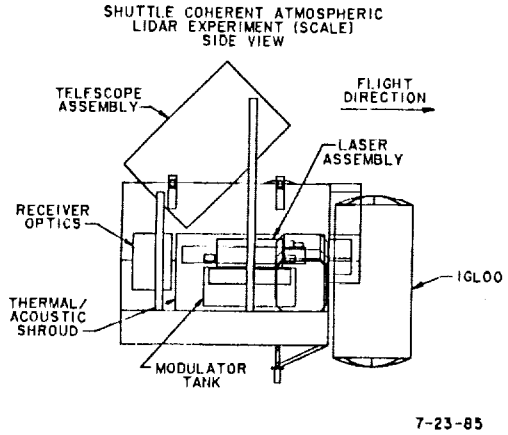

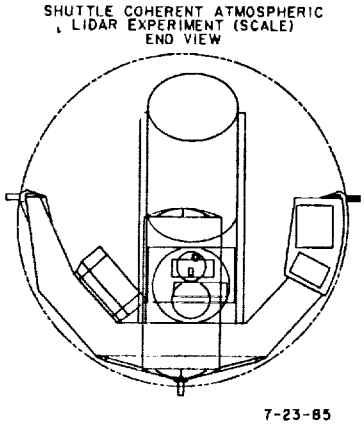

Figure 7 SCALE Apparatus on Spacelab Pallet

SCALE ELECTRICAL POWER BUDGET

SCIENCE INSTRUMENTS	POWER REQUIRED (WATTS)
LASER (MECHANICAL)	75
LASER (ELECTRICAL) AT 25 Hz REPETITION RATE	1,300
GAS PROCESSOR	180
THERMAL (ONE PUMP)	315
C^3	100
OPTICAL/STRUCTURAL	250
	2,220
SPACELAB (IGLOO AND PALLET)	
C&DH (W/HDR OPTION)	1,955
THERMAL	375
DISTRIBUTION AND CABLE LOSS (5%)	111
CONTINGENCY (15%)	333
TOTAL	4,994 WATTS

Figure 9 Power Budget

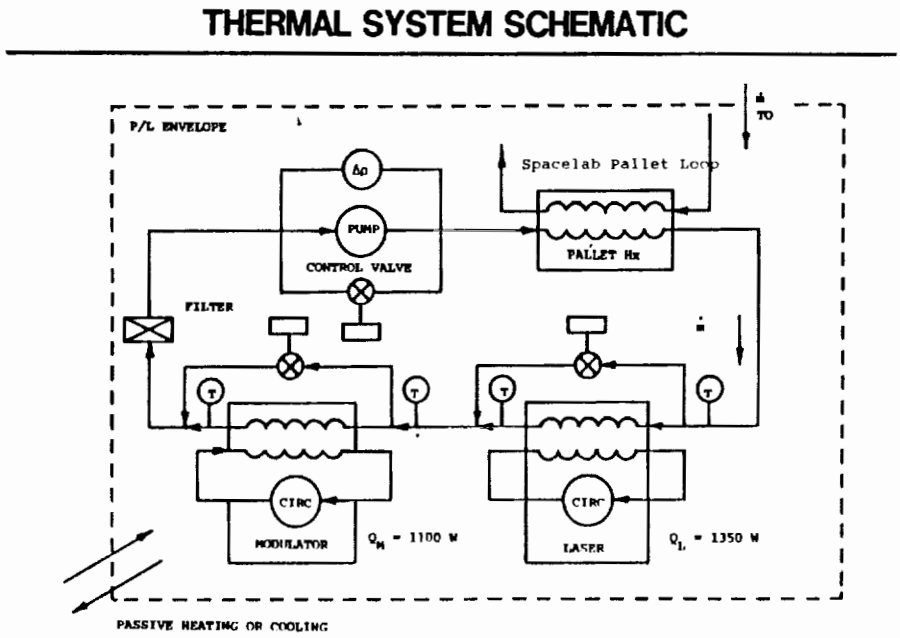

Figure 10 Thermal System

SCALE

CDMS REQUIREMENTS

- HOUSEKEEPING
  - 120 KB/S DOWNLINK
  - REQUIRES SHUTTLE STATUS (POSITION, ATTITUDE, ETC.)
  - TEMPERATURE, PRESSURE, VOLTAGE, POWER, ETC. FROM EXPERIMENT
- SCIENCE DATA
  - RAW DATA
    - UP TO 3.5 MB/S DOWNLINK
  - PROCESSED DATA
    - 18 KB/S DOWNLINK
    - PROCESSED BY EXPERIMENT
    - DOPPLER MOMENTS AND CALCULATIONS
- VIDEO DATA
  - BORESIGHTED TV CAMERA
  - 4.5 MHZ CHANNEL
  - MAY RECORD DURING PEAK DATA DOWNLINK
- TOTAL DATA REQUIREMENT
  - 3.6 MB/S PLUS TV CHANNEL
  - DOWNLINK ALL DATA DURING NORMAL OPERATION
  - RECORD DATA WHILE IN MANEUVER
  - DOWNLINK RECORDED DATA WHILE OVER TARGETS OF NO INTEREST

Figure 11 Command and Data Management System

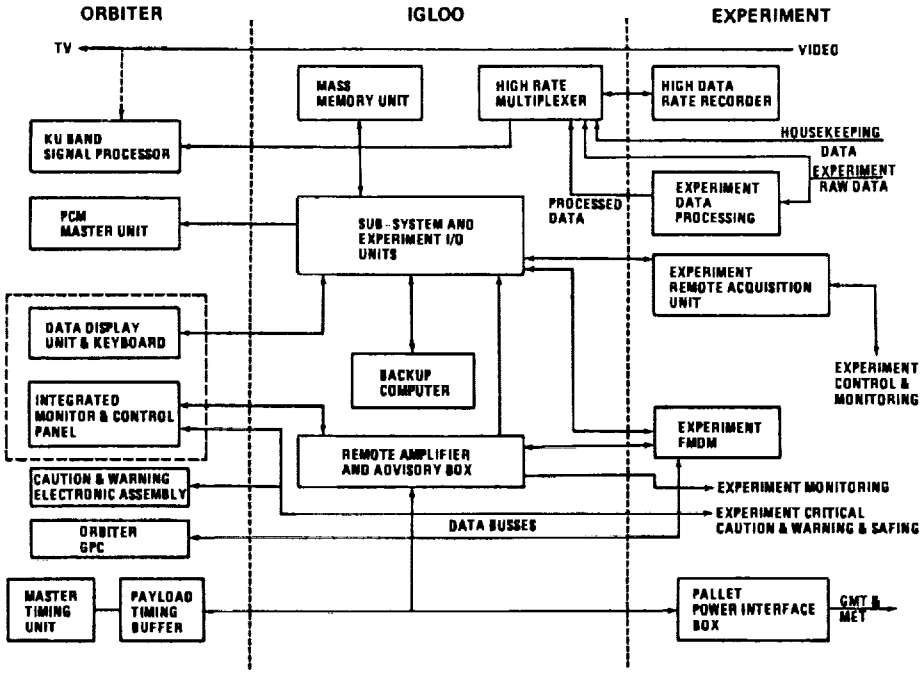

Figure 12 Command and Data Management Configuration

Optics, including that associated with the laser transmitter and the heterodyne interferometer, will be designed to withstand the launch loads without realignment. Preliminary calculations indicate that this is possible using current technology. Estimates of the needed structures were made and included in the weights summary presented below. One of the areas of interest in the optics design will be the lag angle compensation system, which will account for the fact that the scanning laser transmitter/receiver will not be pointing quite the same direction when the transmitted pulse has had time to echo back from the atmosphere. A preliminary optics design indicates that the lag angle compensation can be accomplished within the optical train using present technology.

Since the laser operates at approximately 10 microns, the telescope does not need to be built to the same tolerances as for visible or uv operation. Preliminary study confirmed that the telescope primary mirror can be made of diamond-turned aluminum, and the entire telescope will fit within the 1.25 m diameter by 2 m long envelope shown below.

5. SHUTTLE ACCOMMODATIONS

A standard Spacelab pallet with support igloo was chosen, because of its power availability. Figure 7 shows four views of the preliminary concept drawings of the SCALE instrument in the Spacelab pallet. The telescope support structure shown is schematic only and will consist of a spaceframe structure attached to the indicated pallet hard points.

Figure 8 gives the weight summary that is the result of the preliminary laser and structures analyses. It can be seen that it is well within the Spacelab pallet limitations. The electrical power budget is given in figure 9. The pulse repetition rate was chosen to bring the power up to the available 5 kw. If some of the estimated power loads or contingency are less than assumed, the repetition rate can be increased, since the basic laser design will support 50 Hz operation. The 25 Hz rate will be sufficient to meet all the scientific and engineering goals of the experiment. The thermal control system schematic is shown in figure 10. Thermal loads are within the Spacelab pallet capabilities. The Command and Data Management System (CDMS) requirements are given in figure 11, and a schematic in figure 12. Data requirements are within the standard capabilities of the Spacelab pallet system.

Signal processing requirements dictate that the returned signal be shifted to the receiver passband so that the gross Doppler shift due to the spacecraft motion be removed to allow processing of the much smaller atmospheric motions. The accuracy of the Shuttle attitude measurement is not sufficient to be able to calculate the entire shift, so that some type of scanning circuit may be needed. This is within the capabilities of present technology. Shuttle propellant usage for the rotation maneuver is given in figure 13, and the total propellant consumed per day is

SCALE
WEIGHT SUMMARY (KG)

SUBSYSTEM	WEIGHT
LASER (MECHANICAL)	125
LASER (ELECTRICAL)	680
GAS PROCESSOR	30
THERMAL	48
C^3	30
OPTICS ASSEMBLY	30
STRUCTURAL SUBSYSTEM	150
ACOUSTIC SHELL & LEAD FOAM	300
TABLE & SPACE FRAME INCL. REC. OPTICS	100
COMPRESSOR TANK LINES, VAL., PRES. REG.	20
SUBTOTAL LASER EQUIPMENT	1513
TELESCOPE	605
MTG STR	67
CONTINGENCY 10%	220
TOTAL EXPERIMENT WEIGHT	2405
MDE	
EXP. HX	14
COLD PLATES + SPRT FOR (3) + PLUMB.	52
TOTAL PALLET PAYLOAD	2471

NOTE: SPACELAB PALLET NOMINAL LOAD CARRYING CAPABILITY FOR PAYLOAD AND MISSION DEPENDENT EQUIPMENT (MDE), WITH AN IGLOO, IS 2880 KG.

Figure 8 Weight Summary

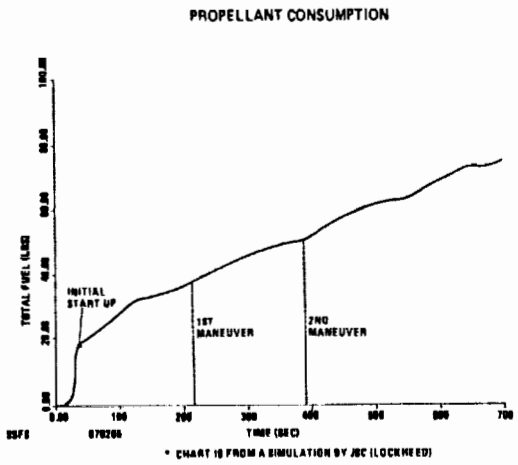

Figure 13 Propellant Consumption During Maneuver

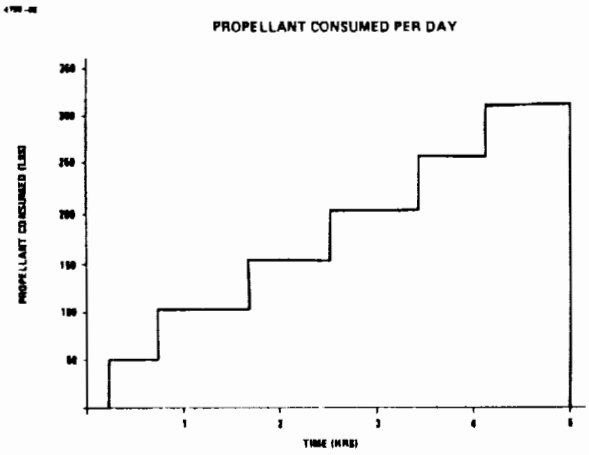

Figure 14 Propellant Consumption During Day

given in figure 14. The total usage for a 5 day mission is within the Shuttle capabilities. At the chosen 185 km altitude, the pointing will be within 10 deg of vertical at the end of the 180 sec maneuver if no corrections are made to maintain vertical during the Shuttle 360 deg rotation. This amount of deviation from the vertical should pose no difficulty to the wind estimation, thus this may be the preferred mode.

6. CONCLUSIONS

The results of the study have confirmed that there are no engineering or technology "show stoppers" to the design of the Shuttle Coherent Atmospheric Lidar Experiment. The scientific and engineering questions that will be answered and demonstrated by this experiment encompass nearly all of those remaining before a free-flying Doppler Lidar wind profiler can be designed and built. This experiment will be an economical and necessary step along the way toward the goal of true global wind measurement. The necessary cost data are currently being prepared for presentation to NASA HQ for phase B preliminary experiment design.

ACKNOWLEDGMENTS

The laser study was prepared by S. Moody and the staff of Spectra Technology Corp. Wind field estimates were done by G. Emmitt of Simpson Weather Associates. Optics and telescope consultation was done by D. Korsch of Korsch Optics Inc. The Spacelab accommodations study was done by the staff of the MSFC Preliminary Design group.

S36-47
84496

THE WINDSAT CONCEPT FOR MEASURING THE GLOBAL WIND FIELD

N93-70335

R. Milton Huffaker*

Coherent Technologies, Inc.
Boulder, Colorado, USA

1. INTRODUCTION

The Wave Propagation Laboratory of the National Oceanic and Atmospheric Administration's (NOAA) Environmental Research Laboratories has investigated the feasibility of measuring the global wind field by using an infrared coherent laser radar under a joint program with the U.S. Air Force Space Division Defense Meteorological Satellite Program (DMSP). These studies considered both the analytical and hardware feasibility of a space-borne global wind-measuring coherent laser radar (WINDSAT). Objectives and requirements of the Air Force Defense Meteorological Satellite Program were used in the study. The vertical distributions of the horizontal wind field were required throughout the troposphere with 300-km square horizontal and 1-km vertical resolution with a measurement accuracy of 1 m s^{-1}. Complete global coverage was required. The lidar system performance should also be scaleable to operational satellite conditions. The analytical studies were performed for both a 300-km altitude Space Shuttle orbit and an operational polar orbit of 800-km altitude (Huffaker, 1978; Huffaker et al., 1980). A hardware definition study was performed for a space Shuttle demonstration test flight (Lockheed Missiles and Space Co., 1981). Studies have also been conducted to determine the feasibility of mounting a WINDSAT payload on an Advanced TIROS-N spacecraft (RCA Corporation, 1983).

Winds are the most critical atmospheric parameter in the global numerical model forecasts, as shown in studies performed by several groups on the sensitivity of the models to meteorological parameters (Daly, 1980). Bengtsson (1981) in an analysis of First Global GARP Experiment (FGGE) data indicated that by using accurate wind information, skilled forecasts were possible for up to seven days. The NASA Goddard Space Flight Center has performed simulation studies using global numerical models to determine the impact that WINDSAT would have on the global forecasts.

A recent report (National Academy of Sciences, 1980), of the National Academy of Science Select Committee on the National Weather Service concluded that "there is a consensus among modelers, whether doing operational forecasting or research, that wind information is critical to continued improvement in forecasting." Citing the lack of currently implemented techniques capable of yielding the complete set of data required, they focused on a coherent lidar as "... the only concept now in sight that promises to provide an operational, truly global wind determination system in the future," and strongly endorsed its development.

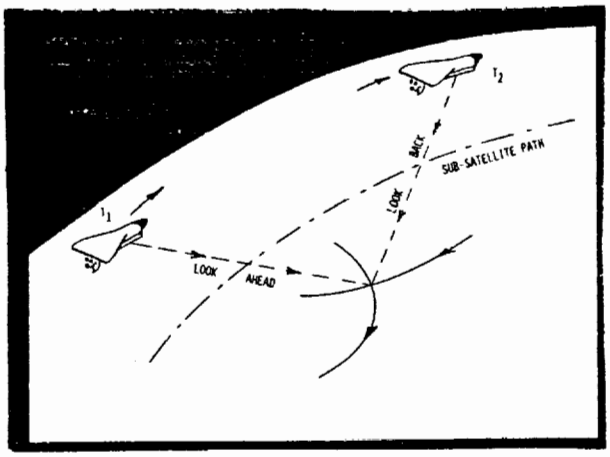

Fig. 1. Geometry of the satellite-borne lidar wind measurement.

2. CONCEPT DESCRIPTION

Laser radiation backscattered from the naturally occurring aerosols is collected by the receiving optics of the WINDSAT lidar and is coherently detected. The lidar system measures the radial wind component along the line of sight of the transmitted pulse, the height resolution determined by the pulse duration. Two or more observations from different directions are required from each region to determine both components of the horizontal wind velocity (Fig. 1).

The basic pulsed CO_2 coherent laser radar for global wind measurement consists of a stable, single frequency CO_2 transverse excited atmospheric (TEA) laser, interferometer, transmit-

*Work was performed when employed at the NOAA/ Wave Propagation Laboratory.

receive optics with scanning telescope, attitude control system, an infrared detector, a velocity-frequency analyzer, and a data processor and display. TEA lasers have very high coherence and gain characteristics and can generate several joules of energy per pulse. It is this improvement in laser technology which makes global wind monitoring possible.

3. PROGRAM APPROACH

Determination of the analytical feasibility of a pulsed coherent lidar system for global wind monitoring involves an analysis of the complex interaction of (1) atmospheric absorption, scattering, and refractive turbulence effects, (2) meteorological parameters such as turbulence, wind shear, and non-uniformity of conditions, (3) signal and data processing, (4) optimum instrument characteristics for coherent detection, (5) satellite environment and operational constraints, (6)design testing, and (7) systems analysis to insure the proper interaction of objectives capabilities, and requirements. An efficient evaluation necessitates the use of a complex computer simulation model. The WINDSAT lidar computer simulation integrates the listed variables into a software package capable of simulating any region of the globe.

4. COMPUTER SIMULATION

The satellite lidar computer simulation was developed to assess the overall system feasibility. Modeling the atmosphere anywhere on the globe is done by characterizing the target volume's aerosol backscatter profile, refractive turbulence profile, and its wind field, and also the absorption profile along the propagation path.

The geometry of the lidar system is generalized by locating the target volume relative to the satellite track. In this manner, the atmosphere of the entire globe is simulated, one volume at a time. The estimate of the wind field in this target volume is affected by lidar pointing errors, inexact satellite motion compensation, finite signal-to-noise ratio, spectral spreading caused by wind shear and turbulence, and smoothing of a nonhomogeneous wind field by least-square data fitting. When the lidar simulation is run by using realistic wind fields, an estimate of the backscatter power and the mean wind velocity (u, v, w) over the entire measuring volume is made. The rms error of this measurement $(\overline{\sigma_{\hat{u}}}, \overline{\sigma_{\hat{v}}}, \overline{\sigma_{\hat{w}}})$ is then computed to evaluate system performance. The simulation assumes a Gaussian laser transmitter beam shape and telescope apodization at the e^{-2} radiance radius. A digital Doppler processor using the complex covariance frequency-velocity estimator is assumed in the basic processing model. Other processing algorithms such as pulse pair, polypulse pair, and a Cramer-Rao lower bound can also be utilized. Figure 2 outlines the structure of the computer simulation.

In the model the global region and geometry are specified, and a scan of the target volume is performed to determine the orientation and location of lidar 'shots'. By utilizing the model, an example of the density of lidar data samples is shown in Fig. 3, using a laser pulse repetition frequency of 8 Hz and a scan time of 11 sec.

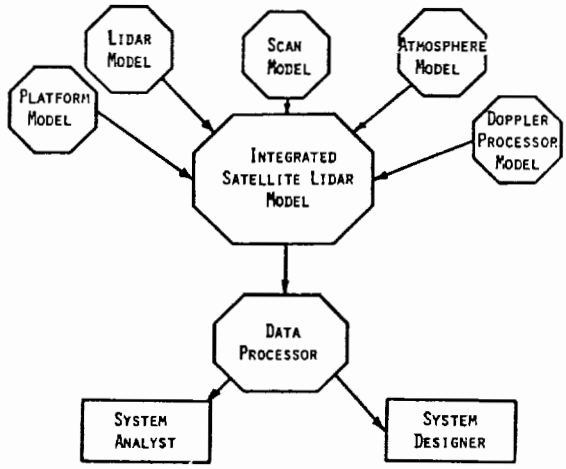

Fig. 2. Satellite lidar computer simulation.

4.1 Instrument Base Parameters

A set of instrument parameters were selected for a Space Shuttle orbit of 300 km and an operational orbit of 800 km. These parameters were selected after evaluating the TEA laser technology, Space Shuttle constraints, and navigation and pointing errors. The parameters selected for use in the computer simulation are shown in Table 1.

Target patch 2 is a volume located 300 to 600 km from the satellite track with dimensions of 300 km along the tracks and 20 km in depth. A conical scan period of 7 or 11 seconds at a variable pulse repetition frequency (PRF) gives a uniform distribution of shots into the patch. The proposed configuration incorporates a 1.25 m diameter telescope, 10-joule/pulse transmitter energy, 6.7 μs pulse duration (corresponding to 1-km range resolution), and a detector and optical system having a total efficiency of 10%. The wavelength of 9.11 m ($^{12}C^{18}O_2$) was chosen because of the low atmospheric absorption at this wavelength and the increased aerosol backscatter. Long-term pointing errors of <50 μrad are achievable using state-of-the-art pointing systems. One of the most stringent requirements of the system is to hold the sensor optical line of sight to within 2 μrad during the 10 ms pulse roundtrip time (short-term pointing error). The assumed 50 kHz local oscillator frequency stability has been demonstrated.

4.2 Atmospheric Effects

The primary atmospheric parameters that affect system performance are aerosol backscatter coefficient, molecular absorption, refractive turbulence, and the presence of clouds. Molecular absorption spectra for CO_2 laser

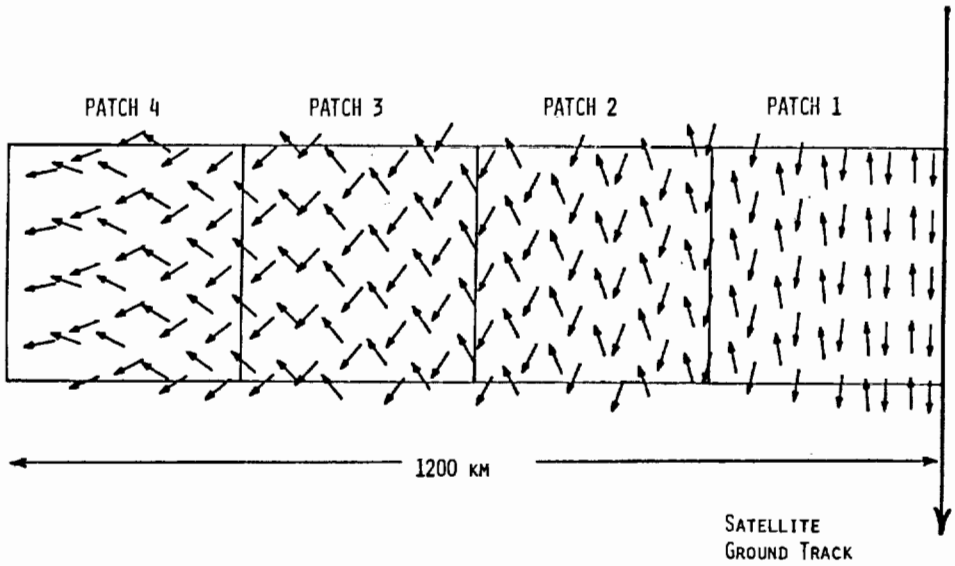

Fig. 3. Measurement pattern from 800 km orbit.

Table 1. Base Case Parameters

	Space Shuttle Orbit	Operational Orbit
Altitude	300 km	800 km
Target Volume (patch)	#2 (300 km x 300 km x 20 km)	(See Fig. 3)
Nadir Angle	62° (600 km reach)	52° (1200 km reach)
Conical Scan Period	7 s	11 s
Pulse Repetition Frequency	8 Hz average, 12 Hz peak	
Wavelength	9.11 μm ($^{12}C^{18}O_2$) 11.19 μm ($^{13}C^{16}O_2$)	
Telescope Diameter	1.25 m	
Pulse Energy 1	10 J	
Pulse Duration	6.7 μs	
Optical-Detector Efficiency	10%	
rms Long-Term Pointing Error	50 μrad	
rms Short-Term Pointing Error	2 μrad	
Local Oscillator Jitter	50 kHz	

wavelengths were computed at 32 heights by using the Air Force Geophysics Laboratory (AFGL) model atmospheres: Tropical, Midlatitude Summer, Midlatitude Winter, Subarctic Summer, and Subarctic Winter (McClatchey and Selby, 1974). Results of the molecular absorption analysis indicated that the $^{13}C^{16}O_2$ (P24) and the $^{12}C^{18}O_2$ (R20) isotope lines have the least amount of total atmospheric absorption.

There is a scarcity of information on global aerosol statistics. The backscatter coefficient β is the quantitative measure of the ability of atmospheric aerosols to scatter energy. Only a limited number of measurements of β have been made at CO_2 laser wavelengths; therefore, we have calculated β from visible extinction measurements (Kondraytyev et al., 1976) by assuming a limited range of size distribution and refractive indices for the aerosols. Figure 4 shows our β models for five AFCRL atmospheres, based on the visible data, plus two "cleaner" models to permit simulations in cases of extremely low backscattering. Inhomogeneities in the backscatter coefficient and speckle effects are included in the computer simulation by requiring that the β values be independent at each range gate. This requirement is accomplished by considering β to be a random variable with log-normal probability density function having a mean value equal to the β given by the curves in Fig. 4

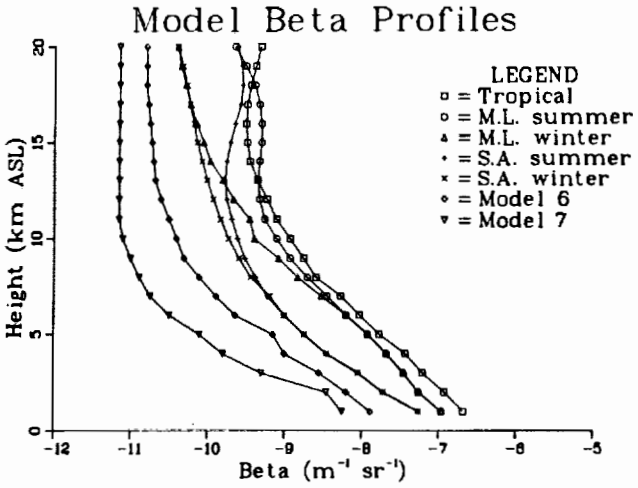

Fig. 4. Profiles of the aerosol backscatter coefficient, β.

4.3 Wind Field Models

Three-dimensional mesoscale wind field realizations were constructed by using simulated two-dimensional (2D) wind fluctuation fields added to a one-dimensional (1D) mean profile. The fluctuation fields were determined by using two-dimensional spatial filtering techniques and observed wind correlation functions. Energy at scales less than 600 km was accommodated and data generated over a 300-km square target volume with 10-km resolution. Wind velocity fluctuations accounted for the energy between 600 and 1 km with the energy at smaller scales parameterized as microscale turbulence. Two correlated wind fields, smooth and disturbed, were used in this study. The smooth wind field had a spectrum with energy cascading smoothly down through the mesoscale. The disturbed field had a spectral bump at 80 km, energy being added into the field at this wavelength.

5. WIND MEASURING PERFORMANCE

The calculated signal-to-noise ratio (SNR) provides a measure of system performance and is used in estimating the wind-measurement accuracy. The lidar equation expresses the detector-shot-noise limited SNR in a bandwidth matched to the transmitted pulse duration as presented by Huffaker (1978)

$$SNR = \frac{\pi \eta J \beta c \tau D^2 K e^{-2\mu R}}{8h\nu \left[R^2(1+D^2/4r_a^2) + (\pi D^2/4\lambda)^2(1-R/f)^2\right]} \quad (1)$$

where η is the overall detector-optics system efficiency,
J is the transmitted pulse energy (J),
β is the atmospheric backscatter coefficient (m^{-1} sr^{-1}),
c is the speed of light (3×10^8 m s^{-1}),
τ is the pulse duration (s),
D is the telescope diameter (m),
K is the beam shape compensation factor (0.46),
μ is the atmospheric absorption coefficient (m^{-1}),
R is the range (m),
$h\nu$ is the photon energy (1.88×10^{-20} J),
r_a is the turbulence-induced transverse coherence radius (m), $0.69\ (R\ C_n^2)^{-3/5}$
C_n^2 is the refractive-index structure parameter ($m^{-2/3}$),
λ is the wavelength (m)
f is the focal distance (m).

Detector output signals having an SNR less than approximately 5 kB cannot be used to accurately estimate the Doppler frequency shift of the returned signal without additional averaging.

The rms radial velocity error depends on the SNR and the velocity width of the received signal as given by Zrnic (1977),

$$\sigma_r = \left[\frac{\lambda \sigma_v}{2\tau}\left(\frac{1}{4\sqrt{\pi}} + \frac{2}{\pi}\frac{1}{SNR} + \frac{1}{16\pi^3 \rho^3 SNR^2}\right)\right]^{1/2} \quad (2)$$

where σ_v is the rms velocity width of received spectrum,
τ is the transmit pulse duration
ρ is the ratio of rms velocity width to the total system velocity width

Equation (2) models the complex covariance processor used in the computer simulation. Although the radial velocity errors may be large, averaging many shots reduces the uncertainty in the calculated horizontal wind.

A summary of the expected rms wind-measurement errors is shown in Figures 5 and 6 by using the smooth wind field model. These computer simulation results represent many computer runs for patches 1 through 4 and a wide range of instrument and atmospheric parameters (wind shear, turbulence, pointing errors, local oscillator laser uncertainty, and the various atmospheric models). The wind-measurement error is $\lesssim 1$ m s^{-1} throughout the troposphere. Errors in measuring the disturbed wind field are only slightly greater.

6. HARDWARE DEFINITION STUDIES OF A GLOBAL WIND MEASURING SATELLITE SYSTEM (WINDSAT)

A Hardware Definition Study has been completed under contract to the Lockheed Missiles and Space Company. The contract effort used as input the results of the NOAA analytical feasibility study. The overall objective of this study was to determine the hardware feasibility of a Space Shuttle-based feasibility demonstration system and to determine the scalability to operational conditions. The hardware study consisted of specifying the lidar system, defining an operation plan and required supporting systems, developing a follow-on program plan for the detailed design, development, and acquisition phases, identifying long-lead items, identifying and planning for required technology developments, and performing a safety analysis.

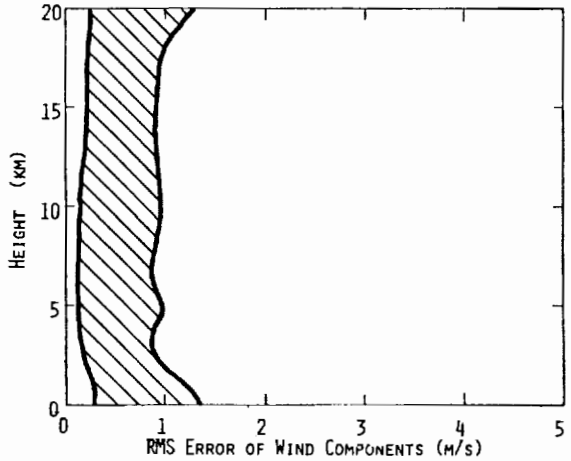

Fig. 5. Estimates of the rms wind-measurement errors for the 300 km orbit. (Base parameters listed in Table 1 were used for patches 1 and 2.)

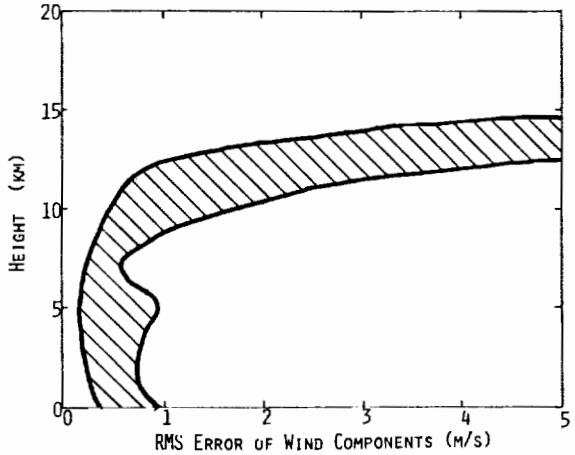

Fig. 6. Estimates of the rms errors for the 800 km orbit. (Base parameters listed in Table 1 were used for all four patches. Across-the-track wind estimates for patch 1 are not included.)

In the selected WINDSAT design, as the Space Shuttle orbits the Earth, the telescope (1.25 m) continuously rotates about the nadir with one rotation every 7 sec and with a laser pulse repetition frequency of 8 sec^{-1} and nadir scan angle of approximately 60°. In the recommended WINDSAT system, an attitude-sensing system is mounted to the stationary base of the telescope to provide the required laser-pointing accuracies. Because of the high telescope scan rate, the return Doppler shifted radiation returns off-axis in the diffraction-limited optical system and a lag-angle compensator is required.

Laser Design - The laser is a 9.11 μm, 10-J pulse, 8 pulses per sec, transverse excited atmospheric (TEA) CO_2 laser with pulse length 3-6 μsec. The unstable resonator oscillator is frequency controlled with a low power CO_2 injection laser. The preferred excitation technique for the Lockheed study was e-beam sustained operation for improved efficiency, laser chirp, and better pulse control. A uv pre-ionized TEA laser was also feasible. No new technology issues were identified.

Optical System Design - A basic Cassegrain telescope collimator with a field flattener was selected. The telescope is continuously rotating and has a 1.25-m-diameter primary. The lag angle compensation (LAC) is accomplished by a fast LAC mirror, which performs a closely controlled one-dimensional rotation, and a closed-loop controlled, two-axis gimbal mirror for compensating vehicle perturbations.

Attitude Determination and Control - A WINDSAT autonomous attitude determination and control system was selected. The attitude determination system consists of two star sensors which update an inertial reference unit (IRU). These components are mounted on the fixed portion of the telescope base.

Signal and Data Processing - The signal and data processing system provides for onboard processing and transmittal of conditioned data to the ground for off-line processing. Conditioned data are compressed by using time-delayed automatic gain control and low-order quantization. Gross Doppler shifts are removed electronically after heterodyne detection. The signal and data processing system does not pose any technology problems, and many hardware implementations of the system are possible.

Power and Weight - This hardware study was performed for the Space Shuttle platform where there is not a severe restriction on power and weight. The estimated power and weight for this research system is 2,340 watts and 830 kg, respectively. This instrument has not been light weighted or optimized for minimum power. The selected WINDSAT design can be scaled down in power and weight to fit an operational platform and still provide adequate performance from an 800 km operational orbital altitude. Studies indicate the operational WINDSAT system will weigh <500 kg and use <1 kW power by light weighting and reducing the laser prf.

The overall WINDSAT system configuration for measuring the global wind field in a feasibility demonstration mode onboard the Space Shuttle and using a Spacelab pallet platform is shown in Fig. 7.

7. OPERATIONAL PLATFORM STUDIES

The analytical and space hardware studies discussed above concluded that it is indeed feasible to measure the global wind field using a coherent laser radar on a space shuttle-space lab pallet platform. A major question was answered in the RCA Study: "Can this WINDSAT concept, as developed in previous studies, be scaled to an operational system?". To address this question, in a joint program with the U.S. Air Force Defense Meteorological Satellite Program, we introduced another series of study efforts which defined the operational system characteristics (by using the WINDSAT simulation) and a conceptual hardware definition study under a contract to the RCA Corporation. A space shuttle launched advanced TIROS N spacecraft was the platform selected for this study.

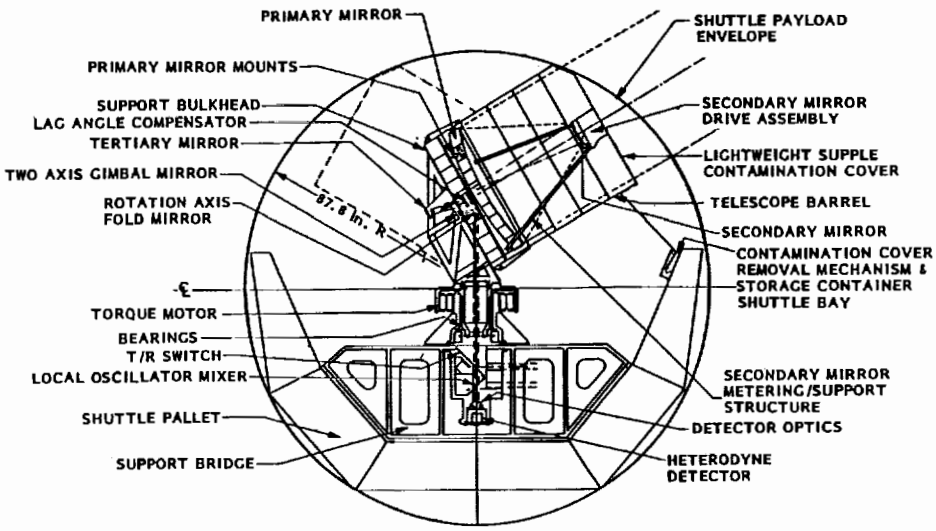

Fig. 7. Side view of recommended lidar design, mounted on the Space Shuttle pallet.

7.1 Computer Simulation of the Operational WINDSAT Performance

Input parameters to the WINDSAT computer simulation were updated to reflect an improved understanding in the areas of aerosol backscatter and signal processing. The expected aerosol backscatter was made more pessimistic reflecting aerosol data obtained in the southern hemisphere. These profiles are shown in Fig. 4 and identified as Models 6 and 7. The minimum in Model 7 reflects a single aerosol measurement made in the Antarctic. The Model 6 profile was selected for determining the characteristics of the operational system. The signal processing algorithms were changed to more realistically reflect present processing capabilities. Zrnic (1979) has developed an expression for the Cramer-Rao bound for velocity estimations, i.e., the theoretical limit on estimator accuracy for a given SNR. For our model of processor performance, we used the error predicted by the Cramer-Rao bound expression multiplied by a factor of 2. Discussions with signal processor manufacturers indicated that this is achievable.

A new set of base parameters for the operational WINDSAT lidar characteristics were established by using the computer simulation. The principal features are:

Optics diameter, m	1.25
Laser pulse energy, J	10
Conical scan period, s	19
Laser pulse repetition frequency, Hz	2

Figures 8 and 9 show the expected wind measuring errors for the along and cross track wind components to be between 1 and 3 m/s.

7.2 Advanced TIROS N Platform Study

Under a contract effort to RCA Corporation, a study has been conducted to determine the compatibility of WINDSAT with an advanced TIROS N spacecraft. Mathematical Sciences Northwest was subcontractor for the laser design and Perkin-Elmer Corporation for the optical system design. Results of this study indicate that the WINDSAT power and weight requirements are within the advanced TIROS N capabilities.

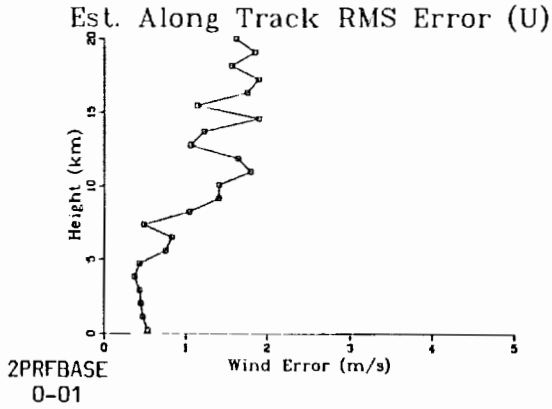

Fig. 8. Estimates of the rms errors along track for the operational 800 km orbit

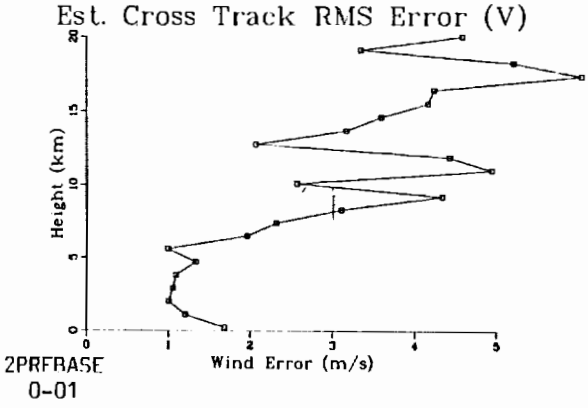

Fig. 9. Estimates of the rms errors cross track of the operational 800 km orbit.

9. CONCLUDING REMARKS

These analytical and hardware feasibility studies indicate that it is indeed feasible to measure the global wind field from a space platform by using a pulsed coherent laser radar. The next steps in the WINDSAT program are (a) to determine global aerosol backscatter statistics, (b) to determine the impact that WINDSAT will have on the accuracy of the global forecasts, (c) to develop an engineering model of WINDSAT for ground and airborne testing, and (d) to establish the preliminary design of the space system.

REFERENCES

Bengtsson, L., 1981: The impact of FGGE on global medium range forecasts. FGGE Conference, Tallahassee, FL, January 1981.

Daly, R., 1980: On the optimal specification of the initial state for deterministic forecasting. Mon. Wea. Rev., 108.

Huffaker, R.M., ed., 1978: Feasibility study of satellite-borne lidar global wind monitoring system. NOAA Tech. Memo. ERL WPL -37.

Huffaker, R.M., T.R. Lawrence, R.J. Keeler, M.J. Post, J.T. Preistley and J.A. Korrell, 1980: Feasibility study of satellite-borne lidar global wind monitoring system Part II. NOAA Tech. Memo. ERL WPL-63.

Kondraytyev, K. Ya., I. Ya. Badinov, G.A. Mikidsky, and E.V. Prokopendo, 1976: Modeling of Real Profiles of Aerosol Attenuation. Tr. Gl. Geofrz. Obs, 262L.

Lockheed Missiles and Space Co., Palo Alto Research Lab., 1981: Global wind measuring satellite system. Report No. LMSC-D767868. Work conducted under NOAA contract NA 79RAC-00127.

McClatchey, R.A., and J.E.A. Selby, 1974: Atmospheric attenuation of laser radiation from 0.7 to 31.27 μm. Air Force Cambridge Research Laboratories, Report No. AFCRL-TR-74-0003.

National Academy of Sciences, 1980: Technological and scientific opportunities for improved weather and hydrological services in the coming decade. Select committee on the National Weather Service, 87 pp.

RCA Astro-Electronics, 1983: Feasibility study of a WINDSAT free-flyer. Final report, NOAA Contract NA82 RAC 00141, Princeton, NJ.

Zrnic, D., 1977: Spectral moments estimated from correlated pulse pairs. IEEE Trans. Aerosp. and Electron Syst., 7, pp. 344.

Zrnic, D., 1979: Estimation of spectral moments for weather echoes. IEEE Trans. Geosci. Elect. GE-17.

DOPPLER LIDAR SAMPLING STRATEGIES AND ACCURACIES--REGIONAL SCALE

G. D. Emmitt

Simpson Weather Associates, Inc.
Charlottesville, Virginia 22902

1. INTRODUCTION

It has been proposed that a Doppler lidar be placed in a polar orbit and scanned to provide estimates of lower tropospheric winds twice per day and with a spatial resolution of 300 km. Initial feasibility studies conducted primarily by NOAA and NASA presented an optimistic outlook for a space-based lidar. The technology appeared within reach and initial computer simulations suggested that acceptable accuracies could be obtained.

Those early studies exposed, however, several potential problem areas which included: (1) the algorithms for computing the wind vectors did not perform well when there were coherent gradients in the wind fields; and (2) the lifetime and power requirements of the lidar put severe restrictions on the pulse repetition frequency (PRF). These two basic problems are currently being addressed by a Doppler lidar simulation study focussed upon three primary objectives:

(i) To develop optimum scan parameters and shot patterns for a satellite-based Doppler lidar

(ii) To develop robust algorithms for computing wind vectors from lidar returns

(iii) To evaluate the impact of coherent mesoscale structures (wind gradients, clouds, aerosols) on up-scale wind estimates.

In the following sections an overview of the simulation efforts will be provided with particular emphasis upon rationale and methodology. Since this research is currently underway, any results shown are meant only as evidence of progress.

2. SIMULATIONS

The errors associated with lidar wind measurements can be divided into two sets: (1) those associated with the detection of aerosol motion and the processing of the lidar return signal to estimate radial velocities within various range gates, and (2) those associated with combining the radial information to estimate the horizontal wind vector for the target volume (in this case 300 x 300 x 1 km^3). The computer simulations being conducted at SWA are focussed upon the latter set of errors, the one exception being the signal-to-noise ratio (SNR) for single lidar shots which is allowed to vary as a function of available aerosols and H_2O absorption. Errors associated with pointing accuracy, lag angle compensation, local oscillator stability, etc., are being addressed by other groups within NASA and NOAA.

2.1 Shot Management Algorithm (SMA)

Given that there will be power and lidar lifetime constraints, it is desirable that the pattern of lidar shots be optimal for resolving the winds on some specified space scale. Initially, the target scale has been defined as synoptic--i.e. wind structures with wavelengths greater than 1000 km. Resolution of smaller scales (e.g., mesoscale) should not be discounted but for current algorithm development we use a 300 km data output grid.

The base set of orbit and lidar parameter used in the SWA simulations are listed in Table 1. A conical scan has been used in all our

Table 1
Orbit/Lidar Parameters for
Space-based Doppler Lidar Simulation Model

Altitude	800 km
Satellite Orbital Speed	7.5 km/sec
Scan Angle from Nadir	56^{o}
Scan Period	20 sec
Shot Frequency (PRF)	8 s^{-1}
Pulse Length	2 km

simulations to date. Part of the resultant shot pattern on the earth's surface is shown in Figure 1. The points to note are the infrequent spatial coincidence of forward and aft shots and the uneven density of shots in the lateral direction.

To optimize the distribution of shots, keeping the PRF constant, a shot management algorithm (SMA) was developed. At present the SMA (i) controls the scanner slew rates and (ii) schedules pulse suppression in regions of low information potential.

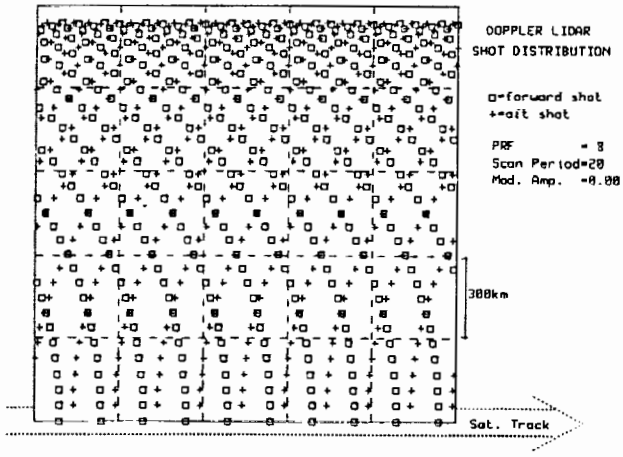

Figure 1. Pattern of lidar shots on the earth's surface for a portion of the total scan domain. The orbit/scan parameters for this pattern are presented in Table 1.

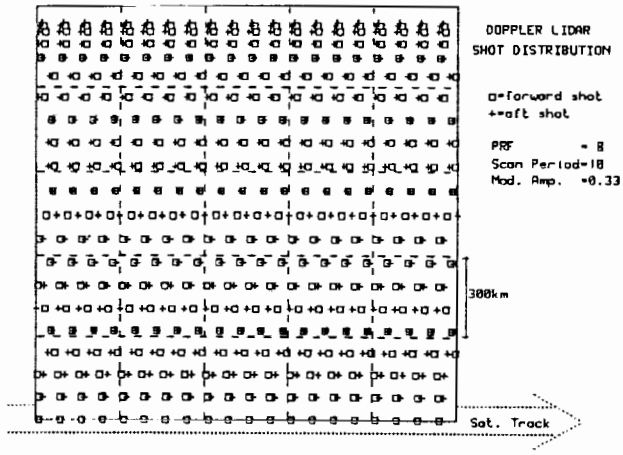

Figure 2. Same as Figure 1 except that a variable scan rate and a scan period of 10 seconds have been used.

An example of one optimization is shown in Figure 2 where the coincidence of forward and aft shots has been greatly improved and the lateral shot distribution has become less skewed to the limb region than for the simple case in Figure 1. Shot suppression is used in areas (along track and far lateral range) prone to large wind estimation errors independent of atmospheric conditions and areas where previous forward shots have had poor signal-to-noise ratios in the cloud-free regions (e.g. above optically dense cirrus).

Currently, the SMA is being modified to include the logic for varying shot density in response to real-time evaluation of signal or wind estimation variances. This change represents a feedback between the wind computation algorithm and the lidar hardware control systems and must be developed in coordination with engineering efforts.

2.2 Multi-pair algorithm (MPA)

As mentioned before, early simulations using a least squares regression (LSR) technique had problems with atmospheric wind fields which were coherent on space scales close to that of the target volume. This failure was due to the correlation between the velocity (dependent variable) and the position vector (supposedly independent variable). If one knew a priori the nature or form of that relationship, then an LSR could still be employed. However, it is assumed that there is no independent knowledge of the coherent or correlated component of the wind field.

A more flexible and informative approach has taken on the form of a multi-pair algorithm (MPA). Given a number of lidar shots into a target volume, the MPA currently consists of 5 major steps:

Step (1) Delete all radial estimates with SNR less than 5 db

Step (2) Form all possible pairs with the remaining shots and compute u and v components from each pair with the assumption that the contribution of vertical speeds are small and/or effectively uncorrelated in the horizontal

Step (3) Assign weighting functions to each pair's wind estimate. These weighting functions are based upon three factors:

(a) Horizontal spatial separation of the shots in a pair--i.e. the closer the shot locations, the more weight assigned

(b) Angular separation of the two shot perspectives in a pair--i.e. the more orthogonal the perspectives, the more weight assigned

(c) Lateral distance from the orbit ground track--i.e. the weighting functions vary depending upon which 300 x 300 km area is being sampled.

Step (4) Combine the weighted pair information to calculate a single set of u and v components for the target volume

Step (5) Perform an analysis of variance for individual shot pair data to characterize the sub-target scale wind field and the representativeness of the single wind estimate.

A consequence of this approach is that the number of pairs effectively used to compute a final wind estimate can vary depending upon the shot pattern. In Figure 3 an error index as a

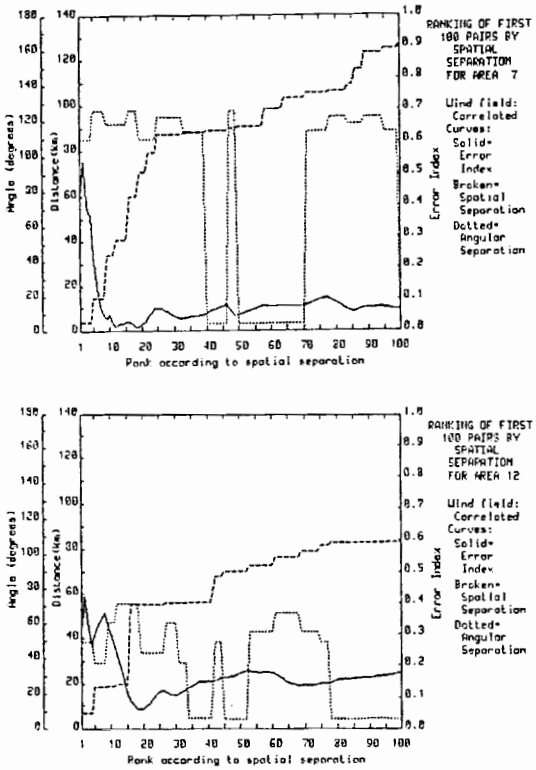

Figure 3. Error Index as a function of the inclusion of more shot pairs on the basis of rank. Rank is determined by spatial separation. The Error Index is equal to a combination of RMS errors in u and v estimates.

function of the spatial weighting factor is shown for two areas; area 7 is mid-range from the ground track and area 12 is near the range limit (1450 km). Note that the minimum in the error index for area 7 is between the best 10 or 20 shot pairs; for area 12 it is between the best 18 or 20 shot pairs. These results lead to two suggestions: (1) either the weighting functions can be adjusted to produce similar error behavior in all areas or (2) one can just use the shots that give the best estimate regardless of their number. Although optimization of the weighting functions is still in progress, the results so far indicate that the errors due to sampling and horizontal wind gradients are on the order of 3-8%.

2.3 Model Mesoscale Atmospheres

To develop the optimum shot patterns and weighting functions, several control or test wind fields were constructed. Basically, they were either fields where the variations from the mean were purely random (uncorrelated) or fields containing linear gradients of the u and v components (correlated). Figures 4 and 5 show how the MPA performed on uncorrelated and correlated test cases. For comparison, Figure 6

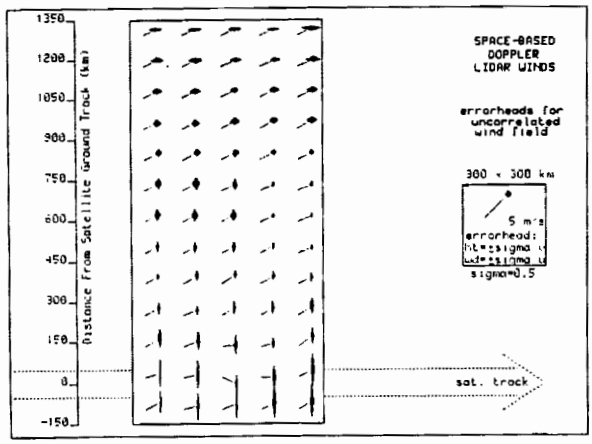

Figure 4. An "errorhead" presentation of the standard deviations in the u and v estimates obtained with the MPA on an uncorrelated wind field where $u = 2\ m\ s^{-1}$, $v = 1\ m\ s^{-1}$, $\sigma_u = \sigma_v = .5\ m\ s^{-1}$.

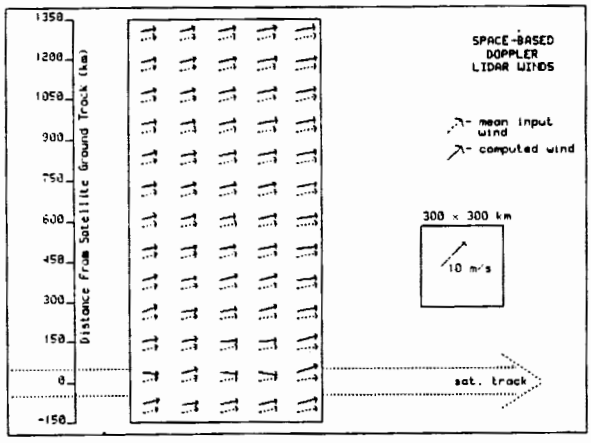

Figure 5. Vector comparison between the control wind field (dashed) and MPA wind estimates (solid) for a correlated wind field where $u_o = 2\ m\ s^{-1}$, $v_o = 1\ m\ s^{-1}$, and $du/dx = 4 \times 10^{-6}\ s^{-1}$.

shows how the LSR technique performed on the same correlated field shown in Figure 5.

More advanced evaluation of the SMA and MPA requires the use of more realistic wind fields than those used for initial development. As mentioned in the introduction, our focus is upon the impact of coherent mesoscale features on up-scale wind estimates. However, there is a broad range of spatial scales involved in Doppler lidar sampling:

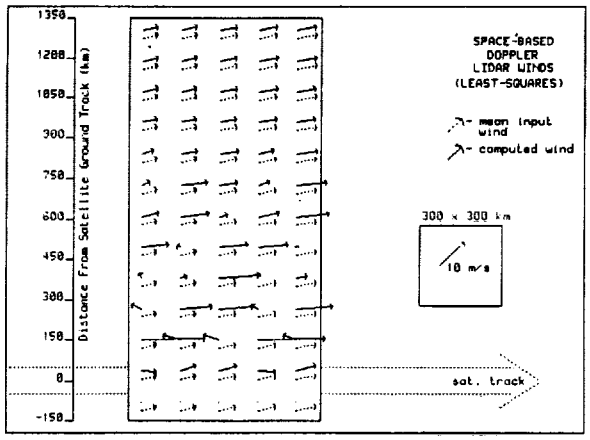

Figure 6. Vector comparison between the control wind field (dashed) and LSR wind estimates for the same correlated field shown in Figure 5.

(i) Laser beam diameter at earth's surface ..... $\sim 10^1$ meters

(ii) Laser pulse length ..... $\sim 10^3$ meters

(iii) Shot separation on earth's surface ..... $\sim 10^4$-10^5 meters

For the present, scales 1 and 2 are accounted for by using empirically derived estimates of the uncertainties in the radial wind estimates ($\sim$0.5-1.0 m s^{-1}). In this case both system and atmospheric error sources are represented. Efforts to isolate the atmospheric components of the error are in progress.

The third scale (10^4-10^5 meters) is associated with the lidar shot pattern and the wind field being sampled. Instead of developing more idealized control fields, we have chosen to use several case studies involving mesoscale phenomena. Initially, we have selected jet streaks, MCC's, sea breezes, mountain flows and tropical storms. For example, the jet streak data set is taken from Shapiro and Kennedy (1981), winds for the sea breeze were obtained from the Pielke mesoscale model, a SESAME 5 case study with diagnosed winds was provided by University of St. Louis researchers Fuelberg and Buechler, and a LAMPS simulation of an AVEVAS II storm system was obtained from Kalb (MSFC). In all cases the cloud fields obtained from satellite imagery were included in the Doppler lidar simulation. A basic assumption of the lidar simulations is that the wind, aerosol, vapor, and cloud fields are frequently correlated. An example taken from a west coast jet is shown in Figures 7 and 8.

In general, the simulations using the case study data sets are indicating that (1) the MPA does well even where the gradients are 10^{-4} s^{-1}

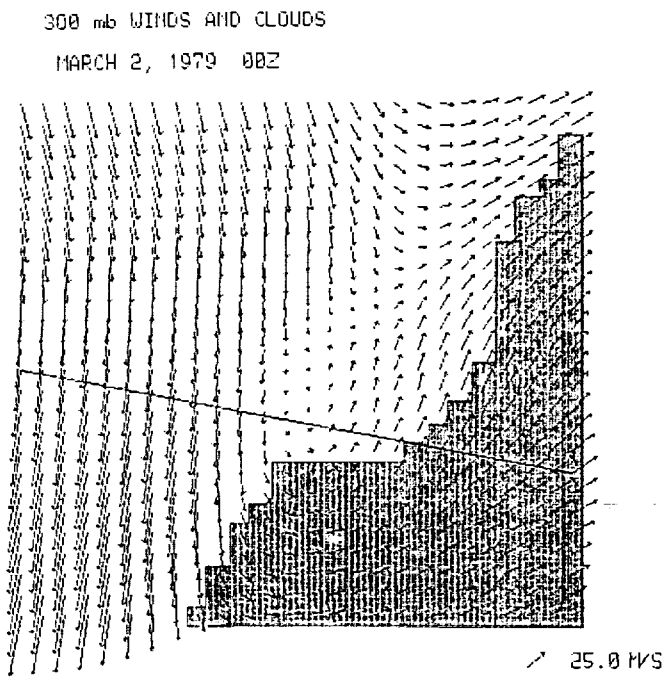

Figure 7. Wind and cloud (shaded area) fields at 300 mb over a 1500 x 1500 km portion of the Pacific coast states on 2 March 1979. The wind data were obtained from National Weather Service charts and special aircraft research flights through the jet streak. The Barnes interpolation scheme was used to produce the maps as presented. Grid spacing is 60 km. The sloping line across the figure denotes a horizontal aircraft track.

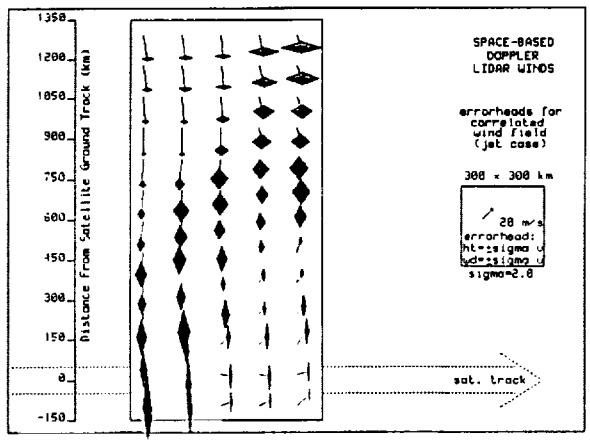

Figure 8. An "errorhead" representation of the MPA winds for a portion of the wind field shown in Figure 7. The width of the "errorhead" is proportional to the standard deviation in the estimates of u for that point; the height is related to the v component deviation.

and (2) the clouds often mask regions of high wind variance and thus minimize a potential error source. One area that is continuing to be difficult is the specification of a representativeness index, i.e., some means of isolating the random and correlated components of the MPA variance data.

3. CONCLUDING REMARKS AND FUTURE PLANS

Although it is too early in the study to draw conclusions with regard to expected errors and general Doppler lidar performance from a space-based platform, the efforts currently indicate that considering only sampling/windfield related errors, there is a basis for optimism in obtaining estimates of the global wind field in cloud-free regions.

Future plans include:

(i) Expand the mesoscale case studies to include a hurricane

(ii) Update the MPA error analyses as better single-shot SNR data becomes available for 10.6 μm and 9.11 μm lasers

(iii) Evaluate synergistic relationships between cloud tracking and Doppler lidar wind measurement techniques

(iv) Incorporate the MPA into experiments using a GCM.

REFERENCE:

Shapiro, M. and Kennedy, 1981: Research aircraft measurements of jet stream geostrophic and ageostrophic winds. JAS, 38, 2642-52.

SOME CLOUD POPULATION STATISTICS

J. William Snow

Air Force Geophysics Laboratory
Hanscom Air Force Base, Massachusetts, USA

1. INTRODUCTION

Photographs of cloud scenes taken from the orbiting space shuttle are being used to assess the overestimation in the amount of cloud cover sensed by satellites at angles other than nadir. Also these photographs and Landsat images indicate that the frequency distributions of clear and of cloudy intervals, at least in simple tropical cloud scenes, may be approximated by common distribution functions.

2. VIEWING-ANGLE CORRECTION

The fact that clouds have vertical as well as horizontal extent is involved in the systematic overestimation of cloud amounts by meteorological satellites, particularly those operating in the visible wavelengths. The satellite cloud cover (SCC) increases as the angle at which the clouds are viewed (ζ) increases.

As an ongoing geophysical research project, the U.S. Air Force is sponsoring the photographing of cloud scenes from the orbiting space shuttle. Target cloud scenes are photographed throughout the viewing angle range from 0° to nearly 85°. The series of photographs thus generated are uniquely suited to quantifying the viewing angle bias in satellite-determined cloud amounts.

In Figure 1 (taken from Snow et al, 1985a) is shown the average SCC for 10 passes of a polar-orbiting satellite over the Atlantic Ocean (dashed curve) and the results of analysing two series of cloud photographs taken during mission 41-D of the space shuttle *Discovery*. The function SCC(ζ) is seen to be smooth and remarkably repeatable and implies a family of curves parameterized by SCC(0), the cloud cover itself.

3. DISTRIBUTIONS OF CLEAR AND CLOUDY INTERVALS

3.1 Pertinence

The introduction of realistic cloud fields into numerical models of the atmosphere and the communication/interaction between surface locations and orbiting space vehicles both have a dependency on the spacial characteristics of clouds. The presence of clouds in atmospheric models by any means other than crude parameterization requires detailed knowledge of real cloud dimensions and spacings. Such information is not abundant. Also, any interaction between orbiting vehicles and the earth's surface, or vice versa, must occur through a variably cloudy troposphere. Particularly within the optical wavelengths, such interaction is seriously impeded by clouds within the line of sight.

For these reasons the quantification of cloudiness in more detail than is possible by the traditional statistics of cloud amount, cloud type, and cloud base-height is required. Useful descriptors for the applications mentioned are the frequency distributions of the clear and the cloudy intervals as they occur in actual cloud populations. (Frequency distribution is taken to be equivalent in meaning to the term histogram.) Such distributions determined from satellite cloud imagery are the principal topic of this report.

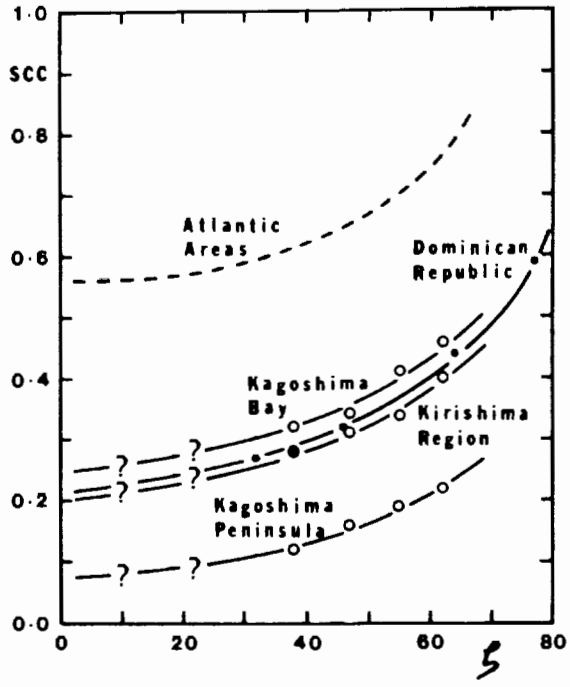

Figure 1. Satellite cloud cover versus viewing angle (ζ). Open circles are Kyushu Island data; solid dots are Dominican Republic data.

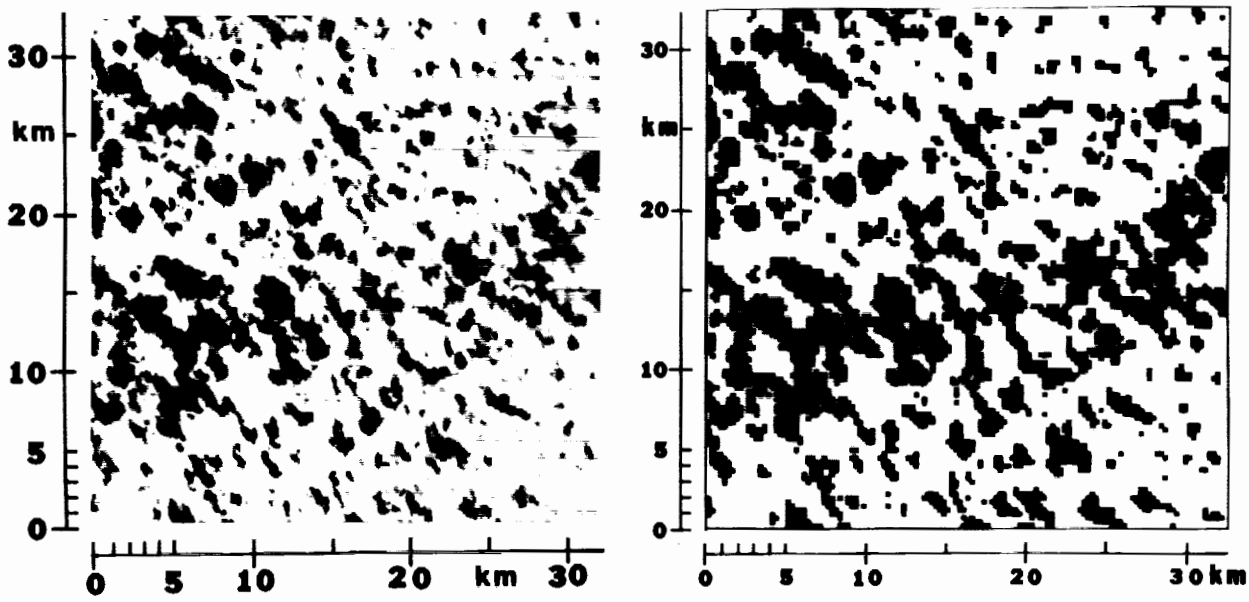

Figure 2. Photograph (left) and computer-generated binary image (right) of clouds over a trade wind island (cloud photo #133 of space shuttle mission 41-D). Clouds are black and background light or white. Cloud cover is 3/10 and threshold brightness is 163 of 256 levels.

3.2 Data

The amount of cloud population information contained in the space shuttle cloud photographs, one of which is reproduced as the left panel of Figure 2, is enormous. Any comprehensive analysis, therefore, requires a digital version of the photograph. Such digital images are being produced from these photographs with a spacial resolution of approximately 60 m. Landsat imagery is the only other available U.S. source of comparable resolution but, as an operational procedure, efforts are made to exclude clouds from these images.

Two shuttle photographs and one Landsat image of cloud scenes are here discussed. All scenes are of tropical cumulus with cloud cover of 3/10 or less: the first two are shuttle photos taken over the eastern Pacific and over an island in the trade wind latitudes, the third is a Landsat scanning-radiometer image taken over the Straits of Florida. Details on location, cloud condition, digitization, and certain mean statistics are given in Table 1.

Table 1. Cloud Scene Statistics

		Eastern Pacific	Trade Wind Island	Straits of Florida
	image type	shuttle photo	shuttle photo	Landsat band 7
location	latitude	~20 S	20 N	~25 N
	surface	ocean	land	ocean
cloud condition	cloud cover	0.20	0.31	0.19
	cloud type	cumulus	trade cu	trade cu
	cloud base	low	low	low
digitization	dimension in pixels	960 x 960	130 x 130	300 x 300
	dimension in km	60 x 60	32½ x 32½	16½ x 16½
	resolution in m	62½	250	55
mean length in m	clear interval	3748	2108	1485
	cloudy interval	911	961	357

The preliminary step in the analysis is to assign a threshold brightness value for the discrimination of background, viz. the surface, from cloud. A new clear/cloudy binary digital image is then generated. All subsequent analysis is accomplished using this version of the cloud scene. The right panel of Figure 2 is the binary version of the shuttle photo shown on the left. (The relative exposures of the photo and the binary image in Figure 2 are only suitable for qualitative comparisons.)

3.3 Scanning Strategy

A 2-dimensional horizontal grid is the basic domain on which numerical models of the atmosphere operate; at each point within the grid variables are sequentially evaluated. Similarly, satellite surveillance of the surface involves a systematic radiometric scanning of the plan-view below. Emulating this point-to-point analysis of a 2-dimensional array, each digitized cloud scene is completely scanned in the same manner as the reader is proceeding through this column of words, specifically line-by-line from left to right, beginning in the uppermost left corner.

The length of every clear interval and every cloudy interval is determined and the histogram of each type of interval is generated. These frequency distributions for one shuttle photo and the Landsat image, plotted on logarithmic ordinates, are given in Figures 3, 4, 5 and 6 as the bold dots with light connecting lines. The total number of intervals within each array, N_t, appears in each figure. For cloudy intervals, Figure 4 and 6, N_t is the sum of all plotted ordinates but for the clear intervals, only the non-overlapping averages of 8 (or 5) individual ordinate values, plotted at the mean x-position, are shown in Figure 3 (or 5). The mean clear or

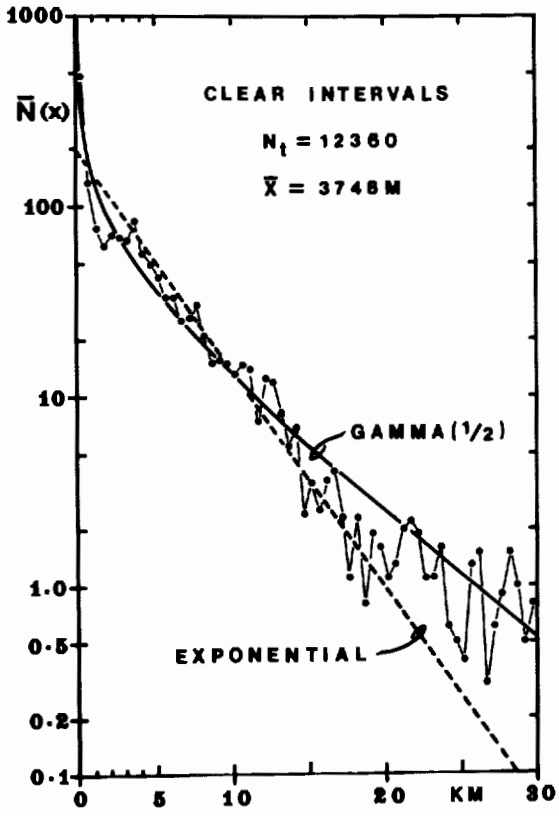

Figure 3. Frequency distribution of clear intervals in cloud photo #298 of space shuttle mission 41D taken over the eastern Pacific, $\ln(\bar{N})$ vs x. Bold dots are values of $\bar{N}$, the average number of clear intervals occurring within 8 pixel-categories (500m total) centered on each dot. x is clear interval length, $\bar{x}$ is mean length of all N_t clear intervals. Solid and dashed curves are hypothetical distributions.

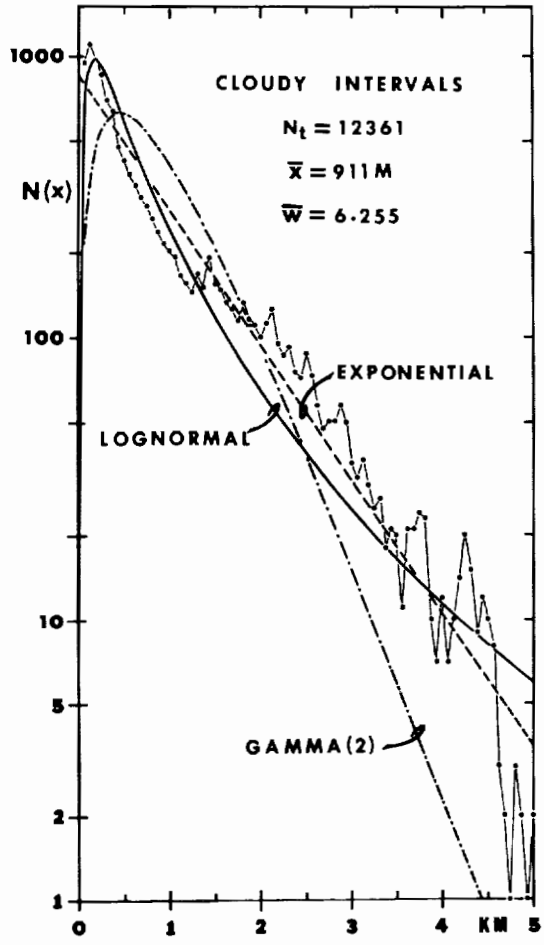

Figure 4. Frequency distribution of cloudy intervals in cloud photo #298 of space shuttle mission 41D taken over the eastern Pacific, ln(N) vs x. Bold dots are individual N-values, x is cloudy interval length, $\bar{x}$ is the mean length of all N_t cloudy intervals, and $\bar{w}$ is $\overline{\ln(x)}$. Solid and dashed curves are hypothetical distributions.

cloudy lengths, $\bar{x}$, for each scene are presented in Table 1 and in the figures. The scanning strategy requires that the ratio of mean lengths (cloudy/clear) be equal to the cloud cover divided by the clear fraction (one minus the cloud cover).

3.4 Discussion

The distributions are all similar in that short intervals are much more common than long ones. In the case of clear intervals, the number continues to increase with decreasing length down to the pixel resolution itself. (This condition occurred in both the unaveraged and averaged data used and/or shown in Figures 3 and 5.) However, for cloudy intervals the modal length is found at one or two pixel-lengths above the resolution limit. All distributions are smooth, especially in the region below 2 to 3 times the mean.

Each histogram has been fitted by at least 2 hypothetical distribution functions, one of which is in all cases the exponential with $\bar{x}$, the mean length, as a normalizing factor for both the exponent and the exponential function itself. (Further details on these distributions are found in most probability texts.) In this form, the exponential distribution is actually a member of the gamma family of distributions, viz. the one having its first parameter $\alpha = 1$. Gamma distributions with $\alpha < 1$ have the characteristic of monotonically increasing in value with decreasing x. The $\alpha = \frac{1}{2}$ distribution, gamma ($\frac{1}{2}$), is fitted to each of the clear interval data sets. Gamma distributions with $\alpha > 1$ attain a mode at a non-vanishing value of x. The $\alpha = 2$ member, gamma (2), is plotted for the data in Figure 4. Also fitted to these cloudy interval data is the lognormal distribution. Any ordinate in Figures 3, 4, 5 or 6 is converted to percent by applying the proper $100/N_t$ factor. To obtain a continuous probability density function, the resolution, given in Table 1, must also be considered.

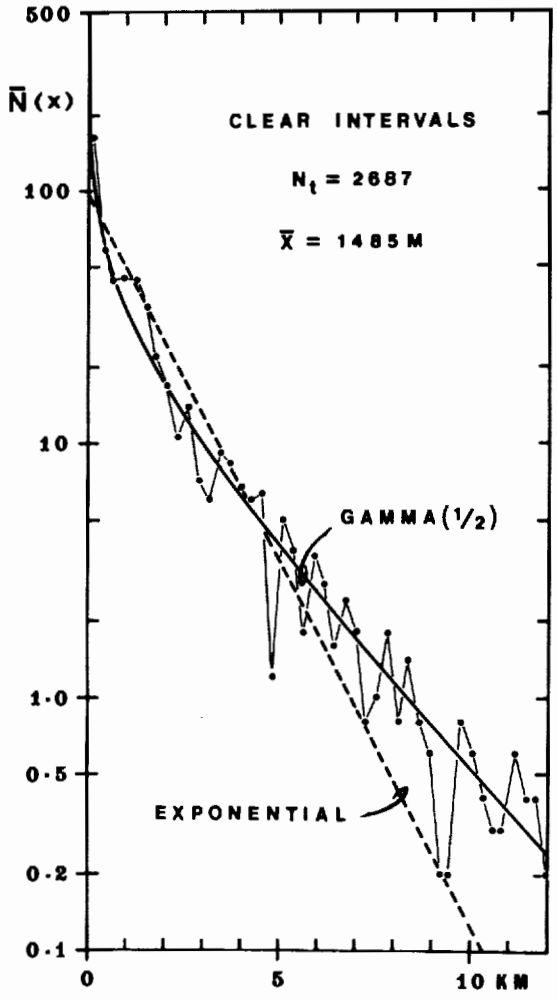

Figure 5. Frequency distribution of clear intervals in a Landsat band 7 image taken over the Straits of Florida, $\ln(\bar{N})$ vs x. Bold dots are values of $\bar{N}$, the average number of clear intervals occurring within 5 pixel-categories (275m total) centered on each dot. x is clear interval length, $\bar{x}$ is the mean length of all N_t clear intervals. Solid and dashed curves are hypothetical distributions.

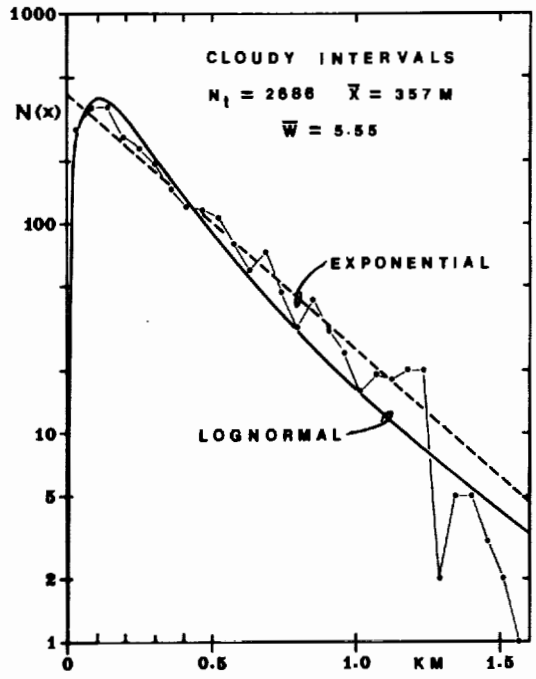

Figure 6. Frequency distribution of cloudy intervals in a Landsat band 7 image taken over the Straits of Florida, $\ln(N)$ vs x. Bold dots are individual N-values, x is cloudy interval length, $\bar{x}$ is the mean length of all N_t cloudy intervals, and $\bar{w}$ is $\overline{\ln(x)}$. Solid and dashed curves are hypothetical distributions.

Table 2. Goodness-of-Fit. Values of Q, the average normalized squared difference.

Distribution	Eastern Pacific clear	cloudy	Trade Wnd Island clear	cloudy	Straits of Florida clear	cloudy
gamma (½)	3.2	---	3.7	---	0.9	---
exponential	11.0	11.0	1.1	3.5	2.7	4.1
gamma (2)	---	106.5	---	6.8	---	8.0
lognormal	---	15.5	---	1.3	---	4.2

In Table 2 is presented a goodness-of-fit study of each data set to candidate hypothetical distributions. The statistic

$$Q = \frac{1}{M} \sum \frac{(N(x_i) - N_i)^2}{N(x_i)}$$

is given there. N_i is the actual number of intervals in the i-th category, $N(x_i)$ is the number given by the theoretical expression, and M is the number of categories. (Since Q is chi-squared divided by M, the smaller its value the better the fit.)

The clear interval histograms for the two oceanic cloud scenes are best approximated by the gamma (½) distribution; the other candidate, the exponential distribution, results in Q-values at least 3 times larger. For the over-land scene, however, the situation is reversed. The exponential distribution provides the best approximation to the clear interval histogram, the gamma (½) resulting in a Q-value more than 3 times larger. (Although the Trade Wind Island figures are not included here, in the region x > 4 km the gamma (½) is an excellent approximation to this clear interval histogram.)

In the cloudy interval cases, the lognormal is the best approximation for the Trade Wind Island scene, either the exponential or the lognormal is equally acceptable for the Straits of Florida scene but the exponential distribution results in the smaller Q-value for the Eastern Pacific scene. From Figure 4, however, it is obvious that even in this scene an approximation provided by the lognormal distribution is superior in the region x < 2 km. It is worthy of note that measurements made in eastern Europe suggest that randomized cloud intervals are distributed lognormally (Feigelson, 1984).

Additionally, the spacial correlations and the spectra have been computed for the cloud scenes. (Reference is directed to Snow et al, 1985b.) Figure 7 contains these functions for the Straits of Florida scene. The spectral peak near recurrency 0.5 km^{-1} (recurrence distance of 2 km) is clearly associated with the predominant oscillation in the correlation function.

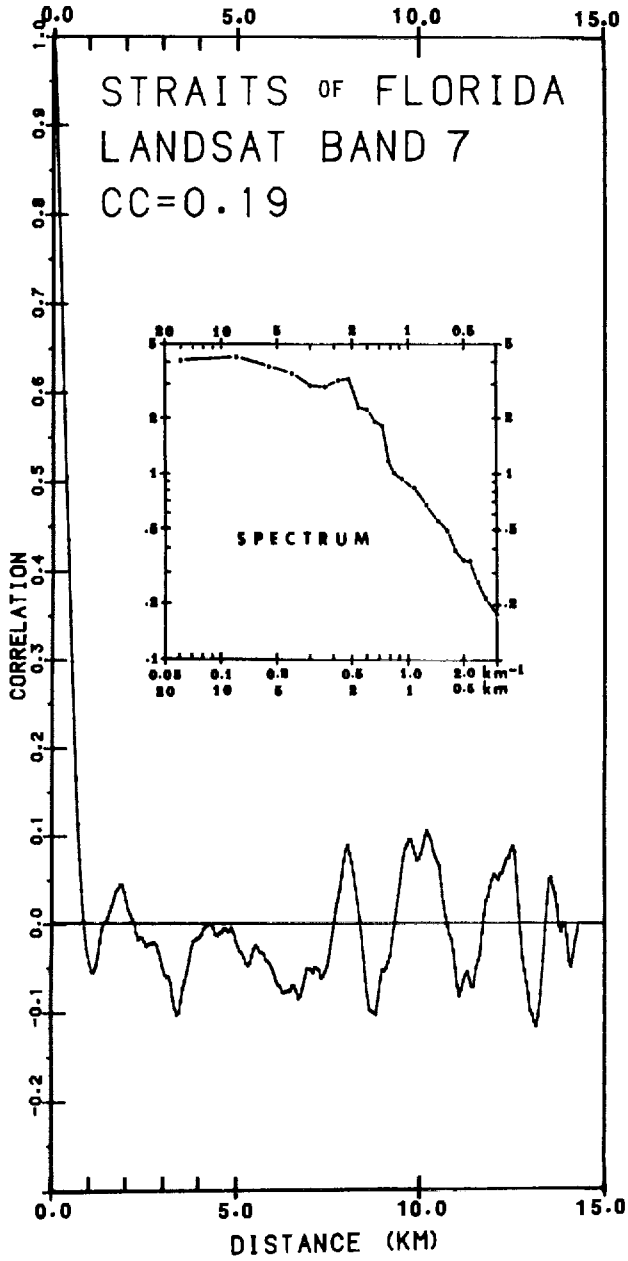

Figure 7. Spacial correlation function and spectrum for the Straits of Florida cloud scene. Spectral strength (variance) is plotted against recurrency (km^{-1}) and recurrence distance (km) on logarithmic scales.

4. CONCLUDING REMARKS

The postulate is made that at least for simple tropical cloud populations, the frequency distributions of clear and cloudy intervals can be approximated by common probability density functions.

Concurrently, the reservation is made that the distribution of clear or of cloudy intervals may not necessarily be of the same form as the distribution of cloud-to-cloud minimum distances or of cloud sizes, respectively. Although the atmospheric physicist may not be completely content, the numerical modeller and the spacecraft tracker are assisted. Given the appropriate theoretical distributions for clear and cloudy intervals, a Monte-Carlo scheme could insure that realistic cloud populations exist within the grid-domain of a model. Also, given these distributions, the computation of operationally significant parameters for space-ground communication, such as the maximum interaction time, is facilitated.

The interval distribution studies using space shuttle cloud photographs is being extended to include a variety of cloud covers and cloud types. For the utilization of common distributions, the link between the distribution type and its parameter(s), for example $\bar{x}$, and the more traditional cloud statistics, specifically cloud amount and cloud type, must be established. The shuttle cloud photo studies also have this as a goal.

Series of photographs of diverse cloud populations are being made to develop usable correction factors for the viewing angle bias contained in satellite cloud amount information.

REFERENCES

Feigelson, E.M. (Ed.), 1984: Radiation in a Cloudy Atmosphere, D. Reidel Publishing Co., Dordrecht, Holland, 293 pp.

Snow, J.W., J.T. Bunting, R.P. d'Entremont, D.D. Grantham, K.R. Hardy, and E.M. Tomlinson, 1985a: Space shuttle cloud photographs assist in correcting meteorological satellite data, EOS Trans. AGU, 66, 489.

Snow, J.W., E.M. Tomlinson, and J.H. Willand, 1985b: Distributions of clear and cloudy intervals and spacial correlations from space shuttle cloud photographs. In Presentations at the Third Tri-Service Clouds Modeling Workshop, D.D. Grantham and J.W. Snow (Eds.), Air Force Geophysics Laboratory, Hanscom AFB, Massachusetts, 75-90.

DISTRIBUTION OF ATMOSPHERIC AEROSOLS AND CO_2 LIDAR BACKSCATTER SIMULATION

G. S. Kent, P. H. Wang, and A. Deepak

Science and Technology Corporation, Hampton, VA 23666

U. O. Farrukh

Hampton University, Hampton, VA 23668

1. INTRODUCTION

Development of a Global Wind Measurement Satellite System (WINDSAT) (NOAA, 1981) requires a knowledge of the global characteristics of the free tropospheric and lower stratospheric aerosol. In particular, there is a need to document the behavior of the aerosol backscattering function, at CO_2 laser wavelengths, β_{CO_2}, as a function of space and time. There is, unfortunately, a relative lack of data for the free troposphere, particularly over the remoter regions of the globe, as compared with that for the boundary layer and the stratosphere. Moreover, because of variations in concentration that occur as a function of space and time, large data sets are required to obtain meaningful averages. A recent study by Kent et al. (1985) uses three distinct tropospheric aerosol data sets in order to obtain an improved global model of the general aerosol characteristics, including variation of β_{CO_2} with latitude, season, and altitude. The current paper summarizes the more important findings of this study.

The main data set used is that obtained by the Stratospheric Aerosol and Gas Experiment I (SAGE I) and Stratospheric Aerosol Measurement II (SAM II) satellite experiments (McCormick et al., 1979). These instruments, although primarily designed for the global measurement of stratospheric aerosol extinction at a wavelength 1 μm (SAGE I also measured ozone and nitrogen dioxide concentrations), are able, in the absence of high altitude clouds, to extend their range of measurements well down into the troposphere. These measurements thus provide a global coverage of the upper free tropospheric aerosol, not obtainable by other techniques. The second data set used is that from the GAMETAG flight series over the Pacific Ocean in 1977 and 1978 (Patterson et al., 1980; Kent et al., 1985). This data set has been used for comparison with the SAGE I/SAM II data, as well as to obtain a factor to convert 1-μm extinction cross sections to the equivalent 10.6 μm. For the free troposphere, these measurements have primarily been made in, or near, the United States.

2. THE SAGE I AND SAM II DATA SETS

Examination of the relative frequency of tropospheric SAGE I and SAM II data, as compared with the total stratospheric data set, shows that in equatorial and northern latitudes, approximately 30% of the observations are made down to an altitude of 5 km. In the southern hemisphere, this fraction rises to about 50%. Individual extinction profiles show a gradual increase in extinction with decreasing altitude with no apparent discontinuity between stratospheric and tropospheric aerosol. A few profiles reach down to the boundary layer, but it is felt that average values for extinction at these levels are likely to be systematically biased toward cleaner, cloud-free atmospheres and they have not been calculated. In the upper free troposphere such a systematic bias is likely to be small. Examination of the probability distributions for extinction values in the upper free troposphere shows a distinctive tail of high extinction values, most likely due to thin high altitude cloud or haze. Formation of a standard data average would result in a bias toward these higher values which are not representative of the background aerosol. Instead, we have chosen to calculate the median extinction rather than the mean extinction as the measure of central tendency. This quantity is related to the probability distribution, itself an important function for WINDSAT modeling and is not appreciably affected by the presence of clouds in the data set. In the stratosphere, because of the low spread in measured extinction values, the mean and median agree closely.

One year of SAGE I and SAM II data has been studied in detail and the variation of 1 μm extinction with latitude, altitude, and season determined. As expected from other measurements made in the troposphere, the aerosol extinction decreases with increasing altitude (Kent et al., 1983), provided there is no major volcanic influence. The analysis also confirmed the very strong hemispheric asymmetry previously noted by Deepak et al. (1982). An attempt was also made to determine any possible systematic differences between the extinction over ocean and land. This analysis was carried out for an altitude of 6 km and except for a possible small difference within the equatorial zone, no significant variation was found. The result confirms that the aerosol residence times in the upper free troposphere are long compared with the zonal circulation times between land and ocean. Figure 1 shows a contour plot of the 1 μm extinction for the period March - May, 1979, the

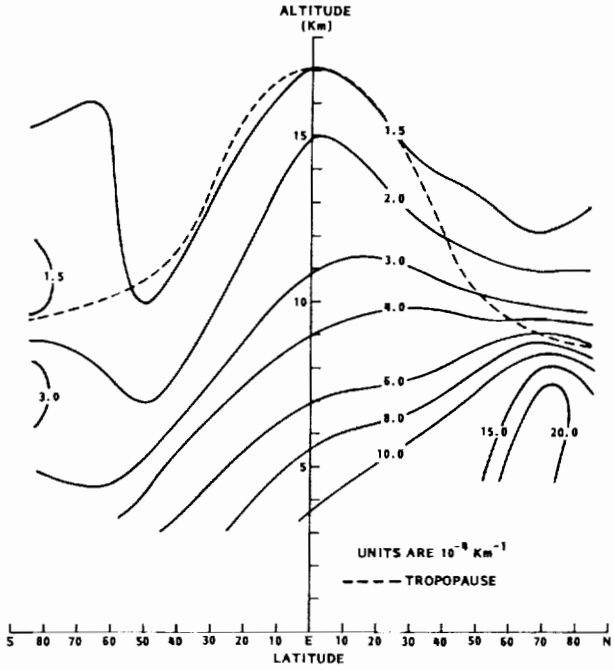

Figure 1. Contour plot of free tropospheric aerosol extinction at 1 μm from SAGE I and SAM II, March-May 1979.

combined data from SAGE I and SAM II covering most of the globe. The strong hemispheric asymmetry and altitude variation is very evident. Superimposed upon this asymmetry, there is found to be a seasonal variation with maximum extinction occurring in local spring-summer and minimum in local fall-winter. Above the tropopause, the extinction is fairly constant globally at a level of about 10^{-4} km^{-1} for the next 5 km in altitude, and then decreases slowly.

3. COMPARISON WITH GAMETAG DATA

Aerosol measurements during the GAMETAG program in 1977 and 1978 have provided the most extensive set of direct measurements of aerosol properties in remote areas. The flights in both years followed an approximately North-South track over the USA and Pacific Ocean, free tropospheric measurements being made between altitudes of 5 and 7 km. Optical counters were used to determine the aerosol size distribution and concentration for radii between 0.126 and 2.34 μm. These distributions have been used to calculate the equivalent optical parameters at other wavelengths, including 1.0 μm and 10.6 μm. Comparison of the calculated 1.0 μm extinction values with those determined from SAGE I/SAM II shows a similar hemispheric asymmetry and good quantitative agreement in the northern hemisphere for both years of GAMETAG data, and in the southern hemisphere for the 1977 data. The 1978 GAMETAG data show somewhat lower values in the southern hemisphere. These size distributions have been used to calculate conversion factors for 1-μm extinction to 10.6-μm backscatter, appropriate to the free troposphere. This factor was found to lie mainly between 10^{-4} and 10^{-3} sr^{-1}, the lower values being associated with the lower levels of 1-μm extinction. These values for the conversion factors have then been applied to the 1-μm SAGE I/SAM II data set to calculate the equivalent values for the 10.6-μm backscatter function and their global behavior. The results of this calculation show that at an altitude of 5 km, the median values for $\beta_{10.6}$ lie between 2-7 x 10^{-10} m^{-1} sr^{-1} in the northern hemisphere and 0.5-2.0 x 10^{-10} m^{-1} sr^{-1} in the southern hemisphere. Near the tropopause, under non-volcanic conditions, the median value falls to about 0.3 x 10^{-10} m^{-1} sr^{-1}.

4. COMPARISON WITH CO_2 MEASUREMENTS

Almost all CO_2 lidar backscatter measurements made in the free troposphere are post-1980. These measurements are thus affected by injected volcanic material from Mt. St. Helens in May 1980 and later volcanic eruptions, including that of El Chichon in March-April 1982. Examination of the SAGE I/SAM II data and independent studies by Post (1984) show that the upper troposphere, above an altitude of about 5 km, becomes strongly modified by presence of volcanic aerosol. This aerosol is injected into the stratosphere from which it is slowly released to the upper troposphere, particularly in middle and high latitudes. Stratospheric concentrations show strong irregularities immediately after an eruption which gradually homogenize and decay with a 1/e time period of the order of 6 months (Kent and McCormick, 1984). Direct comparison of modeled values (based on pre-1980 data) is thus rendered difficult. Analysis and examination of the 1980-1981 SAGE I/SAM II data have not yet been undertaken in any detail. Figure 2 shows the results of a comparison of the modeled values for 1979 with several experimental data sets obtained in northern spring and summer. All modeling and data are for altitudes between 5 and 7 km and the diagram shows three independent experimental CO_2 lidar data sets as well as the values calculated directly from GAMETAG flight data. With the exception of the GAMETAG data for 1978, near the equator and in the southern hemisphere, the general agreement is good. It must be remembered in making the comparison that most of the data have been obtained in different years, including both post- and pre-volcanic periods. Very little experimental data are available for the fall-winter season but comparison of that obtained by NOAA (Post, 1983) with the SAGE I/SAM II model shows good agreement. Intercomparison of the vertical variation of aerosol characteristics presents more problems. The 5-7 km altitude range shown in Figure 2 is fortuitously close to the altitude of minimum volcanic perturbation. Below 5 km, the SAGE I/SAM II data are likely to be systematically biased toward lower extinction values. Above 5 km, all the direct measurements of $\beta_{10.6}$ are affected to some extent by volcanic injection. Further comparison, of the kind shown, requires improved understanding of the

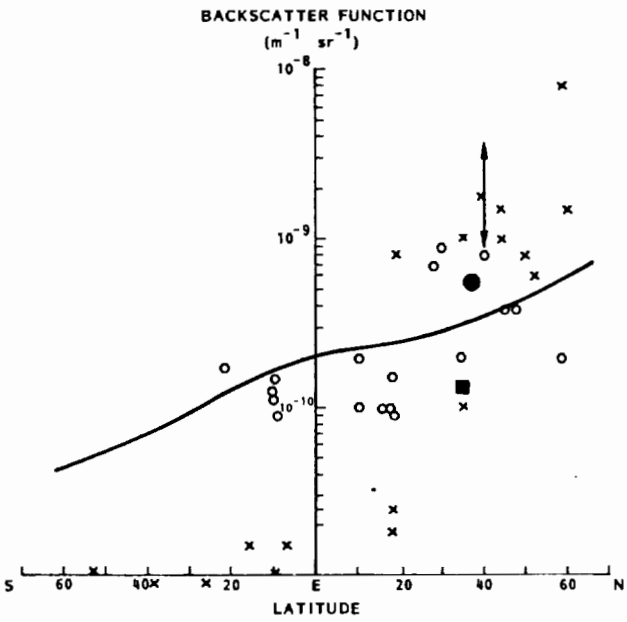

Figure 2. Comparison of modeled and directly measured values of $\beta_{10.6}$ for altitudes between 5 and 7 km, northern hemisphere, spring-summer.

- o 1977 GAMETAG data, 5-7 km
- x 1978 GAMETAG data, 5-7 km
- SAGE I/SAM II, March-May, 1979, 6 km
- Range of NOAA spring-summer seasonal averages, 6 km
- ● Median NASA-MSFC summer value, 6 km (Jones, 1983)
- ■ JPL mean spring-summer value, 6 km (Menzies, 1984, Private Communication)

volcanic aerosol as well as analysis of post-volcanic satellite data sets.

It is also of interest to compare the latitude variation shown in Figures 1 and 2 with that of a 2-D global aerosol model (Rehkopf et al., 1984). This model calculates the steady-state concentrations of tropospheric aerosols based on known sources and sinks as well as transport and loss mechanisms. A strong hemispheric asymmetry was found for particles with radii less than 0.1 μm and a somewhat smaller asymmetry for particles with radii between 0.1 and 1.0 μm. Anthropogenic particle production figured strongly as the cause of the greater concentration in the northern hemisphere.

5. ACKNOWLEDGMENTS

The work reported here was carried out under Contract No. NAS8-35594 from NASA-Marshall Space Flight Center. We are grateful to Dr. D. Fitzjarrald of NASA-MSFC and to Dr. M.P.McCormick and Mr. L. R. McMaster of NASA-LaRC for much encouragement and helpful discussion during the course of the work.

6. REFERENCES

Deepak, A., G. S. Kent, G. K. Yue, 1982: Atmospheric Backscatter Model Development for CO_2 Wavelengths, IFAORS Final Report for NASA-Marshall Space Flight Center, Contract No. NAS8-34427.

Jones, W. D., 1983: Beta System Test Results (1981 and 1982), Second Multi-Agency Workshop on Atmospheric Backscatter at IR Wavelengths, April 12-13, Workshop Notes, pp. 53-70.

Kent, G. S., G. K. Yue, U. O. Farrukh, and A. Deepak, 1983: Modeling atmospheric aerosol backscatter at CO_2 laser wavelengths. I: Aerosol properties, modeling techniques and associated problems, Appl. Opt. 22, 1655-1665.

Kent, G. S., and M. P. McCormick, 1984: SAGE and SAM II measurements of global stratospheric aerosol optical depth and mass loading, J. Geophys. Res. 89, 5303-5314.

Kent, G. S., P. H. Wang, U. Farrukh, A. Deepak, and E. M. Patterson, 1985: Development of a Global Model for Atmospheric Backscatter at CO_2 Wavelengths. Final Report for NASA Contract NAS8-35594, March 1985.

McCormick, M. P., P. Hamill, T. J. Pepin, W. P. Chu, T. J. Swissler, and L. R. McMaster, 1979: Satellite studies of the stratospheric aerosol, Bull. Am. Meteor. Soc. 60, 1038-1046.

NOAA, 1981: Global Wind Measuring Satellite System-WINDSAT, Final Report for NOAA Contract NA 79RA C00127.

Patterson, E. M., C. S. Kiang, A. C. Delany, A. F. Wartburg, A. C. D. Leslie, and B. J. Huebert, 1980: Global measurements of aerosols in remote continental and marine regions: Concentrations, size distributions, and optical properties, J. Geophys. Res. 85, 7361-7376.

Post, M. J., 1983: Atmospheric Aerosol Profiles at CO_2 Wavelengths, 2nd Topical Meeting on Coherent Laser Radar; Technology and Applications, August 1-4, 1983, Aspen, Colorado, Technical Digest, pp. Th B4-1 to Th B4-5.

Post, M. J., 1984: Lidar observations of the El Chichon cloud at λ = 10.6 μm, Geophys. Res. Lett. 1, 846-849.

Rehkopf, J., M. Newiger and H. Grassl, 1984: Stratosphere, Proceedings of a Working Party Meeting, Brussels, 18 May 1984. Ed. A. Ghazi, Commission of the European Communities, 145-171.

S40-47

N93-70339

P_3

AEROSOL MEASUREMENT PROGRAM STRATEGY FOR GLOBAL AEROSOL BACKSCATTER MODEL DEVELOPMENT

David A. Bowdle

Universities Space Research Association
NASA Marshall Space Flight Center, Alabama 35812

1. INTRODUCTION

The purpose of this paper is to propose a balanced program of aerosol backscatter research leading to the development of a global model of aerosol backscatter. Such a model is needed for feasibility studies and systems simulation studies for NASA's prospective satellite-based Doppler lidar wind measurement system. Systems of this kind measure the Doppler shift in the backscatter return from small atmospheric aerosol wind tracers (of order 1 micrometer diameter). The accuracy of the derived local wind estimates and the degree of global wind coverage for such a system are limited by the local availability and by the global-scale distribution of natural aerosol particles.

The discussions here refer primarily to backscatter model requirements at CO_2 wavelengths, which have been selected for most of the Doppler lidar systems studies to date. Model requirements for other potential wavelengths would be similar.

2. CRITICAL MODEL UNCERTAINTIES

Previous studies have shown, both by measurement and by modeling, that aerosol backscatter cross sections at CO_2 wavelengths may often fall below the expected threshold for accurate wind measurements (about 10^{-10} m^{-1} sr^{-1} for current design concepts). These results indicate the need for further research to remove several critical uncertainties.

The global frequency of occurrence and the spatial/temporal scales of variation of low aerosol backscatter domains are not well known. Information is also lacking on the global prevalence of sporadic intrusions of high-backscatter targets (such as subvisible cirrus clouds, residual continental plumes, and volcanic debris) into otherwise clean airmasses. Finally, a better understanding is needed of the physical parameters which determine the magnitude and the spectral dependence of aerosol backscatter at CO_2 wavelengths.

3. PROPOSED BACKSCATTER RESEARCH PROGRAM

A carefully balanced aerosol backscatter research program is necessary to address all three of these critical uncertainties over the required range of spatial and temporal scales. This program should involve a combination of long-term backscatter profile measurements at carefully selected sites, short-term global-scale "snapshots" of backscatter distributions at carefully selected times, detailed short-term measurements of selected aerosol microphysical and optical properties, ongoing backscatter model development, and periodic comparisons between measured and modeled backscatter estimates.

This paper proposes a phased research program to accomplish these goals. Each new phase would provide backscatter information over a spatial, temporal, or spectral range which was previously inaccessible. The research method selected for each phase would be optimized for the new information which is required in that phase. Each succeeding phase would be more difficult and more resource-intensive than the preceding phase. This structure would then allow timely decisions to be made on the trade-offs between the importance of the additional information and the final committment of the required resources. If warranted, work could proceed on several phases simultaneously.

In most cases, this program does not require the development of new instrumentation. Rather, it uses technology which has already been developed or is planned for development for other purposes.

4. PHASE I -- ADVANCED MODELS

Phase I involves the development of global backscatter models from existing global-scale measurements of aerosol optical parameters at wavelengths outside the CO_2 band. Conversion factors between backscatter values at CO_2 wavelengths and the measured optical properties are provided from Mie scattering theory applied to measurements of aerosol size distributions over

the central Pacific Ocean during the Global Atmospheric Measurement Experiment of Tropospheric Aerosols and Gases (GAMETAG, Patterson et al., 1980).

The first such data set includes measurements of aerosol extinction coefficients at 1 micrometer wavelength by the limb occultation method. These data are obtained with the Stratospheric Aerosol Measurement (SAM II) satellite sensor and the Stratospheric Aerosol and Gas Experiment (SAGE I) satellite sensor. Preliminary analysis of these data has been completed.

The second data set includes measurements of aerosol scattering extinction coefficients at mid-visible wavelengths with a high sensitivity multiwavelength integrating nephelometer. These data are obtained at NOAA's Global Monitoring for Climatic Change (GMCC) remote sites, especially at Mauna Loa Observatory on the island of Hawaii (Bodhaine, 1978). Analysis of these data has just begun.

This model development work should be continued and expanded. In particular, analyses of the newly available multi-wavelength SAGE II data should begin as soon as possible.

5. PHASE II -- SATELLITE IMAGERY

Phase II involves the analysis of visible and infrared imagery from geostationary and polar orbiters and from the Space Shuttle. These data would provide a global-scale perspective which is not currently available from any other measurement technique.

Visible imagery can be used to map the spatial and temporal structure of high-backscatter aerosol targets, by using the technique developed by Griggs (1979). This method should be improved to enhance its sensitivity and accuracy for detection and quantification of residual aerosol plumes and also, if possible, to provide at least coarse vertical resolution. Concepts for improving this method are being evaluated.

Infrared imagery in the 6.7-micrometer water vapor channel may also be used to map the spatial and temporal variability of low backscatter regions, if preliminary indications of positive correlations between specific humidity and backscatter are validated. Attempts should be made to explore and validate this correlation.

6. PHASE III -- GROUND BASED CO_2 DOPPLER LIDAR NETWORK

Several research groups now have, or will soon have, operational high-power ground-based pulsed CO_2 Doppler lidars. A committee has been established to define standard methods for calibration, data acquisition, data processing, data recording, and data display. A facility has been established to characterize primary and secondary standard calibration targets from these groups. These actions were taken in anticipation of the formation of a cooperative ground-based network of CO_2 lidar stations.

The long-term backscatter statistics, the detailed vertical profiles, and the internal consistency which could be provided by such a network are not presently attainable with any other aerosol measurement technique. This network should be implemented, and the necessary resources supplied, to obtain backscatter profiles at regular intervals. A central data center should be provided to compile and analyze the backscatter data from the entire network.

7. PHASE IV -- GLOBAL-SCALE BACKSCATTER SURVEY FLIGHTS

A global-scale backscatter survey flight series is expected to be an essential element of the proposed backscatter research program. This research effort would provide several series of "snapshots" of aerosol backscatter from the global scale to the micro-scale -- much as an orbiting Doppler lidar would see it. This kind of information would not be available by any other means until a high-power CO_2 lidar is actually deployed in a low earth orbit.

As presently envisioned, the flight series would require a high-power pulsed CO_2 Doppler lidar with versatile scanning capability to map the three-dimensional backscatter field above, below, and alongside the aircraft flight track. A tuneable, focused continuous wave CO_2 Doppler lidar would be used simultaneously to explore the spectral dependence of backscatter. An array of supporting aerosol instrumentation would be used to measure aerosol size distributions, compositions, and morphologies as well as other selected aerosol optical properties.

Tentative flight plans call for at least two flight series that concentrate on the Pacific Ocean. A spring flight series would allow characterization of the effects of Asian dust plumes on backscatter values in the free troposphere over the mid-Pacific. A winter flight series would allow characterization of worst-case backscatter conditions in regions which exert a strong influence on North American weather patterns. Flight plans would also allow comparisons of latitudinal and longitudinal backscatter variations across the Pacific, and perhaps across portions of the adjoining continents.

A ground-based intercomparison of all the prospective flight instruments will be an integral element of the global survey flights. The optimum site for such a study appears to be the Mauna Loa Observatory, where a long-term aerosol record already exists and where typical mid-tropospheric aerosols can be sampled for long periods of time without the constraints of airborne operations.

8. PHASE V -- SHUTTLE-BASED CO_2 DOPPLER LIDAR

The final phase of the proposed backscatter research program involves the deployment of a space-prototype, high-power, pulsed CO_2 Doppler lidar in low earth orbit -- perhaps on the Space Shuttle. This mission might not be justified solely for the aerosol backscatter assessment effort. However, if such a system is deployed -- perhaps for a technology-plus-science demonstration experiment -- it should be designed to provide accurate measurements of aerosol backscatter with a sensitivity approaching 10^{-10} m^{-1} sr^{-1} in the middle and upper troposphere.

A mission of this kind could map aerosol backscatter on a true global scale, with a sensitivity and spatial resolution far exceeding that available from satellite imagery, and a spatial coverage far exceeding that available from aircraft. Shuttle missions could then be repeated several times, as needed. These missions would be the last major CO_2 backscatter measurement programs before the final development of a free-flying Doppler lidar system in the mid-1990's.

Backscatter distributions could also be mapped with a somewhat less sensitive Shuttle-based 1.06 micrometer Nd:YAG lidar, which is already scheduled for deployment in the late 1980's.

9. GLOBAL AEROSOL BACKSCATTER MODEL

The phased research approach recommended here is well-suited for periodic updates and improvements of a global aerosol backscatter model. This approach would also allow timely inputs from the global model to feasibility and simulation studies for the Doppler lidar system.

It is therefore extremely important that the global model be well-documented, reviewed, and validated. This purpose can be accomplished by the establishment of an expert Scientific Working Group to oversee the model development and measurement activities, by performing rigorous intercomparisons between theoretical and experimental estimates of selected aerosol properties, by maintaining high data quality standards, and by establishing a central data processing site, to manage, analyze, and synthesize the large amounts of data from the various aerosol measurement programs.

10. CONCLUDING REMARKS

The aerosol backscatter research program proposed here should provide enough information to remove the critical uncertainties in existing global aerosol backscatter models. The refined models should be sufficiently complete to define the design of a satellite Doppler lidar system for the measurement of global wind fields in the troposphere and lower stratosphere. The phased research approach would allow timely decisions to be made on the trade-offs between the requirements for additional information and the final committment of the resources which are required to obtain the additional information.

ACKNOWLEDGMENTS

This research was carried out by Universities Space Research Association for the National Aeronautics and Space Administration under contract NAS8-35919. Support under this contract is gratefully acknowledged.

REFERENCES

Bodhaine, B., 1978: The Mauna Loa Four Wavelength Nephelometer: Instrument Details and Three Years of Observations. NOAA Tech. Rept. ERL 396-ARL-5. Boulder, CO, 39 pp.

Griggs, M., 1979: Satellite Observations of Atmospheric Aerosols during the EOMET Cruise. J. Atmos. Sci., 36, 695-698.

Patterson, E. M., C. S. Kiang, A. C. Delaney, A. F. Wartburg, A. C. D. Leslie, and B. J. Huebert, 1980: Global measurements of aerosols in remote continental and marine regions: Concentrations, size distributions, and optical properties. J. Geophys. Res., 85, C12, 7361-7376.

DEVELOP A PLAN FOR ESTABLISHING GLOBAL AEROSOL BACKSCATTER COEFFICIENT DATA BASE

Ho-Pen Chang
Gary G. Worley
Walter Frost

FWG Associates, Inc.
Tullahoma, Tennessee 37388

1. INTRODUCTION

A potential improvement on measuring atmospheric winds by using a coherent Doppler system has led to a need for detailed knowledge concerning the aerosol backscattering characteristics, especially at CO_2 wavelengths. In order to meet this requirement, a plan of study has been developed to establish a global data base of atmospheric aerosol backscattering coefficients.

2. DISCUSSION

An extensive literature search was carried out using the NASA/RECON system under the major headings, aerosols and aerosol measurements; utilizing the DTIC system, literature was identified under the major headings, aerosol models and aerosol measurements. Approximately 1500 sources have been identified and over 70 papers/reports have been collected and reviewed in detail. Synopses of these papers and reports are fitted into a tabulated form. As an example, Table 1 shows the synopsis of the measurement of GAMETAG (Global Atmospheric Measurement Experiment of Tropospheric Aerosols and Gases) (Patterson et al., 1980). The forms include basic information, as shown in Table 1, for each aerosol measurement activity.

Part of the current interest is to identify the existing data gaps from a geographical point of view. The existing aerosol measurements in the literature have been located on the maps for different layers (troposphere and stratosphere) in various regions (Pacific Ocean, Atlantic Ocean, Indian Ocean, Arctic, and Antarctic). For example, Figure 1 shows the location of the aerosol measurements in the Pacific Ocean area, which includes the ocean, North America, Australia, and East Asia. This figure shows tropospheric aerosol measurements only. The solid line represents aircraft measurements and the dashed line designates a ship measurement. The dots indicate that aerosol measurements have been done over that area. A number at the dot is corresponding to the reference paper/report used. Number 18 in Figure 1 is the paper whose synopsis is shown in Table 1. Most measurements were carried out in North America. Compared with the number of continental aerosol measurements, marine aerosol measurements are insufficient for global coverage. Further measurements for both continental and marine aerosols are necessary.

Most existing lidar systems representatives were contacted and reported by Deepak et al. (1982). The hardware characteristics and the future plans for these systems have been updated by a letter survey. As an example, Table 2 shows the updated information about the lidar system of CRIRO, Division of Atmospheric Research, Aspendale, Victoria, Australia. So far, responses to the letter survey have been received from 50 percent of the total requests.

3. CONCLUDING REMARKS

Based on the literature review, summaries of the aerosol measurements will be presented in the near future, to include the composition, concentration, particle size distribution, and other characteristics of the atmospheric aerosol distribution. The available data on the aerosol backscattering coefficient (especially at CO_2 wavelengths) will be presented. Moreover, identification of the remaining data gaps will be reported. By referring to the characteristics of existing lidar systems and their future applications, a plan to establish a global data base of aerosol backscatter coefficients will be recommended in a future report.

REFERENCES

Deepak, A., G. S. Kent, and G. K. Yue, 1982: Atmospheric Backscatter Model Development for CO_2 Wavelengths. IFAORS Technical Report 189. Institute for Atmospheric Optics and Remote Sensing, P.O. Box P, Hampton, VA 23666.

Patterson, E. M., C. S. Kiang, A. C. Delany, A. F. Wartburg, A. C. D. Leslie, and B. J. Huebert, 1980: Global Measurements of Aerosols in Remote Continental and Marine Regions: Concentrations, Size Distributions, and Optical Properties. Journal of Geoph. Res., 85(C12):7361-7376, Dec. 20.

TABLE 1. Synopsis of a Paper.

Reference	
Location of Measurement	A. Pacific Ocean (18 Hawaiian islands through New Zealand; latitude range 50° S - 35° N) B. Western United States C. Canada D. Alaska
Date of Measurement	A. August 1977 and August 1978 at local noon
Altitude of Measurement	A. Mid-tropospheric region (5-6 km altitude) B. Planetary boundary layer (0-2 km altitude) C. Measurements to link A. and B. regions
Instrumentation	A. National Center for Atmospheric Research (NCAR) electra aircraft B. Two optical particle counter systems developed by particle measurements systems (PMS) were used 1. Active scattering aerosol spectrometer and classical scattering spectrometer probe (ASAS-CSSP) 2. Forward scatter spectrometer probe (FSSP)
Aerosol Composition	A. Clear air B. Continental aerosols: sulfate, large particles (Al, Si, Ca, Ti, K, Fe) Size = 0.1 μm to 3 μm C. Marine aerosols: sea-salt component (Cl, Ca, SO_4, NO_3, NH_4^+). Size = 0.1 μm to 3 μm
Aerosol Concentration	A. Continental aerosol: 1. Boundary layer: 10 μgm^{-3} 2. Free troposphere: 0.2 μgm^{-3} B. Marine aerosol: 1. Boundary layer: 12 μgm^{-3} 2. Free troposphere: 0.15 μgm^{-3}
Remarks	A. Phase I operation of GAMETAG B. Total aerosol and crustal component concentrations show a general decrease from north to south C. Continental aerosol population consists of crustal aerosols with r > 0.5 μm (two-mode) D. Marine aerosol has very large increase in particle number and volume upon entering the marine boundary layer E. The GAMETAG data set is going to be used in the development of a global model for atmospheric backscatter at CO_2 wavelengths

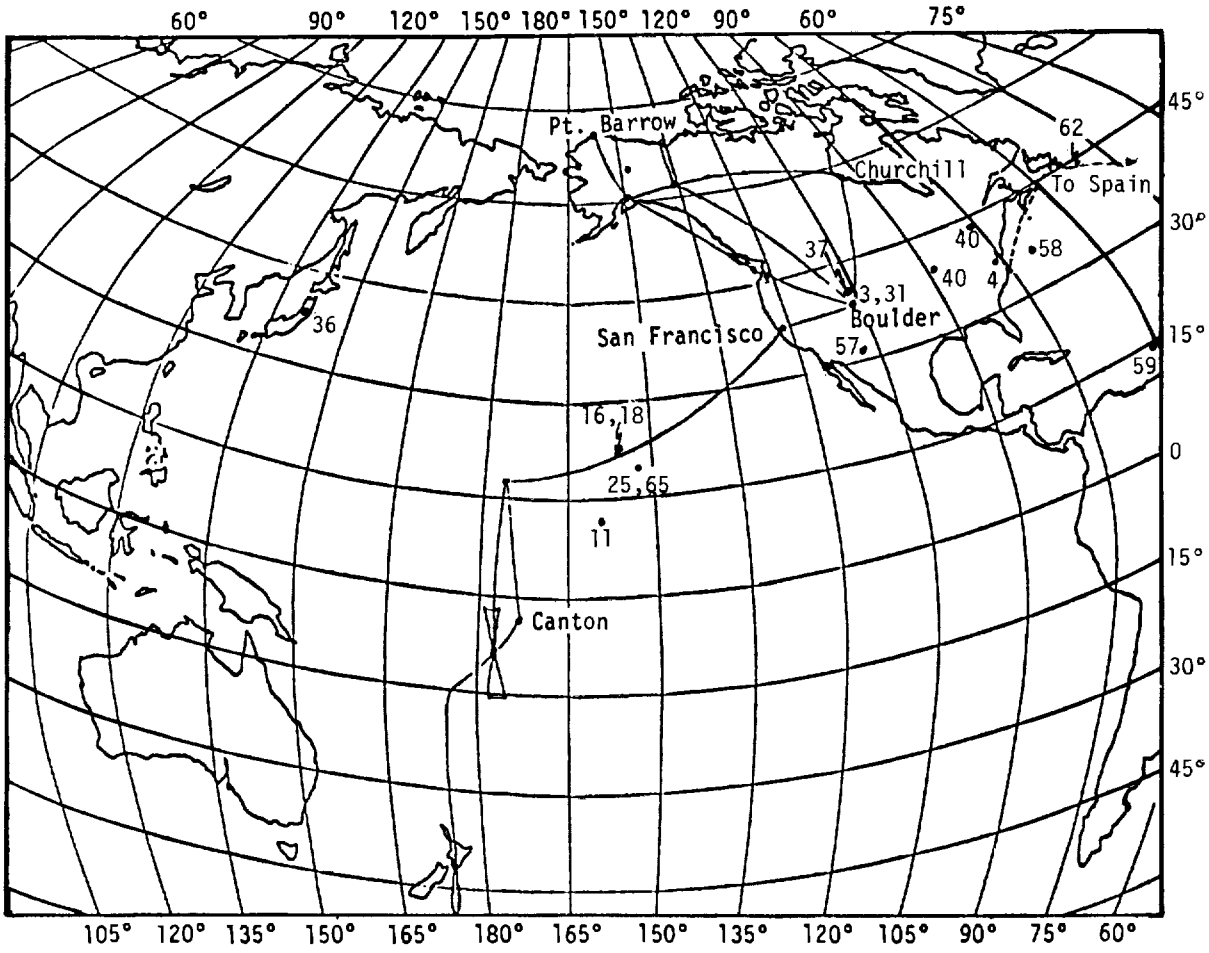

Figure 1. Tropospheric aerosol measurements in the Pacific Ocean area (numbers at dots indicate reference report used).

TABLE 2. Updated Information on a Lidar System.

Stations (No. of Systems)	Principal Research Worker(s)	Period of Operation	Data Measured	Characteristics of the System (wavelength used, power, duration, etc.)	Notes
CSIRO, Division of Atmospheric Research, Aspendale, Victoria, Australia	C. M. R. Platt	1979-1981	High clouds	0.694 nm 0.5 Joules	An extensive program to measure the optical properties of high clouds. Also some data on tropospheric aerosol profiles.
	J. C. Scott	1981-	ISCCP--applications middle and high clouds	Repeat	
		1982-1986	Stratospheric aerosol	Repeat	Not analyzed fully. Some work in conjuction with SAGE program.
		1984	Boundary layer and upper tropospheric aerosols	0.694 nm 0.5 Joules and 9 to 11 μm CO_2 lidar 2 weeks Oct. 84	Comparative measurements with ruby lidar, CO_2 lidar (CSIRO developed) and aircraft direct sampling, data still being analyzed.

Recent Publications:

1. Platt, C. M. R. (1981): The Effect of Cirrus of Varying Optical Depth on the Extraterrestrial Radiative Flux, Q. J. Roy. Met. Soc, 107:671-678.

2. Platt, C. M. R., and G. L. Stephens (1982): The Interaction of Clouds and Radiation, Aust. Met. Mag., 30(1):97-105.

3. Platt, C. M. R. (1983): On the Bispectral Method for Cloud Parameter Determination from Satellite VISSR Data: Separating Broken Cloud and Semitransparent Cloud, J. Appl. Met., 22: 429-439.

4. Platt, C. M. R. (1983): Cirrus Clouds in Tropical Australia, Weatherwise, 36:132-133.

5. Platt, C. M. R., and A. C. Dilley (1984): Determination of the Cirrus Particle Single Scattering Phase Function from Lidar and Solar Radiometric Data, Applied Optics, 23:380-386.

6. Heymsfield, A. J., and C. M. R. Platt (1984): A Parameterization of the Particle Size Spectrum of Ice Clouds in Terms of Ambient Temperature and the Ice Water Content, J. Atmos. Sci., 41:846-855.

7. Platt, C. M. R., A. C. Dilley, J. C. Scott, I. Barton, and G. L. Stephens (1984): Remote Sounding of High Clouds, V: Infrared Properties and Structure of Tropical Thunderstorm Anvils, J. Clim. and Appl. Met., Vol. 1, Sept. issue.

Future Plans: (1) Ruby lidar and satellite comparisons of high and middle clouds for ISCCP.
(2) More aerosol measurements with ruby and CO_2 lidar and aircraft, in conjunction with NASA (WINDSAT applications).
(3) CO_2 lidar profiling of water vapor, plumes, etc.
(4) Development of coherent CO_2 lidar.

Omit TO END

AUTHOR INDEX

APPENDIX A

TECHNICAL PROGRAM
of the
SYMPOSIUM AND WORKSHOP
ON GLOBAL WIND MEASUREMENTS

29 July–1 August 1985 Columbia Inn, Columbia, Maryland

SUNDAY EVENING, 28 July 1985

6:00 - 8:00 REGISTRATION and RECEPTION

MONDAY, 29 July 1985

8:30 am Welcoming Remarks
Robert J. Curran, NASA Headquarters
Wayman E. Baker, NASA/GSFC

PLENARY SESSION I
METEOROLOGICAL USES OF WIND MEASUREMENTS

I-A: Atmospheric Scales of Motion
Chairman: **William D. Bonner,** NOAA/NMC/NWS

8:40 Introduction and Overview
William D. Bonner, NOAA/NMC/NWS

8:50 I-A.1 The Relative Importance of Mass and Wind Data in the Current Global Observing System
Eugenia Kalnay, NASA/GSFC

9:10 I-A.2 The Analysis and Forecast Sensitivity to Tropical Wind Data
Jan Paegle, University of Utah

9:30 I-A.3 Tropical Upper Tropospheric Motion Field
T.N. Krishnamurti, Florida State University

9:50 REFRESHMENT BREAK

10:10 I-A.4 Observation Requirements for the Regional Scale
Louis W. Uccellini, NASA/GSFC

10:30 I-A.5 The NMC Regional Analysis System
Geoffrey I. DiMego, NOAA/NMC

10:50 I-A.6 The Impact of Mesoscale Data on the Simulation of a Mesoscale Convective Weather System
J. Michael Fritsch, Penn State University

11:10	I-A.7	DOD Operational Applications of Wind Measurements ***Allan C. Ramsay,*** OUSDRE
11:30	I-A.8	Use of Ground-Based Wind Profiles in Mesoscale Forecasting ***Thomas W. Schlatter,*** NOAA/ERL
11:50	I-A.9	Severe Wind Flows of Small Spatial and Temporal Scales: The Microburst and Related Phenomena ***Rita D. Roberts*** and John McCarthy, NCAR
12:10	pm	LUNCH
1:30	I-A.10	Mesoscale Applications of Cloud-Track Winds in a Baroclinic Atmosphere ***Steven E. Koch,*** NASA/GSFC

I-B: Observing System Simulation Experiments
Chairman: **Robert M. Atlas,** NASA/GSFC

1:50	I-B.1	Observing System Simulation Experiments at GSFC ***Robert M. Atlas,*** NASA/GSFC
2:10	I-B.2	Design of a Windsat Observing System Simulation Experiment ***Clifford H. Dey*** and Charles P. Arnold, Jr., NOAA/NMC
2:30	I-B.3	Results of an Observing System Simulation Experiment Based on the Proposed Windsat Instrument ***Charles P. Arnold, Jr.*** and Clifford H. Dey, NOAA/NMC
2:50		REFRESHMENT BREAK
3:10	I-B.4	Use of Wind Data in Global Modeling ***Jean Pailleux***, ECMWF
3:30	I-B.5	Calculation of Geopotential and Temperature Fields from an Array of Nearly Continuous Wind Observations ***Ying-Hwa Kuo*** and Richard Anthes, NCAR
3:50 - 5:00		Planning Meeting for Workshop Participants
5:30		ICEBREAKER

TUESDAY, 30 July 1985

PLENARY SESSION II
WIND SENSING TECHNIQUES

8:30	am	Introduction and Overview ***James W. Bilbro***, NASA/MSFC

II-A: Operational Wind Sensing Techniques
Chairman: **Fred Brock**, University of Hawaii

8:35		Introduction ***Fred Brock***, University of Hawaii

8:50	II-A.1	Balloon Probing Techniques ***James Arnold***, NASA/MSFC
9:10	II-A.2	Reference Level Winds from Balloon Platforms ***Vincent E. Lally***, NCAR
9:30	II-A.3	Balloon-Based Interferometric Techniques ***David Rees***, University College of London
9:50	II-A.4	Aircraft/ASDAR ***James K. Sparkman, Jr.***, NOAA
10:10		REFRESHMENT BREAK
10:30	II-A.5	Cloud and Water Vapor Wind Measurements from Geostationary Satellites ***Tod Stewart,*** William L. Smith, and W.P. Menzel, University of Wisconsin
10:50	II-A.6	Improving the Quality, Coverage, and Utilization of Cloud Motion Derived Winds ***William E. Shenk***, NASA/GSFC
11:10	II-A.7	Interferometric Winds ***W.R. Skinner***, University of Michigan
11:30	II-A.8	Inferred Winds ***John H. Ward***, NOAA/NMC
11:50		LUNCH

II-B: Potential Space-Borne Techniques

Chairman: **Milton Huffaker**, Coherent Technologies, Inc.

1:10		Introduction and Overview ***Milton Huffaker***, Coherent Technologies, Inc.
1:20	II-B.1	Doppler Radar Wind Profilers ***Richard G. Strauch***, NOAA/ERL
1:40	II-B.2	Gas Correlation Remote Sensing of Stratospheric and Mesospheric Wind ***Daniel J. McCleese***, and Jack S. Margolis, Jet Propulsion Laboratory
2:00	II-B.3	Satellite Scatterometers for Oceanic Surface Wind Measurements ***M.H. Freilich,*** F.K. Li, P.S. Callahan, and C. Winn, Jet Propulsion Laboratory
2:20	II-B.4	Incoherent, Excimer Laser Based, Doppler Lidar System ***I. Stuart McDermid,*** J.B. Laudenslager, and D. Rees, Jet Propulsion Laboratory
2:40	II-B.5	Development of a 0.5 μm Incoherent Doppler Lidar for Space Application ***Ari Rosenberg*** and Jeff Sroga, RCA Astro Electronics
3:00		REFRESHMENT BREAK

3:20	II-B.6	Aerosol Pattern Correlation ***Ed Eloranta***, University of Wisconsin
3:40	II-B.7	Coherent Doppler Lidar-Current US 9–11 μm Systems ***Freeman F. Hall***, NOAA/WPL
4:00	II-B.8	Current European Systems ***Michael Vaughan***, Royal Signals and Radar Establishment
4:20	II-B.9	1.06 μm Systems ***Robert Byer***, Stanford University
4:40	II-B.10	A Discussion of the Effects of Wavelength on Coherent Doppler Lidar Performance ***T.R. Lawrence***, NOAA/WPL
5:00	II-B.11	Comparison of Coherent and Incoherent Doppler Lidar Systems ***Robert T. Menzies***, Jet Propulsion Laboratory
7:00 - 9:00		POOLSIDE BARBECUE

WEDNESDAY, 31 July 1985

II-B: Potential Space-Borne Techniques (Continued)

8:30	II-B.12	Lockheed Windsat Study ***Steve Martin***, Lockheed Missile & Space Co., Inc.
8:50	II-B.13	Windsat Free-Flyer Using the Advanced TIROS-N Satellite ***Herbert M. Gurk***, Paul F. Kaskiewiez and Wolf P. Altman, RCA Astro Electronics
9:10	II-B.14	Shuttle Demonstration Study ***D. Fitzjarrald***, NASA/MSFC

PLENARY SESSION III
MEASUREMENT SIMULATION STUDIES
Chairman: **Freeman F. Hall**, NOAA/ERL

9:35		Introduction ***Freeman F. Hall***, NOAA/ERL
9:40	III.1	Global Sampling Strategies and Accuracies ***R. Milton Huffaker***, Coherent Technologies, Inc.
10:00		REFRESHMENT BREAK
10:20	III.2	Doppler Lidar Sampling Strategies and Accuracies-Regional Scale ***G. David Emmitt***, Simpson Weather Associates, Inc.
10:40	III.3	Cloud Obscurations and Statistics ***W. Snow***, Air Force Geophysics Lab
11:00	III.4	Distribution of Atmospheric Aerosols and CO_2 Lidar Backscatter Simulation ***G.S. Kent***, U. Farrukh, P. Wang and A. Deepak, Science and Technology Corp.

11:20	III.5	Aerosol Sampling Strategies for a Global Aerosol Model ***David A. Bowdle***, NASA/MSFC
11:40	III.6	Global Aerosol Distribution Walter Frost and ***Gary G. Worley***, FWG Associates, Inc.
12:00	pm	LUNCH
1:00 - 5:00		Working Groups Prepare Recommendations and Draft Workshop Report

SPECIAL SESSION:
AIR FORCE DEVELOPMENTS TOWARD SPACE WIND SENSING
Chairman: **Vince Falcone**, Air Force Geophysics Laboratory

7:30	pm	Introduction ***Vince Falcone***, Air Force Geophysics Laboratory
7:40	SS.1	DMSP Lidar Program ***Gary L. Duke*** and Richard Higgins, DMSP/Space Division
8:00	SS.2	New Avenues for Lidar Technology ***Milton Birnbaum***, New Advances for Lidar Technology
8:20	SS.3	Ground-Based Lidar Measurements of Stratospheric and Mesospheric Density and Aerosols ***D. Sipler,*** R. Philbrick, C. Bix, and M. Gardner, Air Force Geophysics Laboratory
8:40	SS.4	AFGL Mobile CO_2 Doppler Lidar ***S. Alejandro***, Air Force Geophysics Laboratory
9:00	SS.5	Backscatter Measurements from a Balloon-Borne Lidar ***D. Bedo*** and R. Swirbalus, Air Force Geophysics Laboratory

THURSDAY, 1 August 1985

PLENARY SESSION IV

8:30 - 12:00	Amend Report and Finalize Recommendations of Working Groups
12:00	ADJOURN

APPENDIX B

LIST OF CONTRIBUTORS

V.J. Abreu
The University of Michigan

W.P. Altman
RCA Advanced Technology Laboratory

R.A. Anthes
National Center for Atmospheric Research

C.P. Arnold
NOAA National Environmental Satellite, Data, and Information Service

R. Atlas
NASA Goddard Space Flight Center

W.E. Baker
NASA Goddard Space Flight Center

R. Beranek
NASA Marshall Space Flight Center

J. Bilbro
NASA Marshall Space Flight Center

W.J. Bostelman
NOAA National Meteorological Center

D.A. Bowdle
NASA Marshall Space Flight Center

F.V. Brock
National Center for Atmospheric Research

R.L. Byer
Stanford University

P. Callahan
Jet Propulsion Laboratory

H.-P. Chang
FWG Associates, Inc.

A. Deepak
Science and Technology Corporation

C.H. Dey
NOAA National Meteorological Center

E.W. Eloranta
University of Wisconsin

G.D. Emmitt
Simpson Weather Associates, Inc.

U.O. Farrukh
Hampton University

D. Fitzjarrald
NASA Marshall Space Flight Center

M. Freilich
Jet Propulsion Laboratory

J.M. Fritsch
The Pennsylvania State University

W. Frost
FWG Associates, Inc.

H.M. Gurk
RCA Astro-Electronics Division

M. Halem
NASA Goddard Space Flight Center

F.F. Hall
NOAA Environmental Research Laboratories

C.M. Hayden
NOAA National Environmental Satellite, Data and Information Service

P.B. Hays
The University of Michigan

R.M. Huffaker
Coherent Technologies, Inc.

J.C. Jusem
NASA Goddard Space Flight Center

E. Kalnay
NASA Goddard Space Flight Center

T.J. Kane
Stanford University

P.F. Kaskiewicz
RCA Astro-Electronics Division

G.S. Kent
Science and Technology Corporation

S.E. Koch
NASA Goddard Space Flight Center

T. N. Krishnamurti
Florida State University

Y.-H. Kuo
National Center for Atmospheric Research

V.E. Lally
National Center for Atmospheric Research

J.B. Laudenslager
Jet Propulsion Laboratory

T.R. Lawrence
NOAA Environmental Research Laboratories

F. Li
Jet Propulsion Laboratory

J. Mabry
NASA Marshall Space Flight Center

J.S. Margolis
Jet Propulsion Laboratory

S.C. Martin
Lockheed Palo Alto Research Laboratory

J. McCarthy
National Center for Atmospheric Research

D.J. McCleese
Jet Propulsion Laboratory

I.S. McDermid
Jet Propulsion Laboratory

R.T. Menzies
Jet Propulsion Laboratory

J.S. Osmundson
Lockheed Palo Alto Research Laboratory

J. Paegle
University of Utah

J. Pailleux
European Centre for Medium Range Weather Forecasts

J. Pfaendtner
NASA Goddard Space Flight Center

A.C. Ramsay
Office of the Under Secretary of Defense for Research and Engineering

D. Rees
University College London

D. Reuter
NASA Goddard Space Flight Center

R.D. Roberts
National Center for Atmospheric Research

A. Rosenberg
RCA Astro-Electronics

T.W. Schlatter
NOAA Environmental Research Laboratories

W.E. Shenk
NASA Goddard Space Flight Center

W.R. Skinner
The University of Michigan

G.J. Smidt
NOAA National Weather Service

J.W. Snow
Air Force Geophysics Laboratory

J.K. Sparkman
NOAA National Environmental Satellite, Data, and Information Service

J. Sroga
RCA Astro-Electronics

T.R. Stewart
Cooperative Institute for Meteorological Satellite Studies

R.G. Strauch
NOAA Environmental Research Laboratories

J. Susskind
NASA Goddard Space Flight Center

L.W. Uccellini
NASA Goddard Space Flight Center

J.M. Vaughan
Royal Signals and Radar Establishment

P.H. Wang
Science and Technology Corporation

C. Winn
Jet Propulsion Laboratory

G.G. Worley
FWG Associates, Inc.

D.-L. Zhang
The Pennsylvania State University